UNIVERSITAT POLITÈCNICA DE CATALUNYA BARCELONATECH

Construction and post-construction performance of vertical breakwaters on soft soils: the Port of Barcelona case

Manuel Ricardo Madrid Argomedo

CONSTRUCTION AND POST-CONSTRUCTION PERFORMANCE OF VERTICAL BREAKWATERS ON SOFT SOILS

The Port of Barcelona case

by

Manuel Ricardo Madrid Argomedo

A thesis submitted in partial fulfilment of the requirements for the degree of Doctor of Philosophy

Department of Civil and Environmental Engineering
Section of Geotechnical Engineering and Geosciences
Universitat Politècnica de Catalunya
BARCELONA TECH
Advisor:
Antonio Gens Solé

Barcelona
April 2021

Dedicated to my loving father

Manuel Madrid

Abstract

The design and construction of vertical caisson breakwaters on soft soils represents a significant challenge for the engineering of marine structures. Past experience reveals that this type of structures is sometimes prone to failure or to undergo excessive settlements. Cyclic loading due to storm wave action adds an addtional degree of complexity. This Thesis present the performance of a wide-ranging set of geotechnical activities to address the key issues of stability, large caisson displacements and cyclic loading effects in the context of the construction of vertical breakwaters. They include site investigation operations (involving laboratory tests, in situ tests and field tests), constitutive models for soft clays (under static and cyclic conditions), instrumentation and monitoring systems, numerical modelling of the breakwater during and after construction and the evaluation of stability under static and cyclic loads. The construction and performance of a vertical breakwater built on the soft soils of the Port of Barcelona provides the focal point to integrate the description of those activities in a joint and structured manner.

After reviewing the main aspects associated with the construction and performance of vertical breakwaters, the behaviour of the soft foundation soil is examined. Laboratory tests, in situ tests and a large scale instrumented preload test are considered. Particular attention is paid to undrained shear strength, small strain stiffness, compressibility characteristics and cyclic loading effects. Soil behaviour is then modelled by a range of different constitutive laws of different degrees of complexity. The proper representation of strength anisotropy, long-term creep and cyclic behaviour is explicitly addressed.

An extensive monitoring system for the measurement of pore pressures and soil movements has been installed before construction and, following the loss of a number of sensors, after caisson emplacement as well. A novel feature of the instrumentation was the installation of sensors on the front and on the base of the caisson to measure the hydraulic response to the impact of sea waves. The monitoring data has provided the necessary information to achieve a sounder knowledge of the behaviour of the breakwater at different stages of construction and post-construction, including the response under storm loading.

Numerical analyses have been carried out towards achieving a better understanding of the breakwater behaviour during construction, post-construction and under cyclic loads. The interplay between monitoring observations, construction history and simulation results is highlighted. Special attention has been given to the evaluation of stability during construction and post-construction. Whenever relevant, the observations provided by the monitoring system are incorporated in the evaluation; the measurement of the evolution of pore pressures has proved important to ensure the safety of the caisson during construction. Breakwater stability under cyclic loading has also been evaluated using both simplified and advanced methods.

This ensemble of works performed in the context of a well-documented case history should prove of benefit for the design and construction of similar structures founded on soft ground.

Keywords: Vertical breakwater, consolidation, cyclic mobility, creep, undrained strength, residual pore pressure, constitutive modelling, site investigation, storm loading

Agradecimientos

Ha sido un largo y difícil recorrido, un sueño que inicio en Barcelona con el Master en Métodos Numéricos y que termina finalmente en Lima, mi ciudad natal. Sin duda, una experiencia inolvidable y de amplio crecimiento tanto a nivel personal como profesional. Crecimiento que no habría sido posible sin el apoyo y contribución de muchas personas, quienes muy gentilmente, me brindaron su amistad y apoyo, y contribuyeron con su experiencia y conocimiento, a quienes quiero agradecer en estas líneas.

En primer lugar, mi mayor agradecimiento y admiración al Prof. Antonio Gens, por la confianza y oportunidad de trabajar en el emblemático proyecto de Ampliación del Puerto de Barcelona. Sin su asesoría y extraordinario conocimiento geotécnico, no habría sido posible completar esta tesis.

Debo agradecer igualmente al Prof. Eduardo Alonso, otro genio de la geotecnia, trabajar bajo su co-dirección en las obras del puerto, ha sido todo un aprendizaje.

A Javier Uzcanga, quien, con su trabajo y empeño a cargo de la dirección técnica de la Autoridad Portuaria de Barcelona, supo sacar adelante los tantos proyectos de investigación que se llevaron a cabo en el Puerto y que finalmente forman parte de esta tesis.

Agradezco igualmente a todos los profesores de la Sección de Ingeniería del Terreno, Cartográfica y Geofísica, por los valiosos conocimientos impartidos durante mi paso por el doctorado. En especial a Enrique Romero, a cargo del Laboratorio de Geotecnia, por transmitir su brillante conocimiento en interpretación de los ensayos de laboratorio.

Quiero agradecer a mis colegas y amigos, Dani Tarragó y Amadeu Deu, excelentes profesionales con quienes me toco trabajar en los proyectos del Puerto. Expresar mi mayor aprecio a Sergio Samat y Nubia Gonzales, con quienes inicie esta travesía. A Rodrigo, Tere, Clara, Mauricio, Christian, Ernesto, Nuria, Enrique, German, Jubert, Vladimir, Khanta, Andres, Abel y muchos otros, por los inolvidables momentos que compartimos e hicieron de mi estadía en Barcelona toda una experiencia multicultural.

A mis colegas de la Universidad de Lima, en especial a Alexandre Almeida, por ayudarme en mi regreso a la actividad académica y confiar en el trabajo que vengo desarrollando.

Debo agradecer también a CIMNE, por la beca que permitió financiar mis estudios de doctorado, durante mi estadía en Barcelona.

Finalmente, agradezco mi familia, en especial a mis padres Manuel y Teresa, por su gran amor y apoyo incondicional. Papá sé que desde el cielo guías nuestro camino. A mis hermanos Martin y Rosemarie y a mis hijos Eduardo y Adriana por ser siempre mi mayor motivación.

Table of content

List de Figures

List of Tables

Chapter 1

INTRODUCTION

1.1 GENERAL BACKGROUND

In recent decades, trade and industry have grown significantly, creating a need to expand the areas of operations of the major ports. Although the economic crisis of 2007 stopped some of the projected expansion plans, the industry seems to have recovered the growing trend of expansion as observed in Spanish ports (mainly Valencia, Barcelona, Vigo, Bilbao and Algeciras). This expansion is usually done through reclaimed land, and at water depths that are enough to allow traffic of large ships. Therefore, it is necessary to build breakwaters, increasingly farther from the coastline and therefore founded at greater depths. Building breakwaters with traditional sloping embankment geometry is often unattractive under these conditions. Some of the reasons for this include: the high cost of work (that sometimes it is simply unfeasible), a greater impact on the marine environment, less quality control in construction, longer construction times and maintenance difficulties. By contrast, breakwaters with concrete caissons seem to reduce all these problems and therefore their use is becoming more common in Europe. In Spain, since the end of the 20th century, about 32.2 km of dykes have been built, of which, 15.4 km correspond to slope type breakwaters and 16.8 km of vertical breakwaters (Gutiérrez & Grassa, 2015), which shows a marked tendency toward the construction of vertical breakwaters (see Table 1-1).

The use of vertical breakwater in harbour works is not new. Many vertical breakwaters were built during the early decades of last century. The catastrophic failure of a number of them, however, caused that for many years this structural type was almost left aside. Oumeraci (1994) did a review of the main causes that produce failure of these breakwaters. Table 1-2 presents the cases that were studied and shows some characteristics regarding the design of these breakwaters, as well as the reasons that led to the collapse of these structures, which were attributed mainly to deficiency in the hydraulic definition of wave load, although geotechnical failures such as overturning, sliding and settlements have also been reported. Negro et al (2001) did also a review of the collapse of several vertical breakwaters, with similar conclusions.

As explained by Franco (1994) failures occurring in Italy were initially due to the impact of the waves, which exceeded the design conditions, but later, advances in estimation of waves design made the wave loading problem less common, and changed the tendency in favour of differential settlements problems due to poor bearing capacity and large compressibility of the foundation soil.

Table 1-1. Breakwaters built in Spain since the end of last century (Gutierrez & Grassa, 2015).

Slope dikes built since the late 20th century									
Denomination	**L(m)**	**D_{max}(m)**	**B(m)**	**C(m)**	**H(m)**	**W(t)**	**S(H/V)**	**$H_{Sdesign}$ (m)**	**T**
Torres, Gijón	1.450	-22	-	22	44	145	2:1	9,5	4,6
Ferrol, Puerto exterior	1.100	-33	-15	18	51	90	3,5:2	7,60	4,5
Coruña, Puerto exterior	4.000	-42	-28	25	67	150	2:1	15,1	4,5
Valencia, Ampliación norte	1.123	-16	-9	12	28	35	3:2	6,3	1
Este, Barcelona	2.165	-20	-10	12	32	50	3,5:2	7,3	0
Sur. Tramos 1-3 Barcelona	3.100	-23/-27	-14	11		40	1,75:1	7,3	0
Bocana. Norte Barcelona	1.000	-25,2	-10	11	35,2	40	3:2	6,4	0
Alicante	1.200	-16	-8	7,5	23,5	20	3:2	4,4	0
Esfinge. Las Palmas	302	-39	-10	15	54	56	3:2	7,3	3,0
Total length: 15 340 m									
Vertical dikes built since the end of the 20th century									
Denomination	**L(m)**	**D_{max}(m)**	**B(m)**	**C(m)**	**W(m)**	**H(m)**	**$H_{Sdesign}$(m)**	**H(m)**	
Norte. Gijón	1.588	-30	-24,75	24	32,01	48,75	9,5	4,6	
Isla Verde. Algeciras	1.750	-43	32,5	7,5	21,4	40	4,8	1,3	
Levante. Málaga	1.200	-20	-20	10	21,1	30	6,3	0,8	
Motril	550	-20	-12	7,5	21,1	91,5	6,3		
Ampliación Escombreras	1.955	-52	-28	8	24	32	8,1	0,6	
Valencia. Ampliación norte	2.271	-16	-	13	19,17	29	6,3	1	
Sagunto	1.204	-15	-	9	19,6	24	6,4	0	
Levante. Castellón	440	-12	-13	12	19,6	25	7,3	0,5	
Levante. Prolongación. Castellón	358	-15	-13	12	19,6	25	7,3	0,5	
Sur. Castellón	819	-16	-12,5	12	15	5,20	7,3	0,5	
Prolongación Tarragona	736	-30	-21,5	8	24	29,5	7	0	
Sur. Tramo 2. Barcelona	1.700	-20	-15	11	24,4	26	7,6	0	
Bocana Norte. Barcelona	450	-29	-17,5	6	19,6	25,5	6,4	0	
Botafoc. Ibiza	615	-25	-20	7	21,1	27	6,3	0	
Reina Sofía. Las Palmas	490	-40	-26	12,2	24	38,2	7,3	3,0	
Esfinge. Las Palmas	664	-33	-26	12,2	24,6	38,2	7,3	3,0	
Total length: 16 830 m									

L = length, Dmax =seabed level, B= berm level, C= crown wall level, Wt= rockfill weight, W= caisson width, H = caisson height, Hs = significant wave height, T= tide, S= Slope

At the beginning of 21st century, the Port Authority of Barcelona started an ambitious plan to extend the port area; it was called the 'Plan Delta' and involved the construction of new breakwaters and quays. The expansion of Barcelona Port was not free of failures during construction; on the night of 10 to 11 November 2001 a storm with a significant wave height of 4.50 m caused damage to several areas of the harbour, and in particular to the construction of a new caisson dyke of the North Entrance. The most serious damages occurred in the final sector, where 4 of the 21 caissons had already been placed. The two central caissons practically disappeared, and the end caisson sank in its entirety. Puzrin et al (2010) concluded that the failure and the deep sinking of caissons are explained by a strength-loss mechanism associated with liquefaction phenomenon due to the cyclic wave loading.

Also, at Barcelona Port, during the construction of Muelle Prat, after one year of caisson placement and also consolidation of foundation soil, on January 1 of 2007 a failure of 15 caissons occurred during the process of back filling. Investigations performed about the failure indicated the reason of collapse was the liquefaction of the hydraulic fill (Tarragó, 2021).

Another failure that occurred in Spain, was that at the Port of Malaga on July 19, 2004 when a preload was being performed on the dock backfill. Also, on May 3, 2004 a big storm with waves up to 8m almost completely destroyed the crown wall of the west dyke of the Port of Motril (Granada). Similarly, damage occurred in the breakwater crown wall of the harbour of Ceuta on March 1, 2005 due to a heavy storm.

Table 1-2. Vertical breakwaters failures (Oumeraci, 1994).

Breakwater (country, year)	**H/T**		**Foundation Soil**	**B** h_c	**d**	h_b	**Cause of failure**
	Design	**Now**					
Madras (India, 1881)	-	-	-	7.3 9.1	22	14.6	Breaking waves and overtopping, drag and erosion (tilt towards the sea).
Bizerta (Tunes, 1915)	-	-	-	8 13	17	10.0	Breaking waves and overtopping, erosion in embankment.
Valencia (Spain, 1926)	-	7/14	Fine sand, mud	12 14.4	12	4.0	Exceeded design wave, breaking waves and overtopping, drag and erosion (slope to sea).
Antofagasta (Chile,1928-29)	6/8	9/15 8/47	-	10 16.9	30	12	Exceeded design wave, No-monolithic, breaking waves.
Catania (Italy, 1930-33)	6/7	7/9 7.5/12	Dense sand	12 20	17.5	-	Exceeded design wave, No-monolithic, breaking waves and overtopping, differential settlement (slide and tilt towards the sea).
Genova (Italy, 1955)	5.5/7	7/12	Fine sand	12 17.9	17.5	8/7	Exceeded design wave, No-monolithic, breaking waves and overtopping (slip).
Algiers (Argelia, 1930-1934)	5/7.4	6.5/11 9/14	Silty sand, mud	11 21.6	20	7.7	Exceeded design wave, breaking waves and overtopping, differential settlement, embankment erosion (tilt toward the sea).
Niigata (Japan, 1976)	7/13	7/13.5	Silty sand	15	17	4.0	Breaking waves and overtopping, differential settlement (tilt toward the sea).
Bari (Italy, 1974)	-	-	-	9.5 15	15.5	5	Exceeded design wave, breaking waves, embankment erosion

Breakwater (country, year)	H/T		Foundation Soil	B h_c	d	h_b	Cause of failure
	Design	Now					
Palermo (Italy, 1973)	5.5/7	6.1/11.3	-	9 26	36	36	Exceeded design wave, breaking waves, embankment erosion
Nápoles (Italia, 1987	-	5	-	13 18	19	-	Breaking waves (Sliding and overturning).
Mashike (Japan)	5.5/10	6.6/12	-	14.5 6.0	7	2.8	Exceeded design wave, breaking waves and overtopping (sliding=2.9m).
Fukaura (Japan)	7.6/11	6.3/13	-	20.5 12.5	15	4.3	Breaking waves and overtopping, embankment erosion (sliding=3.0m).
Sakata (Japan)	3.3/8.8	5.5/13	-	6.5 10	7.0	2.5	Exceeded design wave, breaking waves, differential settlement (sliding and tilt toward coast).
Onahama (Japan)	6.1/14	6.1/14	-	15 13.5	16	9	Breaking waves, embankment erosion (sliding).
Niigata-West pier (Japan)	7.5/13.5	7.5/11	-	18 17.5	18	6.5	Breaking waves and overtopping, embankment erosion (sliding=26m).
Niigata- West dike (Japan)	7/13	7.1/13.5	-	15 18	15	4	Breaking waves and overtopping, differential settlement.

H = wave height (m); T = period (s); B = caisson width; h_c = caisson height; d = draught; h_b = embankment height.

Recent development in wave measurement systems, instrumentation, scale models, advances in mechanics and wave interaction with vertical structures, allow the definition of the design storm in a more accurate way. In fact, many of the failures occurred in the past were due to an incorrect definition and interpretation of design storms, as indicated in Table 1-2.

On the other hand, the geotechnical problems are usually surrounded by a number of uncertainties in model calculations, identification of failure mechanisms and the definition of design parameters. Additionally, the mechanisms of failure observed in breakwaters are associated with the dynamic nature of the wave loads and the transient phenomenon that governs the structure-foundation interaction. Therefore, due to the complexity of the phenomena involved, it is necessary a periodic review of the methods used for the design of vertical breakwaters, which includes an interaction between the hydraulic, geotechnical and structural aspects.

In this context and, in order to improve standards of construction of vertical breakwaters, a research project PROVERBS (Probabilistic Design Tools for Vertical Breakwaters) was created within the program research MAST (Marine Science and Technology research Programme of the European Union). It was a multidisciplinary project involving 23 European institutions during the period from 1996 to 1999. The objective of this project was to develop probabilistic design tools to be applied in

vertical breakwaters. To this end, a review of the structural, hydraulic and geotechnical issues was performed (Oumeraci et al. 2001).

In Spain, a technical committee responsible for drafting the "Recommendations for Maritime Works" (Program ROM) was formed in 1987. Publications of this commission serve as a guide to the various State agencies and private companies in the design, construction, maintenance and exploitation of marine constructions. Specifically, the ROM 0.5: Geotechnical Recommendations for Maritime Works was published in 1994. The whole program ROM (now Project Marine and Port Works) was subjected to an integral review, producing an updated version of ROM 0.5 in 2005, this new version is currently in force.

In the ROM 0.5 there are recommendations and guidelines to be followed to study the stability and settlements of vertical breakwaters. In particular, failure mechanisms are defined for these structures, including: Global Stability, Plastic Overturning, subsidence and slides, and describes analytical methods for each. Additionally, recommendations are given for calculations using slope stability methods. When these standards have been put into practice, either in 1994 or 2005, they have caused some controversy, because the application of the ROM's expressions seems to lead to conservative designs. Experience in several projects, including the port of Barcelona indicates that the use of computer programs can lead to different solutions depending on the criteria adopted in the design.

Because of these difficulties, the Port Engineering Technical Committee of the Technical Association of Ports and Coasts (ATPYC) created the working group: "Analysis of Structures Using Two-Dimensional Slope Stability Programs" in October 2005. The group comprised a total of 17 institutions (both state and private), including the UPC. The group's goal was to develop a set of recommendations and proposals for the solution of geotechnical problems in marine works using commercial programs; among the issues to consider was the case of breakwaters and quays constructed with caissons (Pita et al, 2007). It is evident, however, that the limit equilibrium methods examined by the working group have significant drawbacks and, more importantly, they do not contribute to an enhanced understanding of the behaviour of the soil-structure system throughout its lifetime.

In summary, vertical breakwaters are structures that are subjected to complex loading and have proved to be prone to failure or to undergoing excessive settlements, especially when founded on soft soils. It is thus appropriate to go beyond conventional practice to improve the design methodology and behaviour understanding using the full scope of modern geotechnical tools of site investigation, instrumentation and numerical analysis.

1.2 AIMS AND OBJECTIVES OF THE THESIS

The construction of vertical breakwaters on soft soils involves a series of key geotechnical issues that include stability, caisson displacements (in the short and in the long term) and behaviour under cyclic loads associated with storm wave loading. To address adequately those issues, it is necessary to employ

a variety of geotechnical tools such as site investigation (involving laboratory tests, in situ tests and field tests), constitutive models for soft clays (under static and cyclic conditions), instrumentation and monitoring, numerical modelling of the breakwater behaviour during and after construction and a detailed evaluation of stability under static and cyclic loading. All those activities have been performed in the case of the construction of a large vertical breakwater founded on soft soil at the Port of Barcelona that provides a focal point for the combined application of this wide-range set of geotechnical approaches.

During site investigation, special attention has been paid to the determination of the undrained shear strength, the key parameter controlling stability, under static and cyclic conditions. Undrained shear strength has been determined from laboratory tests and in situ tests, such as CPTu tests and vane tests. Laboratory tests have included triaxial tests, simple shear tests, cyclic triaxial tests and cyclic simple shear tests. The other key parameter is soil compressibility that largely controls breakwater settlements; it has been evaluated by in situ and laboratory tests but, also, from the backanalysis of an instrumented preload test.

To observe the performance of the vertical breakwater during and after construction, an advanced instrumentation system including piezometers and inclinometers, has been installed before construction and, after the loss of a number of sensors, after caisson emplacement as well. The monitoring data has provided the necessary information to examine the behaviour of the breakwater at different stages of construction and post-construction. A novel feature of the instrumentation was the installation of sensors to measure the hydraulic force caused by the impact of the sea waves, thus allowing a better knowledge of the breakwater's behaviour under wave-induced cyclic loading.

A better understanding of the breakwater behaviour is greatly assisted by the performance of appropriate numerical simulations. Essential components of the numerical analyses are the constitutive models selected to represent the mechanical behaviour of the soil in the calculations. Several constitutive laws have been employed in the simulations; they have been carefully calibrated using the results from the laboratory, in situ and field tests performed as part of the site investigation. Specific features such as anisotropy, creep and cyclic loading have been particularly considered. Numerical analyses of the breakwater during and after construction have been carried out, including the consideration of cyclic effects due to storm loads. The interplay between monitoring observations, construction history and simulation results is highlighted. Stability evaluations, using both advanced and simplified methods, are given especial attention as it is often the main geotechnical problem of a vertical breakwater constructed on soft soils.

In summary, the main objective of the Thesis is to describe and discuss this wide-ranging set of geotechnical activities in the context of this case history. They include conventional and advanced testing, a large-scale preload test, instrumentation of the foundations ground, instrumentation of

caissons, application and calibration of several constitutive models, performance of numerical analyses to simulate the various stages of construction and post-construction, and the assessment of stability under static and cyclic load conditions. The case of the vertical breakwater in the Barcelona Port provides the necessary focal point to integrate all the activities performed, in a joint and structured manner. Naturally, the fact that the work described here has been carried out in the research context of a Ph.D. Thesis means that the tools and techniques employed are able to go beyond standard practice. In this way, full benefit can be drawn from this well documented and relevant case history.

1.3 OUTLINE OF THE THESIS

This thesis is organized in eight chapters, each of which has a separate and distinct function, as described below.

Chapter 2 presents a general review of important issues associated with vertical breakwaters behaviour relevant to the research. This chapter starts with a review of the procedures or methods to evaluate external loads (static and cyclic) affecting breakwaters. Also, the way how the sea wave loads were established for the Barcelona Breakwaters design is discussed. Phenomena associated with geotechnical behaviour of the breakwater are then reviewed such as failure modes, settlements, pore pressure evolution and stiffness degradation during cyclic loading. Also, the dynamic behaviour of the breakwater is considered in the context of a two degrees of freedom analytical equation of motion.

Chapter 3 describes the mechanical behaviour of the soft soils of the Port of Barcelona, focusing on four relevant aspects: undrained shear strength, behaviour in the small strain range, cyclic undrained resistance and soil compressibility. For soil compressibility, a large-scale instrumented preload test was performed allowing the calculation models and parameters to be adequately calibrated.

Chapter 4. This chapter investigates the ability of various constitutive soils models to reproduce the experimental behaviour observed in different tests. Specifically, the undrained resistance behaviour, cyclic behaviour and creep behaviour are evaluated. The performance of the models has been assessed based on the degree of agreement between experimental measurements and model predictions. For this task, several models available in the Plaxis code were chosen: the soft soil model (SS), the anisotropic S-Clay1 model, the UBC3D-PLM liquefaction model, and the soft soil creep model (SSC).

Chapter 5 is devoted to the examination of the field performance of the vertical breakwater in Barcelona Port based on the records obtained from the geotechnical instrumentation of the foundation. The response of the breakwater is discussed based on pore pressure and settlement measurements that are compared with the classical theory of consolidation under increasing loads. Finally, the recorded cyclic response observed under three storms is described and discussed.

Chapter 6 presents first the numerical simulation of Barcelona's breakwater under the static loads applied during construction and post-construction. Results of horizontal and vertical displacements and

also pore water pressures computed using the Soft Soil and S-Clay1 models are presented and compared with field measurements. Subsequently, the dynamic analysis of the breakwater under a large storm using the UBC3D-PLM model is presented and the results compared with the pore pressures measured during the storm.

In Chapter 7, the stability of the breakwater under static and cyclic loads is discussed. First, a series of factor of safety definitions appropriate for the assessment of the breakwater stability are proposed. The definitions are consistent with the finite element methodology applied. Afterwards, a series of simulations that include analyses using undrained and effective stress strength parameters are performed. They consider the design hypothesis of full dissipation of pore pressure but also the more real condition of partial dissipation as measured with the instrumentation. Finally, a simplified methodology for assessing stability under cyclic loading is presented based on the interaction diagram constructed from the simple shear tests results.

Chapter 8 summarises the main conclusions that can be drawn from the results of the research and presents some recommendations for future work.

In addition, the thesis includes two Appendices.

Appendix I presents the equipment and procedures used in the geotechnical instrumentation of the vertical caisson breakwater in the Port of Barcelona. Measurements of pore pressure and settlements of the breakwater, recorded during the different stages of the structure's construction are presented. They allowed a better understanding of the breakwater's behaviour under static and wave-induced cyclic loading.

Appendix II describes the procedures and results obtained from the instrumentation installed in one caisson to monitor the effects of storm loading. Pressures from sea waves impacting on the front face of the caisson and the uplift pressure during three large storms were recorded and analysed in order to establish a pattern of pressure variation potentially useful for design.

Chapter 2

GENERAL ASPECTS OF VERTICAL BREAKWATER PERFORMANCE

2.1 INTRODUCTION

The main purpose of a harbour breakwater is to give protection against wave attacks on berths, manoeuvring areas, and port facilities (Vicinanza et al 2019), permitting in this way the operational activities in the Port. Due to this inherent purpose, vertical breakwaters are subjected to many cycles of waves hitting during a storm, which mean, static and dynamic loads are transmitted to the foundation soils during their operational life. This special characteristic transforms the problem of bearing capacity of caissons into a complex problem of soil-structure-water interaction. Therefore, the response of breakwaters is closely linked to the definition of loads with which they interact. Two types of behaviour can be defined in this way: static behaviour (produce by non-breaking waves, dead loads, and live loads) and cyclic behaviour (produce by breaking waves, impact waves and seismic loads). Static behaviour involves study of stability problems, failure modes, and settlements while cyclic behaviour refers mainly to stiffness degradation, built up of pore pressure, cyclic mobility and liquefaction of soils (in some cases). Although a definition of breakwater response based on load type seems appropriate from a point of view of laboratory experimentation or design methodologies, it could be better for performance investigation of breakwaters to use the classical definition of short- and long-term performance. Duncan et al (2014) proposed the following definitions: *"Short term refers to conditions during or following construction—the time immediately following the change in load"* and long-term conditions: "*After a period of time, the clay foundation would reach a drained condition, and the drained analysis would be performed because long term and drained conditions carry exactly the same meaning. Both of these terms refer to the condition where drainage equilibrium has been reached and there are no excess pore pressures due to external loads*". These definitions of short and long-term periods involve implicitly the time and excess pore pressure dissipation (hydro-mechanical process) but they do not make clear where the boundary between both is.

Juran & Elias (1991) also suggest an alternative definition: "Short-term performance is defined by a time-independent load-displacement relationship, while an assessment of the long-term performance should account for the effect of time-dependent phenomena such as creep and

relaxation". From this definition, the short-term performance of breakwaters should include all phenomena where interstitial excess pore pressure do not have time to dissipate (pore pressure built-up), corresponding to the undrained response of soil under static or cyclic load and long term response refers to those processes in which dissipation of interstitial pore pressure takes place (consolidation) or viscous effects occur (creep), corresponding to drained or partially drained response. For the purpose of this thesis short- and long-term performance is associated to construction and post construction phases of the breakwater. A schematic representation of short- and long-term definitions is show in Figure 2-1.

The most important force to be considered in the design is the wave force acting on the caisson wall. Although recent efforts have improved methods to define wave loads, due to their random nature, there is not yet a fully reliable method, so frequently large-scale physical model are required. Of course, hydraulic aspects of definitions of wave pressures are a very large topic that is beyond the scope of this research, but even so it was considered relevant to investigate breakwater performance, as it cannot be left aside. Wave loads were introduced into the analysis of breakwater performance by directly measuring of the water pressure in front of the wall and measuring the uplift pressure at the caisson base during various storms. This relevant information has permitted to verify the most commonly used methods of wave loads computation.

In this chapter, a brief review of theories and methods to describe fundamental aspects of breakwater behaviour is presented, focusing on what is useful for interpreting results of this investigation from a point of view of short and long-term performance. Basically, the performance of breakwaters is described by two parameters: pore pressure and settlements. Both are susceptible to be measured with relative precision by the instrumentation system. From these two parameters, it is possible to derive and identify the behaviour of the breakwater foundation during construction and post-construction. Characteristics like gain of undrained strength under consolidation or phenomena like stiffness degradation, creep, liquefaction or cyclic mobility are all of primary concern because they are relevant in the analysis of breakwaters.

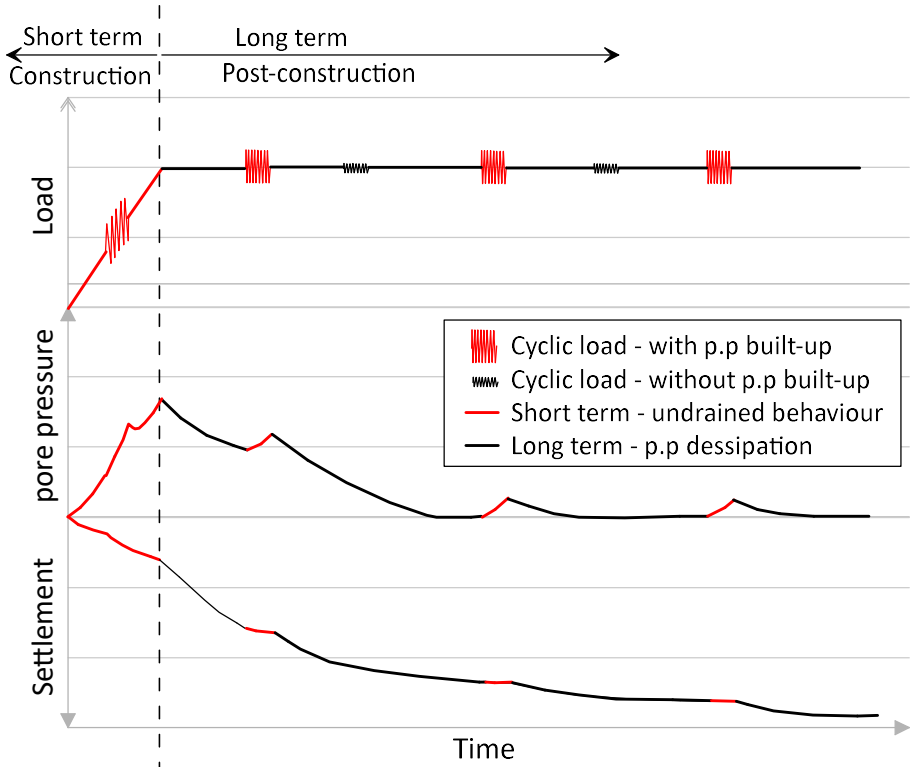

Figure 2-1. Schematic representation of short- and long-term definitions

2.2 LOADS ON BREAKWATER

Several typologies and shapes of vertical breakwaters have been designed and constructed around the world, including composite breakwater, perforated breakwater and armoured caisson breakwater (Figure 2-2). Composite type, which involves large thickness of earth embankment as support for the vertical caisson, is most common in Spain as described by Gutierrez-Serret et al (2010). These structures are subject to a combination of environmental forces such as waves, marine currents, winds, and sometimes earthquakes. Probably the main source of loading are the ocean storms which apply relatively large horizontal loads and overturning moments. The lateral load is usually an important fraction of the vertical load, and therefore, the overturning moment is also very large causing large eccentricity on caisson foundation. This characteristic adds complexity to the analysis of caissons foundations. Experiences on vertical breakwater and quays constructed at Spain, show that these structures can be subject to lateral forces as great as 45% of its vertical load (see Table 2-1 and Figure 2-3 based on compilation from Port Authority of Barcelona, 2007).

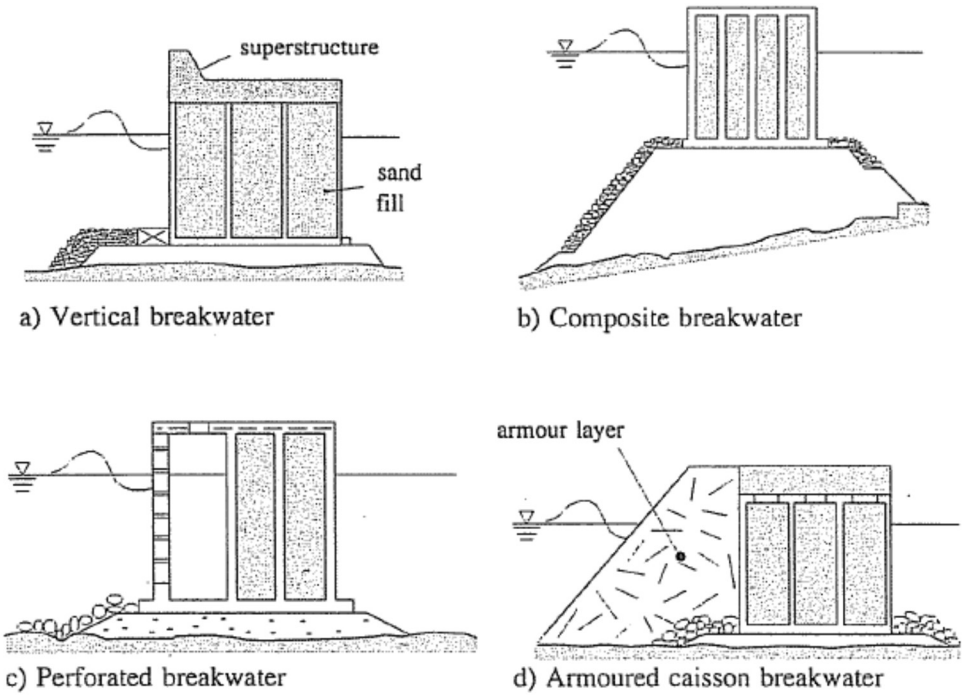

Figure 2-2. Main types of vertical breakwaters (Oumeraci et al, 2001)

Table 2-1. Characteristics of some Spanish quays and vertical breakwaters (APB, 2007)

N°	Name	Port	Top Level (m)	Foundation Level (m)	Height (m)	Width (m)	V' (kN/m)	H (kN/m)	H/V' (%)
1	Muelle Sur y Oeste San Juan de Nieva	Avilés	6.3	-12	18.3	12.6	2898	1272.4	43.9
2	Muelle n° 3	Bilbao	6.85	-20	26.85	18.6	5839	2043.4	35.0
3	Muelle de las Azucenas	Motril	3.5	-14	17.5	13.6	2654	738	27.8
4	Muelles comerciales	Baleares	2	-11	13	9.68	1346	630	46.8
5	Muelle Norte de Isla Verde	Algeciras	3	-18.4	21.4	12.88	2912	1263.8	43.4
6	Muelle Ferrazo	Villagarcia	5.5	-13	18.5	12.5	2800	1231.4	44.0
7	Prolongación muelle Darsena Norte	Valencia	2.7	-16.5	19.2	10.62	2155	781.1	36.2
8	Muelle del Bajo de la Cabezuela	Cádiz	6	-15	21	13.5	3400	1210.1	35.6
9	Muelle de Leon y Castillo	Las Palmas	4.5	-19	23.5	15.55	4045	1271.5	31.4
10	Muelle de Málaga	Málaga	3	-16	19	15.55	3173	1250	39.4
11	Muelle adosado	Barcelona	2.5	-16	18.5	12.56	2443	900	36.8
12	Prat I	Barcelona	3.7	-16	19.7	18.5	4021	1130	28.1
13	Prat II	Barcelona	3.7	-16.5	20.2	12.07	2679	1070	39.9
14	Dique Sur	Barcelona	3.5	-26	29	24.4	4874	1071	22.0

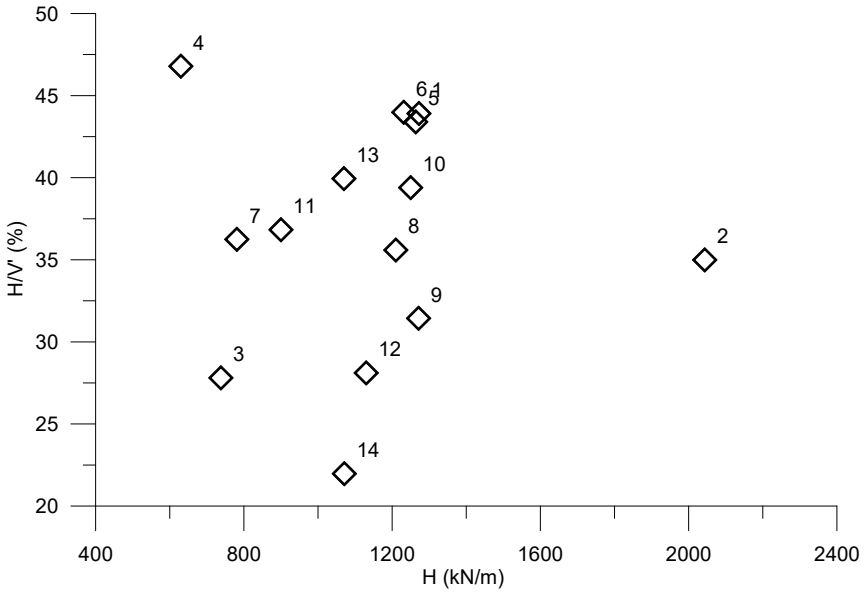

Figure 2-3. Ratio between horizontal to vertical loads of some Spanish vertical breakwaters

2.2.1 Self-weight of caisson and embankment

Dead load is the main concern in predicting settlements in a breakwater founded in soft soil. Therefore, the first step to investigate the performance of a breakwater is to estimate the self-weight of the structure during each phase of construction. What appear a straightforward task involves some difficulties in relation to embankment construction, because quarry run and rip rap material density is difficult to measure directly, typically these materials are dumped over the seabed, and the geometry of the embankment is controlled through periodic bathymetry. Weight of concrete elements like the caissons, beams, slabs and crown wall are easier to establish based on geometry. In the case of caissons, the cells are filled with dredged material, for which an average weight is considered based on the volume of concrete and fill material.

2.2.2 Sea waves

The main forces that act over a vertical wall breakwater are due to sea wave loading, which in general consists of two components: the hydrostatic pressure due to the instantaneous water depth at the wall, and the dynamic pressure component due to the accelerations of the water particles. The last depends on several geometric characteristics and in case of a vertical wall can be described on three ways:

a) Non-breaking Waves

These are waves do not trap an air pocket against the wall (see Figure 2-4a). The pressure at the wall has a gentle variation in time and is almost in phase with the wave elevation. Wave loads of this type are called pulsating or quasi-static loads because the period is much larger than the natural period of oscillation of the structures. As indicated in the Coastal Engineering Manual EM 1110-

2-1100, for conventional caisson breakwaters the period is approximately one order of magnitude larger. Consequently, this wave load can be treated like a static load in stability calculations.

b) Breaking (plunging) waves with almost vertical fronts

Waves that break in a plunging mode develop an almost vertical front before they curl over (see Figure 2-4b). If this almost vertical front occurs just prior to the contact with the wall, then very high pressures are generated having extremely short durations. Only a negligible amount of air is entrapped, resulting in a very large single peaked force followed by very small force oscillations. The duration of the pressure peak is on the order of hundredths of a second (EM 1110-2-1100).

c) Breaking (plunging) waves with large air pockets

If a large amount of air is entrapped in a pocket, a double peaked force is produced followed by pronounced force oscillations (EM 1110-2-1100) as shown in see Figure 2-4c. The first and largest peak is induced by the wave crest hitting the structure at point A, and it is similar to a hammer shock. The second peak is induced by the subsequent maximum compression of the air pocket at point B, and it is referred to as compression shock, (Lundgren 1969). In the literature this wave loading is often called the “Bagnold type”. The force oscillations are due to the pulsation of the air pocket. The double peaks have typical spacing in the range of milliseconds to hundredths of a second. The period of the force oscillations is in the range 0.2-1.0 sec.

Oumeraci et al (1995) suggest a further classification of the wave loads based on the purpose and the failure modes for which they are used: quasi-static loading (which may induce an overall failure of the structure), impact loading (causing local overall failure and structural failure modes) and cyclic loading (causing fatigue and stepwise failure).

Figure 2-5 shows a system (parameter map) for identifying types of wave loadings on the vertical breakwater as a function of structure geometry and wave characteristics (Kortenhaus and Oumeraci, 1998). Considering that impact loads definition is still a matter of discussion, the geometry of breakwater must try to avoid generation of impact loads.

On the other hand, it is important to note that resultant forces may change their direction as the wave move on the structure, passing from crest to trough. Figure 2-6 shows distribution of pore pressure at front and rear face of caisson breakwater, for both conditions. Also, wave overtopping of vertical walls provides a reduction in the total force and moment because the pressure distribution is truncated, but at the same time the wave may impact over the caisson, increasing the vertical load. Overtopping can also create seaward pressure on the rear wall because of saturation of backfill.

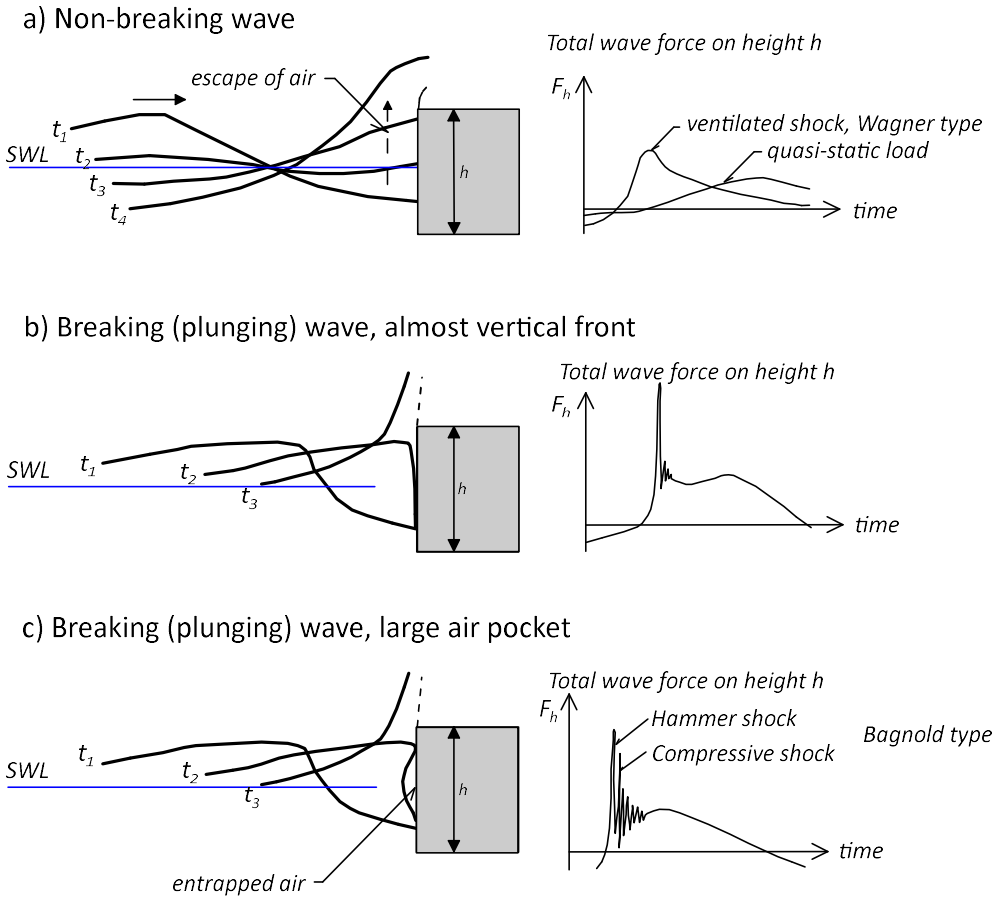

Figure 2-4. Waves forces on wall caissons from non-breaking and breaking waves (Coastal Engineering Manual, 2008).

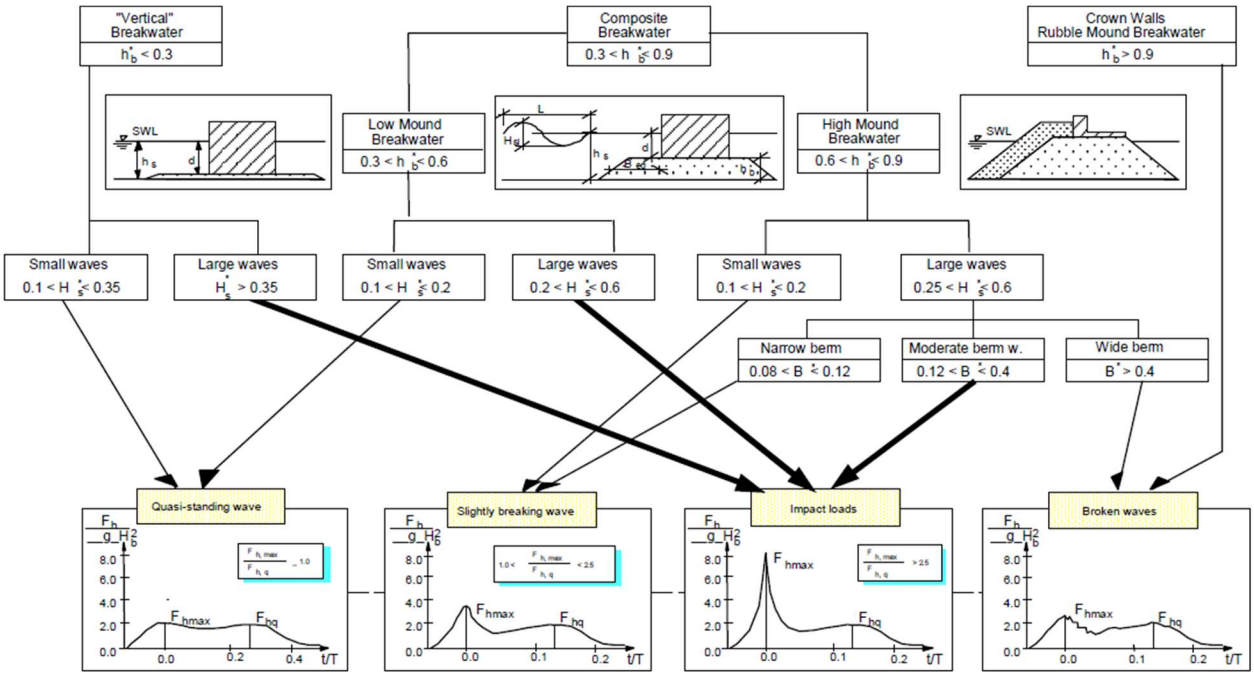

where $h_b^* = h_b/h_s$, $H_s^* = H_{si}/h_s$, $B^* = B_{eq}/L_{pi}$

Figure 2-5. Parameter map (Kortenhaus and Oumeraci, 1998)

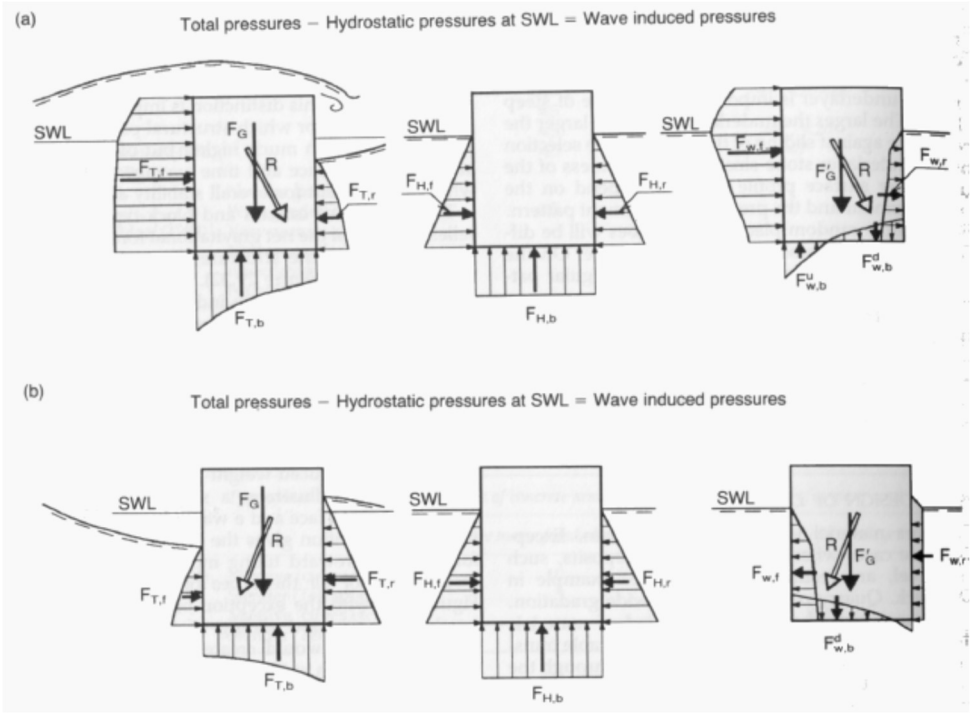

Figure 2-6. Wave induce loads on a vertical wall caisson (a) Wave crest at front and rear face (b) wave trough at front and rear face (C.E.M, 2008).

Several analytical formulas have been developed to estimate the wave force, but Goda´s formula (Goda, 1974) and their extensions (Tanimoto and Kimura, 1985; Takahashi and Hosoyamada, 1994; Takahashi et al, 1994) are probably the most used in engineering practice. Table 2-2 shows a summary of the formulas and their respective types of wave in which they are applied, as recommended by the Coastal Engineering Manual, EM 1110-2-1100.

Table 2-2. Recommended formulas to compute wave load (Coastal Engineering Manual, 2008)

Formula	Wave type	Structure type	CEM Table
Sainflou formula (modified by Miche-Rundgen, 1958)	Standing	Impermeable vertical wall	VI-5-52
Goda formula	2-D oblique	Impermeable vertical wall	VI-5-53
Goda formula (modified by Takahashi, Tanimoto, and Shimosako 1994)	Provoked breaking	Impermeable vertical wall	VI-5-54
Goda formula forces and moments	Provoked breaking	Impermeable vertical wall	VI-5-55
Goda formula (modified by Tanimoto and Kimura 1985)	2-D head-on	Impermeable inclined wall	VI-5-56
Goda formula (modified by Takahashi and Hosoyamada 1994)	2-D head-on	Impermeable sloping top	VI-5-57
Goda formula (modified by Takahashi, Tanimoto and Shimosako 1990)	2-D head-on	Horizontal composite structure	VI-5-58
Goda formula (modified by Takahashi, Tanimoto and Shimosako 1994)	3-D head-on	Vertical slit wall	VI-5-59

For standing waves, the method developed by Sainflou in 1928 on the basis of the linear theory is best suited for long and less steep waves. Rundgren (1958) based on the work of Miche (1944) proposed an approach that give satisfactory results for steep waves (Miche-Rundgren method). Wave pressures following the Sainflou-method (1928) are defined as:

$$p_1 = (p_2 + \rho_w g h_s)\frac{H + \delta_0}{h_s + H + \delta_0}$$

$$p_2 = \frac{\rho_w g H}{\cosh(2\pi\, h_s/L)}$$

$$p_3 = \rho_w g (H - \delta_0)$$

$$\delta_0 = \frac{\pi H^2}{L}\cosh\frac{2\pi h_s}{L}$$

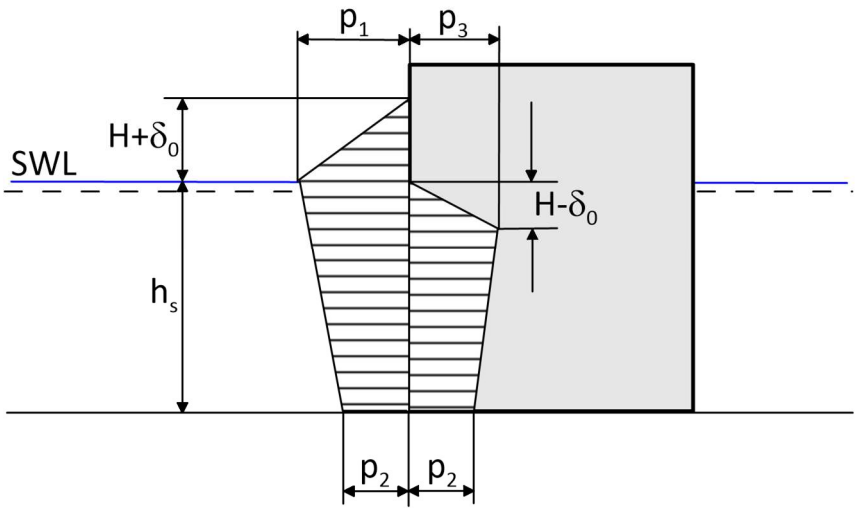

Figure 2-7. Wave pressure distribution by Sainflou's formula

Where:

H = characteristic wave height

p_1 = water pressure at the still water level, corresponding to wave crest

p_2 = water pressure at the base of the vertical wall

p_3 = water pressure at the still water level, corresponding to wave trough

δ_0 = vertical shift in the wave crest and the wave trough at the wall

ρ_w = water density

h_s = water depth at the foot of the structure

L = local wave length

Goda's method (1985) was developed to estimate the horizontal pressure distribution along the vertical face of caisson and the uplift pressure along the caisson bottom for all wave conditions (standing and breaking waves). The following are the Goda's formulas:

$$\eta^* = 0.75\left(1+\cos\beta\right)\lambda_1 H \tag{2.1}$$

$$p_1 = 0.5\left(1+\cos\beta\right)\left(\lambda_1\alpha_1 + \lambda_2\alpha_2\cos^2\beta\right)\rho g H \tag{2.2}$$

$$p_3 = \alpha_3 p_1 \tag{2.3}$$

$$p_4 = \alpha_4 p_1 \tag{2.4}$$

$$p_u = 0.5\left(1+\cos\beta\right)\lambda_3\alpha_1\alpha_3\rho g H \tag{2.5}$$

where $\eta*$ is the water elevation above the still water level, H is the incident wave height in front of the breakwater, β is the angle of incident of wave (angle between wave crest and front of structure), λ_1, λ_2, λ_3, are multiplication factors dependent on the geometry of the structure (for conventional vertical wall structures takes value 1) and α_1, α_2, α_3, α_4, are multiplication factors dependent on the wave conditions and the water depth given by:

$$\alpha_1 = 0.6 + 0.5\left(\frac{4\pi h_s/L_p}{\sinh\left(4\pi h_s/L_p\right)}\right)^2 \tag{2.6}$$

$$\alpha_2 = \min\left(\frac{\left(1-\frac{d}{h_s}\right)\left(\frac{H}{d}\right)^2}{3}, \frac{2d}{H}\right) \tag{2.7}$$

$$\alpha_3 = 1-\left(\frac{d+dc}{h_s}\right)\left(1-\frac{1}{\cosh(2\pi h/L_p)}\right) \tag{2.8}$$

$$\alpha_4 = 1-\frac{R_c^*}{\eta^*} \tag{2.9}$$

Where h_s is the water depth at a distance of $5H_s$, L_p is the wave length, d is the depth of water in front of the caisson, d_c is the height over which the caisson is embedded in the rubble foundation and R_c^* is the minimum of the freeboard R_c and the notional run-up elevation $\eta*$. The following figure shows the geometric definitions of Goda's method.

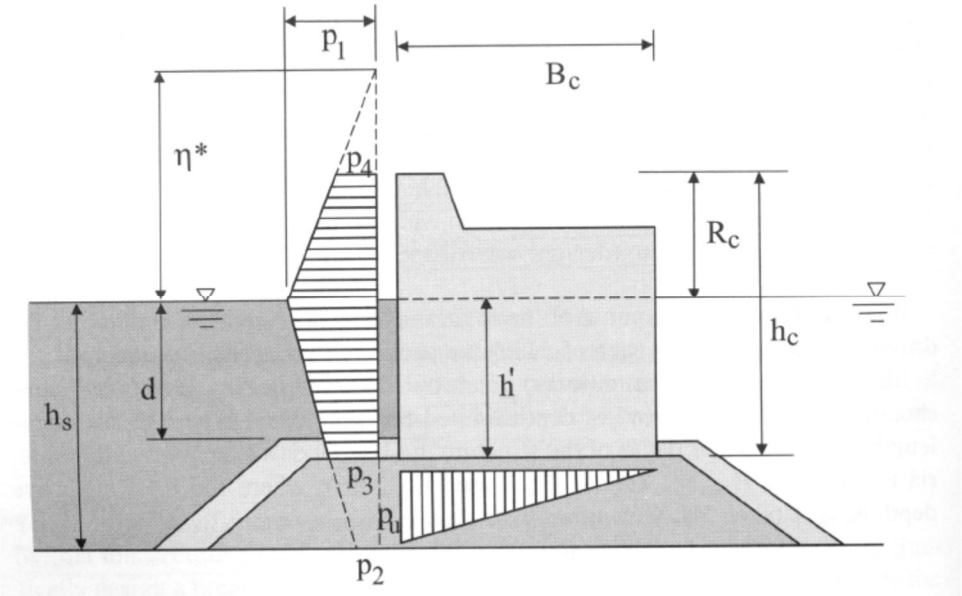

Figure 2-8. Distribution of wave pressure on a vertical breakwater (Goda, 1985)

Once the wave pressures are known, the wave forces can be calculated by integration as follow:

$$F_{h,Goda} = \frac{1}{2}\left(p_1 + p_4\right) R_c^* + \frac{1}{2}\left(p_1 + p_3\right)\left(d + d_c\right) \tag{2.10}$$

$$F_{v,Goda} = \frac{1}{2} p_u B_c \tag{2.11}$$

in which B_c is the width of the caisson bottom. The lever arm of the wave forces with respect to the centre of the caisson bottom is given by:

$$l_{h,Goda} = d + d_c + \frac{R_c^{*2}\left(p_1 + 2p_4\right) - \left(d + d_c\right)^2\left(p_1 + 2p_3\right)}{3R_c^*\left(p_1 + p_4\right) + 3\left(d + d_c\right)\left(p_1 + p_3\right)} \tag{2.12}$$

$$l_{v,Goda} = \frac{1}{6} B_c \tag{2.13}$$

Using the expressions for the wave forces and the lever arm, the total moment due to the wave forces can be calculated by:

$$M_{Goda} = l_{h,Goda} \cdot F_{h,Goda} + l_{vGoda} \cdot F_{vGoda} \tag{2.14}$$

Although Goda's formula are the most used design formula for wave impact loads (Goda, 1985; Takahashi et al. 1994), studies under the PROVERBS project (Oumeraci et al, 2001) have measured short duration wave impact much higher than would be predicted by Goda´s method. More sophisticated procedures to predict impact loading have been proposed in the framework of PROVERBS Project. This procedure enables to predict horizontal impact wave force as a function

of the relative rise time t_r (see Figure 2-9) and also the dynamic response characteristics of the structure and its foundation.

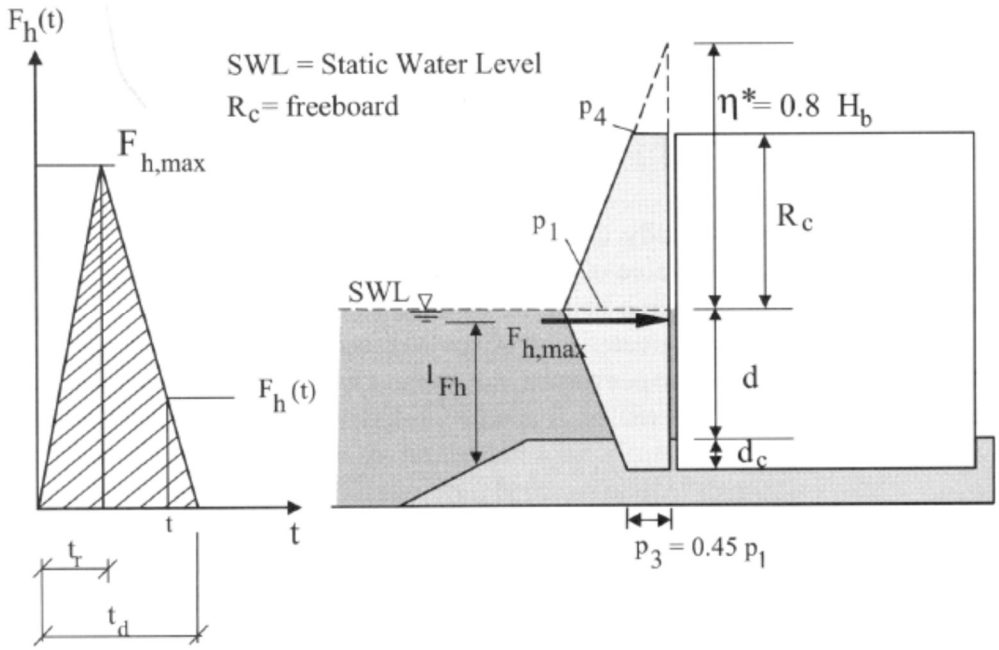

Figure 2-9. Vertical pressure distribution at the breakwater (Oumeraci et al, 2001)

It was shown that the maximum horizontal impact force could be given by

$$F_h = F_h^* \rho g H_b^2 \qquad 2.15$$

Where H_b is the individual or maximum wave height at breaking and the relative maximum wave force F_h^* can be calculated using the following Generalised Extreme Value (GEV) distribution:

$$F_h^* = \frac{\alpha}{\gamma}\left(1 - \gamma \ln P\right) + \beta \qquad 2.16$$

Where P is the probability of non-exceedance of impact forces (P value larger than 90%) and α, γ and β are the scale, shape and location parameters of the GEV distribution, given as a function of the bed slopes (Oumeraci et al, 2001).

Oumeraci et al, 2001 also provide a similar statistical procedure to calculate the uplift pore pressure distribution underneath vertical breakwater. A triangular distribution form is assumed to remain constant over time, with the maximum pressure at the time of the maximum uplift force. The pressure underneath the shoreward side of the breakwater p_{ru} can be calculated as follows:

$$p_{ru} = \rho g H_b \left(\frac{H_b}{h_s} - 0.1 \right) \qquad 2.17$$

And the pressure underneath the seaward side p_u can be calculated as follows:

$$p_u = \frac{2F_{u,\max}}{B_c} - p_{ru} \qquad 2.18$$

where B_c is the caisson width, $F_{u,max}$ is the maximum uplift force calculated for impact conditions and p_{ru} is the pressure at the shoreward side of the structure. The pressure p_u calculated in this way represents an upper bound. Another upper bound is $p_u = p_3$.

All the methods described uses the water level (H) as the main input parameter, which is an important design parameter for calculating forces and moments on vertical walls. Usually, it is defined as the significant wave height (H_s), which correspond to the average height of the highest third part of the waves in a wave field.

Field measurements of wave pressures and hydraulic model tests (Oumeraci et al., 1991) showed that wave forces under non-breaking waves conditions on many structures were often larger than the ones predicted by Goda prediction methods. This can be ascribed to several uncertainties generated from two main sources: the maximum individual wave height in a wave field and the Goda wave force model.

The distribution of individual wave heights in a wave field can generally be assumed to follow a Rayleigh distribution, in which there is only one parameter, the significant wave height H_s. Consequently, $F_H(H)$ the probability that a wave chosen at random in a sea state with parameter H_s has height less than H can be calculated with the cumulative distribution function:

$$F_H(H) = 1 - e^{-2\left(\frac{H}{Hs}\right)^2} \qquad 2.19$$

By considering the maximum wave height in a wave field, and assuming that such waves have independent and identically distributed heights, the distribution of the maximum wave height during the storm, H_{max}, is:

$$F_{H\max}(H) = \left(1 - e^{-2\left(\frac{H}{Hs}\right)^2}\right)^N \qquad 2.20$$

Where N denotes the number of individual waves in the wave field. For given values of H_s and N it is now possible to derive the ratio between the significant wave height and the maximum individual wave height. For 1000 waves, the most probable maximum height is found to be $1.868H_S$ and $H_s=1.6H_{mean}$.

2.2.3 Wave loading at Barcelona breakwater

Based on PROVERBS parameter response map for prediction of the type of wave loading acting on vertical breakwaters, South breakwater is classified as Lower mound breakwater ($h_b^*=h_b/h_s$ =

0.33), which mean that quasi-standing waves are generated for significant height waves (Hs) lower than 4.0m (H_s*=H_s/h_s<0.2) and impact load are generated for H_s higher than 4.0m (H_s*>0.2). Geometric characteristics of South breakwater are shown in Table 2-2.

Table 2-3. Classification of wave load for Barcelona Breakwater following the parameter map of Kortenhaus and Oumeraci (1998)

Characteristic	Symbol	Phase III
Berm height (m)	hb	6.7
Depth water (m)	hs	20
Significant wave height (m)	Hs	5
Berm length (m)	Beq	60
Wave length (m)	L	104.6
Relative berm height	hb*	0.33
Relative wave height	Hs*	0.25
Relative berm width	B*	0.57
Type of breakwater	-	Composite Breakwater
Type of berm	-	Low Mound Breakwater
Type of waves	-	Large waves
Classification of the wave loads	-	Impact loads

When breaking waves condition cannot be avoided, then an extensive model investigation and a complete dynamic analysis of structure and foundation must be carried out. Port Authority of Barcelona commissioned several studies of sea wave behaviour in scaled physical hydraulic and numerical models (GPO-Europrincipia, 2001) and established the design storm to be used in the dynamic stability analysis of breakwater. Table 2-4 and Table 2-5 show the relevant storm characteristics that were consider for the design of construction phases III and IV, respectively. It is assumed that this particular storm has a return period of 100 years. The number of wave impact and their forces (horizontal and uplift forces) were computed using Goda formulation and Rayleigh distribution. It is observed that high magnitude waves, which are believed to be significant for the stability, have a low number of impacts, but those of small magnitude are repeated hundreds of times. Points of horizontal load application (d) are measured from the base of the caissons.

Table 2-4: Design storm. Phase III. South Breakwater. Crown wall level + 6m. Significant wave Hs=4.85m. Number of waves impacting breakwater.

Wave height [m]	Number of waves		Total number of waves	H [kN/m]	d [m]	SD [kN/m]
	H_s=3 m (36 h, T=11s.)	H_s=5 m (12h, T=11s)				
1-2	1172	198	1369	213.4	9.77	148.5
2-3	826	240	1066	341.6	10.28	223.4
3-4	318	209	527	475.0	10.62	297.0
4-5	73	142	215	685.0	10.65	299.0
5-6	10	79	89	825.4	10.74	305.0
6-7	1	36	37	870.5	10.80	308.5
7-8	0	14	14	920.0	10.00	315.0
8-9	0	4	4	1011.5	10.36	310.5
9-10	0	1	1	1410.1	11.46	331.5
10-11	0	0	0	1528.0	11.15	440.0
11-12	0	0	0	1559.3	11.38	357.8

H=Horizontal wave force, d=Point of load application, SD = Uplift force

Table 2-5: Design storm. Phase IV. South Breakwater. Crown wall level + 11m. Significant wave Hs=6.5m. Number of waves impacting breakwater.

Wave height [m]	Number of waves			Total number of waves	H [kN/m]	d [m]	SD [kN/m]
	Hs = 3 m (36 h, T=11s.)	Hs = 5 m (12h, T=11s)	Hs = 6.5 m (6h, T=16s)				
1-2*	1172	198	89	1485	213.4	9.77	148.5
2-3*	826	240	122	1188	341.7	10.28	223.4
3-4*	318	209	129	656	482.7	10.79	297.0
4-5*	73	142	114	329			
5-6*	10	79	87	176	890.9	11.62	532.4
6-7	1	36	58	95			
7-8	0	14	35	48	1749.1	13.75	283.0
8-9	0	4	18	23	1859.0	14.16	397.7
9-10	0	1	9	10	1994.2	14.39	472.2
10-11	0	0	4	4	2234.7	14.28	538.7
11-12	0	0	1	1	2413.3	14.13	622.4
12-13	0	0	0	0			

H=Horizontal wave force, d=Point of load application, SD = Uplift force

2.3 STRESS PATH INDUCED BY VERTICAL BREAKWATERS

In general, breakwaters have similar features of embankments, but their function and also their natural location are generally different. As a consequence, procedures of construction, work schedule, and planning are completely different, which also affect the geotechnical response of foundation soils. Embankments foundation is one of the classical problems of soil mechanics and references to problems of stability or large settlements have been widely reported (i.e.

Bjerrum,1972; Marsland and Powell, 1977; Koutsoftas and Ladd, 1985; Hunter and Fell, 2003; Stark et al., 2018). On the contrary, the technical references about foundation of the breakwater are limited to codes and design guides. Not many case studies are found in the literature or these are limited to the classical slope type of breakwater (i.e. Chung et al, 2006). Many aspects of soil behaviour and constitutive modelling developed during the last decades have permitted characterising the main aspects of typical breakwater behaviour, such as identifying the controlling parameters, assessing the validity of simplified methods of analysis, developing empirical relationships and discuss the ways in which further advances can be made in predicting breakwater performance.

When describing the breakwater behaviour under static collapse load, it is interesting to make a simile with an embankment, which are structures intensely studied, for example Jardine and High (1987) describe the process of collapse of an embankment in two phases:

Phase I correspond to the initial foundation response to load, which is characterized by a stiff behaviour with small ground movement. In this phase, the increase in pore pressure as loading takes place is observed, and also some dissipation is apparent.

Phase II commences when a critical high of fill has reached. In this phase the foundation response becomes much softer with far larger settlements and horizontal displacements developing as construction continues. The rate of pore pressure dissipation under the center line reduces sharply and somewhat larger pore pressure changes become apparent beyond the toe of the embankment. The construction may continue but with each fill increment, the settlement rate accelerates and eventually cracks form in the fill and overall collapse occur.

To illustrate this behaviour, a hypothetical vertical breakwater is simulated with aid of a finite element model and the Hardening soil model with small strain stiffness (HSS) model. Model geometry is an adapted symmetric version from the original geometry of the South breakwater in Barcelona. Light overconsolidation is permitted in the foundation soils in order to include the effect of dredging works and the construction process is carried out with a coupled hydro-mechanical analysis type.

The model shows that the stress path away from the center line experience rotation of principal stress directions (α), in similar way as observed in embankments, but with a more complex combination of shear modes (as can be seen in Figure 2-10). As a consequence, failure develop under active ($0<\alpha<-30$), simple shear ($-30<\alpha<-60$) and passive ($-60<\alpha<-90$) plain strain condition.

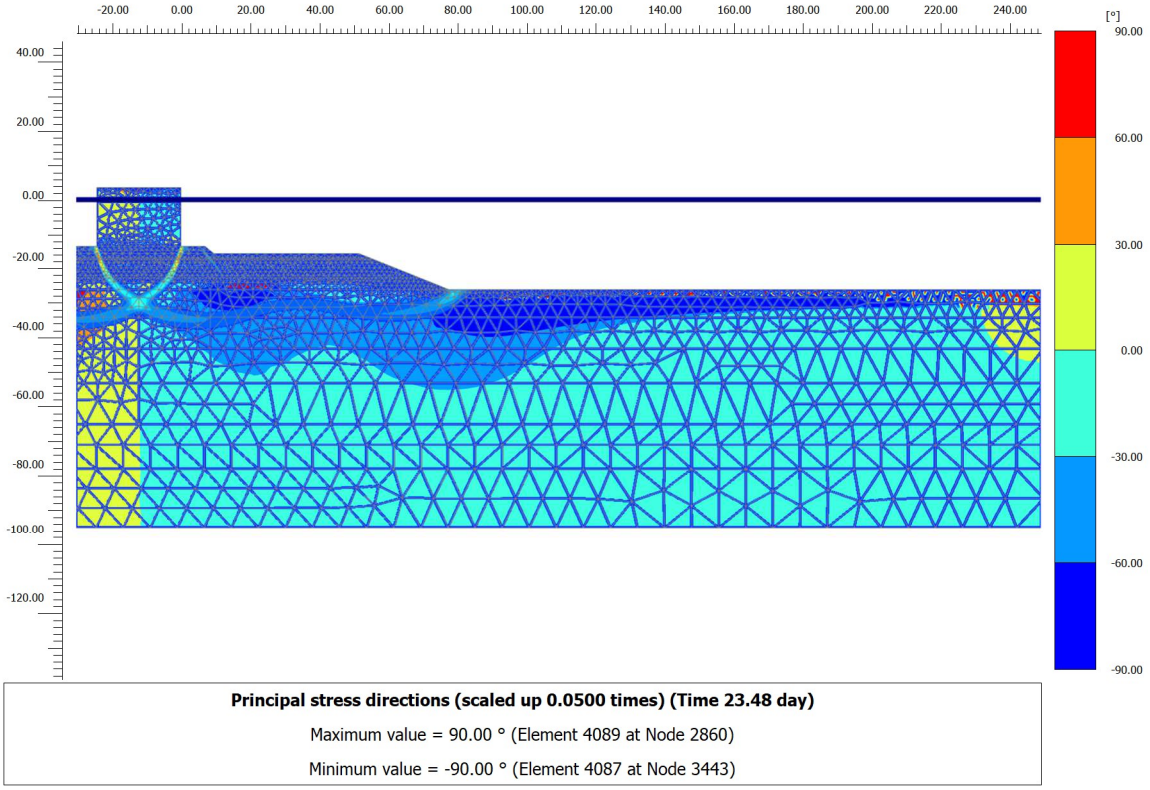

Figure 2-10. Principal stress directions and failure surface computed in a hypothetic breakwater case

Various points in the foundation soil were selected in order to explorer the stress path followed during construction process. Figure 2-11 shows stress paths of selected point beneath the center line of the breakwater and Figure 2-12 shows points at the failure surface. As observed, initially while the soil remains in unyielded state the response is stiff, and small shear induces changes in pore pressure. Also, dissipation of pore pressure can take place, however until yield occurs these give only minor changes in undrained shear strength.

The soil responds in a different way when the stress path reaches the yield surface, shear stress changes lead to larger increase in shear strain and pore pressure, in fact at this stage the soil is deforming plastically.

The process of yielding progress as the height of the embankment is increasing, but it is not until the caisson is placed on the embankment that the foundation soil finally collapses. When points at the center line reach a yielding state, the total stress paths tends to incline sharply to the right in order to maintain equilibrium, which generates extra horizontal loads for neighbourhood points, brings them closer to yield state, at the same time in other zones the total stress remains constant, but the pore pressure continues increasing and pushes the stress path towards yield (Figure 2-13).

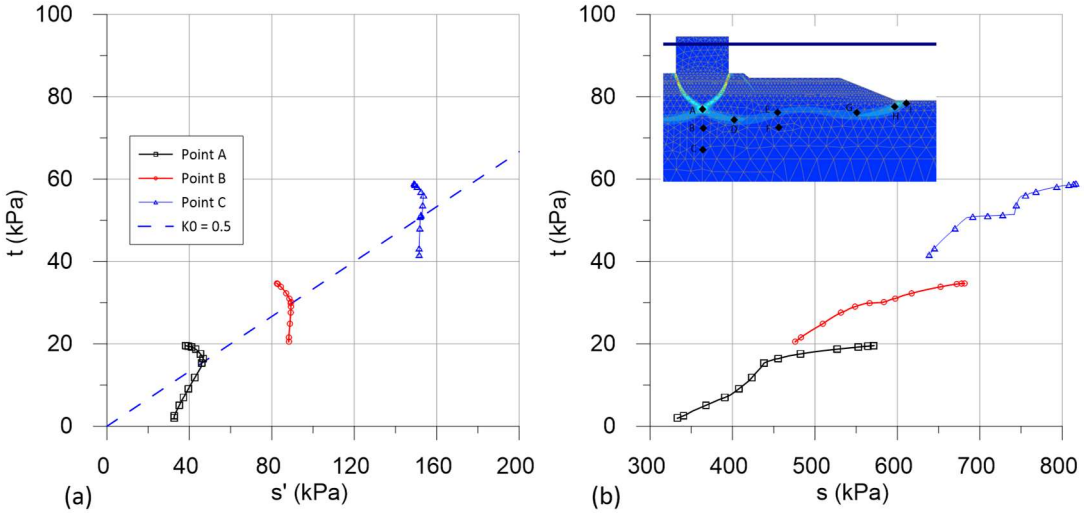

Figure 2-11. Stress paths during loading for points beneath the center line of breakwater (a) effective stress path (b) total stress path.

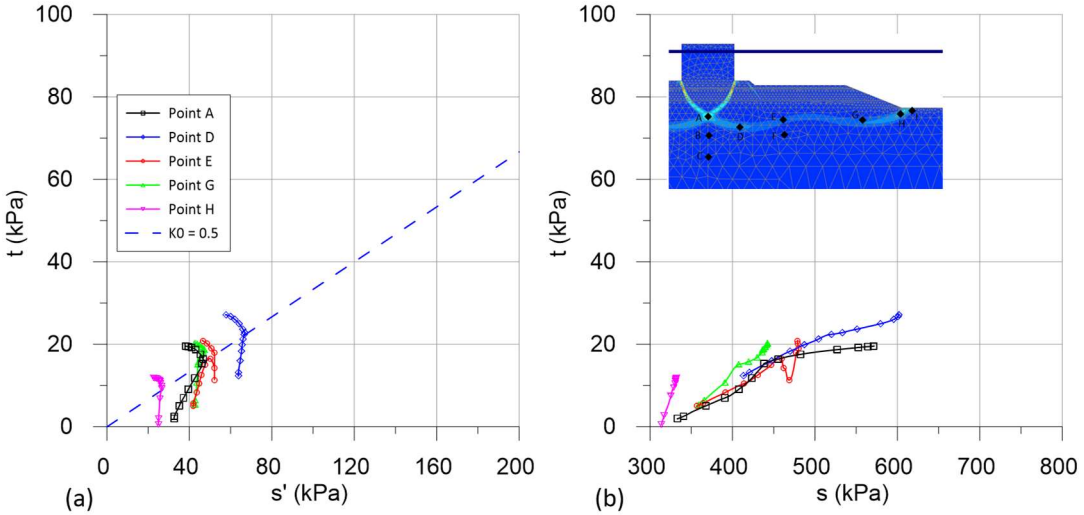

Figure 2-12. Stress paths during loading for points in the failure surface. (a) effective stress path (b) total stress path.

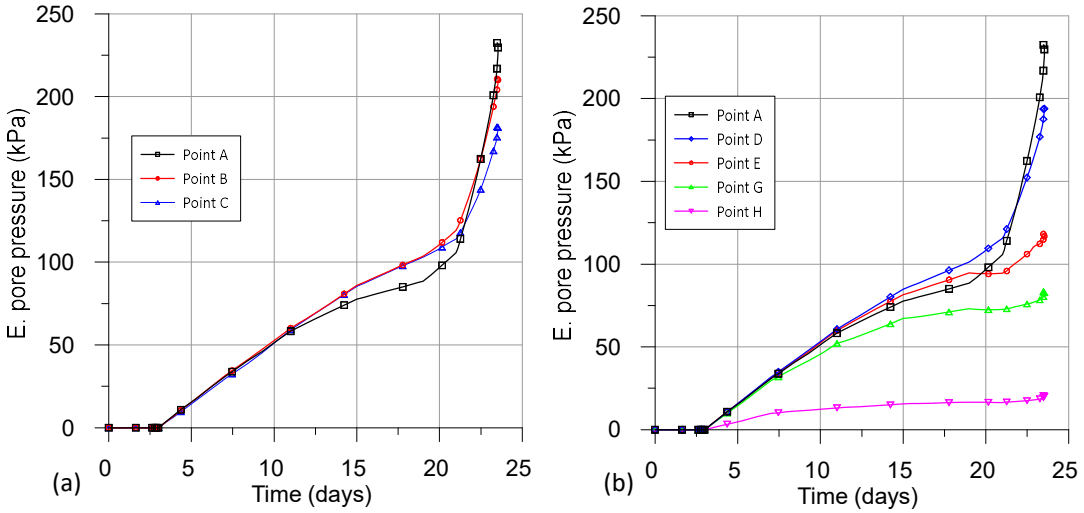

Figure 2-13. Pore pressure predicted by the model at several points (a) points at center line (b) points at the failure surface.

2.4 EVOLUTION OF PORE PRESSURE AND STIFFNESS DEGRADATION

Prediction of pore-water pressure in response to load changes is a main factor to study the performance of a breakwater during the construction phase and during the service life of the breakwater. An increase in pore pressure results in a reduction of the shear strength of soil, changing stability conditions, and sometimes it causes failure when the pore pressure rises to the point that the resistance of soil drops below the acting stress. Construction loads (static) and also the cyclic and impact loads from waves (dynamic loads), are the main responsible for changes of pore pressures, whose mechanism responds to complex hydro-mechanical interactions between soil skeleton and pore fluid.

Loading imposed by a storm can generate pore pressures in soils with poor drainage capacity, which are accumulated at each loading cycle, causing a reduction in effective stress in some areas of foundation soil, and lead to reduced strength and stiffness, this phenomenon is usually known as 'cyclic instability' and in extreme cases can lead to a state of liquefaction.

According to Elsafti and Oumeraci (2016), when water waves attack a marine gravity structure, such as a vertical breakwater, the underlying seabed is affected in two ways: Directly from water waves and indirectly by the breakwater motion induced by water wave loads. As a consequence, pore pressures tend to increase causing the breakwater to fail under certain conditions. Several failures were described by Oumeraci (1994), including the seaward tilt, which was also observed in centrifuge tests (Zhang et al, 2009). Although an explanation for the seaward tilt failure is still unsatisfactory, it has been attributed to several mechanisms, including seabed scour or soil liquefaction underneath the breakwater heel (seaward side). Also, breakwater foundation failures may include the stepwise liquefaction, usually accompanied with significant residual pore pressure as described by De Groot et al (2006).

Kudella et al (2006) found that the caisson-induced pore pressure due to breaking wave impact, is much more significant than the wave induced pore pressure, because it is capable of generating residual pore pressures, whereas non-breaking waves can generate only transient pore pressure without any (residual) pressure build up. The experiments were developed to simulated unfavorable seabed and drainage conditions, similar to those of a loose sand bed with thin clay or silt layers. Following this work, only partial liquefaction can occur in the seabed underneath a caisson breakwater, even under unfavourable drainage conditions. This is due to the large confining effective stresses induced by the own weight of the caisson breakwater.

The main factors that increase the probability of residual pore pressure generation are pore fluid stiffness, soil relative density, ratio of drainage to loading periods and ratio of cyclic shear stress to vertical effective stress (Kudella and Oumeraci, 2004).

Sumer et al. (2008) performed simplified experiments to simulate caisson breakwater movements with a rocking plate over a soil box with the objective to study the effect of the rocking amplitude and frequency on seabed response. Complete liquefaction was observed during some of the experiments, which is explained by the absence of the higher confining pressures that provide the weight of the structure.

An appropriate mathematical formulation to properly modelling seabed response to water waves is required. These fully dynamic governing equation for the interaction of solid and fluid media were first derived by Biot (1941, 1956, 1962a and 1962b) and later generalized to the incremental form by Zienkiewicz (1982), Zienkiewicz and Shiomi (1984) and Zienkiewicz et al (1990a and 1990b) where the non-linear material behaviour was included. The complete formulation is described herein as the 'fully dynamic' (FD), to distinguish it from the simplified u–p formulation, referred to as 'partially dynamic' (PD) and from Biot's original formulation referred to as 'quasi-static' (QS). The fully coupled general equations are briefly described below, follow the Zienkiewicz et al (1999) derivation, where more detail on it can be found.

The overall equilibrium or momentum balance relation for the soil-fluid mixture is described in a Lagrangian framework for the control volume $dV = dx \cdot dy \cdot dz$ as:

$$\nabla \cdot \boldsymbol{\sigma} - \rho \frac{\partial^2 \mathbf{u}}{\partial t^2} - c \frac{\partial \mathbf{u}}{\partial t} - \rho_f \left(\frac{\partial \mathbf{w}}{\partial t} + \mathbf{w} \cdot \nabla \mathbf{w} \right) + \rho \mathbf{b} = 0 \qquad 2.21$$

Where $\boldsymbol{\sigma}$ is the total stress tensor, $\mathbf{u}$ is the displacement vector, $\mathbf{w}$ is the average (Darcy's) velocity of percolating fluid, c is damping coefficient, $\mathbf{b}$ is the body force per unit mass vector, ρ_f is the density of the fluid, ρ is the total density of the solid-fluid mixture defined as:

$$\rho = n\rho_f + (1-n)\rho_s \qquad 2.22$$

Where ρ_f and n are the density of the solid particle and porosity, respectively.

The momentum balance of the fluid phase alone considering the same control volume in an Eulerian framework and assuming the solid phase is the reference:

$$-\nabla p - \mathbf{R} - \rho_f \frac{\partial^2 \mathbf{u}}{\partial t^2} - \rho_f \left(\frac{\partial \mathbf{w}}{\partial t} + \mathbf{w} \cdot \nabla \mathbf{w} \right) \Big/ n + \rho_f \mathbf{b} = 0 \qquad 2.23$$

Where p is the pore pressure and $\mathbf{R}$ represents the viscous drag forces which, can be defined according to the Darcy seepage law as:

$$\mathbf{R}\mathbf{k} = \mathbf{w}\rho_f g \qquad 2.24$$

Where **k** is the permeability tensor.

Finally, the mass balance of flow is described as:

$$\nabla \cdot \mathbf{w} + \frac{\partial \varepsilon_v}{\partial t} + \frac{n}{K_f}\frac{\partial p}{\partial t} + \frac{(1-n)}{K_s}\frac{\partial p}{\partial t} - \frac{K_T}{K_f}\left(\frac{\partial \varepsilon_v}{\partial t} + \frac{1}{K_S}\frac{\partial p}{\partial t}\right) = 0 \qquad 2.25$$

If the factor $\alpha = 1 - K_T / K_s$ defined by Zienkiewicz et al (1999) is introduced and assumed to be equal to 1 as typical for soils, the equation is simplified to:

$$\nabla \cdot \mathbf{w} + \frac{\partial \varepsilon_v}{\partial t} + \frac{1}{Q}\frac{\partial p}{\partial t} = 0 \qquad 2.26$$

Where,

$$\frac{1}{Q} = \frac{n}{K_f} + \frac{\alpha - n}{K_s} = \frac{n}{K_f} + \frac{1-n}{K_s} \qquad 2.27$$

In this equation, K_s is the bulk of modulus solid grains, K_f is the bulk of modulus of fluid, and K_T is the average bulk modulus of solid skeleton.

It is often useful to describe pore pressure changes under undrained conditions with the aid of so-called pore pressure coefficients described in the pioneering work of Skempton (1954):

$$\Delta p = B\left[\Delta\sigma_3 + A\left(\Delta\sigma_3 - \Delta\sigma_3\right)\right] \qquad 2.28$$

The pore pressure parameter A is not a soil constant, varies with the stresses and strains and depends on the past history of the soil. Bishop (1973) demonstrated analytically the expression for the pore pressure coefficient B for a fully saturated porous medium:

$$B = \frac{\Delta p}{\Delta \sigma} = \frac{1}{1 + n\dfrac{C_w - C_s}{C - C_s}} \qquad 2.29$$

In which C_w = compressibility of water = 0.048×10^{-5} vol/vol per kPa. C_w is approximately 25 times greater than C_s, which is in the range of 0.001-0.003 x 10^{-5} vol/vol per kPa for most geological materials. C is compressibility of soil skeleton.

These pore pressure parameters are implicit in the dynamic formulation described by Zienkiewicz et al (1999). In this way, for undrained behaviour with $\nabla \cdot \mathbf{w} = 0$ we have from eq. 2.26:

$$dp = -Q\alpha d\varepsilon_v \qquad 2.30$$

And after assuming that the material is isotropic, the original Skempton (1954) B soil parameter is derived as:

$$B = \frac{\alpha}{K_T/Q + \alpha^2} = \frac{1}{1 + n(K_T/K_f)} \tag{2.31}$$

The pore pressure parameter B should be unity for saturated soils but will be lower than unity for soils with compressible pore fluids, or for porous materials in which the compressibility of the matrix is of the same order as the compressibility of the pore fluid.

Lade and de Boer (1997) presented a more detailed treatment of the compressibility of the grains and derived a more comprehensive formulation of B. Two additional compressibilities were defined related to changes on pore pressure. The expression for the parameter B is derived on the basis of volumetric compatibility between the outside reduction in volume of an element and the inside volumetric compression of the components of the element, which finally yields:

$$B = \frac{\Delta p}{\Delta \sigma} = \frac{1}{\left[1 + n\dfrac{C_w}{C_{sks} - C_{gs}} + \dfrac{(1-n)C_{gu} - C_{sku}}{C_{sks} - C_{gs}}\right]} \tag{2.32}$$

Where, C_{sks} is compressibility of skeleton due to change in total confining pressure and C_{gs} is compressibility of grains due to change in total confining pressure. C_{gu} is compressibility of grains due to a pore pressure change, C_{sku} is the compressibility of the skeleton due to a pore pressure change, and n is porosity.

The terms that contain the variable **w** can be neglected from the governing equations to produce a simplified system known as the u-p form (PD):

$$\nabla \cdot \boldsymbol{\sigma} - \rho \frac{\partial^2 \mathbf{u}}{\partial t^2} - c\frac{\partial \mathbf{u}}{\partial t} + \rho \mathbf{b} = 0 \tag{2.33}$$

$$\nabla \cdot \mathbf{k}\left(-\nabla p - \rho_f \frac{\partial^2 \mathbf{u}}{\partial t^2} + \rho_f \mathbf{b}\right) + \frac{\partial \varepsilon_v}{\partial t} + \frac{1}{Q}\frac{\partial p}{\partial t} = 0 \tag{2.34}$$

Applying finite element discretisation using a Galerkin procedure, with the same interpolation functions used for displacements and pore pressures and incorporating prescribed boundary conditions, we finally obtain:

$$\mathbf{M}\ddot{\mathbf{u}} + \mathbf{C}\dot{\mathbf{u}} + \mathbf{K}\mathbf{u} - \mathbf{L}\mathbf{p} - \mathbf{f}_1 = 0 \tag{2.35}$$

$$\mathbf{L}^T\dot{\mathbf{u}} + \mathbf{H}\mathbf{p} + \mathbf{S}\dot{\mathbf{p}} - \mathbf{f}_2 = 0 \tag{2.36}$$

Where,

$$\mathbf{M} = \int \mathbf{N}^T \rho \mathbf{N} dV \tag{2.37}$$

$$\mathbf{K} = \int \mathbf{B}^T \mathbf{D} \mathbf{B} dV \tag{2.38}$$

$$\mathbf{L} = \int \mathbf{B}^T m \mathbf{N} dV \tag{2.39}$$

$$\mathbf{H} = \int \nabla \mathbf{N}^T k \nabla \mathbf{N} dV \tag{2.40}$$

$$S = \int \mathbf{N}^T \frac{1}{Q} \mathbf{N} dV \tag{2.41}$$

$$\mathbf{C} = \alpha \mathbf{M} + \beta \mathbf{K} \tag{2.42}$$

$$\mathbf{f}_1 = \int \mathbf{N}^T \rho \mathbf{b} dV + \int \mathbf{N}^T \mathbf{t} dS \tag{2.43}$$

$$\mathbf{f}_2 = -\int \mathbf{N}^T \nabla^T \mathbf{k} \rho_f \mathbf{b} dV + \int \mathbf{N}^T \mathbf{q} dS \tag{2.44}$$

The damping matrix C is formulated as a function of the mass and stiffness matrices, using the Rayleigh damping coefficients α and β. Note also that the contribution of solid acceleration in the flow equation was neglected. These equations are incorporated in the finite element code Plaxis (Brinkgreve et al., 2017), which was used for the simulations described in this thesis.

Jeng and Cha (2003) proposed a simple relation for the boundary between the QS and the FD solutions based on the two dimensionless parameters π1 and π2, defined by Zienkiewicz et al (1980), concluding that for most cases in the wave-induced seabed response both the PD and FD solutions yield almost identical results.

Ülker et al. (2009) propose a more general classification, indicating that the inclusion of the inertial terms (FD formulation) have a significant influence on the seabed response. However, in case of soils with small permeability (i.e. clays), the quasi-static approach is sufficiently approximate, except for very low period waves. For highly permeable soils, such as gravel, the FD formulation should be used. In other cases, many factors must be evaluated (e.g. soil permeability, wave period, water depth and degree of saturation of soil) before considering which formulation must be used. Also, it concluded that a maximum discrepancy of 3% is considered between the results obtained from the three formulations. In this study, it was clear that the degree of saturation of soil generally affects the pore pressure response obtained from the FD, PD and QS formulations. As the saturation

increases, larger pore pressures are obtained in the seabed and the differences between the pore pressure responses obtained from the three formulations increase.

Ulker et al (2012) performed parametric studies to investigate the impact of waves and seabed parameters on the induced pore response around a caisson breakwater using the three possible formulations with respect to the inclusion of inertial terms. Analyses show that the partial dynamic formulation produces the highest response amplitudes as compared to the fully dynamic formulation, which is the most complete form. Likewise, it was observed that stresses of very high magnitude develop in the corners of the breakwater due to the rocking movement of the caisson caused by the breaking waves. It should be noted that in these analyses a linear elastic behaviour of the material was used, which greatly influences the observed response.

Another aspect of modelling soil response to water waves refers to the constitutive model used in the formulation. In this context, to simulate residual pore pressure and residual deformations caused by cyclic loading, the soil constitutive model should be able to capture plasticity induced by cycles of loading and unloading rather than by monotonic loading. Therefore, the classical plasticity models (for example, the Cam-Clay model) are not suitable for cyclic loads, because, in many cases, the stress states will fall within the yield surface and a purely elastic response will be obtained.

Stickle et al. (2013) implemented a dynamic structural model to study cohesive soil seabed underneath a rubble foundation of a caisson breakwater with the u–p formulation. The constitutive model used for the seabed is a combination of both a nonlinear elastic model and a generalised plasticity model.

Jeng and Ou (2010) developed a three-dimensional model for the elastoplastic behaviour of seabed around a vertical breakwater. The seabed was treated as a porous medium according to the u–p approximation of the Biot's equations using a generalised plasticity model. In their model, the poro-elastoplastic model is capable of capturing both mechanisms of pore pressure development (instantaneous and residual) simultaneously. They found that the poroelastic models underestimate the liquefaction depth as opposed to poro-elastoplastic models.

Excess pore pressure cannot be generated (undrained conditions) or volume changes (drained conditions) cannot occur until gross particles sliding does not occur (Dobry et al, 1982; Vucetic, 1994). The shear strain corresponding to the initiation of gross sliding is called the volumetric threshold shear strain γ_{tv}. Soils exhibit linear elastic behaviour below a linear cyclic threshold shear strain γ_{tl} that is approximately 30 times smaller than γ_{tv}. Between the linear threshold shear strain (γ_{tl}) and volumetric threshold shear strain (γ_{tv}), the soils begin to exhibit non-linear behaviour, but remain largely recoverable, since the microstructure of the soils remains unchanged. Beyond the volumetric threshold shear strain(γ_{tv}), the soils become heavily non-linear and inelastic. The soil

microstructure changes irreversibly when the shear strain exceeds the volumetric threshold shear strain (γ_{tv}), which finally degrades the stiffness of soil. Based on experimental evidence Vucetic (1994) suggest that the volumetric threshold shear strain increase with plasticity index (PI) (that was later confirmed by Hsu and Vucetic, 2004) and determined that the threshold shear strains have a negligible effect with the OCR value (Hsu and Vucetic, 2006).

The degradation of soil stiffness is primarily a function of the level of cyclic stress within the soil mass. To roughly account for variation in soil stiffness, NGI (1998) has proposed a simplified soil " trough" model, in which the soil mass is divided into a finite number of depressions over depth D and it is assumed to generate a constant shear strain within each individual channel. The model thus allows calculating the stiffness and shear displacement within each channel as a function of the stress level. For clay the effect of cyclic loading on the stiffness can be found by evaluation of the degradation within each trough using the strain accumulation method, which was proposed by Andersen (1976). The cyclic shear strain accumulation procedure uses the cyclic shear strain as a memory to quantify the effect of cyclic loading.

To study the evolution of pore pressure of Barcelona breakwater foundation, a geotechnical instrumentation was installed under the breakwater to capture the characteristics of the ground response during construction and also under cyclic loading produced by large storms. Records of pore pressure during construction and large representative storm was interpreted under the framework of elastoplastic model. Chapter 5 examines this issue in detail.

2.5 DYNAMIC BEHAVIOUR

Due to inertia effects the load transferred from wave impact to the foundation differs from the load that would occur if a stationary hydraulic load with the same peak value would occur. To investigate this effect Oumeraci and Kortenhaus (1994) established the concept of 'dynamic load factor' as a relation between the peak hydraulic load and the equivalent stationary hydraulic load.

$$F_{stat} = \nu_L F_{dyn,\max} \tag{2.45}$$

Also, similar factor can be defined in terms of response (deformation), which is called the 'dynamic resistance factor' (ν_d) and defined as the ratio between the maximum actual response (dynamic) and the maximum static response. This factor can be estimated using a simplified mass-spring-dashpot system with two degree of freedom (2DOF) for representing the horizontal movement (sway) and rotational movement (roll) in a coupled way. The model is largely described in Oumeraci and Kortenhaus (1994) and represents the movement of one isolated caisson or a small number of caissons. The model was verified with hindcasts of several large-scale and full-scale tests performed in the Netherlands on behalf of the Oosterschelde works (Meijers, 1994). More refined models which incorporate the interaction between caissons was developed in the framework

of PROVERBS, but for the purposes of this thesis, the simplified 2DOF model is considered sufficient to verify the numerical model described in Chapter 6. The equations of motion of the 2DOF model can be written as:

$$\begin{aligned} &M_{11}\ddot{x} + D_{11}\dot{x} + D_{12}\dot{y} + K_{11}x + K_{12}y = F_h(t) \\ &M_{22}\ddot{y} + D_{21}\dot{x} + D_{22}\dot{y} + K_{21}x + K_{22}y = F_h(t)\left(h - y_M\right) + F_v(t)\left(x_M - v\right) \end{aligned} \quad 2.46$$

Where M, K and D are the mass, spring and dash-pot matrix of parameters, respectively. The dynamic response of caissons is influence by the interaction with foundation soil and seawater around the caisson. In this way, contribution to mass, stiffness and damping matrix are partly due to rubble foundation, subsoil and seawater. So, the total mass matrix is obtained by considering the mass of caisson, the hydrodynamic mass and the geodynamic mass:

$$\begin{aligned} M_{11} &= \rho_c h_c B L_c + 1.086\rho_w d^2 L_c + 0.76\rho_s R^3 \left/ \left(2-\mu\right)\right. \\ M_{22} &= \rho_c h_c B L_c \left[\left(h_c^2 + B^2/4\right)/3\right] + 0.420\rho_w d^4 L_c + 0.64\rho_s R_i^5 \left/ \left(1-\mu\right)\right. \end{aligned} \quad 2.47$$

Stiffness diagonal mass matrix terms can be derived from Savinov (1955) as recommended by Oumeraci and Kortenhaus (1994):

$$\begin{aligned} k_x &= 0.7C_0\left(1+2\left(B+L\right)/A\right)\sqrt{p/p_0}\,A \\ k_y &= 2C_0\left(1+2\left(B+L\right)/A\right)\sqrt{p/p_0}\,I \end{aligned} \quad 2.48$$

Where the elastic uniform compression coefficient C_0 was adopted as 260 kN/m^3 (soil type 1). Finally, the stiffness matrix was defined as:

$$\begin{aligned} K_{11} &= k_x \\ K_{12} &= k_x\left(H_c - y_M\right) \\ K_{21} &= k_x\left(H_c - y_M\right) \\ K_{22} &= k_y + k_x\left(H_c - y_M\right)^2 \end{aligned} \quad 2.49$$

Damping influence on the dynamic load factor is rather limited (Pedersen, 1997). Significant influence probably occurs only if the foundation is near to failure, in that case plastic deformation dominates the process and a dash-pot does not model the plastic deformation correctly. This effect should be modelled with an appropriate constitutive soil model (not considered at this section). The damping coefficients were determined experimentally by pendulum tests on the caisson prototype by Oumeraci et al (1992) and is described as follows:

$$d_x = 2\sqrt{\frac{\delta_x^2}{4\pi^2+\delta_x^2}}\sqrt{k_x M_{11}}$$
$$d_y = 2\sqrt{\frac{\delta_y^2}{4\pi^2+\delta_y^2}}\sqrt{k_y M_{22}} \qquad 2.50$$

Where δ_x and δ_y are the logarithmic decrement for the horizontal and rotational motion, respectively:

$$\delta_x = \ln\left[\frac{x(t)}{x(t+T_x)}\right]$$
$$\delta_y = \ln\left[\frac{y(t)}{y(t+T_y)}\right] \qquad 2.51$$

Where x(t) is the horizontal motion of the structure, y(t) is the rotational motion of the structure, T_x and T_y are the period of the horizontal and rotational oscillations, respectively, and *t* is the time. Finally, the damping matrix is defined as:

$$D_{11} = d_x$$
$$D_{12} = d_x\left(H_c - y_M\right)$$
$$D_{21} = d_x\left(H_c - y_M\right)$$
$$D_{22} = d_y + d_x\left(H_c - y_M\right)^2 \qquad 2.52$$

This set of differential equations can be solved numerically using the Runge-Kutta method (Press et al, 1988) implemented in Matlab. An isolated impulse force of symmetric triangular shape was defined to excite the model, with a horizontal force Fh_{max}=1011kN/m and uplift force Fv = 310kN/m as defined in section 2.2.3. Using the equations previously defined in relation with the Barcelona caissons geometry, the parameters of the model were:

$$M = \begin{bmatrix} 299745 & 0 \\ 0 & 3823324 \end{bmatrix}$$
$$K = \begin{bmatrix} 3744773 & 7489546 \\ 7489546 & 545809329 \end{bmatrix} \qquad 2.53$$
$$D = \begin{bmatrix} 54297 & 108595 \\ 108595 & 2526014 \end{bmatrix}$$

Results of the analytical model are presented in the Figure 2-14. Displacement (swap mode) under static and dynamic load condition are compared and the dynamic resistance factor v_d is computed as 0.77. In order to determine the natural frequency of vibration, the time-history signal was transformed to the frequency domain using the Fast Fourier Transform (FFT). Figure 2-15 shows

that the dominant frequency of the model is about 0.53 Hz. Lee et al (2013) carried out prototype tests on a 2D wave generating flume with water level variation, in order to study the vibration characteristic of caissons. They observed that the natural frequency gradually increases as the water level decreases. Thus, 22.05% of the natural frequency increases when the water level decreases by 12.9% of the caisson height. In addition, it was observed that the damping ratio shows a tendency to reduce as the water level decreases.

The dynamic response factor v_d can also be computed with the caisson array model developed in the framework of Proverbs project as shown in the Figure 2-16. As observed in this figure, for $T_d/T_n<0.5$ the response to every impulsive force shape is similar. Between $0.5<T_d/T_n<1$ the observed response is an amplification effect of almost 1.4 times. Finally, for $T_d/T_n>1$ the response is different for a symmetric (or moderately asymmetric) loading compared to an asymmetric loading (i.e. loading cases of long duration) the first case is well represented by the static model, while the second one causes a relevant overshooting. For a triangular impulse force with a duration time (T_d) of 0.5 s, a response factor (v_d) of 0.75 is obtained which is consistent with the one obtained in the simplified model.

The dynamic characteristics investigated with the simplified model are then used to verify the finite element model described in section 6.3.

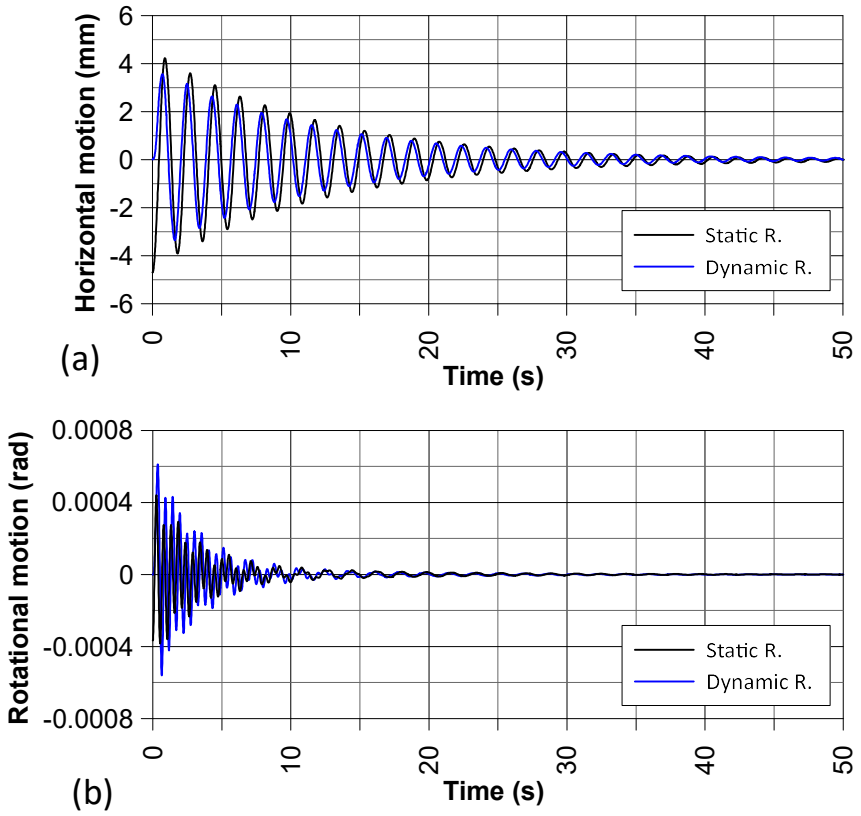

Figure 2-14. Displacement (swap mode) computed with the analytical model.

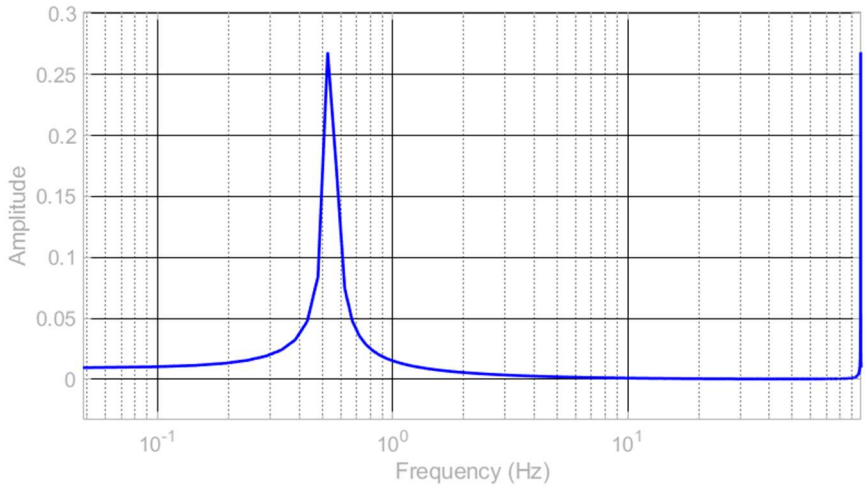

Figure 2-15. Fourier spectrum computed with the results of analytical model.

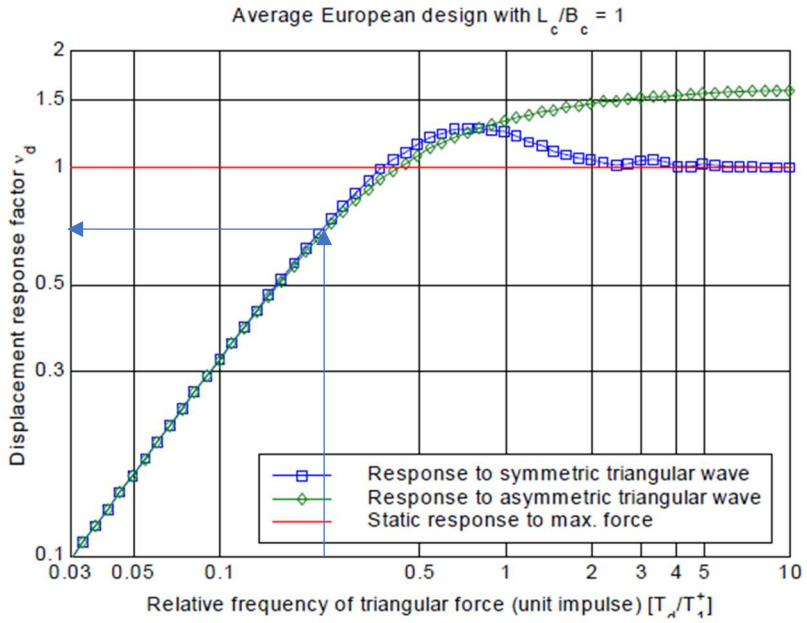

Figure 2-16. Dynamic response factor as a function of the ratio between impact duration t_d and natural period T_N for two values of impact rise time t_r with and without some damping (de Groot et al, 1995).

2.6 FAILURE MODES AND STABILITY ANALYSIS

Stability problems are concerned with the collapse of the structure, which is produced when the shear stresses required to maintain equilibrium reach or exceed the available shearing resistance on some potential failure surface. The way this potential failure surface is defined depends not only on the structure, but also on soil properties and boundary conditions and define the mode or mechanism of failure. In case of breakwater, De Groot (2001) defines four basic modes of geotechnical failure: sliding along the base, bearing capacity failure in rubble, bearing capacity failure in subsoil, and settlement by consolidation, creep or erosion in fine grained soil. However, from a mechanical point of view, geotechnical failures modes can be classified as follow (Figure 2-2):

- Overturning
- Sliding of caisson
- Global Instability or bearing capacity

Settlements, although is the reason of many observed past failures of breakwaters, are not in themselves a failure mechanism, rather is a response of soil under certain conditions, mainly due effective stress changes. Of course, settlements must be within tolerable limits in order to satisfy serviceability criteria and avoid damage to the structure. Uncontrolled settlement can lead the breakwaters to not fulfil its function and finally to collapse of the structure, this is the reason why it is very important to estimate the magnitude of ground settlement, rate of settlement and the maximum allowable settlement, especially in soft soil foundations.

There are several methods of stability analysis but currently the most used ones are limit equilibrium analysis, and stress-strain analysis with the finite element method. Regardless of the method used, stability analysis is usually expressed as a factor of safety, which is the ratio of capacity (shear strength of the soil) to demand (shear stress induced on the potential failure surface). Also, the factor of safety can be viewed as the factor by which the strength of the soil would have to be divided to bring the structure to an instable condition. Loads and factors affecting stability must be determined in the best way and, not less importantly, the soil response must be idealized in an approximate enough model.

2.6.1.1 Overturning

The basic form of the overturning mechanism corresponds to a problem of statics that does not depend on soil properties. Soil is assumed to be fully rigid so that overturning is defined as the rotation with respect to the heel of caisson.

Sekiguchi & Omaki (1992) developed a theory of overturning, proposed and solved the equation of motion, which shows that the angle of rotation of caisson during a storm depends on the structural properties of the caisson (inertial and geometric properties) and the wave period. Also, it is noted that waves of a longer wave period are more threatening to stability of a given caisson against overturning, than the waves of a shorter wave period are, if wave amplitudes are the same magnitude.

Following Sekiguchi & Omaki (1992) formulation, it is noted that caissons are more vulnerable to overturn when some initial degree of deformation is present to trigger overturning. That means overturning can be interpreted as two stages process: first stage corresponds to deformation of foundation as a response of the highly eccentric load induced by wave storm; once the caisson has reached a potentially unstable position, start the second stage, which correspond to overturning itself.

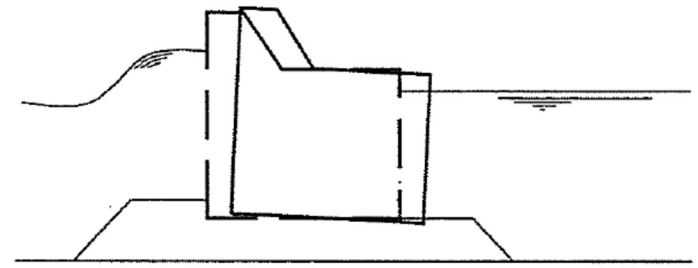

(a)

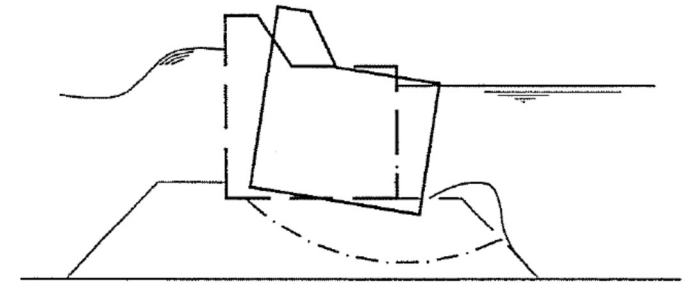

(b)

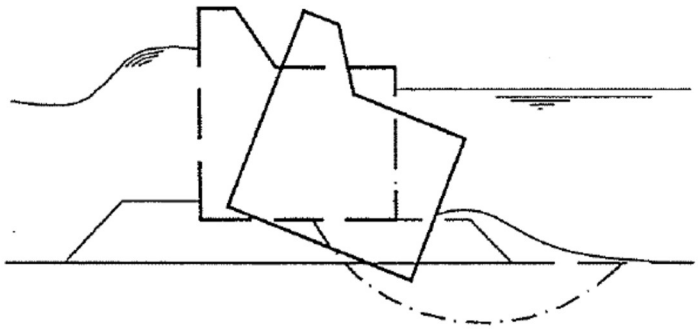

(c)

Figure 2-1. Failure modes of vertical breakwaters (a) Sliding, (b) Overturning (c) Global instability with failure in rubble (c) Global instability with failure in subsoil (PROVERBS, 2001)

Spanish code ROM 0.5-05, defines two types of overturning: rigid overturning and plastic overturning. The first one, refers to the static problem, in which the caisson rotate around the caisson heel over a totally rigid base and the last one introduces a local plastic zone in the contact of caisson foot and embankment. This plastic zone is a result of the large load eccentricity, which produce soil failure and subsequent overturning. ROM 0.5-0.5 develop a procedure to estimate horizontal load that cause soil plastification based on the general bearing capacity equation and compute the safety factor for overturning as the relation between the horizontal load that produce plastification and the initial horizontal load. It seems that this procedure confuses a local bearing capacity mechanism with overturning. In this way, failure does not necessarily imply overturning, but can be the trigger for overturning.

To evaluated stability condition against overturning the resultant of forces must be computed and their projection on the caisson base must be verified to be on the central third of the base. Also, a factor of safety against overturning can be defined as a relation of moments:

$$F = \frac{M_r}{M_o} \tag{2.54}$$

Where:

M_r = moments of forces tending to resist overturning about the heel
M_o = moments of forces tending to overturn about the heel

2.6.1.2 Sliding

Following ROM 0.5-0.5 the factor of safety against sliding may be expressed by the equation:

$$F \leq \frac{H_f}{H} \tag{2.55}$$

Where:
H_f = Horizontal driving forces that produce failure
H = Initial horizontal acting force
F = Factor of safety (usually 1.5 under static condition)

Unlike overturning, the sliding failure mode is related to the shear strength parameters of the foundation.

2.6.1.3 Global instability

Sliding and global instability are both modes of failure related to the shear strength of soil. The main difference between both is on shape of the failure surface, for sliding it is defined in the interface between caisson and rubble mound, while for global stability the failure surfaces may cross the rubble mound and pass through the foundation soil (Figure 2-2). Although limit equilibrium analysis can be used in order to assess the factor of safety, in this investigation the stress-strain analysis is preferred, which has the advantage of being able to identify the most likely mode of failure, locating critical zones of stress, and also predicting the effects of breakwater failure. The accuracy of stress-strain analysis is strongly influenced by the way the constitutive model reproduces the stress-strain behaviour of soil, which is an important topic in this thesis.

The classical problem of bearing capacity is also a problem of stability and therefore, using the traditional equations of bearing capacity (Terzaghi, 1943) and the respective factors for considering the effect of eccentricity and inclination of the load (Meyerhof 1953; Brinch-Hansen 1970; Vesic 1975), at first seem directly applicable to the problem of port caissons. However, due to the action

of large forces of waves that occur during storms, caissons are exposed to a set of vertical loads, horizontal, and moment (VHM), which combined lead to complex failure mechanisms (Sekiguchi & Ohmaki, 1992). In these situations, traditional bearing capacity equations lead to quite conservative results. Research on foundations in homogeneous clays have shown that under combined loading (VHM) traditional equations may underestimate the true bearing load up to more than 20% (Ukritchon et al. 1998).

The problem of course is much more complex as it departs from the traditional problem of a foundation on homogeneous soil. Vertical breakwaters on soft soils (such as the ones constructed at the Port of Barcelona) often consist of a reinforced concrete caisson founded on an embankment rockfill. For such situations, there are no analytical solutions. In the absence of analytical solutions to study the bearing capacity of caissons founded over rockfill embankments, which in turn are subjected to the action of combined loads (VHM), numerical tools are preferred. The finite element method is presented as the most attractive alternative. In this way, not only the bearing capacity problem is treated, but also the global stability under several conditions of loads is dealt with.

There is enough experience in the use of finite elements to study problems of soil-structure interaction in service, having books and manuals with recommendations for practical application (i.e. Potts & Zdravkovic, 2001; Potts, 2002). However, its use under ultimate limit state conditions, to estimate factors of safety in geotechnical projects, requires some special care, both in numerical methodology and the criteria for establishing the stability conditions. This difficulty is of special interest in incompressible materials (such as clays in undrained conditions), since several studies have reported an erroneous stiffening stress-strain response, a phenomenon known as 'locking' and reported in literature by several researchers (Sloan & Randolph 1982; de Borst & Vermeer 1984, Yu & Netherton 2000).

In the framework of finite element analysis, the method of strength parameter reduction is becoming a standard for stability analysis. In this approach, the shear strength parameters tanφ and c of the soil as well as the tensile strength are successively reduced until failure of the structure occurs. In this way safety factor at a given stage of the analysis is defined as:

$$SF = \frac{\tan\varphi_{input}}{\tan\varphi_{reduced}} = \frac{c_{input}}{c_{reduced}} = \frac{S_{u,input}}{S_{u,reduced}} = \frac{Tensile\_strength_{input}}{Tensile\_strength_{reduced}} \qquad 2.56$$

Where the subscript 'input' refers to the properties entered in the material sets and subscript 'reduce' refer to the reduced values used in the analysis. This definition is equivalent to the one used in the limit equilibrium method, moreover, investigation has shown that stability analysis using the finite element method produce nearly the same factor of safety as the limit equilibrium method (Griffiths and Lane, 1999).

The definition of failure surface is natural in a finite element model, through the zones in which the shear strength of the soil is insufficient to resist the shear stresses, so it depends on soil properties, geometry of the model and loading conditions. Figure 2-8 shows a caisson founded over a rubble mound embankment on soft soil, while Figure 2-9 show the same rubble mound embankment, but now over a hard soil. Keeping all the numerical parameters constant, the failure surfaces obtained after the phi-c reduction computation show different mode of failure, in the first case it shows a global instability mechanism and in the last case it shows a sliding mode of failure.

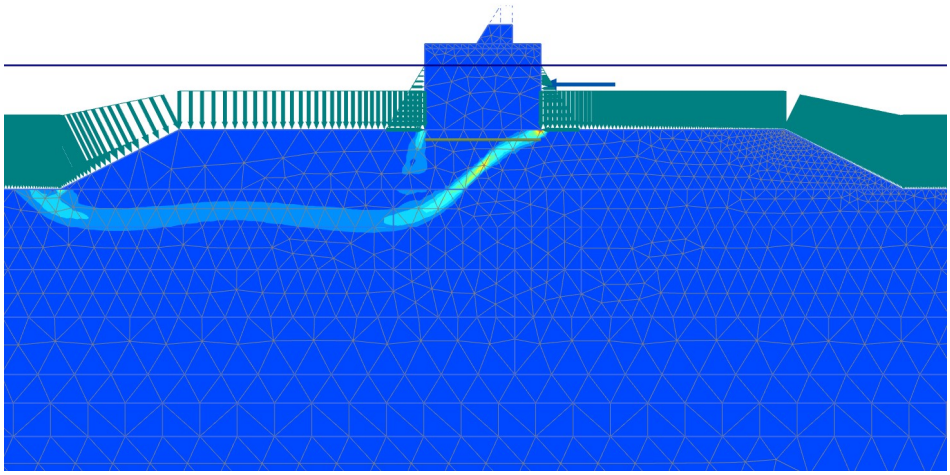

Figure 2-17. Caisson founded on rigid embankment over soft soil.

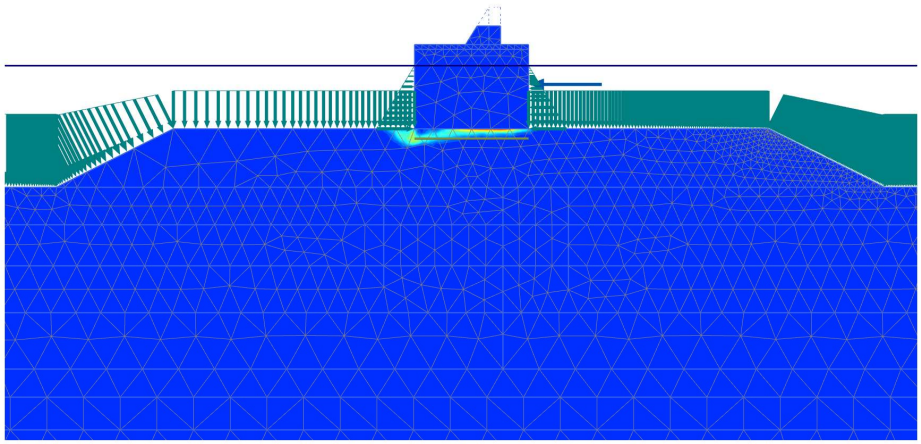

Figure 2-18. Caisson founded on rigid embankment over hard soil.

This thesis intends to approach the study of the stability of caissons breakwater from two perspectives: First, the bearing capacity of caissons and other modes of failure related with short term condition are treated, both under static and cyclic loads. After that, the long-term behaviour is studied. Chapter 7 is devoted to the analysis of stability in the context of the construction of the Barcelona breakwater.

2.7 SETTLEMENTS

To make estimates of settlement it is quite usual to separate primary consolidation and secondary compression:

- Primary consolidation, which occurs during the dissipation of interstitial pore pressure behaves according to Terzaghi's theory or the more general Biot's theory.
- Secondary compression, which corresponds to deformations that occur after interstitial pore pressures have dissipated.

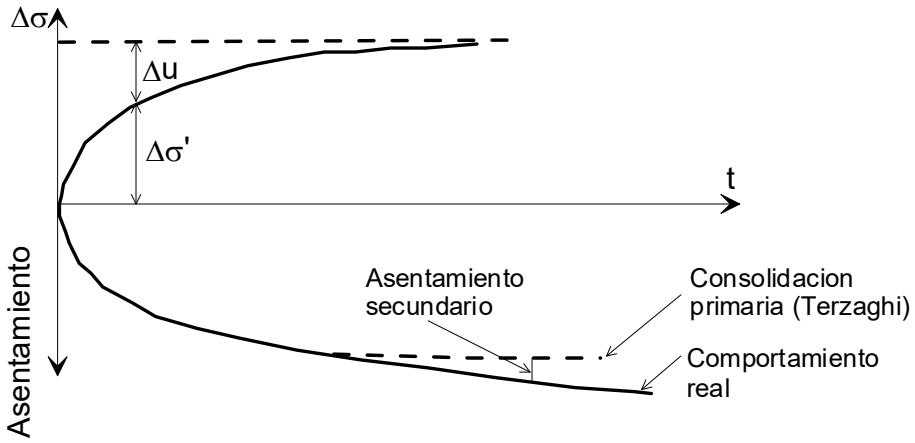

Figure 2-19. Diagram representing the phenomenon of secondary compression

Even though the behaviour of a breakwater is better represented by 2D or 3D models, a simplified analysis based on the one-dimensional consolidation of the soil is appropriate to quickly interpret the evolution of pore pressures and settlements during the construction process. Terzaghi's consolidation theory was extended by Olson (1977) to consider the case of time-dependent loads, which is more suitable for use in a stage construction procedure of a breakwater. For the case corresponding to a ramp load, the primary consolidation equations are:

$$T \le T_c; \overline{u} = \sum \frac{2q_c}{M^3 T_c} \sin \frac{Mz}{H} \left[1 - \exp(-M^2 T)\right] \qquad 2.57$$

$$U_v = \frac{T}{T_c}\left\{1 - \frac{2}{T}\sum \frac{1}{M^4}\left[1 - \exp(-M^2 T)\right]\right\} \qquad 2.58$$

$$T \ge T_c; \overline{u} = \sum \frac{2q_c}{M^3 T_c}\left[\exp(M^2 T_c) - 1\right] \sin \frac{Mz}{H}\left[\exp(-M^2 T)\right] \qquad 2.59$$

$$U_v = 1 - \frac{2}{T_c}\sum \frac{1}{M^4}\left[\exp(M^2 T_c) - 1\right] \exp(-M^2 T) \qquad 2.60$$

In which, $T_c = \frac{c_v t_c}{H^2}$ is the time factor at the end of construction, q_c is the ultimate applied load and $M = \frac{1}{2}\pi\left(2m+1\right)$.

Experimental evidence has shown the existence of delayed deformations not directly associable to hydrodynamic phenomena described with the classical theory of consolidation. In the 30s, Buisman (1936) reports differences with respect to the results predicted by Terzaghi's consolidation theory. These differences consisted mainly of an increase in settlement even when the interstitial pore pressure had already largely dissipated (see Figure 2-19). In this case, the viscosity of the solid skeleton plays an important role when the soil is loaded. This type of viscous or rheological deformation is often referred to as secondary compression or creep deformation to distinguish it from the hydrodynamic deformation, often referred to as primary consolidation. In reality, the distinction between both types of deformations is not clear because secondary compression occurs as part of the primary consolidation phase, especially in soft clays.

A simple way to quantify secondary compression is through the secondary coefficient of consolidation, which is defined as the slope of the last part of the settlement - log (t) curve for each of the loading steps of a consolidation test. In order to make dimensionless the mentioned slope is expressed in terms of deformation instead of settlements.

$$C_\alpha = \frac{\varepsilon}{\Delta \log t} = \frac{\Delta H / H_0}{\log\left(t/t_0\right)} = \frac{\left(H_0 - H\right)/H_0}{\log\left(t/t_0\right)} \tag{2.61}$$

Where H_0 is the original height of the sample corresponding to time t_0.

A simple procedure for the calculation of secondary settlements in practice (NAVFAC DM-7.1, 1986) is to multiply C_α by the thickness of the compressible stratum and by $\log(t/t_0)$, where t_0 is the time that marks the end of the primary consolidation and t is the time for which the secondary settlement is sought (useful life of the structure). Of course, a calculation of this type is very conditioned by the choice of t_0 that is always uncertain. In this sense, the practical calculation of secondary settlements of real structures is still unsatisfactory.

Bjerrum (1967) in his Rankine Lecture shows the effect of time on the mechanical behaviour of Drammen clay, proposing a unique relationship between the void ratio, vertical pressure and time; this relationship is represented by slightly curved parallel lines (see Figure 2-20). An additional curve represents the undrained shear strength of the clay as a function of the soil void ratio, indicating that an increase in soil strength is effectively achieved under a constant load, since delayed compression occurs over time. These ideas provide the background for the development of advanced time-dependent constitutive models, such as the 'Soft Soil Creep' model, which incorporates volumetric hardening as a function of time.

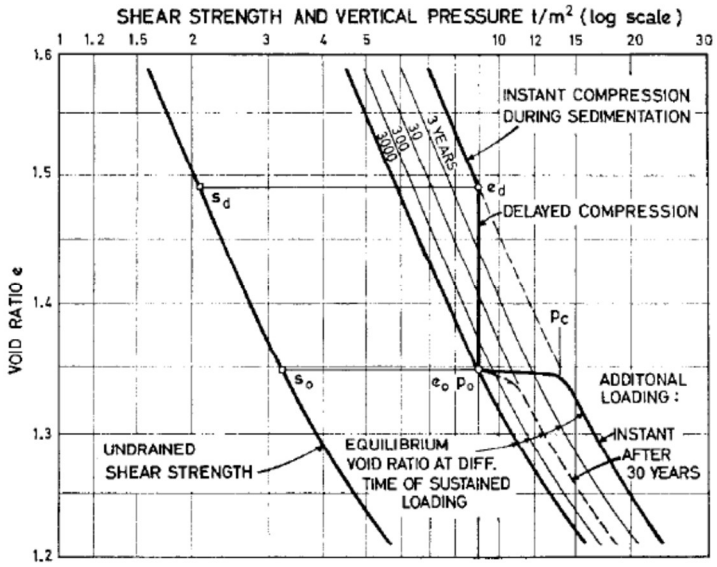

Figure 2-20. Compressibility and shear resistance of a clay that presents a secondary compression (Bjerrum, 1967).

Bjerrum goes further and introduces the terms “instant compression” and “delayed compression” to describe the reaction of clay with respect to an increase in effective stresses; terms that differ from the classical concepts of “primary compression” and “secondary compression”, which separate compression into components that occur before and after the excess pore pressure has dissipated.

The differences between both concepts can be seen conceptually in Figure 2-21. The dotted line shows the reaction of a soil structure in the event that the water pressure in the pores of the clay was unable to slow the compression, and the applied load was instantaneously transmitted to the structure of the clay as an effective stress. This curve defines the instantaneous and delayed compression. On the other hand, considering the permeability of the soil and the viscosity of the water, it is clear that the effective stress will increase gradually as the pressure in the pores dissipates and the compression will adjust to the behaviour of the full line. As the time required to dissipate the excess pressure in the pores depends on several factors such as the thickness of the clay strata, their permeability and the drainage conditions, the separation of the compression of the soil in its primary and secondary components is highly arbitrary; hence Bjerrum suggests that this division is not adequate to describe the behaviour of soil structure with respect to effective stresses. This type of division is equally inconvenient in the implementation of constitutive models that could be used in numerical simulations.

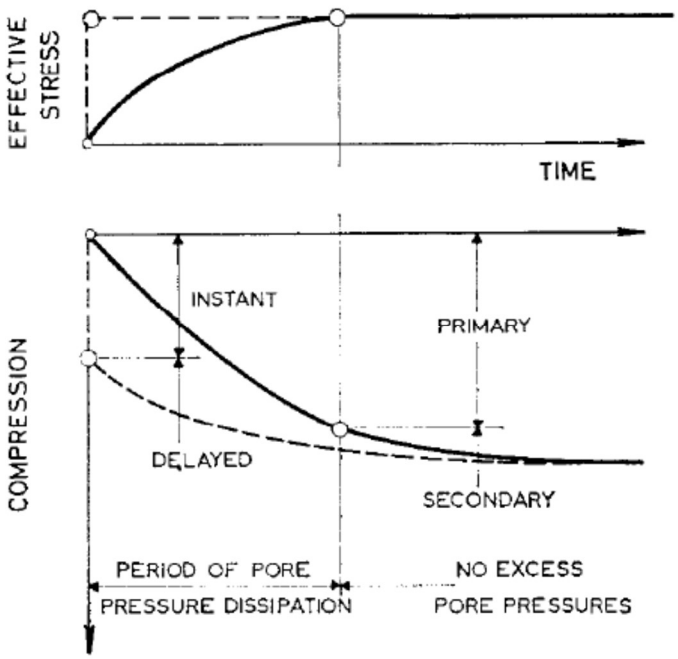

Figure 2-21. Comparison between instantaneous and delayed compression with primary and secondary consolidation (Bjerrum, 1967).

Another important aspect that Bjerrum emphasizes, is related to the really slow velocity with which the water flows in the clays, which governs the velocity of volumetric change during the application of loads. In this sense, the hydrodynamic delay, which is insignificant for the relatively small velocity of volume changes that prevails during delayed compression, completely governs the instantaneous compression rate. Also, if the pressure increase is less than preconsolidation pressure minus the initial stress (p_c-p_0), the pressure in the pores will dissipate rapidly. In this case the instantaneous compressibility will be small and the total amount of water flowing from the soil during the consolidation will also be relatively small. Therefore, as the increase in effective stress exceeds p_c, the importance of the hydrodynamic delay increases. In Figure 2-22 a system of curves shows the type of consolidation curves that can be found for different load increases in relation to p_c. This situation makes the determination of the time in which the primary consolidation ends even more difficult.

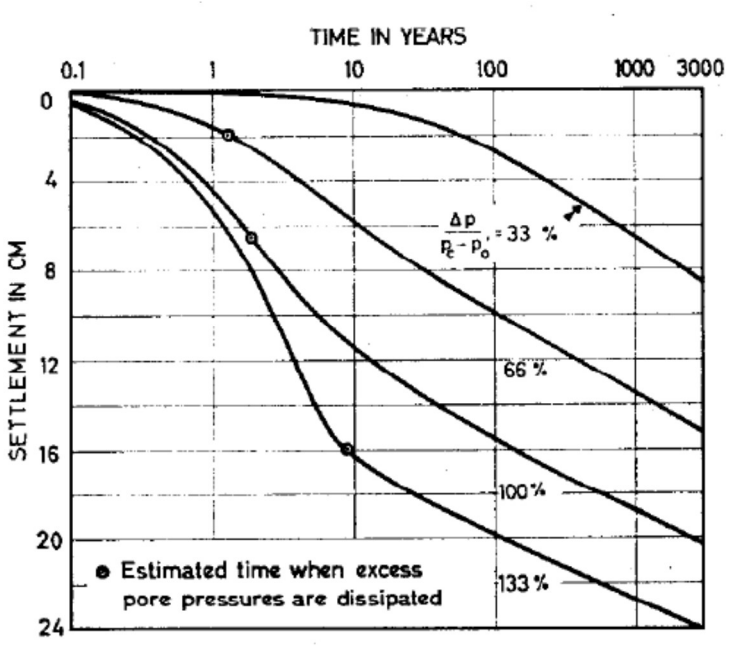

Figure 2-22. Different consolidation curves indicating the end of primary consolidation (Bjerrum, 1967).

The ideas proposed by Bjerrum are the basis for the subsequent development of visco-plastic models such as the 'Soft Soil Creep' model, which is described in the next chapter. However, it is also possible to obtain simple solutions by using classical theory, incorporating the secondary compression component and the preconsolidation pressure in the equation. In this way, a more general expression, which can be easily programmed in a spreadsheet is as follows:

$$\Delta e = C_s \log\left(\frac{p'_c}{p'_0}\right) + C_c \log\left(\frac{p'_f}{p'_c}\right) + C_\alpha \log\left(\frac{t_{eoc}+t}{t_{eoc}}\right) \tag{2.62}$$

Where: C_s is the slope that corresponds to the unloaded-reloaded section and t_{eoc} is the time corresponding to the end of the primary consolidation. In this case the secondary deformations depend exclusively on the coefficient C_α, which can be modified to introduce the effect of the preconsolidation pressure and the increase of effective stresses. Alonso et al (2000) proposed the following equation to compute the increase in vertical secondary deformation $\varepsilon_2^s - \varepsilon_1^s$ due to a time variation from t_1 to t_2:

$$\varepsilon_2^s - \varepsilon_1^s = \begin{cases} \dfrac{\sigma'_2 - \sigma'_0}{\sigma'_{ref}}\left(C_{\alpha\,min} + (C_{\alpha\,max} - C_{\alpha\,min})\exp[-C_{\alpha\,dec}(OCR_1 - 1)]\right)\log\left(\dfrac{t_2 - t^*}{t_1 - t^*}\right), & \text{si } t_2 > 0.848\dfrac{H^2}{c_v} \\ 0, & \text{si } t_2 \le 0.848\dfrac{H^2}{c_v} \end{cases} \tag{2.63}$$

Where:

σ'_2 vertical effective stress at time t_2

σ'_0 Initial vertical effective stress at $t_0 = 0$

σ'_{ref} Reference vertical stress

$C_{\alpha\ max}$ Maximum secundary compression index (OCR = 1) for $\sigma' = \sigma'_{ref}$

$C_{\alpha\ min}$ Minimum secundary compression index (OCR = ∞) for $\sigma' = \sigma'_{ref}$

$C_{\alpha\ dec}$ Transition coefficient between $C_{\alpha\ max}$ and $C_{\alpha\ min}$ for $\sigma' = \sigma'_{ref}$

OCR_1 Over consolidation ratio at time t_1

H Half layer thickness

C_v Coefficient of consolidation

t * Time used for smoothing the solution

2.8 SUMMARY AND CONCLUSIONS

This chapter presents a description of some specific aspects of breakwaters, that are useful to interpret the performance of Barcelona Port breakwater at the stages of construction and post-construction. The first part of the chapter has been devoted to review the various types of loads acting on the breakwater, focusing on estimating the sea waves load. Three different types of wave load were identified: Non-breaking wave, breaking wave and breaking wave with large air pocket (Impact load). The parameter map proposed by Kortenhaus and Oumeraci (1998) to identify types of wave load on the vertical breakwater based on the geometry of the breakwater and the characteristics of the wave has proved useful to evaluate the typical wave of the Barcelona breakwater, which resulted in an "impact load" type wave classification.

Although more sophisticated procedures have been proposed to predict impact loading under the PROVERBS Project (Oumeraci et al, 2001), Goda's formula remains the most widely used design formula for wave impact loads, possibly due to its practicality. For this reason, the Goda formulas have been used to establish the impact load of the waves and the Rayleigh distribution to calculate the number of waves impacts and their horizontal and uplift forces applied in the stability analysis of Barcelona breakwater described in the Chapter 7.

Stress path followed during construction of a typical breakwater were computed with a finite element model. This model shows that the stress path away from the center line experience rotation of principal stress directions, as a consequence, failure develop under active ($0<\alpha<-30$), simple shear ($-30<\alpha<-60$) and passive ($-60<\alpha<-90$) plain strain mode.

Modelling the evolution of pore pressures as a result of the application of wave loading requires a suitable mathematical formulation. Various formulations have been derived and used in the context of numerical models (generally finite element models), mainly based on the work of Zienkiewicz (1982). The fully coupled governing equation can be reduced to a two-variables form, which is

called u-p formulation or partial dynamic formulation, furthermore, the inertial term can be neglected to derive the quasi-static formulation. Ulker et al (2009) have shown that the differences between these simplified formulations and the fully dynamic formulation are negligible for low permeability soils.

Even if at present time there are adequate models to simulate the soil skeleton–pore fluids interaction accurately in the sea floor dynamics framework (Ulker et al., 2010, 2012), this is not yet the case for the constitutive models required to reproduce satisfactorily the seabed soil response. Most soil models used in the investigations of sea floor dynamics have been limited to the poroelastic model (Jeng, 2003). Only a few studies (Sekiguchi et al., 1995; Richwien and Wang, 2000; Pastor et al., 2006; Stickle, 2010, Elsafti and Oumeraci, 2016) have incorporated advanced constitutive relations that are able to represent properly the features of soil response under cyclic loading.

An important issue of a vertical breakwater is the dynamic behaviour during a storm. This factor can be estimated using a simplified mass-spring-dashpot system with two degree of freedom (2DOF) for representing the horizontal movement (sway) and rotational movement (roll) in a coupled way. In this sense, a simplified model described by Oumeraci and Kortenhaus (1994) was used, which represents the movement of an isolated caisson or a small number of caissons. The set of differential equations was solved numerically using the Runge-Kutta method (Press et al, 1988) implemented in Matlab considering the parameters of the Barcelona breakwater. The results made it possible to identify the dominant frequency of the model at approximately 0.53 Hz. This result is significant to subsequently verify that the dynamic model developed in finite elements captures the expected vibration frequencies.

The typical failure modes identified in the vertical breakwater analysis (overturning, sliding and global instability) and the recommendations for their evaluation were described first as recommended in various codes (i.e. ROM 0.5) and secondly in the context of finite element models, used to derive to the safety factors defined in chapter 7 to analyse the stability of the breakwater.

The analysis of the failure modes of caisson breakwaters has revealed the significance of the consideration of dynamic approaches for stability analysis, because the successive build up and dissipation of pore pressures strongly affect the mechanical behaviour of soils. It becomes more significant for cases of soils with higher permeability under higher frequency loading.

Last, and not least, it is the issue of breakwater settlements. Interpretation of the measurements described in Chapter 5 requires a framework derived from consolidation theory. More precisely, the theory of consolidation under variable loads in time (Olson, 1977) is suitable for a construction process in stages. In addition, as it is typical in soft soils, secondary compression or creep constitutes a relevant part of the total settlement. The ideas of Bjerrum (1967) have been described

as the basis for the soft soil creep model described in Chapter 4 to simulate the long-term behaviour of the breakwater.

Chapter 3

MECHANICAL BEHAVIOUR OF THE BARCELONA PORT SOFT SOIL - EXPERIMENTAL EVIDENCE

3.1 INTRODUCTION

Understanding and interpreting the mechanical behaviour of soft soil is a key element to asses stability and settlement of breakwaters. It is noted that the mechanical response of soft clays is greatly influenced by the depositional environment (composition and fabric) in which the clay was formed and the post-depositional changes (stress-time history and chemical history) to which the clay was subjected (Hight et al, 1987). In that sense, slow rates of deposition are often associated with soils of open structure and lower density and therefore more compressive under breakwater loading (Leonards and Altschaeffl, 1964). Structure is also responsible of anisotropic behaviour observed in natural clays. As defined by Burland (1990) the structure of a natural soil consists of the combination between the fabric, representing the arrangement of the particles and pore space, and the bonding representing the interparticle forces between the clay particles.

Descriptions on this chapter are based on the extensive laboratory investigation of Port Barcelona clay developed during breakwater construction project at several times (RODIO, 1996; EURO GEOTECNICA, 1999; UPC, 1997; UPC, 2001; NGI, 2002; NGI, 2009, CEDEX, 2008; UPC, 2008). Although careful techniques were employed in field and laboratory work, it is always difficult to obtained good quality samples to study behaviour of soft soil. To reduce the influence of sample disturbance, all triaxial tests were performed following the recompression technique SHANSEP (Stress History and Normalized Soil Engineering Properties) developed by Ladd and Foott (1974). Samples were consolidated well beyond the initial vertical stress (estimated from the depth of samples), at several stress states along the K_0 line before shearing.

In this Chapter, the mechanical behaviour of soft clay, under monotonic and cyclic loading is described. Undrained strength and stiffness of soft clay is examined under several shear modes associated with the stress path follow in breakwater projects, which included compression and extension K_0 triaxial tests, static and cyclic simple shear tests and resonant column tests. The experimental results of several clays available in the literature are analysed and compared with tests performed on undisturbed samples of Port of Barcelona clay.

For the purposes of this thesis soft soil will be defined as clay or silty clay, normally or lightly overconsolidated which is geologically young with no significant post depositional effects. The main characteristic of these soils is the large deformation produced under construction loads, which could lead to failure of the breakwater. Post-depositional effects are less pronounced in more recent deltaic soft clays, like Barcelona Port clay, and therefore they are not studied in this thesis.

3.2 UNDRAINED STRENGTH

The strength of a soil is largely influenced by drainage conditions during shear, which can be described as undrained (full generation of pore pressure), drained (full dissipation of pore pressure) or partially drained (partial dissipation of pore pressure) mainly depending on the permeability of soils and velocity of application of load increments. Figure 3-1 shows schematically the effect of drainage conditions and stress history (defined in terms of over consolidation ratio, OCR) on shear strength of soil. In a soft clay which is normally or lightly overconsolidated, undrained strength is likely to be lower than drained strength, and as a result, undrained stability is likely to be more critical than drained stability. The opposite is observed to happen in heavily overconsolidated clays.

The undrained shear strength (s_u) is a key parameter for the design of a breakwater, especially when it must be built on soft clay soil, as is the case of the Port of Barcelona. s_u is affected by the mode of testing, boundary conditions, rate of loading, confining stress level, initial stress state and other variables. A schematic representation of undrained strength of soils is shown in Figure 3-2 (Hight et al, 1987). This figure shows the undrained strength as a function of α, the direction of the major principal stress to the vertical and b, the relative magnitude of the intermediate principal stress ($b=(\sigma2-\sigma3)/(\sigma1-\sigma3)$). Also illustrated in this figure are the undrained strength measured in conventional laboratory tests. Plane strain conditions, which are most likely to apply beneath a long breakwater are shown hatched in this figure. Moreover, as described by D'Ignazio (2016), the undrained response of soft soils is influenced by the following factors: preconsolidation pressure (stress history), strain rate, Creep and aging (time history), and anisotropy (direction and magnitude of imposed stress increment).

The complexity of this parameter means that its determination must be made through an exhaustive investigation. Taken this in mind, the laboratory testing program which included several modes of shearing was performed: unconfined compression tests (UC), Compression triaxial test (TC), extension triaxial test (TE) and simple shear tests (DSS). Also, field determination of undrained strength was made by means of vane (VT) and cone penetration tests (CPTu).

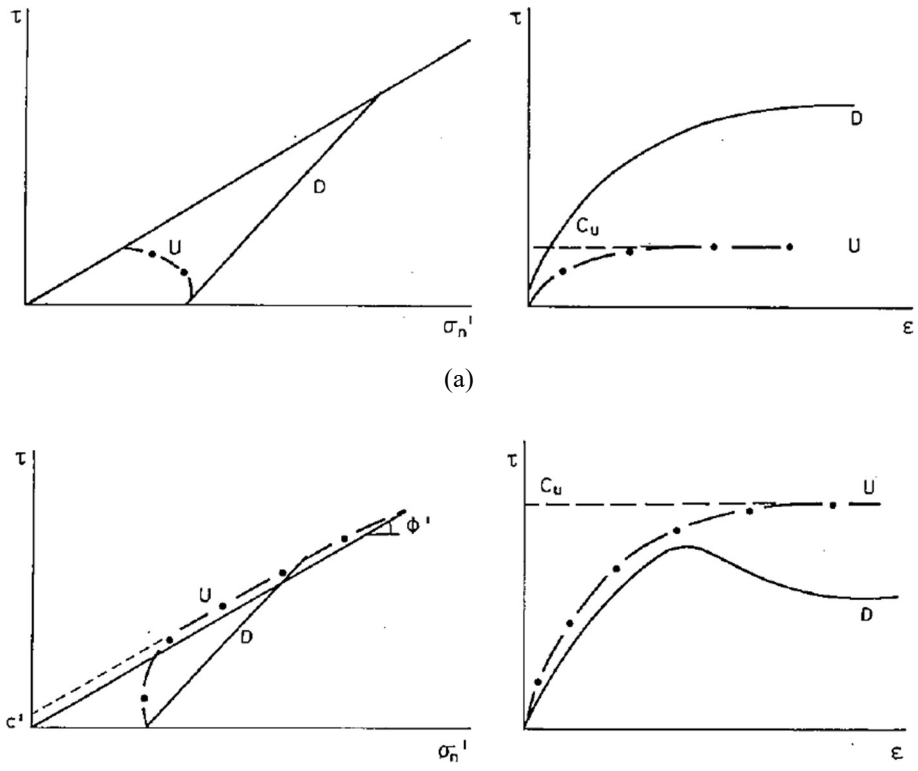

Figure 3-1. Drained (D) and undrained (U) shear in (a) normally or lightly overconsolidated clay and (b) heavily overconsolidated clay (Hight et al, 1987)

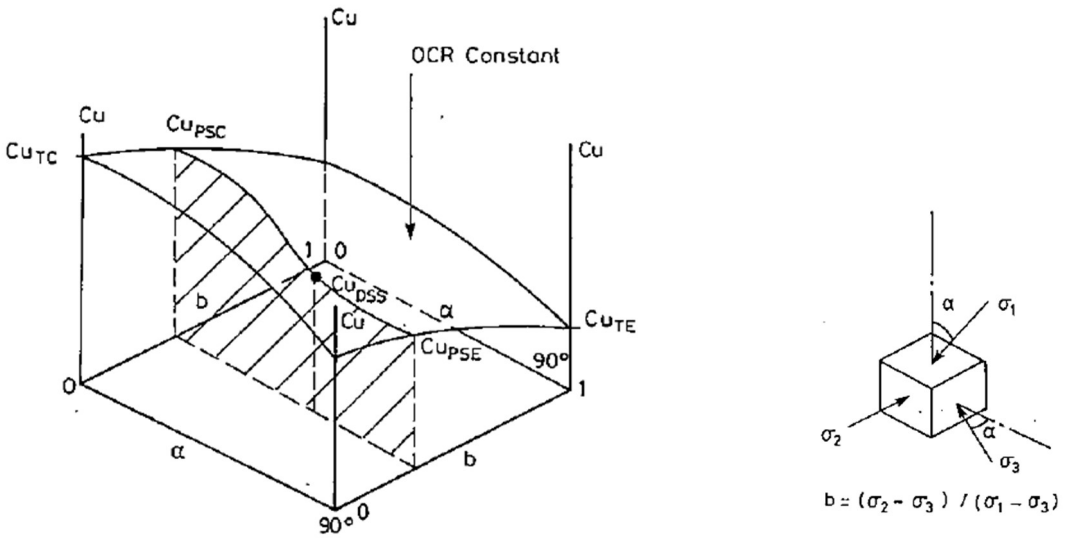

Figure 3-2. Effects of shearing direction and stress state on undrained strength (Cu_{TC} triaxial compression, Cu_{TE} triaxial extension, Cu_{PSC} plane strain compression, Cu_{PSE} plane strain extension, Cu_{DSS} plane strain simple shear) (Hight et al, 1987).

3.2.1 Static undrained strength of normally or lightly overconsolidated clay in triaxial compression and extension (S_u)

The observed behaviour of normally consolidated (K_0=0.5) Port of Barcelona clay during undrained triaxial compression and extension is presented in Figure 3-3a. Results are presented normalised with respect to the mean consolidation pressure, p_0. Stress controlled procedure was followed during undrained triaxial compression shearing at a rate of 10-50 kPa/h and strain-controlled procedure for triaxial extension with a rate of shear of -2 to -5 mm/h. Specimen dimensions of 50mm diameter x 100 mm high were tested. Detailed descriptions of these tests can be found in Laboratory Report by UPC (2001). The key features to note on these tests are:

- A peak undrained strength Su_{pTC}, is mobilised at a small shear strain in triaxial compression (less than 0.1%), while in triaxial extension the maximum strength Su_{TE} is observed at a large strain (around 12-15%). (Figure 3-3b).
- There is an apparent strain softening behaviour (the strength mobilised at large strains, $Su_{ult,}$ is lower than the strength at small strain, Su_p) observed in triaxial compression and extension, mainly due to the effect of the area correction **(**Figure 3-3b). For shear strains lower than 20% as usual in standard triaxial tests, slight differences between peak and ultimate strength is observed in compression, while in extension the maximum strength is reached at about 20% of strain. Certainly, in a compression test in which the deviator stress is steadily increased, catastrophic failure occurs and the specimen deforms rapidly until the limit of load piston carriage.
- The strength in triaxial extension, Su_{TE}, is considerably lower than corresponding to triaxial compression, Su_{pTC} or Su_{ult}. The average ratio of undrained strength in compression and extension Su_{pTC}/Su_{TE} is about 2.0 (Figure 3-3b).
- The ultimate stress ratio is similar for triaxial compression and extension (equivalent to ϕ'=30º), although triaxial extension seems to show some dispersion ranging between 25º and 30º) (Figure 3-3a).

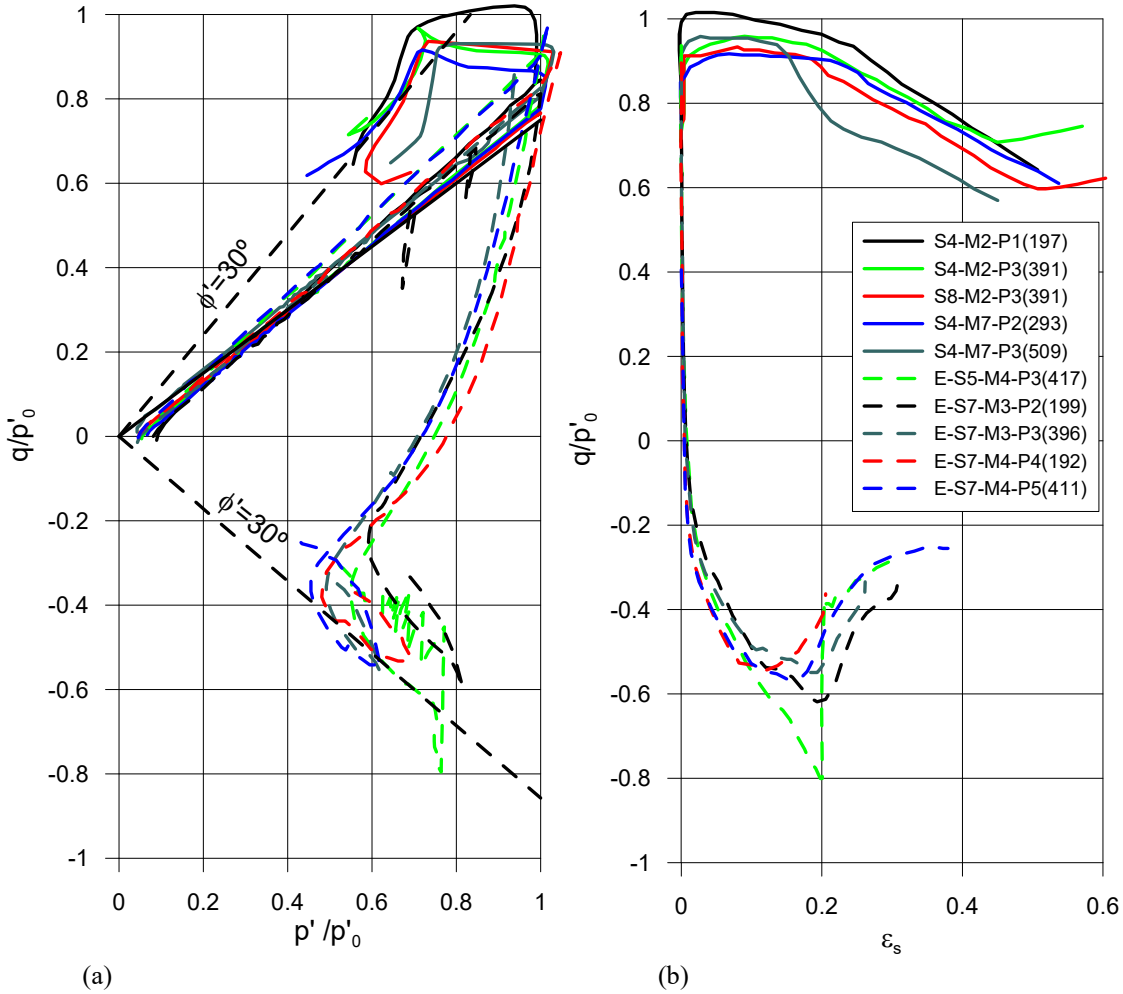

Figure 3-3. (a) Normalised effective triaxial stress path and (b) stress-strain characteristics followed in different triaxial tests of Barcelona's Port samples.

In order to reproduce several in situ conditions, each triaxial specimen is normally K_0 consolidated to several vertical effective stresses, σ'_{vp}, larger o equal to the in situ vertical stress. A total of 29 CAU triaxial compression tests and 12 CAU triaxial extension tests were carried out. Figure 3-4 shows results of triaxial compression and extension of two of these samples. The shape of the effective stress path is almost the same for each stress level, indicating that they are all normalisable. Also, the peak and ultimate strength (ε_s=15%) is observed to increase linearly with preconsolidation stress (Figure 3-5). Average strength ratios Su_{pTC}/σ'_v = 0.33 (compression) and Su_{TE}/σ'_v = 0.19 (extension) are obtained from all triaxial tests performed.

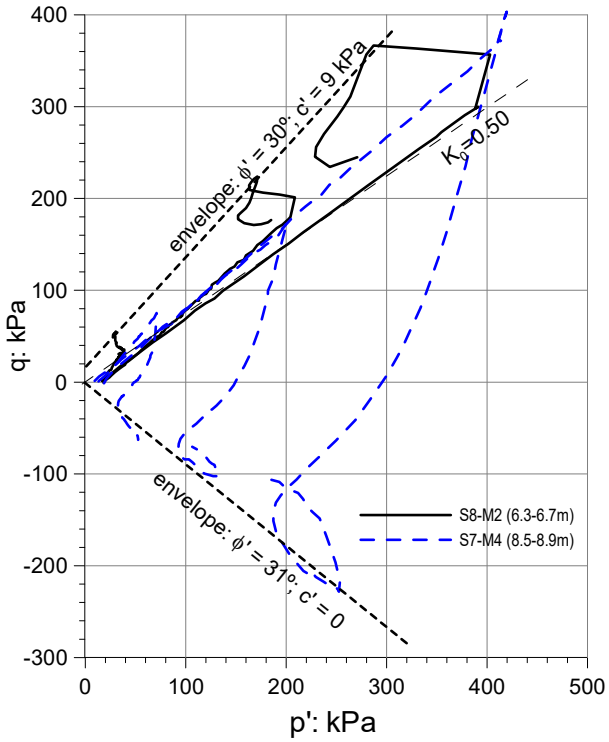

Figure 3-4. Effective triaxial stress path followed in two samples of Barcelona's Port clay.

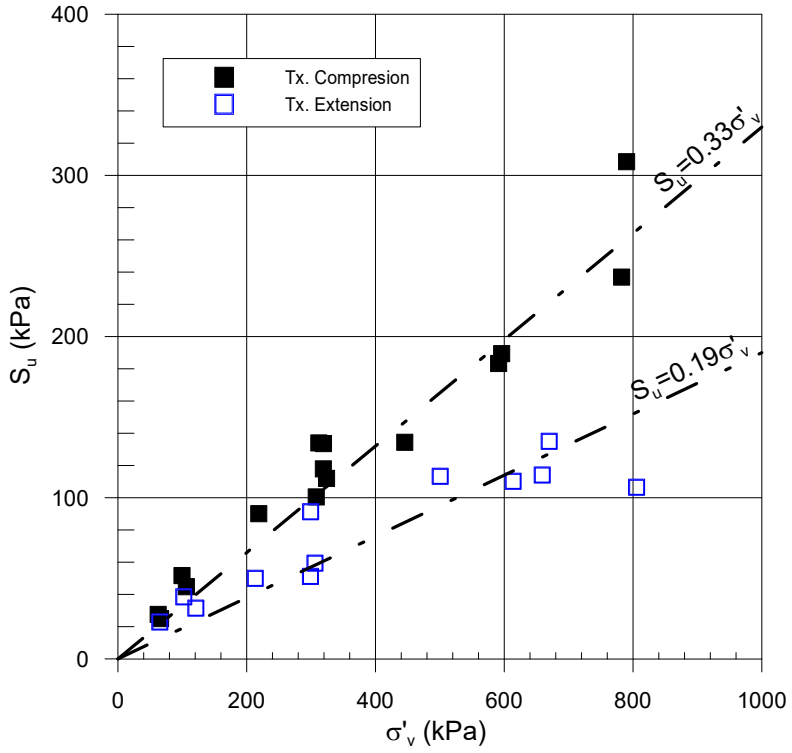

Figure 3-5. Undrained strength of different triaxial tests on Barcelona's Port clay

As indicated by Hight et al (1987), the ultimate strengths are related to water content and a line (the critical state line, CSL) can be defined linking the ultimate states in each test in a plot of *e* versus log p'. Figure 3-6 shows the ultimate state of samples after undrained shearing in triaxial compression tests. The average CSL for all these points is also shown, this line is parallel to the

average virgin consolidation line (VCL). For reference, a typical compression line obtained in a K_0 consolidation stage of one triaxial tests is also shown. From this line is observed that overconsolidated state remains until mean stress reach about 80 kPa, where the soil turns normally consolidated and compression line become straight and parallel to the average VCL.

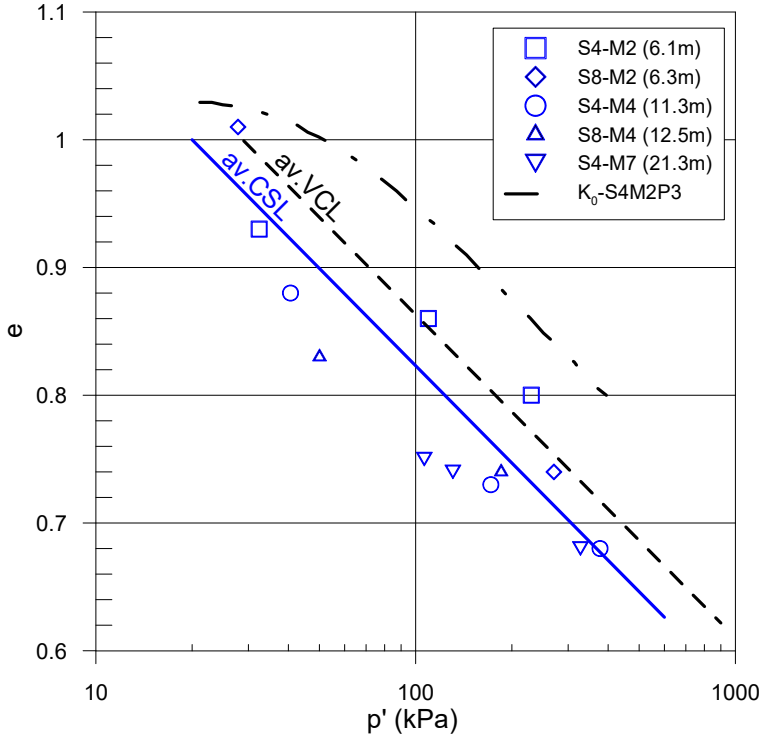

Figure 3-6**.** Ultimate state of samples under triaxial compression tests after undrained shearing (Port of Barcelona clay).

The pattern of behaviour of Port of Barcelona clay is compared with other K_0 normally consolidated clays of different composition. The normalised effective stress paths of this clays, which have a wide range of plasticity, are superimposed with one representative triaxial test of the Barcelona Port clay in Figure 3-7. In accordance with Hight et al (1987), the following characteristics are observed from this figure:

- The angle of shearing resistance ϕ in triaxial compression, generally reduces with increasing PI.
- The effective stress path in triaxial compression is more constrained (between K_0 and K_f line) than in triaxial extension and shows much less dependence on PI.
- Stress path rotate to the right with increasing plasticity, giving rise to an increase in undrained strength in triaxial extension with PI.
- Undrained brittleness in triaxial compression reduces with increasing PI.
- The strength ratio S_{uTC}/σ'_{vc}, reduces as PI increases, while S_{uTE}/σ'_{vc} increases (see Figure 3-8), because the effect of anisotropy in strength increases as plasticity reduces (Hight et al, 1987).

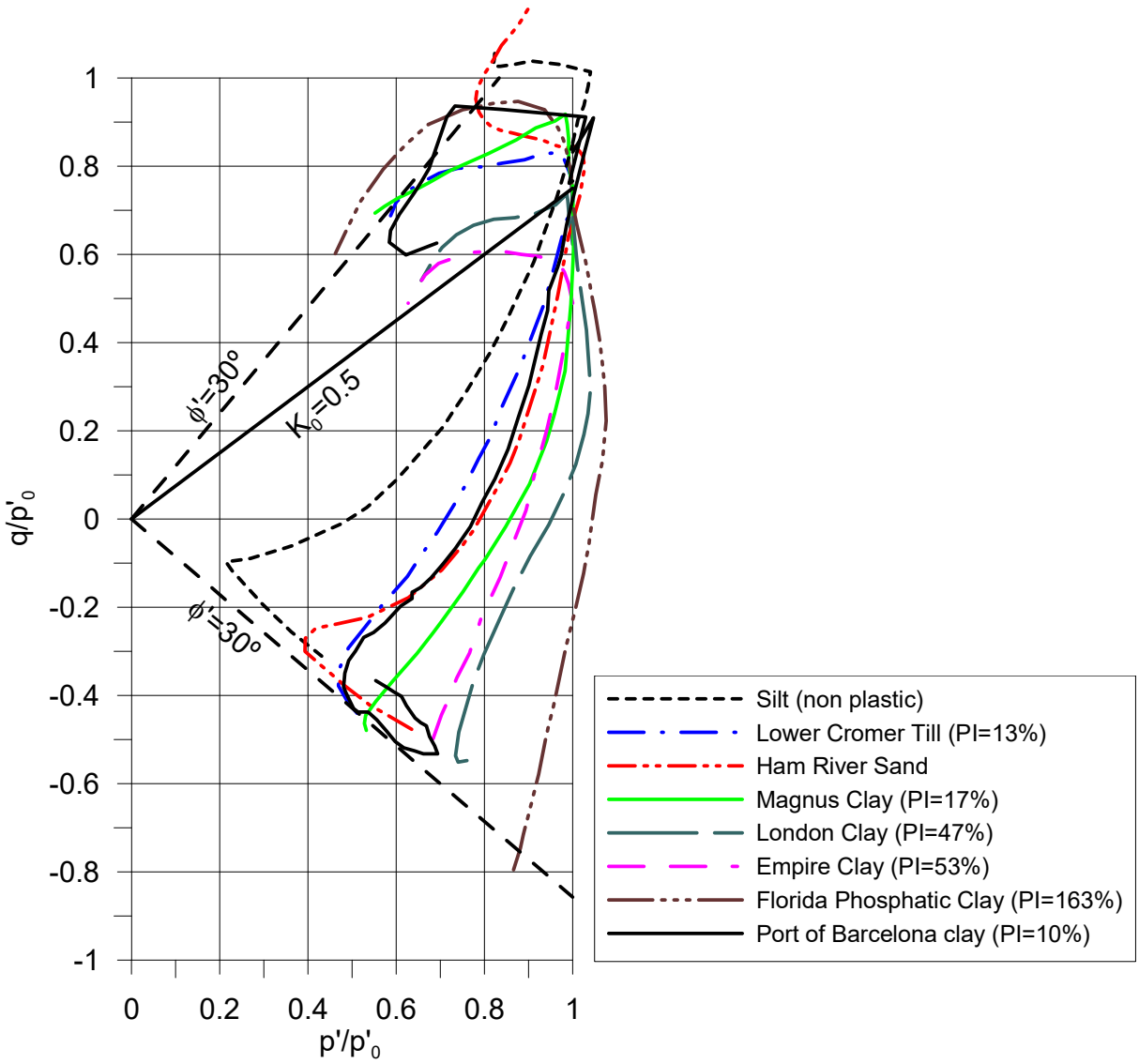

Figure 3-7. Normalised effective stress path for normally consolidated clays of different composition.

3.2.2 Static undrained strength of overconsolidated clay in triaxial compression and extension (S_u)

Overconsolidated soils shows similar patterns of behaviour as normally consolidated soils, but some characteristics depends on the OCR. As described by Hight et al (1987) the undrained brittleness observed in triaxial compression tests of normally or lightly overconsolidated clays reduces with increasing OCR and the shear strain to mobilise peak strength increases, while in triaxial extension the response remains non-brittle (Figure 3-9). Also, the strength ratios, Su_{PTC}/σ'_v, Su_{ultTC}/σ'_v and Su_{PTE}/σ'_v are observed to increase with OCR (Figure 3-10). When the strength ratios for overconsolidated clay $(S_u/\sigma'_v)_{oc}$ is normalised with respect to the strength ratio for normally consolidated state $(S_u/\sigma'_v)_{nc}$, a unique curve for compression and extension shear mode is produced.

In the same way as in normally consolidated case, it is observed that the undrained strengths are significantly lower in triaxial extension than in triaxial compression.

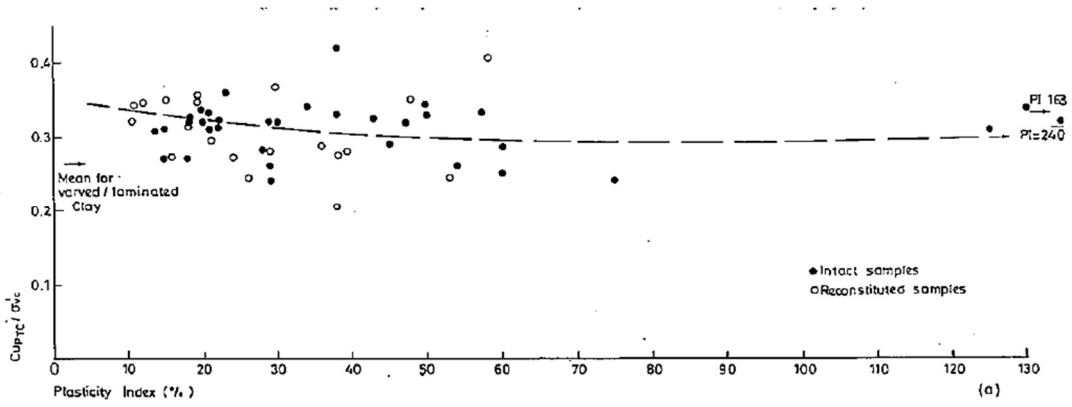

(a)

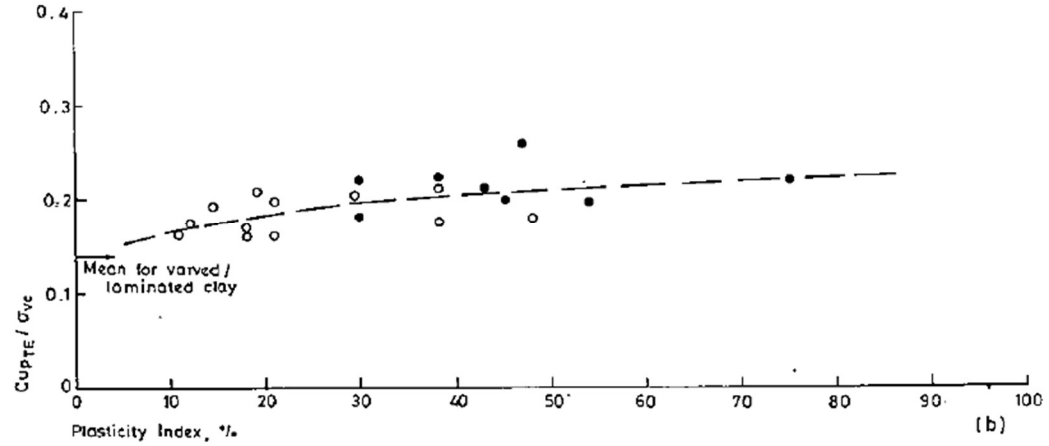

(b)

Figure 3-8**.** Strength ratios for normally consolidated clays a) Triaxial compression, b) Triaxial extension (Hight et al, 1987)

The same pattern of behaviour described for Lower Cromer Till is observed in other young or reconstituted overconsolidated clays (See Figure 3-11). Not strongly dependence on PI is observed. However, as described by Hight et al (1987), there is a dependence on plasticity at higher PIs (PI>25%) and high OCR, due to the tendency of more plastic clay to bifurcate due to the dilatant behaviour that is characteristic of high OCR.

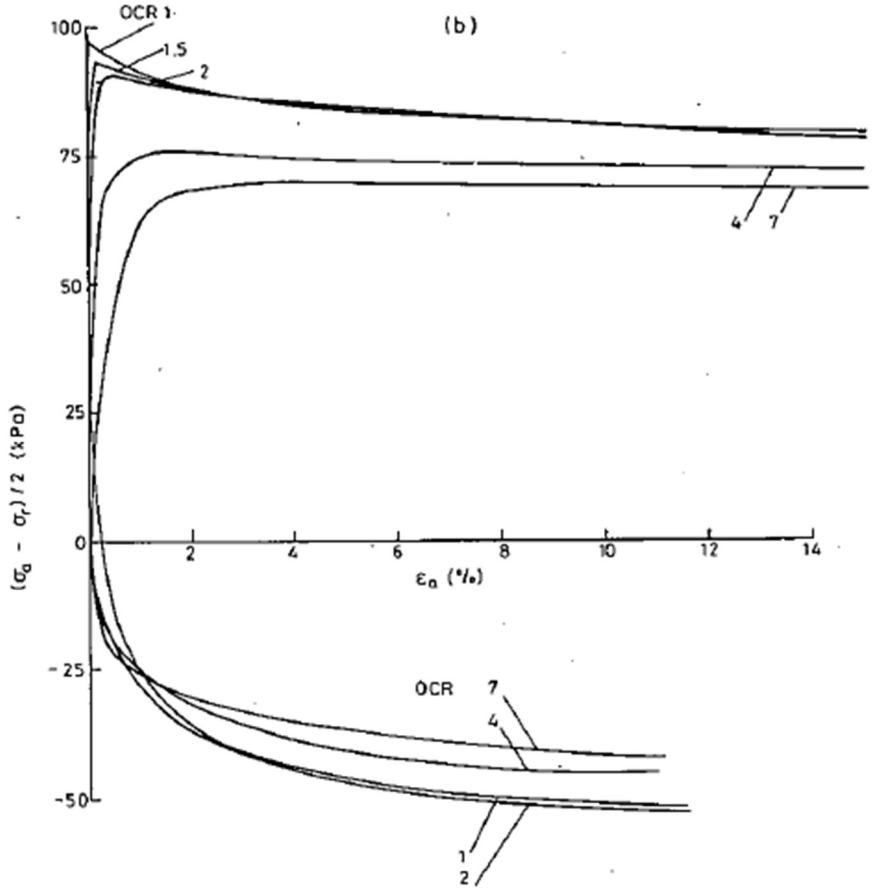

Figure 3-9. Stress-strain behaviour of overconsolidated reconstituted low plasticity clay in triaxial compression and extension (Hight et al, 1987).

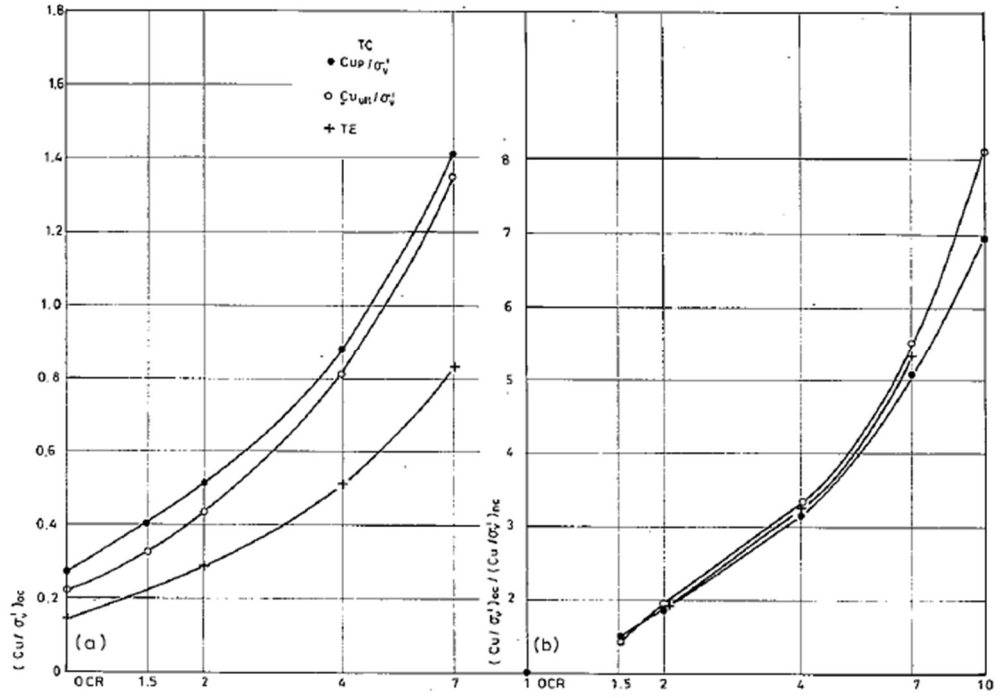

Figure 3-10. Strength ratios for overconsolidated Lower Cromer Till. a) $(S_u/\sigma'_v)_{oc}$ versus OCR and b) $(S_u/\sigma'_v)_{oc}/(S_u/\sigma'_v)_{nc}$ versus OCR. (Hight et al, 1987).

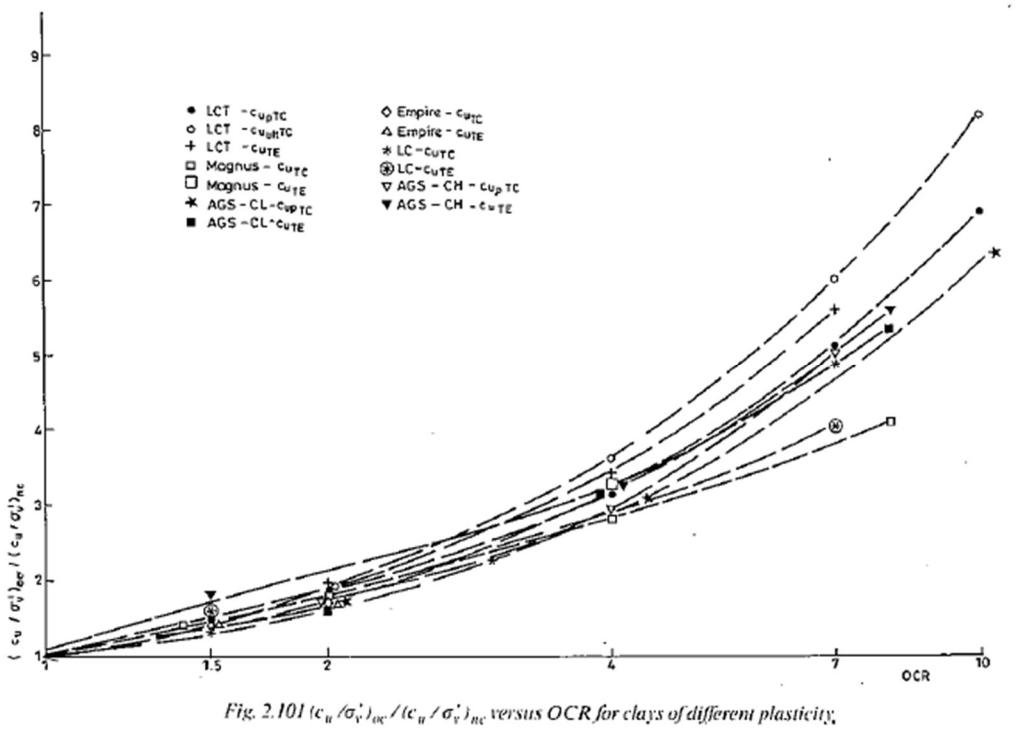

Fig. 2.101 $(c_u/\sigma'_v)_{oc}/(c_u/\sigma'_v)_{nc}$ versus OCR for clays of different plasticity.

Figure 3-11. $(S_u/\sigma'_v)_{oc}/(S_u/\sigma'_v)_{nc}$ versus OCR for clays of different plasticity (Hight et al, 1987)

3.2.3 Static undrained strength of Normally or lightly overconsolidated clay in Direct Simple Shear Tests (Su_{DSS})

Simple shear is a deformation-controlled mode of shearing in which conditions of zero horizontal deformation in the direction of shear and plane strain in the orthogonal direction are enforced. The undrained condition is simulated by continuously adjusting the vertical stress so that the specimen height is kept constant (thereby keeping constant volume). The change in vertical stress is assumed to be equal to the change in pore water pressure that would have occurred during a truly undrained test. Comparative tests at NGI have shown that this assumption is valid (Lacasse and B. Raadim, 1987).

In the DSS test, only the horizontal shear stresses, τ_h, vertical stress, σ'_v and horizontal shear strain, γ are measured. However, these are not sufficient to define the full stress or strain state. Also stress non-uniformities occur because complementary shear stresses cannot develop on the vertical boundaries of the specimen. As such, assumptions with regard to the specimen stress state must be made to construct the Mohr circle and determine the undrained shear strength $s_u = (\sigma_1-\sigma_3)/2$. Typically, the undrained shear strength from the DSS test is taken as τ_{hmax} or defined as the shear stress at certain shear strain (usually 15%) if no distinct peak occurred at lower strain levels.

Wijewickreme et al (2013) studied the stress state in the DSS test using 3D discrete element analysis. Results for the constant volume simulation shows that at the center point of the specimen the shear stresses acting on the horizontal and vertical planes are close to maximum shear stress at

shear strain of 12-15%, which correspond well to the undrained strength. For larger shear strain there is a tendency showing that the maximum shear stress would act on inclined planes and the stress state on the horizontal plane seems to be closer to that for maximum stress obliquity.

A total of twelve static direct simple shear tests were performed by NGI on ten selected samples of Barcelona Port, from boreholes S-5, S-10, S-11, S-1 and NS-1. All samples were in the depth interval 12 to 24m. Before shearing, the samples were consolidated to a vertical stress larger than the estimated preconsolidation stress, in this way all samples were tested under OCR=1 condition. Post depositional effects (if any) have been obliterated by consolidating well beyond the apparent preconsolidation pressure. Standard rate of shearing of 5% shear strain per hour was used. Detailed procedures of these tests are described in the Geotechnical testing report of NGI (2002). Bjerrum and Landva (1966) and Andresen et al (1979) described the apparatus used for this test.

Results of DSS tests are shown in Figure 3-12, where the stress path is defined by the horizontal shear stress, τ_h and vertical effective stress, σ'_v. As soon as the horizontal shear stress start to increase the soil shows stiff behaviour, immediately the vertical stress has to reduce in order to maintain the constant volume, the stress path moves to the left until it reaches what it seen to be a boundary line. The same data are presented in normalised form using the vertical effective stress of consolidation as normalising parameter in Figure 3-13. It is shown that specimens sheared under normal effective stresses reproducing in situ stress conditions showed higher strength ratios than specimens consolidated to higher effective stress values. This is an indication of some (small) overconsolidation effects due to natural creep or aging phenomena. Taking $S_{uDSS} = \tau_{hmax}$, the average strength ratio, $S_{uDSS}/\sigma'_v = 0.25$ in this mode of shearing is lower than in triaxial compression, $S_{upTC}/\sigma'_{vp} = 0.33$, but higher than in triaxial extension, $Su_{TE}/\sigma'_{vp} = 0.19$.

Figure 3-14 show the stress path follow by the Boston blue clay at several OCR in simple shear (Ladd and Edgers, 1972). It is observed that the data for the normally consolidated soil forms a bounding surface for the overconsolidated soil. The overconsolidated soil is stiff until the effective stress path approaches the boundary provided by the normally consolidated soil.

Plastic index (PI) and OCR shows a similar effect as observed in triaxial test over the undrained strength. From Figure 3-15 it is evident that the strength ratio S_{uDSS}/σ'_v increases with PI in a similar way as in triaxial compression tests.

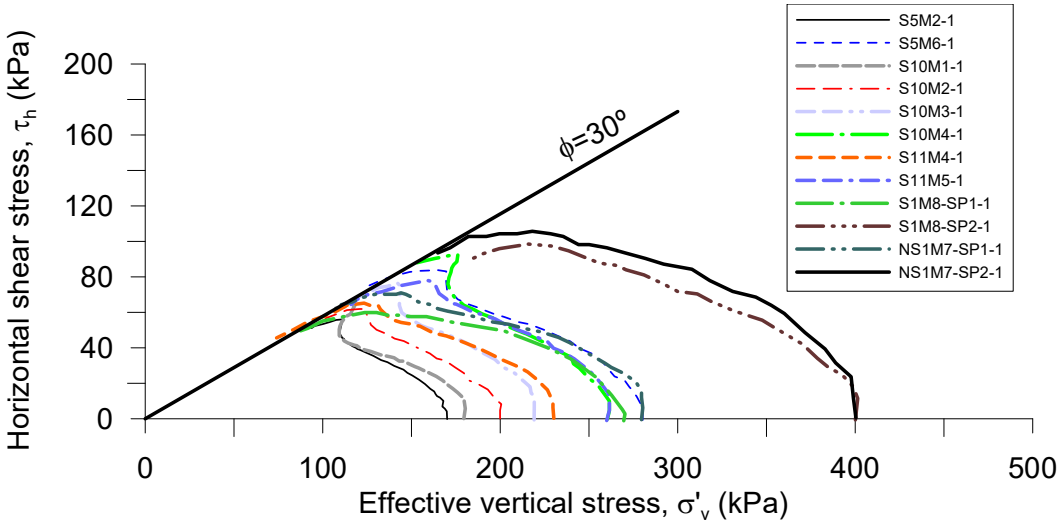

Figure 3-12. Stress path followed in DSS tests.

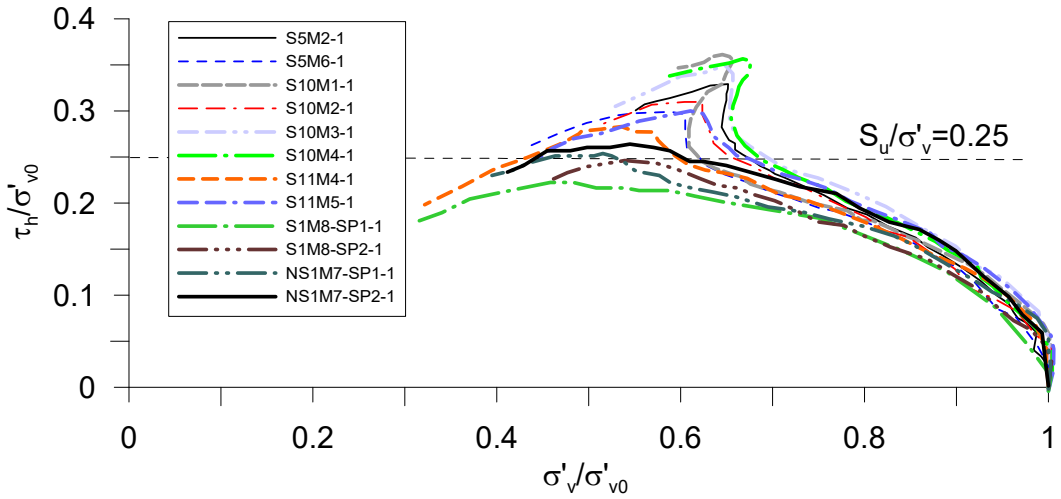

Figure 3-13. Normalised stress path followed in DSS tests.

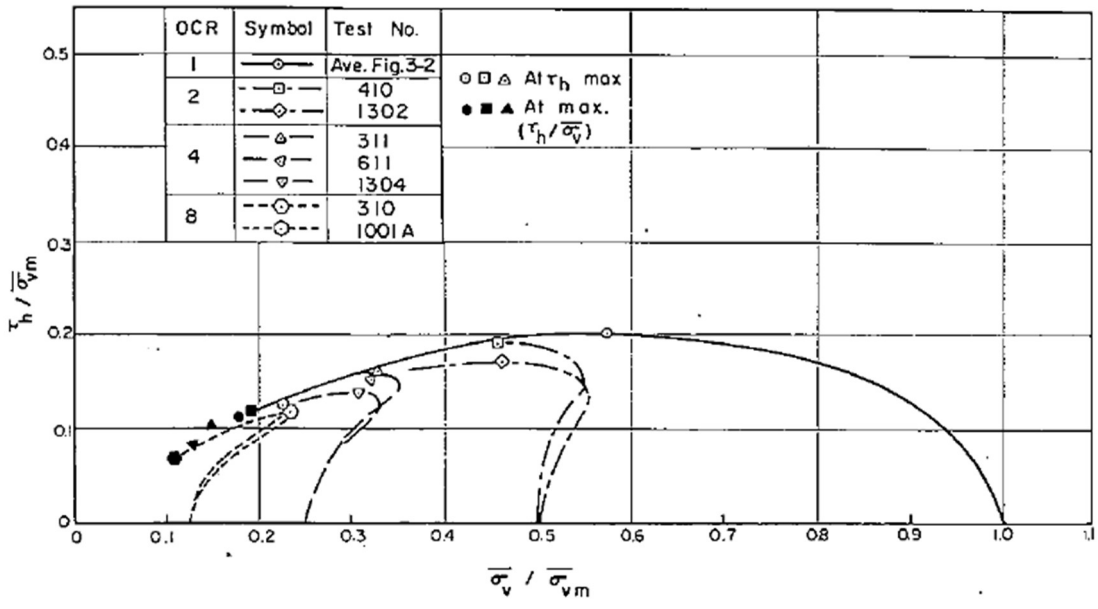

Figure 3-14. Behaviour of reconstituted Boston Blue Clay in simple shear (from Ladd and Edgers, 1972).

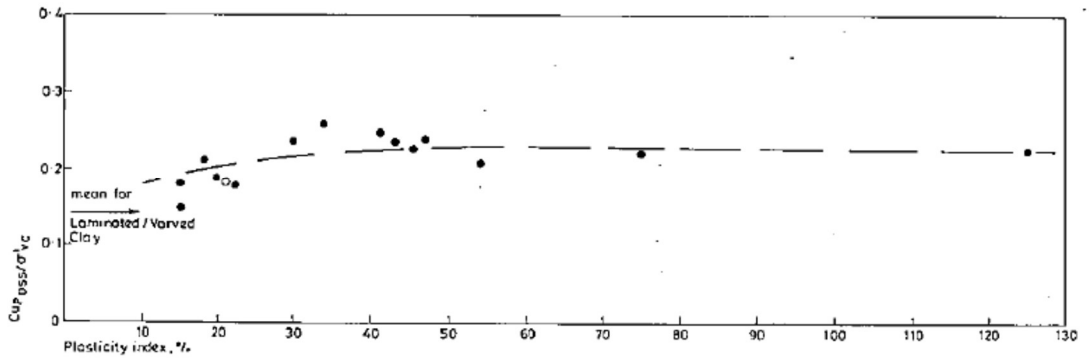

Figure 3-15. Strength ratios for normally consolidated soil in simple shear (Hight et al, 1987)

Data of the strength ratio (S_u/σ'_{v0}) plotted against the overconsolidation ratio OCR from undrained simple shear tests on six clays reported for Ladd et al (1977) are show in Figure 3-16. Samples in these tests were initially K_0 consolidated before shearing. Figure 3-17 shows the same data in normalized form, indicating a narrow band.

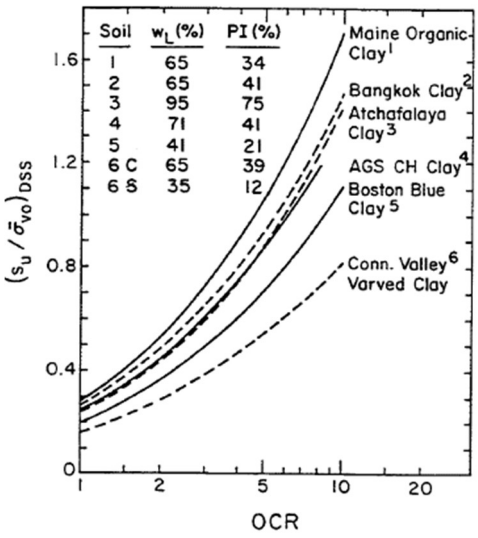

Figure 3-16. s_u/σ'_{v0} versus OCR, Ladd et al (1977)

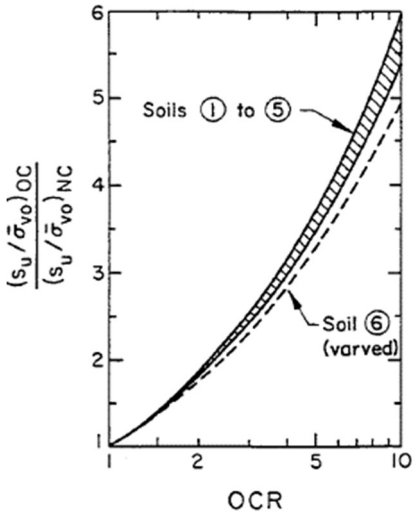

Figure 3-17. Normalized s_u/σ'_{v0} versus OCR, Ladd et al (1977)

Based on this data, the following general equation was suggested by Ladd et al (1977):

$$\frac{\left(s_u/\sigma'_{v0}\right)_{OC}}{\left(s_u/\sigma'_{v0}\right)_{NC}} = OCR^m \qquad 3.1$$

With m=0.8. However, a better fit is obtained if m reduces from 0.85 to 0.75 with increasing OCR.

Based on the same tests, for low to moderate plasticity soils, Jamiolkowski et al (1985) proposed the following relation:

$$s_u/\sigma'_{v0} = (0.23 \pm 0.04) OCR^{0.8} \qquad 3.2$$

3.2.4 Undrained strength from other tests

The undrained shear strength of Port of Barcelona clay was also investigated from 24 unconfined compression tests of clay samples, providing the follow relationship: $s_u=0.215\sigma'_v$. This low undrained strength ratio may be attributed to damage to the microstructure and the associated reduction of mean effective stress during sampling (Tsuchida, 2000; Rocchi et al, 2013).

Another source of data for s_u derives from in situ tests. Interpretation of CPTu tests results in values of undrained strength increasing linearly with depth. The following relationship was estimated: $s_u=0.24\sigma'_v$. Vane tests were also performed, but these tests showed a large scatter in the undrained strength, an effect that was probably due to the existence of sand stratification.

Figure 3-18 summarizes the different estimations of undrained strength at Port of Barcelona clay. In case of short-term analysis of the stability of breakwaters with isotropic models, the relationship obtained through simple shear tests is preferred: $s_u=0.25\sigma'_v$. This value is consistent with the strength ratio value proposed by Ladd and Foot (1974): $s_u/\sigma'_{vc} = S \cdot OCR^m$ (where parameters S and m vary in the range $0.24<S<0.27$ and $0.61<m<0.77$) (OCR = 1 in this case).

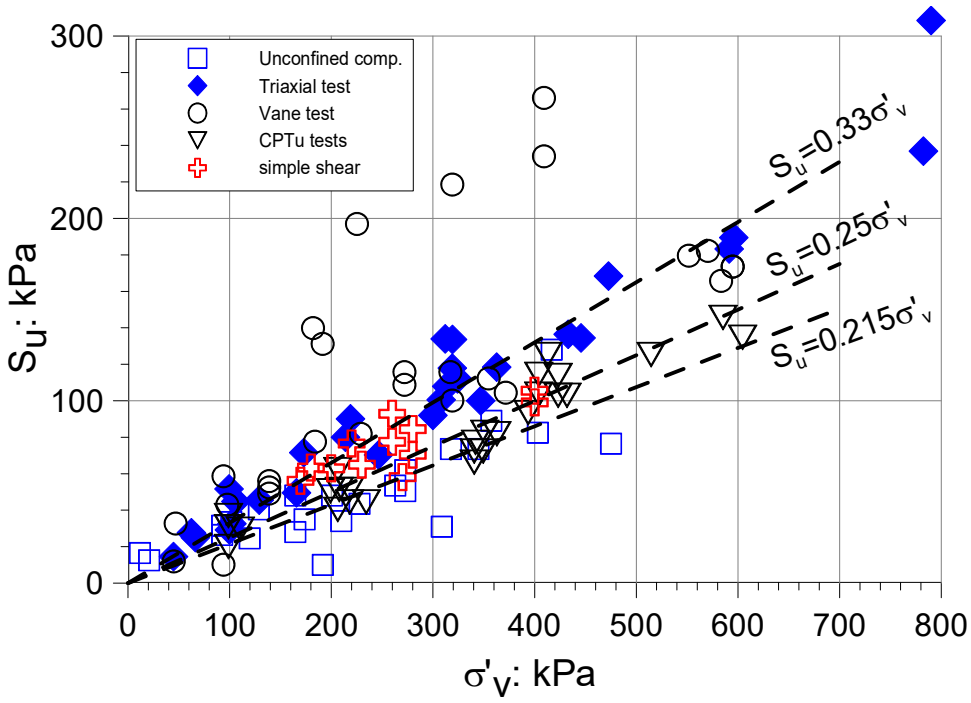

Figure 3-18. Undrained shear strength. Summary of results

3.3 STIFFNESS-STRAIN BEHAVIOUR AND SMALL DEFORMATION STIFFNESS

The stiffness – strain relationships of soils is known to be non-linear. Experimental evidence shows that the stiffness decreases with increasing strain in a similar way during dynamic tests (Anderson & Richart, 1976) than static conventional triaxial tests (Jardine, Symes & Burland, 1984). Also, experimental tests on the Lower Cromer Till clay shows that stiffness is higher during unloading in triaxial extension than during loading in triaxial compression (Gens, 1982).

Georgiannou et al (1991) observed that for reconstituted soils the shear moduli start to decay and becomes non-linear beyond a threshold value of strain related to the plasticity index, which ranges from about 0.001% in case of low-plasticity soils to about 0.01% for plastic clays. Experimental observations have shown that soil behaviour within the region of very small strain is linear and elastic and the stress-strain loops show little or no hysteresis, which means that the behaviour is conservative and little or no energy is dissipated (Papa, Silvestri & Vinale, 1988; Silvestri, 1991). Also, volumetric and shear deformations is observed to be fully recoverable and uncoupled, indicating that no pore pressures are generated during undrained shear (Lo Presti, 1989; Georgiannou *et al.,* 1991; Silvestri, 1991). Therefore, shear strain higher than the threshold value must be necessary to accumulate residual pore pressures.

Result of testing on London clay performed by Viggiani and Atkinson (1995), shows that the value of G_{max} depends on the current state (determined by both the current stress and the overconsolidation ratio) and is unaffected by structure and fabric.

Santagata et al (2007) carried out an extensive program of triaxial tests on samples of reconstituted Boston Blue Clay using a stress-path triaxial device equipped with the small strain measuring system developed at MIT. These tests confirm that at very small strains, the behaviour of the soil is linear. The linear behaviour extends further to about 0.0015% axial strain, after which the stress-strain curve becomes increasingly nonlinear.

Experimental evidence also shows that the rate, amplitude and direction of shear strain influence the behaviour of stiffness. In this way, a direct comparison between the shear modulus obtained from dynamic tests (resonant column) and the very small strain shear modulus relevant to monotonic loading in triaxial compression or extension tests is difficult, as the rates of strain and the modes of shearing are very different in these two types of test. Vardanega & Bolton (2013), analysed a large database of dynamic and static tests performed on silts and clays and proposed a method to normalize and merge static and dynamic tests data, based on rate effects adjustments. This method was used to produce stiffness-strain curves for Barcelona's Port soils as explained later.

Low strain properties of port of Barcelona soils were investigated in resonant column tests. In this test a cylindrical sample of soil is subjected to harmonic torsional loading, starting from a low frequency, which is gradually increased until the response (strain amplitude) reaches a maximum. The frequency that produces the maximum response is the fundamental frequency and is related to the low strain stiffness. Although the stiffness of soil can be evaluated at shearing strains ranging from 0.00001 % to 1%, results are only reliable in the region of very small strain, since the analyses of resonant column tests assumes that the behaviour of the soil is linear and elastic (Isenhower, 1979).

Resonant column test samples were isotropically consolidated at confining pressures of 100, 200 and 400 kPa before the harmonic loading was applied. The loading frequency was initially set at low value (15Hz) and then gradually increased in order to match the fundamental frequency of the specimen. Shear Modulus determined from resonant column and compression and extension triaxial tests are collected in Figure 3-19, Figure 3-20 and Figure 3-21 for confining pressure of 100, 200 and 400 kPa, respectively. These pictures show the degradation of stiffness with shear strain from both resonant-column and anisotropic triaxial tests. As expected, stiffness curves do not coincide, but all them show similar tendency.

Several semiempirical expressions for the maximum shear modulus (G_0) have been proposed through the years, among them maybe the most used expression is the one proposed by Hardin (1978), which is a general expression that relate the maximum shear modulus G_0 with a function of the void ratio and the mean effective stress:

$$G_0 = Sf(e)OCR^k p_a^{1-n} p'^n \qquad 3.3$$

where S is a dimensionless coefficient which depends on the nature of the soil, *f(e)* is a function of the void ratio, usually $f(e)=1/(0.3+0.7e^2)$, *p'* is the mean effective stress, p_a is the atmospheric pressure and *OCR* is the overconsolidation ratio. Hardin & Drnevich, (1972) show that the stress exponent *n* is less than 1.0 and the exponent *k* increases as the plasticity index increases, taking values k = 0, 0.18, 0.30, 0.41, 0.48, and 0.5 (for plasticity index Ip values of 0, 0.2, 0.4, 0.6, 0.8, and 1.0, respectively).

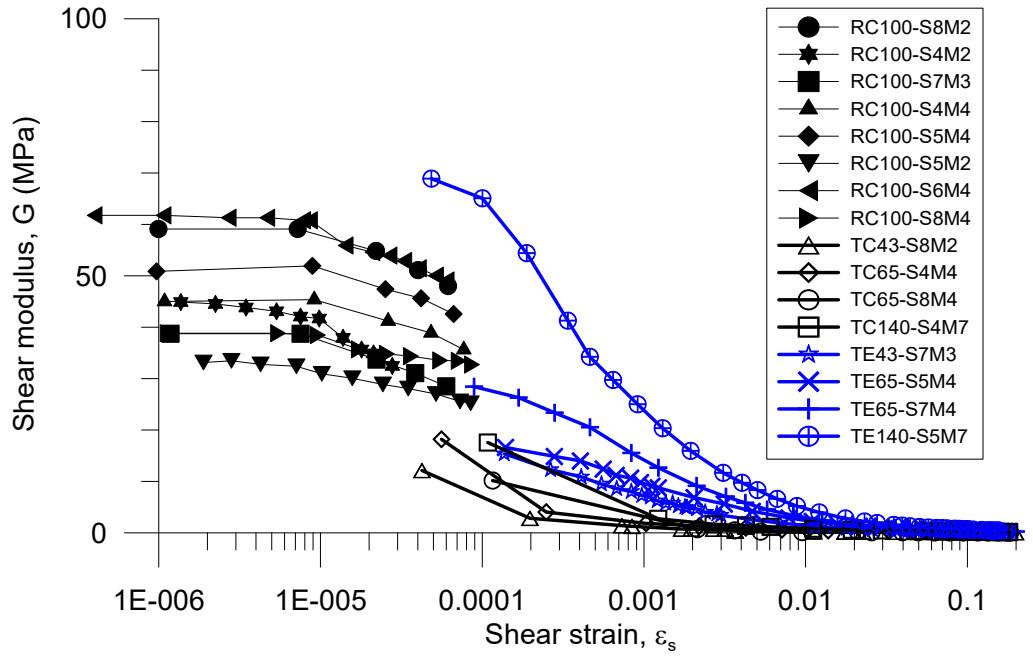

Figure 3-19. Variation of shear moduli with shear strain in resonant column and triaxial tests (p'=100kPa).

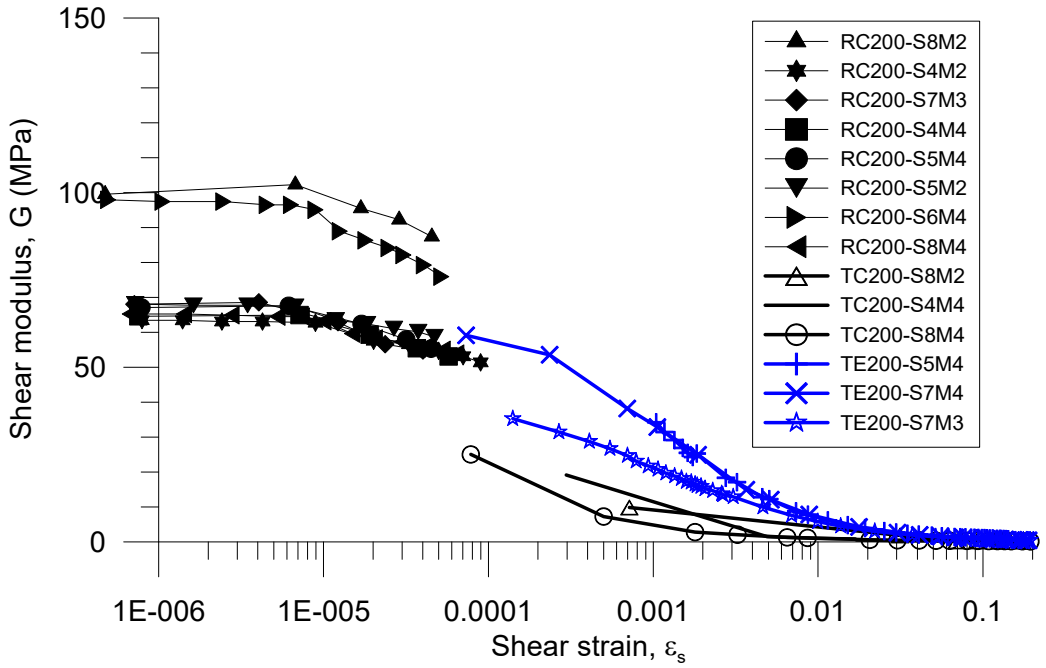

Figure 3-20. Variation of shear moduli with shear strain in resonant column and triaxial tests (p'=200kPa).

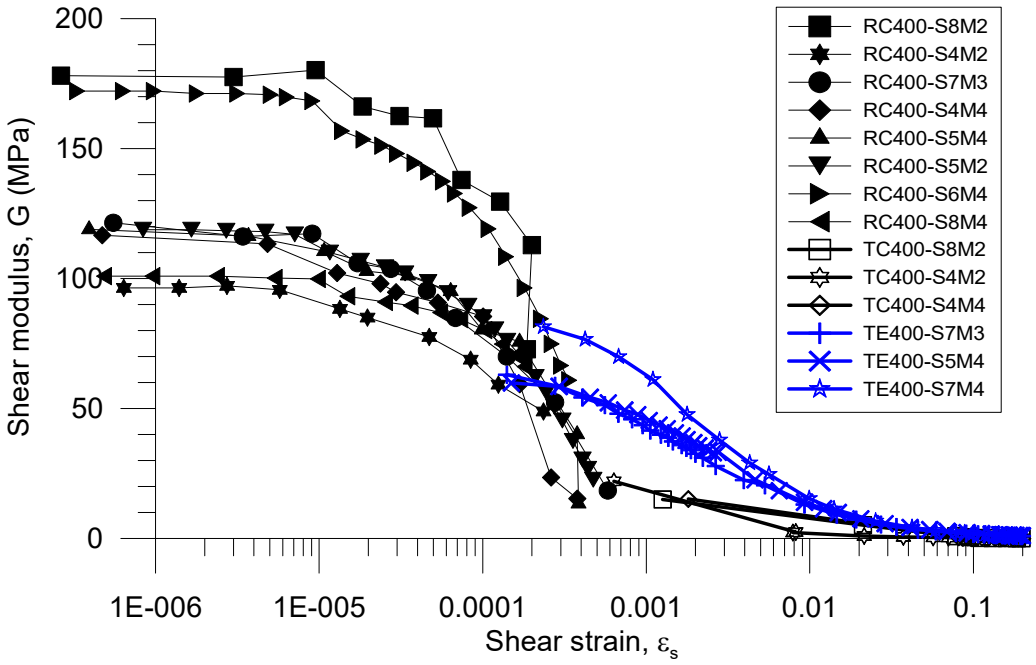

Figure 3-21. Variation of shear moduli with shear strain in resonant column and triaxial tests (p'=400kPa).

Shibuya et al. (1997) introduced an empirical expression which includes an alternate void ratio function for estimate the shear modulus G_{max} of normally consolidated clays under the current state of stresses.

$$\frac{G_{max}}{p'_r} = \frac{B}{(1+e)^{2.4}} \left(\frac{p'}{p'_r} \right)^{0.5} \qquad 3.4$$

In Shibuya et al (1997) the factor B for soft clays in equation 3.4 ranged from 18,000 to 30,000, with an average of about 24,000. Vardanega & Bolton (2013) used a data base of G_{max} reported in the literature and computed the factor B for several clays and silts, producing an average value of 20000 and an upper limit of 50000 (for highly plastic silts). Results from resonant column tests performed in soil samples of Port of Barcelona were compared with this data base and they seem to fit better with a value of B=30000 as shown in Figure 3-22.

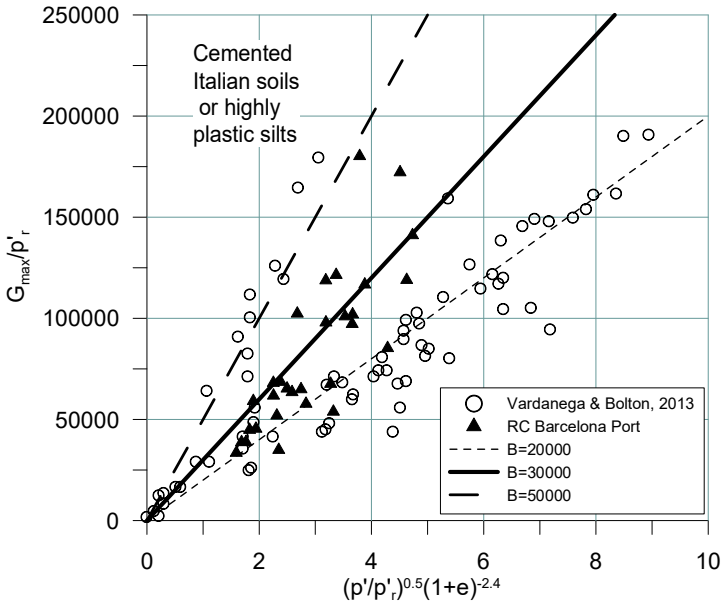

Figure 3-22. Factor B for the database collected by Vardanega & Bolton (2013), comparing with Barcelona Port tests.

Through experimental data on kaolin clay, Viggiani & Atkinson (1995) came to the same general form for the equation that relates the shear stiffness at very small strain G_{max} with the current stress, as proposed by Wroth & Houlsby (1985) for the shear modulus of sands. Also, the increased of G_{max} with log R_0 (overconsolidation ratio) is given in a similar way as that reported by Houlsby & Wroth (1991):

$$\frac{G_{max}}{p_r} = A\left(\frac{p'}{p_r}\right)^n R_0^{\,m} \qquad 3.5$$

Values for parameters A, n and m are shown in Figure 3-23 against plasticity index for different clayed soil tested.

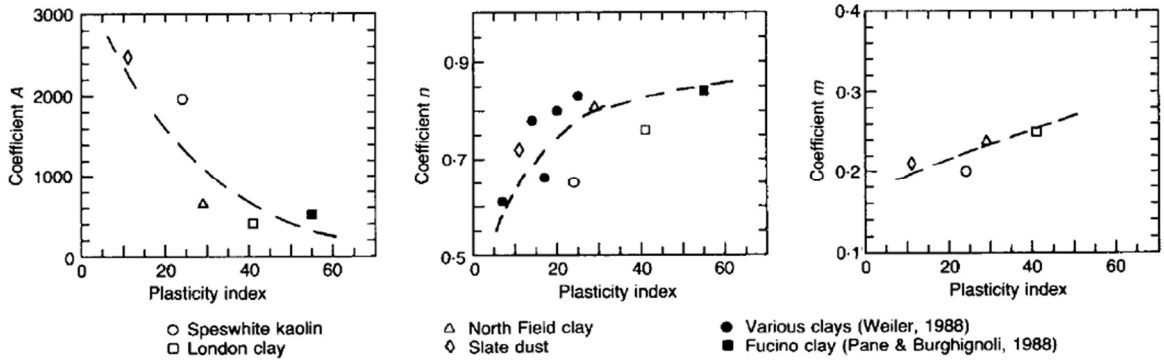

Figure 3-23. Variation of stiffness parameters for G_{max} with plasticity index (Viggiani & Atkinson. 1995)

Vardanega & Bolton (2013) presented an alternative form of the expression 3.5, which is based on the modified compression indexes λ* and κ* defined in the axes log(ν) - log(p') as suggested by Butterfield (1979).

$$\frac{G_{max}}{p_r} = \frac{B}{v_n^{\alpha}} \left(\frac{p'}{p_r} \right)^{\kappa + \alpha\lambda^*} \left(\frac{p'_{max}}{p'} \right)^{\alpha\left(\lambda^* - \kappa^*\right)} \qquad 3.6$$

This equation has the same form as Eq. 3.5, in which A, n, and m are soil constants given as $A = B / v_n^{\alpha}$, $n = \kappa + \alpha\lambda^*$ and $m = \alpha\left(\lambda^* - \kappa^*\right)$.

All these empirical equations have been proved for Barcelona's Port clay and the results are compared with the shear modulus measured in resonant column tests (see Figure 3-24). Although some dispersion is observed, this figure shows clearly some tendency to decrease the modulus with increasing void ratio and also to increase the modulus with increasing density.

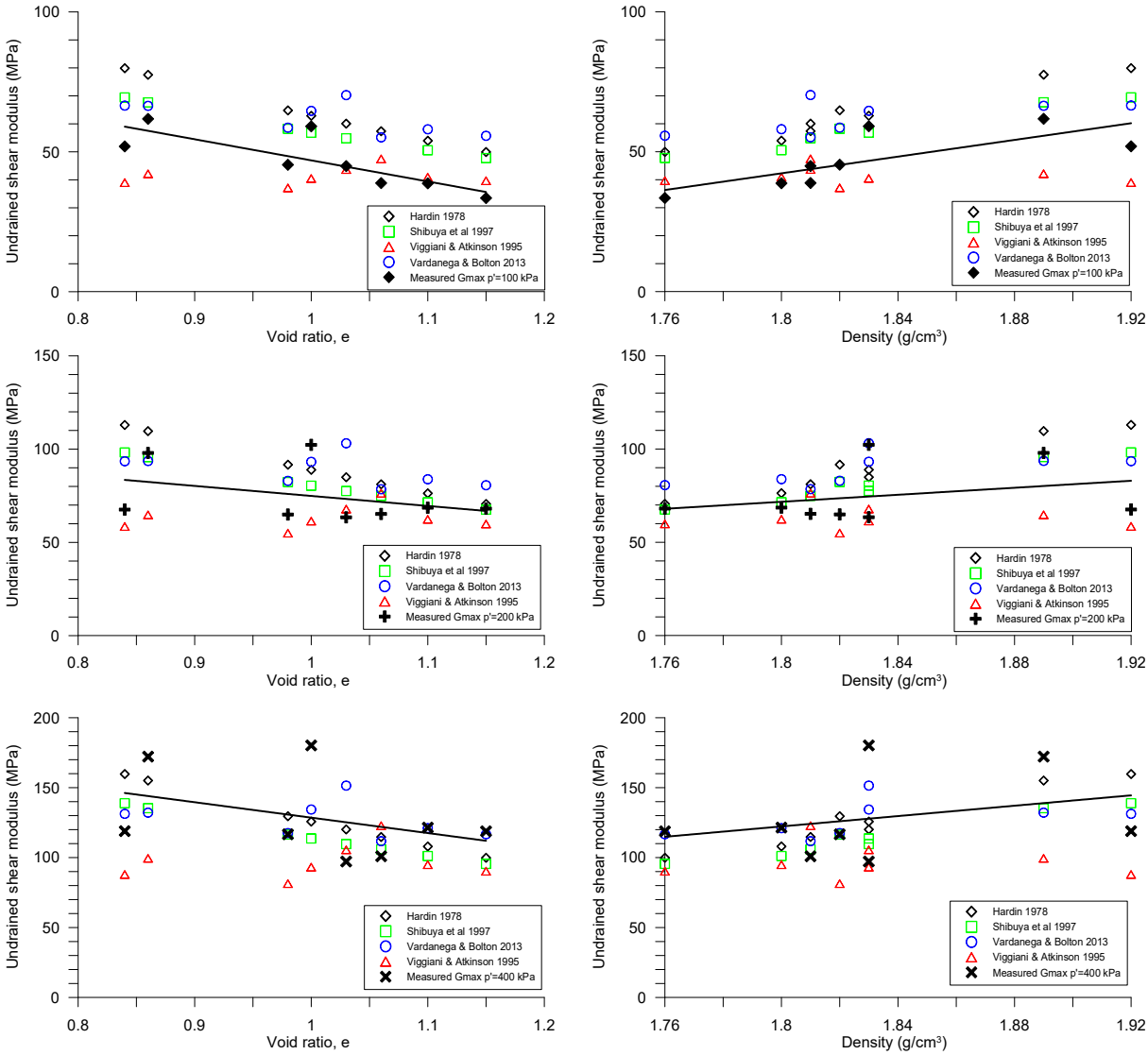

Figure 3-24. Comparison of shear modulus computed with empirical equations and the measured G_{max} from resonant column tests at Port of Barcelona clay.

Vardanega and Bolton (2011a) suggested that resonant-column and static triaxial test data could be merged within a stiffness curve using a simple rate-effect adjustment, which could be static for

foundation analysis or dynamic for earthquake problems. The rate effect is assumed to be a 5% increase in stiffness per factor of 10 increase in plastic strain rate $\dot{\gamma}_z$ (similar to that finding of Lo Presti et al., 1997 and d'Onofrio et al, 1999). It is assumed that the onset of grain slippage (and the first instance of $G<G_{max}$) occurs at 10^{-5} strain, and that only strains greater than this will lead to rate effects (γ - 10^{-5}). So, the rate-linked reduction factor Z on the stiffness measured in a resonant column test is taken as:

$$Z = \left\{1 + 0.05 \log_{10}\left[\frac{100\pi\left(\gamma - 10^{-5}\right)}{10^{-6}}\right]\right\} \tag{3.7}$$

The shear modulus is finally corrected by $G=G_{measured}/Z$. This relation was used to produces stiffness degradation curve for Barcelona Port clay.

On the other hand, several authors have shown that the stress-strain curves, can be adequately described by a hyperbolic law (Konder, 1963; Duncan and Chang, 1970, and Hardin and Drnevich, 1972). The most used is that proposed by Hardin and Drnevic:

$$\frac{G}{G_{\max}} = \frac{1}{1 + \left(\frac{\gamma}{\gamma_{ref}}\right)} \tag{3.8}$$

where γ_{ref} is the threshold shear strain. This definition has the feature that secant shear stiffness reduces to half of its initial maximum value when $\gamma = \gamma_{ref}$. In an attempt to better fit the data available at small strain range, Darendeli (2001) and Zhang et al. (2005) both raised the normalized shear strain (γ/γ_{ref}) to a power of α, in this way:

$$\frac{G}{G_{\max}} = \frac{1}{1 + \left(\frac{\gamma}{\gamma_{ref}}\right)^{\alpha}} \tag{3.9}$$

Also, Dos Santos and Correia (2001) suggest an alternative normalization factor, called the reference threshold shear strain $\gamma_{ref} = \gamma_{0.7}$ defined as the shear strain for which the secant shear modulus G_s reduces to about 70% of its initial value. In this regard, equation 3.9 is modified as:

$$\frac{G}{G_{\max}} = \frac{1}{1 + a\left(\frac{\gamma}{\gamma_{0.7}}\right)} \tag{3.10}$$

Where a=0.385. This equation is adopted in the Hardening Soil model with small-strain stiffness (HSSmall) implemented in the FE code Plaxis.

The value of the reference shear strain γ_{ref} is closely related to the concept of volumetric threshold shear strain γ_{tv} and is not easy to determine. Although experimental data shows that its value increase with plasticity index and strain rate in cohesive soils and with the mean effective stress in cohesionless soils (Dos Santos and Correia, 2001).

Empirical relation for the reference shear strain (γ_{ref}), that relate it with the plasticity index has been proposed by Vardanega & Bolton (2013), but as explained by its authors there is a 50% uncertainty in the predicted value. This relation is expressed as follow:

$$\gamma_{ref} = J\left(\frac{IP}{1000}\right) \qquad 3.11$$

where Ip is plasticity index (expressed numerically, not as a percentage); J is 2.2 for data with the static adjustment applied and J is 3.7 for data with the dynamic adjustment applied.

Figure 3-25 show the normalized stiffness from resonant column and triaxial tests of Barcelona's Port clay compared to the static and dynamic adjustment curve constructed for IP =10%, which is the average plasticity for Barcelona Port clay and Figure 3-26 shows the statically adjustment test data compared to the degradation stiffness curve for static and dynamic adjustment plotted in a normalized stiffness (G/G_{max}) and shear strain plane ($\gamma/\gamma ref$). Better agreement appears to be obtained when the data tests are adjusted for rate effect. Also, the stiffness degradation curve as defined in the HSS model was also fitted to the static and dynamic curves using the parameter $\gamma_{0.7}$ set to $1.5x10^{-4}$ (static) and $7x10^{-5}$ (dynamic). Figure 3-27 shows this comparison, where is clear that the dynamic curve is much better fitted with the HSS model.

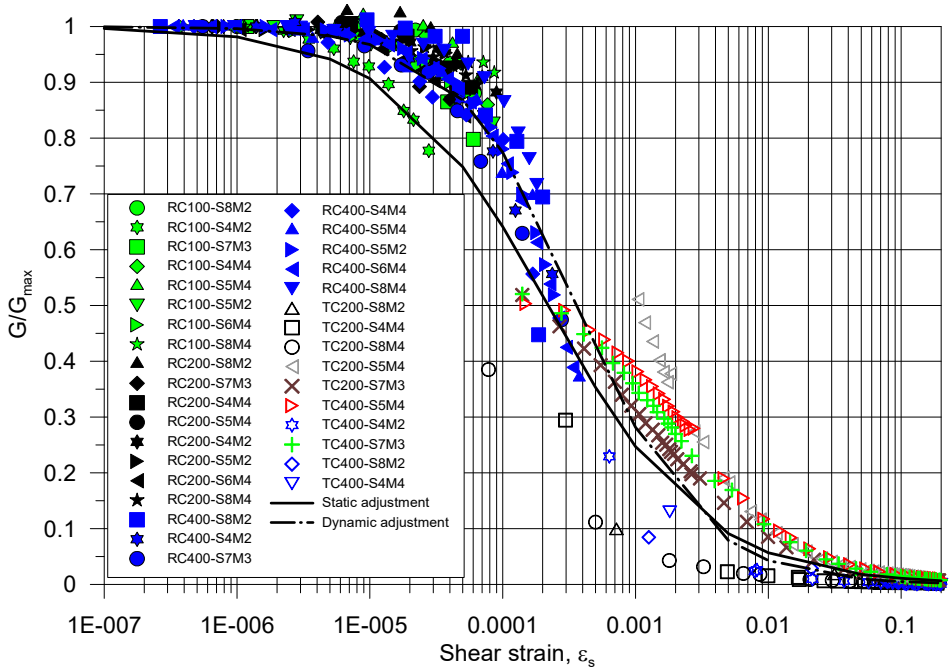

Figure 3-25. Normalized shear modulus versus shear strain from resonant column and triaxial tests compared to the static and dynamic adjustment curve.

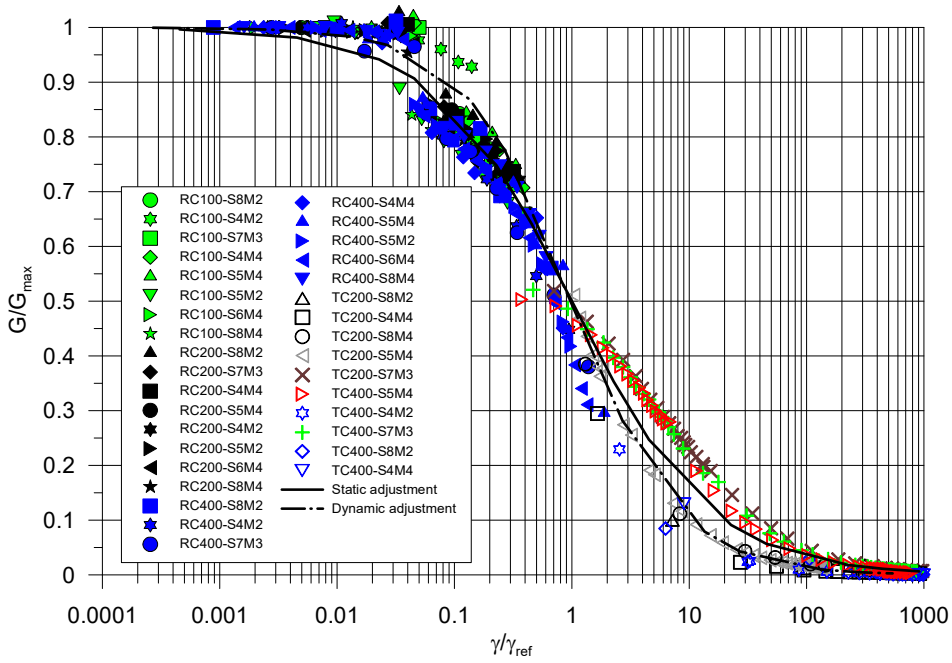

Figure 3-26. Comparison of the statically adjustment resonant column tests data with the normalized stiffness degradation curve for static and dynamic adjustment (IP=10%).

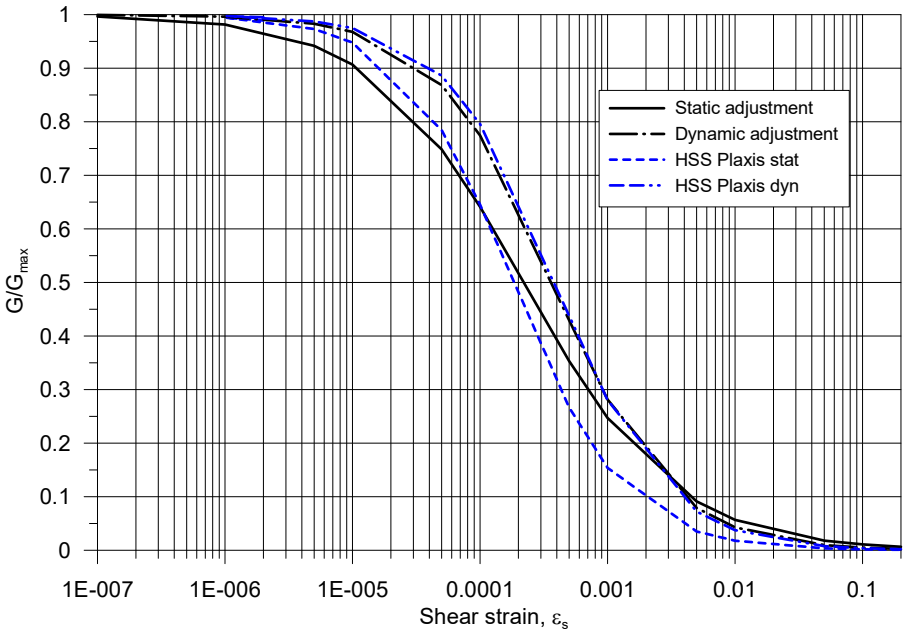

Figure 3-27. HSS model adjustment for static and dynamic stiffness degradation curve.

3.4 CYCLIC UNDRAINED STRENGTH

Breakwaters are subjected to cyclic wave loading. Storms are the primary source of energy that may cause cyclic loading on foundation soils. Cyclic loading tends to break down the soil structure and cause a tendency for volumetric reduction in the soil. If the conditions are undrained, as in the case of clays or silts, volumetric changes will be prevented by the low volumetric compressibility of the water, inducing an increase of the pore pressure, characterized by a permanent pore-pressure component u_p, and a cyclic pore pressure component u_{cy}. The increased pore pressure reduces de effective stresses in the soil, resulting in increased permanent γ_p and cyclic γ_{cy} shear strain with time (Andersen, 2009). Figure 3-28 shows definition of average and cyclic shear stress, pore pressure and shear strain generated under cyclic loading.

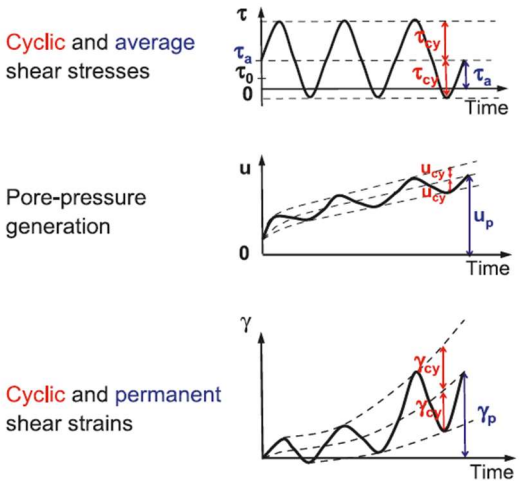

Figure 3-28. Definition of average and cyclic shear stress, pore pressure and shear strain (after Andersen 2009).

The soil beneath a vertical breakwater is subjected to various stress conditions, which produce several loading modes (e.g. triaxial and simple shear). Cyclic behaviour depends on a combination of both, average and cyclic shear stress, but also different response is observed under triaxial and simple shear conditions. Of course, phenomena like cyclic mobility or, in extreme conditions, liquefaction of foundation soils, strongly influence the strength that the soil can mobilize under cyclic strain or stress. Figure 3-29 shows a schematic representation of the stress conditions along a potential failure surface beneath a vertical breakwater under cyclic loading.

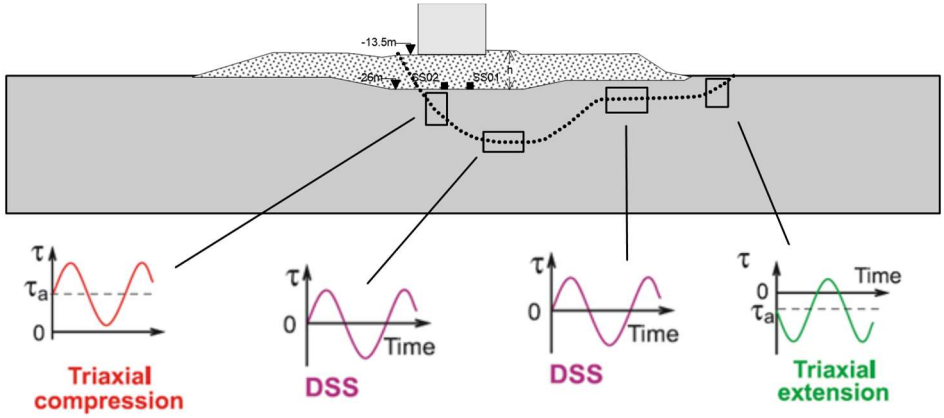

Figure 3-29. Schematic representation of stress conditions beneath a vertical breakwater.

The behaviour of Barcelona Port clay under cyclic loading was investigated through cyclic triaxial tests performed at the Geotechnical Laboratory of UPC and cyclic simple shear test at NGI and CEDEX.

A Bishop and Wesley (1975) type of triaxial stress-path cells was used at UPC to perform cyclic triaxial tests. Soil samples were isotropically or anisotropically (K_0) consolidated before the undrained cyclic stress was applied. Deviatoric cyclic loading ended when failure conditions were reached or, else, when a maximum number of 500 cycles was attained. Samples which did not reach failure during cyclic loading were finally sheared under a monotonic deviatoric loading. A constant frequency of 0.2 and 0.5 Hz was selected.

Figure 3-30a show a cyclic effective stress path followed by an isotropically consolidated sample. Excess pore pressure developed during cyclic shearing (see Figure 3-31a) takes the effective stress path towards the failure envelope (from B to C). Although stress path is still far from the envelope, degradation of stiffness is clearly observed (see Figure 3-30b). The drop of cyclic shear stress amplitude observed in the test is due to changes of sample stiffness because tests were performed in a controlled strain mode.

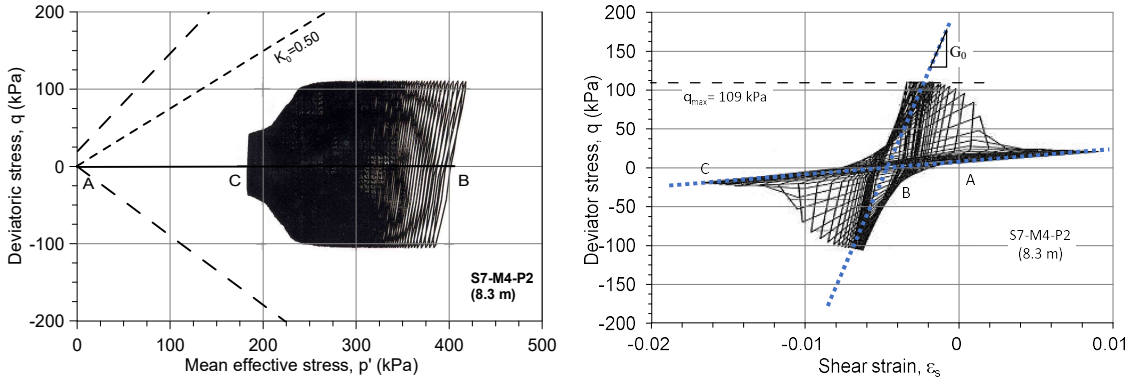

(a) (b)

Figure 3-30. Isotropically consolidated cyclic triaxial test (a) Effective stress path in. (b) Cyclic stress-strain curve

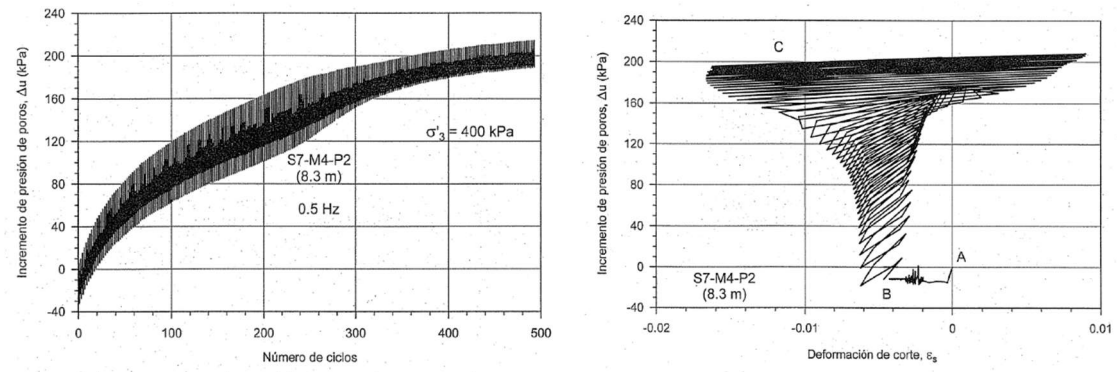

(a) (b)

Figure 3-31. Excess pore pressure evolution in a cyclic triaxial test under isotropic compression as a function of (a) number of cycles (b) shear strains.

Figure 3-32a show the effective stress path followed in a typical triaxial test of a sample consolidated under K_0 condition (AB), subjected to undrained cyclic load (BC) and finally sheared under undrained condition (CD) by a monotonic deviator stress. It was observed that the mobilized undrained strength at the end of the cyclic load was very high (as observed in Figure 3-33b, after a period of pore water pressure generation, dilatant strains take place reducing the pore pressure and increasing the undrained strength). These tests have shown that the undrained strength mobilized after cyclic loading is similar or even higher than the static strength. The stress-strain behaviour of two identical samples tested under similar conditions, but different amplitude of cyclic deviator stress is shown in Figure 3-34. In case of samples S5-M2, changes in monotonic strength do not seem to be significant, probably because cyclic loading induced minor structural changes in the soil. But, in case of samples S6-M4, behaviour was different. The specimen subjected to larger cyclic deviator stress show softening behaviour.

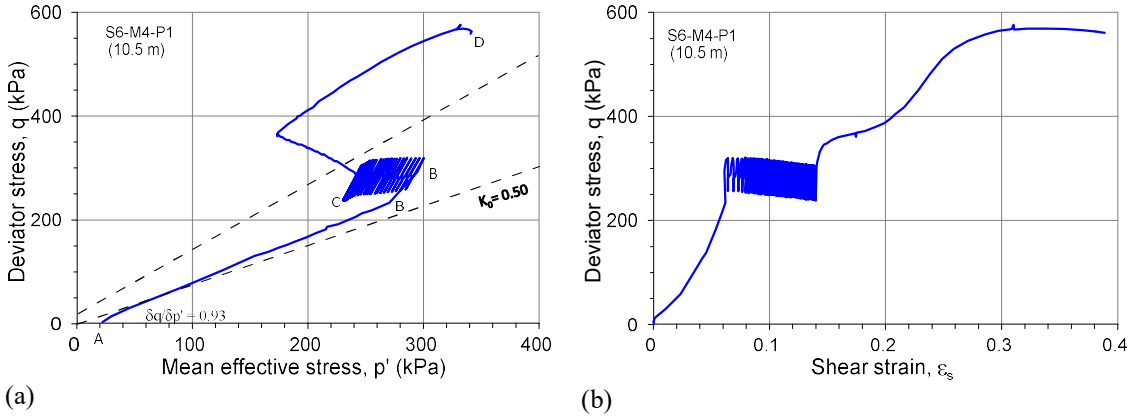

(a) (b)

Figure 3-32. Effective stress path followed in a cyclic triaxial test after the K_0 consolidation.

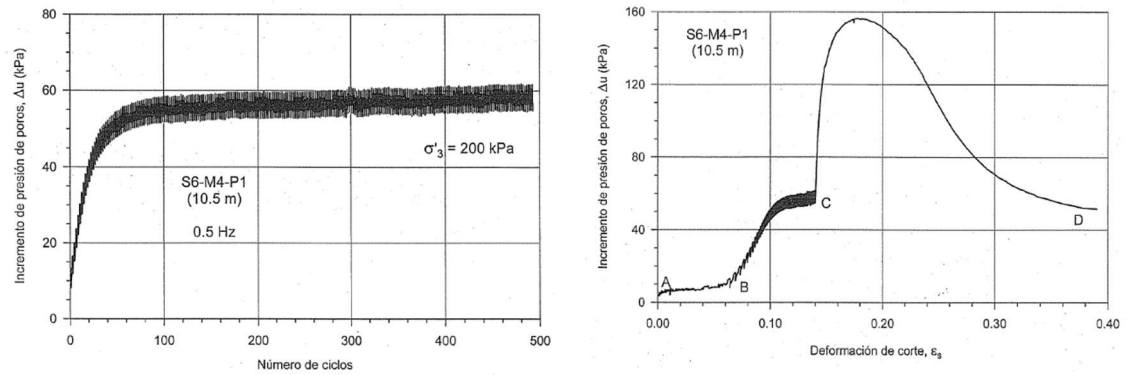

(a) (b)

Figure 3-33. Excess pore pressure evolution in a cyclic triaxial test after the K_0 consolidation as a function of (a) number of cycles (b) shear strains.

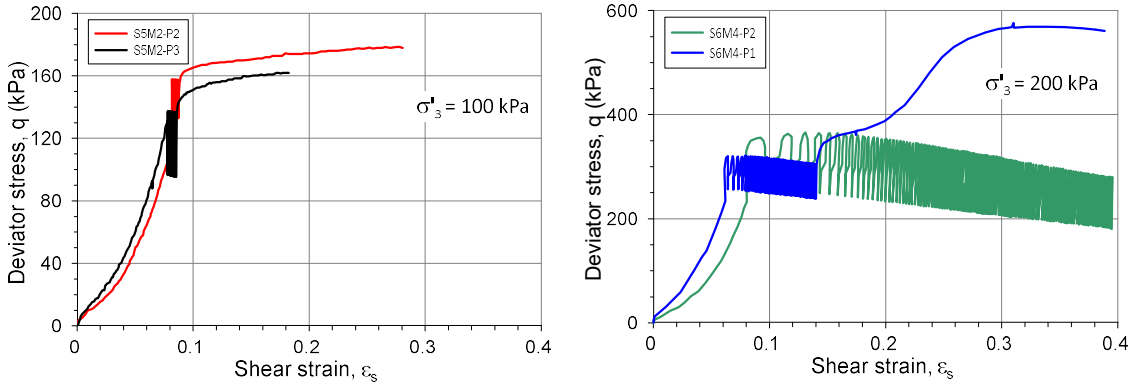

(a) (b)

Figure 3-34. Stress-strain behaviour of cyclic triaxial test under different amplitude of cyclic deviator stress. (a) confining pressure 100kPa (b) confining pressure 200 kPa.

Pore pressures reached at the final cyclic deviatoric stress of the triaxial tests were used to compute the pore pressure ratio (similar to the Skempton A_f parameter) as a relation between the permanent pore pressure and the double amplitude cyclic deviatoric stress. Figure 3-35a shows the pore pressure ratio in relation to the normalized deviatoric stress. It is observed that increased of pore pressure is mainly around 20% of deviatoric cyclic stress for both type of triaxial tests (isotropic and anisotropic), but some exceptions were also observed with tests that reached 50% or even 100%

of deviatoric cyclic stress. For comparison, the A_f values obtained with the static triaxial tests were also included in this figure. Triaxial extension tests show A_f values similar to those obtained with cyclic tests, something that is not observed in triaxial compression tests, which show a quite different pattern with A_f values greater than 1.0. It is worth noting that this feature occurs mainly in samples taken from the upper stratum, where void ratios were higher. Somewhat lower A_f values were found in samples from the intermediate stratum.

Furthermore, the pore pressure ratio $r_u = \Delta u_f/\sigma'_3$, frequently used to define the onset of soil liquefaction (Kramer, 1996), was calculated from the static and cyclic triaxial tests, as shown in Figure 3-35b Results of triaxial extension tests are not included in this figure, since pore pressures are mainly negative in these tests. It is observed that r_u is well below 1.0, with maximum values reached in the isotropic cyclic tests of the order of 0.6.

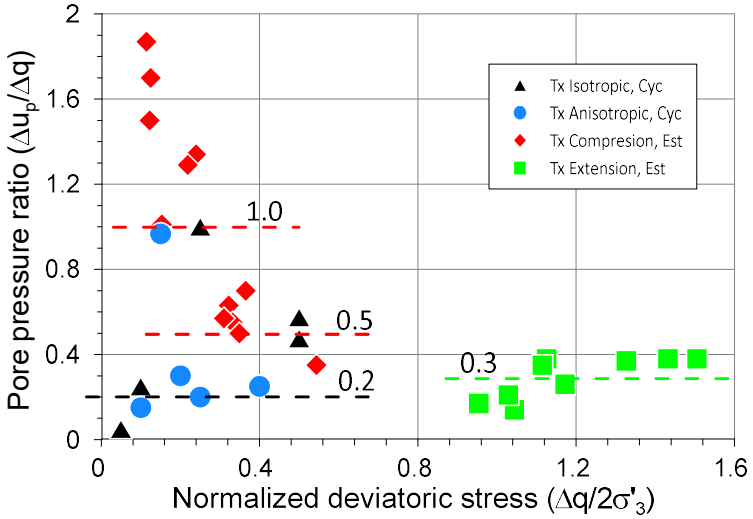

(a)

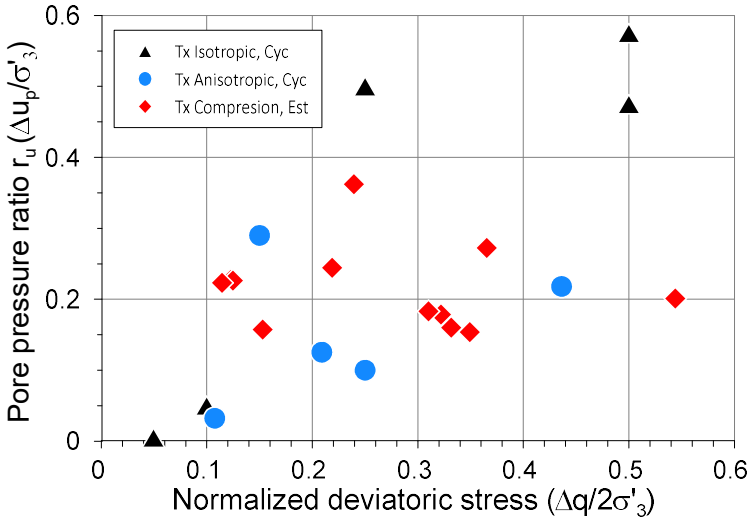

(b)

Figure 3-35. Pore pressure ratio at failure in relation to the normalized deviatoric stress

Wang et al (2018) studied the induced pore pressure during cyclic loading stages in triaxial tests of a marine silty clay. Results have demonstrated that the maximum normalized cyclic-induced pore pressure $\Delta u_{cy}/p_0$ increase with the increase in q_{cy}/p_0, and the initial shear stress q_s/p_0 have a minor effect (see Figure 3-36).

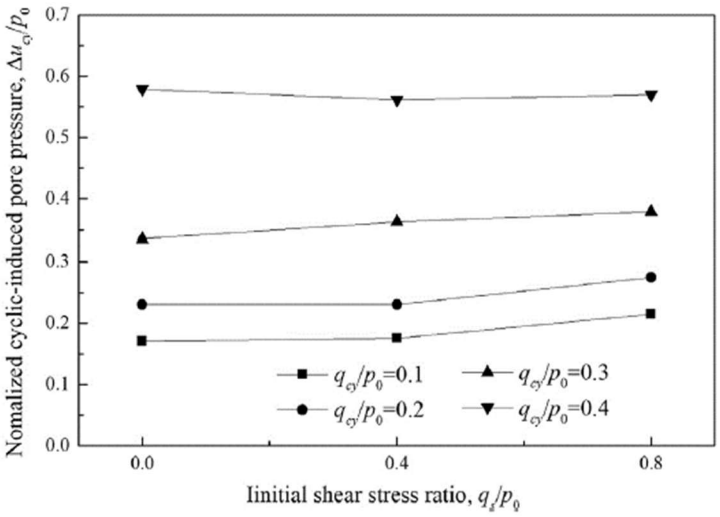

Figure 3-36. Normalized cyclic induced pore pressure $\Delta u_{cy}/p_0$ in relation to the initial deviatoric stress ratio q_s/p_0 (Wang et al, 2018)

Triaxial tests results were complemented with 17 cyclic simple shear tests (DSS). Figure 3-37 shows the stress-strain response of three cyclic simple shear tests performed at Cedex, which were identified as A, B and C. Samples were subjected to cyclic shear stress of 16 kPa, 32kPa and 40 kPa, respectively. After 1900 cycles of load, a small stiffness reduction was observed in test A, while samples in test B and C reached the failure criteria (10% of shear strain) at 250 and 5 cycles of load, respectively. These tests demonstrate the effect of cyclic deviator stress in the degradation of soil stiffness.

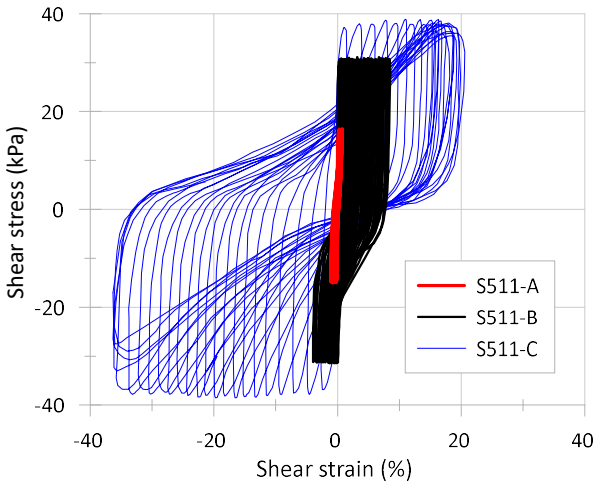

Figure 3-37. Stress-strain behaviour of cyclic simple shear test

An additional specimen was tested (test D) at CEDEX, with an initial shear stress of 16 kPa applied before start the cycled loading of 16 kPa. The aim of this test, was to probe the effect of applying different average shear stress, maintaining the same cyclic deviatoric stress. As expected, soil was able to withstand 2000 cycles of load, although a smaller stiffness degradation can be observed when compared to that obtained in test A under the same cyclic deviator stress (see Figure 3-38). Also, a lower deformation in the hysteresis cycles was observed in this case. Sample A appears to be more affected by the sign change in shear stress. Cyclic direct simple shear tests performed at NGI have shown a similar behaviour.

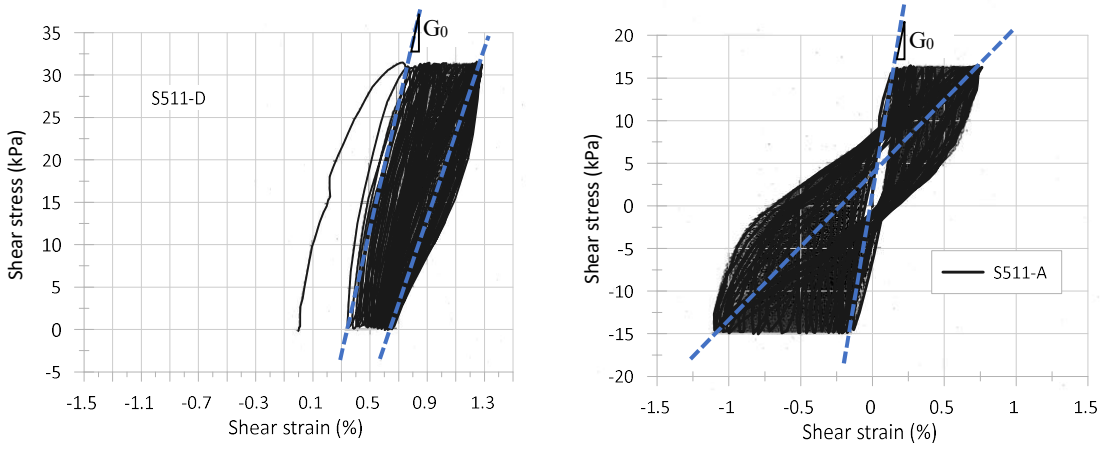

(a) (b)

Figure 3-38. Stress-strain behaviour of cyclic simple shear test (a) initial average shear stress $\tau_a = 16$ kPa, (b) initial average shear stress $\tau_a = 0$ kPa.

Post-cyclic undrained shear strength was also investigated using the direct simple shear tests (DSS) and triaxial tests (Tx). In this case, some samples were subjected to monotonic deviator stress after the cyclic stage. Normalized undrained shear strength obtained from the static tests (DDS and Tx) are compared with the normalized undrained shear strength reached after the cyclic stages in Figure 3-39. In the various shear modes of the static tests performed (DSS, TXC, TxE), the shear strength ratio (s_u / σ'_{v0}) is almost constant, not influenced by increasing σ'_{v0}. On the contrary, the post-cyclic response seems to behave differently. For consolidation stresses less than 230 kPa, a large scatter is observed, but the post-cyclic resistance is generally greater than the static resistance. For confining stresses greater than 230 kPa, post-cyclic strength tends to be less than static strength. It is also worth noting that higher values of post-cyclic resistance were obtained in samples from the upper stratum, where the clay content was lower than 9%. In this sense, the scatter of the results can be explained, in part due to the lack of homogeneity of the soil.

Post-cyclic shear-induced pore pressure $\Delta u_{post}/p_0$ was also studied by Wang et al (2018). Contractant and dilatant behaviour was observed to be controlled by the magnitude of q_s/p_0 and q_{cy}/p_0. At smaller q_s/p_0 and q_{cy}/p_0, the development in accumulated pore pressure of specimens is below some critical value during post-cyclic shear, and thus the specimens contract. However, with

the increase in q_s/p_0 and q_{cy}/p_0, the accumulated pore pressure for specimens reach and exceed the critical value, and hence the dilatant behaviour is exhibited by the soil.

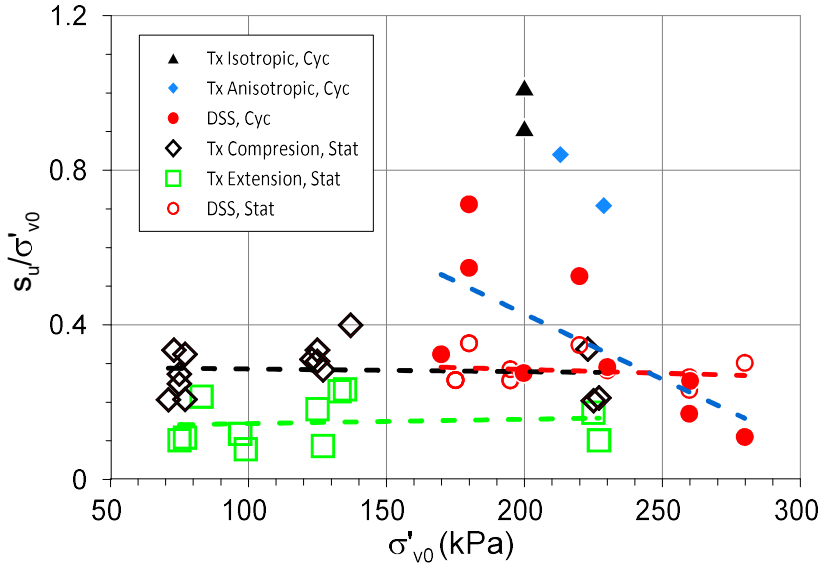

Figure 3-39. Post cyclic undrained strength compare to static undrained strength.

Post-cyclic degradation strength rate can be characterized by the relation between post-cyclic monotonic shear strength ($S_{u,cy}$) and the static monotonic shear strength ($S_{u,st}$), $\beta = S_{u,cy} / S_{u,st}$. Figure 3-40 shows that β decreases with decreasing q_s/p_0 and increasing q_{cy}/p_0, and its rate of decrease increases with increasing q_{cy}/p_0. Wang et al (2018) noted that the post cyclic effective stress path for different number of cycles tends to a common line, which was called the Equivalent Hvorslev line (EHL) (see Figure 3-41). Although this line is not affected by the number of load cycles, it seems that an increase of q_s/p_0 or q_{cy}/p_0 leads to an increase in the slope of EHL, and for larger values of q_s/p_0 and q_{cy}/p_0 it becomes closer to the CSL. Increase of post-cyclic degradation rate and the slope of EHL are both associated with changes in the fabric of clay specimens. With small q_s/p_0 and q_{cy}/p_0, the fabric of the specimen may not be changed during cyclic loading, and the behaviour of post-cyclic strength degradation is mainly caused by the development of cyclic-induced pore pressure. As q_s/p_0 and q_{cy}/p_0 increase, the arrangement of clay grains is changed during cycling and the post-cyclic strength is affected by the change in the fabric of clay specimens.

Erken and Ulker (2008) evaluated the post-cyclic monotonic strength of fine-grained soil with plasticity index varying from 5 to 18 in the torsional test apparatus. It was found that if soil undergoes a cyclic shear strain level below certain yield strain, reduction on monotonic strength is limited, but when the cyclic shear strain level is larger than the yield strain, the monotonic strength decreases down to 40% of the initial strength. Similar conclusion was arrived by Andersen (2015) in relation to a quick clay and the Drammen clay, using the DSS tests (see Figure 3-42). It was noted that the reduction in static shear strength can be significant if the cyclic loading generates large cyclic shear strains, which exceeds the peak strain in virgin monotonic shearing.

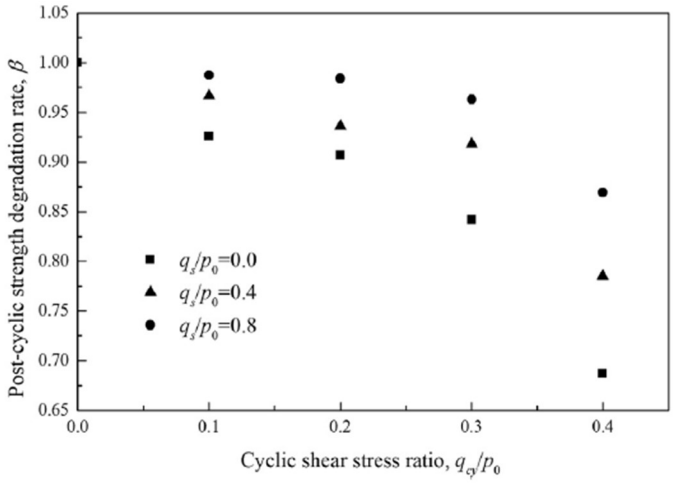

Figure 3-40. Post cyclic undrained strength degradation ratio versus cyclic shear stress ratio (Wang et al, 2018).

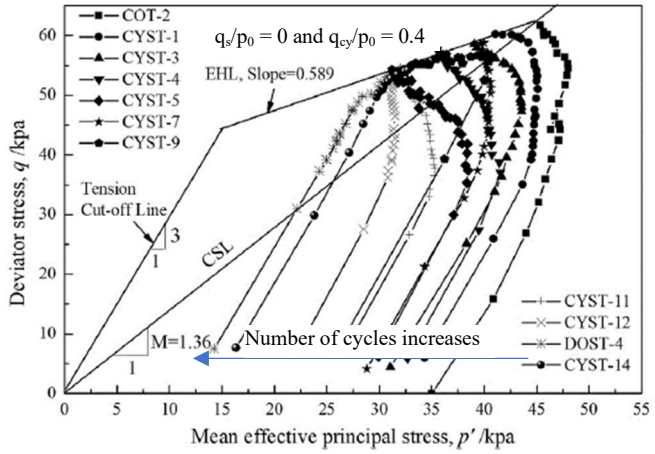

Figure 3-41. Post cyclic effective stress path for different number of cycles (Wang et al, 2018).

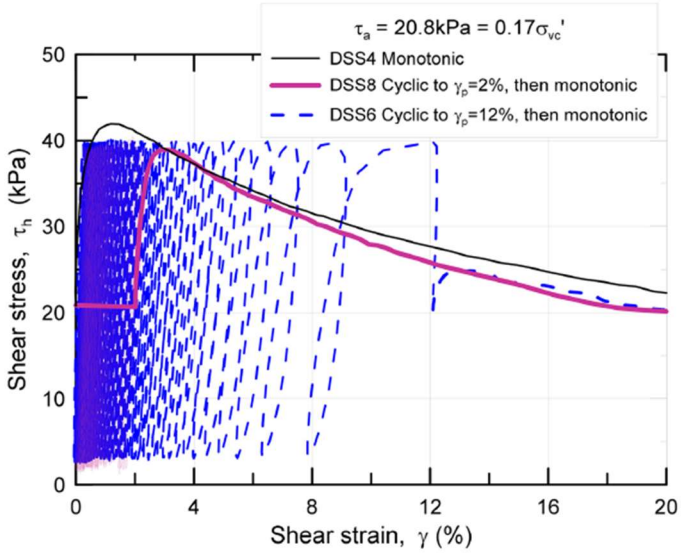

Figure 3-42. Typical results of monotonic tests and tests with cyclic loading followed by monotonic loading (Andersen, 2009).

3.4.1 Cyclic interaction diagram

Results from DSS and Tx tests have been summarized in the interaction diagrams shown in Figure 3-43. This diagram shows a relationship between the normalized average shear stress τ_a/σ'_{vc}, normalized cyclic shear stress τ_{cy}/σ'_{vc} and the number of cycles to reach the failure criteria. In this way, it is possible to define failure envelopes for a given combination of average and normalized cyclic shear stress, allowing to define stable and unstable zones.

The cyclic triaxial tests performed at UPC (UPC, 2001) have allowed constructing the interaction diagram show in Figure 3-43 (a). The stable zone is indicated in this figure by condition $0<\tau_{cyc}/\sigma'_{vc} < 0.14$ if $0<\tau_{ave}/\sigma'_{vc} < 0.26$ and $0< (\tau_{ave} + \tau_{cyc})/\sigma'_{vc} < 0.40$ if $0.26<\tau_{ave}/\sigma'_{vc} < 0.40$. In the same way, the cyclic simple shear tests performed at NGI (NGI, 2002) have permitted define the interaction diagram show in Figure 3-43 (b). In this figure, data for the Norwegian Drammen clay (Goulois et al, 1985) in normal consolidate state, is also included. Figure 3-43 (b) shows the approximate bounds of these combinations for two different loading conditions (40 impacts and 1000 impacts). The normalised cyclic shear stress τ_{cy}/σ'_{vc}, for low values of the normalized average shear stress, is close to 0.16 for 40 loading cycles and to 0.10 for 1000 loading cycles. The static simple shear test led to a safe undrained shear strength value defined by the relation $\tau_{cy}/\sigma'_{vc}+\tau_a/\sigma'_{vc}=0.25$, which was the reference value used to define the undrained strength of Barcelona Port clay. Although it is difficult to compare stress condition of the triaxial test with that of the simple shear test, the results show that the simple shear tests lead to a more conservative failure envelope than the triaxial tests.

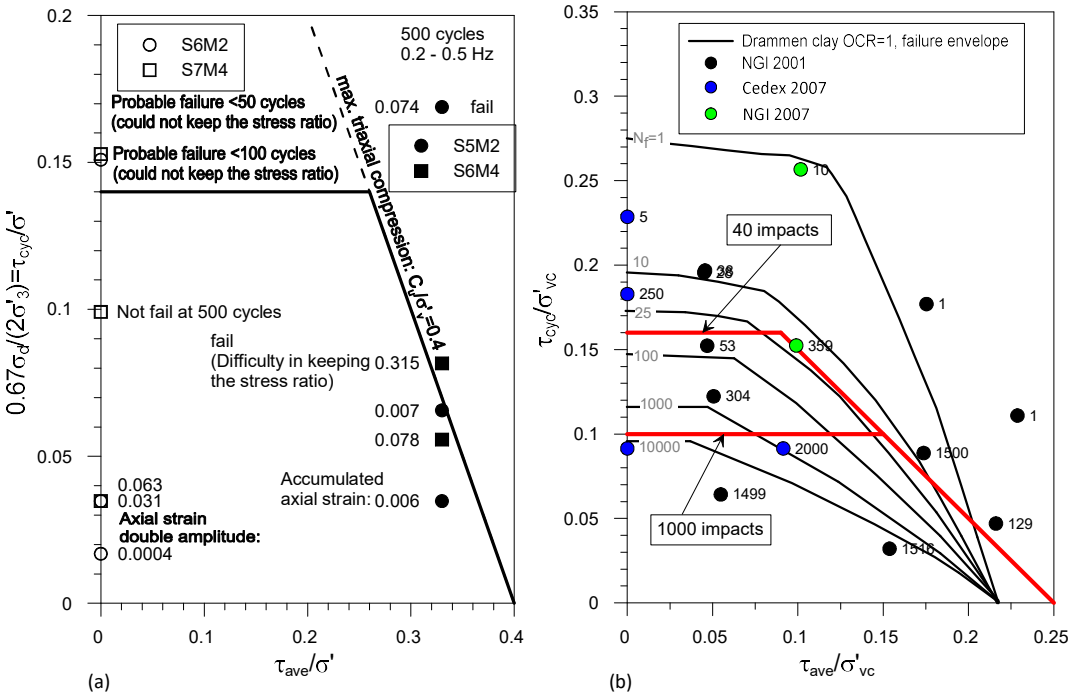

Figure 3-43. Cyclic interaction diagram normalized to effective stress (a) based on cyclic triaxial test (b) based on cyclic simple shear test.

As suggested by Andersen & Lauritzsen (1988), cyclic strength of clay is best normalized by the static shear strength. This normalization has the advantage of being much less influenced by overconsolidation ratio, OCR, than normalization by effective stress. Data for Barcelona Port clay was also normalized by the undrained strength as shown in Figure 3-44. Separate diagrams are presented for DSS and triaxial tests. As reference, the contour diagram for Drammen clay is also included in the plots. The number written beside each point represent the number of cycles to failure, the average shear strain (γ_a) and the cyclic shear strain (γ_{cy}) for that test. Failure was defined as either γ_a or γ_{cy} reaches 10%. Contours defining the combinations of τ_a and τ_{cy} that cause failure after different number of cycles were drawn by interpolation. In addition, the contour of equal shear strain was included in the diagram for the DSS tests. The diagram in Figure 3-44b shows that in DSS tests the contour lines follow two typical failure modes regardless of the number of cycles: first, on the upper flat part of each curve, defined for small to moderate τ_a values, γ_{cy} is the dominant strain, and for large τ_a values corresponding to the sector on a negative slope, γ_a controls deformation at the failure. In triaxial tests, Figure 3-44a shows a similar pattern, but with the cyclic shear stress τ_{cy} increasing until the change of strain mode occurs for small or moderate τ_a values.

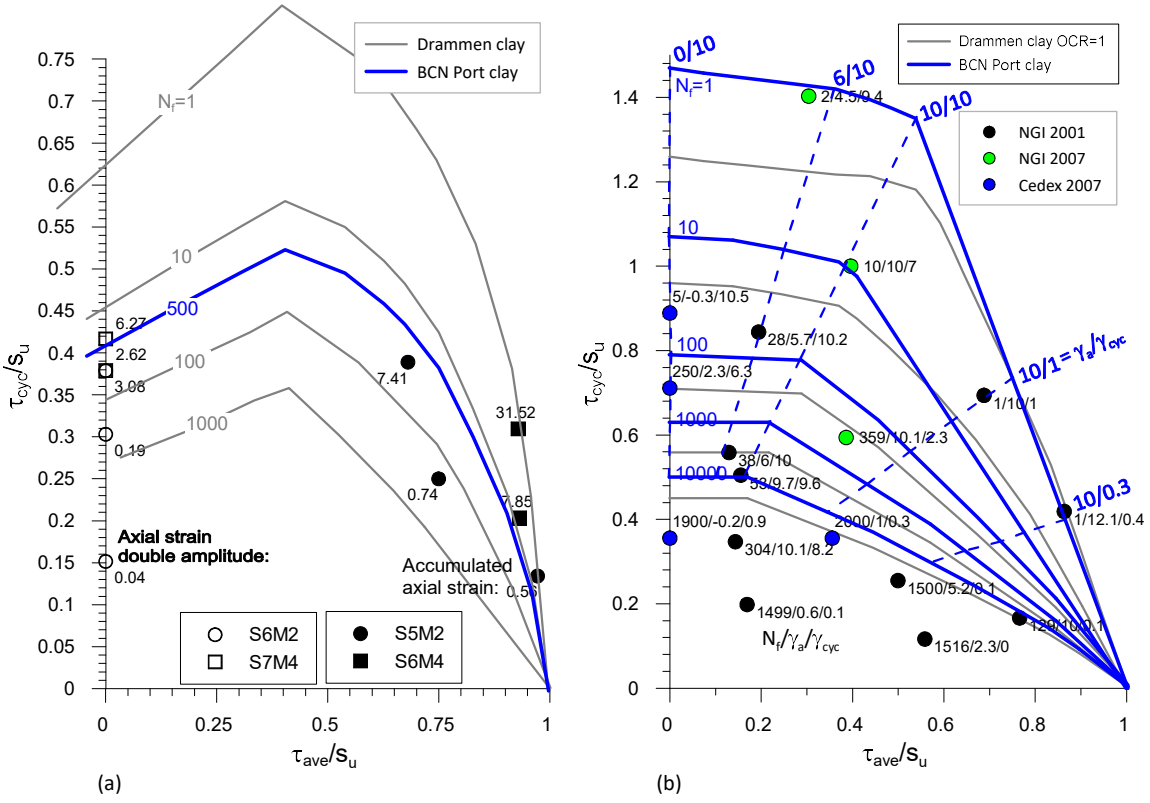

Figure 3-44. Cyclic interaction diagram normalized to undrained static strength (a) based on cyclic triaxial test (b) based on cyclic simple shear test.

Finally, the cyclic shear strength $\tau_{f,cy}$ defined as the peak shear stress that can be mobilized during the cyclic loading (Andersen & Lauritzsen, 1988) as the sum of the average and cyclic shear stress at failure $\tau_{f,cy} = (\tau_a + \tau_{cy})_f$. The cyclic shear strength can be determined from the diagrams in Figure

3-44. The result is presented Figure 3-45a for the compression triaxial tests and Figure 3-45b for DSS tests. This diagram show that the cyclic shear strength depends on τ_a, the cyclic load history (i.e. number of cycles), and the type of test (i.e. the stress path). For the triaxial extension tests, insufficient data was available to draw the contours. The discontinuity observed in the diagram is due to the change of sign corresponding to the shear deformation in extension and compression.

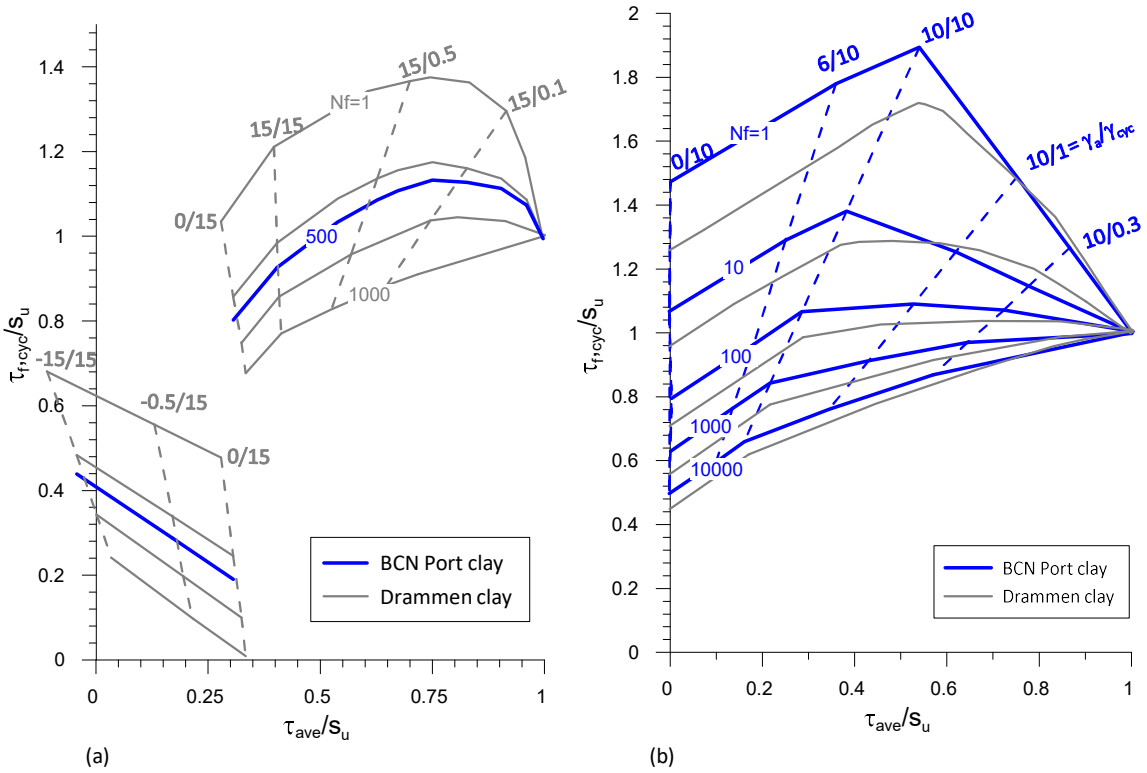

Figure 3-45. (a) Cyclic triaxial compression shear strength (b) Cyclic DSS shear strength.

3.5 COMPRESSION BEHAVIOUR AND CONSOLIDATION

Knowledge of compression behaviour is required to assess settlements of a breakwater, which is a fundamental aspect of design on soft soils. In this way, Barcelona Port clay compression behaviour was first investigated through conventional and long term oedometric tests. To do that, an extensive geotechnical offshore campaign was performed (Rodio, 1996; Eurogeotécnica S.A, 1999). Compression index C_c, swelling index C_s, coefficient of secondary compression C_α and coefficient of consolidation C_v were established from these tests. Taking into account that the prediction of settlement is a key factor in the future behaviour of the breakwater, and also that serious damage occurred to several sensors of the geotechnical instrumentation of the breakwater during construction, in order to obtain greater confidence in the compressibility parameters, it was decided to perform a well-instrumented preload test on the shoreline of the Port of Barcelona in front of the breakwater. Boreholes and CPTu tests were also performed, and undisturbed samples were tested

in oedometer cells (UPC, 2008). The coefficient of consolidation was also determined in CPTU dissipation tests performed at several depths. CPTU tests provided also a detailed soil profile.

The load test, which has an extension of 80x160m, was instrumented by means of several piezometers and four sliding micrometers (Kovari and Amstad, 1982) capable of monitoring vertical deformation at 1 m intervals. Vertical deformations were monitored up to a depth of 60m. Special emphasis was given to evaluating creep behaviour.

In general, a reasonable agreement between preload tests results and laboratory tests on samples was found as described later in this section.

3.5.1 Compressibility characteristics from oedometric tests

The objective of these tests is to determine the parameters of compressibility of a soil under lateral confinement condition according to different vertical effective stress applied in successive steps of loading (consolidation) and unloading (swelling). During the development of the project to expand the Port of Barcelona, oedometric tests have been carried out in different stages, the results of which are included in this section. The tests carried out during the development of this thesis correspond to the 2008 campaign on the preload test site. This section focuses primarily on the results of these tests.

3.5.1.1 Oedometric Test Equipment

Standard Maier oedometer cells and ETI type were used. The sample holder ring has dimensions of 70mm in diameter and 20mm in height in the case of Maier cells and 50mm in diameter and 20mm in height in the case of the ETI cells. The loads were applied by a reaction system provided with a lever arm that allows the loads to be amplified to a ratio of 1:8. All tests were carried out with double drainage, that is, porous stones were used both in the lower part and in the upper part of the sample. The deformations were measured with 0.01mm precision micrometers.

3.5.1.2 Test procedure

- Conventional oedometer tests

The samples were extracted from the borehole using 'Shelby' tubes. In the laboratory the 'Shelby' were carefully opened avoiding as much as possible any type of disturbance to the sample. Once the sample was extracted, it was cut so that it can be placed in the ring of the oedometric cell and then the sample is cut at the height of the ring (the ring has previously been lubricated). The excess material is used to determine the initial water content of the samples.

The oedometric cell is assembled by inserting the ring with the sample, together with the porous stones and the loading piston. The samples are ready to start the test when the oedometric cell is installed in the load application system.

Before applying the load steps, the samples are saturated with distilled water for a minimum period of 1 day.

All tests were carried out with loading and unloading stages; in this way it is possible to evaluate both the compressibility in primary load (C_c) and the compressibility in unload -reload path (C_s). Increases of loads of 1-day duration were applied successively, starting from an initial setting load of 5 kPa up to a maximum vertical stress of 3200 kPa. A summary of loading steps followed by the different laboratories is show in Table 3-4.

Table 3-1. Summary of Loading step

Laboratory	Loading steps (kPa)												
PAYMA 1996	6.3	12.5	25.0	50	100	200	400	800	1600	3200	800	100	12.5
INEMA 1999	5	50	100	200	600	1200	2400	500	100	5.0			
UPC 2008	5	50	100	200	400	800	200	50					

- Long term oedometer tests

In addition to the conventional tests performed on the breakwater soil samples, long term oedometric tests were carried out in samples extracted from the preload test site in order to evaluate the creep characteristics of the materials under slightly overconsolidation conditions.

These are tests with stages of loading, unloading and final reload until reaching a degree of overconsolidation (OCR) between 1.10 and 1.30, as expected during breakwater construction. Once the desired overconsolidation is achieved, creep is controlled for a period of 3 months (See Figure 3-46 for the case of the oedometer test 8). Oedometric tests with similar characteristics, but with shorter creep periods and larger OCRs were performed by Alonso et al (2002).

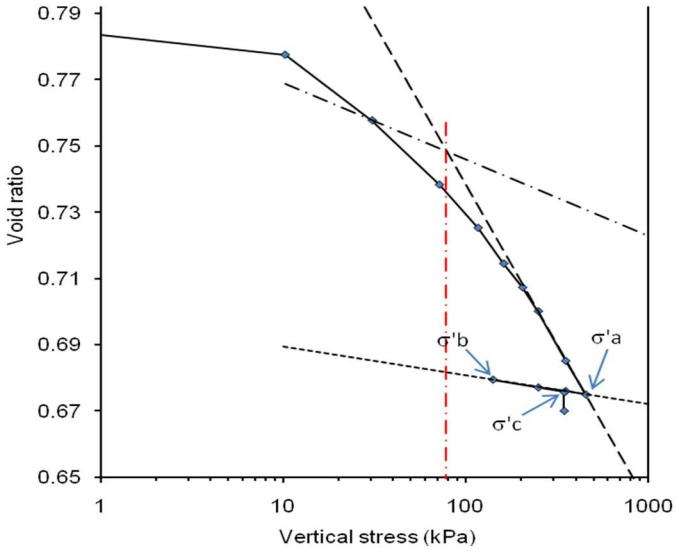

Figure 3-46. Load history followed in the oedometer test 8.

3.5.1.3 Procedure for interpreting results

For each load step, the primary consolidation coefficient (C_v), the secondary consolidation coefficient (C_α), permeability (k) and the oedometric module (E_m) was examined. Do to that, a one-dimensional consolidation model was implemented in a spreadsheet, which allows the adjustment of settlement curves in the laboratory with those of the consolidation model of Terzaghi (1943), using the SOLVER tool. The deformation of the soil in oedometric conditions can be interpreted as the sum of a set of 3 deformation mechanisms: instantaneous deformations, deformation by primary consolidation and deformation by secondary consolidation. These three components are incorporated into the spreadsheet as follows.

- Initial settlement: It corresponds to the settlements that occur when applying the load, as a result of the accommodation of the particles, or the compression of small amounts of air trapped in the soil.

$$s_i = d_0 \tag{3.12}$$

- Primary settlement: Associated with the hydro-mechanical process is defined according to the theory of Terzaghi (1943). The degree of consolidation is calculated from the analytical solution of the consolidation equation, in this case the first 4 terms of the following series have been used:

$$U = 1 - \sum_{m=0}^{m=\infty} \frac{2}{M^2} \exp\left(-M^2 T_V\right) \tag{3.13}$$

Where:

$$M = \frac{\pi}{2}(2m+1) \tag{3.14}$$

$$T_V = \frac{c_v t}{H_{dr}^2} \tag{3.15}$$

H_{dr} is the drain distance of the sample; c_v is the consolidation coefficient and t is time. The settlement corresponding to the primary consolidation is calculated using the equation:

$$s_p = h_0 m_\alpha \Delta \sigma'_v U \tag{3.16}$$

Where, h_0 is the initial height of the sample, m_α is the compressibility coefficient and $\Delta\sigma'_v$ is the increase in effective tension produced by the settlement.

- Secondary settlement: The secondary consolidation coefficient C_α is defined as the ratio between the variation of vertical deformation ($\Delta\varepsilon$) over a logarithmic time cycle, measured after the end of the primary consolidation:

$$C_\alpha = \frac{\Delta \varepsilon}{\Delta \log t} \tag{3.17}$$

In the model, secondary settlement is calculated from time t_{90} that corresponds to 90% of the primary consolidation ($t > t_{90}$).

$$s_s = H_0 C_\alpha \log(t / t_{90}) \tag{3.18}$$

Where, H_0, is initial height of the sample.

Finally, the settlement measured in the tests is compared with the total settlement of the model ($s=s_i+s_p+s_s$). The adjustment parameters are C_v, C_α, m_α y d_0.

Permeability has been calculated from the consolidation coefficient, according to the following relationship:

$$k = \frac{\gamma_w C_v}{E_m} \tag{3.19}$$

Where: γ_w is the specific weight of water and E_m is the oedometric module of the soil (inverse of m_α).

3.5.1.4 Test results

Parameters derived from oedometer tests (compression index, swelling index ratio, coefficient of consolidation, coefficient of secondary compression) are presented in Table 3-2. Coefficient C_v and C_α have been determined for an increase of load equivalent to that experienced by a point under breakwater. The value of the compression index C_c and swelling index C_s are shown versus depth in Figure 3-47. It is noted that C_c values varies from 0.1 to 0.3 and Cs from 0.013 to 0.05. The ratio of Cc/Cs varies mainly between 4 and 8.

It is valuable to compare the results obtained in the laboratory against some of the most common correlations. Based on modified Cam Clay model, Wroth and Wood (1978) showed that C_c can be estimated as follows:

$$C_c = 0.5 G_s (PI/100) \tag{3.20}$$

In which G_s=specific gravity of solids. Using typical G_s=2.7 for clays gives:

$$C_c \approx PI/74 \tag{3.21}$$

Table 3-2. Results obtained from oedometer tests

Bore.	Sample	Depth	w0	e	γ_s	γ_n	γ_d	C_c	C_s	C_v (cm^2/s)	C_α	SUCS
AS3	G260 I6	11.0–11.6	40.1	0.994	2.59	1.86	1.42	0.297	0.051	2.78E-03	4.87E-03	OL-ML
	G264 I10	19.0–19.6	30.9	0.801	2.69	2.03	1.60	0.223	0.03	4.22E-03	2.28E-03	CL
	G266 I12	23.0–23.6	26.6	0.72	2.73	1.97	1.56	0.185	0.025	6.95E-03	2.50E-03	CL-ML
	G272 I18	35.0–35.6	33.5	0.883	2.71	1.92	1.47	0.227	0.04	2.13E-03	3.90E-03	CL
AS4	G275 I1	1.0–1.6	33.3	0.817	2.69	1.74	1.26	0.151	0.013	2.70E-04	8.30E-03	CL
	G278 I4	13.0–13.6	40.1	1.083	2.72	1.81	1.33	0.24	0.05	5.50E-03	3.00E-03	CL
	G281 I7	25.0–25.6	30.4	0.802	2.70	1.92	1.49	0.212	0.03	4.40E-03	2.30E-03	CL
S4	M-6	16-17	27.4	0.704	2.703	1.98	1.55	0.131	0.032	8.15E-03	5.62E-03	CL
	M-9	32-33	29	0.843	2.71	1.90	1.47	0.141	0.018	6.87E-03	3.67E-03	ML
	M-12	47-48	35.8	0.961	2.688	1.86	1.37	0.222	0.045	6.91E-04	5.72E-03	CL
S5	M-6	18-19	27.4	0.782	2.691	1.92	1.51	0.120	0.016	1.49E-02	5.86E-03	ML
	M-9	32-33	30.8	0.831	2.700	1.93	1.48	0.150	0.035	3.81E-02	7.60E-03	CL
	M-12	63-64	20.7	0.559	2.698	2.09	1.73	0.099	0.013	3.04E-03	2.13E-03	SC
S6	M-6	20-21	27.6	0.750	2.713	1.98	1.55	0.201	0.050	7.95E-03	3.46E-03	ML
	M-9	33-34	24.1	0.753	2.699	1.91	1.54	0.191	0.018	4.33E-03	2.71E-03	CL
	M-12	56-57	20.8	0.603	2.709	2.04	1.69	0.121	0.020	8.87E-03	2.29E-03	CL
	M-15	77-78	20.8	0.583	2.706	2.07	1.71	0.151	0.030	3.61E-03	3.18E-03	ML-OL
SPz	M-1	71-72	26.0	0.778	2.702	1.92	1.52	0.141	0.039	5.73E-03	5.11E-03	SM
5.1	M-4	84.5-85.5	22.6	0.612	2.708	2.06	1.68	0.201	0.051	7.30E-03	4.02E-03	CL
	M-7	95-96	18.3	0.504	2.708	2.13	1.80	0.100	0.013	4.49E-03	4.24E-03	SM

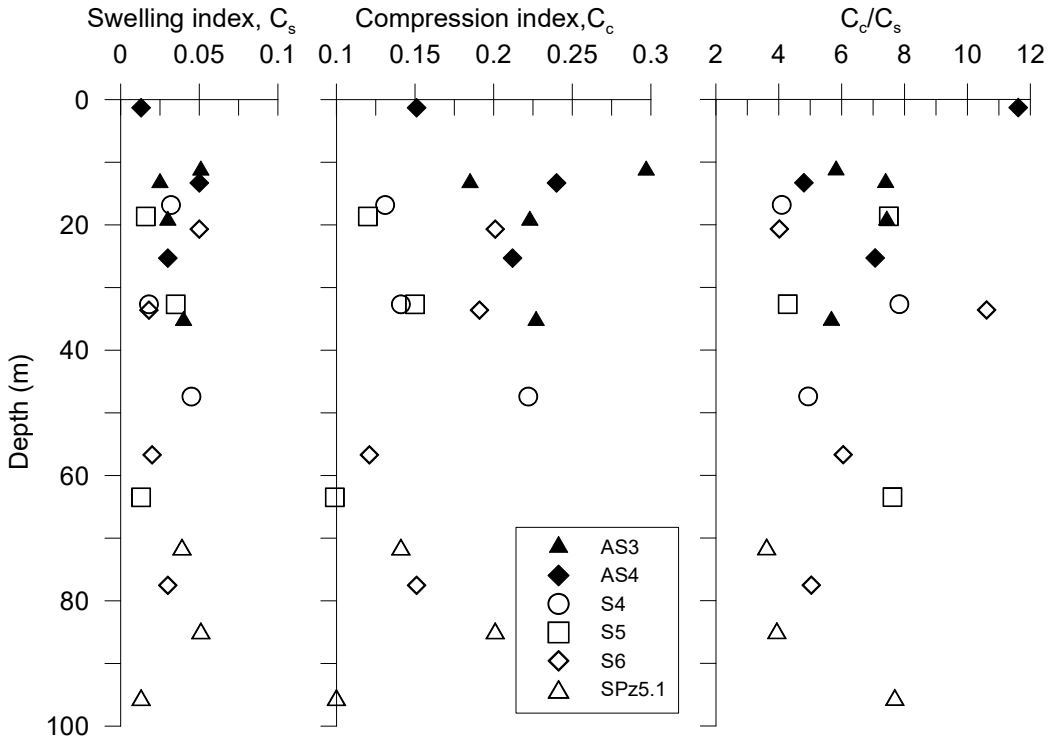

Figure 3-47. Swelling and compression index obtained from oedometer tests

In the same way, the unload-reload index can be calculated as:

$$C_s = C_c (1 - \Lambda) \tag{3.22}$$

Using the typical value of Λ=0.8 with Gs =2.7 gives:

$$C_s \approx PI / 370 \tag{3.23}$$

Both correlations are compared with the results of oedometer tests in Figure 3-48. Also shown in this figure are the collected data by Kulhawy and Mayne (1990), which shows agreement between measured values of C_c and C_s and those predicted using the modified Cam Clay model.

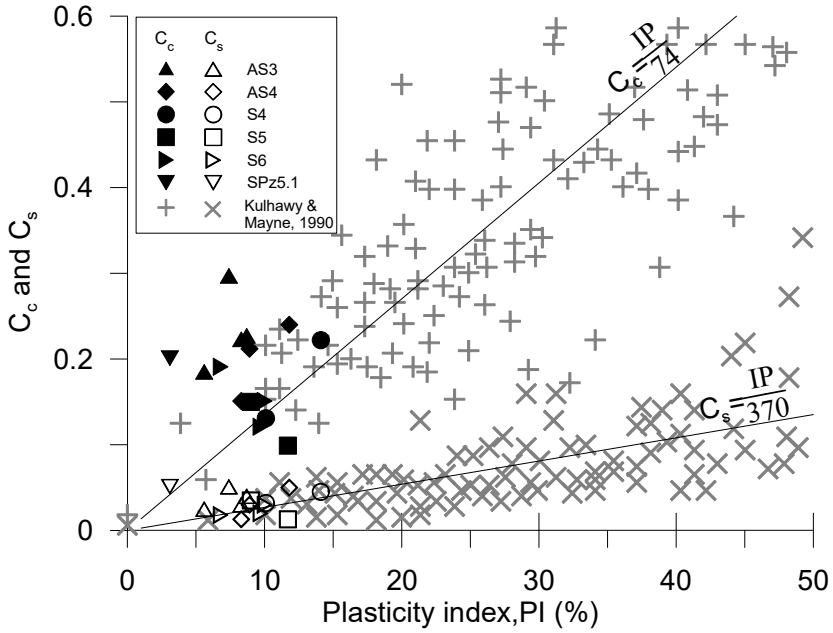

Figure 3-48. Compression and expansion indices as a function of plasticity index.

The C_c values of the clay soils in Barcelona Port, are also correlated with natural moisture content, liquid limit and void ratio, as shown in Figure 3-49. It was found that C_c correlate fairly well with these parameters. Some empirical equations used to estimate the value of C_c are listed in Table 3-3.

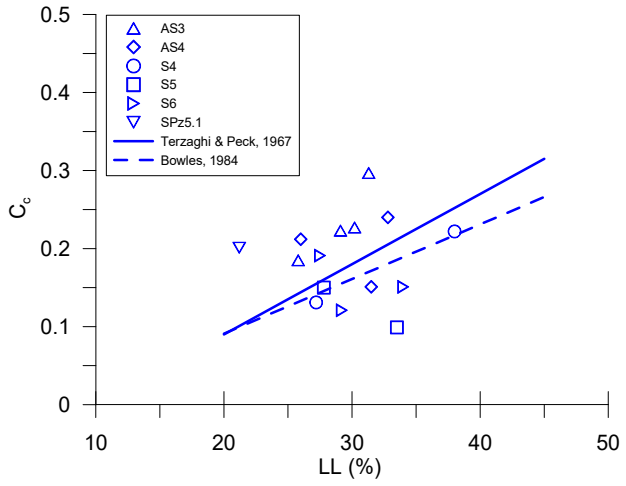

(a)

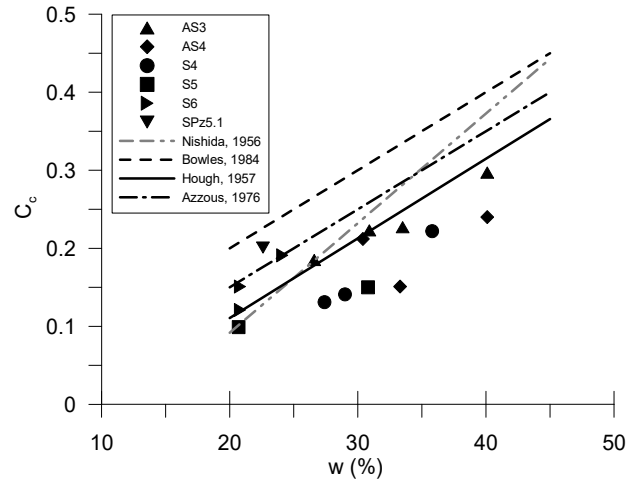

(b)

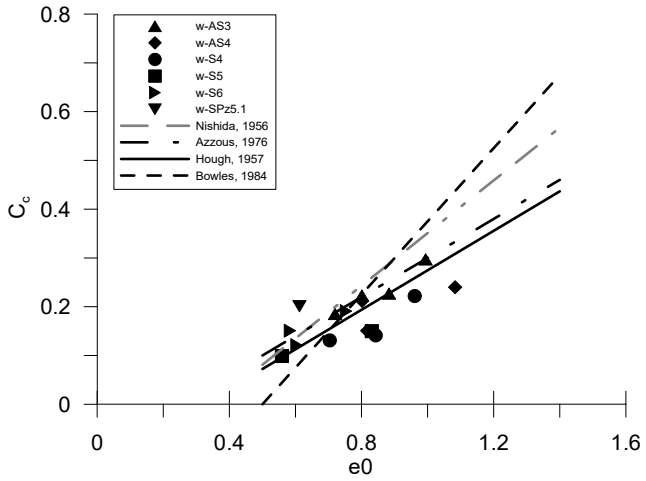

(c)

Figure 3-49. Correlation of compression index C_c, with the (a) liquid limit *LL*, (b) natural moisture content *w* and (c) void ratio e, for Barcelona Port clay

Table 3-3. Empirical equations to predict C_c

$C_c = 0.54(e_0 - 0.35)$	Nishida 1956	Undisturbed clay
$C_c = 0.0054(2.6w_n - 35)$	Nishida 1956	Undisturbed clay
$C_c = 0.4(e_0 - 0.25)$	Azzouz et al 1976	Clays in USA and Greece
$C_c = 0.01(w_n - 5)$	Azzouz et al 1976	Clays in USA and Greece
$C_c = 0.4049(e_0 - 0.3216)$	Hough 1957	Silt, clay, silty clay and inorganic soil
$C_c = 0.0102(w_n - 9.15)$	Hough 1957	Silt, clay, silty clay and inorganic soil
$C_c = 0.009(LL - 10)$	Terzaghi & Peck 1967	Normally consolidated, moderately sensitive
$C_c = 0.01(w_n)$	Bowles 1984	Chicago clays and Alberta Province in Canada
$C_c = 0.007(LL - 7)$	Bowles 1984	Remoulded clays

Values of the coefficient of consolidation, C_v obtained from the last load step of oedometer tests are presented in Figure 3-50. It is observed that value of C_v varies mainly from $2x10^{-3}$ to $1x10^{-2}$ cm/s^2.

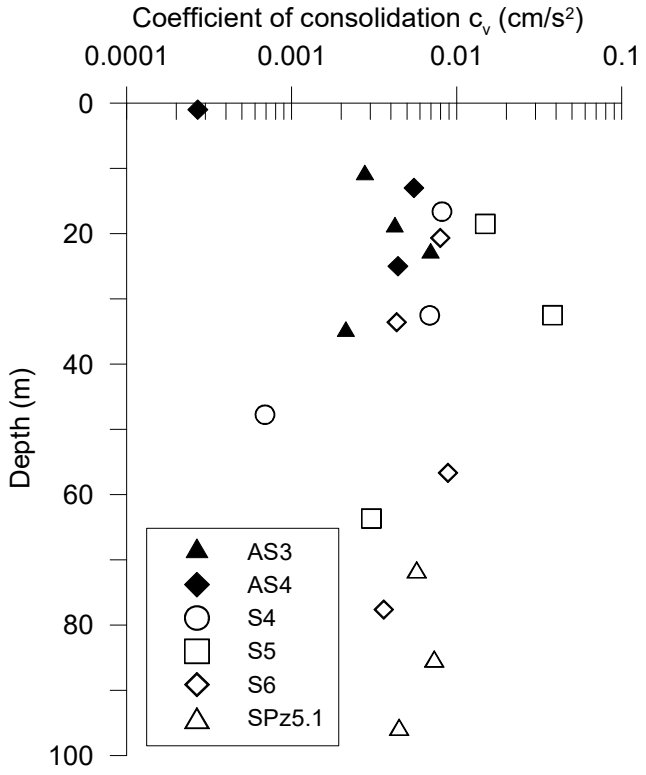

Figure 3-50. Coefficient of consolidation from oedometer tests.

Table 3-4 shows a summary with the main parameters obtained from long term oedometer tests. The maximum secondary consolidation coefficient C_{α_max} coincides with the normally consolidated soil states, while the minimum secondary consolidation coefficient C_{α_min} corresponds to overconsolidated soil. Unlike conventional tests where it is only possible to obtain the maximum secondary consolidation coefficient, long-term tests allow obtaining values for these two parameters.

Table 3-4. Summary of oedometric tests.

Id	Sample	Depth (m)	UCS	w (%)	LL	LP	%<Nº200	γn (kN/m³)	γd (kN/m³)	e0	Cc	Cs	Cv (cm²/s)	Cα (max)	Cα (min)	k (cm/s)
EDO-1	M4-Sh3	6.0	CL	26.15	34	19	89.89	19.4	15.4	0.755	0.152	0.005	4.23E-03	5.11E-03	2.00E-03	6.02E-08
EDO-2	M4-Sh6	16.0	SM	21.23	NP	NP	20.52	18.2	15	0.795	0.094	0.005	8.00E-02	2.30E-03	9.99E-04	3.12E-08
EDO-3	M4-Sh9	33.0	CL	20.54	34	21	97.07	18.8	15.6	0.733	0.107	0.006	1.25E-02	2.75E-03	3.23E-03	3.73E-08
EDO-4	M4-Sh11	45.0	ML	22.72	NP	NP	65.6	19.7	16.1	0.681	0.157	0.019	6.17E-04	4.54E-03	-	1.10E-09
EDO-5	M4-Sh10	39.0	SP-SM	12.64	NP	NP	7.8	16.4	14.6	0.853	0.132	0.009	2.17E-03	3.73E-03	-	4.26E-09
EDO-6	M4-Sh13	57.0	CL	18.96	36	19	98.08	20.9	17.5	0.54	0.122	0.021	8.78E-03	3.59E-03	-	1.31E-08
EDO-7	M1-SH3	18.0	SP-SM	9.5	NP	NP	10.1	14.2	12.9	1.09	0.129	0.008	3.98E-03	3.61E-03	-	9.11E-09
EDO-8	M1-SH4	21.0	SM	10.64	NP	NP	17	16.6	15	0.796	0.097	0.009	4.01E-03	2.11E-03	1.29E-03	5.39E-09
EDO-9	M4-SH1	2.0	SP	13.42	NP	NP	3.98	20.6	18.1	0.49	0.050	0.004	2.07E-02	1.73E-03	-	3.92E-08
EDO-10	M2-Sh2	16.0	SP	22.69	NP	NP	5.4	20.8	16.9	0.596	0.056	0.008	3.75E-03	2.00E-03	9.00E-04	5.47E-08
EDO-11	M3-Sh2	24.0	CL	12.87	33	19	92.1	18.5	16.4	0.647	0.086	0.009	3.68E-03	1.88E-03	2.00E-03	1.18E-07
EDO-12	M2-Sh3	27.0	CL	36.34	35	20	95.2	18.1	13.3	1.029	0.192	0.012	1.57E-02	5.83E-03	2.00E-03	1.25E-07
EDO-13	M3-Sh4	42.0	CL	24.01	36	21	92.6	19.4	15.3	0.763	0.130	0.009	2.32E-03	2.49E-03	1.88E-03	1.66E-09
EDO-14	M3-Sh5	48.0	ML	21.13	NP	NP	74.5	20.1	16.6	0.625	0.103	0.003	4.66E-04	2.02E-03	6.36E-03	4.95E-10

SUCS = unified soil classification system; LL = liquid limit; IP = plastic index; w = moisture content; γ_n = natural specific weight; γ_d = dry specific gravity; e_0 = void ratio; C_c = Compressibility coefficient; C_s = Swelling coefficient; C_v = Consolidation coefficient; C_{α_max} = Maximum secondary consolidation coefficient; C_{α_min} = Minimum secondary consolidation coefficient; k = permeability

3.5.1.5 Consolidation curves

Figure 3-51 shows the consolidation curves of the reloaded steps obtained in the long-term oedometer tests. It is well known that the primary consolidation time in reloaded stages is reduced compared to the case of normally consolidated samples, so that the primary consolidation in these loading steps is virtually negligible. Only in a few cases, the change in slope, that indicates the end of the primary consolidation is perceived. The fact that the readings were taken manually makes it difficult to observe these changes of slopes, which occur at very short times.

On the other hand, Figure 3-51 indicates that the classical theory of secondary consolidation, which considers secondary deformation as a straight line with slope C_α, is applicable only to the first section of the tests, for times greater than 10,000 minutes, that is, in the long term, a systematic change in slope is observed in all the curves shown, thus moving away from the behaviour described by classical theory.

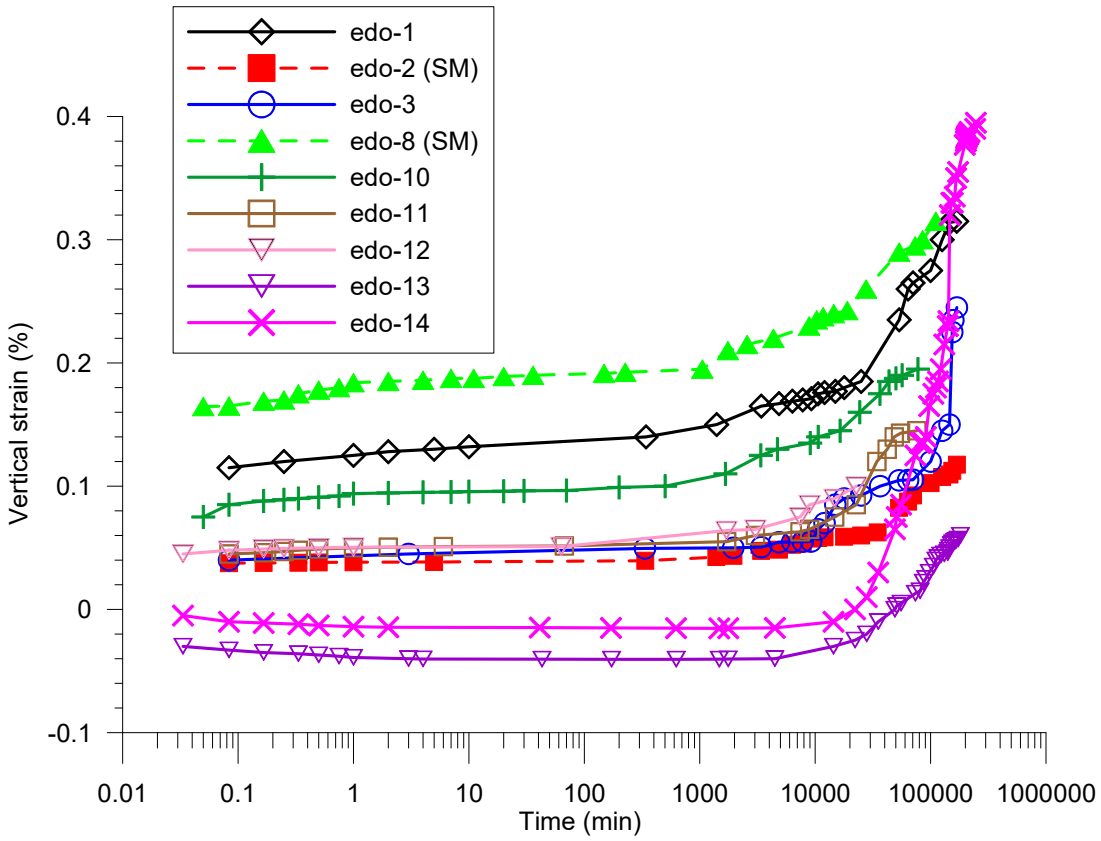

Figure 3-51. Consolidation curves of the tests carried out during the reload stage.

The value of the initial deformation is influenced by the value of the void ratio at the beginning of the loading stage and the respective load increase. In Figure 3-52, the void ratio values are shown at the beginning of the last loading step applied to the samples. In general, the value of the void ratio obtained is around 0.6, with the exception of sample Edo-12, where 0.90 was obtained. This

would indicate that the value of the initial deformation observed in the curves of Figure 3-51, would be predominantly influenced by the increase in applied load.

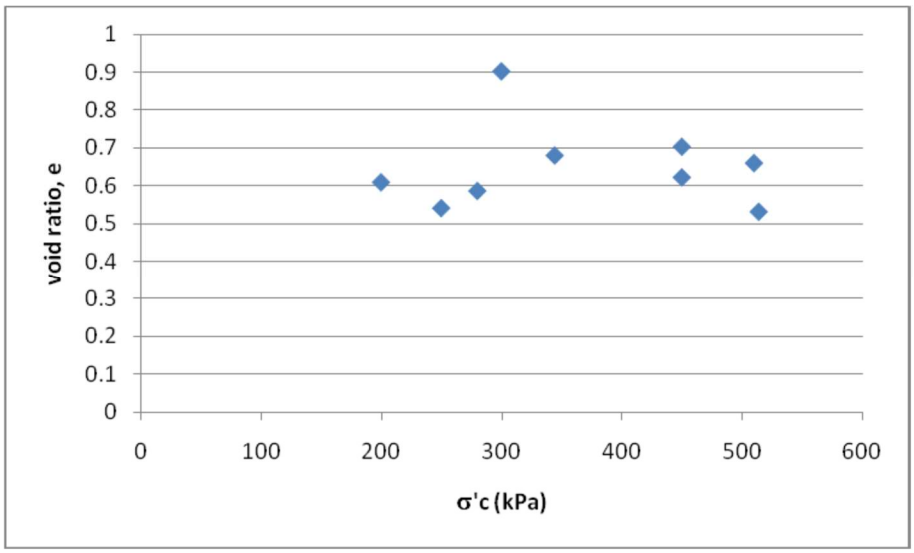

Figure 3-52. Values of void ratio with the final load applied to the samples.

3.5.1.6 Influence of overconsolidation ratio

The tests were conducted so that the degree of overconsolidation will vary between 1.1 and 1.3 (slightly overconsolidated clay). As can be seen in Figure 3-53, the secondary consolidation coefficient C_α is drastically reduced with the increase in the degree of overconsolidation. As shown in Figure 3-54 in all cases tested, C_α is reduced around 1% to 10% of the initial value; However, in long-term tests it was observed that C_α cannot be characterized with a single slope, as it is non-linear, so that C_α changes its slope reaching values close to the initial normally consolidated state.

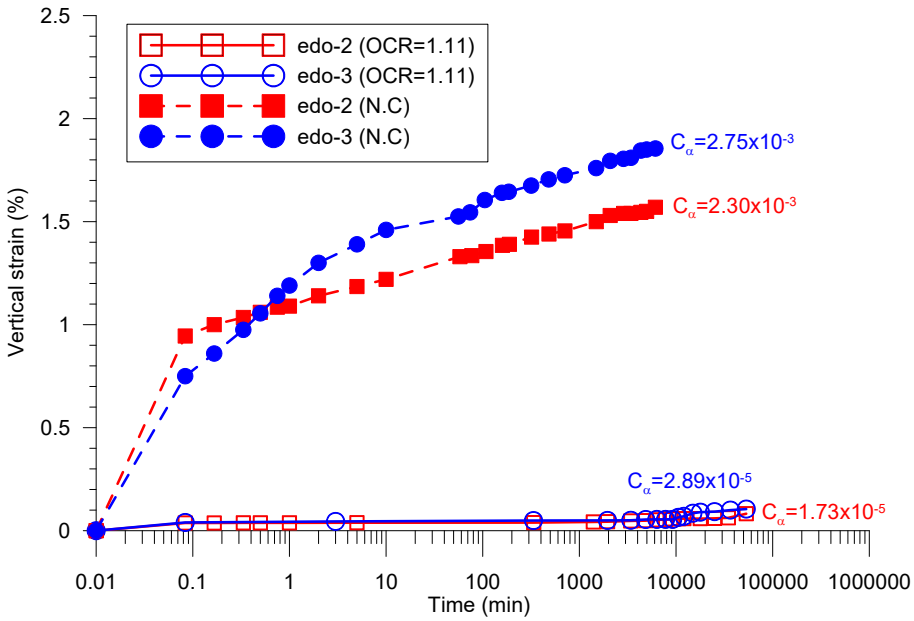

Figure 3-53. Consolidation curves of two different samples under the normally consolidated and overconsolidated condition.

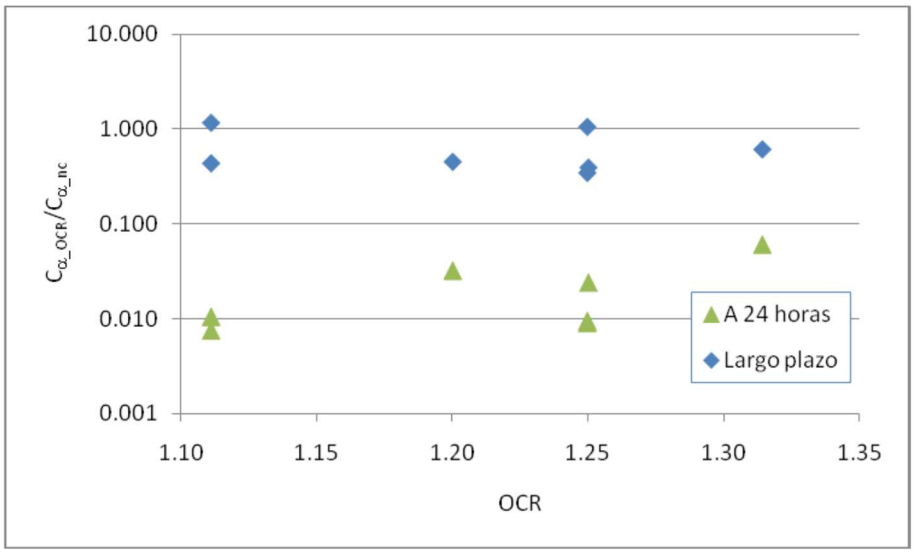

Figure 3-54. Relationship between Cα in normally consolidated and overconsolidated samples versus the degree of overconsolidation

3.5.1.7 Influence of load increase

The effect of the load increase on the secondary consolidation coefficient can be seen by plotting C_α with respect to the ratio σ'_c/σ'_b, which is a measure of the load increase. The value of C_α obtained during the first 24 hours of the test versus σ'_c/σ'_b is shown in Figure 3-55. As expected, as the increase in load is greater, the value of C_α is also greater. On the other hand, when plotting the C_α values corresponding to the final section of the test, these are close to the $2x10^{-3}$ value, regardless of the initial load increase (see Figure 3-56).

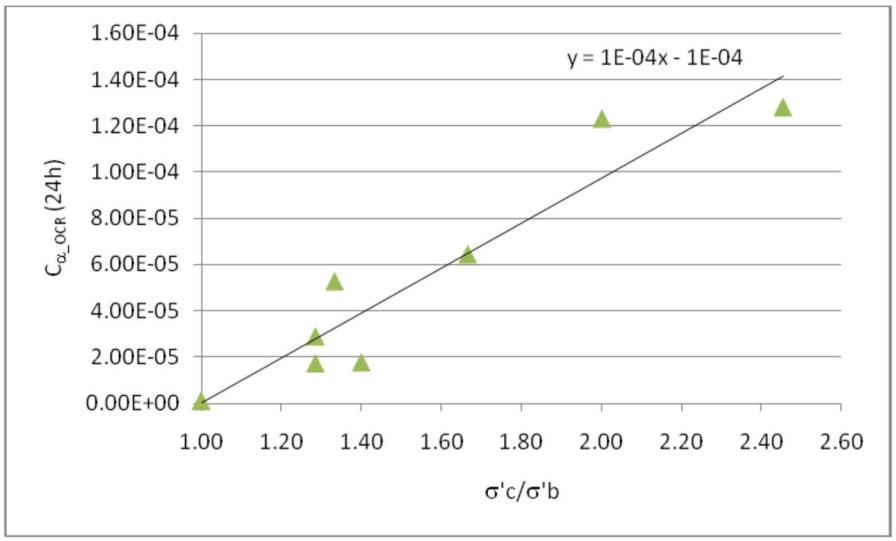

Figure 3-55. Effect of load increase in C_α in the short term

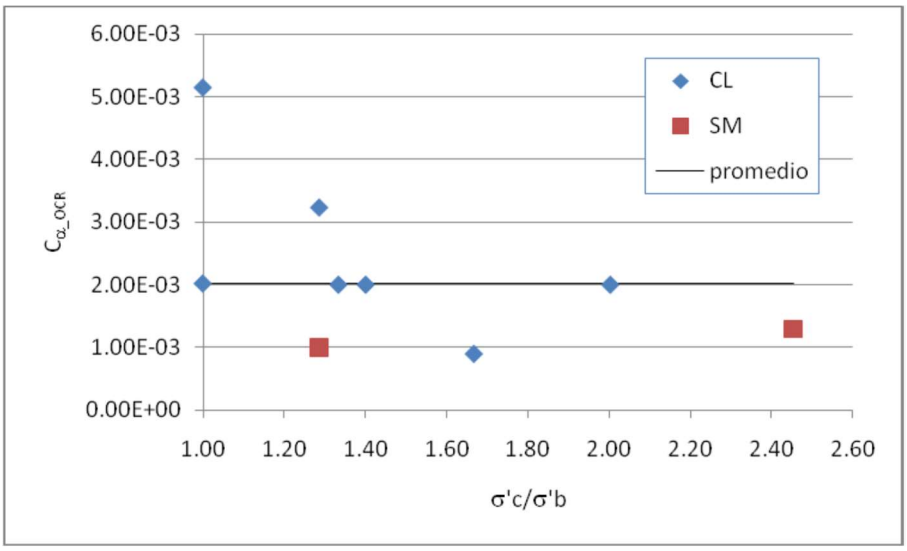

Figure 3-56. Effect of load increase in C_α in the long term

3.5.2 Compressibility characteristics from a large-scale preload test

The construction of new breakwaters at the Barcelona Harbour requires an accurate assessment of settlement in order to limit future settlements under the design loads. Although compressibility parameter was established from undisturbed samples, it was decided to use computational methods to compute settlements. A preloading test was selected as a convenient tool to perform this task.

Difficulties arise in practice because of the limitations to determine precisely the geometry of the consolidating foundation soils. The nature of internal drainage, the "in situ" primary and secondary deformability and the development in time of settlements after loading are difficult to establish on the basis of conventional soil investigation procedures. As a further example of difficulties encountered, the secondary compression rate is controlled by the overconsolidation ratio (OCR), a variable changing in space and time, which depends on a number of aspects describe in the previous section: the initial OCR profile, the actual stress distribution and the preloading times.

The preloading test occupied a 160 m x 80 m rectangular area (see Figure 3-57) and was located on land in front of the breakwater. Sliding Micrometers provided an accurate record of vertical deformations at 1m intervals. Piezometers of the vibrating wire type offered time records of pore pressures at some depths during the loading, consolidation and unloading stages. Both types of instruments could be directly compared with model predictions.

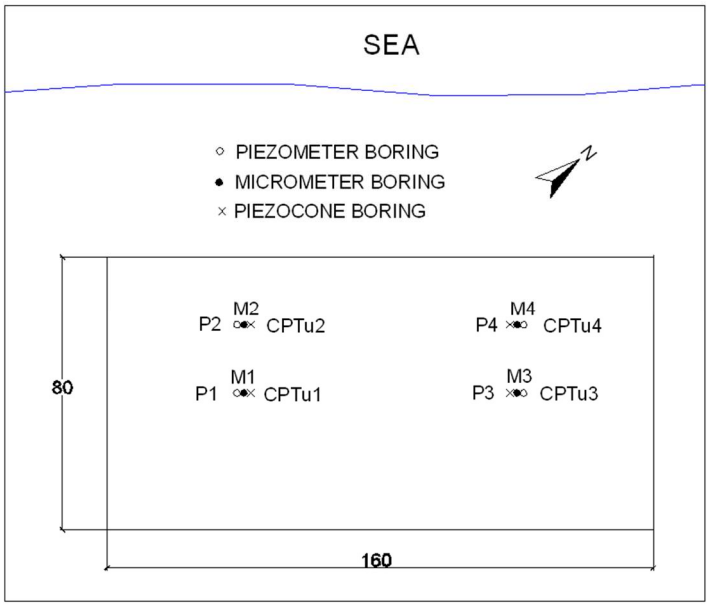

Figure 3-57. Preloaded area (180 m x 60 m). Location of CPTU tests and borings for continuous extensometers and piezometers.

3.5.2.1 Soil profile at the preload test site

The soil profile at zone of preload test is, in general terms, described by a sequence of fine sands, silts, and clays as shown in Figure 3-58a. A granular substratum provides a stiff lower boundary. CPTU tests provided a detailed picture of layering (Figure 3-58b) which is only approximately correlated with the visual description of the stratigraphic sequence. The stratigraphic profile is totally compatible with that at the breakwater location, when compared from level -20m downwards.

Micrometers were also fundamental to identify precisely the detailed soil layering in terms of its stiffness. Therefore, they provide additional information to the data derived from Cone Penetration Tests with pore pressure measurements, CPTU's.

Clayey levels were classified as CL (Low plasticity Clay) or ML (Low plasticity silt), following the Unified Soil Classification System. Liquid limits and plasticity indices remain in the range 34-36% and 13-17% respectively. However, a significant proportion of the profile is classified as silts, sandy silts and sands of no plasticity. These latter soils are less relevant for the breakwater settlement computation.

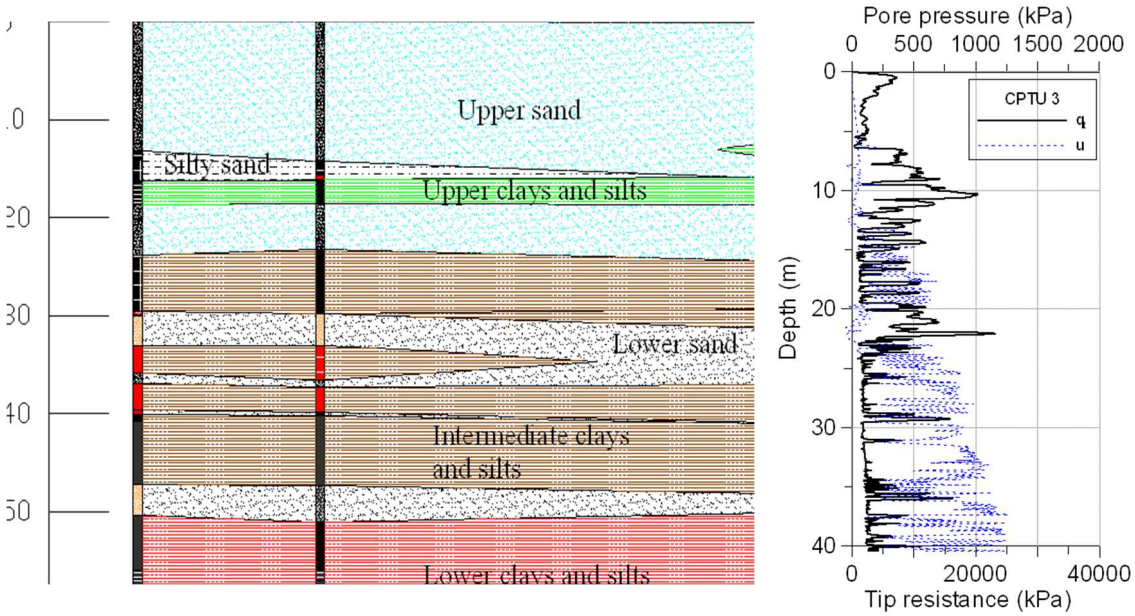

(a) (b)

Figure 3-58. a) Stratigraphic soil profile derived from samples recovered in borings. b) Tip resistance and pore pressure response of CPTU 3.

The void ratio measured in recovered samples is quite variable. Fine clayey and silt materials reach values of e = 0.85 – 1.1 but there are also denser sandy levels (e = 0.5 – 0.7). Measured confined virgin compression coefficients (oedometer tests) for the softer layers lie in the range C_c= 0.1 – 0.2. In sandy layers this coefficient may reduce to C_c= 0.05. Measured coefficients of consolidation span a wide range ($8x10^{-2}$ cm^2/s for sandy soils to $5x10^{-4}$ cm^2/s for the more plastic ones). Measured secondary compression rates were rather uniform for all the samples tested (14 tests): C_α= 1.7 to 5.8 x 10^{-3}. Table 3-5 provides a summary of the geotechnical properties of the foundation soils.

Table 3-5. Geotechnical properties of foundation soils

Layers	UCS	LL (%)	PI (%)	e	C_c	C_s	c_v (cm^2/s)	C_α
Clayey soils	CL – ML	34 – 36	13 – 17	0.85 – 1.1	0.1 – 0.2	0.005 – 0.021	$5x10^{-4}$	$1.88x10^{-3}$ – $5.1x10^{-3}$
Sandy soils	SP – SM	-	-	0.5 – 0.7	0.05	0.004 – 0.008	$8x10^{-2}$	$1.7x10^{-3}$ – $3.7x10^{-3}$

3.5.2.2 Geotechnical instrumentation

The test embankment reached a maximum elevation of 10.5 m over mean sea level. A reference time t = 0 was established as the origin of instrument readings (28.10. 05). Most of the embankment loading was applied in the interval t = 160 to 170 days. Then the embankment remained at full height until it was unloaded to h = 6.50 m in the period t = 370 - 390 days and a further lowering to h = 2.50 m from t = 460 to t = 480 days. Figure 3-59 shows the sequence of loading, consolidation and unloading.

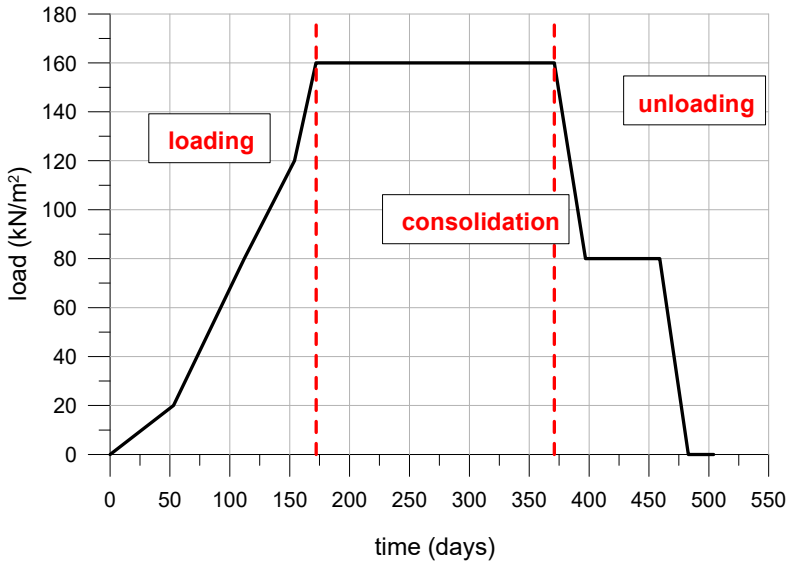

Figure 3-59. Stages of loading, consolidation and unloading.

The preload test instrumentation consists of 4 sliding micrometers and 4 piezometer chains consisting of 3 sensors each. The sliding micrometers allow obtaining records of the vertical deformation in each meter of ground up to the installed depth of 60 meters. In this way, it was possible to obtain a complete profile of vertical deformations, which in turn can be integrated to obtain the profile of vertical settlements. On the other hand, piezometers made it possible to obtain pore pressure measurements that are useful to control soil consolidation. Additionally, topographic control plates have been installed that allow the control of settlements at the base of the embankment. These measurements allow contrasting the measurements obtained with the sliding micrometers, increasing the reliability of the measurements.

Some of the results obtained with the geotechnical instrumentation are described below and were used to calibrate the numerical model that is described in later chapters.

3.5.2.3 Sliding micrometers

The sliding micrometer was developed at the Swiss Federal Institute of Technology (Kovari et al, 1979). It is a precision instrument to measure deformations, and determinate the complete distribution of deformations and axial displacement along a measurement line; it can be used in rock, concrete or soil. It uses a specially designed measuring casing that contains couplings with metallic measuring marks spaced at 1m intervals. The casing is installed in a 100 mm diameter borehole.

The readings are made with a probe that is inserted into the case and moves step by step through each of the marks. By rotating the probe 45º and pulling the guide bar, the two probe heads are tensioned between two adjacent measurement marks. A linear displacement transducer (LVDT)

inside the probe is activated and the measured values are transmitted over a cable to a digital readout unit. A scheme of this instrument is shown in Figure 3-60.

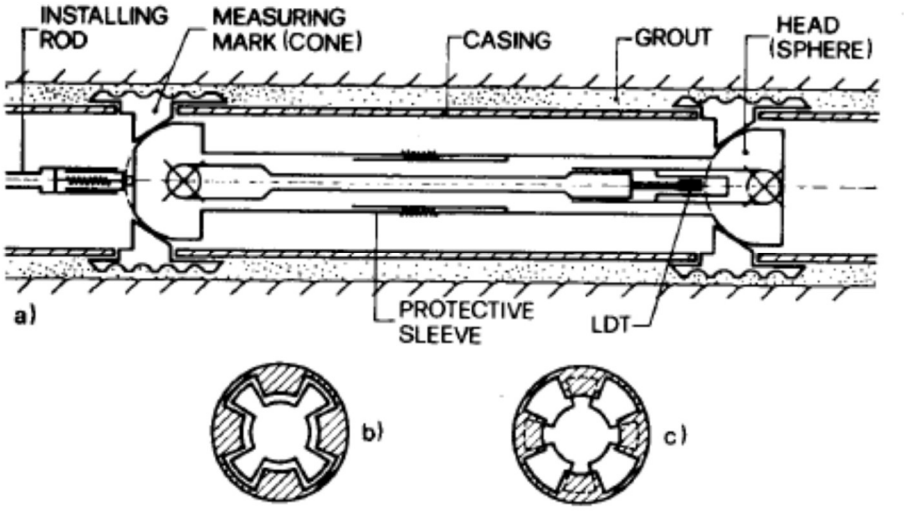

Figure 3-60. Sliding micrometer, a) schematic view, b) sliding position, c) measuring position. (Kovári et al, 1979)

Figure 3-61 to Figure 3-64 show the vertical deformation profile and the settlement profile obtained from the sliding micrometers after one year of measurements. The vertical deformation records obtained indicate the existence of stratified soils in the study area. These stratifications show different compressibility characteristics. The high compressibility of materials located between 10 and 35 meters deep is highlighted. From a depth of 35 meters, the compressibility of the materials is gradually reduced, probably as a consequence of the greater overconsolidation that occurred at those levels due to the decrease in the lower piezometric level, due to the exploitation of the lower aquifer. These measurements were made during the construction period of the preload embankment and in the 6 months after the embankment construction. The plots show the sequence of highly deformable layers in the first 30 - 35 m. Maximum measured deformations reached 45mm/m (4.5%). The plot shows also a progressive stiffening of the soil profile below a depth of 35m.

In Figure 3-65 to Figure 3-68, the vertical deformation-time curves obtained at different depths are shown for each of the installed micrometers. These curves reflect the variability in the compressibility characteristics of the materials found at different depths. Similarly, during the unloading of the embankment, deformation measurements were taken, these are shown in Figure 3-69 to Figure 3-72. Interpretation of these measurements was performed using the 1D consolidation model described in section 2.7. The model parameters were adjusted iteratively layer by layer until a good match with the measurements was achieved (Micrometer 2 was used as a reference for this task). The results of this adjustment are shown in Table 3-6. Also, Figure 3-75 shows the results of the different tests carried out to investigate the soil compressibility. It it observed that soil compressibility parameters (C_c, C_s, C_v, C_α) obtained from the 1D consolidation

model are in good agreedment with those derived from oedometric tests. The compression coefficient varies mainly between 0.1 and 0.3, while the swelling coefficient varies between 0.01 to 0.05. In general, a greater scatter of results is observed in the coefficient of consolidation, which changes from a minimum of about $2x10^{-4}$ to 0.1 cm^2/s. The coefficient of secondary consolidation seems to be the less variable, obtaining similar results with the different testing techniques used (mean value of $2x10^{-3}$).

The integration of micrometer deformations from an assumed fixed point at a depth of 60 m provides a settlement record during the loading period. The four installed micrometers led to similar settlements – time plots, as shown in Figure 3-73 for the loading stage. Maximum settlements reached 0.65m. Independent topographic surveys provided similar results which is an indication of the stiff character of foundations soils below the depth of 65 m. Unloading the embankment in two steps resulted in a rebound measured also by the micrometers (Figure 3-74). It should also be noted in these two figures that the settlement curves calculated with the 1D consolidation model agree quite well with the measured settlements.

Micrometers delivered also time records of relative displacements for 'virtual' layers 1 m thick extending from the soil surface to the lower gravels. They were most useful to create and validate soil deformation models as illustrated in the next chapter.

Table 3-6. Parameters used for the 1D consolidation model

Material	e_0	Depth (m)	C_s	C_c	c_v (m^2/d)	c_{α_max}	c_{α_min}	$c_{\alpha dec}$	σ_{ref} (kN/m^2)	t*
clay 1	0,80	12-14	0.0124	0.180	0.0025	0.0050	0.0002	13	100	15
clay 2	0,80	25-26	0.0140	0.3500	0.0006	0.0080	0.0002	13	100	15
clay 3	0,80	34.5-36	0.0180	0.260	0.0008	0.0060	0.0002	13	100	15
clay 4	0,80	21-22 23-24	0.0100	0.1700	0.0005	0.0040	0.0002	13	100	15
clay 5	0,80	15-17	0.0100	0.2300	0.0030	0.0080	0.0002	13	100	15
clay 6	0,80	31-32	0.0250	0.550	0.0006	0.0080	0.0004	13	100	15
clay 7	0,80	37.5-39 41-42 49-50	0.0220	0.200	0.0008	0.0060	0.0002	13	100	15
clay 8	0,80	45-48	0.0150	0.090	0.0030	0.0040	0.0002	13	100	15
clay 9	0,80	43-44	0.0240	0.200	0.0003	0.0050	0.0002	13	100	15
clay 10	0,80	51-52	0.0150	0.230	0.0008	0.0040	0.0002	13	100	15
clay 11	0,80	27-29	0.0230	0.200	0.0009	0.0060	0.0002	13	100	15
clay 12	0,80	53-56	0.0090	0.150	0.0040	0.0040	0.0002	13	100	15
clay 13	0,80	9-10	0.0110	0.1035	0.0006	0.0040	0.0001	13	100	15
clay 14	0,80	5-7	0.0100	0.0900	0.0016	0.0040	0.0002	13	100	15

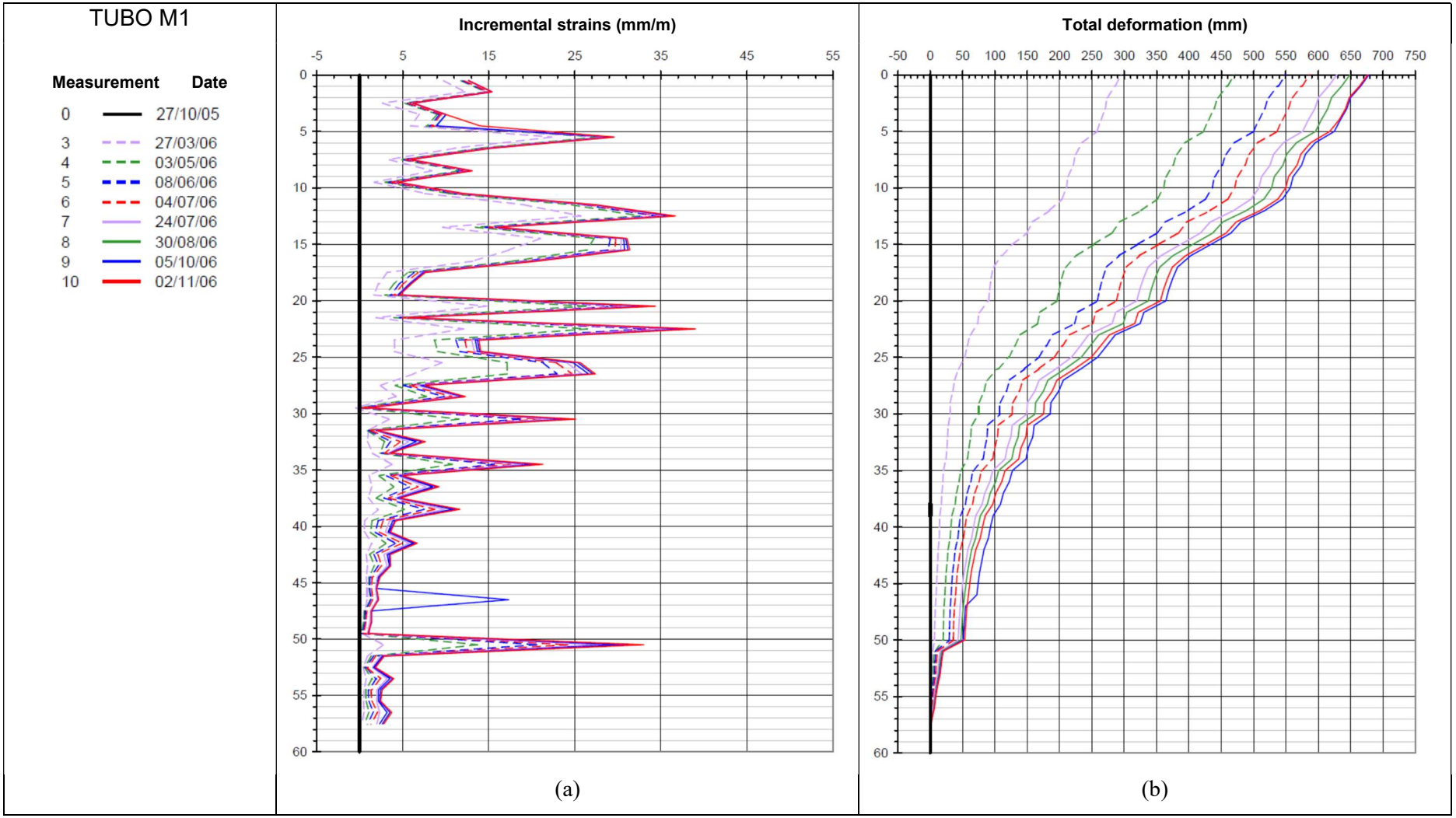

Figure 3-61. Micrometer 1. (a) Vertical deformation profile and (b) vertical settlement profile.

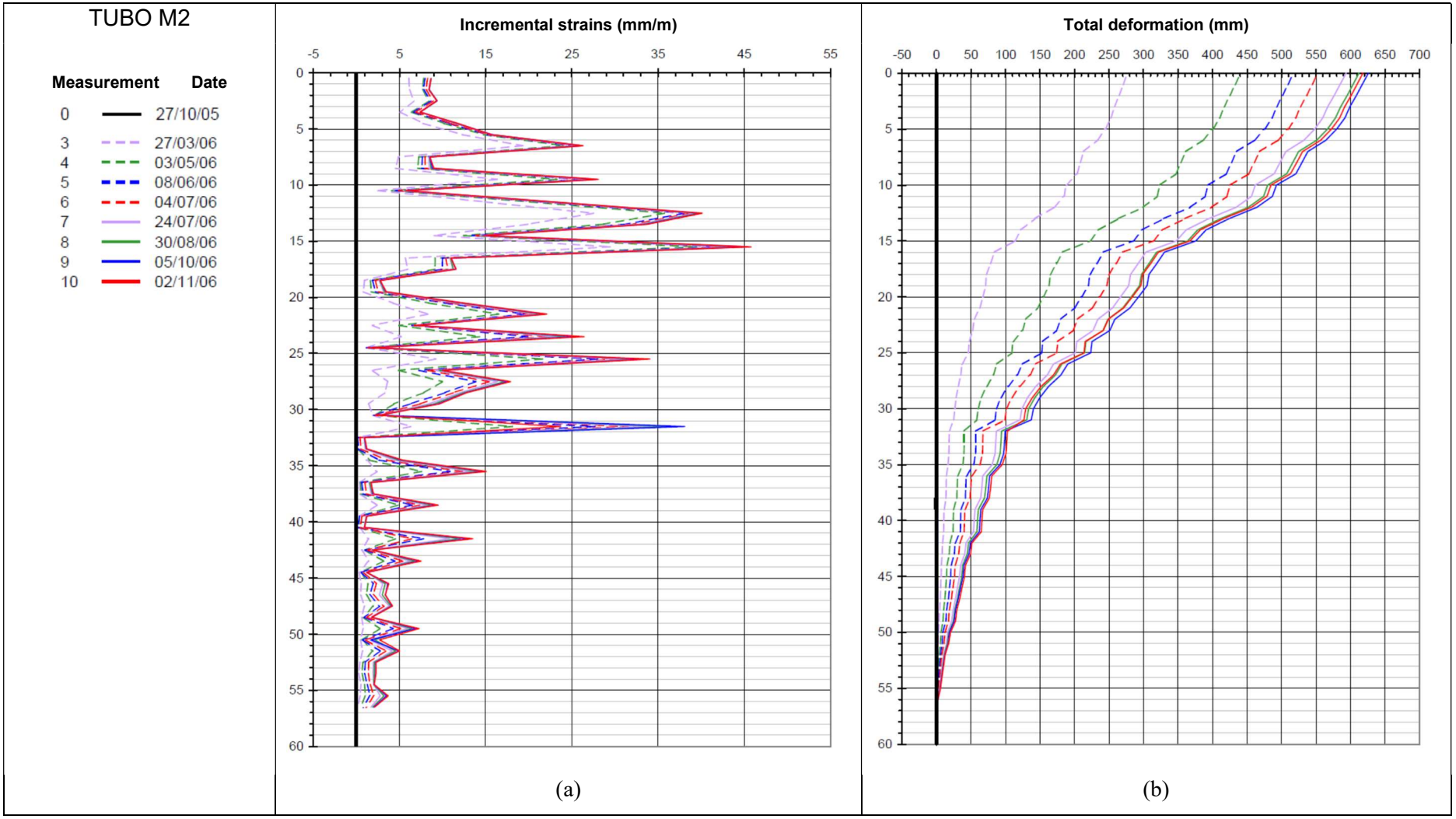

Figure 3-62. Micrometer 2. (a) Vertical deformation profile and (b) vertical settlement profile.

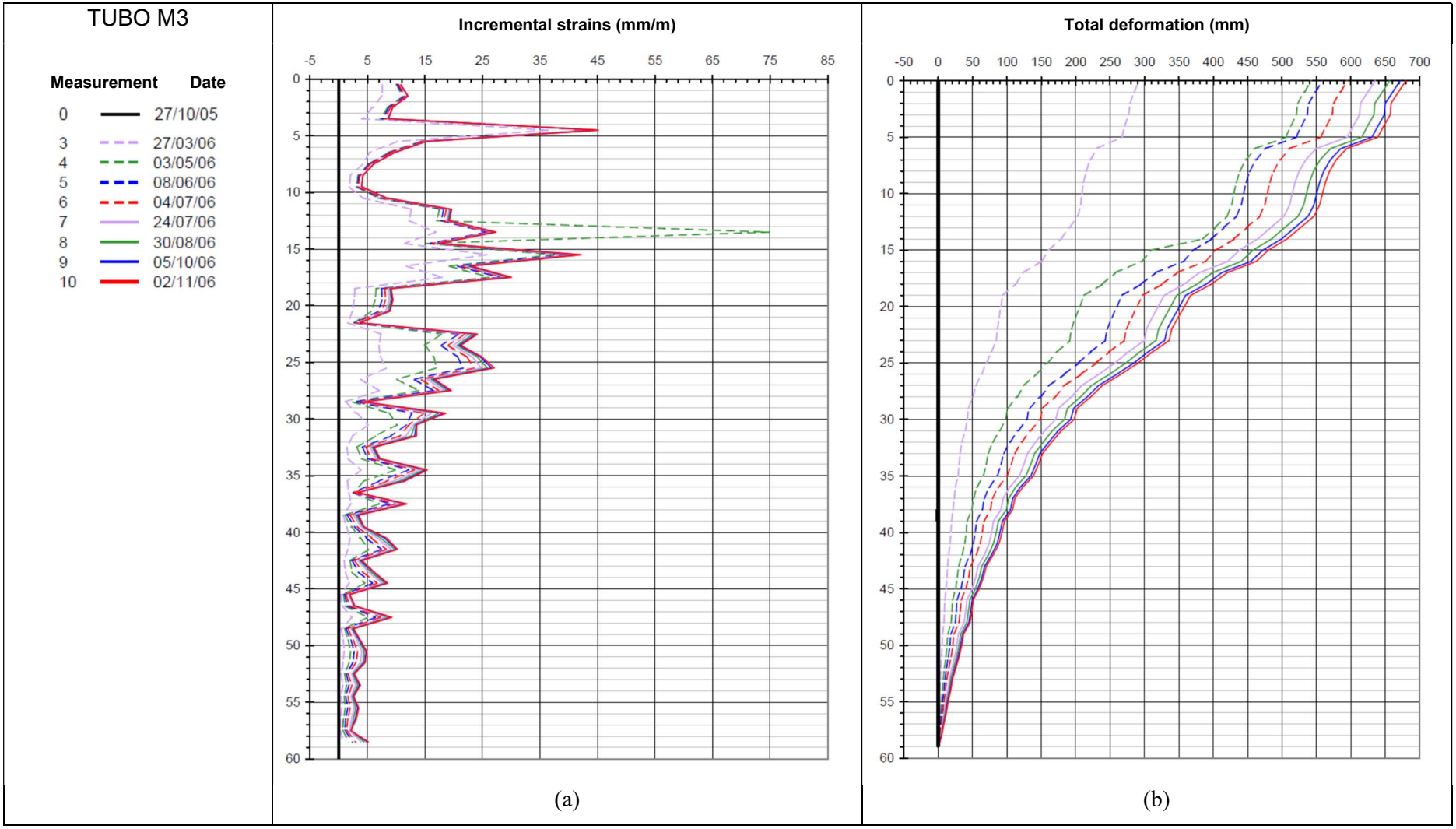

Figure 3-63. Micrometer 3. (a) Vertical deformation profile and (b) vertical settlement profile.

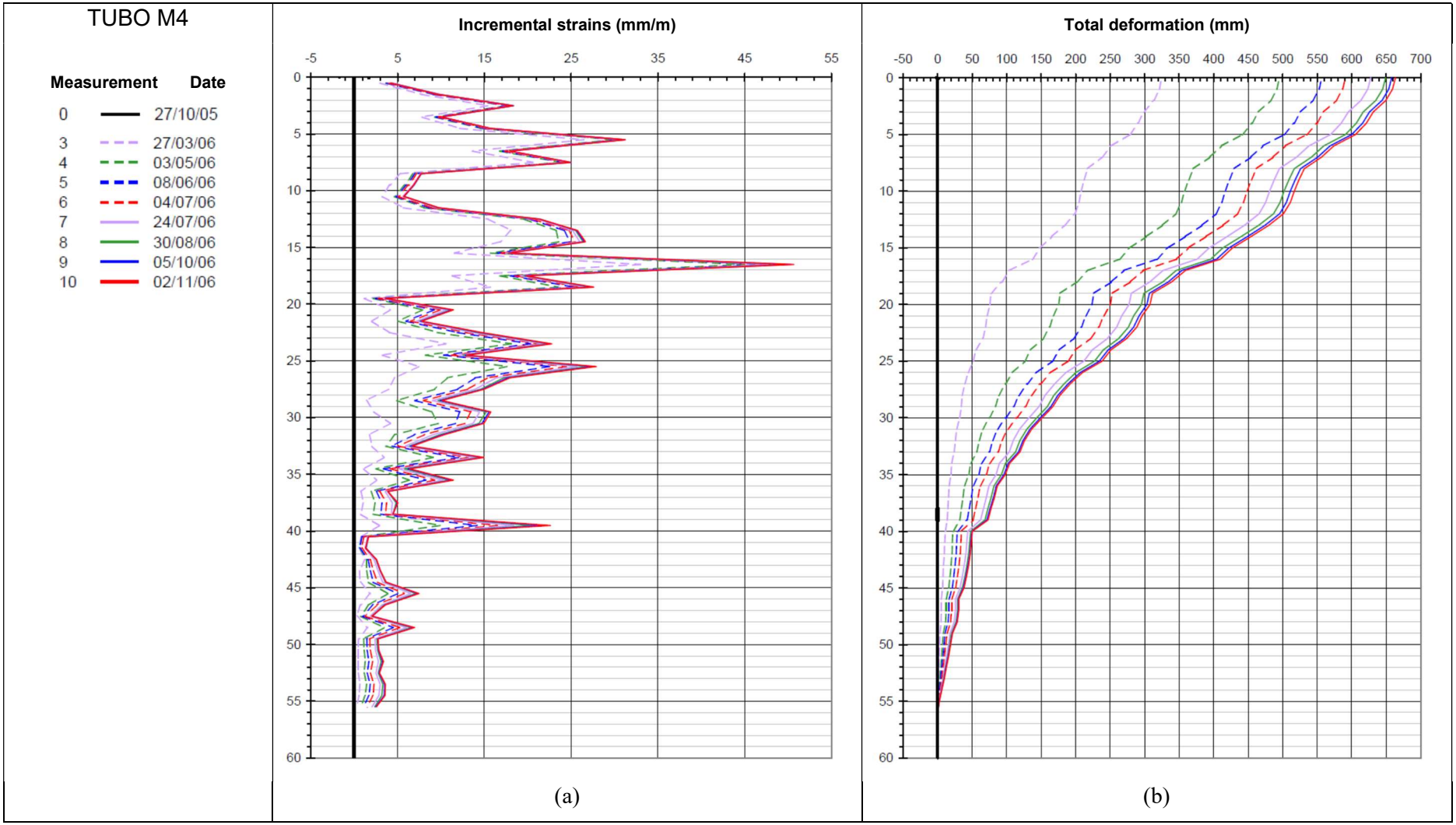

Figure 3-64. Micrometer 4. (a) Vertical deformation profile and (b) vertical settlement profile.

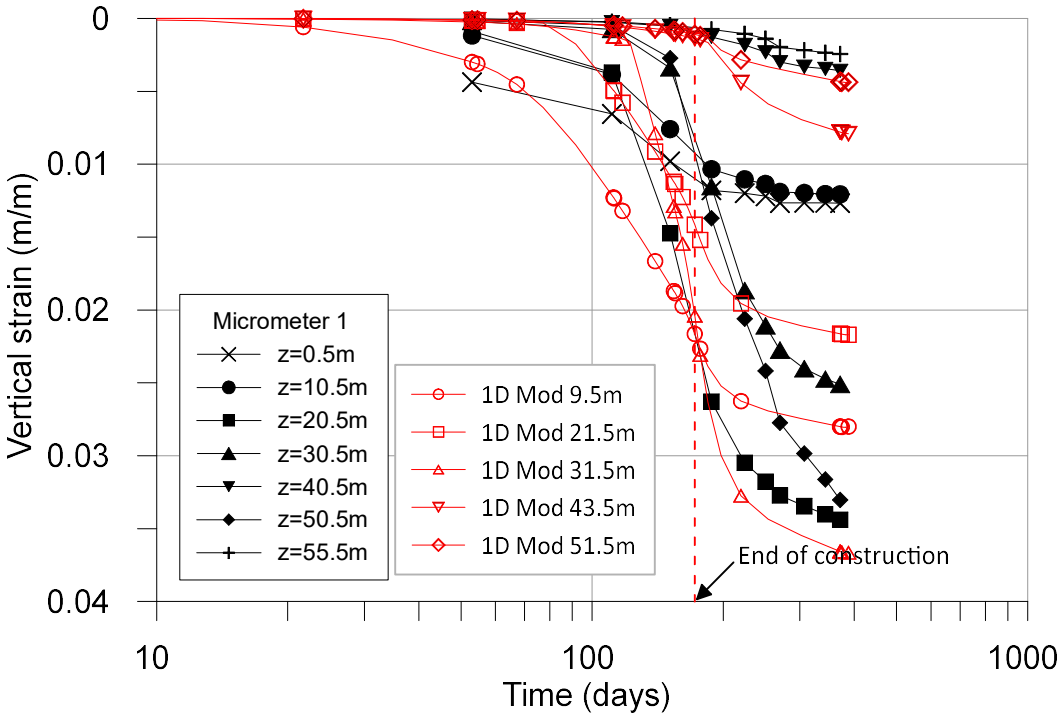

Figure 3-65. Vertical deformation at different depths, on micrometer 1

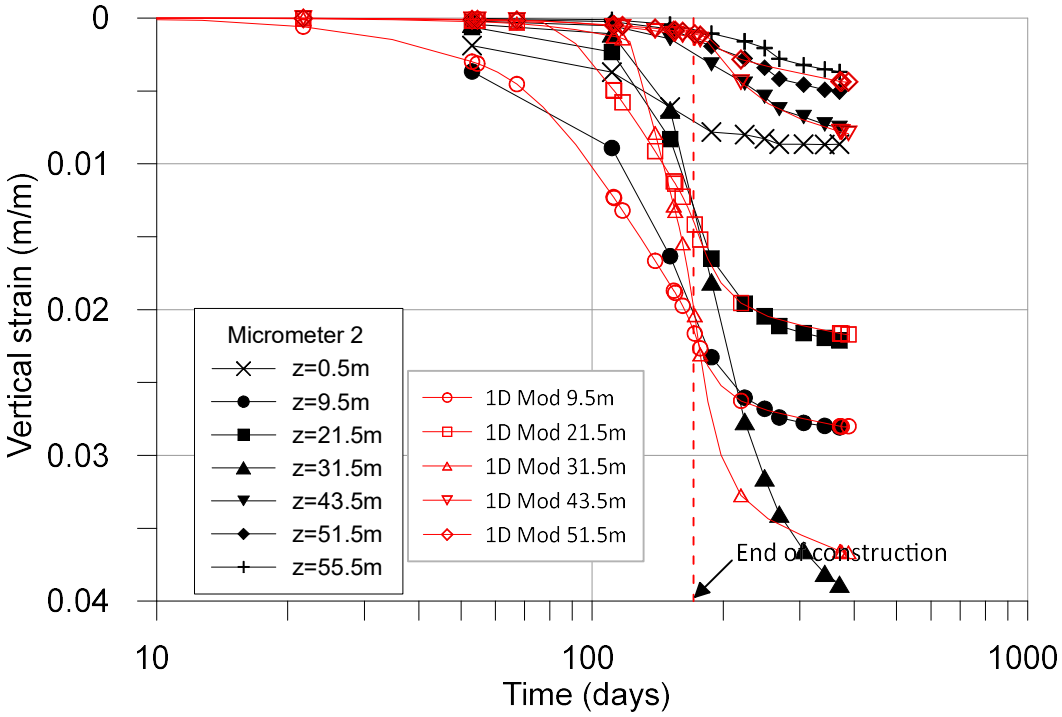

Figure 3-66. Vertical deformation at different depths, on micrometer 2

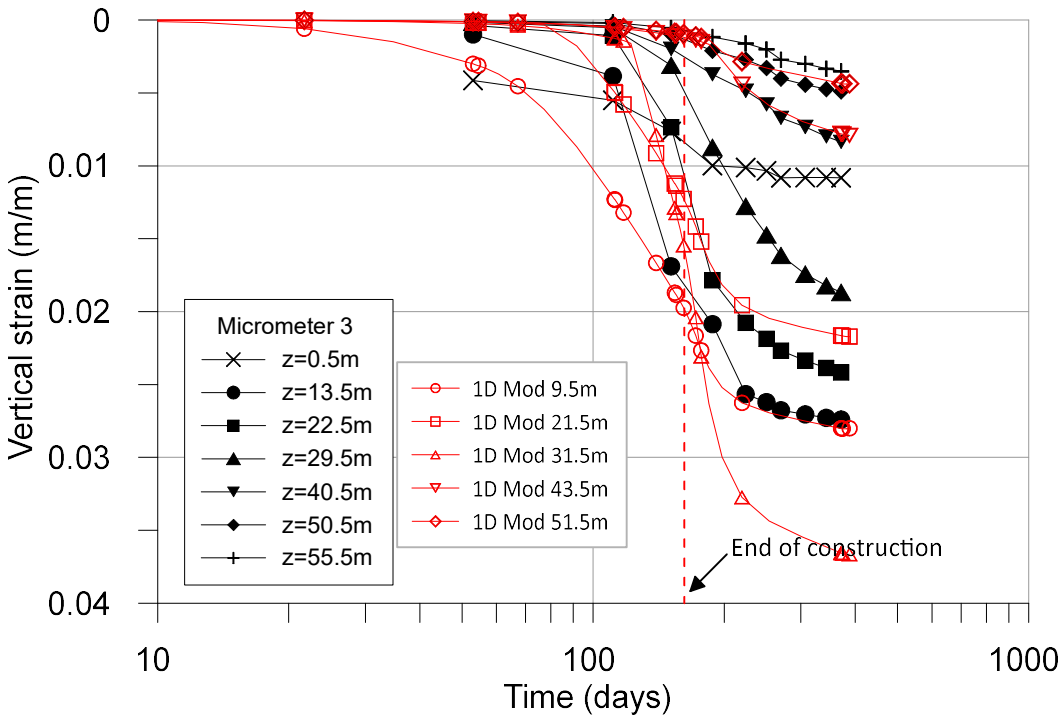

Figure 3-67. Vertical deformation at different depths, on micrometer 3

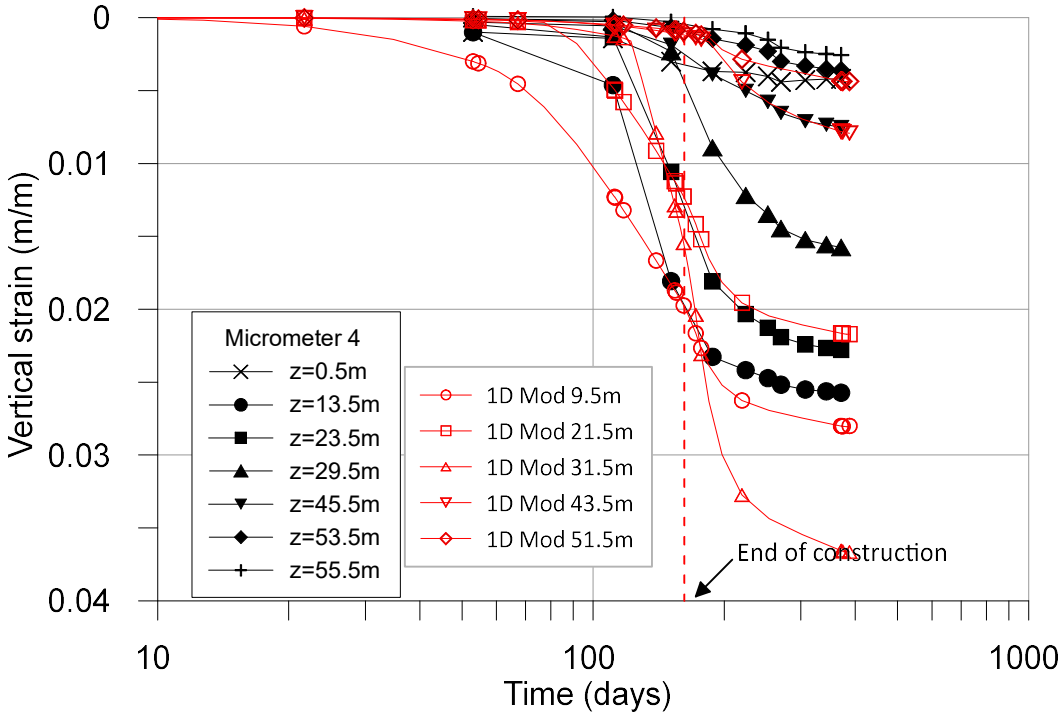

Figure 3-68. Vertical deformation at different depths, on micrometer 4

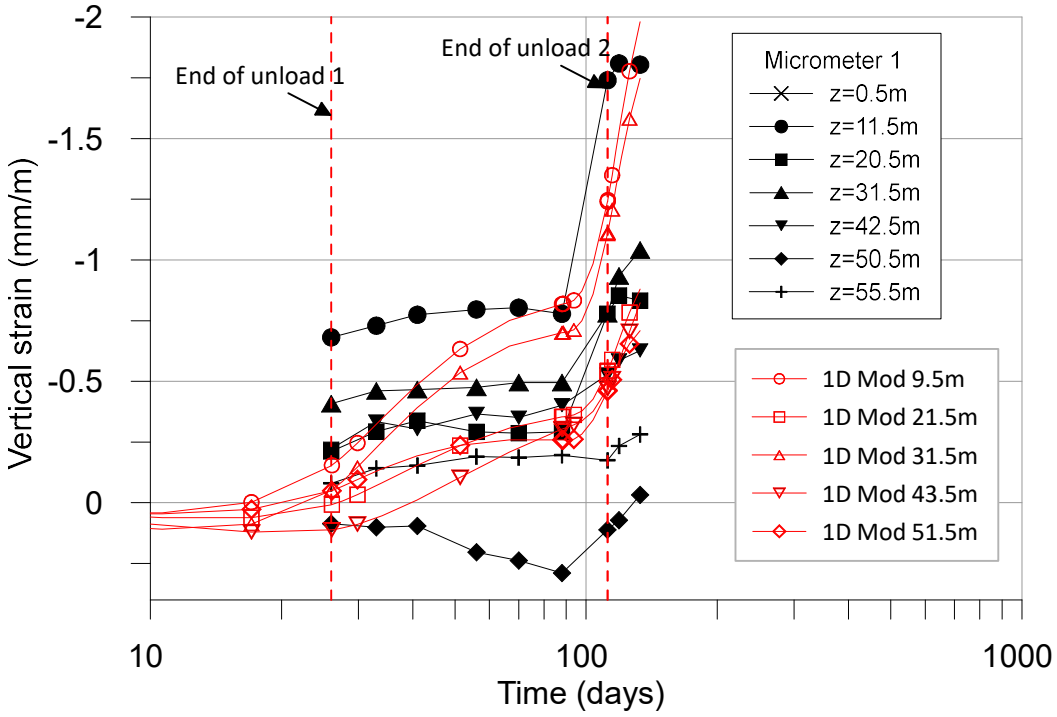

Figure 3-69. Vertical deformations in micrometer 1 during unloading, at different depths.

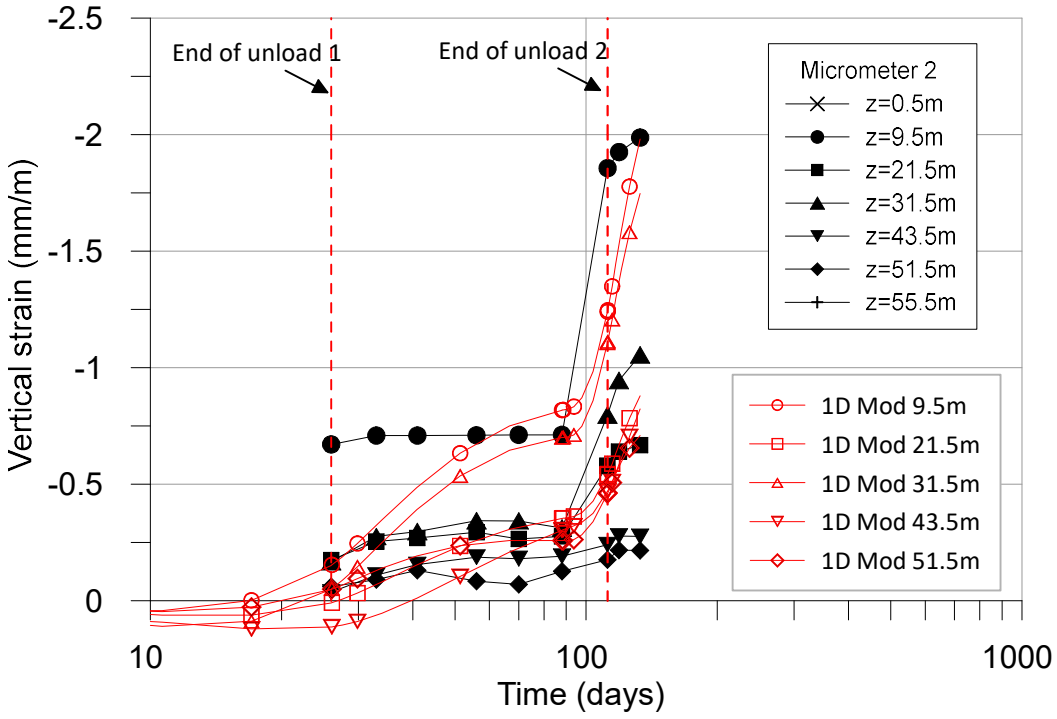

Figure 3-70. Vertical deformations in micrometer 2 during unloading, at different depths.

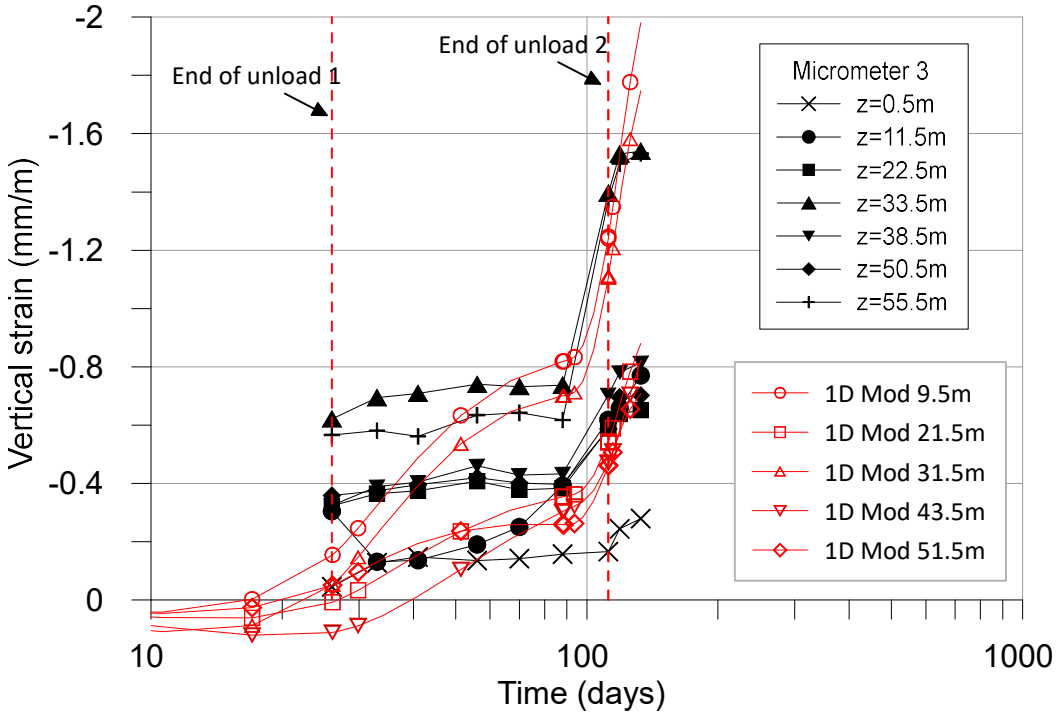

Figure 3-71. Vertical deformations in micrometer 3 during unloading, at different depths.

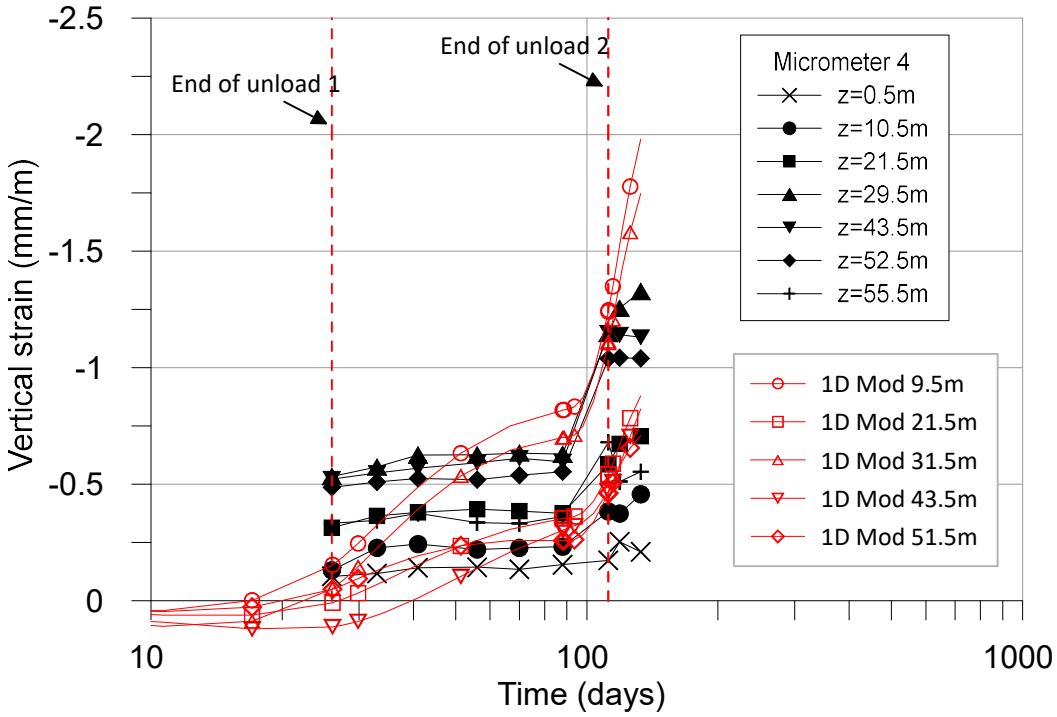

Figure 3-72. Vertical deformations in micrometer 4 during unloading, at different depths.

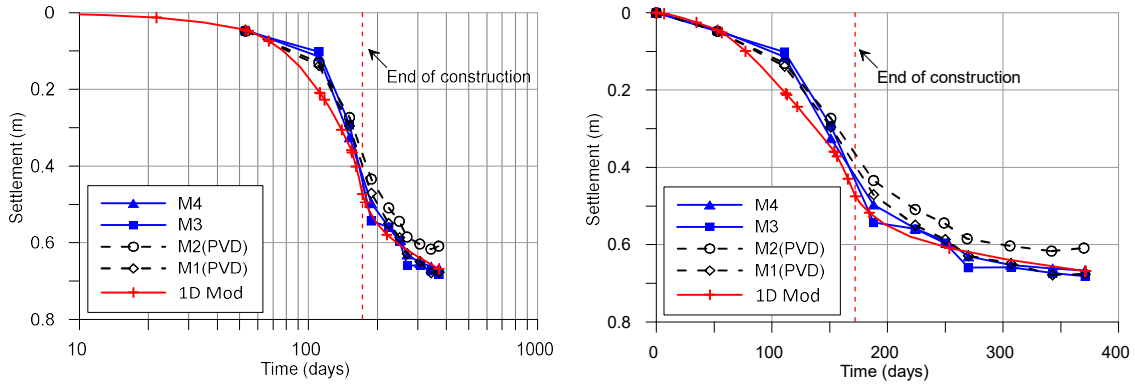

Figure 3-73. Evolution of settlements over time during the loading stage (a) logarithmic scale (b) arithmetic scale.

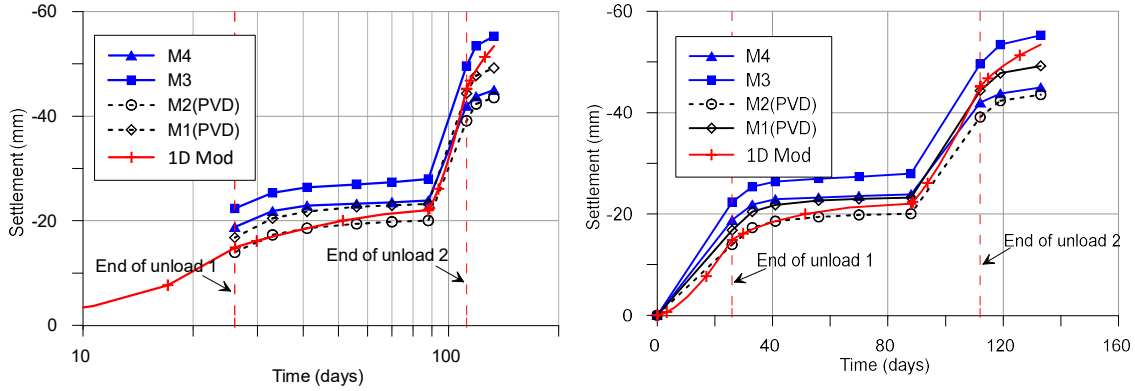

Figure 3-74. Evolution of settlements over time during the unload stage (a) logarithmic scale (b) arithmetic scale

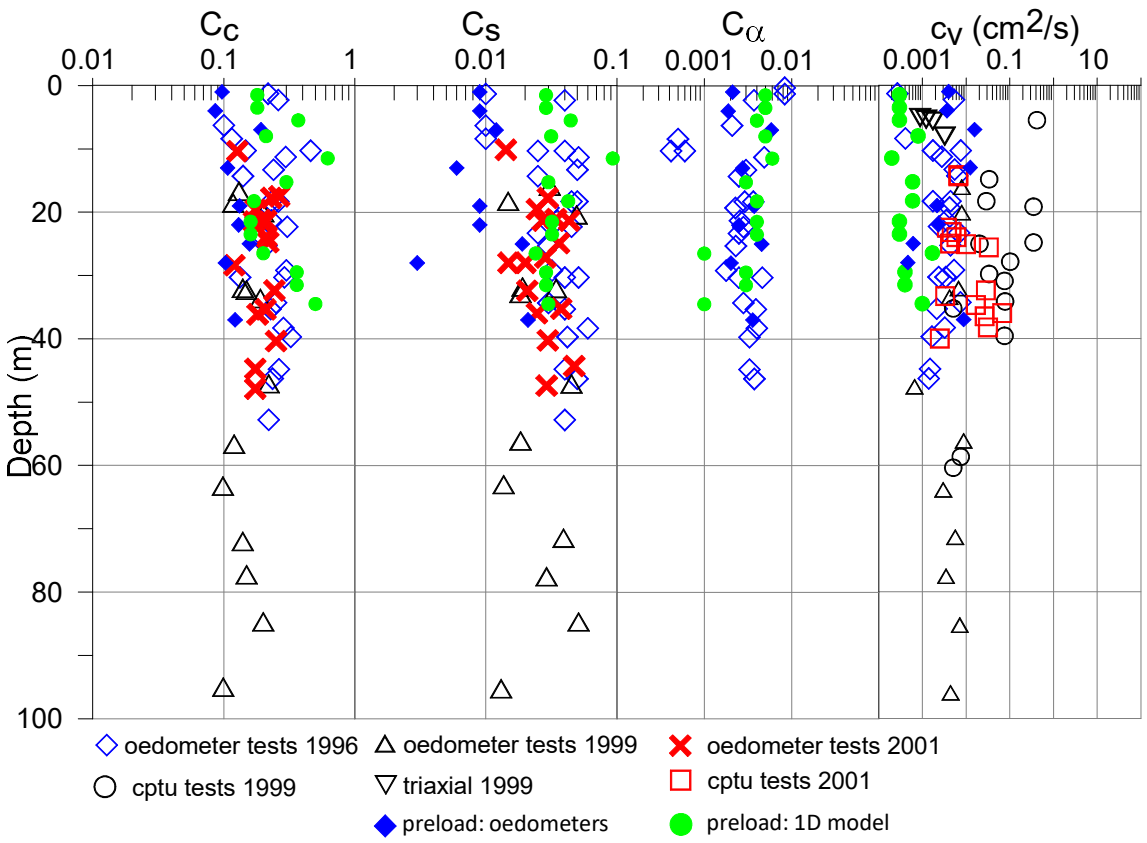

Figure 3-75. Variation of clay compressibility parameters with depth

3.5.2.4 Piezometers

Four strings of commercial vibrating wire piezometers were installed. A detailed description of the working principle of these instruments can be found in J. Dunnicliff (1993). In each chain, 3 piezometers were installed at different depths.

Installed piezometers measure total water pressure, so to calculate excess pore pressures it is necessary to know the depth of installation of the piezometer and the groundwater level. Excess pore pressure is calculated as the difference between total pressure and hydrostatic pressure.

Piezometers reacted also to loading-unloading in the manner shown in Figure 3-76 to Figure 3-79 for the three piezometers installed in borehole P1 to P4, respectively. The plot shows the excess pore pressure over the hydrostatic value. Also, some of the temporary increase in pore pressures, at constant embankment preloading, is attributed to other earth loading operations taking place in the vicinity of the preloading test, which is specially noted in the sensors located at depths greater than 30 meters. Piezometers installed at depths of less than 30 meters also seem to be affected by these increases in pore pressures, however, in these instruments, some dissipation of pore pressures is observed.

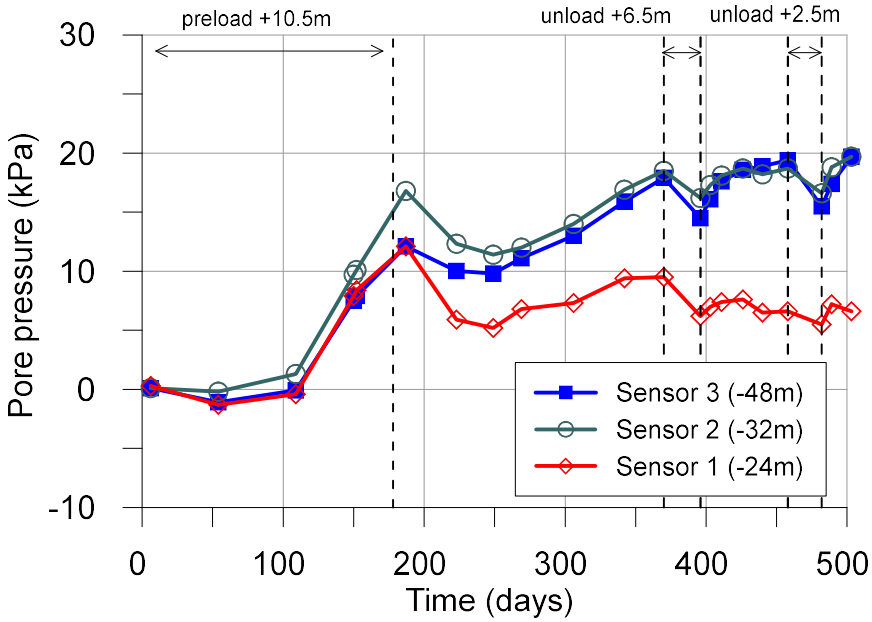

Figure 3-76. Time readings in sensors 1, 2 and 3 in piezometer borehole P1.

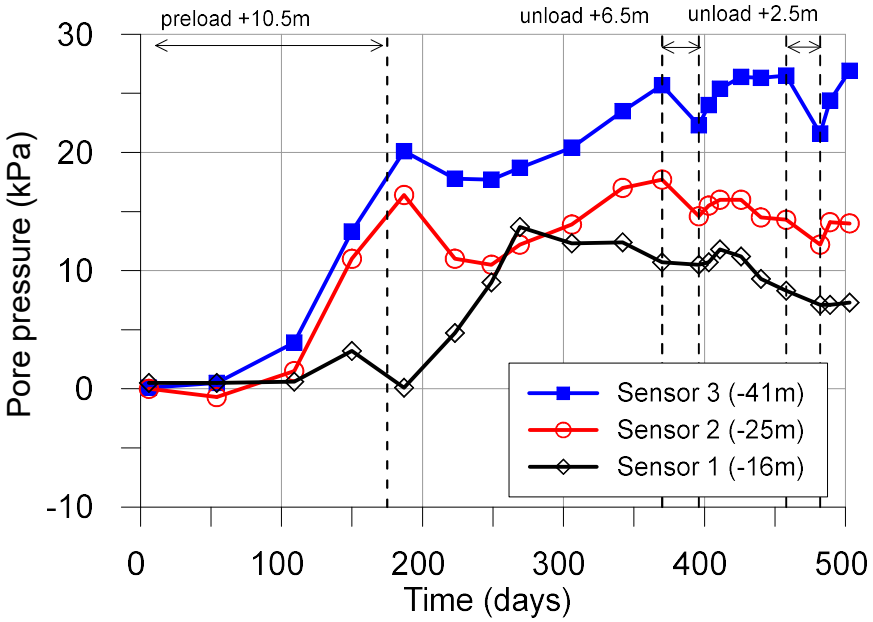

Figure 3-77. Time readings in sensors 1, 2 and 3 in piezometer borehole P2

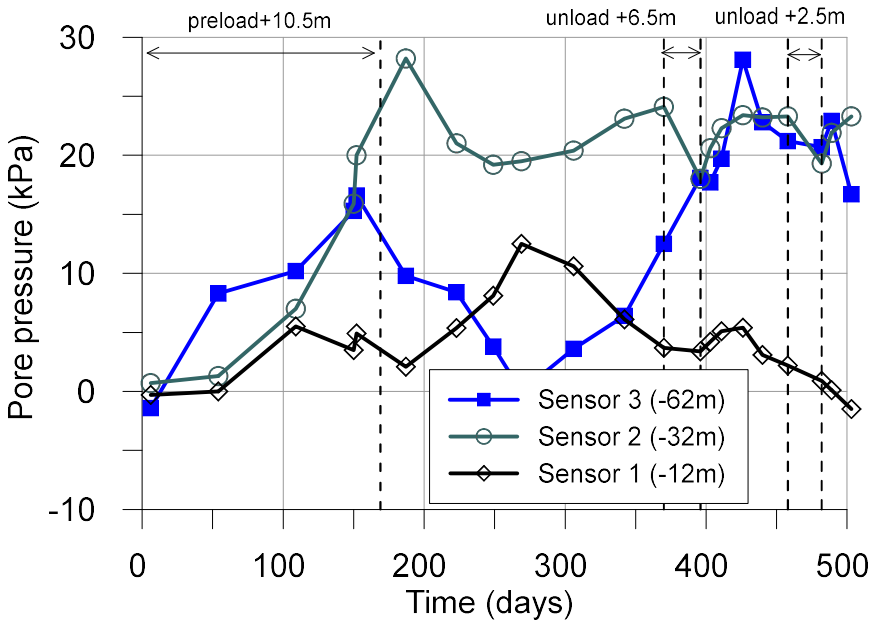

Figure 3-78. Time readings in sensors 1, 2 and 3 in piezometer borehole P3

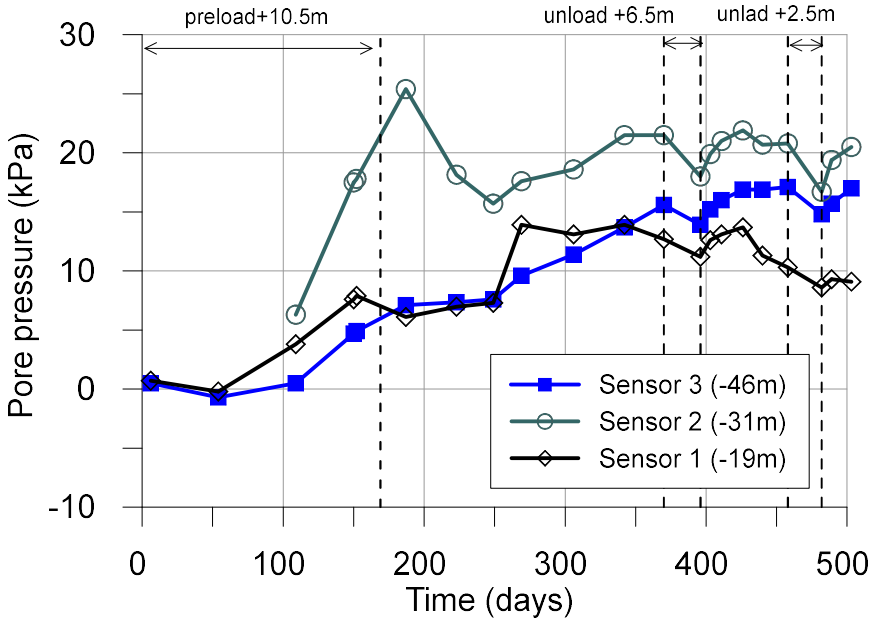

Figure 3-79. Time readings in sensors 1, 2 and 3 in piezometer borehole P4.

Figure 3-80 shows the distribution of excess pore pressures measured under the embankment at the end of the embankment construction, and compared with the values measured at the beginning of the preload embankment construction. At the beginning of the embankment construction the pore pressures correspond to approximately hydrostatic conditions. Later, with the construction of the embankment, there are increases of up to 2m over the hydrostatic pressure. The maximum pore pressures are observed between 30 and 40 meters deep. Likewise, it can be observed by the shape of the pore pressure distribution, that pressure dissipation occurs in the lower contour, consisting of a layer of gravel, and in the upper contour limited by the embankment.

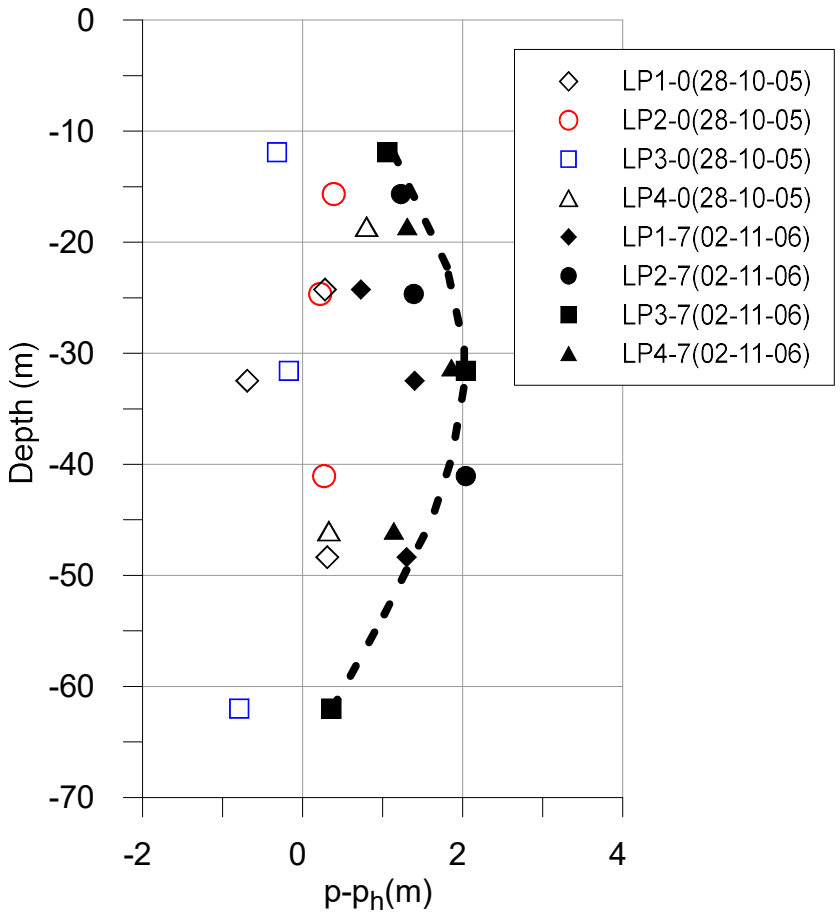

Figure 3-80. Excess pore pressures in piezometer chains measured at the beginning (filled symbols) and at the end of consolidation (open symbols)

3.5.2.5 Topographic control

A total of 24 metal plates in the embankment and 18 metal plates outside the embankment were installed. There were 40x40cm in size. These plates were installed at the base of the preload embankment and allow carrying out a control of settlements by means of conventional topographic devices. The plates have a special design that allows metal rods to be screwed in as the preload embankment grows. The plates have been placed in three alignments (section A, section B and section C), as shown in Figure 3-81.

Additionally, once the first 2 meters of the embankment had been reached, 16 more interior plates were placed, called DI. The arrangement of these plates is also shown in Figure 3-81.

Figure 3-82 shows the settlements measured in 4 interior control plates of section A, these are compared with the settlements measured in micrometers M1 and M3. The coincidence between these two types of measurements (performed with two totally different methodologies) is an indication of the reliability of the vertical deformation data obtained with the sliding micrometers. Figure 3-83 and Figure 3-84 compare settlement values obtained in sections B and C, respectively.

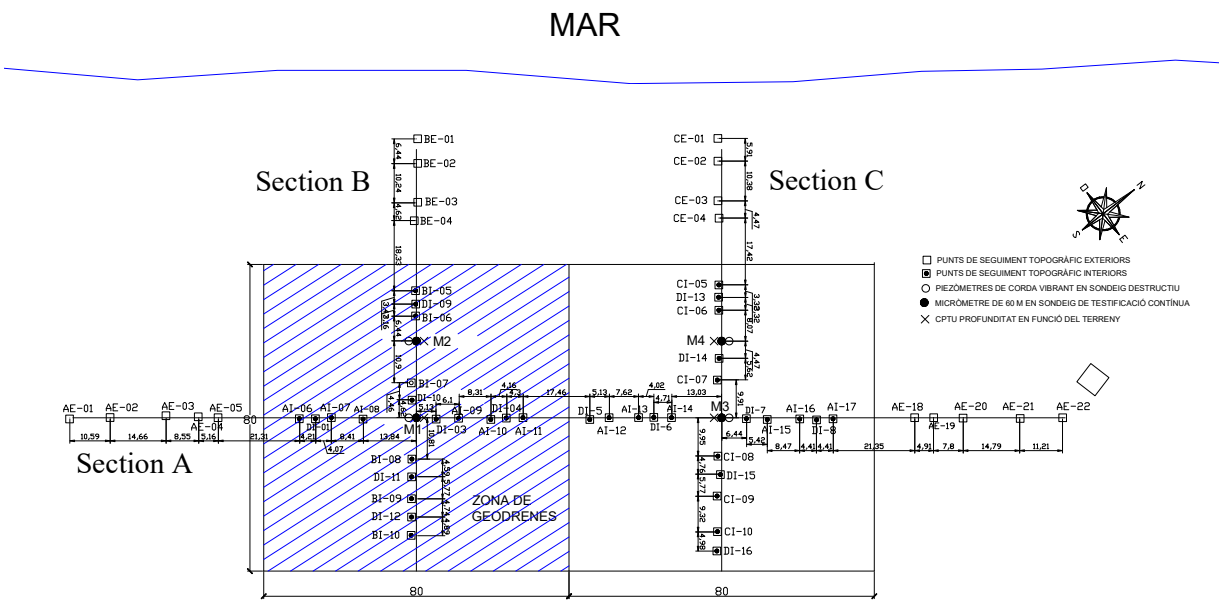

Figure 3-81. Location of topographic control points.

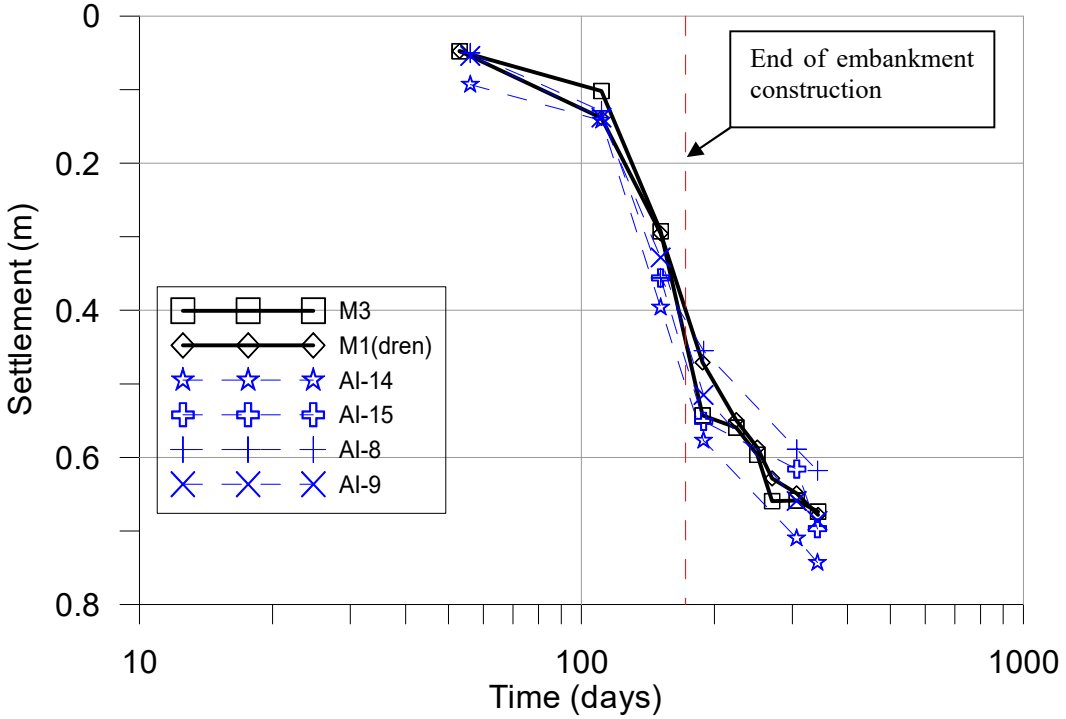

Figure 3-82. Settlements in topographic control points of section A.

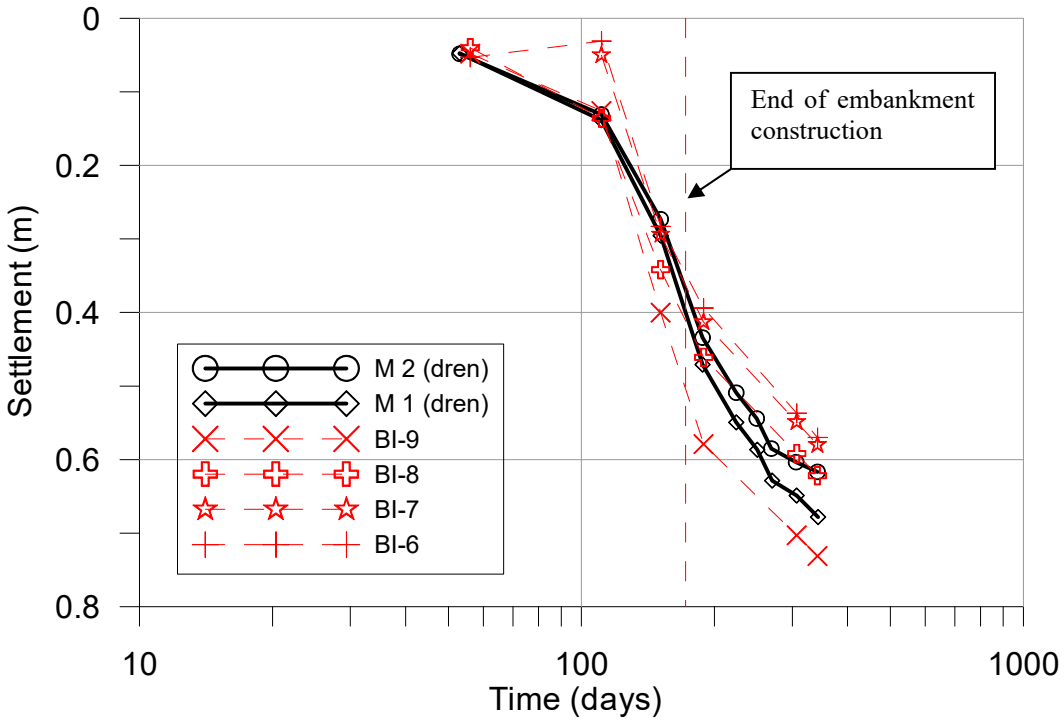

Figure 3-83. Settlements in topographic control points of section B.

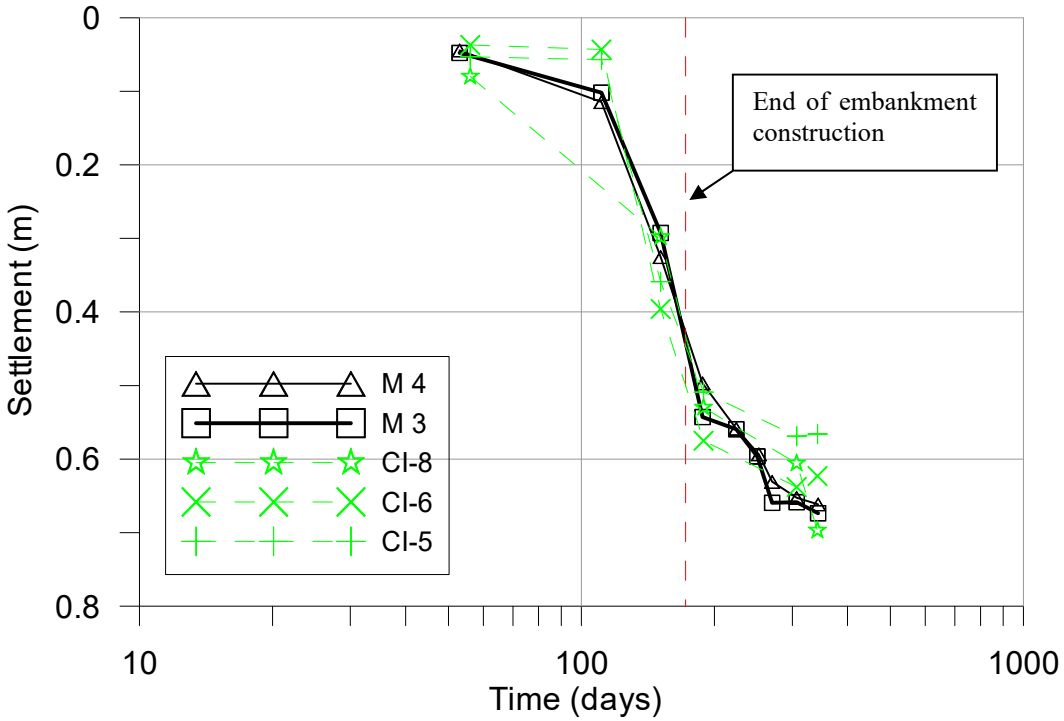

Figure 3-84. Settlements in topographic control points of section C.

3.6 SUMMARY AND CONCLUSIONS

In this Chapter, the mechanical behaviour of soft soil in relation to the performance of breakwaters has been discussed based on an extensive laboratory investigation. Particular emphasis was given to the following aspects:

3.6.1 Undrained shear strength

Undrained shear strength is the most important parameter in stability calculations of breakwaters, and, therefore, it was carefully and reliably assessed. It is a rather complex parameter influenced by several variables, such as, anisotropy, the dependency on preconsolidation pressure, strain rate and creep effects. These aspects are often neglected in breakwater design, as extensive testing would be required for a thorough understanding of the phenomena. Therefore, stability analyses of breakwaters are normally conducted as total stress analysis using an average isotropic undrained shear strength.

In stability analysis of embankments and caisson breakwaters, the undrained shear strength is known to vary along the slip surface based on orientation and magnitude of the major principal stresses. Bjerrum (1973) proposed a simple approach to model the varying anisotropic undrained shear strength along a slip surface. The method consisted of measuring undrained shear strength through triaxial compression and extension tests together with direct simple shear tests, on samples anisotropically consolidated before shearing, at stress level representative of the in-situ conditions. This approach is called "ADP", where "A" stands for active, "D" for direct shear and "P" for passive.

Another important aspect, for staged construction in soft soils, is related to the increase in undrained shear strength as a consequence of the increase in the preconsolidation pressure due to consolidation under an external load (e.g. embankment and caissons load), as suggested by Eq. **¡Error! No se encuentra el origen de la referencia.**. Several modes of undrained shear strength were investigated from undisturbed samples obtained at the south breakwater site, which include extension and compression triaxial tests and simple shear tests. The consolidation pressure was systematically varied in these tests. In this way, a general approach of the anisotropic undrained strength of soft soil was established. Results show that the average undrained strength ratio, $S_{uDSS}/\sigma'_v = 0.25$ in the mode of simple shearing is lower than in triaxial compression, $S_{upTC}/\sigma'_{vp} = 0.33$, but higher than in triaxial extension, $Su_{TE}/\sigma'_{vp} = 0.19$. Results were contrasted with well accepted results of similar clays reported in technical literature, showing good agreement.

3.6.2 Stiffness-strain behaviour

Several investigations have demonstrated that finite element analysis predictive capabilities are enhanced when using a small strain non-linear type of soil model.

The stiffness characteristics at a small strain level of Port of Barcelona Clays was investigated with the resonant column test for several confining conditions. Also, the stiffness-strain relationship of soil was stablished from the triaxial tests. The resonant column and triaxial tests data were merged within a unique stiffness curve using the rate-effect adjustment proposed by Vardanega and Bolton (2011a).

Experimental evidence reported in the literature has shown that several parameters influence the small-strain stiffness. Among them, void ratio and mean stress are probably the parameters that most strongly affect the small-strain stiffness. For this reason, most of the empirical formulas adopt the form proposed by Hardin (1978). All the empirical equations tried estimate the G_{max} values reasonably well when compared with the resonant column results; however, the parameters used in the equations need to be calibrated.

The concept of using the reference shear strain ($\gamma_{0.7}$) to approximate the volumetric threshold shear strain (γ_{tv}) was validated by Likitlersuang et al (2013). This parameter is used in the hardening soil model with small strain stiffness (HSS) and usually related to the plasticity index in cohesive soils. For the Barcelona's Port clay, the $\gamma_{0.7}$ value was set to $1.5x10^{-4}$ for static analysis and $7x10^{-5}$ for dynamic problems, which are comparable with the predicted values from Vardanega and Bolton (2013) empirical relationship.

3.6.3 Cyclic behaviour

Another important aspect of breakwater performance, especially in relation to vertical breakwaters, is related to the response of the foundation soil to cyclic loads imposed by sea waves. Two questions arise from this problem: One concerns stress conditions that generate pore pressures high enough to produce cyclic mobility or liquefaction and reduce the undrained strength of foundation soil. And the second refers to the available undrained post cyclic strength which could affect the stability of the breakwater. Dynamic triaxial tests and cyclic simple shear tests were performed in order to answer these questions.

The generation of pore pressures was investigated from cyclic isotropic and anisotropic triaxial tests. The pore pressure ratio $r_u = \Delta u_f/\sigma_3$ calculated from the triaxial tests was well below 1.0, whatever value of normalized cyclic deviator stress ($\Delta q_f/2\sigma_3$) was applied to the samples (**Figure 3-35**b). A clear relationship between normalized deviatoric stress and r_u was also observed, indicating that the induced pore pressure increases with increasing deviatoric stress, but the initial stress state appears to have a minor effect. The most critical condition was obtained in the cyclic isotropic test with a normalized deviatoric stress of 0.50 (stress reversal occurs), in this case the maximum values obtained for r_u were of the order of 0.6. The stress reversal could have a significant effect on pore pressure response, as indicated by Dobry et al (1982), the rate of pore pressure

generation increases with increasing degree of reversal. Cyclic mobility is expected for these stress conditions.

Post cyclic undrained strength was also investigated using the direct simple shear tests (DSS) and triaxial tests (Tx). It is observed that the undrained strength available after a cyclic loading is mainly influenced by the magnitude of cyclic shear stress ratio $\tau_{cy}/\sigma_{v'0}$, the initial shear stress ratio $\tau_{ave}/\sigma_{v'0}$ and the clay content. For the test conditions considered, in relation to the Barcelona breakwater, with $\tau_{cy}/\sigma_{v'0}$ lower than 0.20 and $\tau_{ave}/\sigma_{v'0}$ lower than 0.23, no structural changes were evidenced in the soil and therefore the undrained resistance available after stress cycles remains the same and it is sometimes even higher. The latter is explained by the low clay content (<9%) found in the samples from the higher levels.

The cyclic triaxial tests performed at UPC and the cyclic simple shear tests performed at NGI and CEDEX have also permitted defining the interaction diagram show in Figure 3-43a for triaxial stress condition and Figure 3-43b for simple shear stress condition. These diagrams define failure envelopes based on a combination of average and normalized cyclic shear stress, allowing the definition of stable and unstable zones. The results show that the simple shear tests lead to a more conservative interaction diagram than the triaxial tests. Therefore, this was used to analyses the cyclic stability of the breakwater as described in Chapter 7.

The cyclic shear strength can also be determined from the interactions diagrams as shown in Figure 3-45a for the compression triaxial tests and Figure 3-45b for DSS tests. This diagram show that the cyclic shear strength depends on τ_a, the cyclic load history (i.e. number of cycles), and the type of test (i.e. the stress path).

3.6.4 Compressibility and consolidation

Compressibility characteristics for settlement analysis were first studied with oedometric tests and then with a large-scale instrumented preload test.

Standard soil investigation techniques (borings, sample testing, laboratory tests and penetration tests) are classical procedures to approach the settlement analysis. However, its precision and reliability are not exempt from uncertainties, such as the quality of the samples used in the tests, the number of samples, the heterogeneous stratigraphic profile of the soil, estimation of the compressibility parameters from a graphic method, among others. Because of this, direct determination of soil deformability in 1 m intervals provided by precision extensometers associated with a preloading test is preferred.

The extensometers provide, in a sense, a compression test for each one of a large set of layers 1 m thick. Short term loading, unloading and long-term deformations can be accurately measured and interpreted with the 1D consolidation model. The technique may allow a direct interpretation of

data but if used in connection with soil models it leads to accurate prediction tools which can be later applied to predicting long term soil behaviour under breakwater construction.

A FEM technique using an elastoplastic creep model, have been validated through the extensometer readings as explained in the next chapter.

Figure 3-75 shows all the compressibility parameters obtained at different depths from undisturbed samples of breakwater places and preload zone.

Chapter 4

MODELLING THE BEHAVIOUR OF BARCELONA PORT SOFT SOIL

4.1 INTRODUCTION

When a soil is subjected to an increasing load, a soil deformation process is immediately activated. At the beginning, this deformation depends on the conditions and characteristics of soil drainage, and is usually accompanied by an increase of interstitial pressures. The evolution and subsequent dissipation of these pressures can be interpreted according to the theory of primary consolidation proposed by Terzaghi (1943) or the more general formulation of Biot (1955). Of course, the complex interaction between soil structure and interstitial fluid, must be described in a framework of mathematical equations: momentum balance for the soil-fluid mixture, momentum balance of the fluid and mass balance of flow. In these equations, the constitutive relationships and the effective stress definition play an important role to introduce features of soil behaviour into the governing equations.

As explained previously, several features of soil behaviour are of particular interest to modelling vertical breakwaters constructed on soft soils. In fact, any breakwater analysis must incorporate constitutive models capable of correctly simulating the undrained strength under several load conditions, cyclic behaviour as liquefaction or cyclic mobility due to seawave loads, stiffness degradation, and creep behaviour. Creep is of recognized importance in geotechnical problems where long-term behaviour is of interest, as occurs in the foundation of special structures on soft soils, whose serviceability can be affected by time-delayed settlements.

Today, there exists a great variety of soil models able to deal with most of the observed features of mechanical behaviour of soils under given conditions of temperature, drainage conditions, velocity of load application, stress path, history of load, etc. Some of them are restricted to academic use, because of the large number of parameters they use, which makes their uses in practice difficult. However, another group of models that address some specific feature of soil behaviour, with a reduced number of soil parameters, have been implemented in various commercial softwares. In this respect, the FE Plaxis code was chosen to simulate the performance of breakwater in this thesis, because it incorporates some of the most used models in engineering practice.

The aim of this chapter is to try various constitutive models (see Table 4-1) useful to analyse some specific aspect of the vertical breakwater performance, such as undrained behaviour in relation to the safety condition, cyclic behaviour during storms and long-term settlements (creep behaviour). The calibration of these models is carried out in this chapter, using results of laboratory tests and, in subsequent chapters, it is corroborated with data from geotechnical instrumentation.

Table 4-1. Summary of constitutive models and related feature

Feature of soil behaviour	Soil model
Undrained Strength	Soft soil
	S-Clay1S
Cyclic behaviour	UBC3D-PLM
Small strain and stiffness degradation	HS small
Creep behaviour	Soft soil creep

4.2 MODELLING UNDRAINED BEHAVIOR

4.2.1 Undrained analysis in the context of finite element models

Soil constitutive models are usually formulated in effective stress variables, which is necessary for situations where gain of strength during soil consolidation is relevant for construction, typically in soft soils. In this case, the effective stress path calculated from the constitutive model must match the undrained strength of soil. To do this, the constitutive model must be able to generate realistic pore pressures. In the context of finite element formulation, undrained analysis can be done using two approaches: undrained effective analysis with effective stiffness parameters or undrained total stress analysis with undrained parameters. In the first one, the effective stiffness is transformed into undrained stiffness parameters, with the alternative to define strength parameters in terms of effective or total stress. The latter one is completely defined in term of total stress, both stiffness and strength parameter are undrained. A brief description of the first alternative is given below, based on Plaxis software implementation (Brinkgreve et al, 2017).

4.2.1.1 Undrained analysis with effective stress parameters

In the framework of finite element analysis, constitutive models are formulated generally in terms of effective stress. In order to perform undrained analysis, the generation of pore pressure should be reproduced correctly. Although some models are able to do undrained analysis with undrained parameters, this approach does not permit the computation of the increase of shear strength with consolidation, which is an important characteristic to simulate construction process of breakwaters on soft soils.

According to Terzaghi's principle, stresses in the soil are divided into effective stresses, $\underline{\sigma}$', and active pore pressure p_{active}, which generally correspond to water in the pore, p_w. Water is considered not to sustain any shear stresses. As a result, effective shear stresses are equal to total shear stresses. Moreover, water pressure is considered to be fully isotropic, so all pore pressure components are equal. Terzaghi's equation of effective stress is expressed as:

$$\underline{\sigma} = \underline{\sigma}' + m p_{active} \tag{4.1}$$

Where:

$$p_{active} = \alpha S_e p_w \tag{4.2}$$

$$m^T = \begin{bmatrix} 1 & 1 & 1 & 0 & 0 & 0 \end{bmatrix} \tag{4.3}$$

α is Biot's pore pressure coefficient and S_e is the effective degree of saturation. Considering incompressible grains, Biot's coefficient α is equal to unity (α = 1).

Pore water pressure is assumed to be formed by two components, the steady state pore stress, p_{steady}, and the excess pore stress, p_{excess}:

$$p_w = p_{steady} + p_{excess} \tag{4.4}$$

Steady state pore pressures correspond to the hydrostatic water pressure or the pore pressure obtained from a steady-state groundwater flow calculation. Excess pore pressures are generated as a response of an external load in the case of undrained material behaviour or during a consolidation analysis. Since the time derivative of the steady state component equals zero, it follows:

$$\dot{p}_w = \dot{p}_{excess} \tag{4.5}$$

According to Hooke's law, the relation between effective stress and strain rate is expressed as:

$$\begin{bmatrix} \dot{\varepsilon}^e_{xx} \\ \dot{\varepsilon}^e_{yy} \\ \dot{\varepsilon}^e_{zz} \\ \dot{\gamma}^e_{xy} \\ \dot{\gamma}^e_{yz} \\ \dot{\gamma}^e_{zx} \end{bmatrix} = \frac{1}{E'} \begin{bmatrix} 1 & -\nu' & -\nu' & 0 & 0 & 0 \\ -\nu' & 1 & -\nu' & 0 & 0 & 0 \\ -\nu' & -\nu' & 1 & 0 & 0 & 0 \\ 0 & 0 & 0 & 2+2\nu' & 0 & 0 \\ 0 & 0 & 0 & 0 & 2+2\nu' & 0 \\ 0 & 0 & 0 & 0 & 0 & 2+2\nu' \end{bmatrix} \begin{bmatrix} \dot{\sigma}_{xx} - \alpha \dot{p}_w \\ \dot{\sigma}_{yy} - \alpha \dot{p}_w \\ \dot{\sigma}_{zz} - \alpha \dot{p}_w \\ \dot{\sigma}_{xy} \\ \dot{\sigma}_{yz} \\ \dot{\sigma}_{zx} \end{bmatrix} \tag{4.6}$$

Considering slightly compressible water, the rate of excess pore pressure is written as:

$$\dot{p}_{excess} = \frac{\alpha \dot{\varepsilon}_v}{n C_w + (\alpha - n) C_s} \tag{4.7}$$

Where $C_w = 1/K_w$ and $C_s = 1/K_s$, in which K_w is the bulk modulus of the water, K_s is the bulk modulus of the solid material, C_w is the compressibility of the water, C_s is the compressibility of the solid material and n is the soil porosity.

$$n = \frac{e_0}{1+e_0}$$

where e_0 is the initial void ratio.

The inverted form of Hooke's law may be written also in terms of the total stress rates and the undrained parameters E_u and υ_u:

$$\begin{bmatrix} \dot{\varepsilon}^e_{xx} \\ \dot{\varepsilon}^e_{yy} \\ \dot{\varepsilon}^e_{zz} \\ \dot{\gamma}^e_{xy} \\ \dot{\gamma}^e_{yz} \\ \dot{\gamma}^e_{zx} \end{bmatrix} = \frac{1}{E_u} \begin{bmatrix} 1 & -\nu_u & -\nu_u & 0 & 0 & 0 \\ -\nu_u & 1 & -\nu_u & 0 & 0 & 0 \\ -\nu_u & -\nu_u & 1 & 0 & 0 & 0 \\ 0 & 0 & 0 & 2+2\nu_u & 0 & 0 \\ 0 & 0 & 0 & 0 & 2+2\nu_u & 0 \\ 0 & 0 & 0 & 0 & 0 & 2+2\nu_u \end{bmatrix} \begin{bmatrix} \dot{\sigma}_{xx} \\ \dot{\sigma}_{yy} \\ \dot{\sigma}_{zz} \\ \dot{\sigma}_{xy} \\ \dot{\sigma}_{yz} \\ \dot{\sigma}_{zx} \end{bmatrix} \tag{4.8}$$

Where:

$$E_u = 2G(1+\nu_u);\quad \nu_u = \frac{3\nu' + \alpha B(1-2\nu')}{3-\alpha B(1-2\nu')};\quad B = \frac{\alpha}{\alpha + n\left(\frac{K'}{K_w} + \alpha - 1\right)} \tag{4.9}$$

B is called the Skempton's B-parameter. In this way, undrained behaviour of soils can be simulated transforming the effective parameters G and υ' into undrained parameters E_u and υ_u. Note that the index u is used to indicate auxiliary parameters for undrained soil.

Fully incompressible behaviour is obtained for $\upsilon_u = 0.5$. However, taking $\upsilon_u = 0.5$ leads to singularity of the stiffness matrix. In order to avoid numerical problems caused by an extremely low compressibility of water, υ_u is usually taken as 0.495, which makes the undrained soil body slightly compressible. In order to ensure realistic computational results, the bulk modulus of the water must be high compared with the bulk modulus of the soil skeleton, i.e. $K_w >> nK'$. The bulk modulus of water can be obtained from the following equation (for α=1):

$$\frac{K_w}{n} = \frac{3(\nu_u - \nu')}{(1-2\nu_u)(1+\nu')}K' = \frac{0.495-\nu'}{1+\nu'}300K' \geq 30K' \tag{4.10}$$

Hence, K_w/n is larger than 30K', at least for $\upsilon' \leq 0.35$ and $\alpha = 1$. The bulk stiffness of water K_w, calculated in this way, is a numerical value related to the soil stiffness. It could be lower than or equal to the real bulk stiffness of pure water, K^0_w (2×10^6 kN/m^2).

4.2.2 Soft Soil Model

The Soft Soil (SS) model is one of the most used models implemented into the Plaxis FE code for normal or slightly overconsolidated soils. It was chosen for use in this research because it shares some characteristics of the well-known Modified Cam clay model (MCC) (Roscoe and Burland, 1968), which has been shown to simulate the basic deformation characteristics of clays (Wood, 1990). Furthermore, the SS model has the advantage that the failure behaviour is controlled independently of the yield surface, through the Mohr-Coulomb criterion, which can be easily calibrated to reproduce undrained resistance. The model uses the modified compression index λ* and swelling index κ*, which differs from the original proposed by Burland (1965). The difference is that λ* and κ* are a function of the volumetric strain rather than the void ratio. A brief description of SS Model is presented in this section, but a detail description can be found in the material models manual of Plaxis (Brinkgreve et al, 2017).

The elliptical shape yield surface, similar to that of MCC model, but displaced by c'cotϕ is defined in general stress space as:

$$\frac{q^2}{\left(M(\theta)\right)^2\left(p'+c'\cot\phi'\right)}-(p_p^{'}-p')=0 \tag{4.11}$$

where θ is Lode's angle and the Mohr-Coulomb failure envelope is defined as:

$$q=M_{\phi'}(\theta)\left(p'+c'\cot\phi'\right) \tag{4.12}$$

As in the MCC model the parameter M define the height of the ellipse and the isotropic pre-consolidation stress p_p determine the size of the ellipse along p' axis (see Figure 4-1). The value of M is determined based on the coefficient of lateral earth pressure K_0^{nc} (Brinkgreve, 1994).

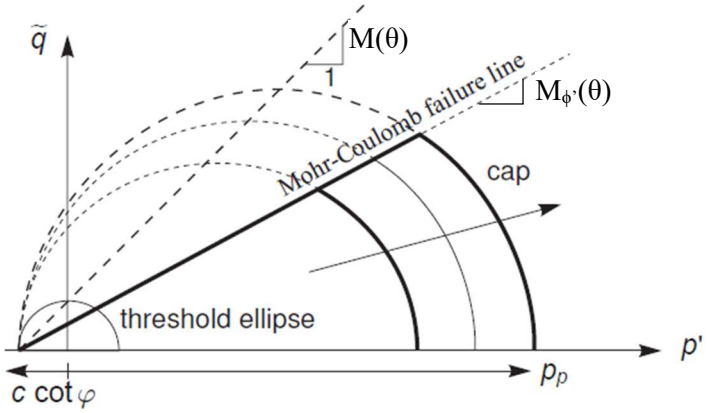

Figure 4-1. Yield surface and failure envelope

The value of p_p increases exponentially with volumetric plastic strain following the hardening relation:

$$p_p = p_p^0 \exp\left(\frac{-\varepsilon_v^p}{\lambda^* - \kappa^*}\right) \tag{4.13}$$

p_p^0 is the initial value of the pre-consolidation stress. If the soil is over-consolidated, information is required about the Over Consolidated Ratio (OCR), which is usually defined in term of vertical effective stress history ($OCR=\sigma_p/\sigma'_{v0}$). In Plaxis the pre-consolidation stress σ_p is used to compute the equivalent isotropic pre-consolidation stress p_p, which determine the initial position of the cap-type surface of Soft Soil model. In this way, OCR is defined in Plaxis as follow:

$$OCR = \frac{p'_p}{p'_{eq}} \tag{4.14}$$

Where the equivalent isotropic stress is:

$$p'_{eq} = p' + \frac{q^2}{M^2\left(p' + c\cot\phi\right)} \tag{4.15}$$

The undrained strength can be easily derived from the equations of the SS model for triaxial compression in relation to some initial stress state of soil, following a procedure similar to that described by Wood (1990) in relation to the MCC model. To do that, it is better to work with the variables $\overline{p'} = p' + c'\cot\phi'$ and $\overline{p_p} = p_p + c'\cot\phi'$ and change the yield surface and the failure envelope to these variables. Figure 4-2 shows geometric relations used to derive s_u from the SS model.

Finally, the undrained strength deduced for triaxial tests is obtained as follow:

$$s_u = \frac{M_{\phi'}\overline{p'_i}}{2}\left(\overline{OCR}_i \frac{\overline{p'_{eq\,i}}}{\overline{p'_i}} \frac{M^2}{M_{\phi'}^2 + M^2}\right)^{\left(\frac{\lambda-\kappa}{\lambda}\right)}$$

or, alternatively,

$$s_u = \frac{M_{\phi'}\left(p'_i + c'\cot\phi\right)}{2}\left(\overline{OCR}_i \frac{p'_{eqi} + c'\cot\phi}{p'_i + c'\cot\phi} \frac{M^2}{M_{\phi'}^2 + M^2}\right)^{\left(\frac{\lambda-\kappa}{\lambda}\right)} \tag{4.16}$$

The value of s_u (triaxial compression) can be easily computed from the soil model parameters and the initial stress state.

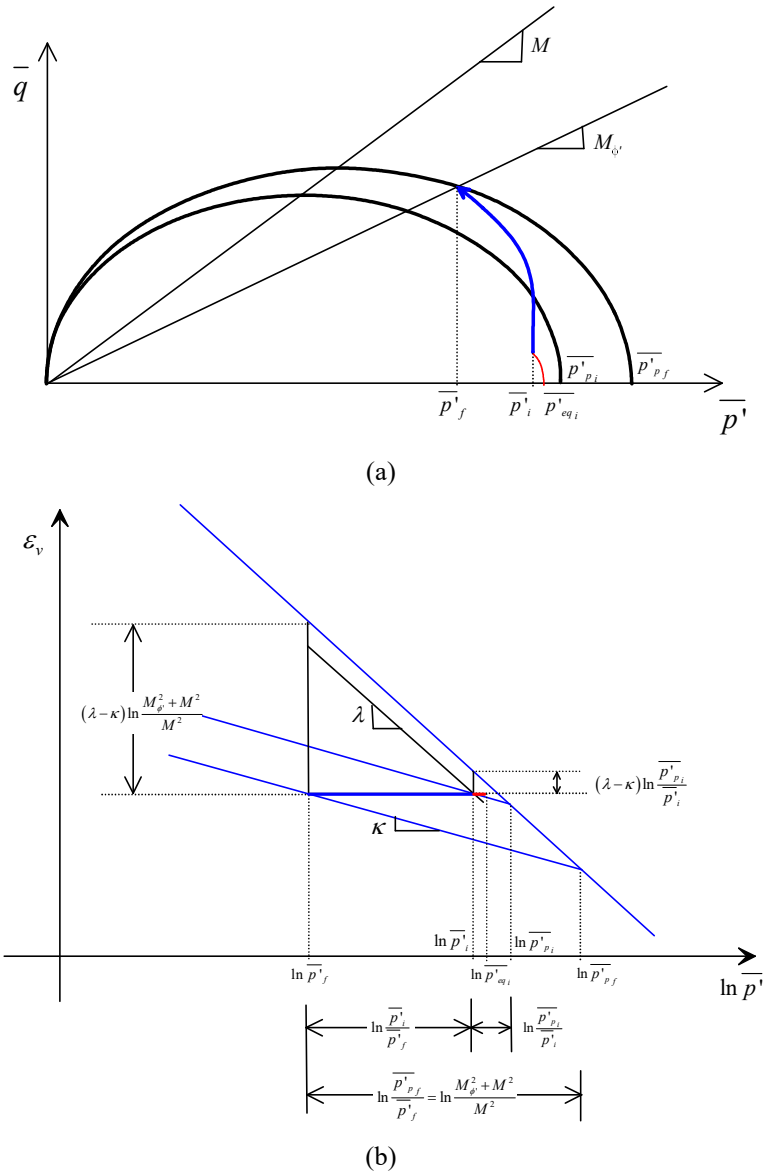

Figure 4-2. Schematic definitions of undrained test on lightly over-consolidated soil with the SS model (a) Yield surface in p':q plane (b) ε_v:ln p' compression plane.

Soil parameters were selected after an iterative process of matching the results of simulation with the real soil response of triaxial tests performed on samples of Barcelona Port. The properties of the soft clay material finally adopted are listed in Table 4-2 for the SS model.

Table 4-2. Material parameters of SS model for triaxial simulations

Model	γ_{unsat} **[kN/m^3]**	γ_{sat} **[kN/m^3]**	ϕ **[°]**	**c [kN/m^2]**	K_0^{nc}	λ^*	κ^*	e_0	υ_{ur}	**k [m/d]**
Axisymmetric	18.5	18.5	30	9	0.658	0.050	0.01	0.8	0.15	$8.64\text{x}10^{-4}$
Plane strain	18.5	18.5	20	1	0.658	0.050	0.01	0.8	0.15	$8.64\text{x}10^{-4}$

4.2.3 Hardening Soil model with small-strain stiffness (HSS)

The HSS model is an enhanced version of the Hardening Soil model (HS) implemented in Plaxis (Schanz et al, 1999), which include in its formulation, the very small-strain soil stiffness and its non-linear dependency on strain amplitude. The model distinguishes between two types of hardening: shear hardening used to simulate irreversible deformations due to a deviatoric load and compression hardening to simulate irreversible plastic deformations due to isotropic compression. The model incorporates the Mohr-Coulomb failure criterion to define soil resistance, but unlike the perfect elasto-plastic Mohr-Coulomb model, the yield surface of the HSS model can expand in the principal stress space due to plastic deformations. When consider stress path of standard drained triaxial tests the model gives the hyperbolic stress strain curve proposed by Duncan & Chang (1970).

In triaxial p-q space the shear hardening function is defined as:

$$f = \frac{2}{E_i}\frac{q}{1-q/q_a} - \frac{2q}{E_{ur}} - \gamma^p \qquad 4.17$$

Where:

$$E_i = \frac{2E_{50}}{2-R_f} \qquad 4.18$$

$$E_{50} = E_{50}^{ref}\left(\frac{c\cos\phi - \sigma_3' \sin\phi}{c\cos\phi - p^{ref}\sin\phi}\right)^m \qquad 4.19$$

$$E_{ur} = E_{ur}^{ref}\left(\frac{c\cos\phi - \sigma_3' \sin\phi}{c\cos\phi - p^{ref}\sin\phi}\right)^m \qquad 4.20$$

The failure ratio is $R_f = q_f / q_a$; E_{50}^{ref} is the reference stiffness modulus and E_{ur}^{ref} is the reference unloading-reloading modulus corresponding to the reference pressure p^{ref}. It is observed that the shape of the yield loci depends on the exponent m. Figure 4-3 shows the shape of yield loci for increasing values of γ^p and m=0.5.

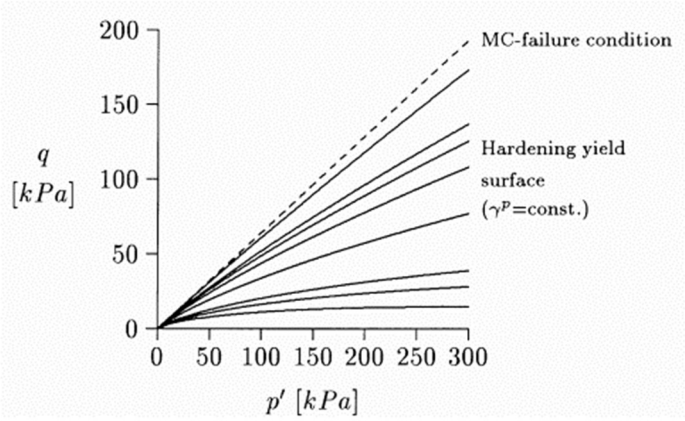

Figure 4-3. Yield loci for various values of γp and m=0.5 (Schanz et al, 1999).

The HSS model involves a relationship between rates of volumetric plastic strain $\dot{\varepsilon}_v^p$ and shear plastic strain $\dot{\gamma}^p$, as follow:

$$\dot{\varepsilon}_v^p = \sin(\psi_m)\dot{\gamma}^p \tag{4.21}$$

The mobilised dilatancy angle ψ_m follows the stress-dilatancy theory (Rowe, 1962, 1971):

$$\sin\psi_m = \frac{\sin\phi_m - \sin\phi_{cv}}{1 - \sin\phi_m \sin\phi_{cv}} \tag{4.22}$$

Where ϕ_{cv} is the critical state friction angle and the mobilised friction angle ϕ_m is defined as:

$$\sin\phi_m = \frac{\sigma_1' - \sigma_3'}{\sigma_1' + \sigma_3' - 2c\cot\phi} \tag{4.23}$$

The mobilised dilatancy angle ψ_m follows Rowe's theory for larger values of the mobilised friction angle ϕ_m, whereas for small mobilised friction angles and for negative values of ψ_m, is taken zero.

A second yield surface is introduced to close the elastic region and simulate compressive behaviour. The cap yield surface takes the form of an ellipse with its centre point in the origin. The magnitude of the yield cap is determined by the isotropic preconsolidation stress p_p and its aspect ratio is controlled by Mp_p (see Figure 4-4). The ellipse is used both as a yield surface and as a plastic potential (associated plasticity) and is defined as follow:

$$f_c = \frac{q^2}{M^2} + p'^2 - p_p^2 \tag{4.24}$$

Where M is an auxiliary parameter related to K_0. The hardening law relating $\dot{p}_p$ to volumetric cap strain $\dot{\varepsilon}_v^{pc}$ is:

$$\dot{\varepsilon}_v^{pc} = \frac{Ks/Kc}{K_s^{ref}}\left[\left(\frac{p_p + c\cot\phi}{p^{ref} + c\cot\phi}\right)^{-m}\right]\dot{p}_p \qquad 4.25$$

in which K_s^{ref} is the reference bulk modulus in unloading / reloading:

$$K_s^{ref} = \frac{E_{ur}^{ref}}{3(1-2\nu_{ur})} \qquad 4.26$$

and K_s/K_c is the ratio of bulk moduli in isotropic swelling and primary isotropic compression, which can be approximate as:

$$K_s / K_c \approx \frac{E_{ur}^{ref}}{E_{oed}^{ref}} \frac{K_0^{nc}}{(1+2K_0^{nc})(1-2\nu_{ur})} \qquad 4.27$$

In this way, K_0^{nc}, E_{ur}^{ref} and E_{edo}^{ref} determine the magnitude of M and K_s/K_c respectively. E_{50}^{ref} controls the magnitude of the plastic strains that are associated with the shear yield surface and E_{edo}^{ref} is used to control the magnitude of plastic strains from the yield cap.

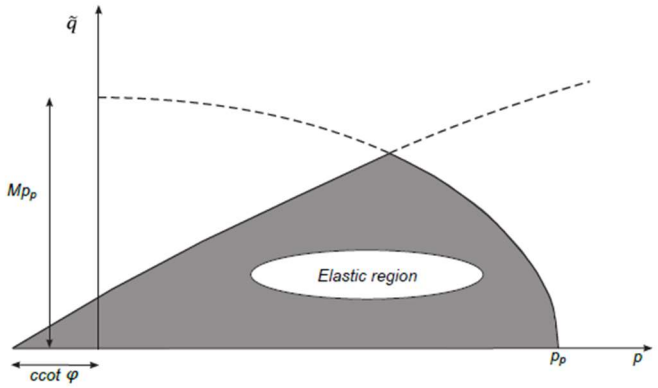

Figure 4-4. Yield surfaces in the p-q plane.

Additionally, the HSS model allows to simulate the non-linear behaviour of the soil in small strain range. For which, it incorporates a non-linear relation between degradation of stiffness and increase in deformations following the hyperbolic law suggested by Dos Santos and Correia (2001) (see eq. 3.10). The model introduces two additional parameters $\gamma_{0.7}$ and G_0. The parameter $\gamma_{0.7}$ is the shear

deformation for which the stiffness modulus has degraded to 70% of its initial value in small strain, G_0. The stress dependency of G_0 is taken into account with the power law, as follow:

$$G_0 = G_0^{ref}\left(\frac{c\cos\phi - \sigma_3' \sin\phi}{c\cos\phi - p^{ref}\sin\phi}\right)^m \qquad 4.28$$

The model parameters used to simulate triaxial tests shown later in this chapter are indicated in Table 4-3. More details about the HSS model can be found in Benz, T. (2006).

Table 4-3. Material parameters of HSS model for triaxial simulations

Model	ϕ [°]	c [kN/m²]	ψ [°]	m	E_{50} [kN/m²]	E_{oed} [kN/m²]	E_{ur} [kN/m²]	G_0 [kN/m²]	$\gamma_{0.7}$	k [m/d]
Axisymmetric	30	9	0	1	5000	3600	14000	65000	$7x10^{-5}$	$8.64x10^{-4}$
Plane strain	30	9	0	1	5000	3600	14000	65000	0.15	$8.64x10^{-4}$

4.2.4 S-CLAY1S model

This model is an extension of the critical state models, with anisotropy of plastic behaviour represented through an inclined yield surface. A rotational hardening rule permits modelling the development or erasure of fabric anisotropy during plastic straining. The model S-clay1 was proposed initially by Wheeler (1997) and was subsequently modified by Näätänen et al (1999) and Wheeler et al (2003). Karstunen et al. (2005) introduce the concept of intrinsic yield surface (Gens and Nova 1993) into the S-Clay1 model to simulate destructuration (Leroueil et al. 1979), this model was called S-Clay1S. In three-dimensional stress space the yield surface of the S-CLAY1S model is a sheared ellipsoid (Figure 4-5), given by:

$$\frac{3}{2}\left[\left\{\boldsymbol{\sigma}_d - p'\boldsymbol{\alpha}_d\right\}^T\left\{\boldsymbol{\sigma}_d - p'\boldsymbol{\alpha}_d\right\}\right] - \left[M^2 - \frac{3}{2}\left\{\boldsymbol{\alpha}_d\right\}^T\left\{\boldsymbol{\alpha}_d\right\}\right]\left(p'_m - p'\right)p' = 0 \qquad 4.29$$

where $\boldsymbol{\sigma}_d$ = deviatoric stress tensor; p' = mean effective stress; and $\boldsymbol{\alpha}_d$ = dimensionless second order tensor describing the fabric anisotropy, called the deviatoric fabric tensor (Wheeler et al, 2003), M = critical state value of the stress ratio in triaxial space and the state parameter p'_m defines the size of the natural yield surface of the clay.

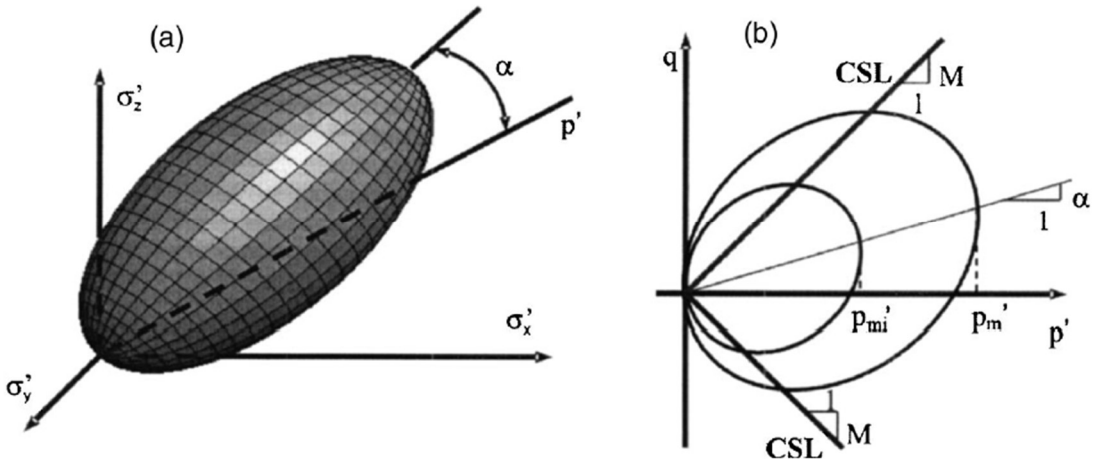

Figure 4-5. S-CLAY1S yield surface in: a) three-dimensional stress space and b) triaxial stress space

The intrinsic yield surface is of the same shape and inclination as the yield surface for the natural soil, but with a size p'_{mi} that is related to p'_m by

$$p'_m = (1+x)\, p'_{mi} \tag{4.30}$$

Where x = amount of bonding.

A hardening law for unbonded (reconstituted) soil similar to that of Modified Cam Clay (MCC) is use to relate the increase in size of the intrinsic yield relate to the increments of the plastic volumetric strain ($d\varepsilon_v^p$) as follow:

$$dp'_{mi} = \frac{\upsilon p'_{mi}}{\lambda_i - \kappa} d\varepsilon_\upsilon^p \tag{4.31}$$

where v = specific volume; λ_i = slope of the intrinsic normal compression line in the compression plane (ln p'–v space); and κ = slope of a swelling line in the compression plane.

Plastic straining also produces rotation of the yield surface (evolution of anisotropy), which is controlled by a second hardening law:

$$d\boldsymbol{\alpha}_d = \mu\left(\left[\frac{3\boldsymbol{\eta}}{2} - \boldsymbol{\alpha}_d\right]\left\langle d\varepsilon_\upsilon^p \right\rangle + \beta\left[\frac{\boldsymbol{\eta}}{3} - \boldsymbol{\alpha}_d\right] d\varepsilon_d^p\right) \tag{4.32}$$

where $\boldsymbol{\eta}$ = tensorial equivalent of the stress ratio, defined as $\boldsymbol{\eta} = \boldsymbol{\sigma}_d/p'$; and $d\varepsilon_v^p$ = increment of plastic deviatoric strain. The soil constants μ and β controls the absolute rate at which $\boldsymbol{\alpha}_d$ heads toward its current target value and the relative effectiveness of plastic deviatoric strains and plastic volumetric strains in rotating the yield surface. More details can be found at Wheeler et al (2003).

The S-CLAY-1S assumes that both plastic volumetric strains and plastic deviatoric strains tend to reduce the bonding parameter *x* to zero. A third hardening law describes the degradation of bonding as follow:

$$dx = -ax\left(\left|d\varepsilon_v^p\right| + b\left|d\varepsilon_d^p\right|\right) \qquad 4.33$$

where the soil constant *a* controls the absolute rate of destructuration and *b* controls the relative effectiveness of plastic deviatoric strains and plastic volumetric strains in destroying the bonding, as detailed by Koskinen et al. (2002a).

The S-CLAY-1S reduces to the S-CLAY-1 model by setting the initial value of the state parameter *x* to zero and using an apparent value of λ (determined from an oedometer test on a natural clay sample), instead of the intrinsic value λ_i of a reconstituted clay. The model can also be reduced to the isotropic Modified Cam Clay model if in addition, the initial values of all terms of α_d and the value of the soil constant μ are set to zero.

Again, as for the SS model, the soil parameters were selected through an iterative trial and error process until the best fit was achieved with the triaxial tests performed in the laboratory. Table 4-4 shows the parameters adopted for the S-Clay1 model.

Table 4-4. Material parameters of S-Clay1S model for triaxial simulations.

Model	γ_{unsat} [kN/m^3]	γ_{sat} [kN/m^3]	κ	ν	λ	M	μ	β	a	b	e_0	α_0	x_0	k [m/d]
Axisymmetric	18.5	18.5	0.02	0.25	0.1	1.2	50	0.1	0	0	0.8	0.6	0	$8.64x10^{-4}$
Plane strain	18.5	18.5	0.02	0.25	0.1	1.2	50	0.1	0	0	0.8	0.6	0	$8.64x10^{-4}$

4.2.5 Triaxial CAU Tests. Axisymmetric model

Numerical simulation of triaxial tests was intended to follow the stress paths of triaxial tests performed on undisturbed samples of Barcelona Port (extension and compression triaxial tests). Isotropic SS model and anisotropic S-Clay1 model were tested. Also, comparison with the Modified Cam-Clay (MCC) model and the Hardening Soil with small-strain stiffness (HSS) model were performed.

Due to the double symmetry of the problem, a quarter of the typical cylindrical specimen of a triaxial test is simulated. The dimensions adopted for the model are similar to those that would have a real soil sample in a laboratory test: 0.05 x 0.025 meters. The model was discretized in 52 triangular elements of 15 nodes as is shown in Figure 4-6.

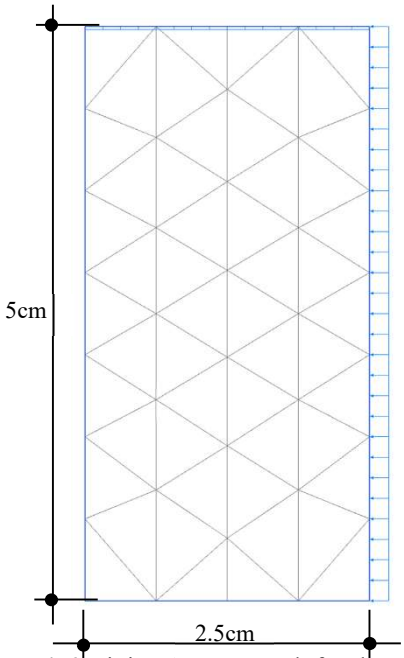

Figure 4-6. Finite element mesh for the triaxial test

Regarding boundary conditions, the displacements in the horizontal and vertical direction were restricted in the left and bottom boundary, respectively. Normal stresses were imposed on the upper and right-side boundary. Also, during shearing of the sample, drainage through the lateral and lower boundaries was not allowed.

Considering that soil samples were really very soft, all samples tested were subjected to an initial phase of isotropic consolidation of 20kPa, in order to move away from the critical state line. After that, the specimen is consolidated following $K_0 = 0.5$ stress path. Stresses were applied in several steps until reaching the specified vertical stress prior to start shearing (σ'_v = 64, 322, 600 kPa). During these phases the dissipation of water pressures is allowed. Finally, once the desired vertical stress is reached, the sample is shearing in an undrained condition. Six different failure conditions were evaluated, three corresponding to compression failure (increasing vertical tension) and three to failure in extension (increasing horizontal tension). In all cases the samples were at a normally consolidated condition (OCR = 1).

4.2.5.1 Results

Results from Isotropic Models

Table 4-5 shows the value of the undrained resistance s_u and the resistance ratio s_u / σ'_v obtained in the simulation of triaxial tests under normally consolidated condition. Samples were sheared under compression and extension (reducing the vertical stress) stress path. Results of the models match quite well the resistance ratio adopted from laboratory tests in compression (aprox. 0.33), but overestimate the value adopted in extension tests (aprox. 0.19). Also, note that the stress ratio computed from the SS and HSS models decreases slightly as vertical stress increases, both in

compression and extension simulation, probably due to the different slope of the failure envelope (Mohr-Coulomb) and the K_0 line.

Figure 4-7 shows a comparison of CAU triaxial tests (blue line) performed under confining pressure of p'=200 kPa and the results of computation with isotropic models Soft Soil (SS), Modified Cam Clay (MCC), and Hardening Soil with Small-Strain Stiffness (HSS). It is observed that the simulation of the triaxial test with the isotropic models predict values of the undrained resistance very close to those defined under compression triaxial stress path, but it results in overprediction of undrained stress in extension triaxial stress path. The SS and HSS models produce quite similar results, because both incorporate a Mohr-Coulomb failure criterion in their formulation, whereas for the MCC model as implemented in Plaxis, the critical state line is comparable with the Drucker-Prager failure line and represents a (circular) cone in principal stress space. Hence, the value of M must be adjusted for each mode of failure tested. Also, it is noted that pore pressure at failure is quite well predicted for all the models tested in compression path, but it is largely over predicted for extension. Similar behaviour is observed for tests under different consolidation stress reached before the shear stages (see Figure 4-8 compression tests and Figure 4-9 extension tests).

Table 4-5. Results obtained in the simulation of the triaxial CAU test

Model	**Compression**			**Extension**		
	σ'_v (kPa)	**s_u (kPa)**	**s_u/σ'_v**	**σ'_v (kPa)**	**s_u (kPa)**	**s_u/σ'_v**
MCC	64.44	19.64	0.304	64.44	19.6	0.304
	323.59	100.81	0.312	323.59	95.87	0.296
	602.82	185.18	0.307	602.82	184.86	0.307
SS	63.29	22.85	0.361	63.29	16.12	0.255
	327.03	103.93	0.318	327.03	74.16	0.227
	609.37	187.05	0.307	609.37	133.44	0.219
HSS	63.71	25.73	0.404	63.71	18.37	0.288
	323.38	110.64	0.342	323.38	79.54	0.246
	601.55	202.10	0.336	601.55	145.32	0.242

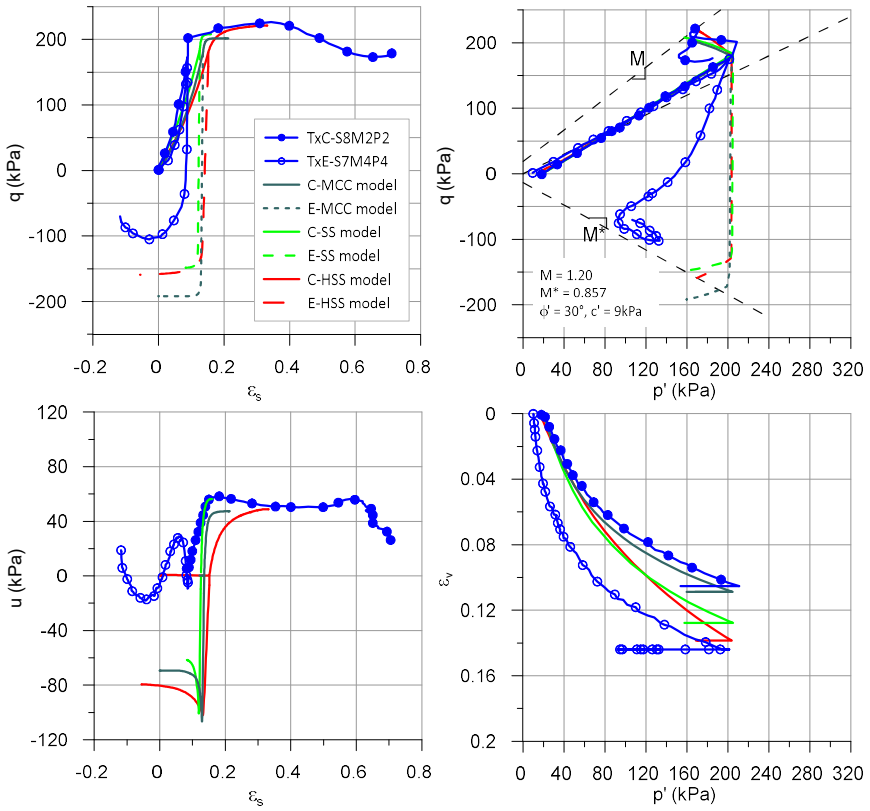

Figure 4-7. Comparison of real CAU triaxial tests (p'=200kPa) with simulation using isotropic constitutive models (MCC, SS and HSSmodels).

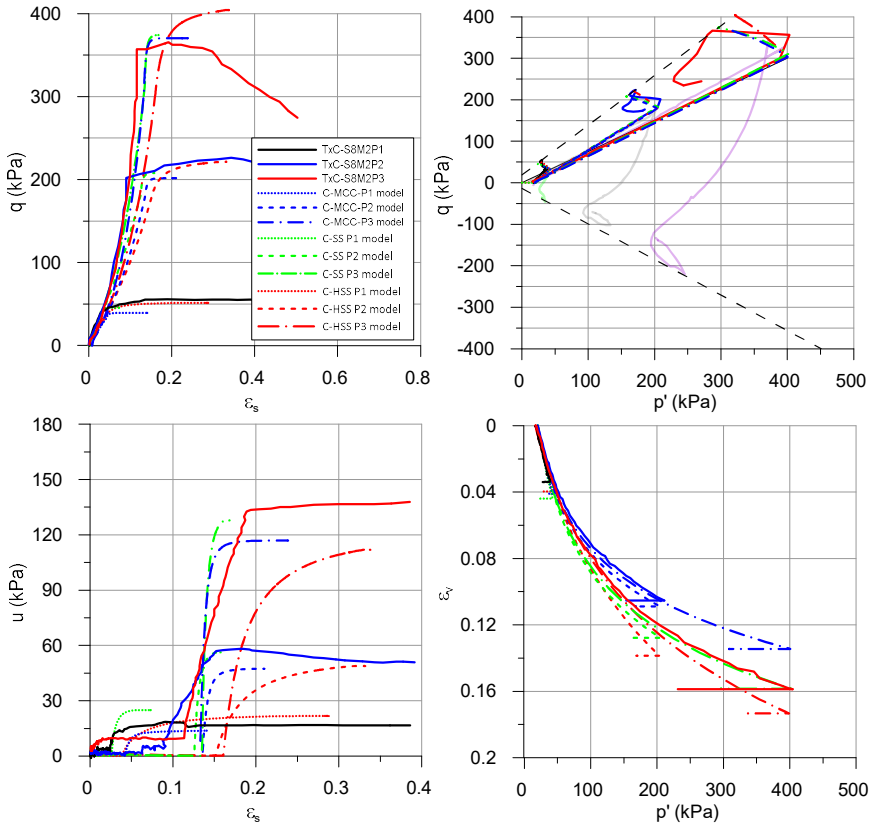

Figure 4-8. Comparison of real compression triaxial tests at confining pressures p´= 43, 200 and 400 kPa with simulation of several triaxial tests using isotropic modes (MCC, SS, HSS).

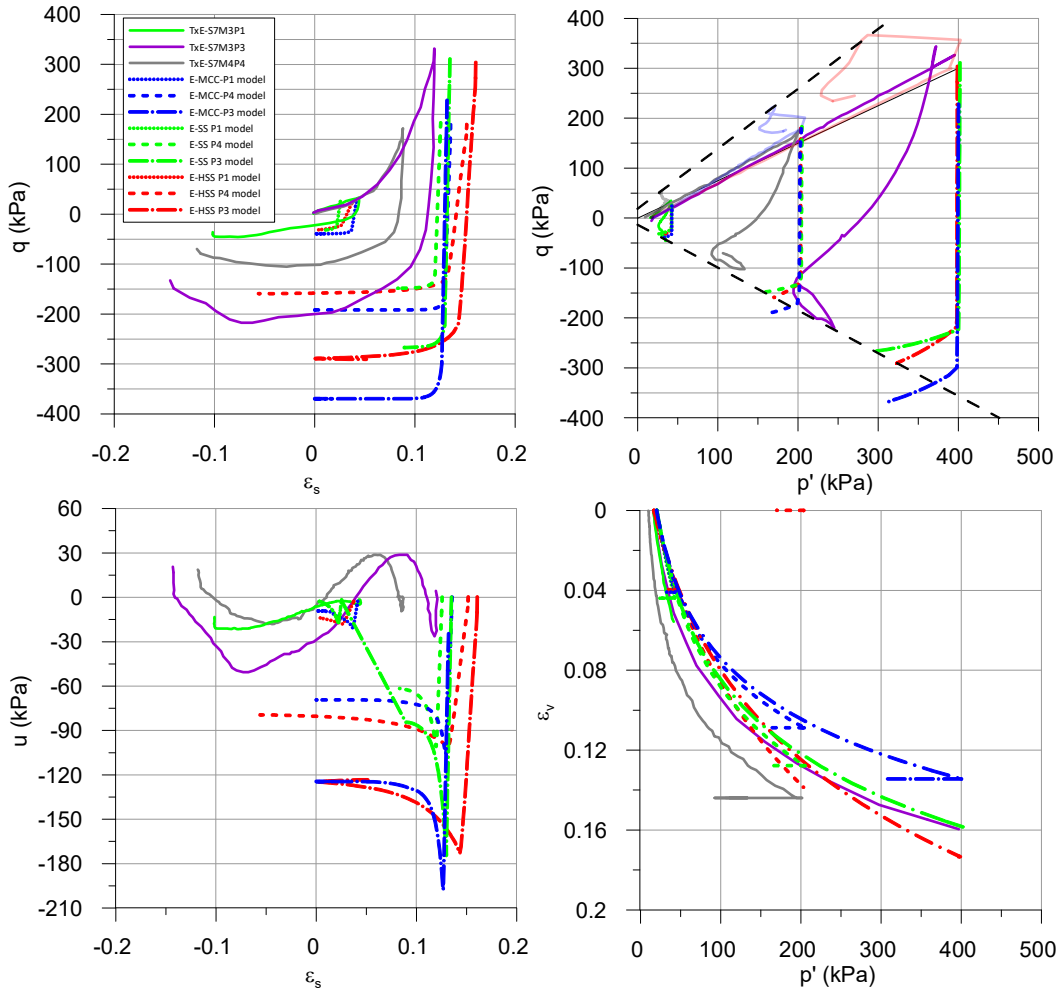

Figure 4-9. Comparison of real extension triaxial tests at confining pressures p´= 43, 200 and 400 kPa with simulation of several triaxial tests using isotropic modes (MCC, SS, HSS).

Results from Anisotropic models

Simulation of triaxial tests with the isotropic models have shown difficulties mainly to predict the extension undrained strength and also the pore pressure development during extension shearing. The effect of these difficulties will be more significant in problems where the extension mode of failure is predominant. Results of simulation with the S-Clay1 model are shown in Figure 4-10. The advantage of the S-Clay1 over the SS model is that stress state reaches the yield surface in extension in a shorter distance due to the rotated yield surface, which imply elastic domain is also shorter than in case of SS model. As expected, the model produces an undrained strength closer to the real one. But it might be even better if the critical state parameter M were different for compression and extension mode of failure. The version of the S-Clay1 model used in this research does not permit this option. The stress-strain behaviour is quite good simulated with the S-Clay1 model both for compression and extension mode of failure. Although, pore pressure is better simulated with the S-Clay1 model compared to the SS model, it is not entirely satisfactory. The laboratory specimen appears to show a dilating behaviour, which makes the pore pressure tend to

decrease. Figure 4-11 shows a comparison between the SS model and the S-Clay1 for simulating triaxial test at different confining pressures. The stress paths followed in compression are quite similar for both models. Note that the failure criterion in the S-Clay1 is defined in term of the critical state parameter, which imply that no cohesion is considered in the model, unlike the SS model, where a M-C failure criterion is adopted. Undrained strength is slightly overpredicted with the S-Clay1 model. Both models reproduce well the compression behaviour.

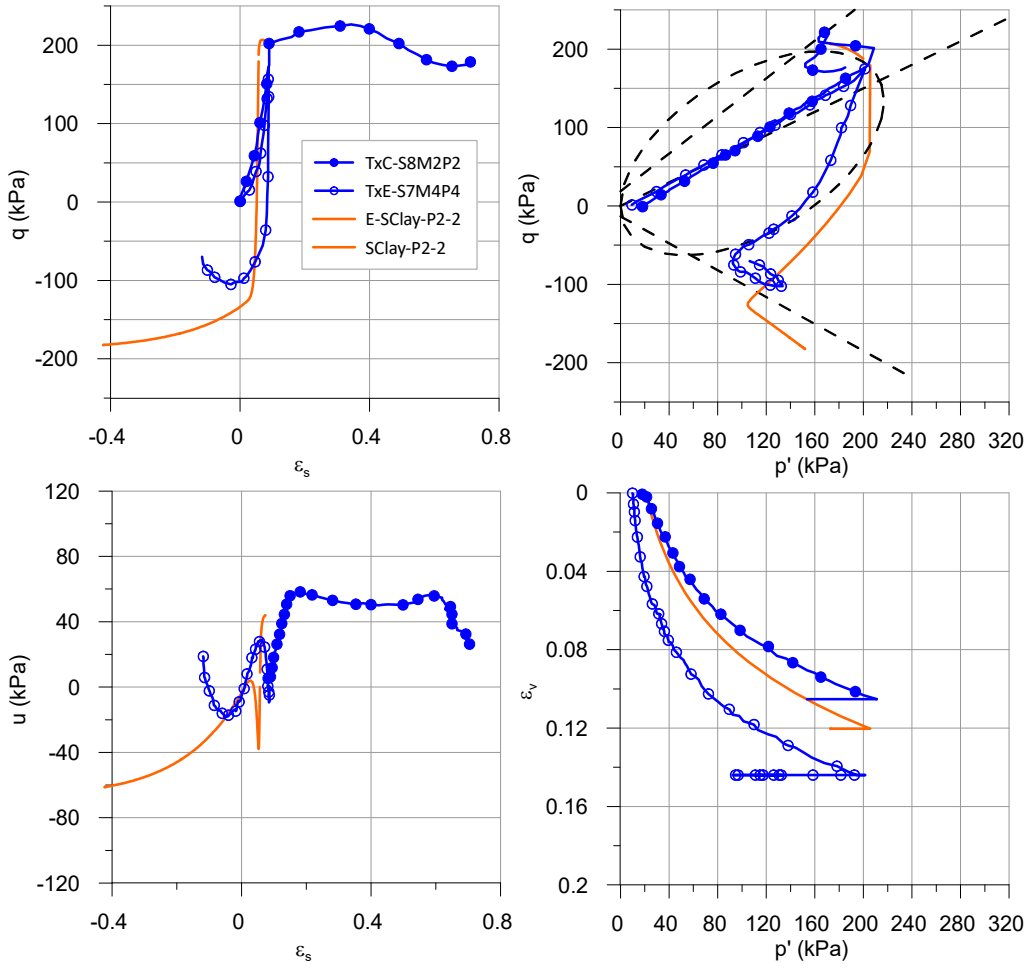

Figure 4-10. Simulation of triaxial test with the S-Clay1 model compared to real triaxial test of Barcelona Port Clay

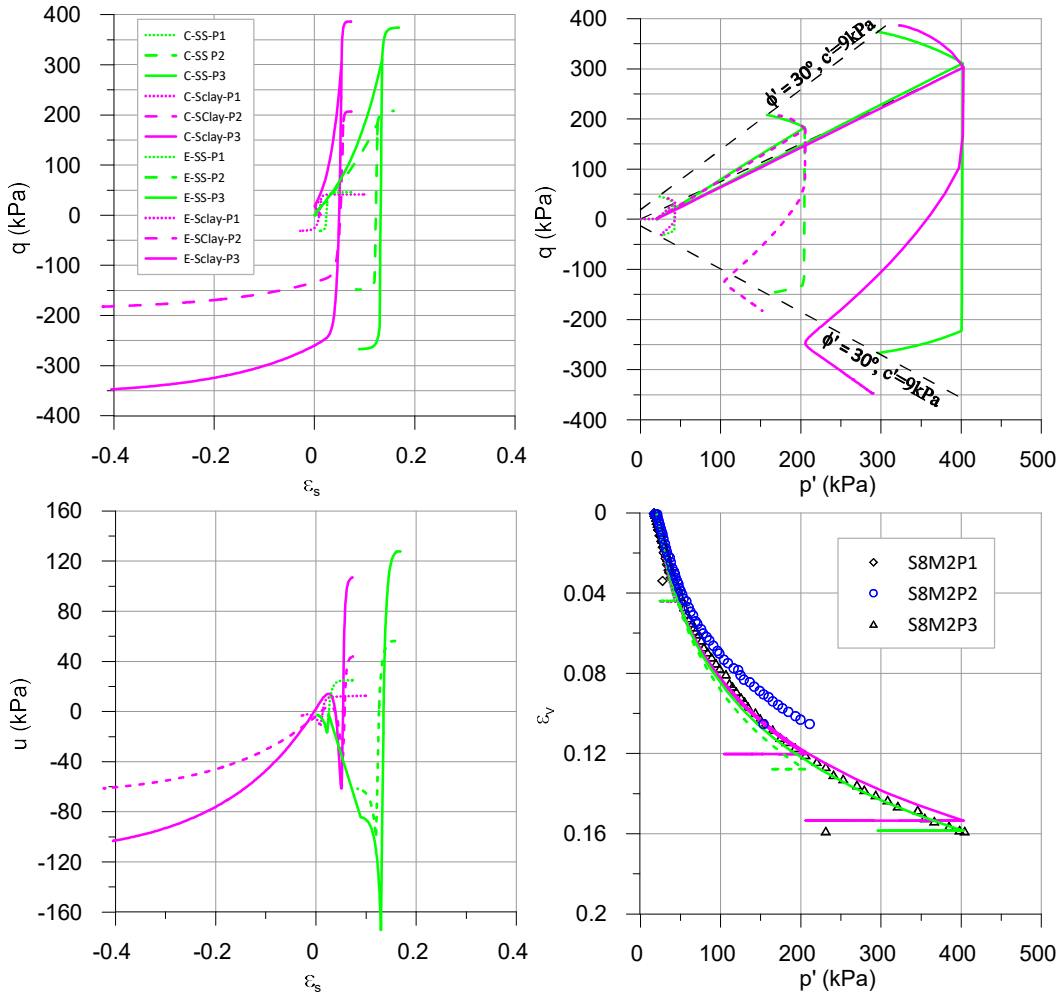

Figure 4-11. Comparison of Simulation of triaxial tests with the SClay-1 and SS model for different confining pressure

4.2.6 Compression and extension tests in plane strain

Similar to the axisymmetric model, only a quarter of the true geometry of a triaxial specimen is simulated. The finite element mesh is exactly the same as that used in the axisymmetric model, as described above, but this time under plane strain conditions, which are most suitable for the analysis of lineal structures such as breakwaters. Again, all stages of a triaxial compression and extension test were simulated.

The boundary conditions and phases of computation are the same as in axisymmetric model. The stresses were applied in different phases during consolidation until reaching the specified vertical stress prior to shearing (σ'_v = 64, 322, 600 kPa). Furthermore, to investigate the undrained strength under different overconsolidated states, some models were unloaded before the shearing stage.

4.2.6.1 Results

Normally consolidated soils (OCR = 1)

Figure 4-12 show results of three simulations of plain strain tests under compression and extension load conditions using isotropic models. Table 4-6 shows the value of the undrained shear strength s_u and the resistance ratio s_u / σ'_v obtained in these simulations. It is noted that the resistance ratio obtained with the MCC model increases notably under plain strain condition compared to the results obtained in the axisymmetric condition (it changes from 0.30 to 0.35 in the simulation of compression and extension tests). As expected, the SS and HSS models produce almost the same undrained strength as their corresponding axisymmetric model, but in plain strain conditions, no difference between compression an extension tests simulation is noted in contrast to what was observed in the axisymmetric model.

It is also noticeable in plane strain tests simulations that computed pore pressures are greater than that obtained in axisymmetric model regardless of the constitutive model used. The volumetric strain computed during K_0 consolidation are almost the same as that obtained with the axisymmetric model.

Table 4-6. Undrained strength computed from the plane strain tests

Model	**Compression**			**Extension**		
	σ'_v (kPa)	**s_u (kPa)**	**s_u/σ'_v**	**σ'_v (kPa)**	**s_u (kPa)**	**s_u/σ'_v**
MCC	65.15	22.87	0.35	65.15	21.96	0.34
	324.15	115.68	0.36	324.15	113.88	0.35
	603.36	213.70	0.35	603.36	212.83	0.35
SS	64.01	23.06	0.360	64.01	22.57	0.353
	326.58	103.54	0.317	326.58	103.35	0.316
	608.83	186.90	0.307	608.83	186.54	0.306
HSS	64.18	25.91	0.404	64.18	25.78	0.402
	324.62	111.05	0.342	324.62	110.94	0.342
	604.70	203.14	0.336	604.70	202.78	0.335

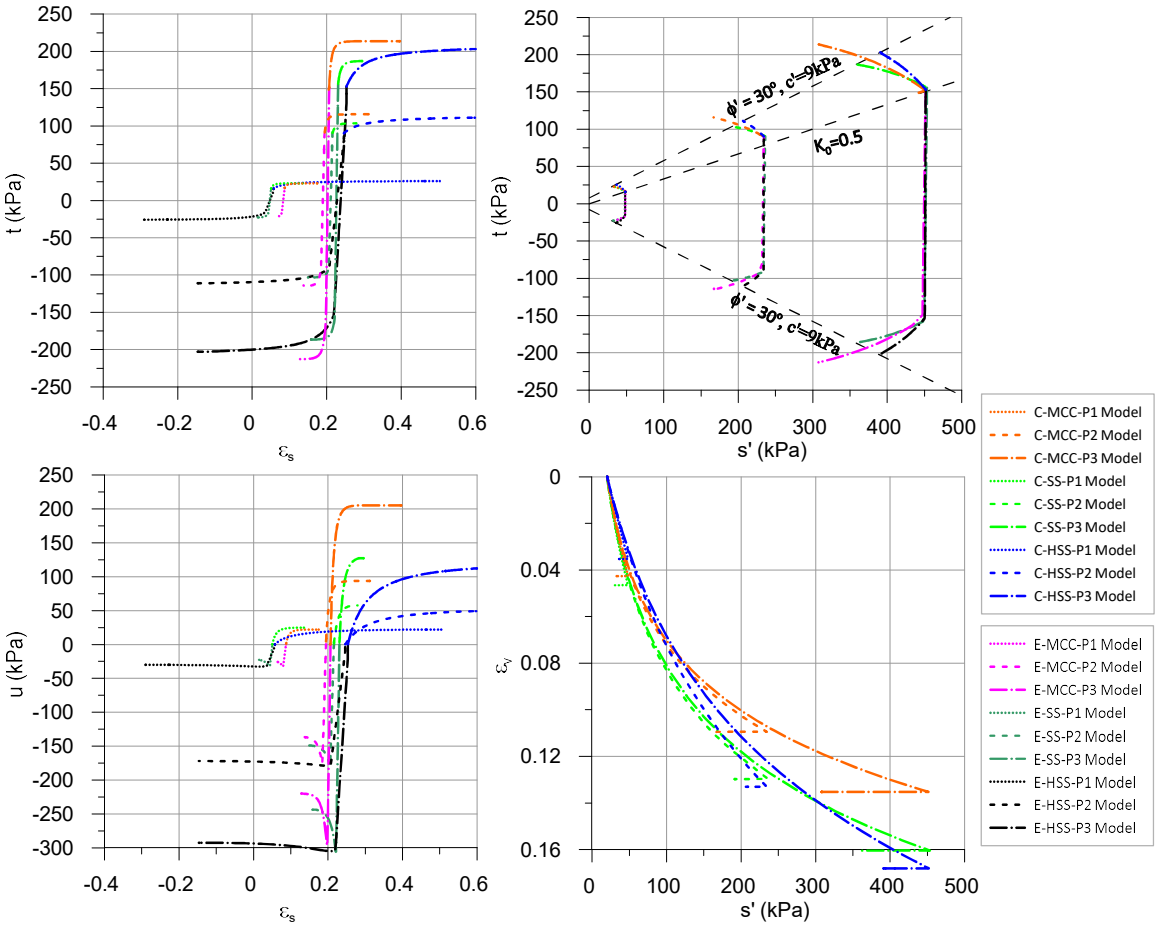

Figure 4-12. Simulation of plain strain tests with isotropic models MCC, SS, and HSS.

The Anisotropic S-Clay1 model was also tested to simulated compression and extension tests in plane strain conditions, results are shown in Figure 4-13. The undrained strength is slightly overpredicted with the S-Clay1 model compared to the results of the SS model, which is especially noticeable at high confining pressure. For low and intermediate confining stress, results are quite similar with both models. The extension stress path obtained with the anisotropic model looks more similar to those obtained in triaxial tests. Furthermore, the volumetric strain is higher with the anisotropic model, even while the pore pressure is markedly lower.

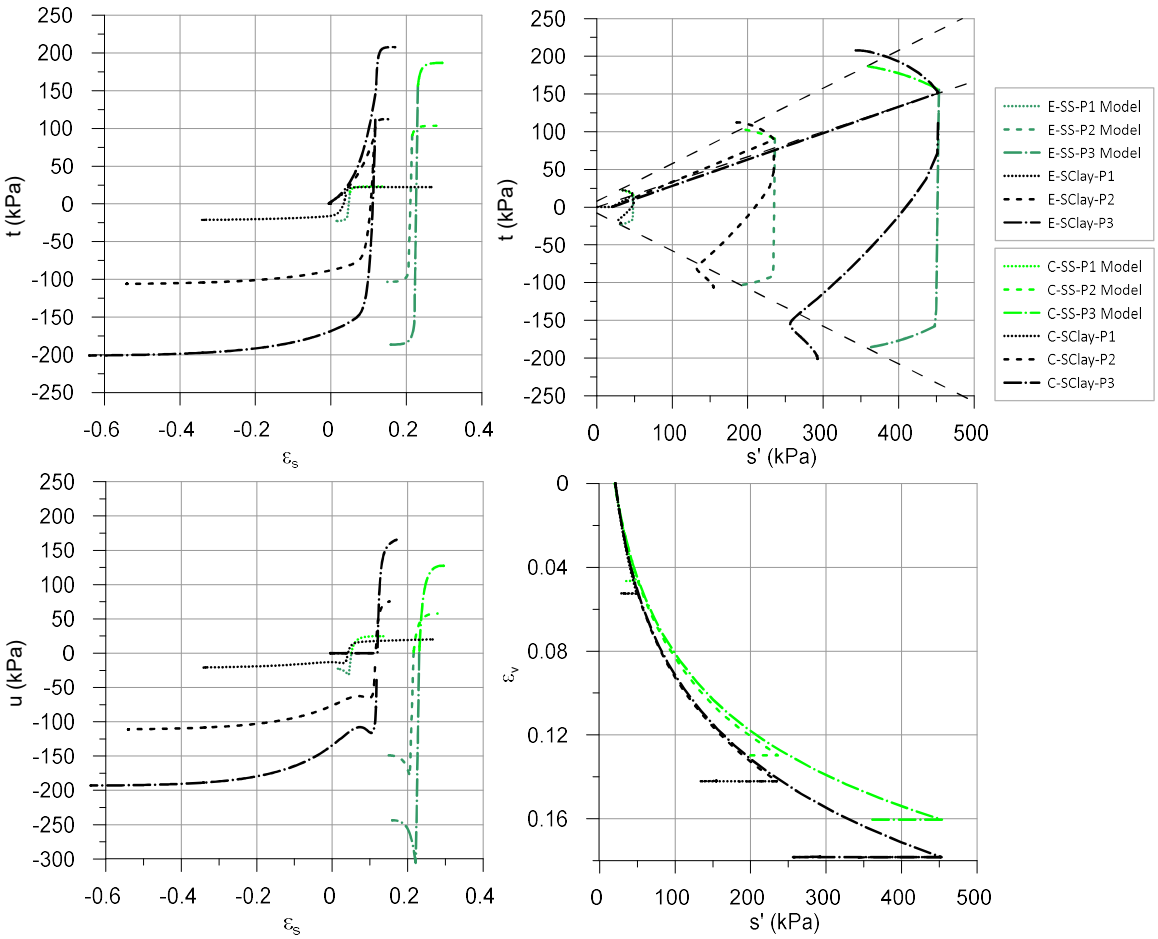

Figure 4-13. Simulation of plain strain test with anisotropic S-Clay1 model compared to isotropic SS model.

Overconsolidated soil (OCR> 1)

As indicated previously different simulations of plane strain tests were carried out, with loading and unloading stages, in order to achieve different levels of overconsolidation in the sample. The stress paths resulting from the simulation of isotropic and anisotropic consolidated triaxial test with the S-clay1 and MCC model are shown in Figure 4-14. The value of M is related to the angle of friction at the failure in the MCC and S-Clay1 model, so that for a friction angle of 20º corresponds a value M = 0.772 and for 30º, M = 1.20. It is observed that the undrained resistance is almost the same for the tests with $K_0 = 1$ and $K_0 = 0.5$ with the S-Clay1 model, although they follow a different stress path. In the case of the MCC model, the final undrained resistance is slightly different in the two cases ($K_0 = 1$ and $K_0 = 0.5$), with a tendency to reach higher values than those obtained with the S-Clay1 model.

Figure 4-15 shows the calculation of the undrained resistance in plane strain tests with different OCR values. The MCC and S-Clay models show a tendency to increase the undrained resistance with the OCR value. In the case of the SS model, there is an increase in s_u up to OCR values of

about 1.25, after that the s_u value is limited, because the failure is governed by the Mohr-Coulomb criterion within the elliptical yield surface.

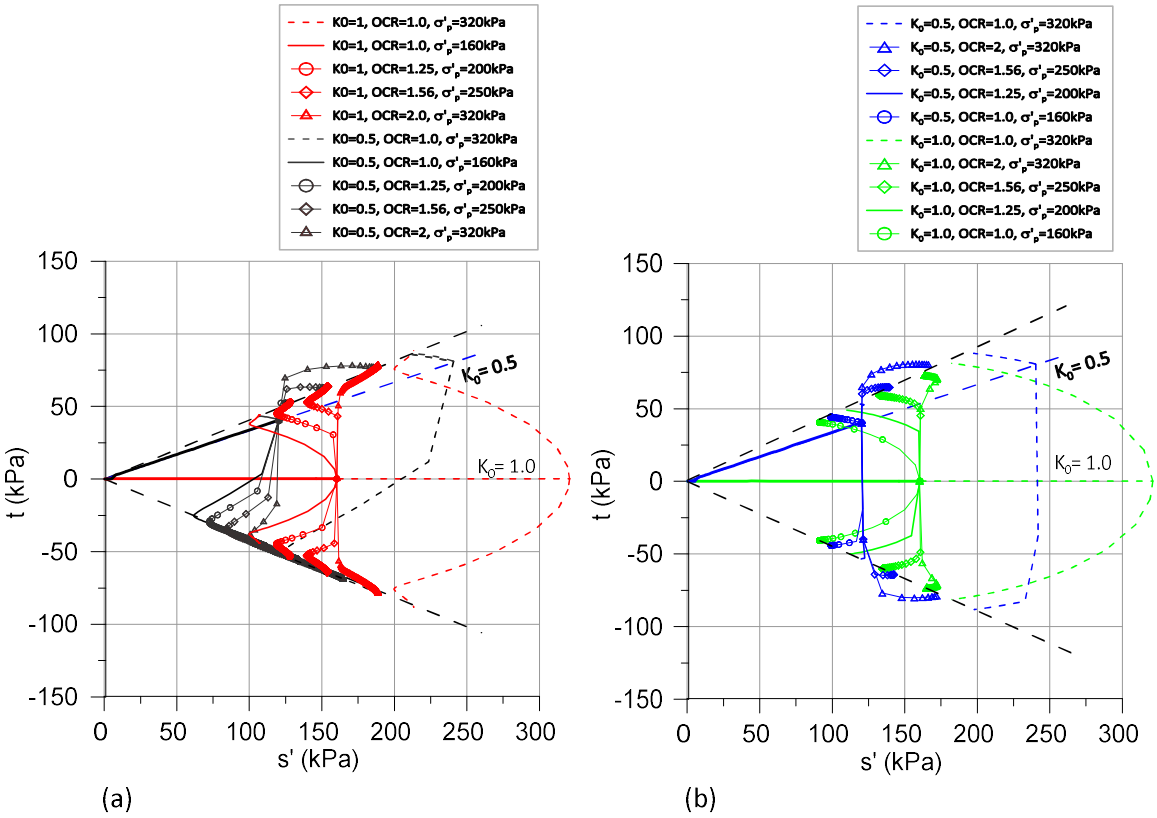

Figure 4-14. Stress path followed under isotropic (K_0=1) and anisotropic consolidation (K_0=0.5) using (a) Sclay model (M=0.772) (b) Modified Cam clay model (M=0.772).

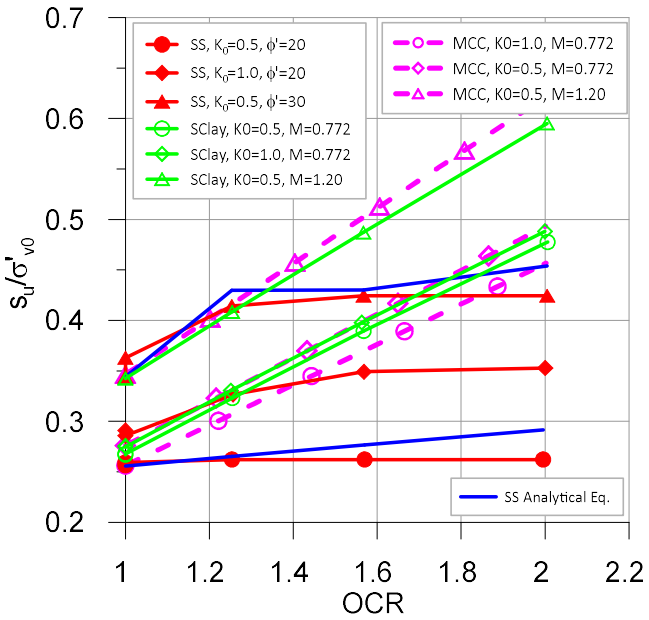

Figure 4-15. Undrained strength at plane strain tests simulations with different OCR values.

The possibility to obtain the desired value of s_u in the SS model while keeping constant the initial stress is by modifying the value of M. This is done by changing the parameter K_0^{NC}. However, there

is a lower limit of the value of s_u that can be obtained in this way. It is given by the fact that M can not be lower than M_ϕ. Some more of flexibility can be obtained by varying κ / λ .

4.2.7 Simple shear tests simulation

The dimensions of the model were similar to those that would have a real soil sample in a laboratory test: 0.02 x 0.10 meters. The model was discretized in 108 higher order triangular elements of 15 nodes and 12 Gauss points. Figure 4-16 shows the finite element mesh used to perform the analyses. Plain strain condition was adopted.

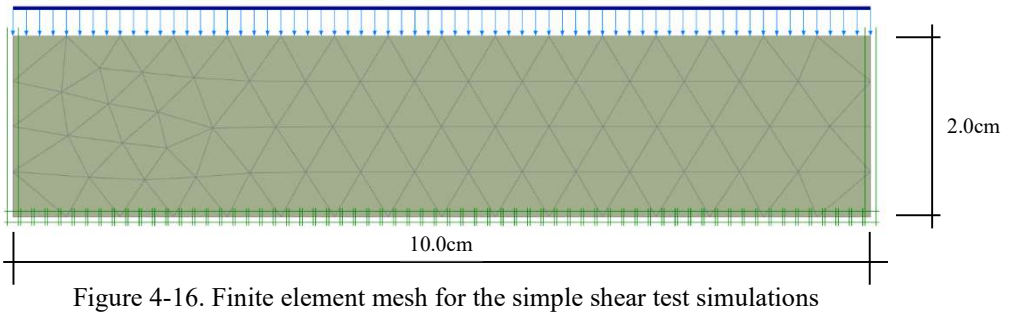

Figure 4-16. Finite element mesh for the simple shear test simulations

To simulate the simple shear test, horizontal displacements were prescribed on the side boundaries, increasing linearly from zero at the base to 0.01m at the upper edge. Likewise, on the upper boundary a horizontal displacement of 0.01 m is established, while in the lower boundary of the model, displacements in the vertical and horizontal directions were restricted.

During the consolidation phase of the sample, free drainage was allowed in the upper and lower boundaries, while drainage was prevented in the lateral boundaries. The vertical stresses increase successively at each step of consolidation loading (10, 20, 40, 80, 160, 200, 250, 320 kPa). Consolidation is allowed for periods of 1 day at each loading step, in order to completely dissipate excess interstitial pressures. In the following loading steps, the vertical stress was reduced to 250, 200 and 160 kPa before the undrained shearing phase start, which produces OCR = 1.28, 1.60 and 2. For the normally consolidated state, the sample was subjected to undrained shearing under a constant vertical stress of 80, 160 and 320 kPa.

4.2.7.1 Results

Normally consolidated soil (OCR=1)

Three simple shear tests were simulated, proceeding to the undrained shearing of the sample when the vertical stresses of 80, 160 and 320 kPa were reached. Figure 4-17 shows the shear stresses τ plotted versus the shear deformations during undrained shearing in the simple shear tests with the MCC, SS and S-Clay1 models. Table 4-7 shows the values of the resistance factor τ/σ'_v obtained from these tests.

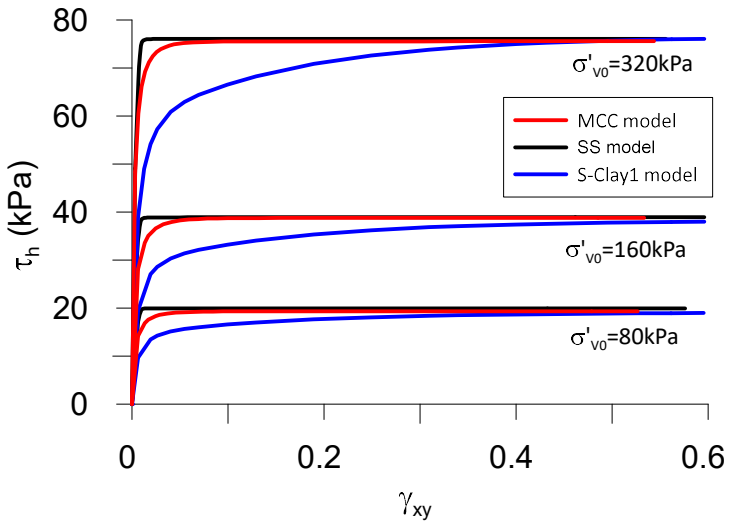

Figure 4-17. Shear stress vs shear strain obtained in the simple shear test simulation.

Table 4-7. Summary of results of simple shear tests simulation

Model	**σ'v (kPa)**	**su (kPa)**	**su/σ'v**
MCC	80	19.07	0.24
	160	38.13	0.24
	320	76.21	0.24
SS	80	20.43	0.26
	160	40.28	0.25
	320	78.80	0.25
S-Clay1	80	19.11	0.24
	160	38.25	0.24
	320	76.40	0.24

These results demonstrate that under the conditions tested (normally consolidated soil) and with the parameters adopted, the simulation of the simple shear test with MCC, SS and S-Clay1 model reproduces approximately the relation that was defined for the undrained resistance of normally consolidated soil of the Port of Barcelona: $s_u = 0.25\sigma_v^{'}$. The S-Clay model requires a high level of shear strain to mobilize the undrained shear resistance. Figure 4-18 shows the stress paths followed in the simulation with the MCC, SS and S-Clay1 models and is compared with the results of laboratory tests. All three models achieve similar undrained strength; however, the SS model generates less pore pressures during shearing.

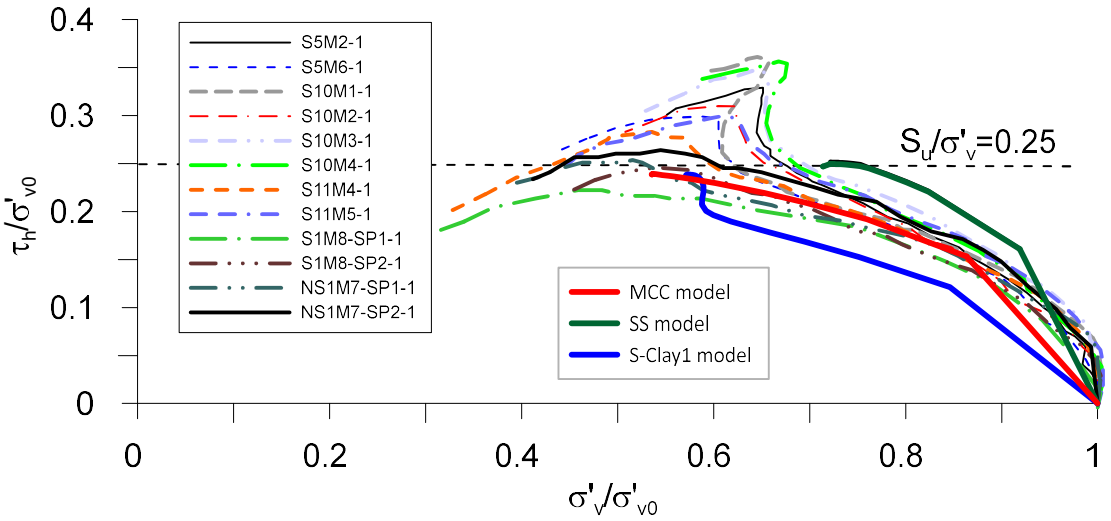

Figure 4-18. Normalized shear stress versus normalized vertical stress obtained in the DSS tests simulation compared with the test results.

Overconsolidated soil (OCR>1)

Figure 4-19 shows the values of the undrained resistance obtained in the simulation of the simple shear test in samples with different OCR values. The results show that for the different values of OCR tested, the MCC and S-clay1 model reproduces quite well the relation of undrained resistance $0.25OCR^{0.8}$; while, the SS model tend to under estimate the undrained resistance when the OCR value increases beyond 1.25.

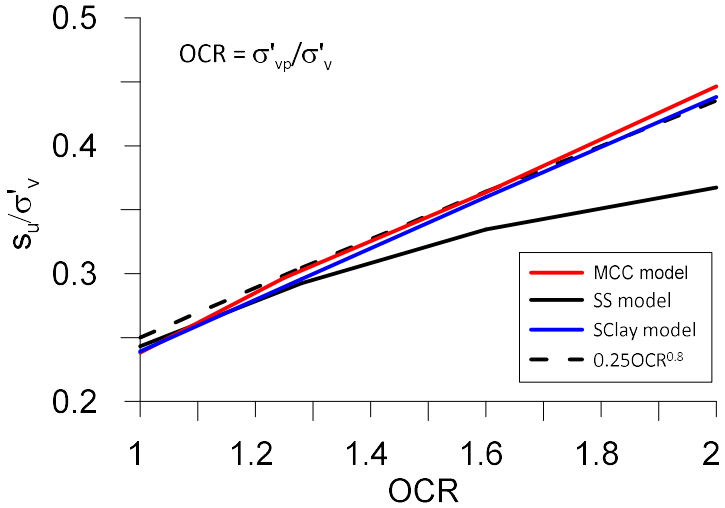

Figure 4-19. Normalized undrained resistance varying with OCR

4.3 MODELING CYCLIC BEHAVIOUR

4.3.1 The UBC3D-PLM Model

The UBC3D-PLM model implemented in Plaxis (Tsegaye,2010; Petalas & Galavi, 2012) is a generalization of the original UBCSAND (University of British Columbia Sand) model introduced by Puebla, Byrne & Phillips (1997) and Beaty & Byrne (1998).

The UBC3D-PLM model uses the Mohr-Coulomb yield condition in a 3D principal stress space for primary loading, and a yield surface with a simplified kinematic hardening rule for secondary loading. Moreover, a modified non-associated plastic potential function based on Drucker-Prager's criterion is used for the primary yield surface, in order to maintain the assumption of stress-strain coaxiality in the deviatoric plane for a stress path beginning from the isotropic line (Tsegaye, 2010).

4.3.1.1 Elastic behaviour

Elastic behaviour of the UBC3D-PLM is defined in terms of the elastic bulk modulus K and the elastic shear modulus G, which are defined by the following equations:

$$K = k_B^{*e} p_{ref} \left(\frac{p'}{p_{ref}} \right)^{me}$$
$$G = k_G^{*e} p_{ref} \left(\frac{p'}{p_{ref}} \right)^{ne} \qquad 4.34$$

where k_B^{*e} and k_G^{*e} are input parameters that represent the bulk and the shear modulus factors respectively, p_{ref} is the reference pressure, *me* and *ne* are parameters that define the rate of stress dependency of stiffness. The model predicts pure elastic behaviour with G_{max} during unloading process.

4.3.1.2 Yield surface

The yield Surface is defined from a set of Mohr-Coulomb functions as follow:

$$f_m = \frac{\sigma_{\max} - \sigma_{\min}}{2} - \left(\frac{\sigma_{\max} + \sigma_{\min}}{2} + c \cot \phi_p \right) \sin \phi_m \qquad 4.35$$

This function defines 6 planes which combined in one figure produces a general 3D surface of the Mohr-Coulomb criterion (Figure 4-20).

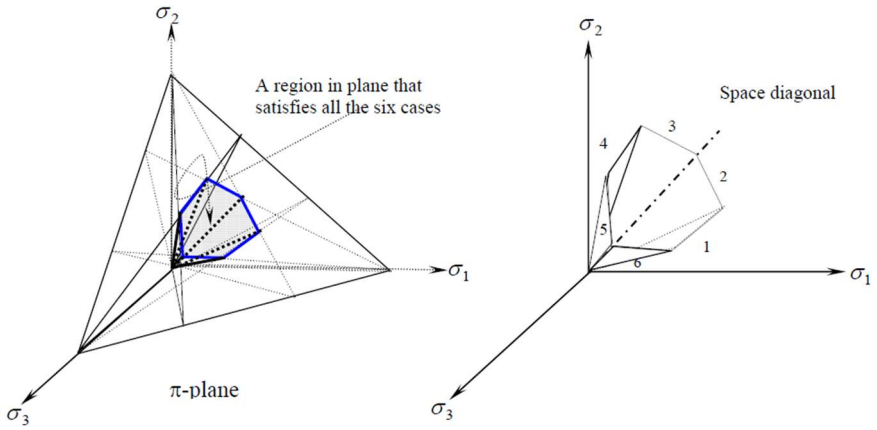

Figure 4-20. General 3D surface of the Mohr-Coulomb criterion.

The mobilised friction angle derived from the Mohr-Coulomb yield criterion, is given as:

$$\sin\phi_{mob} = \frac{\sigma'_1 - \sigma'_3}{\sigma'_1 + \sigma'_3 - 2c\cot\phi_p} \qquad 4.36$$

The projection of the Mohr-Coulomb yield surface in a deviatoric plane is therefore as shown in Figure 4-21:

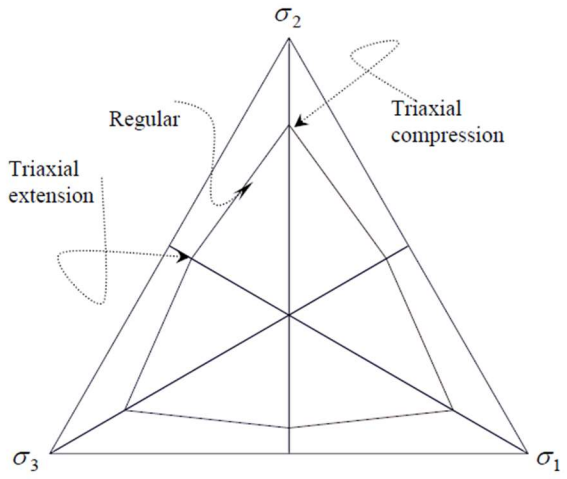

Figure 4-21. Projection of the Mohr-Coulomb yield criterion in π plane

4.3.1.3 Hardening rule

The size of the yield surface is governed with a strain hardening rule (similar to the Hardening Soil model). The hardening rule governs the amount of plastic strain as a result of mobilisation of the shear strength ($sin\phi'_{mob}$).

The hardening rule, as reformulated by Tsegaye (2010) in UBC3D-PLM model, is given as:

$$d\sin\phi_{mob} = 1.5k_G^{*p}\left(\frac{p'}{p_{ref}}\right)^{np}\frac{p_{ref}}{p'}\left(1-\frac{\sin\phi_{mob}}{\sin\phi_p}R_f\right)^2 d\lambda \qquad 4.37$$

where dλ is the plastic strain increment multiplier, k_G^{*p} is the plastic shear modulus factor; *np* is the plastic shear modulus exponent; $sin\phi_{mob}$ is the mobilised friction angle, which is defined by the stress ratio; ϕ_p is the peak friction angle; and R_f is the failure ratio η_f / η_{ult} , ranging from 0.5 to 1.0, η_f is the stress ratio at failure and η_{ult} is the asymptotic stress ratio from the best fit hyperbola.

4.3.1.4 Plastic potential funtion

A non-associated flow rule based on the Drucker-Prager plastic potential function is used in the UBC3D-PLM model (Tsegaye, 2010). The plastic potential function *g* is formulated as:

$$g = q - \frac{6\sin\psi_m}{3-\sin\psi_m}\left(p + c\cot\phi_p\right) \qquad 4.38$$

It is noted that *g* is a cone surface passing through triaxial compression points and it is independent of Lode's angle θ_L and ψ_m is the mobilised dilatancy angle.

4.3.1.5 Flow rule

The flow rule enables specifying the direction of plastic strain at every stress state. Also, flow rules are of great importance in constitutive modelling because they control dilatancy effect which is related to volume changes and strength of soil. In general, the flow rule can be expressed as follows:

$$d\varepsilon^p = d\lambda\frac{\partial Q}{\partial\sigma} \qquad 4.39$$

In the UBC3D-PLM model a simplified version of the well-known Rowe's stress dilatancy relation is used to relates the plastic shear strain to accumulation of plastic volumetric strain.

$$\begin{aligned} d\varepsilon_v^p &= \sin\psi_m d\gamma^p \\ \sin\psi_m &= \sin\phi_m - \sin\phi_{cv} \end{aligned} \qquad 4.40$$

Where $d\varepsilon_v^p$ is the plastic volumetric strain increment and ϕ_{cv} is the constant volume friction angle.

Graphical representation of the modified Rowe's stress dilatancy is show in Figure 4-22, from which the following is observed by Brinkgreve et al (2017):

- There is a unique stress ratio, defined by the constant volume friction angle ϕ_{cv}, for which plastic shear strains do not cause plastic volumetric strains.

- Stress ratios which lie below sin ϕ_{cv} exhibit contractant behaviour, while stress ratios above sin ϕ_{cv} lead to a dilatant response. This means that the constant volume friction angle works as the phase transformation angle.
- The amount of contraction or dilatancy depends on the difference between the current stress ratio and the stress ratio at sin ϕ_{cv}.

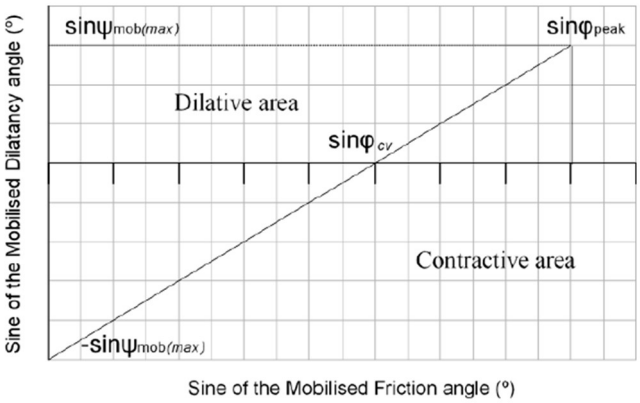

Figure 4-22. Graphical representation of the modified Rowe's flow rule as used in UBC3D-PLM model

Based on the mobilised friction angle, the model is able to identify paths of unloading, loading or reloading. During loading, the friction angle is mobilised, and hardening plasticity occurs. During unloading, pure elastic behaviour is predicted.

Model calibration was a process of trial and error in order to match the model results to the laboratory test results. Table 4-8 shows the best fitted parameters that were finally adopted for the UBC3D-PLM model.

Table 4-8. UBC3D-PLM model parameters for axisymmetric simulations

Model	γ_{unsat} [kN/m^3]	γ_{sat} [kN/m^3]	ϕ_p [°]	ϕ_{cv} [°]	c [kN/m^2]	K_B^e	K_G^e	K_G^p	me	ne	np	f_{dens}	f_{post}	p_{ref}	k [m/d]
Axisymmetric	18.5	18.5	30	29	9	150	150	8000	0.5	0.5	0.5	1.0	0.6	133	$8.64x10^{-4}$
Plane strain	18.5	18.5	30	29	9	300	150	8000	0.5	0.5	0.5	0.2	0.2	133	$8.64x10^{-4}$

4.3.2 Cyclic triaxial test

The UBC3D-PLM model was used to simulate the cyclic triaxial tests. Loading sequence includes an initial anisotropic consolidated stage before application of 500 cycles of loading with a frequency 0.5 Hz. After the cyclic stage the samples were taken to failure under undrained shearing. Geometry and model boundaries were previously described in section 4.2.5. Final simulation results of two samples are presented in Figure 4-23. It is observed that stress- strain behaviour obtained with the model show a good agreement with the test results, but the accumulative pore pressure generated by the model is in excess of what was measured in the laboratory samples, both

during the cyclic stages and during the post-cyclic undrained static shearing. As a results stress path tend to move toward the failure envelope. The post-cyclic undrained strength obtained with the model was slightly lower than that obtained in the laboratory tests. In addition, as reference, the undrained static resistance was calculated with the model, which was slightly higher than the post-cyclic strength, which is explained by the higher pore pressures generated during the simulation of the cyclic load with the model.

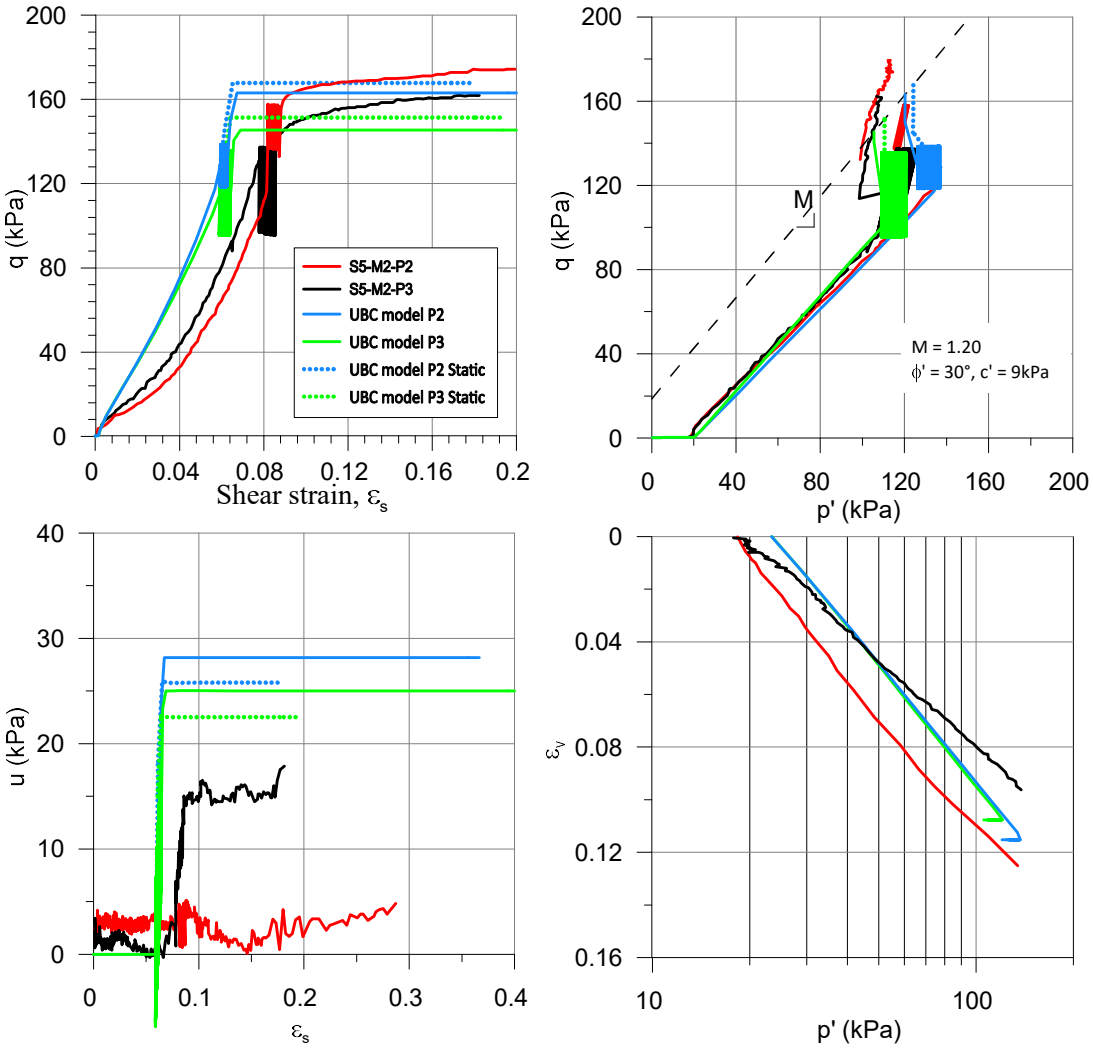

Figure 4-23. Barcelona Port clay cyclic triaxial test simulation with UBC3D-PLM model.

4.3.3 Cyclic simple shear test

The UBC3D-PLM model response was also evaluated against the cyclic simple shear failure mode. A plane strain model was used to simulate five cyclic simple shear tests. Geometry and boundary conditions of the model are similar to those used in the static shear simple test simulation (see section 4.2.7). A wide variety of laboratory test results were chosen to check the model, from samples reaching failure in less than 30 load cycles to samples that do not fail with 1500 load cycles.

Figure 4-24 (a) to (c) shows the results of two simulations corresponding to the tests that did not fail. The samples were subjected to an initial shear stress before starting the cyclic loading stage. During this stage it is observed that the shear deformations obtained in the model do not correctly reproduce the response of the laboratory test. However, the shear deformations calculated with the model in the cyclic phase closely approximate the results of the tests. In contrast, the accumulated pore pressures continue to increase with a greater number of cycles.

Figure 4-24 (d) to (e) shows the simulation results of the shear test that reached failure. Sample S11-M5-P3 failed with 28 load cycles, a significant increase in pore pressures is observed during cyclic shearing, which in turn produces significant shear deformations leading the sample to failure. Numerical simulation of this sample produces somewhat lower accumulated pore pressures compared to laboratory results, yet average shear strains begin to increase rapidly from approximately 15 load cycles until they reach failure a few load cycles later. It is observed that the cyclic shear deformations calculated with the model are significantly lower than those obtained in the laboratory test, but the average deformations are approximately well calculated.

Samples S10-M4-2 and S11-M5-P2 reached failure with 2 load cycles. These tests were started with high initial shear stresses, close to the static undrained resistance of the sample. Pore pressures develop rapidly during the initial static phase and continue to increase during cyclic loading, leading to the rapid development of shear strains. The response observed with the model in relation to pore pressures is not good during the initial static shearing stage, which causes pore pressures to be underestimated and the model requires a greater number of cycles to reach failure.

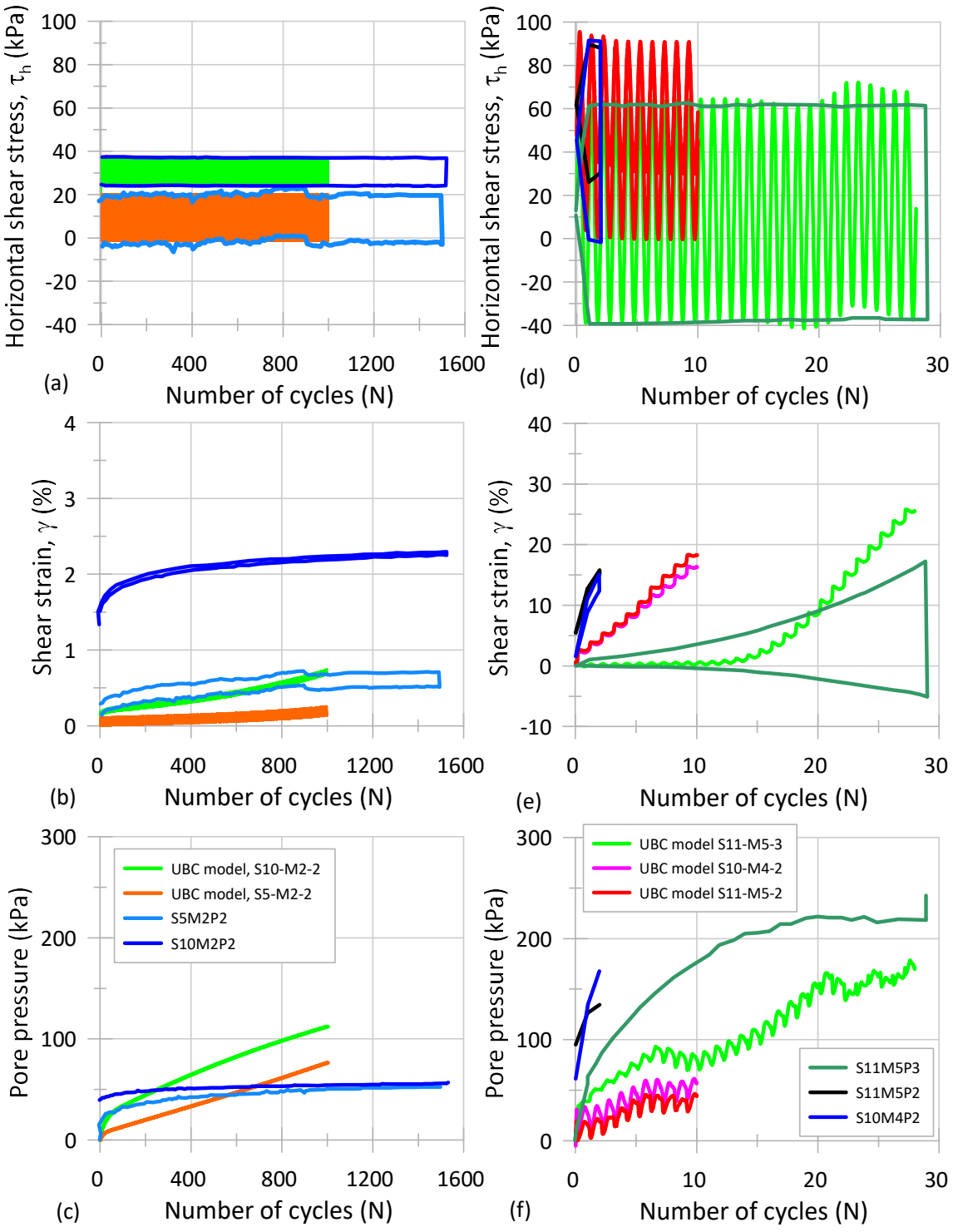

Figure 4-24. Barcelona Port clay cyclic simple shear test simulation with UBC3D-PLM model.

4.4 MODELLING CREEP BEHAVIOUR

4.4.1 Soft Soil Creep model (SSC)

The Soft Soil Creep model is an elasto-viscoplastic model implemented in the Plaxis code. The logarithmic law for unidimensional secondary consolidation was expressed in differential form and subsequently extended to the general state of tensions and deformations by Vermeer & Neher (1999). The procedure for obtaining the differential equation in the one-dimensional case and its generalization is described in the Material Models Manual of Plaxis (Brinkgreve et al, 2017). Below is a brief description of the model.

The classic secondary consolidation model, which defines creep through the secondary consolidation coefficient C_α, is extended to a more general form incorporating concepts of the "Cam Clay" model and the theory of viscoplasticity. In this sense the ellipses of the "Cam Clay" model are used as contours of constant velocities of volumetric deformation (as shown in Figure 4-25), so that, as the soil moves away from the normally consolidated condition, the rate of creep deformation becomes smaller. The formulation of the model allows to reach states of overconsolidation both by creep and unloading, following the ideas proposed by Bjerrum (1967).

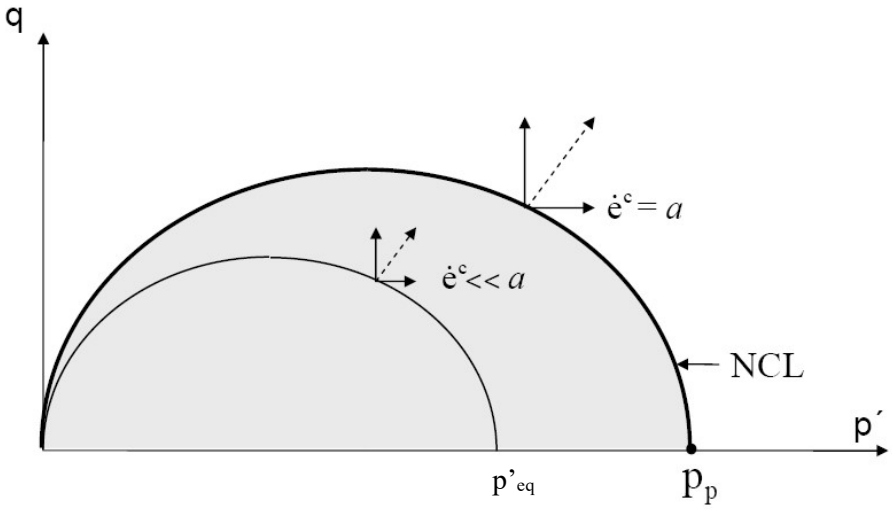

Figure 4-25. Constant velocity of volumetric deformation contours.

In the "Soft Soil Creep" model the deformation rate is decomposed into an elastic part and a part corresponding to creep. As usual in the theory of plasticity, a flow rule for creep strain rate is assumed, and Hooke's law is adopted for the elastic part. Then the following general equation is obtained, formulated based on principal stresses:

$$\dot{\varepsilon}_i = \dot{\varepsilon}_i^e + \dot{\varepsilon}_i^c = D_{ij}^e \dot{\sigma}_j + \Lambda \frac{\partial g}{\partial \sigma_i} \tag{4.41}$$

In this equation the elastic part of the model is given by a logarithmic relationship between the volumetric deformation and the average effective pressure p' as used in the Modified Cam Clay model:

$$D_{ij} = \frac{1}{E_{ur}} \begin{bmatrix} 1 & -\nu_{ur} & -\nu_{ur} \\ -\nu_{ur} & 1 & -\nu_{ur} \\ -\nu_{ur} & -\nu_{ur} & 1 \end{bmatrix}$$

$$E_{ur} = 3(1-2\nu_{ur})\frac{p'}{\kappa^*}$$

Where, E_{ur} = Young's modulus and ν_{ur} Poisson's coefficient, κ* is the modified swelling index as defined in the SS model (Section 4.2.2). The subscript *ur* is indicated to emphasize that both the Young's modulus and the Poisson coefficient determine the unloaded and reloaded behaviour.

In order to derive the creep deformation components, it is assumed that the function of plastic potential *g* is equal to an equivalent pressure p^{eq}.

$$g = p^{eq} \tag{4.42}$$

The equivalent pressure p^{eq} is defined based on the invariants of mean stress *p'* and deviator stress *q*:

$$p^{eq} = p' + \frac{q^2}{M^2 p'} \tag{4.43}$$

From definitions of equivalent pressure p^{eq} and generalized preconsolidation pressure p_p^{eq}, creep volumetric strain ε_v^c can be calculated as:

$$\dot{\varepsilon}_v^c = \frac{\mu^*}{\tau}\left(\frac{p^{eq}}{p_p^{eq}}\right)^{\frac{\lambda^*-\kappa^*}{\mu^*}} \tag{4.44}$$

Where:

$$p_p^{eq} = p_{p0}^{eq} \exp\left(\frac{\varepsilon_v^c}{\lambda^*-\kappa^*}\right) \tag{4.45}$$

From equation (4.41) it follows:

$$\dot{\varepsilon}_v^c = \dot{\varepsilon}_1^c + \dot{\varepsilon}_2^c + \dot{\varepsilon}_3^c = \Lambda\left(\frac{\partial p_{eq}^{'}}{\partial \sigma_1} + \frac{\partial p_{eq}^{'}}{\partial \sigma_2} + \frac{\partial p_{eq}^{'}}{\partial \sigma_3}\right) = \Lambda \frac{\partial p_{eq}^{'}}{\partial p^{'}} = \Lambda\alpha \tag{4.46}$$

The parameter Λ can be calculated from equations (4.44) and (4.46):

$$\Lambda = \frac{1}{\alpha}\frac{\mu^*}{\tau}\left(\frac{p_{eq}^{'}}{p_p}\right)^{\frac{\lambda^*-\kappa^*}{\mu^*}}$$

According to this equation the creep deformation will be less as long as the overconsolidation ratio $OCR = p_p/p'_{eq}$ is greater. The parameter τ is a predefined reference time as 1 day and $\alpha = \partial p_{eq}^{'} \big/ \partial p^{'}$ results:

$$\alpha = 1 - \left(\frac{q/p^{'}}{M}\right)^2$$

In relation to the yield surface, a Mohr-Coulomb type surface is incorporated into the model, as shown in Figure 4-26. In this way, the yield surface is formed by the Mohr-Coulomb failure line and a 'cap' with plastic hardening. This type of surface is suitable for soft soils, where it is expected that material dilation will not occur.

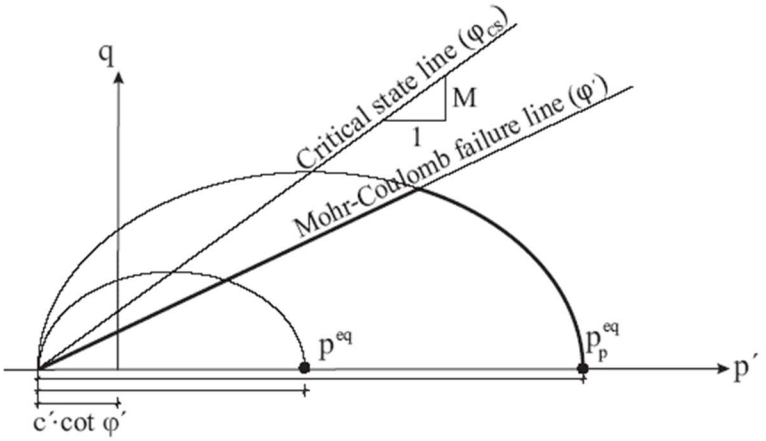

Figure 4-26. Yield surface of the soft soil creep model.

It should be noted that the modified compression indices, modified swelling index and the modified creep index are related to the traditional indices used in the consolidation of soils C_c, C_s, C_α by the following relationships:

$$\lambda^* = \frac{C_c}{2.3(1+e)} \qquad \kappa^* = \frac{2C_s}{2.3(1+e)} \qquad \mu^* = \frac{C_\alpha}{2.3(1+e)}$$

Furthermore, as in the SS model, the parameter M depends on K_0^{NC}, λ^*/κ^* and ν_{ur} and can be approximated by the ratio $M \approx 3.0 - 2.8\, K_0^{NC}$.

In summary, some of the characteristics of the behaviour of a soft soil that can be captured with this type of model according to the formulation described are:

- Stiffness depends on stresses (logarithmic elasticity).
- The model distinguishes between primary load processes and reload-unload processes.
- Incorporates secondary compression (time dependence) that depends on the OCR.
- Incorporates preconsolidation pressure memory.
- Failure according to the Mohr-Coulomb criteria.

The model parameters were adopted from the oedometric tests performed on undisturbed soft clay samples from Port of Barcelona, taking as a reference the average value, as shown in Table 4-9. These parameters were used for the simulation of the oedometric tests. However, in the case of the preload test, the parameters were calibrated for each specific soil layers identified based on the instrumentation of the preload test, as described below.

Table 4-9. Summary of parameters for the Soft Soil Creep model

γ_{unsat}	γ_{sat}	k_x	k_y	λ^*	κ^*	μ	ν	M	C	Phi	Psi
[kN/m^3]	[kN/m^3]	[m/day]	[m/day]	[-]	[-]	[-]	[-]	[-]	[kPa]	[°]	[°]
18.5	18.5	8.64e-4	8.64e-4	0.05	0.01	0.005	0.15	1.117	1	28	0

4.4.2 Oedometric test simulation

In this section the Soft Soil Creep model is used to simulate an oedometric test, with loading, unloading and reloading stages.

Figure 4-27 shows the consolidation curves obtained in the loading stages of the oedometric test simulation. Each load step was applied for 1 day. Subsequently, the applied vertical pressure is reduced and the model is reloaded again. The compressibility curves obtained in the simulation are shown in Figure 4-28. The last load is applied to the model for 100 days, in order to properly distinguish the long-term settlements of secondary consolidation. The value of the last load was defined so that different overconsolidation values of the sample were obtained: OCR of 1.33, 1.6 and 2.0. Figure 4-29 shows the deformation-time curves obtained for the same load increase, and different OCR values. It is observed that at a higher OCR value, the model produces lower values of secondary deformation, even when the increase in load is the same. In addition, the deformation-time curves obtained under the same OCR value are presented in Figure 4-30 with different values of load increase. In this case, discarding the deformations that correspond to the elastic behavior during the application of the load (0.1min), the model gives practically the same value of the secondary deformation. This indicates that the increase in load would not affect the final value of

the secondary deformation. Figure 4-31 shows the secondary deformations, calculated for the same vertical stress (320kPa), but with a load history that produces different values of OCR. The load increase in this case was 160kPa. It is clear that for the higher the OCR values, the secondary deformations are smaller. This can also be seen in Figure 4-32, where results of the secondary deformation obtained in the different calculations performed are shown.

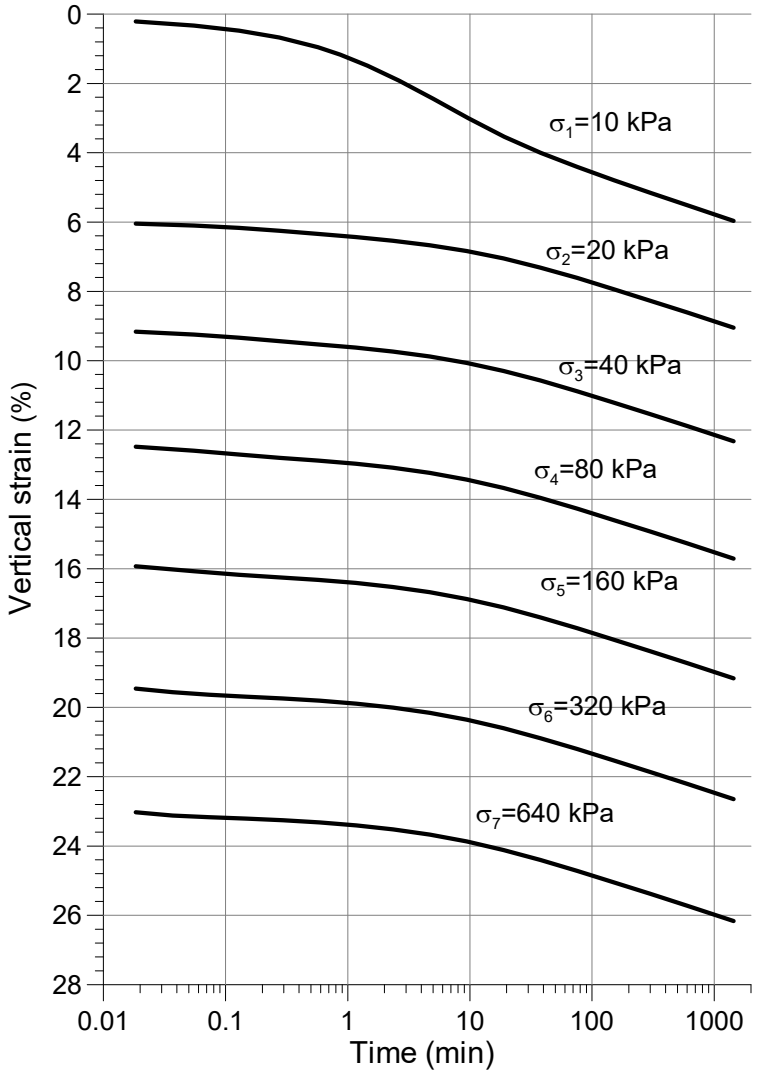

Figure 4-27. Consolidation curve for several load stages.

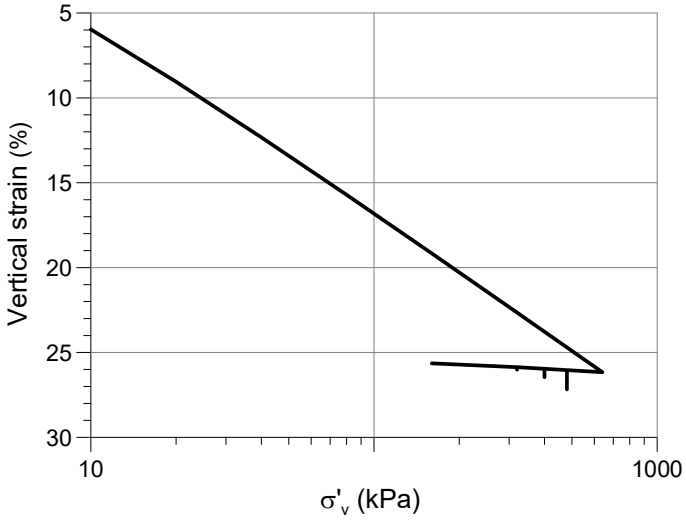

Figure 4-28. Compressibility curve obtained in the simulation of oedometer tests with stages of load, unload and reload.

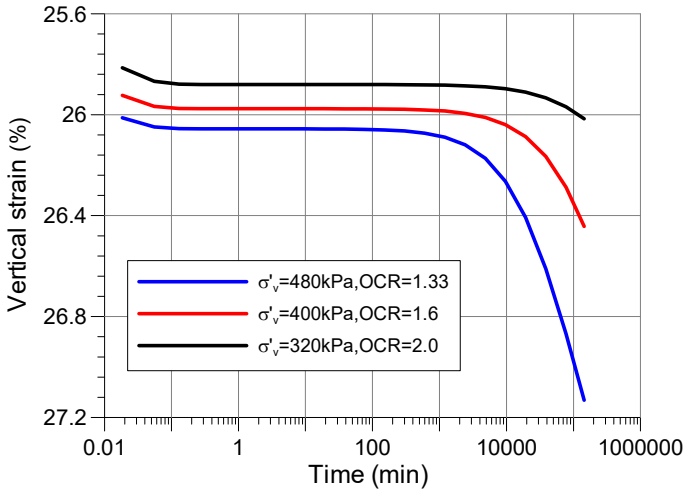

Figure 4-29. Vertical strain obtained under distinct OCR value, with the same load increment Δσ'v=160kPa.

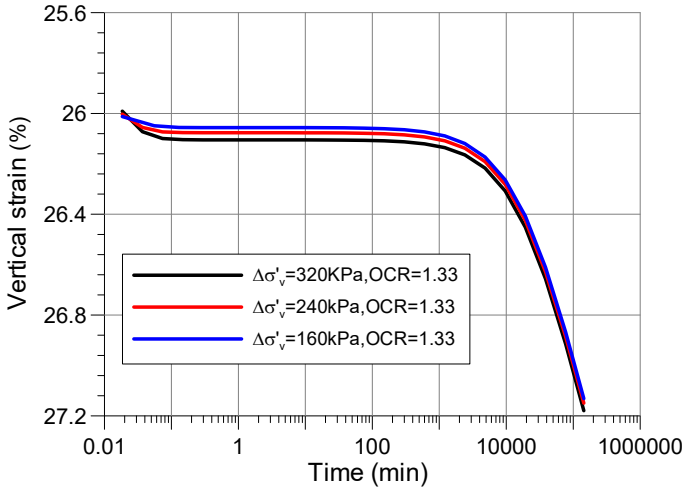

Figure 4-30. Vertical deformation for different load increases, with the same OCR value

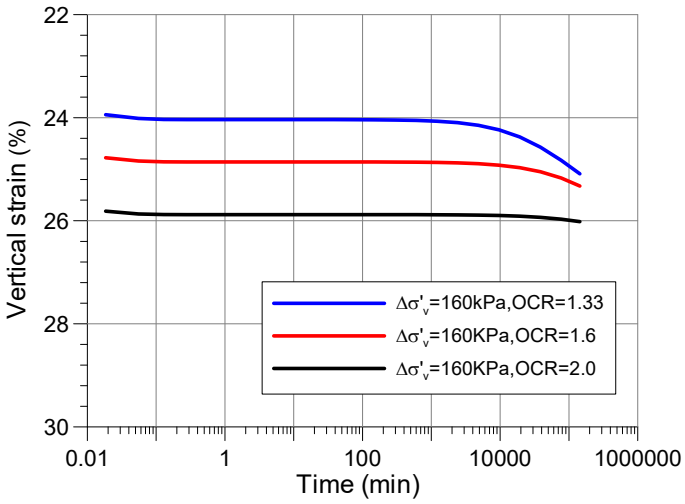

Figure 4-31. Vertical deformation calculated under a vertical stress of 320kPa, load increase 160kPa and different OCR values.

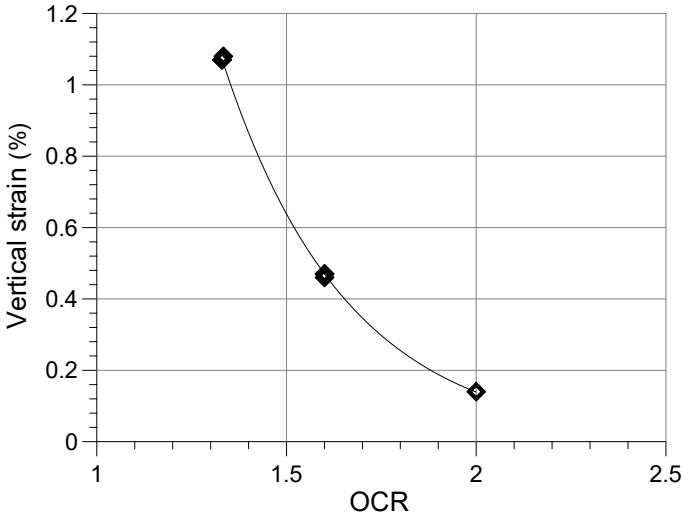

Figure 4-32. Secondary vertical deformation for distinct OCR values.

4.4.3 Large scale preloading test simulation.

Results of the large-scale preloading test described in chapter 3 were used to calibrated a finite element model. The embankment material was represented by a conventional Mohr-Coulomb material. The "Soft Soil Creep" model, described previously, was selected for the natural soil layers.

4.4.3.1 Model geometry

A symmetric geometry with respect to the embankment major axis was defined. Only half of the full section was discretized as shown in Figure 4-34. The soil layering was quite precise and followed the information provided by the four sliding micrometers. Layer thickness varied between 5 m and a minimum value of 1 m.

The finite element mesh used in the analysis is essentially formed by a rectangle 60.0 m high and 150.0 m wide. The chosen width is considered sufficient so that the draining boundary condition, for consolidation purposes, has no influence on the solution. The embankment of the preload has a width of 40 meters at the coronation and a slope of 2: 1. The mesh has been divided horizontally into 35 zones corresponding to the different layers of soil, identified according to the deformability characteristics recorded in the sliding micrometers. In Table 4-10, the depths and the denomination used to identify these materials are indicated, as used in the analyses. It is observed that the sands predominate in the first 20 meters of the model. Between the depths of 20 m and 60 m, there is a predominance of low permeability materials: silt and clays. The material immediately below the modelled area is formed by a competent gravel stratum. Therefore, the lower contour of the modelled area can be considered rigid and with water pressures under constant hydrostatic conditions.

The model geometry is shown in Figure 4-33. The finite element mesh is formed by 2211 triangular elements of 15 nodes (Figure 4-34).

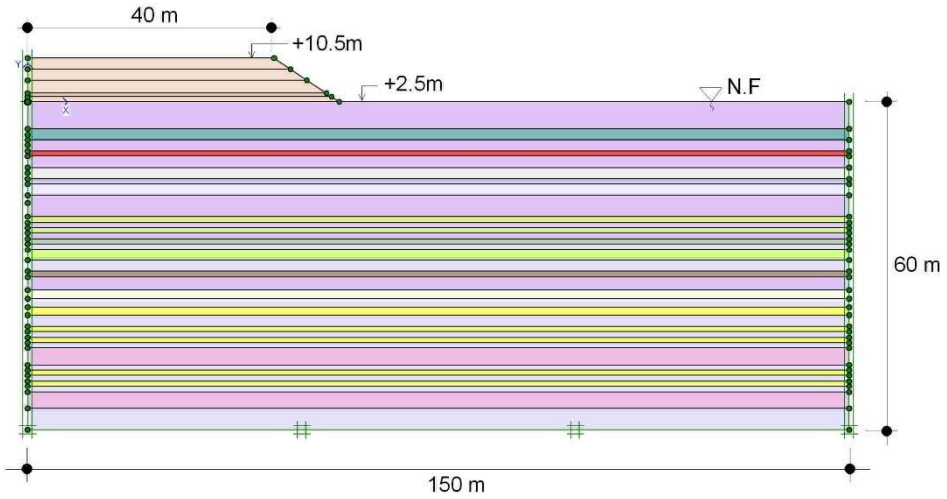

Figure 4-33. FE model geometry

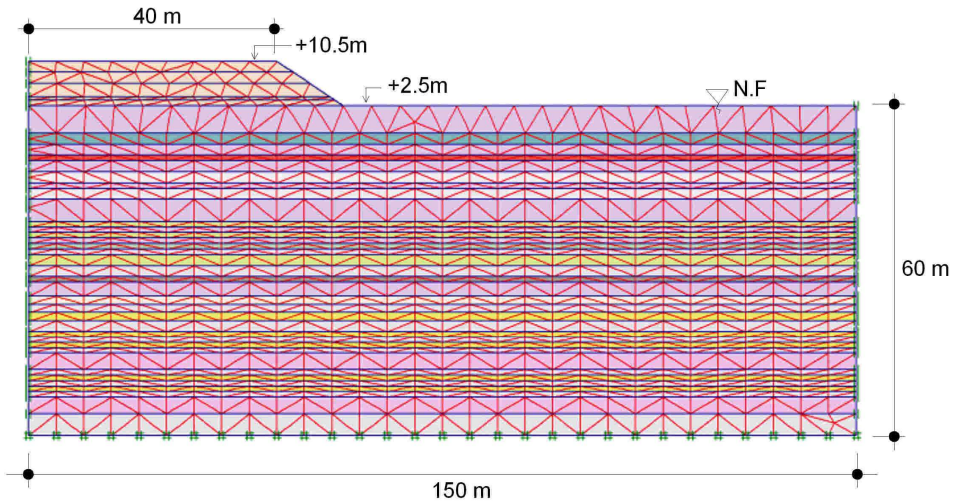

Figure 4-34. Finite element mesh for 2D plane strain analysis.

Table 4-10. Layers and thickness assumed in the analysis.

Layer	material	Depth (m)	Thickness (m)
1	sand 1	0.00-5.00	5.00
2	sand 4	5.00-7.00	2.00
3	sand 1	7.00-9.00	2.00
4	sand 3	9.00-10.00	1.00
5	sand 1	10.00-12.00	2.00
6	clay 1	12.00-14.00	2.00
7	sand 1	14.00-15.00	1.00
8	clay 5	15.00-17.00	2.00
9	sand 1	17.00-21.00	4.00
10	clay 4	21.00-22.00	1.00
11	sand 1	22.00-23.00	1.00
12	clay 4	23.00-24.00	1.00
13	sand 1	24.00-25.00	1.00
14	clay 2	25.00-26.00	1.00
15	sand 2	26.00-27.00	1.00
16	clay 11	27.00-29.00	2.00
17	sand 2	29.00-31.00	2.00
18	clay 6	31.00-32.00	1.00
19	sand 1	32.00-34.50	2.50
20	clay 3	34.50-36.00	1.50
21	sand 2	36.00-37.50	1.50
22	clay 7	37.50-39.00	1.50
23	sand 2	39.00-41.00	2.00
24	clay 7	41.00-42.00	1.00
25	sand 2B	42.00-43.00	1.00
26	clay 9	43.00-44.00	1.00
27	sand 2B	44.00-45.00	1.00
28	clay 8	45.00-48.00	3.00
29	sand 2B	48.00-49.00	1.00
30	clay 7	49.00-50.00	1.00
31	sand 2C	50.00-51.00	1.00
32	clay 10	51.00-52.00	1.00
33	sand 2C	52.00-53.00	1.00
34	clay 12	53.00-56.00	3.00
35	sand 2C	56.00-60.00	4.00

4.4.3.2 Material properties

The process of soil parameters identification was a trial-and-error procedure. Starting at a given distribution of parameters, guided by the available soil description, the CPTU and oedometer tests and the micrometer data, the strains measured at regular intervals within the soil were progressively matched. Table 4-11 shows the parameters assigned to the successive clayey and sandy layers of the finite element model.

Table 4-11. Soft soil creep model parameters used considered in FEM analysis.

Material	γ_{dry} **(kN/m³)**	γ_{wet} **(kN/m³)**	k_x **(cm/s)**	k_y **(cm/s)**	**λ***	**κ***	**μ***	**c'** **(kN/m²)**	**φ'** **(º)**	**ψ (º)**
clay 1	19.0	19.0	$1.5.10^{-5}$	$7.5.10^{-6}$	0.050	$5.0.10^{-3}$	$6.0.10^{-4}$	1	27	0
clay 2	19.0	19.0	$1.5.10^{-5}$	$7.5.10^{-6}$	0.080	$4.0.10^{-3}$	$1.5.10^{-3}$	1	27	0
clay 3	19.0	19.0	$9.3.10^{-8}$	$2.5.10^{-6}$	0.058	$4.0x10^{-3}$	$1.2x10^{-3}$	1	27	0
clay 4	19.0	19.0	$1.6.10^{-7}$	$2.5.10^{-6}$	0.042	$2.5.10^{-3}$	$5.0.10^{-4}$	1	27	0
clay 5	19.0	19.0	$5.0.10^{-7}$	$1.0.10^{-5}$	0.063	$4.0.10^{-3}$	$1.0.10^{-3}$	1	27	0
clay 6	19.0	19.0	$1.6.10^{-7}$	$5.0.10^{-6}$	0.095	$6.0.10^{-3}$	$3.0.10^{-3}$	1	27	0
clay 7	19.0	19.0	$9.3.10^{-8}$	$2.5.10^{-6}$	0.046	$5.0.10^{-3}$	$1.0.10^{-3}$	1	27	0
clay 8	19.0	19.0	$6.9.10^{-8}$	$2.5.10^{-7}$	0.016	$2.0.10^{-3}$	$6.0.10^{-4}$	1	27	0
clay 9	19.0	19.0	$6.9.10^{-8}$	$1.0.10^{-6}$	0.043	$2.5.10^{-3}$	$8.0.10^{-4}$	1	27	0
clay 10	19.0	19.0	$6.9.10^{-8}$	$1.0.10^{-6}$	0.039	$2.0.10^{-3}$	$8.0.10^{-4}$	1	27	0
clay 11	19.0	19.0	$6.9.10^{-8}$	$1.0.10^{-6}$	0.048	$5.0.10^{-3}$	$8.0.10^{-4}$	1	27	0
clay 12	19.0	19.0	$6.9.10^{-8}$	$5.0.10^{-7}$	0.032	$1.5.10^{-3}$	$7.0.10^{-4}$	1	27	0
sand 1	20.0	20.0	$1.2.10^{-4}$	$1.2.10^{-4}$	0.007	$2.0.10^{-3}$	$2.0.10^{-4}$	1	32	0
sand 2	20.0	20.0	$1.2.10^{-4}$	$5.8.10^{-5}$	0.006	$1.1.10^{-3}$	$1.8.10^{-4}$	1	32	0
sand 2B	20.0	20.0	$1.2.10^{-4}$	$2.3.10^{-5}$	0.012	$1.5.10^{-3}$	$4.0.10^{-4}$	1	32	0
sand 2C	20.0	20.0	$1.2.10^{-4}$	$8.1.10^{-6}$	0.015	$1.5.10^{-3}$	$4.0.10^{-4}$	1	32	0
sand 3	20.0	20.0	$1.0.10^{-6}$	$5.0.10^{-7}$	0.025	$4.0.10^{-3}$	$9.0.10^{-4}$	1	30	0
sand 4	20.0	20.0	$1.0.10^{-6}$	$5.0.10^{-7}$	0.021	$3.0.10^{-3}$	$3.0.10^{-4}$	1	30	0

The material used to form the preload embankment has been modelled as "Mohr-Coulomb" type material; the values of the parameters adopted for this material are indicated in Table 4-12.

Table 4-12. Embankment parameters defined as "Mohr-Coulomb"

Material	γ_{dry} (kN/m³)	γ_{wet} (kN/m³)	k_x (cm/s)	k_y (cm/s)	E (kN/m²)	υ	c (kN/m²)	φ (º)	ψ (º)
Embankment	20.0	20.0	$1.2x10^{-3}$	$1.2x10^{-3}$	20000	0.3	1	38	0

4.4.3.3 Boundary conditions

The boundary conditions of the mechanical type used are: (1) horizontal displacements fixed in the vertical boundaries; (2) vertical and horizontal displacements fixed in the lower boundary.

The boundary conditions of the hydraulic type (consolidation) are: in the lower boundary and the outer lateral boundary, the excess water pressure is zero, allowing the flow of water due to the dissipation of excess water pressures. In the axis of symmetry (left lateral boundary) water flow is not allowed.

4.4.3.4 Initial conditions

The water table has been considered on the surface. The initial stresses have been determined by the values of the earth retaing at rest coefficients K_0 set for each material, derived from the Jâky

empirical formula ($K_0 = 1 - \sin\varphi'$). Table 4-13 shows the values considered for each material. The effective vertical stresses at each point are calculated from the specific submerged weights of the materials located above the point vertically. The effective horizontal stresses are obtained by multiplying the effective vertical stresses by K_0.

Table 4-13. K0 values considered for each material.

material	K_0	units
clay 1	0.546	-
clay 2	0.546	-
clay 3	0.546	-
clay 4	0.546	-
clay 5	0.546	-
clay 6	0.546	-
clay 7	0.546	-
clay 8	0.546	-
clay 9	0.546	-
clay 10	0.546	-
clay 11	0.546	-
clay 12	0.546	-
sand 1	0.470	-
sand 2	0.470	-
sand 3	0.500	-
sand 4	0.500	-

It should be noted that these K_0 values correspond to an initial state (at the beginning of the calculations) normally consolidated. In Barcelona, during the 60s industry expansion, a large amount of water was pumped from the lower aquifer, which contributed to overconsolidating the lower stratum (Vazquez-Suñe, 2003). By simulating the lowering and subsequent rise of the groundwater table of the lower aquifer, the overconsolidation of the land can be reproduced, corresponding to the state of the ground at the beginning of the work, which will determine a variation in the values of K_0. Alonso et al (2000) adopted a similar hypothesis in their study of secondary compression of a large water treatment plant, built in the Llogregat delta next to the Port of Barcelona.

4.4.3.5 Phases of analysis

Once geometry, materials properties, boundary conditions and initial conditions have been defined, the loading process is applied, which includes the lowering and raising of the water table and the

construction of the preload embankment. Loading process is summarized in Table 4-14 and explained below.

Phase 0 corresponds to the initial conditions described in the previous section, which imply a normal state of consolidation and a distribution of hydrostatic water pressures corresponding to a groundwater level 0.00 m deep (on the surface).

In the calculation phase 1, the lower water table level is simulated. To do this, the initial pressure distribution (hydrostatic) in the area between 15.0 m and 60.0 m depth is modified, until reaching the pressure distribution obtained by linearly interpolating the water pressures between the water pressure at 15.0 m depth (hydrostatic) and the value of the water pressure at 60.0 m depth (lower than the hydrostatic value of 180kPa, reflecting the decrease in the water table of the lower aquifer). The calculation is of the "plastic" type (without consolidation) and all materials are considered drained, since it is considered that over the years that the lower piezometric level fell, the excesses of water pressures generated were completely dissipated.

In the calculation phase 2 the rising of the lower water table is simulated. For this, the distribution of water pressures reached at the end of the calculation phase 1 in the intermediate zone (between 15.0 m and 60.0 m depth) is modified until the hydrostatic pressure distribution is reached again. The calculation is of the "plastic" type (without consolidation) and all materials are considered drained, since it is considered that the position of the lower water table has been maintained long enough to allow the total dissipation of excess water pressures generated. At the end of this calculation phase, the state of the ground is obtained before the start of the preload. The results of these calculations can be seen in Figure 4-35.

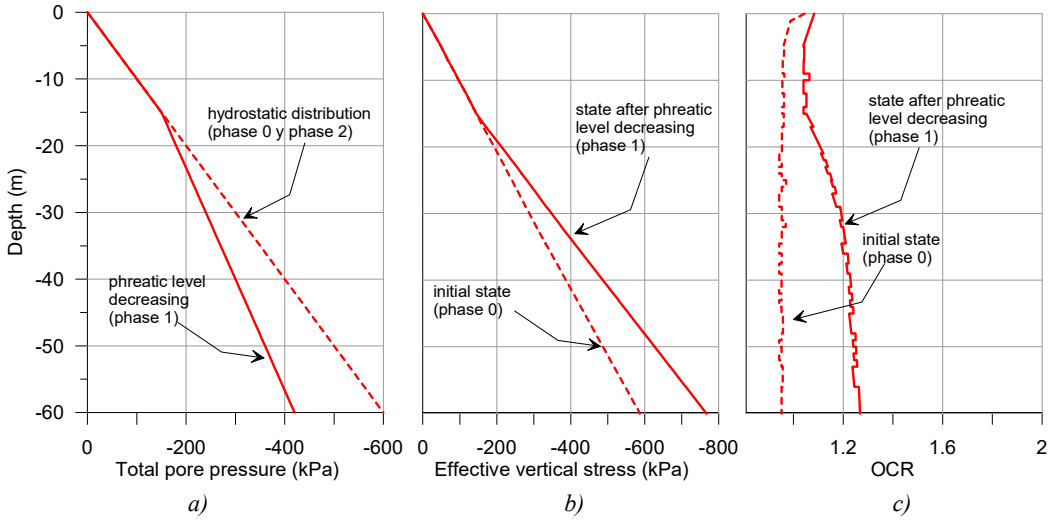

Figure 4-35. Past changes in water pressures and resulting OCR ratio. a) Assumed change in the theoretical hydrostatic profile; b) Associated distribution of vertical effective stresses at steady state; c) Calculated profiles of OCR.

The phases 3 to 6 simulate the construction of the preloading embankment. At the beginning of phase 3 the displacements in all materials are set to zero, since the end of the calculation phase 2 corresponds to the reference state. These calculation phases correspond to the construction of the embankment and reproduce the variation of the height of the embankment with time. In all these calculation phases the 'consolidation' type of analysis was selected (considering primary and secondary consolidation).

The calculation phase 7 corresponds to the consolidation period that produces the ground improvement. This period was extended for a little more than 6 months, after which the embankment unloading stage was started (phases 8 to 11).

Table 4-14. Phases included in the preload test analysis.

Phase	type	Description	Time (days)
0		Intial state	
1	plastic	Descent g.w lower (0.0 m a -18.0 m)	-
2	plastic	Rise g.w lower (-18.0 m a 0.0 m)	-
3	consolidation	Construction of the embankment to h=1.5m	53
4	consolidation	Construction of the embankment to h=4m	59
5	consolidation	Construction of the embankment to h=6m	42
6	consolidation	Construction of the embankment to h=8m	18
7	consolidation	Consolidation period (6 months)	199
8	consolidation	Embankment unload h=4m	26
9	consolidation	Consolidation period	62
10	consolidation	Fully unloaded of embankment h=0m	24
11	consolidation	Consolidation period	21

4.4.3.6 Results

As indicated above, the data from the instrumented preload test was used to calibrate the numerical model. The calibration has allowed to define the parameters of the different materials identified. The results of the model calibration are shown in Figure 4-36 to Figure 4-49. The vertical settlements and deformations shown in these figures refer to the axis of symmetry of the model.

Figure 4-36 shows the settlement calculated with the 2D model and is compared with the settlement measured in the 4 micrometers installed. It is observed that the numerical simulation reproduces the measured settlements quite well. On the other hand, it is interesting to note that there is no significant difference in settlement velocities measured in the area with geodrains with those measured in the preloaded area without geodrains. This is attributed to the presence of sandy layers within the drained thickness (first 20 meters).

Following an iterative process, the deformation parameters λ^*, κ^* and μ^* and the permeability of each of the layers were adjusted. The calculated vertical deformations and the respective measured value at different depths have been plotted in Figure 4-37 to Figure 4-40. Good results have been obtained in most of the points analysed. During the unloading of the embankment, settlement and

deformation measures were also taken, these are compared with the values calculated with the model during the unloading in Figure 4-41 to Figure 4-45. The results indicate that the model is able to simulate the main characteristics of the soil during loading and unloading processes.

The traditional deformation parameters C_c, C_s, and C_α can be easily calculated from the SSC model parameters λ^*, κ^* and μ^*, as indicated in the eq. 4.47. Therefore, the compressibility parameters obtained with the finite element model can be compared with those obtained from the classic 1D consolidation model and with the results of laboratory tests as shown in Figure 4-47. There is a good agreement between the compression parameters resulting from different testing techniques. Again, as expected, a greater scatter is observed in the case of the coefficient of consolidation.

$$\begin{aligned} C_c &= 2.3(1+e)\lambda^* \\ C_s &= 1.15(1+e)\kappa^* \\ C_\alpha &= 2.3(1+e)\mu^* \end{aligned} \qquad 4.47$$

Figure 4-46 shows the excess pore pressure calculated at 3 different points and is compared with the values measured in piezometers at those points. During the loading process the model overestimates the excess pore pressure at the depths of 44 m and 35 m, however, at 55m the model reproduces the measured values quite well. During the consolidation and unloading phases, the greatest discrepancies between the measured values and the response of the model occur. Construction works in nearby areas apparently produced an increased in pore pressures measured in piezometers. It is possible that better adjustments are achieved under a 3-dimensional model.

Finally, the profiles of vertical deformations and vertical displacements measured are compared with those calculated with the model at different times and up to 60 meters depth in Figure 4-48 and Figure 4-49. The coincidence with the model is quite good. This allows to conclude that the model reproduces quite well the deformation characteristics of the soils at the different levels examined up to 60m depth.

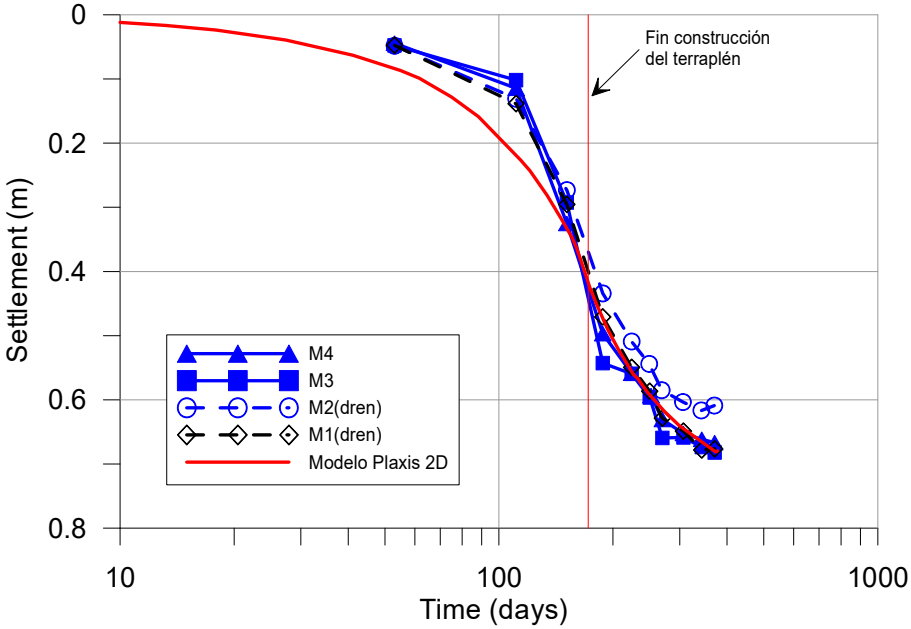

Figure 4-36. Settlement calculated with the model and the settlements measured in the 4 sliding micrometers.

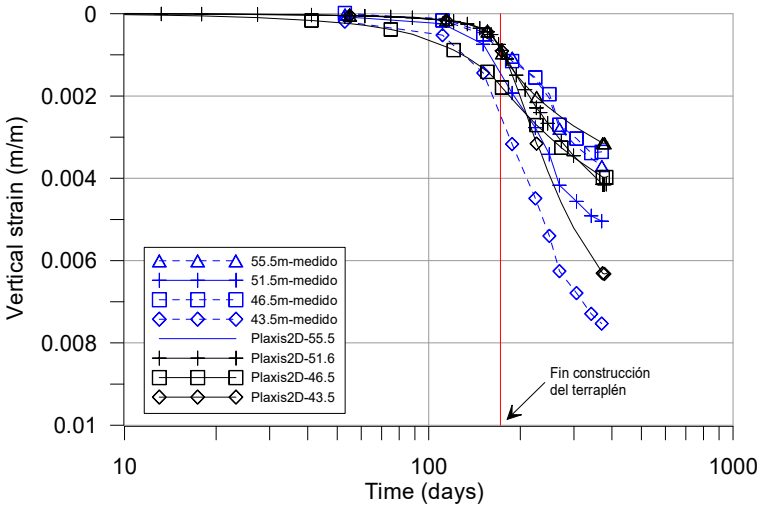

Figure 4-37. Vertical deformation measured and calculated at different depths.

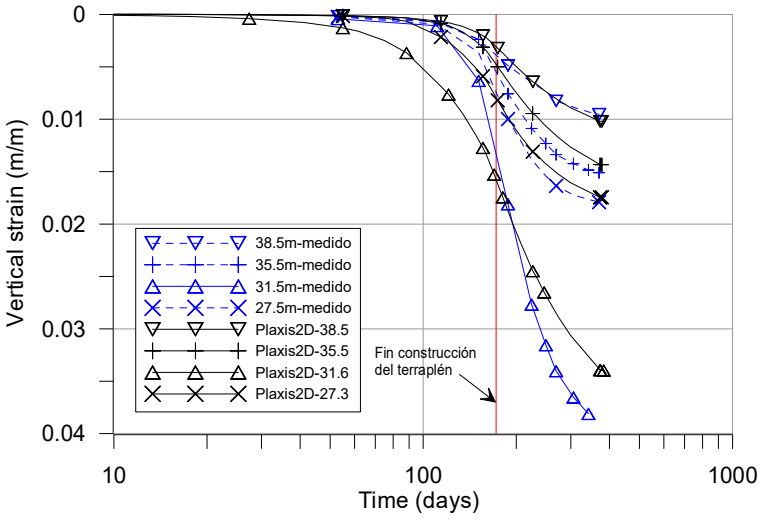

Figure 4-38. Vertical deformation measured and calculated at different depths

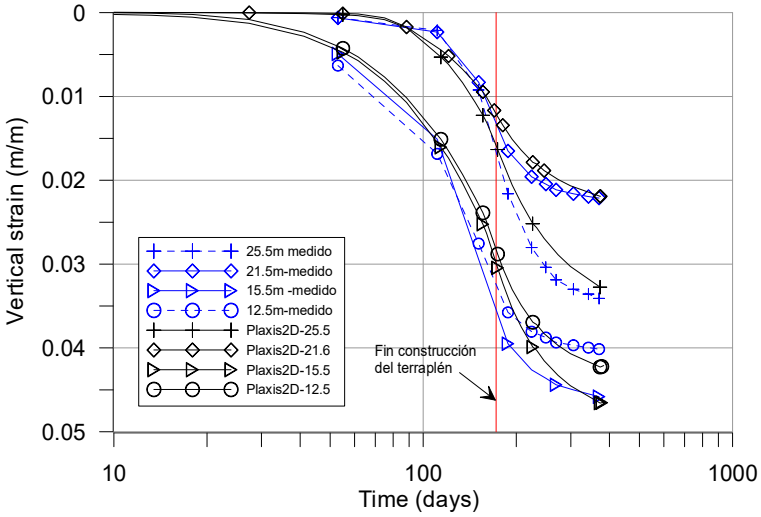

Figure 4-39. Vertical deformation measured and calculated at different depths

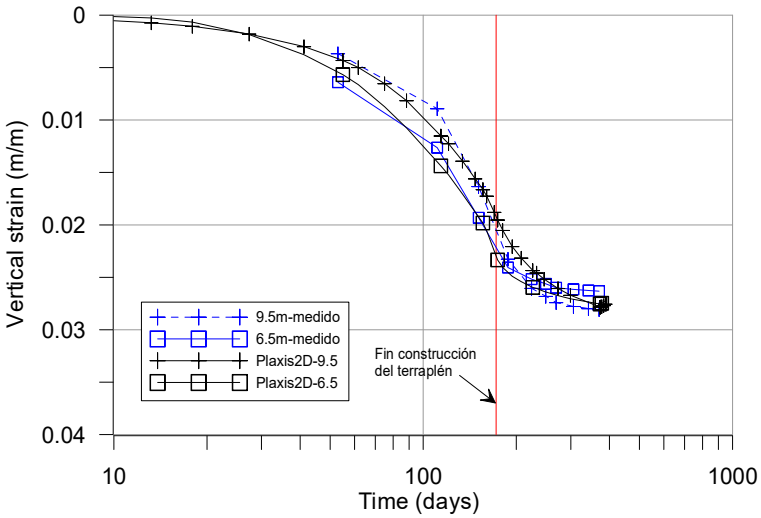

Figure 4-40. Vertical deformation measured and calculated at different depths.

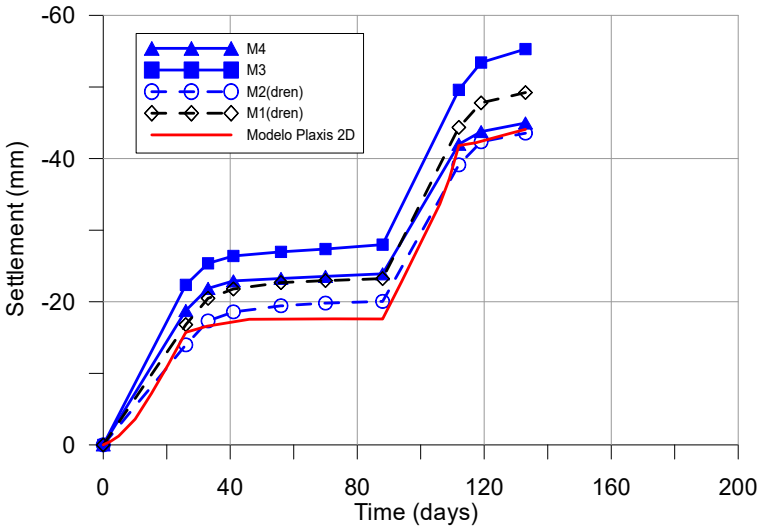

Figure 4-41. Settlement measured in micrometers and calculated during unloading phase.

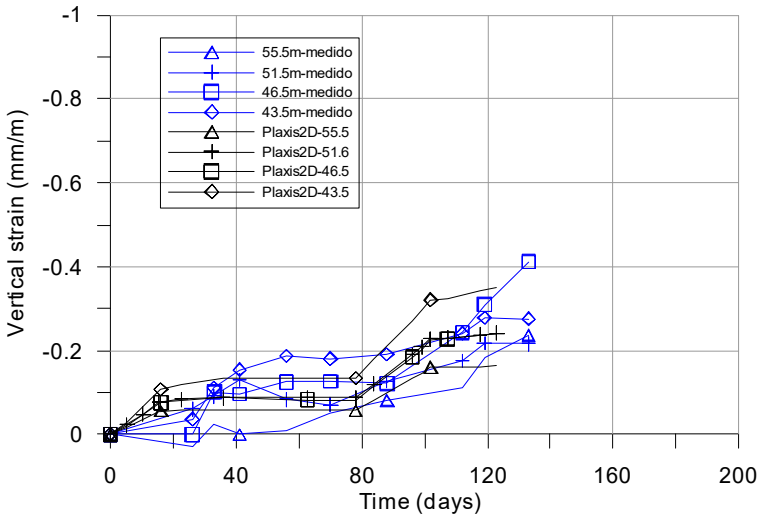

Figure 4-42. Vertical deformation measured and calculated during unloading phase, at different depths.

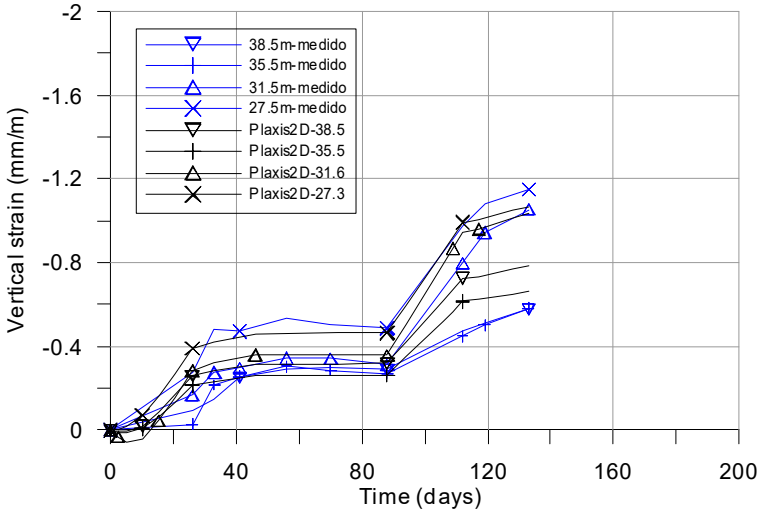

Figure 4-43. Vertical deformation measured and calculated during unloading phase, at different depths.

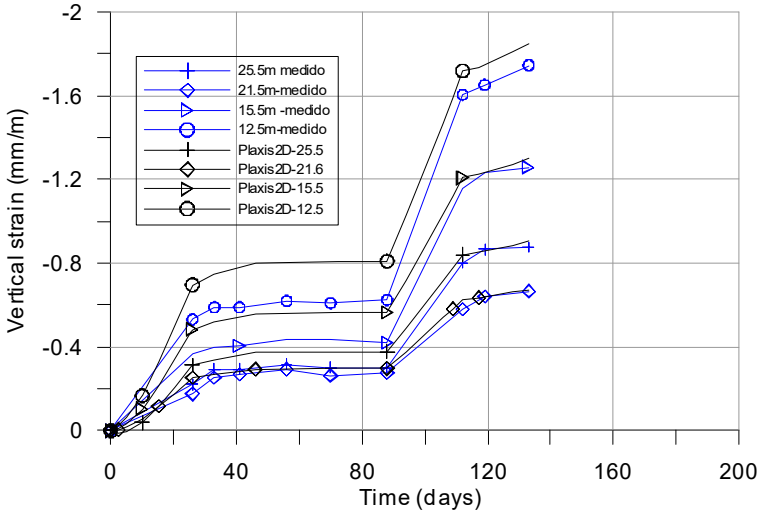

Figure 4-44. Vertical deformation measured and calculated during unloading phase, at different depths.

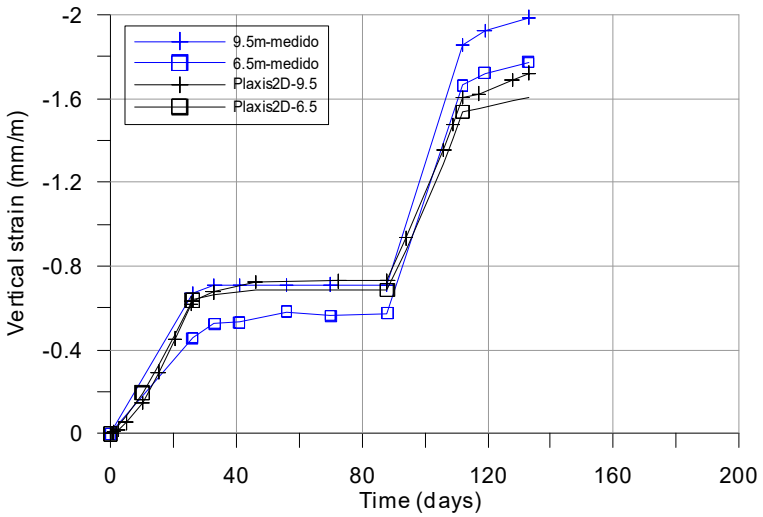

Figure 4-45. Vertical deformation measured and calculated during unloading phase, at different depths, .

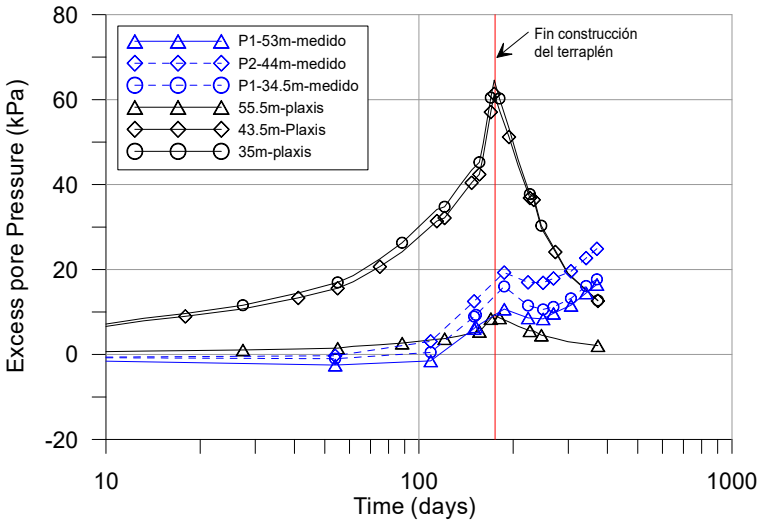

Figure 4-46. Excess pore pressure measured and calculated at different depth.

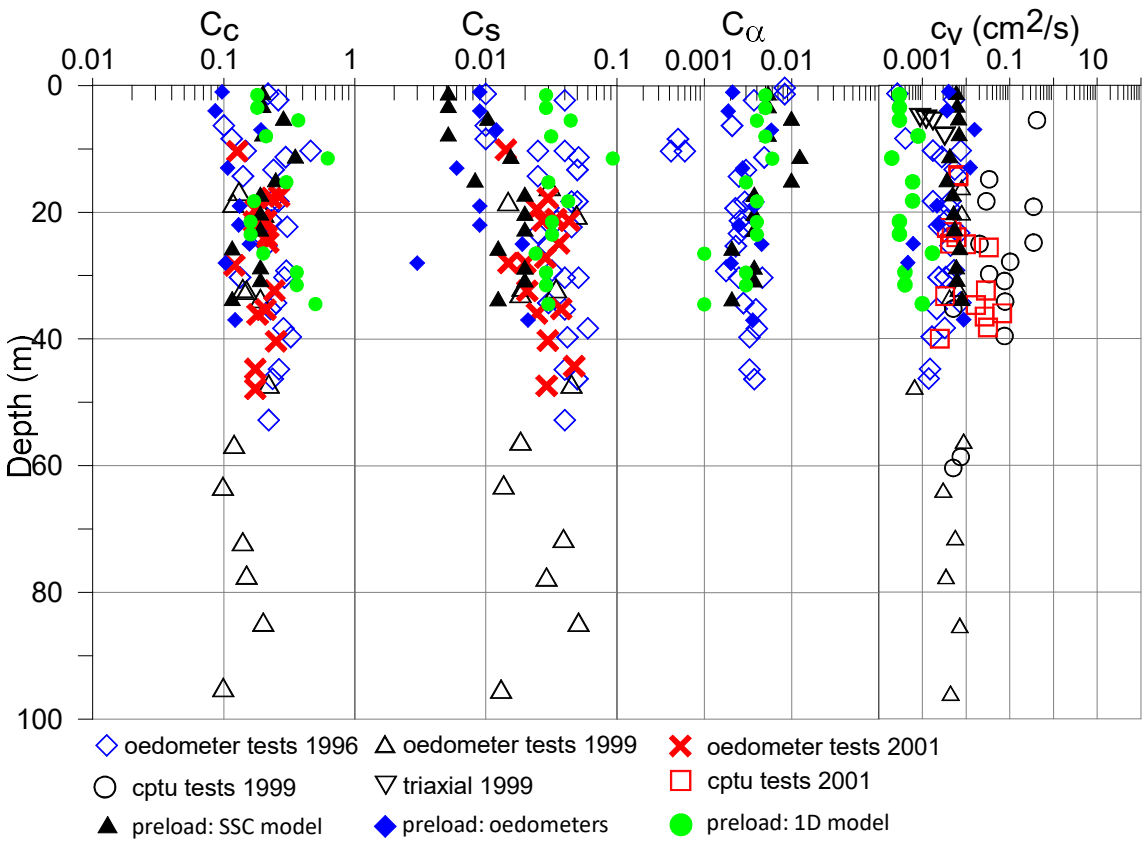

Figure 4-47. Comparison between compression parameters obtained from different testing techniques at the preload site

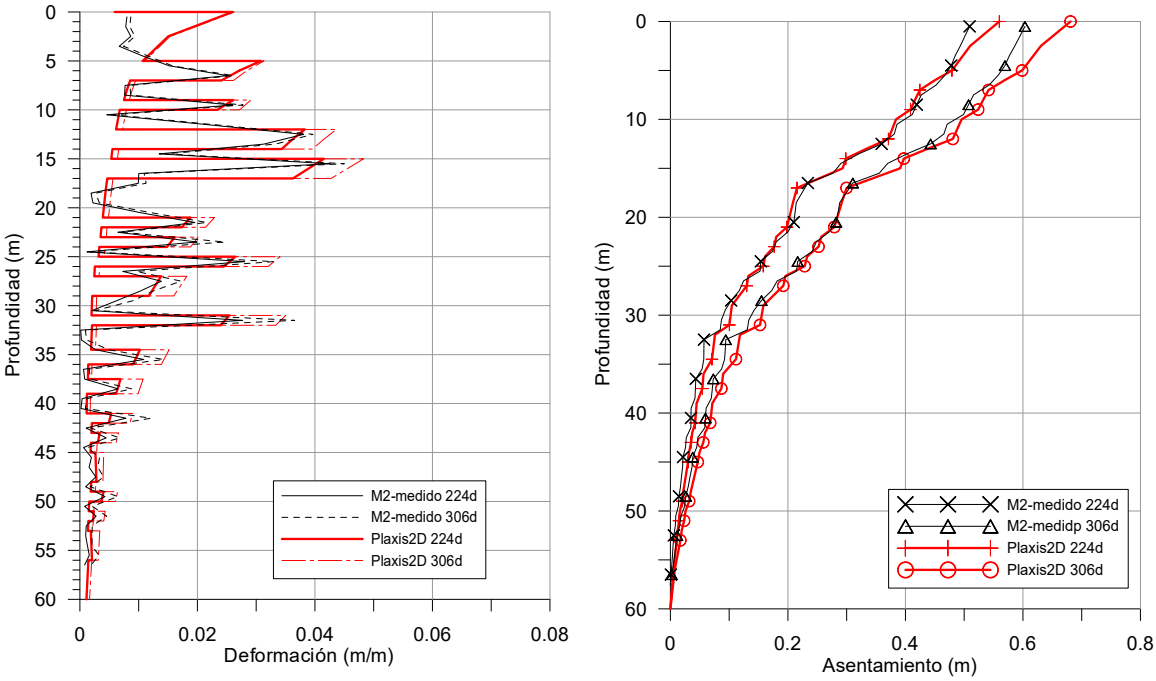

Figure 4-48. a) distribution of vertical deformations measured and calculated after 224 days. b) distribution of vertical displacements measured and calculated at 224 days and 306 days from the beginning of the field measurements.

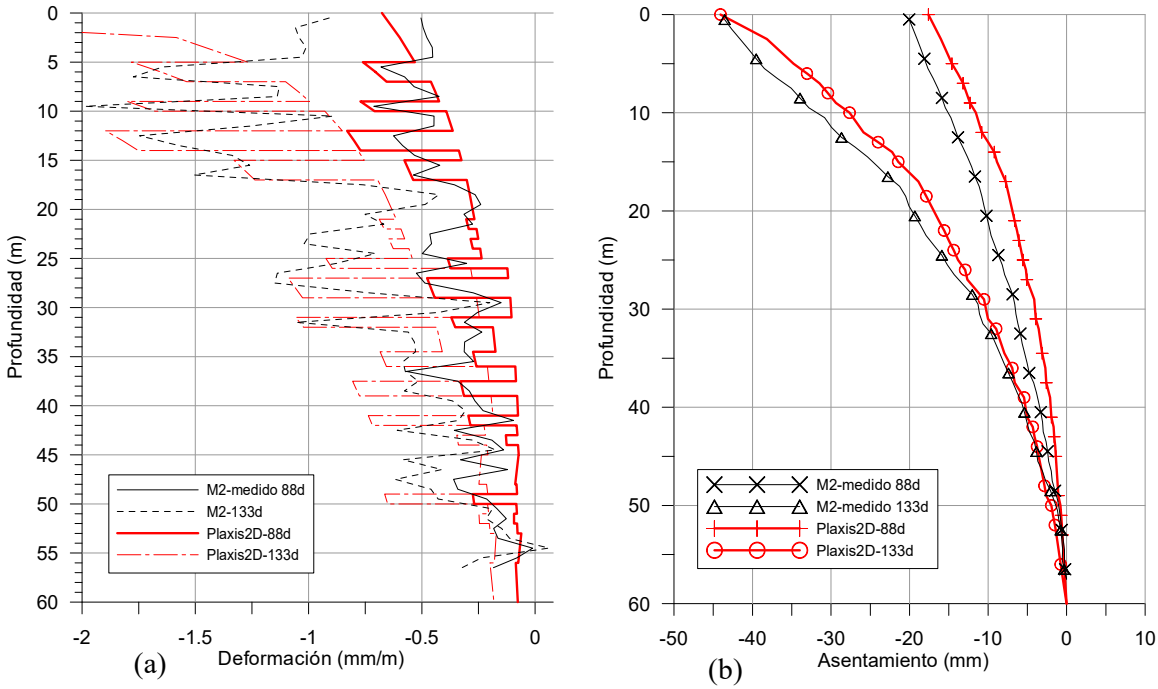

Figure 4-49. a) distribution of vertical deformations measured and calculated at 88 days after discharge. b) distribution of vertical displacements measured and calculated at 88 days and 133 days from the start of the discharge.

4.5 CONCLUSIONS

Different constitutive models are being used for the study of breakwaters stability and deformation, most of them are based on effective strength parameters, which allow the simulation of pore pressure variation. Some constitutive models are, however, based on undrained strength. Predictions in breakwaters problems are however still limited using the available models in either 2D and 3D analyses.

In this chapter, some of the triaxial tests and simple shear tests performed on specimens of undisturbed clayey soil of Port of Barcelona presented in Chapter 3, have been reproduced in the FE Plaxis code using mainly the constitutive models available: Soft Soil, S-Clay1S, UBC3D-PLM, HS-Small, and Soft Soil Creep. The performance of the models has been evaluated based on the level of agreement between the experimental measurements and the numerical predictions of some specific feature associated with the behaviour of breakwaters, such as undrained strength, cyclic behaviour and long-term deformation.

Regarding undrained strength, the SS, HS-Small and the anisotropic S-Clay1S models were checked. Prediction with the well-known Modified Cam Clay model were also included for comparison.

For normally K_0 consolidated soils sheared in triaxial compression, it was found that all models (isotropic or anisotropic) perform in general quite well, with the HSS model producing the highest undrained strength ratio (s_u/σ'_v), but of course with a slight adjustment of the model parameters is

possible to achieve a better prediction of the undrained strength. In the case of triaxial extension tests, it is observed that isotropic models overestimate the resistance of the soil. The pore pressures calculated with these models largely exceed the values measured in the tests. As expected, the anisotropic S-Clay1S model produces a better approximation of undrained resistance in extension, also the pore pressure fits better with this model. It is noted that, for axisymmetric conditions, predictions of extension resistance are less than the compression resistance in all the models, with exception of MCC model that produces the same undrained strength regardless of the applied load mode. For plain strain conditions, all the isotropic models produced the same undrained strength, both in compression and extension loading mode. Only the anisotropic S-Clay1S model was able to distinguish between compression and extension undrained strength. This is because the strength is not associated with a Mohr-Coulomb type failure envelope as in the case of SS and HS-Small models.

The influence of OCR on the undrained resistance is not very relevant in the case of breakwaters founded on soft soils; possibly only during the first stages of construction, in the case of carrying out some dredging of the seabed, there will be a slight overconsolidation of the ground. In any case, in the later stages of construction, with greater loads, the soil returns to the normally consolidated state. Isotropic SS or HSS models, with a Mohr-Coulomb failure envelope, truncate the undrained resistance as the OCR value is increased beyond 1.25.

In the case of simple shear tests, the undrained resistance calculated with all the models results in values very similar to those obtained in the laboratory, the 3 models tested reproduce fairly well the undrained resistance of the soil under normally consolidated conditions. It is also observed that the influence of the OCR on the undrained resistance calculated with the SS model is not as marked as in the case of the tests under triaxial load conditions.

Clearly, anisotropic models have advantages over isotropic models, insofar as they are capable of predicting quite well the undrained resistance of the soil under the three load conditions (compression, extension and simple shear) that are expected to occur under breakwaters. However, if this type of model is not available to perform the stability analysis, it is advisable to calibrate the calculation model, using the undrained resistance obtained from the simple shear tests, which will typically be the predominant mode of failure of a breakwater on soft soils.

Two important characteristics influence the behaviour of a breakwater against cyclic loads. One is the possibility of generation of pore pressures during storms, which could initiate a process of cyclic mobility or liquefaction of the foundation soils, with the subsequent collapse of the structure. And the other one is the degradation of soil stiffness as a consequence of shear deformation cycles. To simulate these phenomena with sufficient approximation, advanced models are required, currently rare in engineering practice. However, recently models have been implemented that capture the

main characteristics of the cyclic behaviour of the soil with a reasonable number of parameters, which facilitates their use in practical engineering, among them, the UBC3D-PLM model (Tsegaye, 2010; Petalas & Galavi, 2013) and the PM4SAND model (Boulanger and Ziotopoulou, 2017). The first is part of the database of models available in Plaxis while the second has recently been implemented as UDSM. The UBC3D-PLM model was selected to simulate the cyclic behaviour of soft soil of the Port of Barcelona. The model was calibrated using the results of cyclic triaxial tests and the cyclic simple shear tests.

The cyclic triaxial tests were consolidated before starting the cyclic deviatoric load stage. Afterwards, post-cyclic undrained resistance was evaluated. During consolidation and the post-cyclic shear stage, the SS model was used. The results show a good prediction of both post-cyclic strength and cyclic behaviour. However, it is observed that the model overpredicts pore pressures during cyclic loading (Figure 4-23). In the case of cyclic shear simulations, the model predictions were not entirely satisfactory. The model can sustain a certain number cycles of shear deformation, after which the accumulation of shear deformations increases rapidly towards excessive values. The pore pressures are underestimated when few numbers of cycles are simulated and, on the contrary, they are overestimated for large numbers of cycles (Figure 4-24).

The study of the compressibility of soft soils is a key factor in defining a breakwater project, both primary and secondary deformations must be considered in these cases. Therefore, in order to adequately reproduce the deformation behaviour of soft soils, it is necessary to have constitutive models that incorporate the creep behaviour of the soil. The SSC model has proven to be effective in adequately reproducing the results of oedometric tests, including effects of secondary compression and the influence of the OCR value, the load increase, and the current stress state, on the deformation (see Figure 4-29 to Figure 4-32).

A large-scale instrumented preloading test provided, through a back-analysis procedure, an accurate distribution of compressibility parameters. Conventional procedures, based on laboratory tests on recovered undisturbed specimens do not achieve the same precision and reliability of the field test. The preload test also provided an accurate distinction between sandy and clay layers. The former is significantly stiffer than the clay levels as reflected in the deformation profile recorded in the preload test (see Figure 4-48).

A backanalysis of deformations measured during the load test was performed using Plaxis Soft Soil Creep model (Vermeer and Neher, 1999). The actual sequence of loading and consolidation was introduced in the model. Their model response is compared with the micrometer –measured vertical displacements at several depths (see Figure 4-37 to Figure 4-40). The agreement is reasonably good. The model is also capable of predicting unloading strains with a good approximation (see Figure 4-42 to Figure 4-45).

Chapter 5

BARCELONA BREAKWATER PERFORMANCE DURING CONSTRUCTION AND POST-CONSTRUCTION

5.1 INTRODUCTION

Geotechnical design and construction of a vertical breakwater founded over low resistance soils imply some special considerations which are treated in this thesis. The main issues to be studied are the assessment of stability (during construction, operational life, and storms) and the prediction of long-term settlements.

A fundamental aspect in the asses of the stability condition of a project is the gain on undrained shear strength of the soils due to the beneficial effect of consolidation due to loads applied previously over the soil. To get this increment of resistance, the consolidation of soils and dissipation of excess pore pressures is needed. The need to get an improvement in soil strength makes it necessary to evaluate the time required to complete the soil consolidation process. Given the uncertainties involved in this process, instrumentation becomes an invaluable tool for controlling the degree of dissipation and settlement. Specifically, the parameters to control are pore pressures and horizontal and vertical displacements.

The construction of Barcelona breakwaters has two main challenges associated with the breakwater typology selected. One is due to the soft characteristic of foundation soils, which means low bearing capacity available, large settlements, and a certain risk of failure. The other refers to the uncertainties about wave interaction with the caisson, and their effect on the cyclic behaviour of the foundation. Experience and lessons learned in a caisson failure at Barcelona (Puzrin et al, 2010) have shown that care should be taken about the cyclic response during storms; it will be a critical issue of design. In this context, a wave pressure measurement system was installed.

This chapter presents the results of almost 8 years of monitoring pore pressures and settlements of the south breakwater of the port of Barcelona during construction and afterwards. Results are discussed in the context of the classical theory of consolidation, previously reported laboratory results, and similar instrumentation on other related projects.

Description of the instrumentation system, installation, performance and monitoring records are presented in detail in Appendix I.

5.2 DESCRIPTION OF THE BARCELONA'S BREAKWATER PROJECT

The extension of Barcelona harbour includes the construction of two breakwaters, the east breakwater of 2165 m length and the south breakwater of 4096 m length. It was planned that the east breakwater and the deepest section of the south breakwater were to be built with vertical caissons founded on an embankment. However, initial planning was modified in the final design. The sections designed as caissons breakwater were reduced to the part of the south breakwater parallel to the shoreline, as shown in Figure 5-1. The rest of the breakwaters were constructed with a conventional rubble mound section. The seabed depth at the east breakwater range between 18 m and 27 m while it was 20 m in the caissons section corresponding to the south vertical breakwater.

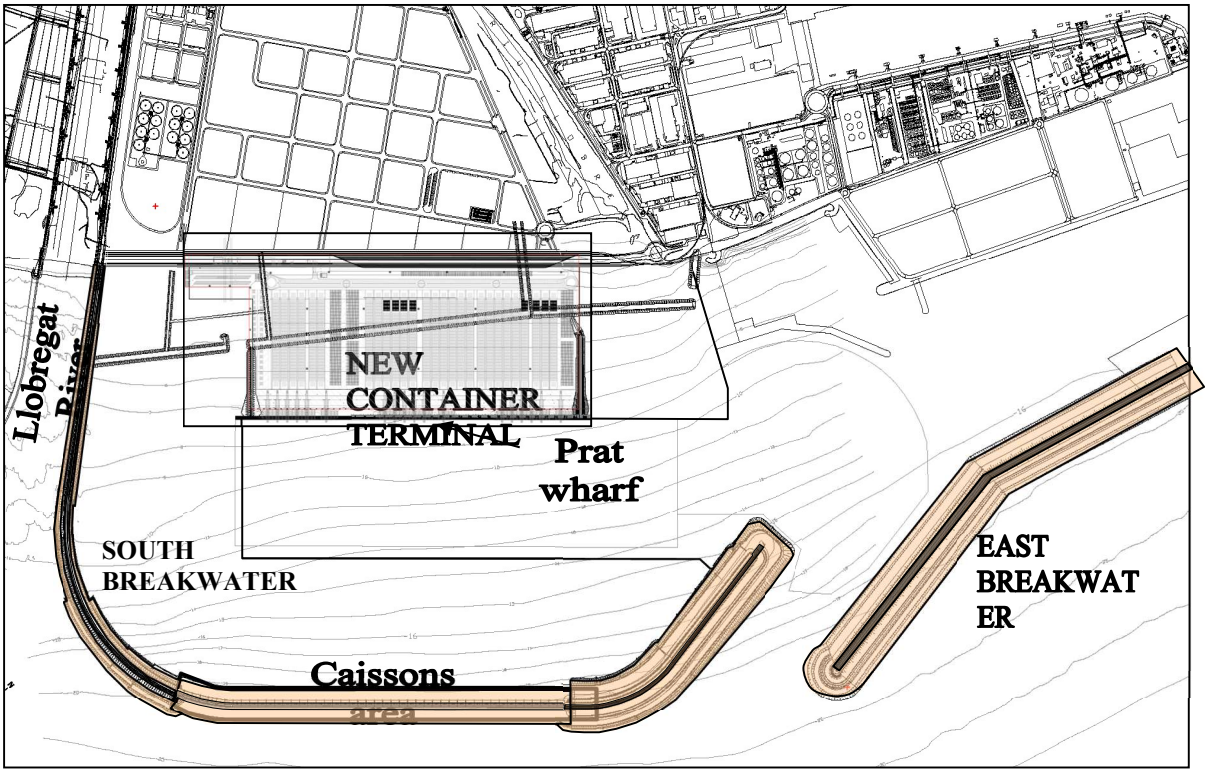

Figure 5-1. Plant view of the new breakwaters at the Port of Barcelona.

The south breakwater presents an alignment with a roughly "L" shape and a total length of 4,096 meters. Given this morphology, as well as the different types of designed sections, the south breakwater was divided into four main sections:

Starting section: corresponds to the first 979 meters, with an alignment mainly perpendicular to the shoreline. The chosen typology is the mound breakwater. Four type-sections were designed in this section (A, B, C and D from land to sea), where the seabed level changes from -2m to -9.0m. The core is formed by rubble mound material, which is covered by the armour layer composed of a natural rockfill of 3 - 6 ton near the shoreline sector or 8-ton concrete blocks in deeper water levels. Slopes in this section vary from 1.75H:1V to 2H:1V. The breakwater is completed with a crown wall, which has a crest level of +6m.

Curved section: it corresponds to the next 1,022 meters, with a curved alignment. The chosen typology is the mound breakwater. Five more non-symmetrical sections with slope 1.75H:1V (seaward side) and 3H:2V (port side) were designed: E, F, G, H and I. In this area, the seabed level varies between -9m to -19m. Before the dumping of the rubble mound begins, a 5m dredge trench was required in this zone. A filter layer of rockfill 1 ton and 0.2 ton cover the rubble mound core. The protection layer composed of concrete blocks of 15ton, 30 ton and 60 ton weight, is located in the outer slope (seaside) whereas the rockfill of 3ton is placed on the inner side. The crown wall crest reaches levels from +7m to +11m. Finally, a stabilization berm 25 to 40m wide is placed on both sides of the breakwater (see Figure 5-2a).

Section parallel to the coast: corresponds to the following 2,095 meters, mainly parallel to the shoreline and constructed on over the level -20m, approximately. The chosen typology is the vertical breakwater, composed of a concrete caisson 24.4m wide placed over a large embankment with 50m berms on both sides of the caissons. The section-type was named K (see Figure 5-2b). The embankment consists of an unclassified rockfill, a 0.3 ton filter layer and a protection layer of 4 ton rockfill that cover the seaward side berm.

End section. Corresponds to the last 500 meters, which form the entrance of the port. The chosen typology for this sector is the mound breakwater.

Figure 5-2 shows the typical geometry for the two typologies adopted in the south breakwater. Although instrumentation data were obtained from the entire project, this thesis deals only with the South breakwater, focusing mainly on the caissons sector.

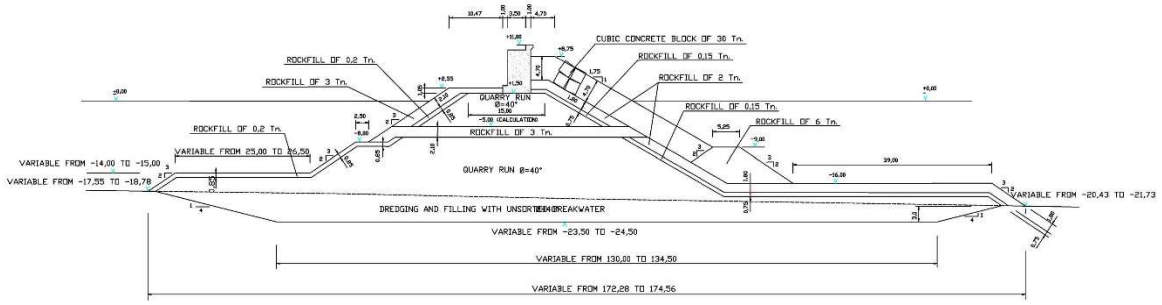

(a)

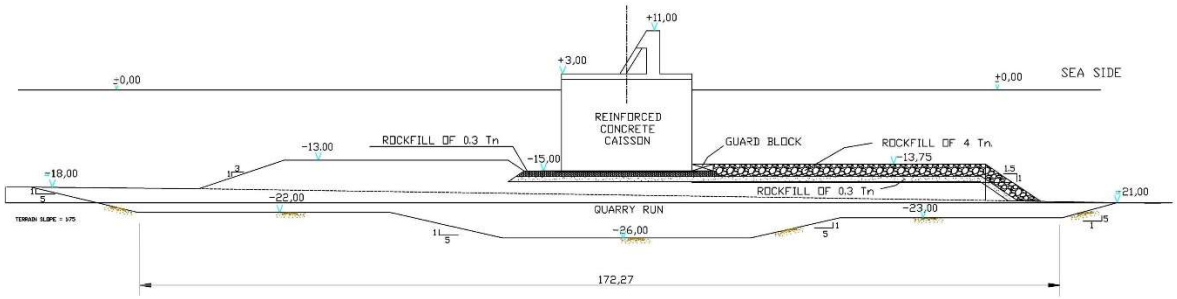

(b)

Figure 5-2. Final typical sections for the south breakwater. a) Section G, b) Section K.

The construction of the vertical breakwater began in June 2003, with the first dredging work, taking about 4 years to complete. Construction was carried out in phases, which were defined in the construction project as follows:

Phase I: dredging and embankment construction over the seabed. 3-5 meters depth of the silts and clays in the seabed soil was replaced by unclassified rockfill material (the same material used to construct the embankment). Rockfill material is transported by barges that, once located in the right position, discharge its contents (see Figure 5-3a). After the core material was dumped, a layer of 0.3 ton rockfill material was placed. Finally, on the area exposed to the wave action a protective layer of 4 ton armour blocks were placed.

Phase II: Placement of caissons and cell filling. In order to ensure stability during this phase, a period of consolidation enough to dissipate the pore pressures developed during embankment construction and, therefore, to produce an improvement in the soil strength was allowed. The project established as a stability requirement, that the total consolidation of the embankment should be completed before starting the placement of the caissons. After installing the caissons to the required location, filling with sand is followed and the closing top slab was constructed (see Figure 5-3b).

Phase III: Construction of the superstructure to form the final geometry of the breakwater. Again, consolidation of the previous phase is a requirement for stability.

Phase IV: Backfill behind the caissons to create quay zones. This phase has not been executed yet, so when this phase of construction starts, soil consolidation due to the caisson will be considered finished.

(a) (b)

Figure 5-3. (a) unclassified rockfill transported in a barge (b)View of caisson filling tasks

Bathymetric surveys were periodically run to control the progress of dumping materials over the dredged area and the seabed during embankment construction. In this way, it was possible to define the sequence of breakwater construction. Longitudinal profiles and cross-sections were continuously plotted. Figure

5-4 shows the evolution of the longitudinal profile between chainage 1+650 to 2+550, that includes instrumentation section 1 and 2.

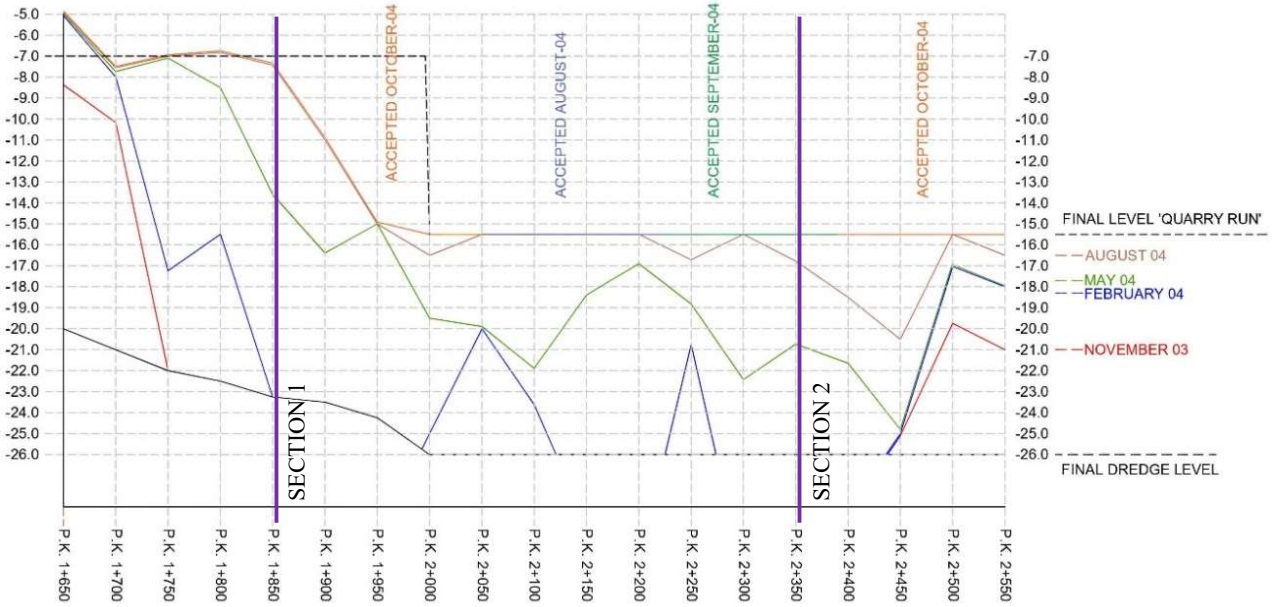

Figure 5-4. Dumping evolution of section 1 and 2 of instrumentation until October 2004

5.3 INSTRUMENTATION

The aim of the instrumentation was to provide advance warning of instability and to control pore pressure dissipation to monitor the gain of undrained shear strength as construction progress. In fact, piezometers measurements were used to establish a safety program of work including mandatory periods of consolidation of 4 months before caisson placement. Also, the interpretation of the evolution of the deformation over time led to change the level of placement of caissons by an additional 1.5m.

The field instrumentation was installed on the surface of the dredged soil, using an innovative method consisting in pushing a casing that contains the chain of sensors until the required depth. A mandrel rig over a mobile platform assisted by a crane mounted on a specialized ship was used for this purpose. In total, 4 sections of instrumentation were installed before the activities of dumping of material to form the embankment began (see Figure 5-5). Typical cross sections of instrumentation were implemented with a chain of 5 piezometers, a chain of 5 settlement cells and 2 chains of in-field inclinometers with 5 sensors each. Piezometers and settlement cells were installed at 5, 10, 15, 25 and 35m depth, while inclinometers reached until 20m depth. Two typical cross-sections of instrumentation are shown in Figure 5-6 (rubble mound breakwater) and Figure 5-7 (vertical breakwater).

Part of the instrumentation system, buoys and data cables suffered frequent damage from maritime traffic and fishing operations. The depth settlement sensors and inclinometers were particularly affected, which were lost in sections 2, 3 and 4. Only the sea side inclinometer in section 1 and the port side inclinometer in section 2 survived during embankment construction.

In June 2009, once the top slabs to close the caissons had been installed, the instrumentation of sections 2, 3 and 4 was replaced maintaining the same setup but without inclinometers. This time the procedure of installation used was the conventional bentonite plug method, consisting of drilling a 4" diameter borehole from the top of the caissons and lower the piezometers into the hole. Unfortunately, the settlement cell system became clogged, so the recorded measurements from those sensors were anomalous. The new instrumentation was active until November 2012.

All the data was transmitted from the junction box by radio communication and received and saved in a server computer installed in the harbour lighthouse. A specific software 'the Geoscope-web' was developed to managed and shared data via the internet. The sampling frequency was configured to store one measurement every hour from each sensor.

Immediately after the emplacement of the caissons, topographic prisms were installed in each corner of the caissons and the settlements were periodically recorded by means of surveying equipment. Also, caisson 9 (corresponding to geotechnical instrumentation section 2) was chosen to install the hydraulic instrumentation. The objective of this instrumentation was to measure the force of the sea waves in order to verify the design hypotheses. Two pressure sensor alignment (A and B) were placed. In each alignment, 8 transducers were placed on the wall, 4 on the base and 2 on the caisson crown wall. Figure 5-8 shows the locarion of the pressure sensors in the instrumented caisson.

A detailed description of the instrumentation is presented in Appendices I and II.

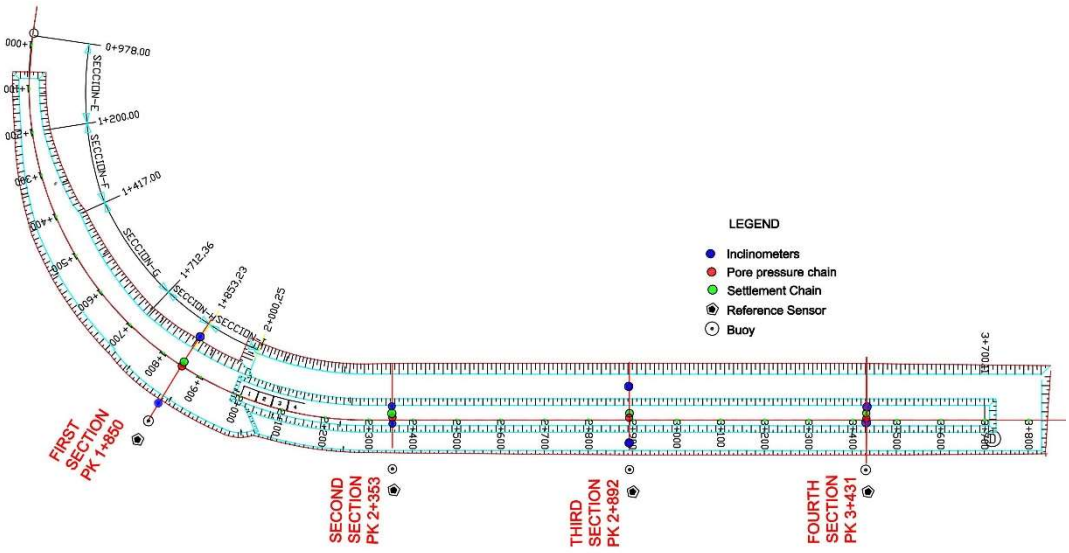

Figure 5-5. Location of instrumented sections in the South Breakwater.

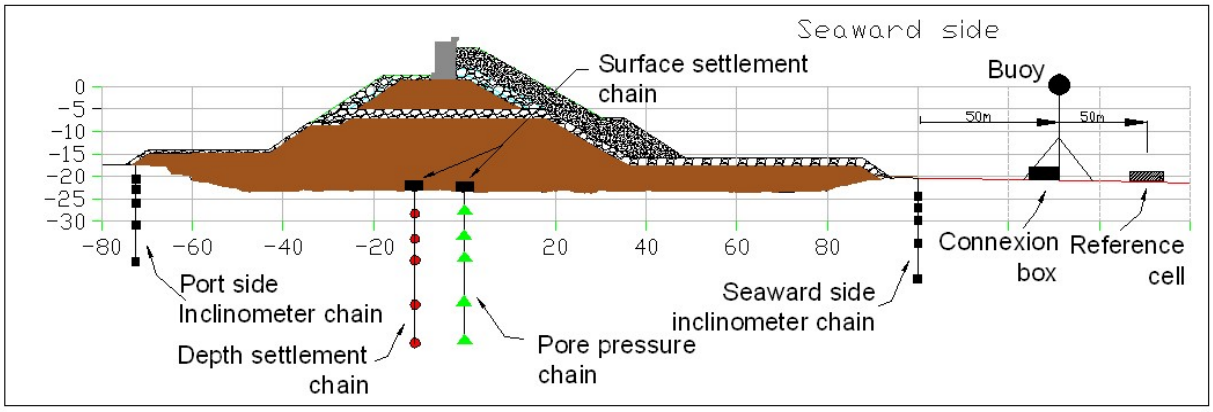

Figure 5-6. Typical cross section for rubble mound breakwater instrumentation.

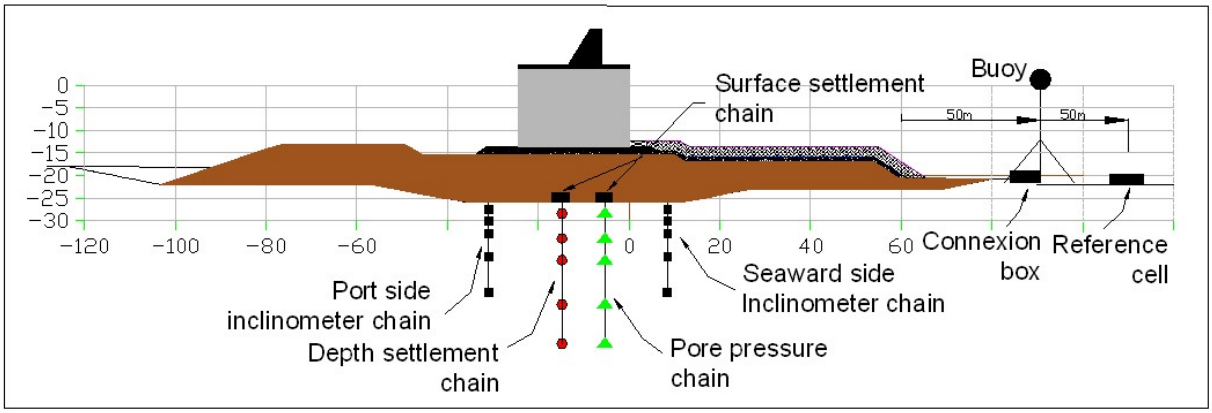

Figure 5-7. Typical cross section for vertical breakwater instrumentation.

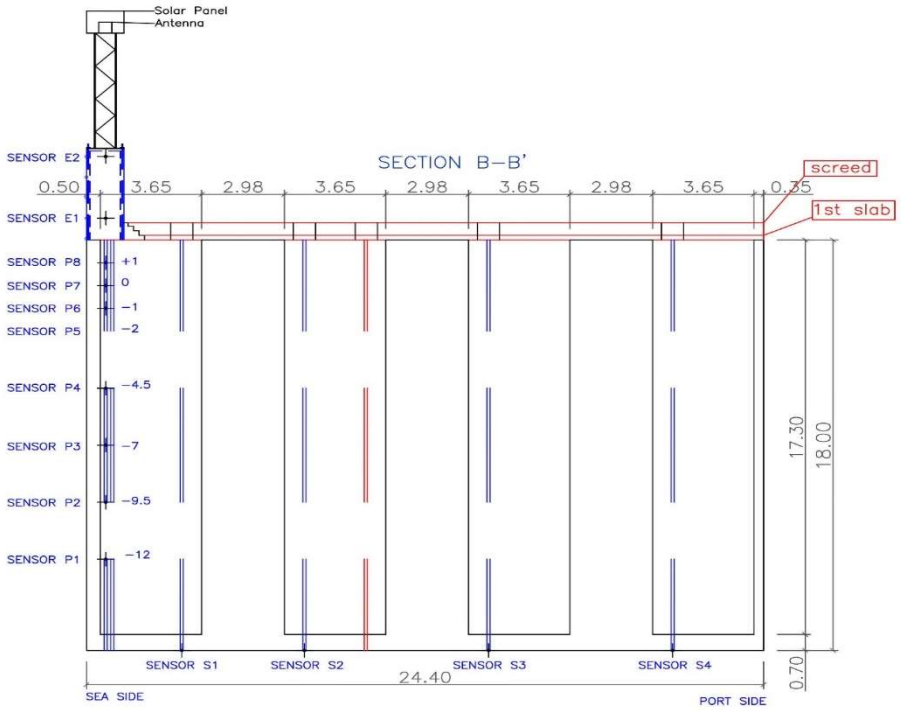

Figure 5-8. Location of the pressure transducers in the instrumented caisson.

5.4 SOIL CONDITIONS

The south breakwater is founded over the prodeltaic sediments of the Llobregat river, which are composed of an upper level of soft clays and silts that extend up to 50m below the seabed. Underlying this stratum appears an intermediate level of gravels and sands, which have a thickness of about 7m. Below a lower level of clays is found, with thickness about 14m and similar characteristics to that of the upper level but denser. Finally, there is a thick layer of gravels and sands that reaches until the end of 120m drilled. The soil profile is shown in Figure 5-9.

The upper sediments are predominantly classified as CL, CL-ML and ML and have numerous intercalations of fine-grain sandy soils and grey colored sandy silts. Figure 5-10 shows the index properties, where it is noted that the liquid limit varies between 20% to 40% and the plastic limit between 15 to 25%. Note also that the liquidity index decreases with depth from a value of about 2.5 at the surface to 0.6 at the lower limit, indicating high compressibility of these strata.

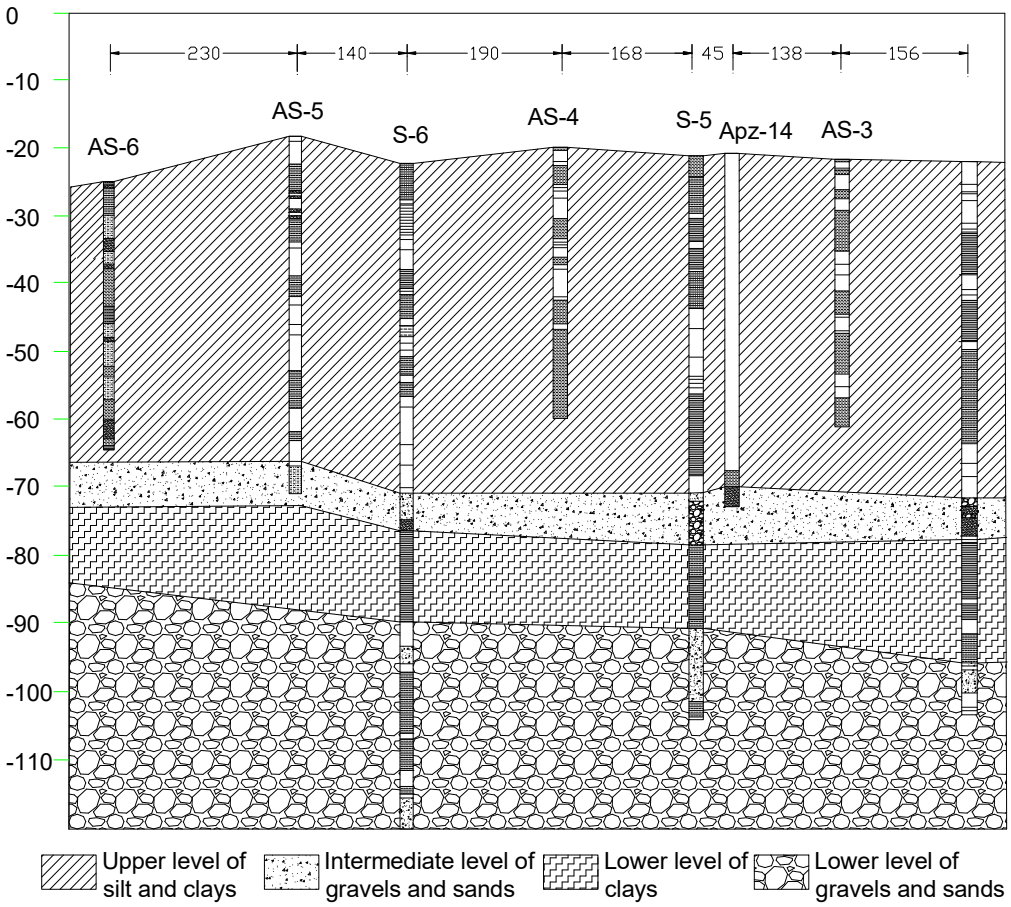

Figure 5-9. Soil profile along the south breakwater

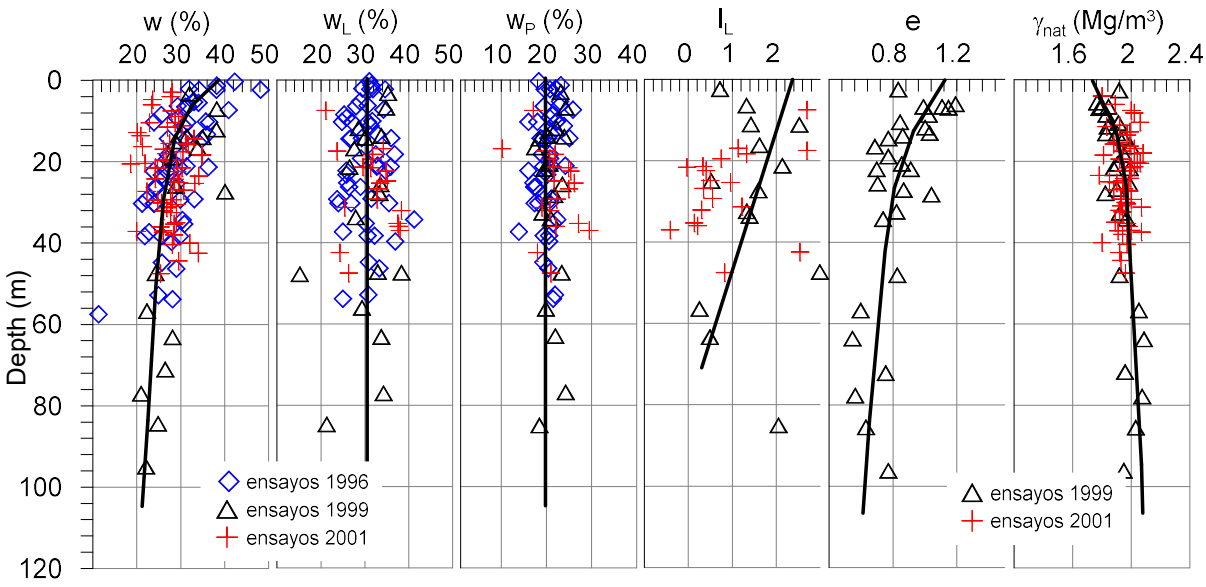

Figure 5-10. Index properties of foundation soils

It is known that undrained shear strength is strongly dependent on the shear mode, and in case of breakwaters, three main modes of shearing are distinguished (see section 0): compression, simple shear and extension. All these three modes were investigated in detail through laboratory tests as described in Chapter 3 and summarized in Figure 5-11. For short term stability evaluation, the undrained shear strength for the dominant shear mode was established as $s_u = 0.25\sigma'_v$.

In situ CPTu tests were also performed that show that the 40 meters of the upper strata correspond to a homogeneous clay stratum; undrained shear strength was also estimated from the empirical correlation to the cone resistance: $s_u = (q_c - \sigma_{v0})/N_k$. As usual for normally consolidated clays, a N_k value of 15 was adopted (Lunne and Kleven, 1981a), matching well with the previously established relationships for simple shear $s_u/\sigma'_v = 0.25$.

Compressibility characteristics were investigated with oedometer tests and an instrumented preload test. Compression index C_c is in the range of 0.125 – 0.24, with a mean value of about 0.20, and swelling index C_s ranging between 0.013 to 0.05. Oedometers tests also give information about the coefficient of consolidation, indicating values between 3×10^{-3} and 1.5×10^{-2} cm^2/s. CPTu dissipation tests also yield values of the coefficient of consolidation varying from 3×10^{-4} to 0.1 cm^2/s, but with more scatter. Finally, the coefficient of secondary compression was estimated to be in the range of 2.1×10^{-3} to 8.3×10^{-3}.

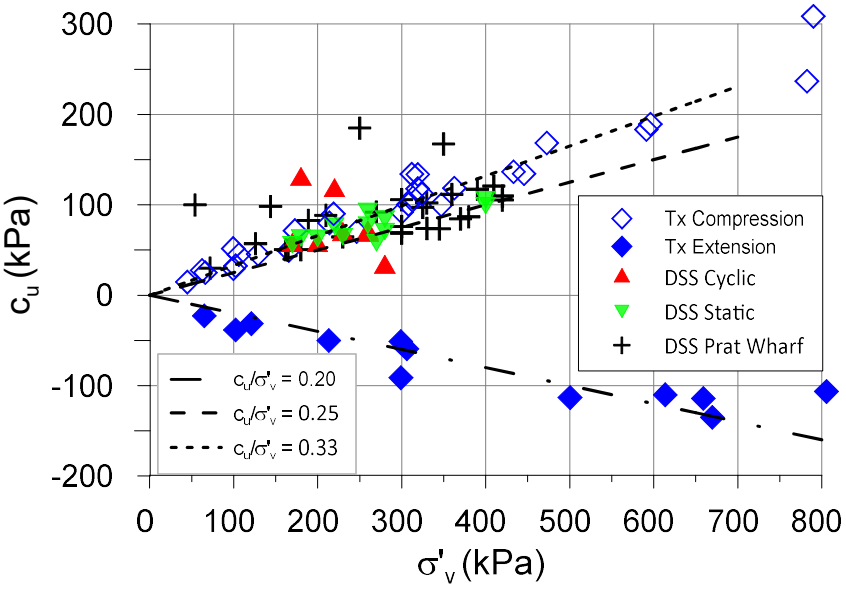

Figure 5-11. Undrained shear strength versus vertical effective stress.

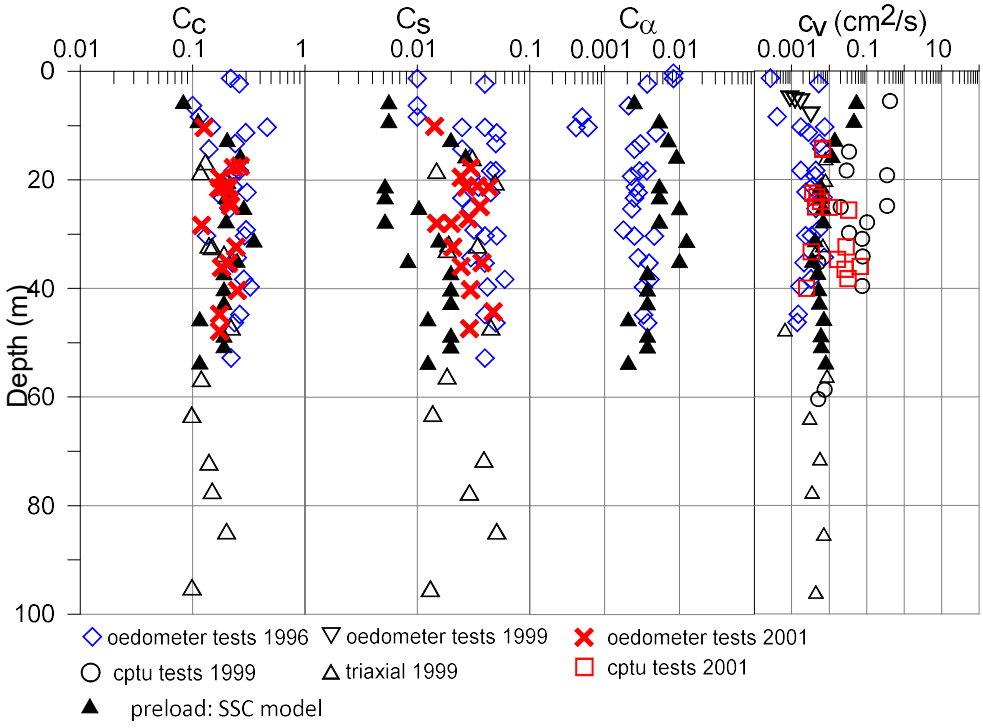

Figure 5-12. Variation of clay compressibility parameters with depth

5.5 FIELD PERFORMANCE

5.5.1 Pore pressures measurement

Piezometers have been placed at five levels in four sections, one of these sections was located under the rubble mound type breakwater (section 1) while the others were placed at the vertical breakwater location as explained before (see Figure 5-5). Unfortunately, many instruments were damaged during the construction work of the embankment, although some of them were repaired quickly others were definitively lost; it was only after the superstructure was constructed that new instrumentation could be

installed. Finally, discontinuous records of about 8 years of monitoring were obtained during construction and post-construction.

Figure 5-13 to Figure 5-16 shows the evolution with time of excess pore pressure (referred to the initial readings) recorded at the instrumented sections, also the history of loading is included in these figures. To calculate the load history, the central point at the base of the embankment was considered, the data from the bathymetry were used to determine the fill height and the daily cell filling reports were used to determine the weight of the caissons. The average unit weight of the embankment was established at 19 kN/m^3 and of the caissons at 21 kN/m^3. It is noted that excess pore pressure built up rapidly during each construction phase but it quickly dissipates in every pause period between construction phases; this tendency is most clearly visible in the upper layers.

Section 1 corresponds to the zone of rubble mound breakwater typology. The stepwise construction strategy was adopted with stops of approximately 30 days for consolidation. Even so, after a lapse of about 120 days and when the embankment reached 18m height, the excess pore pressure had increased to 80 kPa in the upper piezometers. For safety reasons, it was decided to stop the works and allow a long period of consolidation, which lasted until over 10 months. Only the winter protection level was constructed during this period. A very low dissipation rate was observed in the piezometer placed at level -49m and almost null in the piezometer at level -56m (see Figure 5-13), a behaviour that was attributed to soil disturbance resulting from the installation procedure. As explained by Indraratna et al (2015) in a similar case of vertical drainage installation, the penetration and subsequent removal of the steel mandrel disturbs the surrounding soil, changing the permeability and compressibility of the soft clay within the smear zone and affecting the soil consolidation.

Figure 5-14 shows excess pore pressures measured in section 2 of instrumentation. Contrary to section 1, in this case, the embankment has a lower height, approximately 12.5m, and the construction rate was much slower, taking around 10 months for its construction. Under this condition, the excess pore pressure reached a maximum value of 40 kPa in the piezometer placed at the level -33m. Again, the dissipation rate was markedly slow, especially in the piezometers placed at level -48m and -57m, as observed in section 1. Unfortunately, the increase in pore pressure could not be measured during the placing of the caissons, because the instrumentation was damaged. However, new instrumentation was installed after filling the caissons using the conventional method of drilling a borehole from the top of the caissons, which allowed to capture the last phase of dissipation. It was observed that all new piezometers installed show almost the same dissipation ratio, taking more than 5 years to achieve an almost complete dissipation of excess pore pressure.

Section 3 of instrumentation was completely broken before the construction of the embankment at this zone started. Figure 5-15 shows the pore water pressure recorded with the new instrumentation after

about one year from the sinking of caissons. Note that the deepest piezometer (level -62m) records more pore pressure and also the dissipation rate was almost the same in all the piezometers.

The evolution of the pore pressure during the construction of the embankment was measured at three different levels in the instrumentation section number 4 (see Figure 5-16), which could only reach the level -45 m, due to installation problems. Piezometer at level -45m shows almost null rate of dissipation during embankment construction, similar behaviour was observed in section 1 and 2, but at a deeper level. The second installed instrumentation, in contrast, shows a similar rate of dissipation in all the piezometers. The Piezometer at level -33.7m seems to dissipate pressure more easily, compared to the others, probably influenced by its proximity to the upper boundary. Note that in this figure the isolated points correspond to the last reading that could be taken with the initial instrumentation. These measurements approximately coincide with the records of the second instrumentation, taking into account that the sensors are not located in exactly the same position.

Further insight into the ground response is provided by the profile of pore pressure with depth given in Figure 5-17, where the dissipation process is observed along the four sections in the breakwater. During construction, the increment of pore pressure was more noticeable between level -30 to -40 m, which is probably related to the major stress influence from the embankment load. Also, at this level, the rate of dissipation was higher, not so in the lower levels, where the very little dissipation was observed, taking about 5 years to get full dissipation.

Pore pressure records of section 1 and section 2 (which have more information during construction) were checked against the embankment pressure history in Figure 5-18 (section 1) and Figure 5-19 (section 2). Embankment pressure was computed at the central point of the embankment base assuming 3 different unit weights for the embankment material (19, 20 and 21 kN/m^3). Results show that the ratio of pore pressure over embankment pressure ranges from 50% to 60%, this low rate value is related to a slow rate of embankment construction, which allows dissipation of pressure to ensure a satisfactory safety condition. Similar results were obtained in section 2 but, as expected for a lower construction rate, a lower pore pressure was also observed (see Figure 5-19). In an ideal fully saturated soil loaded under undrained condition, the Skempton B parameter can be approximated as the ratio between the increment of pore pressure over the increment of embankment load at the center of the breakwater as shown in Figure 5-20. Load intensity variation with depth was not considered in these figures, so the response of the most superficial piezometer (S1PP05) is considered most representative for B parameter computation. In this condition, B parameter is estimated around 80 to 90%.

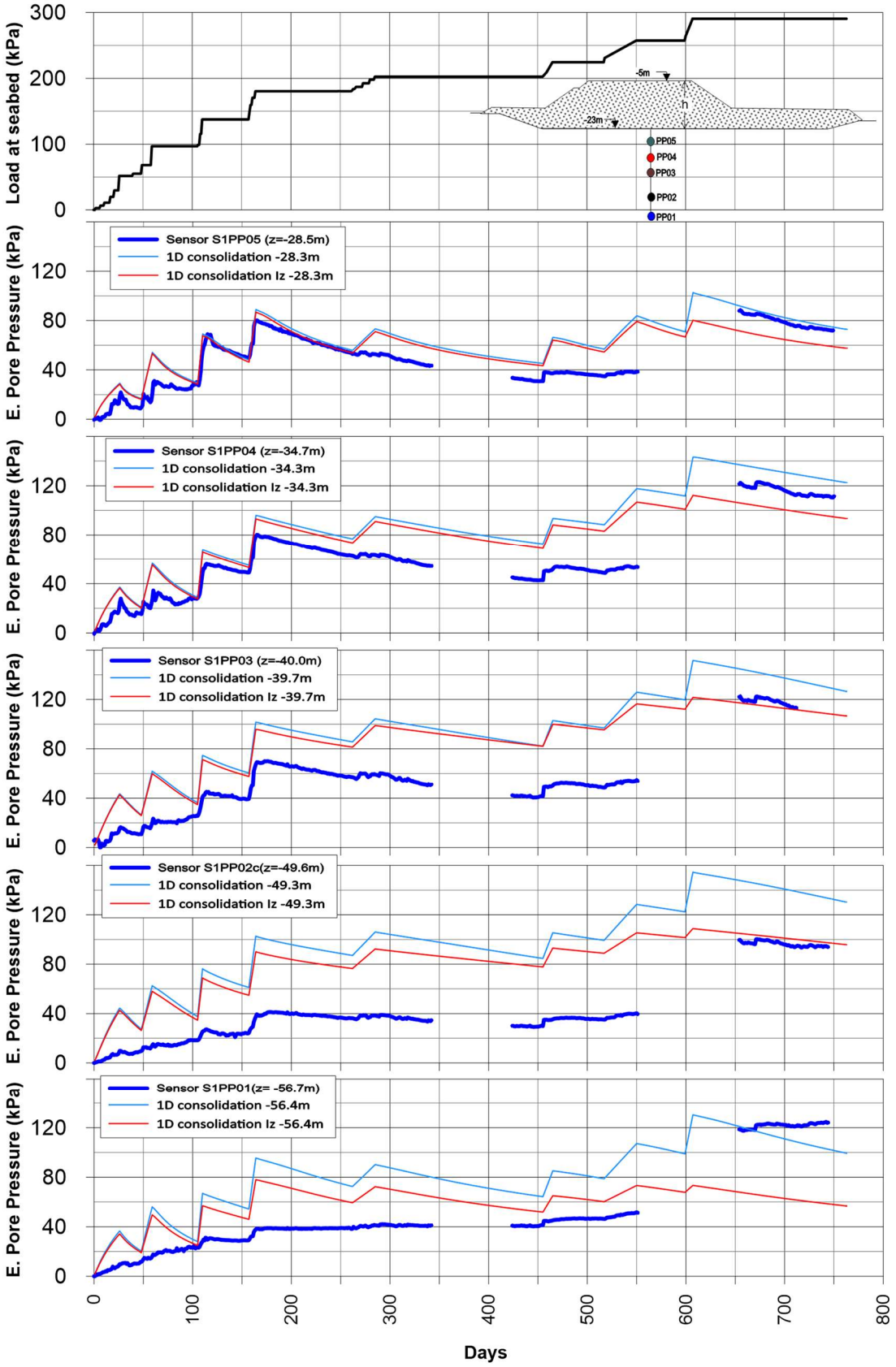

Figure 5-13. Excess pore pressure measured at section 1 of instrumentation

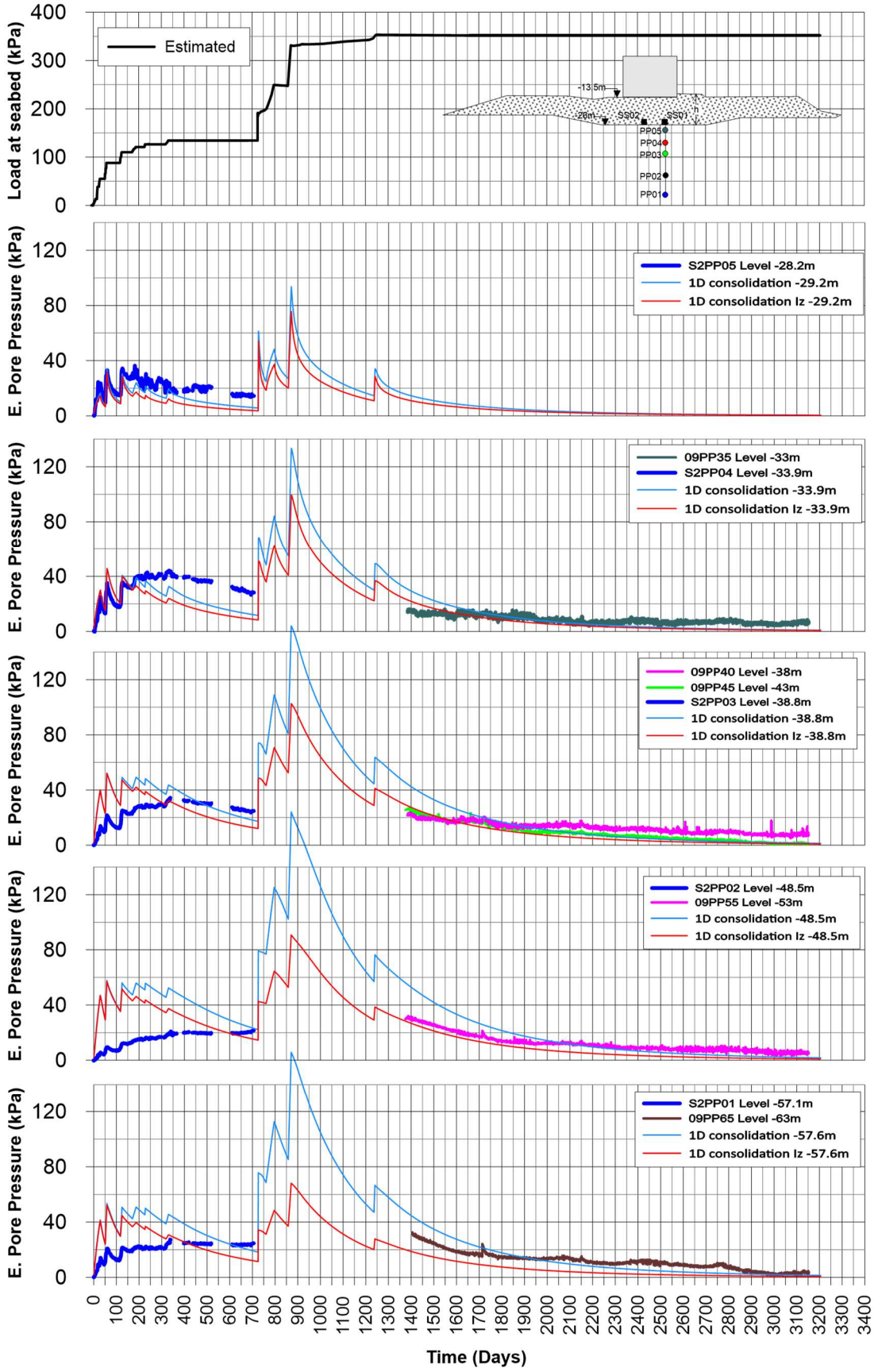

Figure 5-14. Excess pore pressure measured at section 2 of instrumentation.

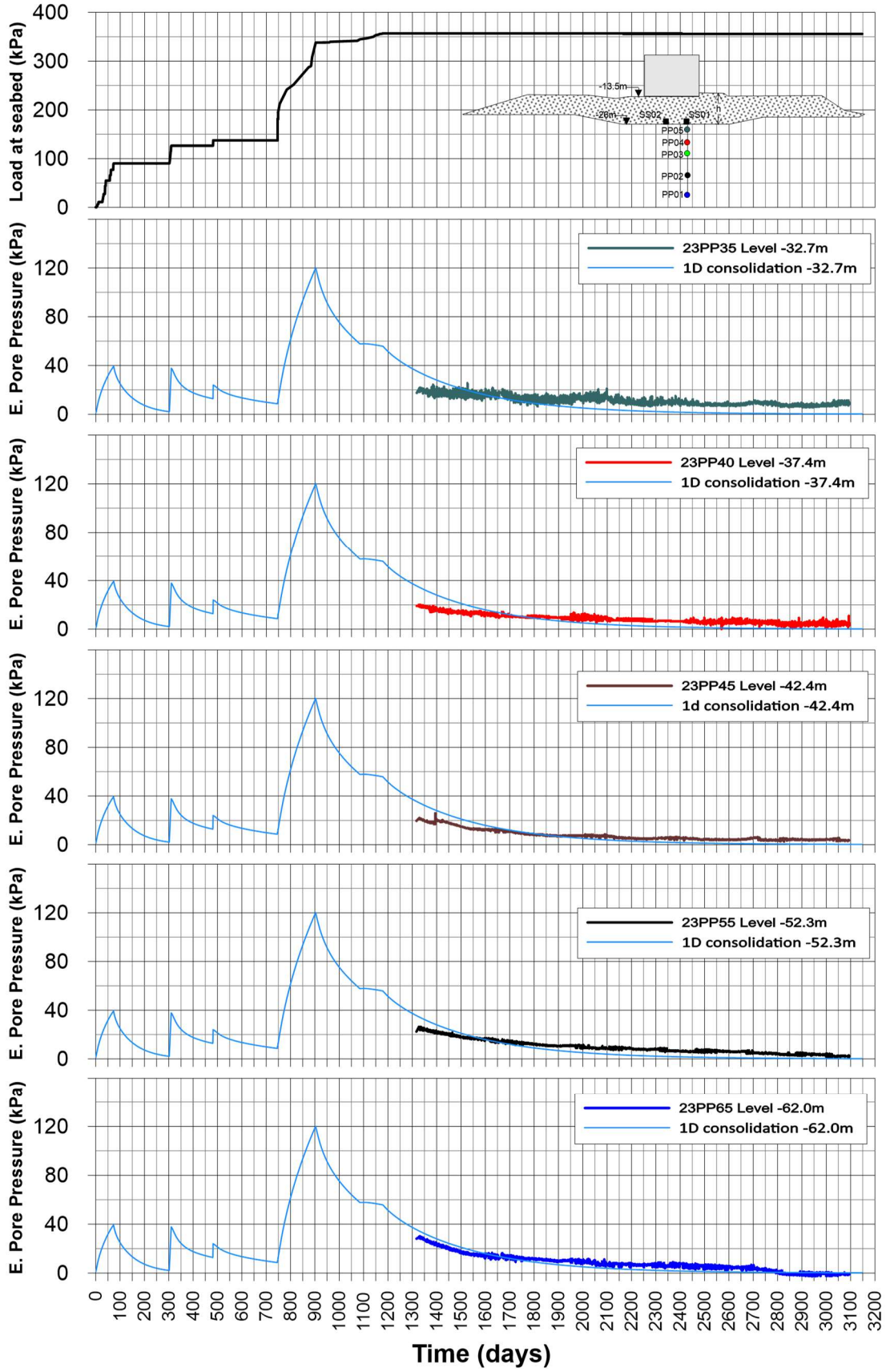

Figure 5-15. Excess pore pressure measured at section 3 of instrumentation.

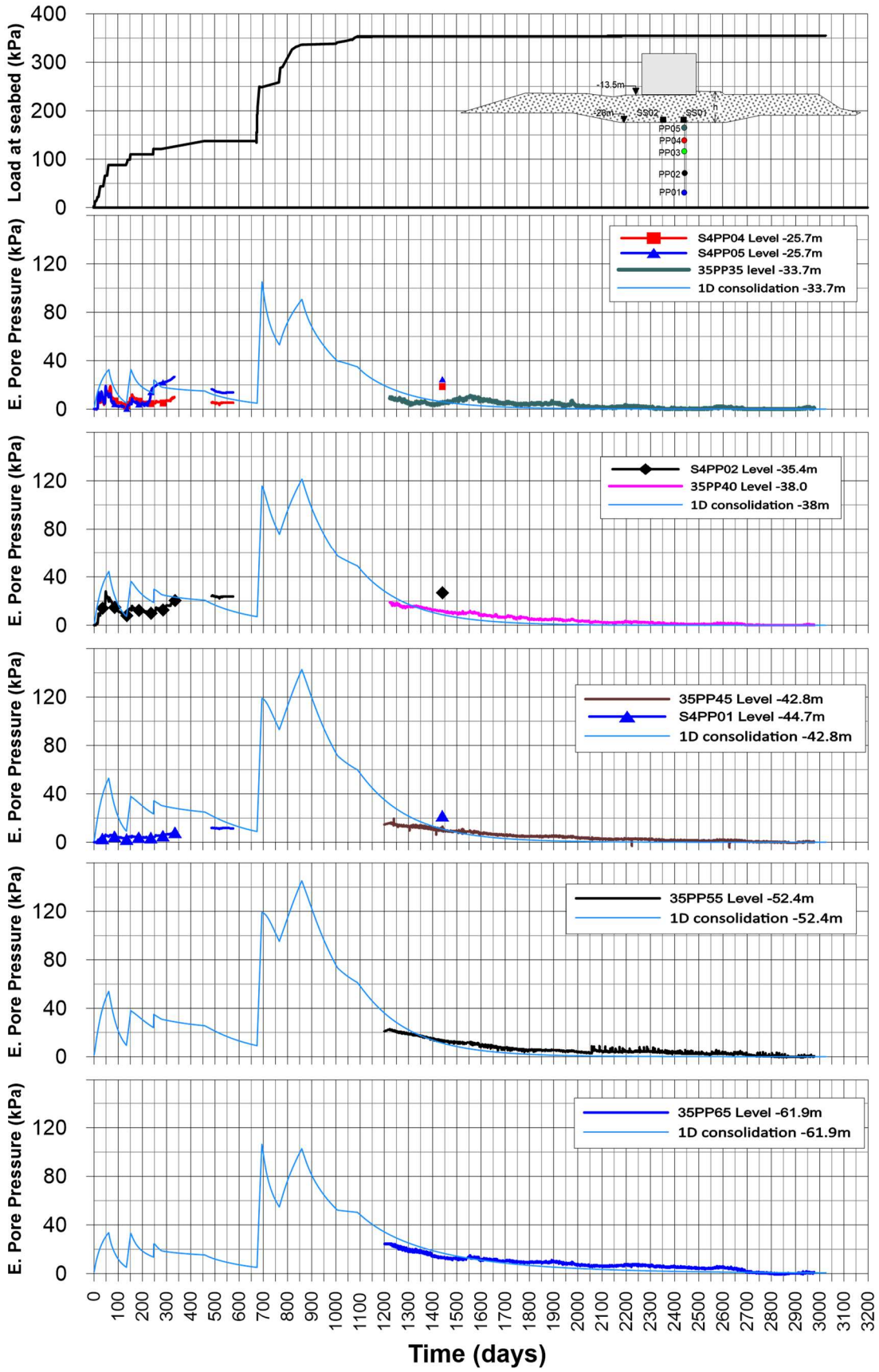

Figure 5-16. Excess pore pressure measured at section 4 of instrumentation.

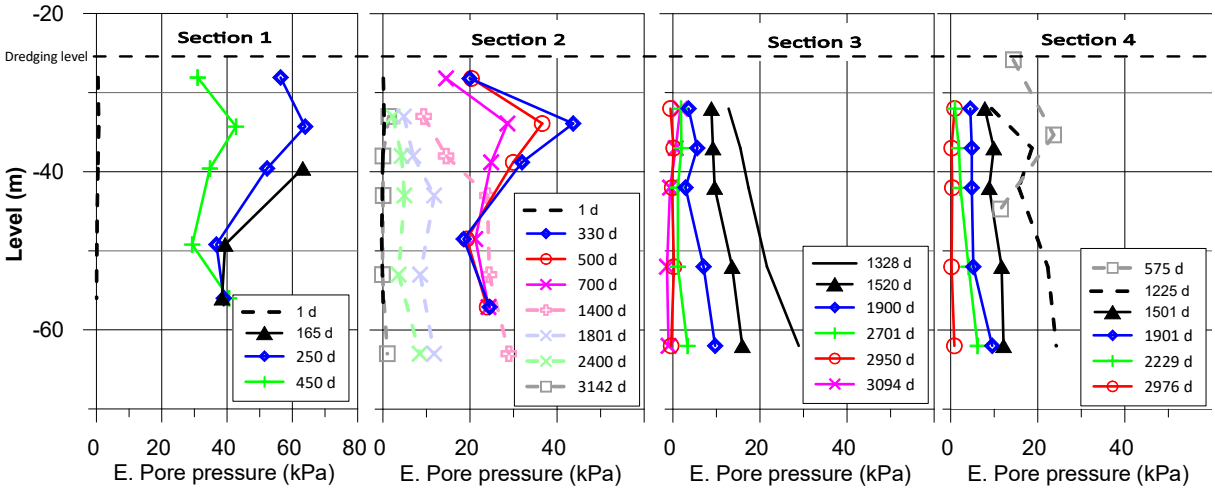

Figure 5-17. Excess pore pressure profile

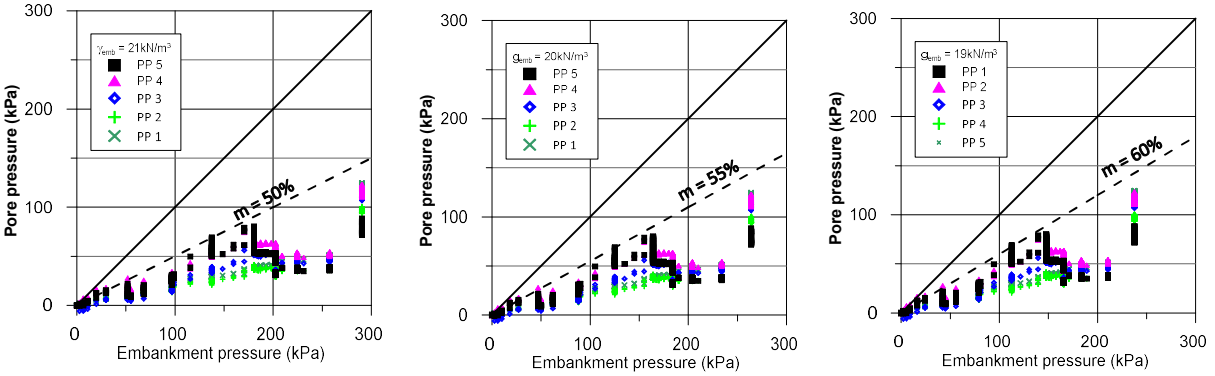

Figure 5-18. Pore pressure response to loading at Section 1 for 165 days of construction

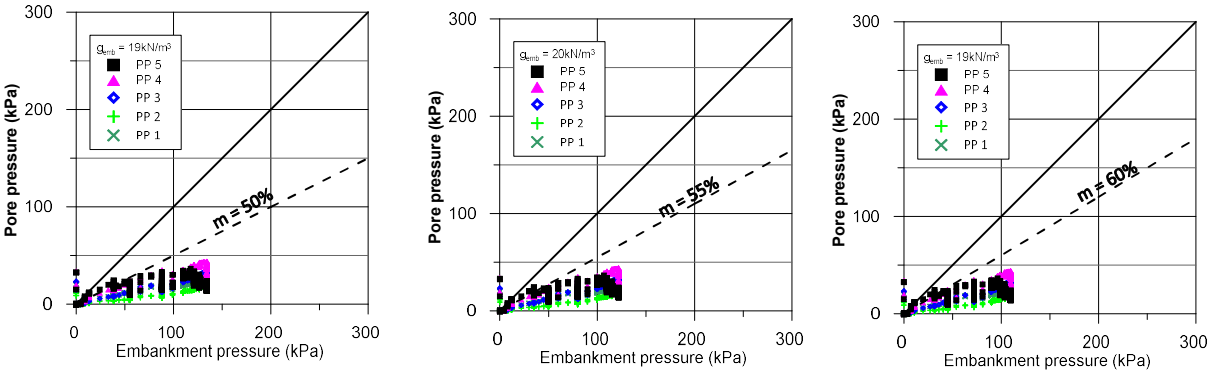

Figure 5-19. Pore pressure response to loading at Section 2 for 690 days of construction

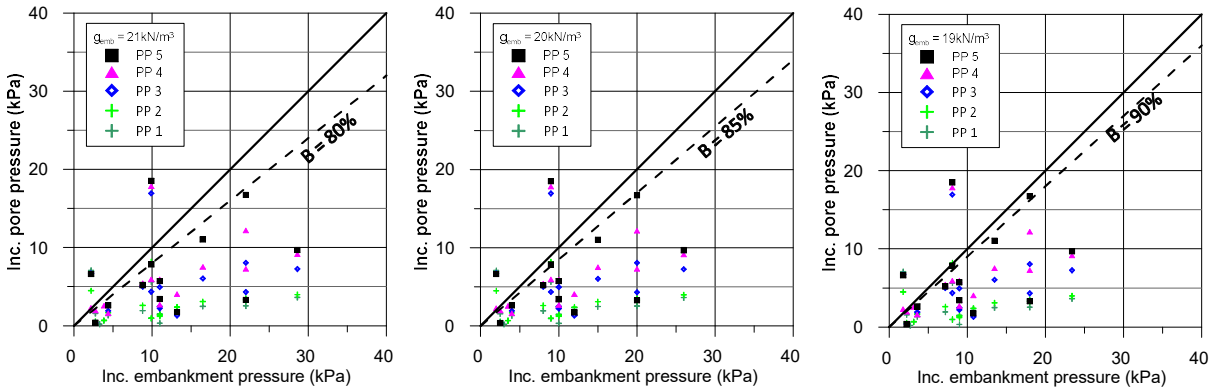

Figure 5-20. Increments of pore pressure versus increments of embankment pressure at Section 1 for 165 days of construction.

Tavenas and Leroueil (1980) proposed that the ratio $B=\Delta u/\Delta\sigma_v$ can be considered as a function of depth in a similar way of an isochrone curve of conventional 1-D consolidation as shown in Figure 5-21, establishing the following relation for pre-yield pore pressure:

$$\frac{\Delta u}{\Delta \sigma_v} = B_i = 0.6 - 2.4\left[\frac{Z}{D} - 0.5\right]^2 \qquad 5.1$$

Where Z is depth and D is the thickness of clay layer. Although Jardine and Hight (1987) suggest that B should depend on the rate of construction, soil permeability, compressibility characteristics, drainage boundary conditions, depth of clay and other details of the layering and soil properties, the pressure ratio B computed from this equation is very similar to the values measured with the instrumentation.

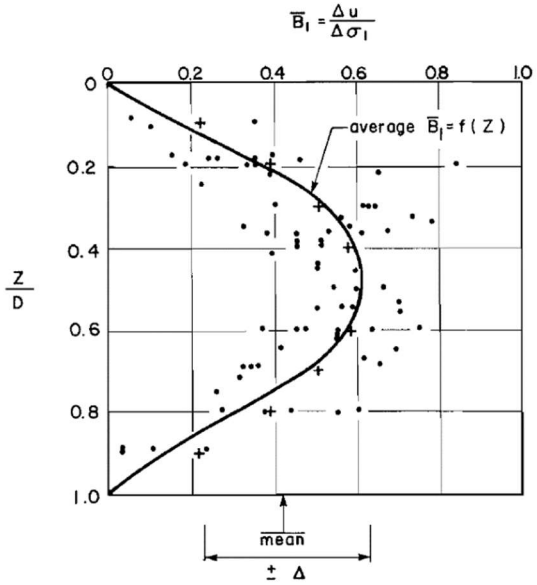

Figure 5-21. Compilation of observed pore pressure in clay foundations at the beginning of embankment construction (Tavenas and Leroueil, 1980).

5.5.2 Horizontal displacement and settlement measurements

Settlements were measured using a special set up of dual piezometers installed at different levels inside a hydraulic line as explaining in Appendix I. The aim of these instruments is to monitor seabed settlements during the construction of the breakwater. As explained before, the construction process implies that a large amount of material is poured from the barges, falling over the instruments. Although the instruments were protected with steel profiles, the protection was not enough and some instruments were damaged, resulting in that only the first two sections could record partial data of settlements. This data is described and analysed below.

Settlements measured in section 1 at four different elevations during the embankment construction are shown in Figure 5-22. Noted that a period to dissipate infiltrated pressures in the hydraulic line is required because these measurements were obtained using piezometers. This inappropriate response is quite noticeable during the first 100 days of construction, as shown in depth settlement sensors readings. Surface settlement readings were recorded for approximately 500 days. The typical primary consolidation curve was observed, the first part of the curve is approximate parabolic, coinciding with the loading process up to 300 days, the magnitude of the settlement in this period is of the order of 80 cm, at which time the breakwater had reached a height of approximately 18 m; then a straight but not horizontal part is observed, which coincides with the winter break period. Finally, when construction starts again, additional settlements of the order of 10cm were observed, until the moment when the instrumentation was damaged. A similar pattern of behaviour was observed in the deeper sensors, but with a lower magnitude of settlement, as expected.

A profile of settlement with depth is shown in Figure 5-23. From this figure is clear the influence of vertical strain reaches at least 40m deep under the seabed, with higher vertical straining being concentrated in the upper strata.

Figure 5-24 compares surface settlement with pore water pressure evolution. A low rate of dissipation and only a reduced magnitude of settlement is observed after the first 60 days of construction, which was expected due to the light overconsolidation induce by the previous dredge works done at the seabed. After that, once the yield point has been reached, the settlement rate and also dissipation seems to increase, even so, partial drainage is maintained in all stages of construction, highlighting the usefulness of the monitoring system of settlements.

As indicated by Tavenas and Leroueil (1980) large ratios of lateral displacement (Δy_m) to settlement (Δs) are expected only when the foundation yields. Lateral displacement estimated with the in-field inclinometer is shown in Figure 5-25. This profile shows a maximum lateral displacement of about 5cm at 763 days from the beginning of construction. This low lateral displacement is associated with the position of the inclinometer casing, which was installed outside the berm. Height of berm of about 5m seems not enough to reach yield at this zone.

Figure 5-26 shows the measured superficial settlement in Section 2. Two phases are distinguished in this figure: the first corresponds to the embankment construction, where the settlement of about 80 cm was measured. It is noted that this embankment was built in almost one year, followed by an additional year of consolidation. Building to a similar embankment height in Section 1 took about 120 days, which was considerably faster than in Section 2; this resulted in a lower pore pressure built-up than in Section 1, in fact the pore pressure reached a maximum value of 40kPa, compared to the 60 kPa measured in section 1 for a similar height. The second phase corresponds to the sinking of the caissons. Topographic control of each corner of the caissons was used to calculated settlement in this phase, an average value of around 160 cm is observed in Figure 5-26. Also, the topographic network of Port of Barcelona was used to monitoring the settlement in the long term up to 10 years after construction. The inclinometer only was active during the embankment construction (717 days) and recorded about 10mm of displacement during this stage (see Figure 5-27).

Tavenas and Leroueil (1980) studied four well-instrumented test embankments and concluded that an important behaviour change occurred when the embankment reaches a critical height H_c, as can be seen in Figure 5-28. Before this critical height is reached, they found the maximum horizontal displacement y_m is related linearly to the center line settlement by mean of equation 5.2 provide that the slope angle (β) of the embankment sides ranges between $0.66 > \tan\beta > 0.4$. In the case of greater angles, equation 5.3 is a better approximation.

$$\Delta y_m = (0.18 \pm 0.09)\Delta s \quad 5.2$$

$$\Delta y_m = (0.91 \pm 0.20)\Delta s \quad 5.3$$

The magnitude of lateral displacement versus settlement measured during embankment construction is shown in Figure 5-29 and is compared with the range of values reported by Tavenas and Leroueil (1980). It is clear that the soil response is out of range of reported data, which is explained by the non-typical embankment geometry of the breakwater with large berms.

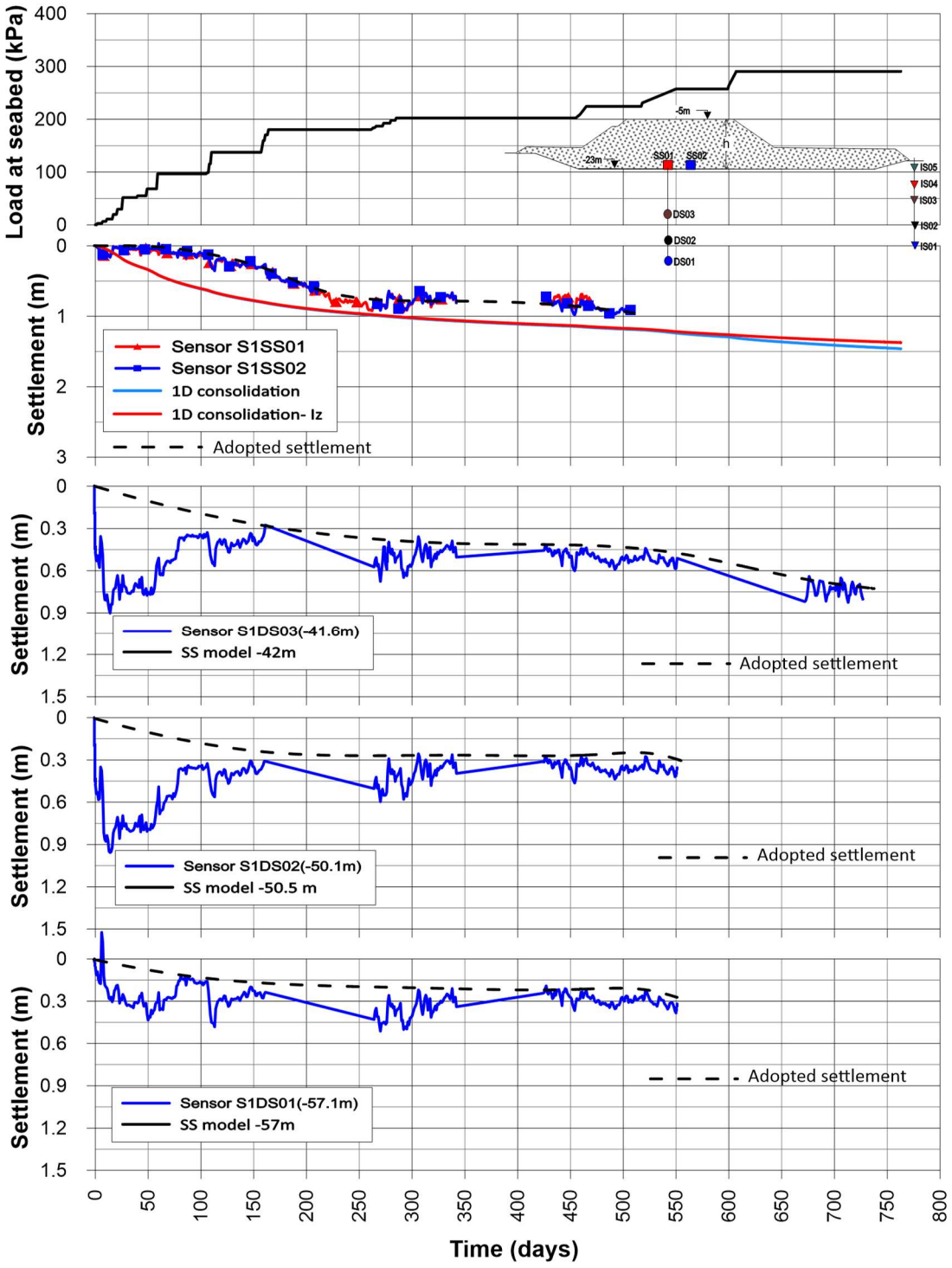

Figure 5-22. Settlements measured at different levels in section 2.

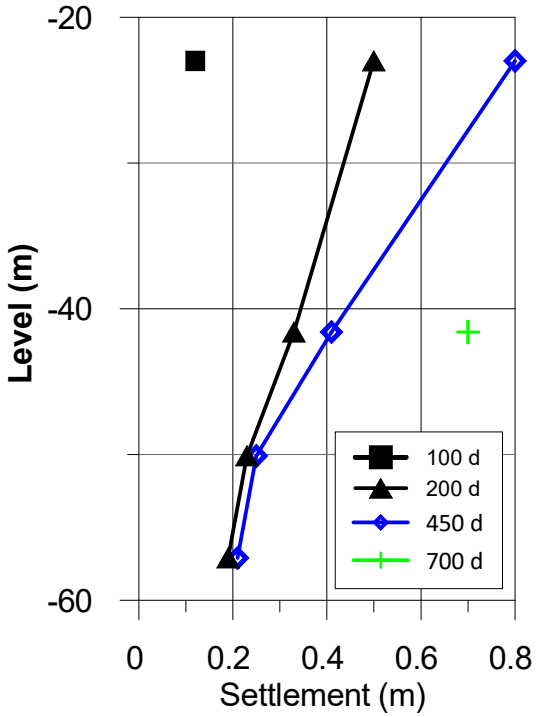

Figure 5-23. Profile of settlement with depth at section 1.

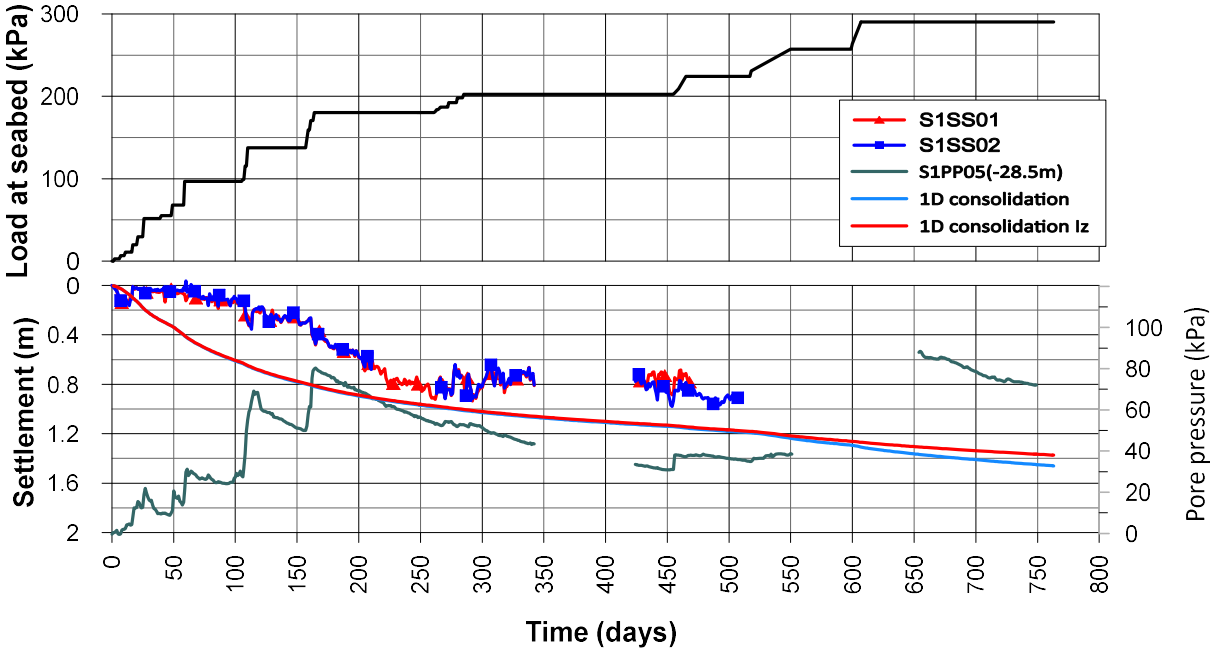

Figure 5-24. Settlement measured at the center line and pore pressure evolution with time at section 1.

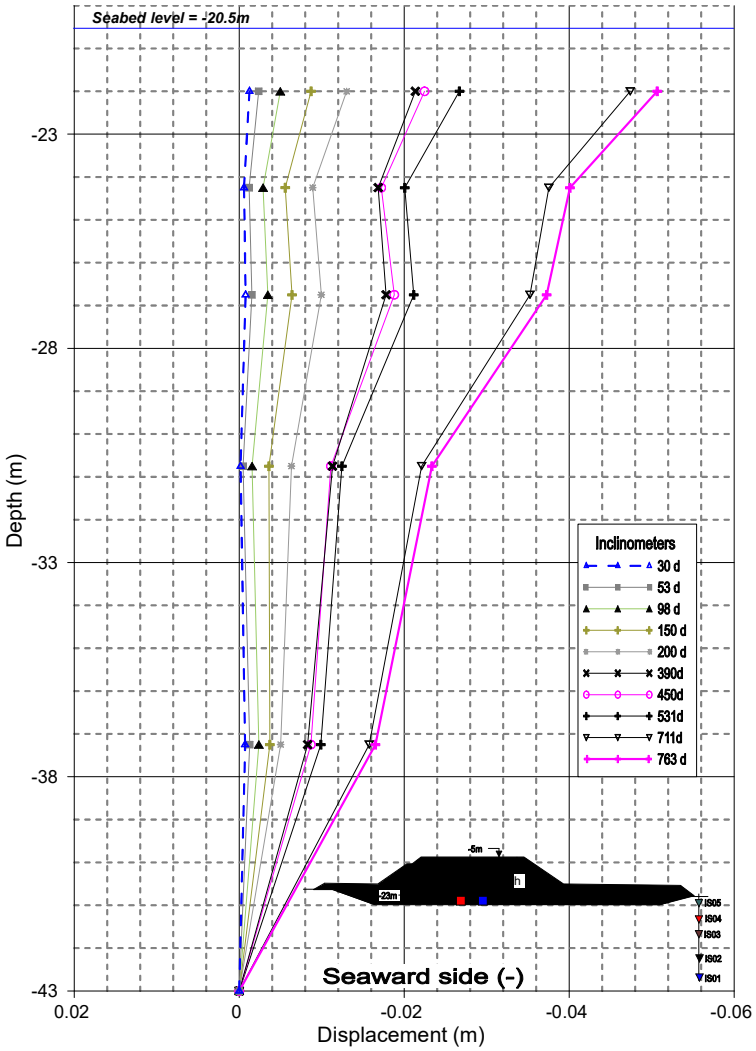

Figure 5-25. Lateral displacement profile recorded with seaward side inclinometer in section 1 after 763 days.

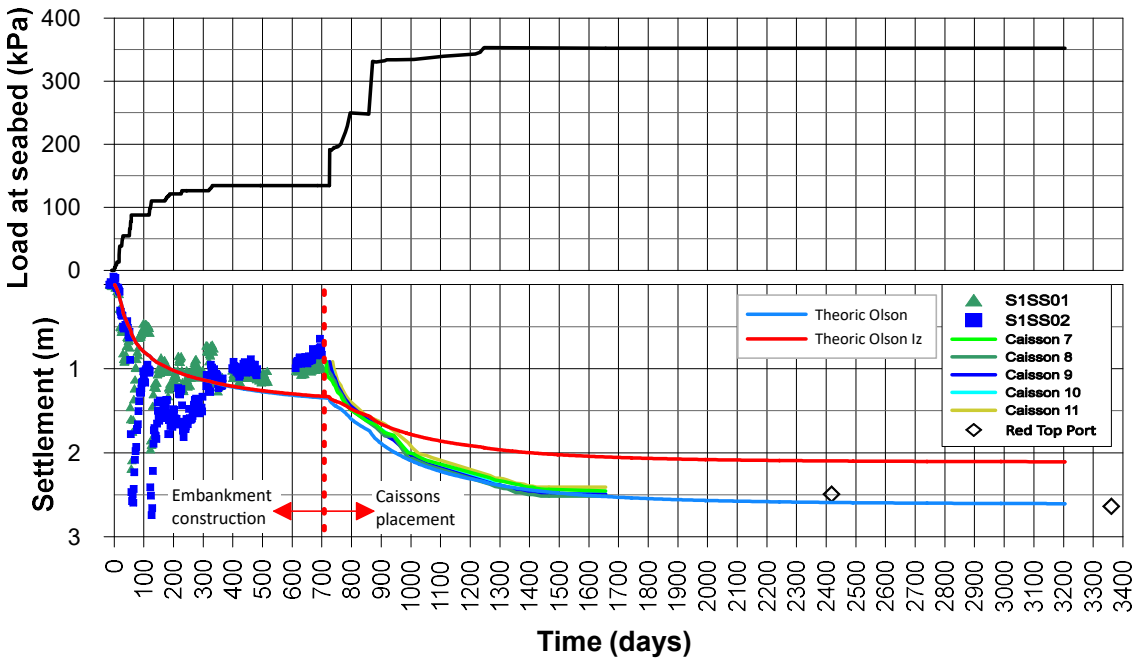

Figure 5-26. Settlement measured during construction and operation of vertical breakwater.

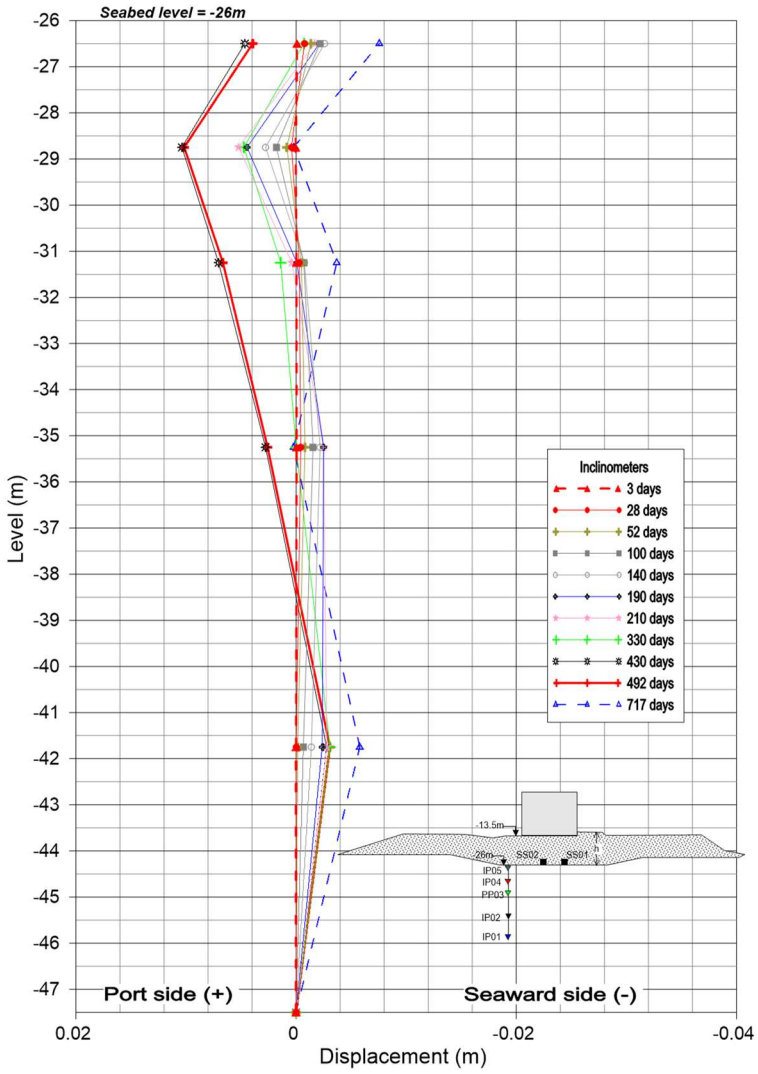

Figure 5-27. Data recorded with the port side inclinometer it section 2 after 717 days.

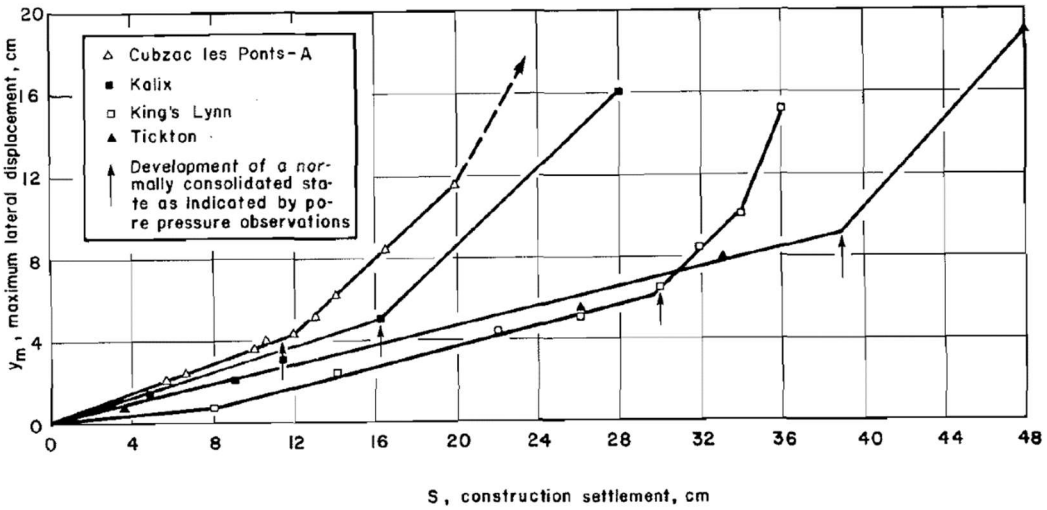

Figure 5-28. Lateral displacement y_m versus settlement during the construction of four test embankments (after Tavenas et al, 1979b).

Figure 5-29. Lateral displacement y_m versus settlement measured at the breakwater

5.5.3 Observed cyclic response

Breakwaters will be subjected to large cyclic and impact loads from waves. These waves can transmit cyclic shear stress to the foundation soil through the interaction with the caissons. After some cyclic stress reversals and depending on certain conditions (like magnitude, frequency, number of cyclic and drainage conditions), a gradual accumulation of pore pressure may develop, which in turn could lead to a reduction of effective stress, and consequently reduction of strength and stiffness. This phenomenon is explained by Andersen (2009) as a tendency for volumetric reduction caused by the breakdown of soil structure but prevented by the low compressibility of water, then pore pressures must develop to withstand the external loads. This process is generally known as liquefaction or cyclic mobility and has been an active topic of research in offshore engineering. There have been many studies on different aspects, especially focus on liquefaction induced by sea waves in sandy soils (Prior et al., 1989; Jeng et al., 2001, 2007; Wang et al., 2001, 2004, 2007; Gao et al., 2011; Geremew, 2013; Kirca et al., 2013; Sumer, 2013; Scholte‘s et al. 2015; Ye et al., 2018).

The stability of a breakwater is an important aspect of the short-term studies, which should be carefully examined at the different stages of the breakwater construction and life. Because the main objective of breakwaters is bringing protection to the port area, response to storms must be included in breakwater short-term stability studies, being liquefaction or cyclic mobility a phenomenon to take into account. Liquefaction has caused damage to offshore structures such as the failure of caissons in silty soil in Barcelona Harbour (Puzrin et at, 2010) or the segments of 16 caissons that failed in 2002 in Yangtze estuary, China (Yan and Zhao 2010).

To investigate this phenomenon complementary hydraulic instrumentation was installed in one caisson. Caisson 9 was selected, which also corresponds with an already installed foundation instrumentation

section (Section 2). Two parallel lines of hydrodynamic sensors (called section A and B) were installed in the caisson, each one, consisting of 8 pressure sensors in the front wall, 2 pressure sensors in the crown wall and 4 additional sensors in the caisson base (see Figure 5-8). The instrumentation was active from October 2007 to October 2010, within which there were several interruptions but, even so, a large amount of data was recorded (sensors were set up to a frequency of data acquisition of 100 Hz). More details of instrumentation are given in Appendix II. Three major storms were examined, with waves of maximum height larger than 6m:

- On December 26, 2008 an east-northeast anticyclonic storm hit the Barcelona coast. Although there was no instrumented record of characteristic waves, journalistic reports indicated that significant wave heights of 4 m and maximum wave height of 6m occurred at the Barcelona harbour. As a reference, maximum waves height of 9m with 10 s period were recorded at Golf of Roses, north of Barcelona (see Figure 5-30).

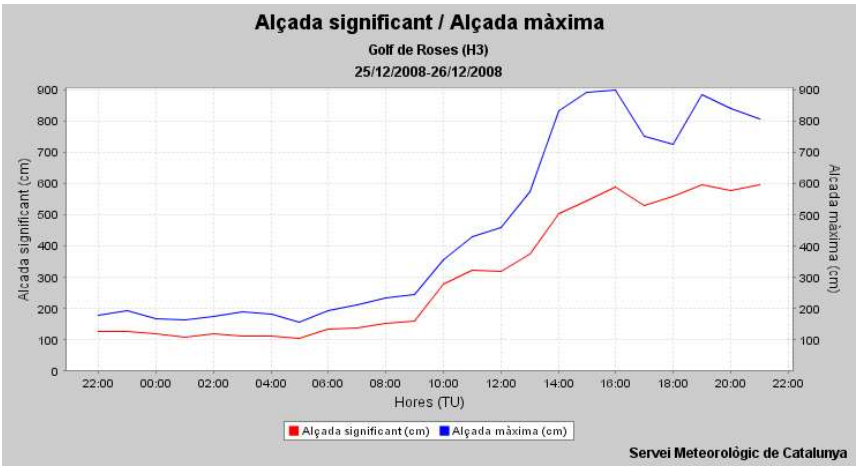

Figure 5-30. Significant and maximum waves height at Golf of Roses, December 26, 2008.

- On December 14, 2009 an intense polar wind from the west and warm ocean surface waters with anomalies of up to 2 °C, generated a storm with a maximum wave height of 6.0m and significant waves of 4m, as recorded at the buoy at the Port of Barcelona.
- Finally, a third storm was recorded at the Port of Barcelona on January 07, 2010 with maximum waves height of 6m and a significant wave height of 3.5m.

Figure 5-31 shows the time history data record on sensors 4 (section A and B) at the wall of the caisson, during the storm of December 26, 2008. When the storm releases the most energy, pressure cycles from 0 to 90 kPa are observed. The violence of the storm was of such magnitude that flooded the data center installed in the harbour lighthouse and caused damage to all systems, so the data recording was truncated before midnight. However, even so, it was possible to show clear evidence of the increase in pore pressures as a response to the cyclic load caused by the storm. All the piezometers installed in the foundation soil recorded a continuous increase in pore pressures during a period of approximately 8 hours of maximum wave attack. The dominant wave period was computed to be 14s.

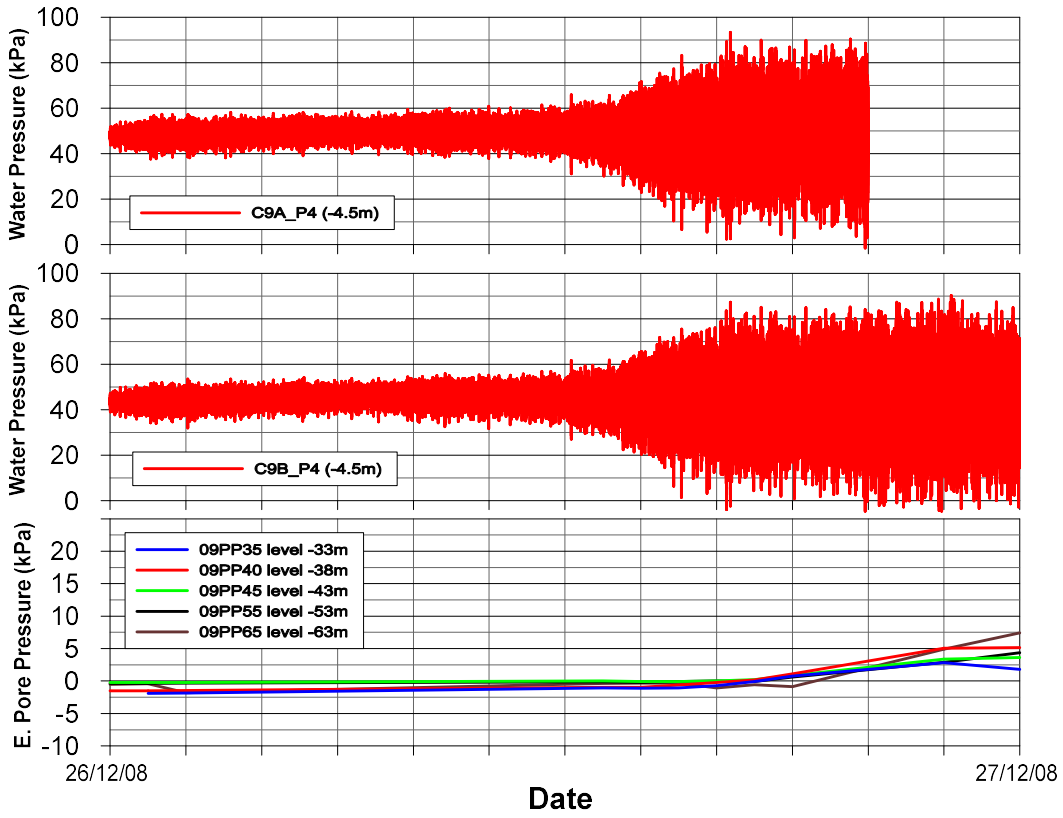

Figure 5-31. Time history record of water pressure at sensor 4 and excess pore pressure measured at foundation, storm of 25 December, 2008.

Data recording from the storm of December 2009 is shown in Figure 5-32. Although the duration of waves breaking is clearly longer than the storm that occurred one year before, in this case, no accumulated pore pressures at the foundation level were observed. Different characteristics of the storms are probably the main reason for this behaviour. When the storm is fully developed, for about 12 to 14 hours, peaks of pressure cycled between 20 to -20 kPa, with some local peaks of 30kPa. However, they do not seem to produce enough energy to develop pore pressures at the foundation.

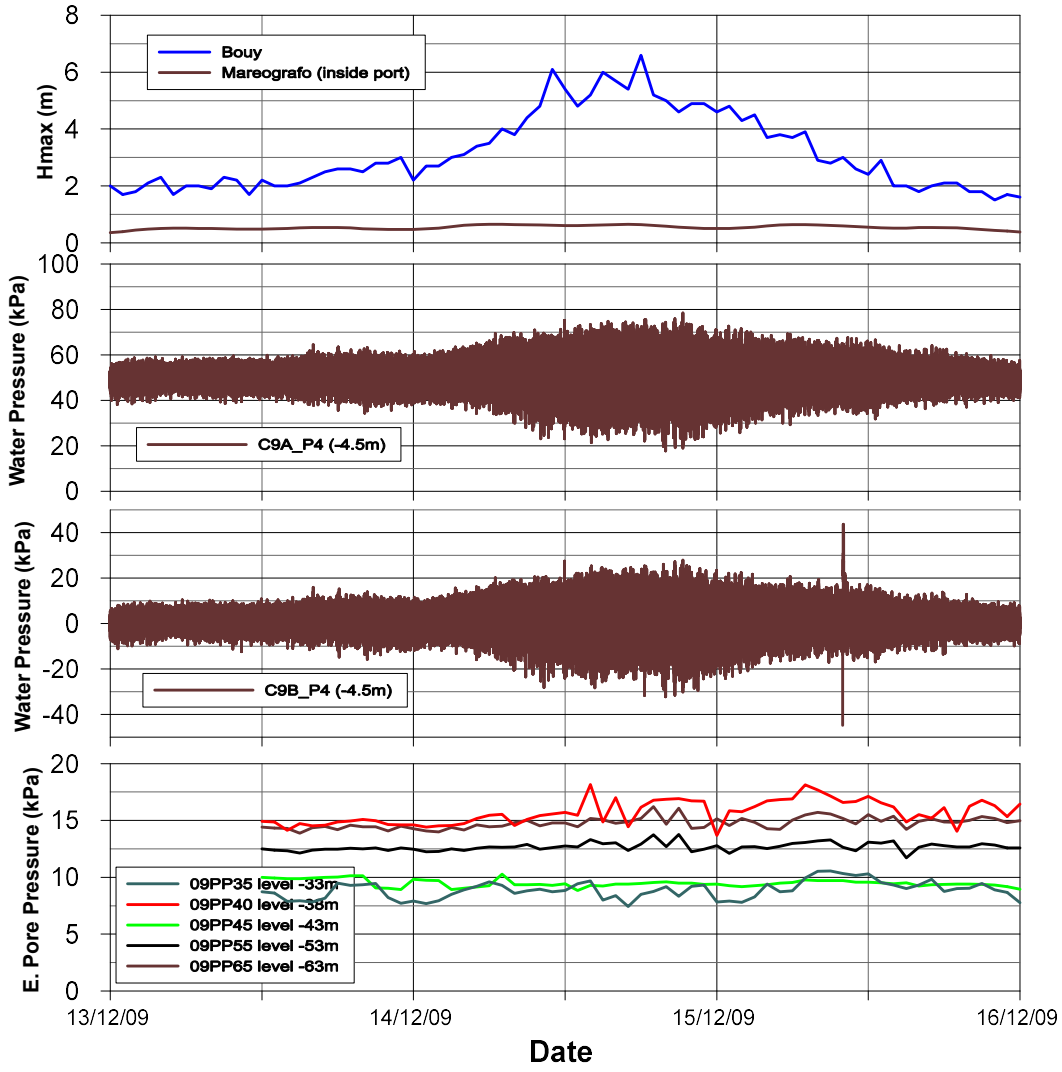

Figure 5-32. Time history record of pore pressure at sensor 4 and excess pore pressure measured at the foundation, storm of 14 December, 2009.

Finally, the time history record of the January 2010 storm is shown in Figure 5-33. It is clear that this storm shares some characteristic with the previous storm, reaching peaks of pressure of 20 kPa, but progressively reducing to 10 kPa as the storm develops, which turns out to be insufficient to generate pore pressures at the foundation.

To distinguish the characteristic shape of waves, a 100 second sector of the data is extracted from each wave record and shown in Figure 5-34. The sinusoidal shape is observed in all records, where the storm of 2008 clearly carries more energy compared to the other two records. The dominant period of wave propagation seems to be in direct proportion to the energy it transmits. For the case of the 2008 storm, it is about 12 to 14 seconds, while for the 2010 storm it is about 8 seconds. In the case of the 2009 storm, a clearly dominant period of wave front is not shown, but it ranges from 7 to 12 seconds. This is also corroborated in the Fourier spectrum shown in Figure 5-35, where a different frequency content is observed in the 3 wave records.

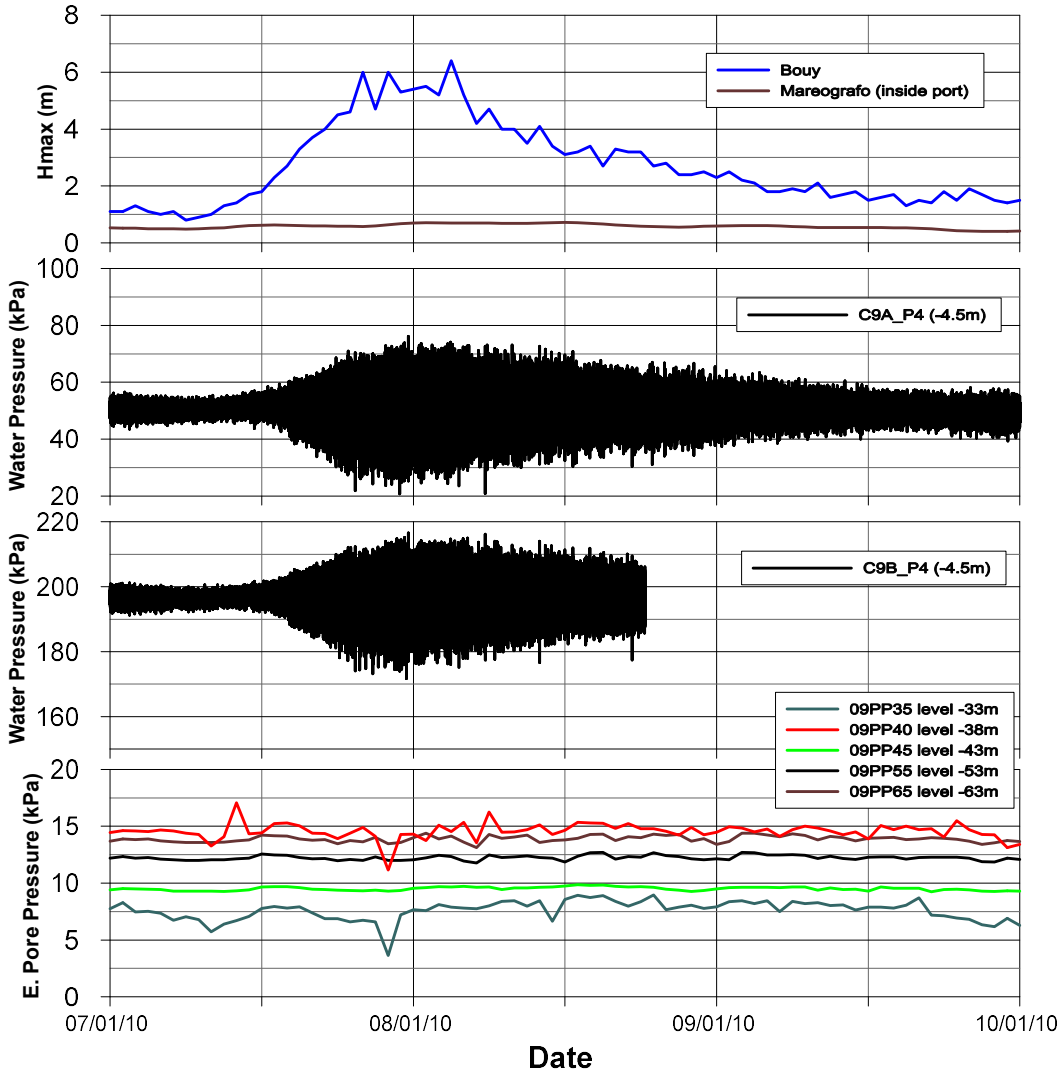

Figure 5-33. Time history record of pore pressure at sensor 4 and excess pore pressure measured at foundation, storm of January 8, 2010.

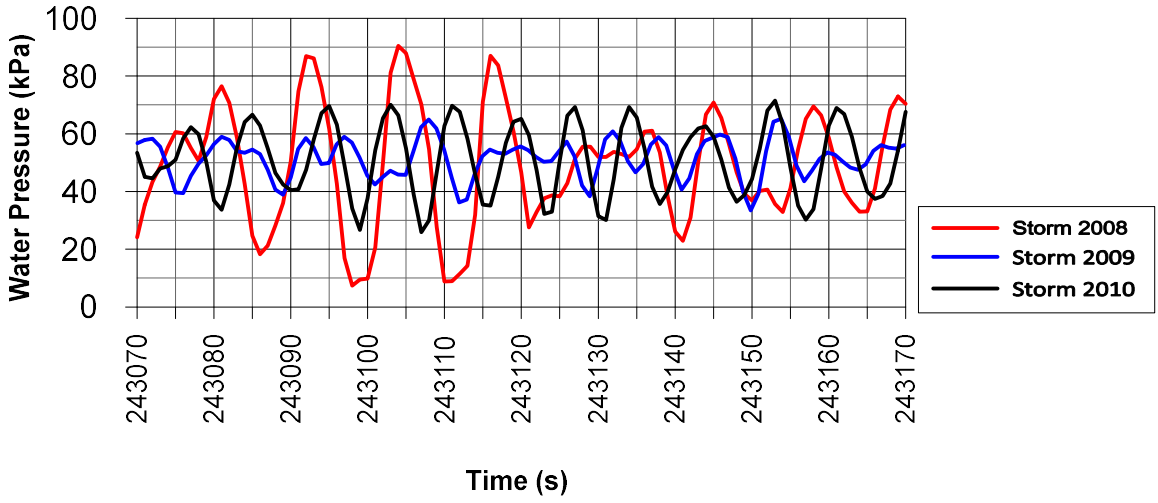

Figure 5-34. Comparison of 100 seconds of wave pressures recorded on sensor 4, corresponding to three storms.

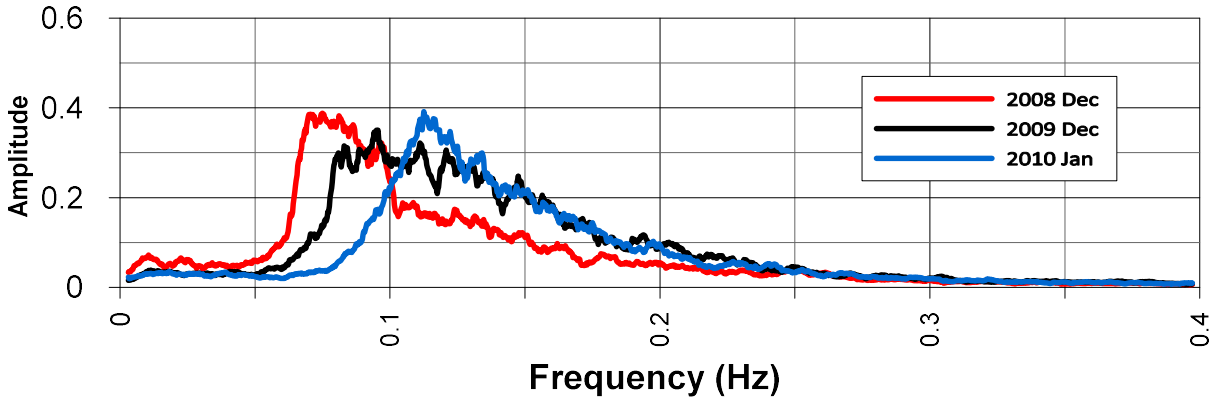

Figure 5-35. Normalized Fourier spectrum of three storms.

The distribution of water pressures due to the impact of sea waves on the caisson is a fundamental parameter to analyse the stability of a breakwater. To estimate the wave load, the traditional Goda formula or the more recent formula proposed by Oumeraci et al (2001) is usually used (see section 2.2.2). However, under certain conditions, these formulas present uncertainties, requiring the use of physical scale models, or in-site instrumentation. In the case of the Port of Barcelona, scale models were made and a caisson was also instrumented so that it was possible to assess the wave loads for subsequent stability analyses.

Figure 5-36 shows the envelope of the maximum and minimum pressure of the waves during the 2008 storm, and it is compared with the pressure calculated with the Goda formula, which in this case was more conservative. The appearance of impact waves at a level of + 3 m is also observed, not considered with the Goda formula. Finally, up-lift pressures values were also recorded at the base of the caisson, in this case Goda's formula also exceeds the measurements.

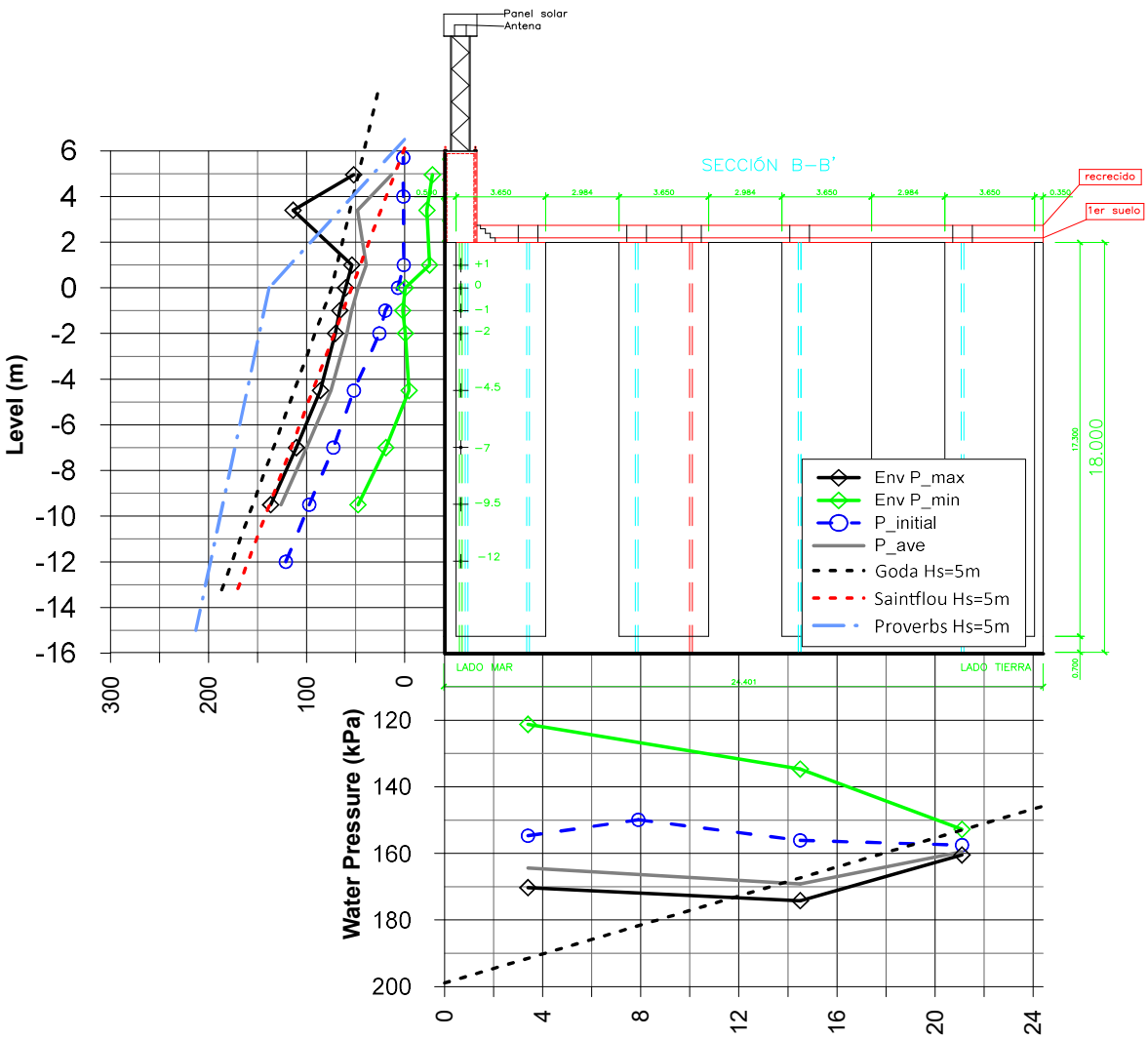

Figure 5-36. Water pressures at the wall and base of the caisson 9, during the 2009 storm.

5.6 CONCLUSIONS

Geotechnical instrumentation for monitoring the performance of a breakwater built on soft soils has proven to be a valuable tool for assessing the progress of consolidation and providing confidence during construction, confirming (or refuting) the soil parameters used at each stage of the project. In this way, if necessary, the soil parameters can be adjusted and the work schedule modified.

A considerable amount of laboratory information was acquired for the deltaic soft clay deposits prior to the construction of the breakwater. Physical characteristics and engineering properties were investigated through extensive laboratory tests conducted at the UPC, NGI, and CEDEX. These include direct simple shear tests, unconfined compression tests and consolidated undrained (CIU) triaxial tests. Laboratory dynamic tests and oedometer consolidation tests were also carried out. A summary of the undrained shear-strength and compressibility characteristics are illustrated in Figure 5-11 and Figure 5-12, respectively. Even when much information is available regarding strength and consolidation parameters from laboratory tests and site investigation, there will always be a high level of uncertainty on soil

properties (due in part to the spatial variability of soil properties) especially those related to the rate of settlement or consolidation, which are essential to assess the increase in resistance of the ground, during each of the construction stages of the project. For this reason, in the case of constructions on soft soils, it is essential to have an instrumentation system that provides continuous monitoring of the significant design parameters.

In the context of the Barcelona breakwater construction project, it was decided to implement an instrumentation system that would allow monitoring the progress of the consolidation of the foundation soil during the construction of the breakwater. The design, installation and maintenance of the instrumentation became a great challenge since there was no previous experience on breakwater instrumentation in these unfavourable offshore conditions. Traditional installation methods of drilling boreholes and grouting operations were discarded because weather conditions make these operations very difficult to perform, and the soil conditions were too weak to use jack-up platforms. An innovative technique of installing the sensors was used, which consists of pushing a casing containing the chain of instruments into the ground until the required depth is reached. This installation method is similar to that used for installing prefabricated vertical drains. Indraratna et al (2015) suggests that during the installation, the penetration and subsequent removal of the steel mandrel disturb the surrounding soil, changing the permeability and compressibility of the soft clay within a smear zone that finally affects the soil consolidation properties. The data recorded in the piezometers installed deeper, where a very slow or almost zero dissipation of pore pressures was observed, seems to corroborate what Indraratna et al (2015) indicated. Although other authors (DiBiagio, 1977 and Dunnicliff, 1993) suggest that the retarded trends in pore water pressure can also be attributed to filter clogging over time, cavitation, chemical alteration or acid corrosion of the filter itself, and electroosmotic effects in certain marine soils. Also, more recently Indraratna et al (2017) observed similar trends in VW piezometers installed around the Australian northern and eastern coastal belt that is predominantly affected by Acid sulphate soil (ASS) conditions where oxidisable pyrite layers cause filter clogging.

The slow dissipation of pore pressures observed in the instrumentation of breakwaters at the Port of Barcelona is however most likely to be explained by a great disturbance of the soil during the installation process; this disturbance seems to be more pronounced at depth where the soil offers more resistance to mandrel penetration. This hypothesis is reinforced by the results obtained with second instrumentation placed in the same position as the initial one, but this time installed by the traditional method, drilling from the top of already installed caissons, a procedure that clearly disturbs the ground less. With this new instrumentation, pressure dissipation was observed continuously in all piezometers as can be seen in Figure 5-14.

The measurements obtained with the instrumentation (pore pressures and settlements) were interpreted using the classical theory of one-dimensional consolidation, extended for the case of time-dependent loads by Olson (1977). The model allows the calculation of pore pressures and settlements caused by a

sequence of loading steps, as is to be expected in the case of staged construction in soft soils. In an attempt to better reproduce the expected stress conditions under embankments and improve the model predictions, the load influence factor concept obtained from elastic theory was incorporated in the model. The load influence factors improved the predictions of pore pressures under the breakwater, which is especially noticeable during the caisson placement stage (see Figure 5-14). Noted that the model parameters were back-calculated using the field data from section 1 of instrumentation (Figure 5-13) and then the same parameters were used to predict pore pressure in sections 2, 3 and 4, reaching a good fit to the measured pore pressure in all cases. The prediction could be further improved by changing the drainage distance of the model.

In the case of settlement predictions, when load influence factors were included in the model, the results were not so good. The short-term prediction overestimates the settlement. But this response could be improved during the early loading stages by introducing a light overconsolidation condition of the soil (expected after dredging works). On the contrary, the long-term settlements are underestimated with the model. But also, in this case, the model's predictions could be easily improved by introducing a secondary consolidation settlement component. The secondary compression may produce a significant increase in settlements long after the primary consolidation is over.

In conclusion, even with a simple consolidation model, a reasonable prediction of pore pressure and rate of settlements can be achieved using back-calculation parameters from instrumentation data, something that can hardly be achieved using laboratory tests. Soil compressibility and strength can be reasonably estimated through laboratory tests or field tests, but, as has been shown (Figure 5-37), the values of consolidation coefficients obtained from laboratory tests are considerably lower than those obtained by instrumentation (at least one order of magnitude lower), this being a key parameter to control a staged construction project on soft soils.

On the other hand, in several numerical and laboratory studies it has been reported that the cyclic action of waves generates pore pressures in the subsoil of breakwaters (Elsafti and Oumeraci, 2016; Ulker et al, 2009; Jeng and Li. 2006, Stickle et al, 2013) which sometimes produces soil liquefaction, mainly in sandy-type soils. However, under certain conditions, the same phenomenon is also expected to occur in fine-grained soils. In any case, this phenomenon had not been recorded before in real site conditions during the occurrence of a storm. The data recorded by the instrumentation of the caissons together with the instrumentation of the foundations during the December 2008 storm in Barcelona, show that under certain storm conditions (periods of 14s, cyclic pressures on the wall of the dyke of about 80kPa), residual pore pressures are generated in clay soils. However, these pressures were of a small magnitude that did not reach to endanger the stability of the breakwater.

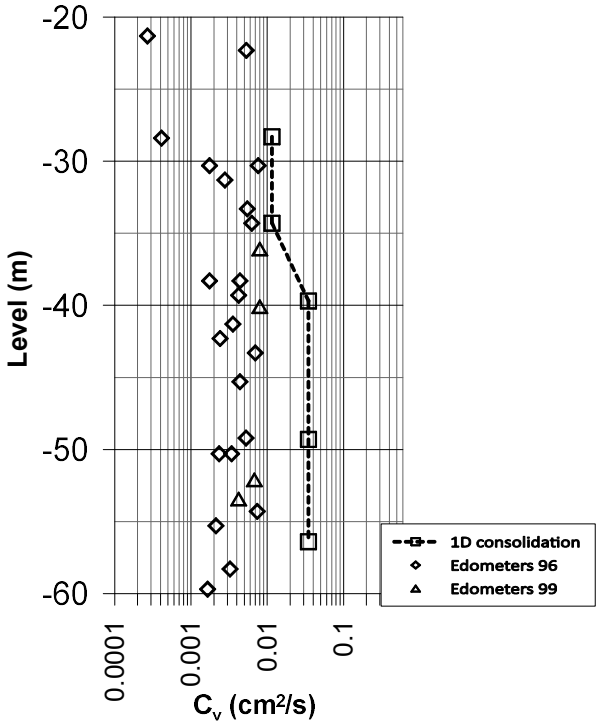

Figure 5-37. Coefficient of consolidation from laboratory tests and back-analysed from the instrumentation

Chapter 6

MODELLING THE PERFORMANCE OF THE BARCELONA BREAKWATER

6.1 INTRODUCTION

The modelling of geotechnical structures such as breakwaters built on soft soils presents some complexities. First, the stress-deformation behaviour of soft soils is quite complex because the behaviour of natural soil is influenced by different characteristics such as anisotropy, creep and destructuration. On the other hand, once the construction phase on the soft ground has been completed and the stability of the breakwater has been assured, the breakwater must be able to withstand dynamic actions caused by the seawaves, adding additional complexity.

Therefore, a breakwater project has three aspects to be evaluated: (i) the evolution of the pore pressure and deformations with time and long-term deformations (ii) safety against failure of the breakwater and foundation soil during construction and post-construction and (iii) response of breakwaters under cyclic loading during storms.

The development of constitutive models has allowed numerical simulations to become more realistic, especially in the field of embankments. Several studies suggest that good approximations to settlements can be achieved with relatively simple models, whereas, to reproduce pore pressures and horizontal displacement properly, it is necessary to use more advanced models, which include some characteristics such as anisotropy, creep or soil destructuration (Tavenas and Leroueil, 1980; Almeida et al., 1986; Ladd et al, 1994; Karstunen et al., 2006). Similar conclusions have also been obtained in numerical simulations of breakwaters using the modified Cam Clay model (Brugger et al., 1998; Chung et al., 2006). Contributions of advanced models to breakwater simulation are explored in this chapter. The South breakwater behaviour has been analysed with different constitutive models for the clayey foundation soil: the isotropic Soft Soil model (SS), the more advanced anisotropic model SClay-1 and the Soft Soil Creep model (SSC) to simulate the long-term settlement of vertical breakwater. Numerical analysis was performed using a fully coupled elasto-plastic finite element analysis for a comparison with the monitored vertical and horizontal displacements and pore water pressures during the construction process. Performance is described based on these measurements and the soil parameters from the ground investigation have been re-evaluated.

The second part of this chapter deals with the behaviour of the dike against the action of cyclic loads caused by storms. The dike instrumentation system allowed the recording of different events over a 3-year period, the largest being the one that occurred in December 2008, which was finally selected to evaluate the dike response. Full dynamic finite element analysis was carried out using the UBC3D-PLM model implemented in the Plaxis code and calibrated under a conservative criterion based on the results of laboratory tests.

Safety against the failure of the breakwater under static or cyclic loads is investigated in the next chapter.

6.2 PERFORMANCE UNDER STATIC LOADS (CONSTRUCTION AND POST-CONSTRUCTION)

6.2.1 Model geometry and boundaries

All the sections instrumented in the south breakwater were simulated. Although Section 1 corresponds to a rubble mound type breakwater, it was the first instrumented section that provided data on the initial stages of construction and therefore was key to establishing the appropriate consolidation times that would allow safe construction. The height of the breakwater at this location is about 26 m, and it is 38 m to the crown of the superstructure. Breakwater geometry of Sections 2 to 4 is the same, with a concrete caisson 24.4m wide and 18m high founded over a large embankment 160m long and about 10m high. The difference between these sections is mainly the construction sequence as explained later.

The foundation soil was assumed to have a permeable rigid boundary at a depth of about 80 m, where a thick layer of gravels was found in the geotechnical investigation campaign. The lateral boundary of the seabed soil was located at a distance of 160 m beyond the embankment toe on the port side and 170 m beyond the toe of the berm on the seaward side to minimise its influence on the results. Permeable boundary conditions were assumed in the analyses at these two limit boundaries of the finite element mesh.

The finite element meshes used in the analysis are presented in Figure 6-1 to Figure 6-4. All breakwater sections were discretized with the 15-noded plane strain triangular elements with 12 Gauss points. This type of element was used in reason of the better ability to simulate the collapse of undrained material (Sloan,S.W. & Randolph, M.F. 1982; De Borst, R. & Vermeer,P.A. 1984). By default, Plaxis generate an unstructured mesh, numerical performance of such meshes is usually better than regular structured meshes to predict the collapse of soil.

In all the analyses, the interfaces between the embankment with the concrete caisson and the backfill materials with the caisson were modelled with nodal compatibility joint elements, assumed to be elastic-plastic and non-dilatant (i.e., $\psi = 0$). The Coulomb criterion is used to distinguish between elastic behaviour, where small displacements can occur within the interface and plastic interface behaviour when permanent slip may occur.

For stability analysis, the uplift force generated during the action of the wave load was considered in the model as a triangular distribution of pressures under the caisson. Physical models of the dike (INHA, 2000) and the hydrodynamic instrumentation described earlier corroborate this approximate shape.

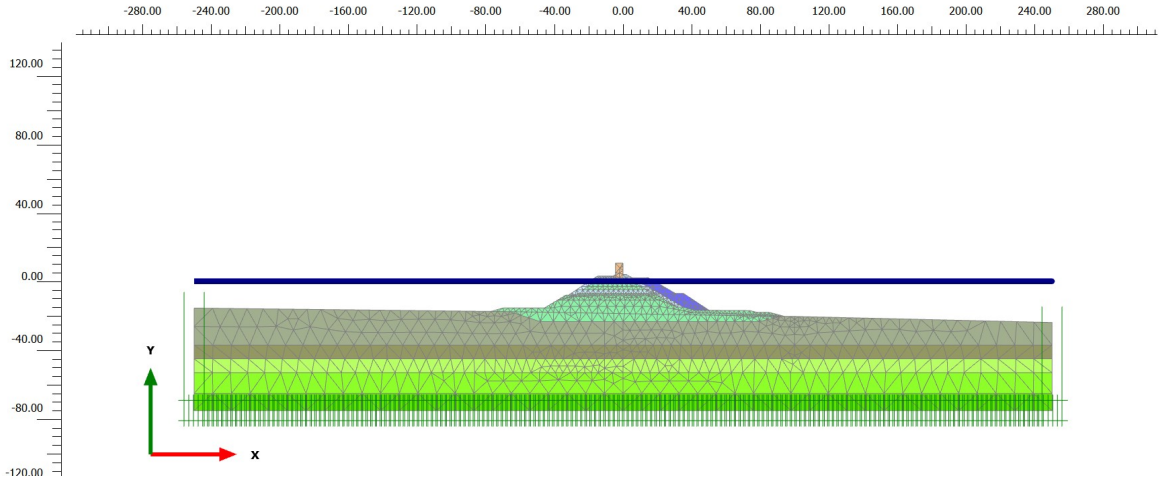

Figure 6-1. Geometry model and finite element mesh of breakwater Section 1

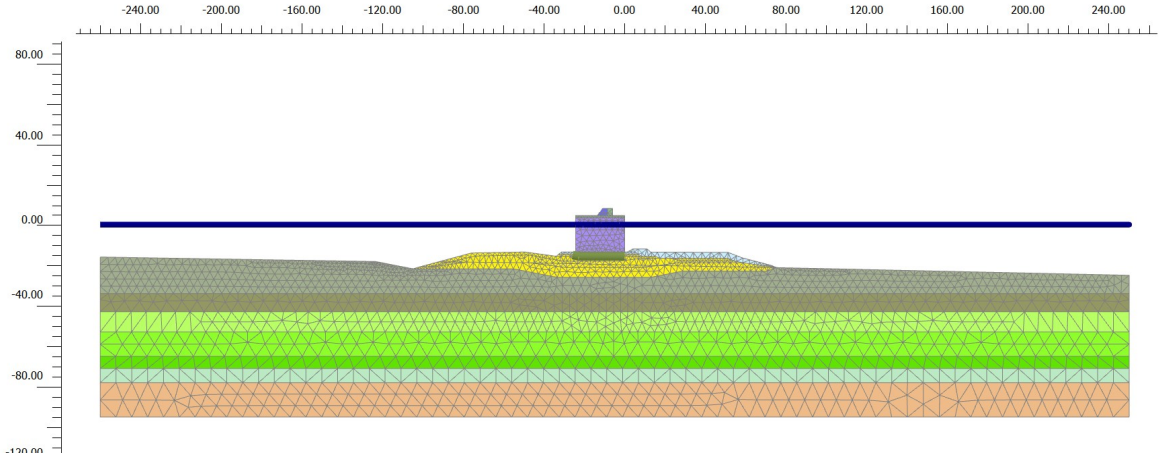

Figure 6-2. Geometry model and finite element mesh of vertical breakwater Section 2

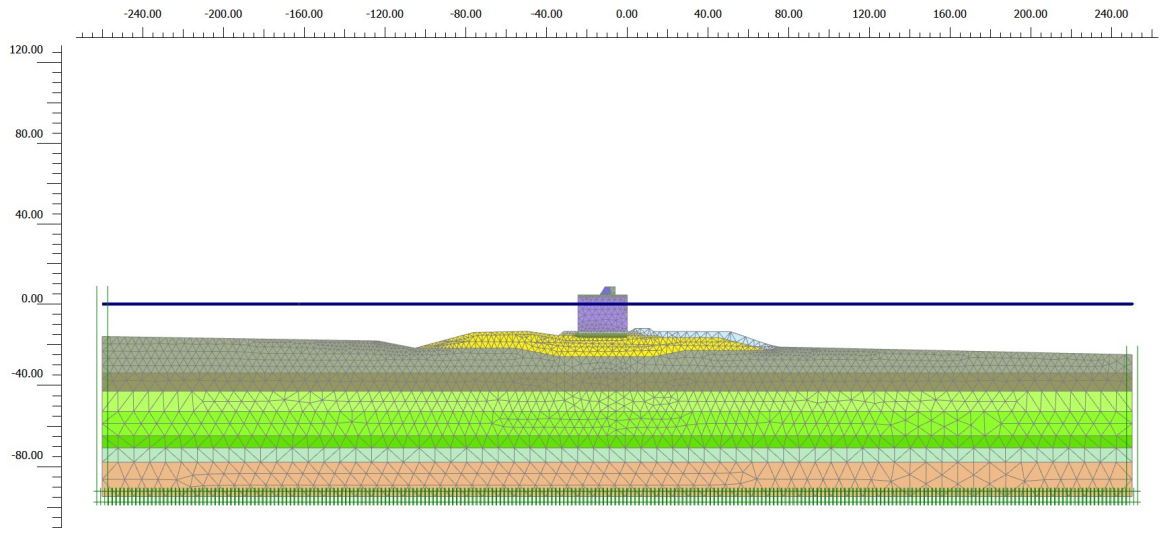

Figure 6-3. Geometry model and finite element mesh of vertical breakwater Section 3.

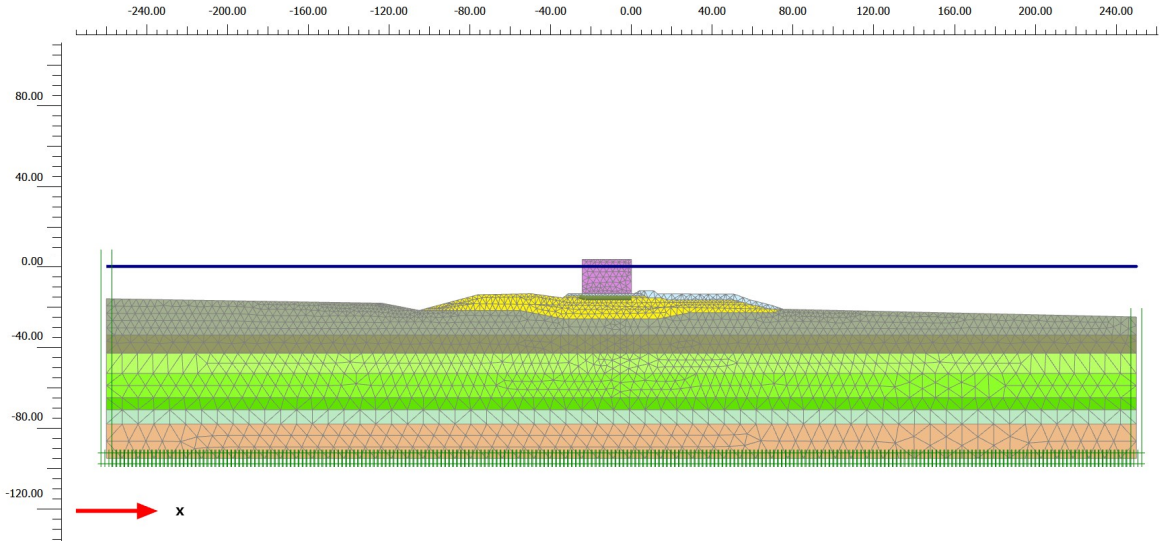

Figure 6-4. Geometry model and finite element mesh of vertical breakwater Section 4.

6.2.2 Materials properties for the analysis

The upper layer of silts and clays was divided into 5 sublayers, associated with the position of the piezometers in Section 2, so that it would be easier to adjust the permeability of the soil to reproduce the measured pore pressure dissipation. The simulations began with a permeability k = 8.64×10^{-4} m/d, the same that was used in the simulations of the laboratory tests (Chapter 4). This permeability value was successively adjusted until the best fit between calculated and measured pore pressures were achieved. The final value of permeability was 2.5 to 5 times higher than the initial value (Table 6-1). Account for the change of permeability due to variations in void ratio during the dissipation analysis was considered according to the formula:

$$\log\left(\frac{k}{k_0}\right) = \frac{\Delta e}{c_k} \tag{6.1}$$

A proper value to c_k-parameter is generally in the order of the compression index C_c as suggested by Brinkgreve et al (2017). In this case, c_k value of 0.15 was adopted for all sublayers.

Numerical simulation of CAU Triaxial and Simple Shear tests were carried out to reproduce the undrained strength relation in the best way possible (see chapter 4). Parameters indicated in the Table 6-1 are required for the Soft Soil model to reproduce the undrained strength ($s_u = 0.25\sigma'_v$) in the simple shear mode of failure, which was considered the dominant mode of shear under the breakwater. Compressibility parameters were also adjusted to better approximate the deformation response observed by the instrumentation. Also, the soil parameters used with the S-Clay1 model are shown in Table 6-2 and for the case of the SSC model the parameters are indicated in Table 6-3.

Table 6-1. Material parameters of Soft Soil model

Material	γ_{unsat} [kN/m^3]	γ_{sat} [kN/m^3]	c [kN/m^2]	ϕ [°]	ψ [°]	λ^*	κ^*	e	K [m/d]
Upper Soft clay 1	18.5	18.5	1.0	20.0	0.0	0.060	0.012	1	$3.32\text{x}10^{-3}$
Upper Soft clay 2	18.5	18.5	1.0	20.0	0.0	0.060	0.012	0.85	$4.32\text{x}10^{-3}$
Upper Soft clay 3	18.5	18.5	1.0	20.0	0.0	0.060	0.012	0.80	$4.32\text{x}10^{-3}$
Upper Soft clay 4	18.5	18.5	1.0	20.0	0.0	0.060	0.012	0.72	$4.32\text{x}10^{-3}$
Upper Soft clay 5	18.5	18.5	1.0	20.0	0.0	0.060	0.012	0.68	$2.16\text{x}10^{-3}$
Lower Soft clay	18.5	18.5	1.0	20.0	0.0	0.060	0.012	0.60	$2.16\text{x}10^{-3}$

Table 6-2. Material parameters of S-Clay1S model.

Model	**γ_{unsat} [kN/m^3]**	**γ_{sat} [kN/m^3]**	**κ**	**ν**	**λ**	**M**	**μ**	**β**	**a**	**b**	**e_0**	**α_0**	**x_0**	**k [m/d]**
Upper Soft clay 1	18.5	18.5	0.016	0.20	0.08	0.772	100	0.76	0	0	1.0	0.46	0	$3.32\text{x}10^{-3}$
Upper Soft clay 2	18.5	18.5	0.016	0.20	0.08	0.772	100	0.76	0	0	0.85	0.46	0	$4.32\text{x}10^{-3}$
Upper Soft clay 3	18.5	18.5	0.016	0.20	0.08	0.772	100	0.76	0	0	0.80	0.46	0	$4.32\text{x}10^{-3}$
Upper Soft clay 4	18.5	18.5	0.016	0.20	0.08	0.772	100	0.76	0	0	0.72	0.46	0	$4.32\text{x}10^{-3}$
Upper Soft clay 5	18.5	18.5	0.016	0.20	0.08	0.772	100	0.76	0	0	0.68	0.46	0	$2.16\text{x}10^{-3}$
Lower Soft clay	18.5	18.5	0.016	0.20	0.08	0.772	100	0.76	0	0	0.60	0.46	0	$2.16\text{x}10^{-3}$

Table 6-3. Material parameters of Soft Soil Creep model

γ_{unsat} [kN/m^3]	γ_{sat} [kN/m^3]	e	$k_x=k_y$ [m/day]	λ^* [-]	κ^* [-]	μ [-]	ν [-]	M [-]	C [kPa]	Φ [°]	ψ [°]
18.5	18.5	3.32e-3	3.32e-3	0.08	0.004	0.0015	0.15	1.214	1	20	0
18.5	18.5	4.32e-3	4.32e-3	0.058	0.004	0.0012	0.15	1.214	1	20	0
18.5	18.5	4.32e-3	4.32e-3	0.046	0.005	0.001	0.15	1.214	1	20	0
18.5	18.5	4.32e-3	4.32e-3	0.039	0.002	0.8e-3	0.15	1.214	1	20	0
18.5	18.5	2.16e-3	2.16e-3	0.039	0.002	0.8e-3	0.15	1.214	1	20	0
20	20	2.16e-3	2.16e-3	0.039	0.002	0.8e-3	0.15	1.214	1	20	0

Embankment and rockfill material parameters were assumed based on local experience. An elasto plastic Morh-Coulomb model was chosen to represent behaviour of these materials. Table 6-4 shows the parameters assumed. Certainly, strength parameters, especially those corresponding to the embankment, have an influence on the final stability of breakwater.

Table 6-4. Embankment and rockfill parameters (Mohr-Coulomb model)

Material	γ_{unsat} [kN/m^3]	γ_{sat} [kN/m^3]	μ [-]	E [kN/m^2]	c [kN/m^2]	ϕ [°]	ψ [°]
Embankment	20.0	20.0	0.30	$20\cdot10^3$	1.0	38.0	0.0
Rockfill	20.0	20.0	0.30	$20\cdot10^3$	1.0	45.0	0.0

The caissons were modelled as elastic material; for this case the unit weight was observed to have a larger influence on breakwater stability than Young modulus. A comprehensive analysis, which included testing of cell fills material, calculation of the cell voids, was done by the contractor to determine the unit weight of the caissons. Table 6-5 shows the best approximation to these parameters.

Table 6-5. Caissons concrete parameters (elastic model)

Material	γ_{unsat} [kN/m^3]	γ_{sat} [kN/m^3]	μ [-]	E [kN/m^2]
Caisson	19.8	19.8	0.25	$2\cdot10^6$

6.2.3 Phases of computation

The construction phases considered in the numerical model are shown in Table 6-6 to Table 6-9. To define the construction process of each section, the periodic bathymetric surveys of the embankment performed as the construction progressed were used. The actual construction times were considered in the analysis.

Table 6-6. Phases of construction consider in the numerical model. Section 1

Phase	Identification	Calculation	Time (days)
0	Initial phase	Plastic + self-weight	-
1	Dredged	Consolidation	-
2	Dumping 1, el. -18.7m	Consolidation	26
3	Consolidation	Consolidation	22
4	Dumping 2, el. -14.5m	Consolidation	11
5	Consolidation	Consolidation	46
6	Dumping 3, el. -10.9	Consolidation	5
7	Consolidation	Consolidation	47
8	Dumping 4, el. -6.7m	Consolidation	7
9	Consolidation	Consolidation	98
10	Winter protection, el. -5m	Consolidation	23
11	Consolidation	Consolidation	170
12	Dumping 5, el. -3m	Consolidation	10
13	Consolidation	Consolidation	52
14	Dumping 6, el. +2.1m	Consolidation	33
15	Consolidation	Consolidation	49
16	Dumping 7, el. +10.5m	Consolidation	8
17	Consolidation	Consolidation	3806

Table 6-7. Phases of construction consider in the numerical model. Section 2

Phase	Identification	Calculation	Time
0	Initial phase	Gravity	-
1	Dredged	Plastic	-
2	Dumping 1	Consolidation	31
3	Consolidation	Consolidation	20
4	Dumping 2	Consolidation	11
5	Consolidation	Consolidation	51
6	Dumping 3	Consolidation	13
7	Consolidation	Consolidation	43
8	Dumping 4	Consolidation	21
9	Consolidation	Consolidation	36
10	Dumping 5	Consolidation	3
11	consolidation	Consolidation	45
12	Dumping 6	Consolidation	5
13	consolidation	Consolidation	40
14	Rockfill	Consolidation	11
15	consolidation	Consolidation	396
16	Caisson placement	Plastic	0
17	Caisson filling	Consolidation	65
18	consolidation	Consolidation	62
19	Caisson filling	Consolidation	13
20	consolidation	Consolidation	13
21	slab	Consolidation	98
22	consolidation	Consolidation	225
23	Crown wall	Consolidation	13
24	consolidation	Consolidation	1990

Table 6-8. Phases of construction consider in the numerical model. Section 3

Phase	Identification	Calculation	Time
0	Initial phase	Gravity	-
1	Dredged	Plastic	-
2	Dumping 1	Consolidation	45
3	Consolidation	Consolidation	10
4	Dumping 2	Consolidation	18
5	Consolidation	Consolidation	229
6	Dumping 3	Consolidation	8
7	Consolidation	Consolidation	70
8	Dumping 4	Consolidation	5
9	Consolidation	Consolidation	96
10	Dumping 5	Consolidation	1
11	consolidation	Consolidation	10
12	Dumping 6	Consolidation	5
13	consolidation	Consolidation	40
14	Rockfill	Consolidation	11
15	consolidation	Consolidation	198
16	Caisson placement	Plastic	0
17	Caisson filling	Consolidation	144
18	consolidation	Consolidation	5
19	Caisson filling	Consolidation	8
20	consolidation	Consolidation	182
21	slab	Consolidation	94
22	consolidation	Consolidation	225
23	Crown wall	Consolidation	13
24	consolidation	Consolidation	1730

Table 6-9. Phases of construction consider in the numerical model. Section 4

Phase	Identification	Calculation	Time
0	Initial phase	Gravity	-
1	Dredged	Plastic	-
2	Dumping 1	Consolidation	61
3	Consolidation	Consolidation	73
4	Dumping 2	Consolidation	18
5	Consolidation	Consolidation	94
6	Dumping 3	Consolidation	4
7	Consolidation	Consolidation	32
8	Dumping 4	Consolidation	30
9	Consolidation	Consolidation	36
10	Dumping 5	Consolidation	6
11	consolidation	Consolidation	45
12	Dumping 6	Consolidation	11
13	consolidation	Consolidation	40
14	Rockfill	Consolidation	11
15	consolidation	Consolidation	216
16	Caisson placement	Plastic	0
17	Caisson filling	Consolidation	20
18	consolidation	Consolidation	72
19	Caisson filling	Consolidation	93
20	consolidation	Consolidation	147
21	slab	Consolidation	83
22	consolidation	Consolidation	225
23	Crown wall	Consolidation	13
24	consolidation	Consolidation	1699

6.2.4 Initial stress state

Establishing the initial stress state in a boundary value problem is the first step in analysing the behaviour of a geotechnical structure. Although, in general, it seems an easy task, in practice it can be complex, because it is influenced by the weight of the material, the history of its formation and the history of fluctuation of ground water, data which are difficult to obtain precisely. All of them define the state of the soil and are expressed by the effective overburden pressure, the overconsolidation ratio (OCR) and the coefficient of earth pressure at rest (K_0), which is the ratio between the horizontal effective stress and the vertical effective stress for a condition of zero lateral strain. The effective overburden pressure and the overconsolidation ratio, OCR, play an important role in determining the engineering behaviour of sediments (Ladd & Foott, 1974).

There have been proposed several equations to calculate K_0 for different types of soil and different soil conditions, both normally and overconsolidated. However, in order to generate directly a stress field that is in equilibrium, it is needed that the soil surface, any soil layers and the phreatic water all be

horizontal. The most accepted equation for a normally consolidated soil was proposed by Jaky (1948) and related K_0 with the friction angle by: $K_0 = 1 - \sin\phi$.

In the context of the finite element Plaxis code, K_0 is based on Jaky's formula (1948) for soils defined as Mohr-Coulumb model. For advanced models like Soft Soil model, Hardening Soil model with small-strain stiffness or the Soft Soil Creep model, K_0 is based on K_0^{nc}, the Overconsolidation ratio (OCR) and the pre-overburden pressure (POP) as follows:

$$K_{0,x} = K_0^{nc} OCR - \frac{\nu_{ur}}{1-\nu_{ur}}\left(OCR - 1\right) + \frac{K_0^{nc} POP - \frac{\nu_{ur}}{1-\nu_{ur}} POP}{\left|\sigma_{yy}^0\right|} \qquad 6.2$$

For non-horizontal strata, the K_0 procedure should produce out of equilibrium stress state and therefore it is not recommended, in this case, the Gravity loading procedure should be used. In this procedure, the initial stresses are generated based on the self-weight of soil, ignoring the OCR and POP parameter, which must be included if needed, in later phases of computation. For Mohr-Coulomb materials the coefficient K_0 depends mainly on the Poisson's ratio, so care must be taken in assuming a Poisson's ratio to produce a realistic K_0 value. When advanced models are used the target K_0^{nc} value is defined before starting the calculation.

The initial stress state of the soil has an important influence in predicting settlement, horizontal displacement and the factor of safety (Fatahi et al, 2012). For this reason, a major effort should be taken to determine it. It is recommended to establish the initial in situ stress based on the use of field test and correlations developed for similar soils. In this investigation, we use oedometer tests and CPTu tests to estimate the preconsolidation pressure. Mayne and Kemper (1988) suggested the following relation with the CPTu tip resistance:

$$\sigma_p^{'} = 0.243\left(q_c\right)^{0.96} \qquad 6.3$$

Also, Kulhawy and Mayne (1990) suggested:

$$\sigma_p^{'} = k\left(q_t - \sigma_{v0}\right) \qquad 6.4$$

As indicated by Kulhawy and Mayne the factor *k* can be expected to range between 0.2 to 0.5, with the higher values of *k* recommended in aged or heavily overconsolidated clays. In this thesis the adopted value was k=0.33.

Figure 6-5 compares the values of preconsolidation pressure obtained in the oedometer tests with that obtained in the CPTu, also included in this figure is the overburden pressure. Oedometer tests show very low preconsolidation pressure, which could indicate incomplete consolidation. Consistent with the

appreciation of Fukuoka & Nakase (1973) that deltaic deposits are usually incompletely consolidated. On the other hand, the preconsolidation pressure obtained with the CPTu and FVT, shows a normally consolidated pattern with some interlayers showing stresses higher than the overburden pressure, probably due to sand or silty sand layers.

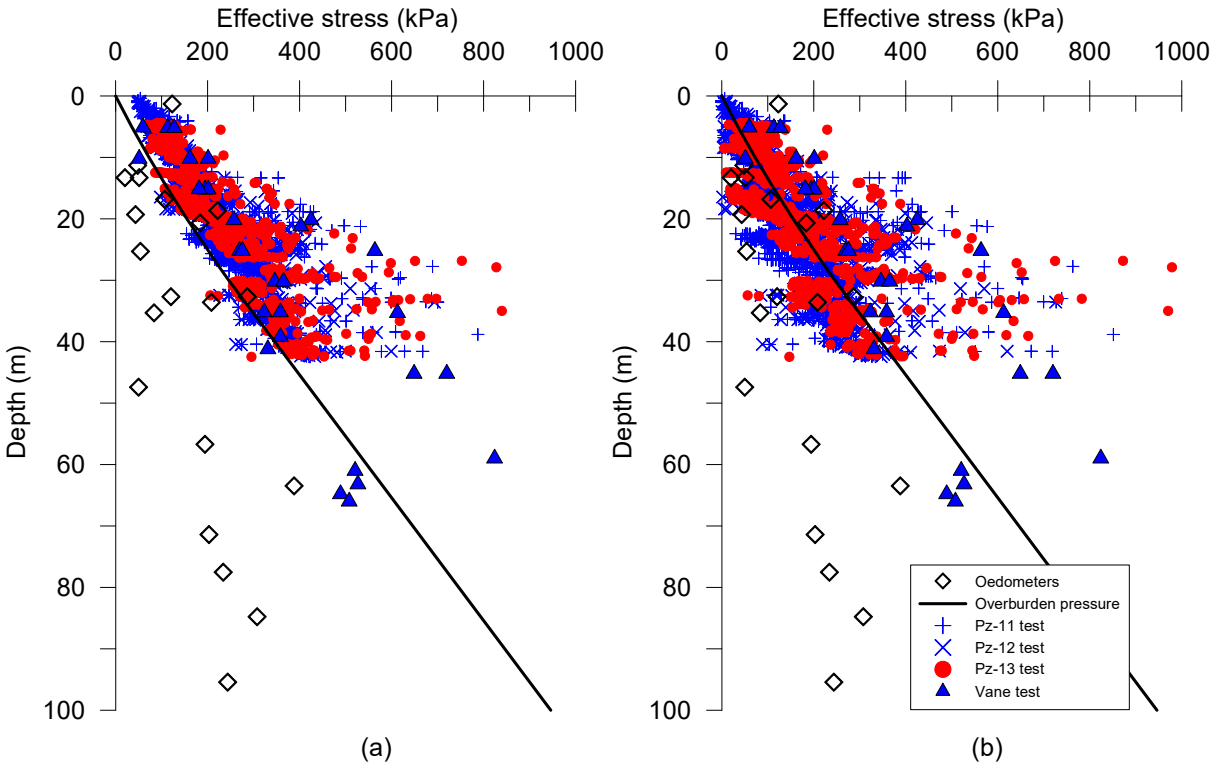

Figure 6-5. Preconsolidation pressure obtained in oedometer and CPTu tests. a) Mayne and Kemper, 1988 b) Kulhawy and Mayne, 1990

Finally, since the piezometers installed do not show anomalous records from the hydrostatic pressure, it was concluded that the foundation soil of breakwater was normally consolidated at the start of breakwater construction. All computations performed considerer the initial state as normally consolidated.

6.2.5 Results and discussion

Results from four different breakwater sections analysed are compared with the field measurements in this section. The isotropic SS model and anisotropic S-Clay1S model were used to simulated breakwater performance during construction and post-construction. Also, results from the simple theoretical consolidation model by Olson are included for comparison.

6.2.5.1 Section 1

Figure 6-6 shows the evolution of pore pressure with time calculated at different levels with the different models. The pore pressure records and the breakwater loading history are included in this figure. The

results of the simulations show good agreement mainly with the upper piezometers (levels -28.5, -34.7 and -40m). Although the dissipation rate observed during the initial loading stages is well reproduced with the models, it tends to decrease with each additional load increase. It is understood that this behaviour is the result of the reduction in permeability as a consequence of the decrease in the void ratio during the consolidation process. Although a rule of logarithmic variation of permeability was included in the models, it is clear that in the last loading stages, the models do not reproduce the dissipation ratio well. Especially noticeable is the very low pressure dissipation rate measured in the lower piezometer (levels -49.6 and 56.7m), which can hardly be followed by any model.

The predicted excess pore water pressure profile under the centreline of the breakwater at different times have been presented in Figure 6-7. As seen in this figure, the models' predictions were similar at a time immediately after construction was completed (607 days), but it overestimated the measured pore pressures. The SS and S-Clay1 models predict a maximum excess pore water pressure of about 140 kPa (at level -30m), while the measured pore pressure at this position was about 125kPa.

The results of both models show a dissipation rate higher than what the measured data shows, as observed in the consolidation period after construction was completed, in this case, the last data recorded is somewhat higher than the predicted values. It is also interesting to note that during the consolidation periods, the greatest differences were observed between the response of the two models, even when the permeability values of both models were equal, which would be explained by the different stiffness. Thus, after a period of 10 months of consolidation since the dike reached 18m in height (day 455), the values predicted by both models were different by about 10kPa. The results were not as good in relation to the lower piezometer, which shows almost no dissipation, possibly due to disturbance of the soil at that level, and in part to pore pressures generated by parallel construction loads carried out in different sectors of the project at the same time that cannot be simulated in a plane strain model.

Predicted settlements versus time at different nodes below the breakwater centerline are presented in Figure 6-8 for a 2-year consolidation time. The settlements predicted with the models show better agreement with the values measured at the lower levels (levels -50 and -57m). In all cases, the settlement predicted with the anisotropic S-CLAY1 model is greater than that calculated with the SS model. In the position immediately under the breakwater (level -23m), the difference is 11cm, while at greater depth this difference is reduced to 8cm. The isotropic SS model gives a lower estimate of about 2.40m for the final settlement, whilst the highest prediction of about 2.51m is given by the S-CLAY1 model. Interestingly, two models with very different shapes for the yield surfaces (SS and S-Clay1) coincidentally predict quite similar vertical deformations. It is noted that the SS model was calibrated with a realistic K_0 value, this parameter has a great influence on settlement predictions (Karstunen et al, 2006). Apparently taking into account anisotropy through a rotational hardening law (S-CLAY1), produces an increase in the predicted final settlement, which explains the higher settlement computed

with the anisotropic model. Furthermore, in the case of the incorporation of destructuration effects, the expected final settlement seems to increase even more (Karstunen et al, 2006).

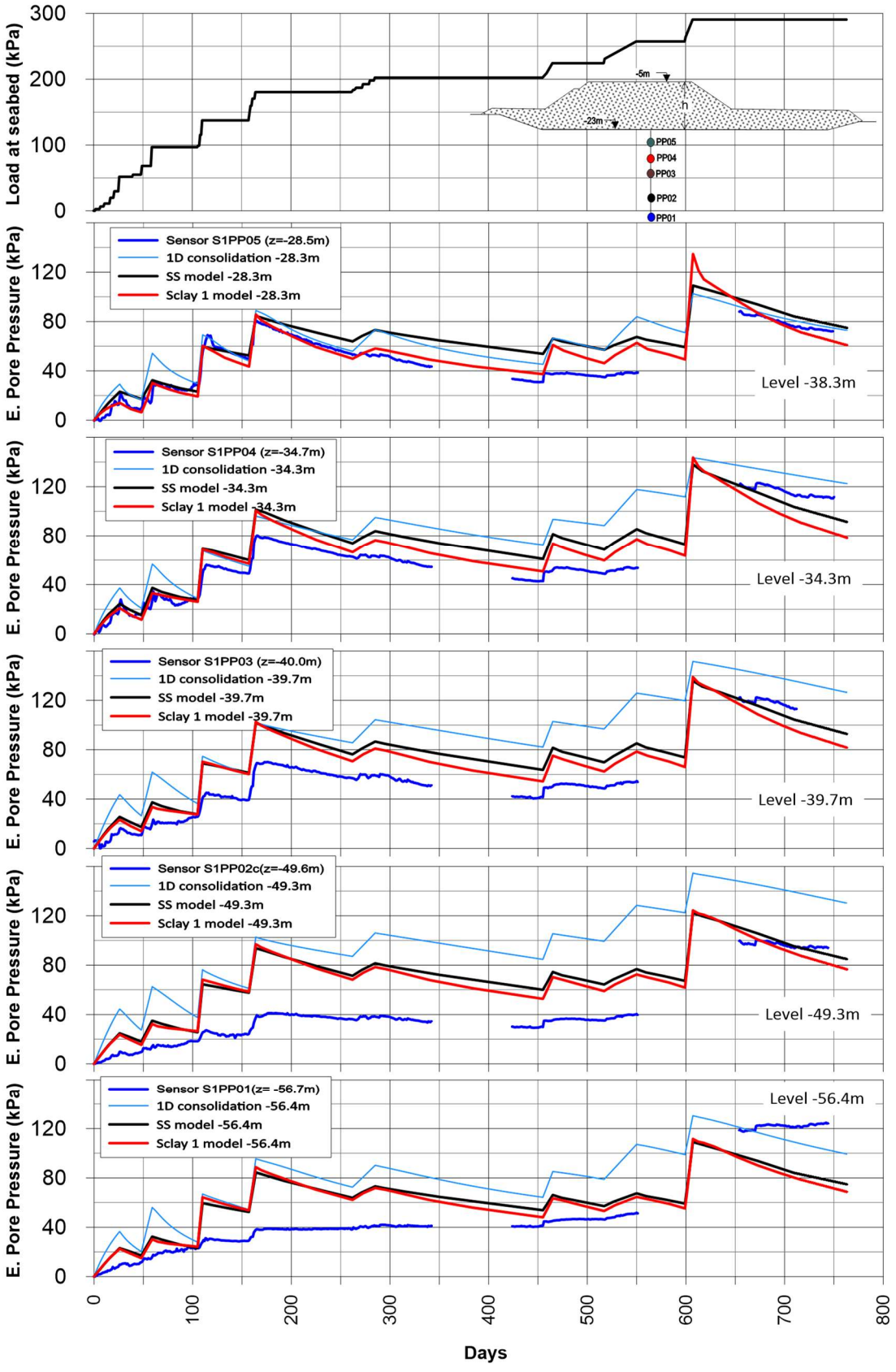

Figure 6-6. Pore pressure evolution with time

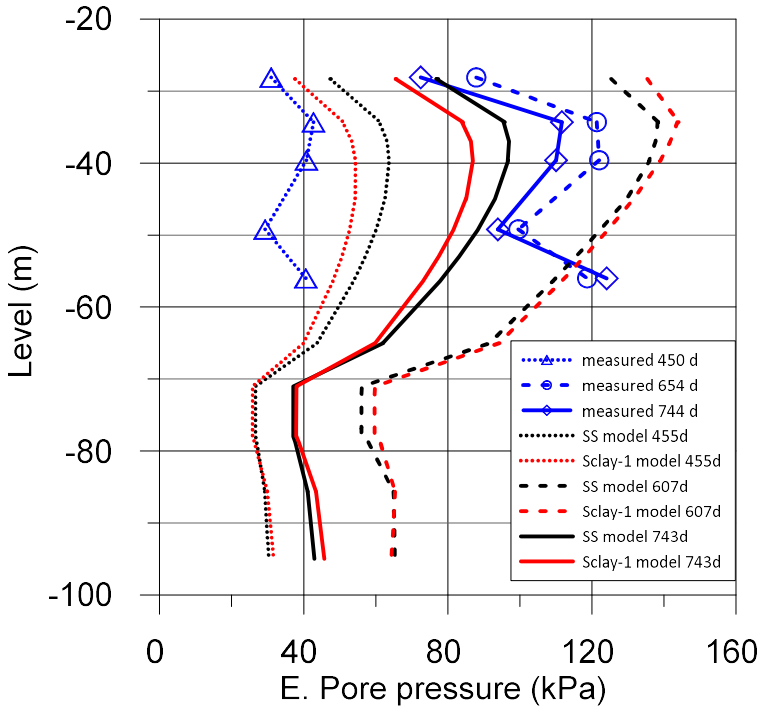

Figure 6-7. Excess pore pressure profile at the cente of breakwater.

The surface settlement profile predicted for three different times (607, 763 and 4413 days) is shown in Figure 6-9. The settlement profiles calculated with the SS and S-Clay1 models in the long term (after 12 years of consolidation) are very similar, with the greatest differences being observed at the ends of the berm, possibly due to the change in direction of the principal stresses. Also, small amounts of surface heave (2.8 - 3.0 cm) out of the embankment are predicted in these areas immediately after construction is completed. The maximum vertical displacement is predicted to be offset from the centerline, due to the non-symmetric geometry of the breakwater. In this case, the zero settlement point is located approximately 90 m (SS model) and 86.5 m (S-Clay1 model) towards the harbour side from the center and 103 m (SS model) and 101 m (S-Clay1) towards the seaside from the center.

The point corresponding to long-term zero settlement is about 200 m from the center, extending to approximately twice the width of the breakwater base, in both models. The S-Clay1 model marginally predicts more settlement than the SS model in both the short and long term (approximately 5 cm), however, the difference between the two predictions is greater (approximately 11 cm) at the intermediate time of 763 days.

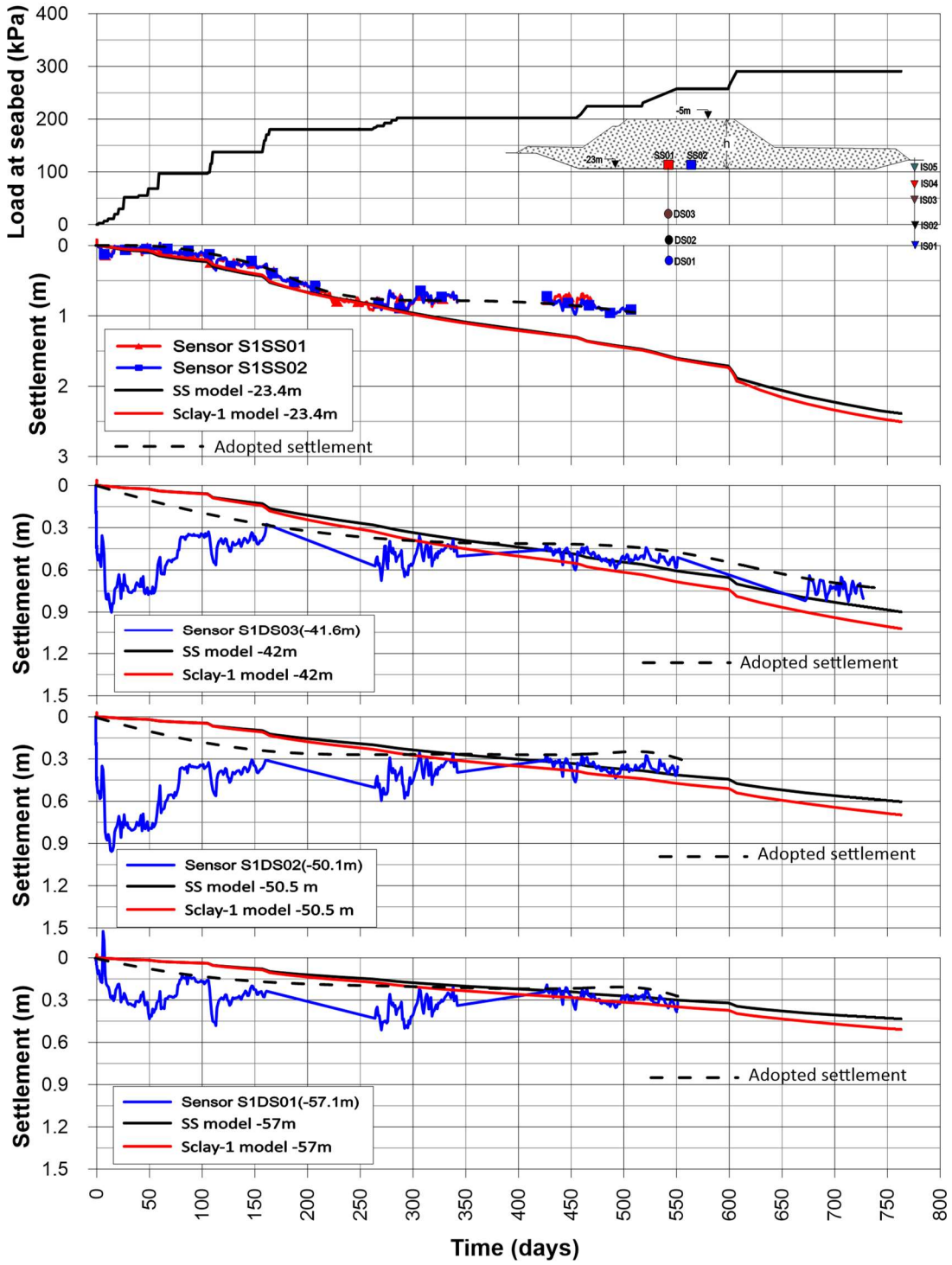

Figure 6-8. Measured and predicted settlement with the FEM models.

The predicted horizontal displacements versus depth under the toe of the breakwater berm are compared with the measurements in Figure 6-10. Both models give different predictions of the horizontal displacements, being S-Clay1 model, which predict significantly larger horizontal displacement than the SS model. In the long term, the horizontal displacement predicted by the S-Clay1 model is even further from the prediction with the SS model. The ratio of the predicted maximum horizontal displacement (u_x) to the vertical settlement (u_y) is, consequently, very different from one model to another: at the end

of construction u_x/u_y is about 0.4 and 1.8% for SS and S-Clay1, respectively, and it is 0.4% and 2.9% in the long term. The ratios of u_x/u_y predicted by the models used are significantly lower than the range suggested by Leroueil et al. (1990), which is attributed to the atypical geometry of the breakwater with large berms.

The largest horizontal displacements predicted with the SS model is 0.01 m, while it is 0.09m with the S-Clay1. Also, it is noted that the predicted maxima with the SS is located at about 6m depth while it is at the ground surface with the S-Clay1.

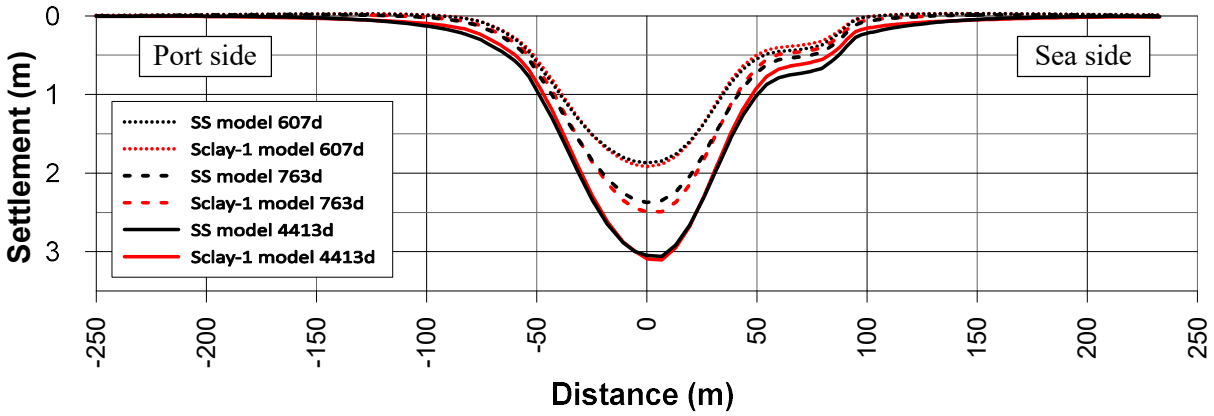

Figure 6-9. Horizontal profile of settlements after construction (607 days) and after long-term consolidation (4413 days).

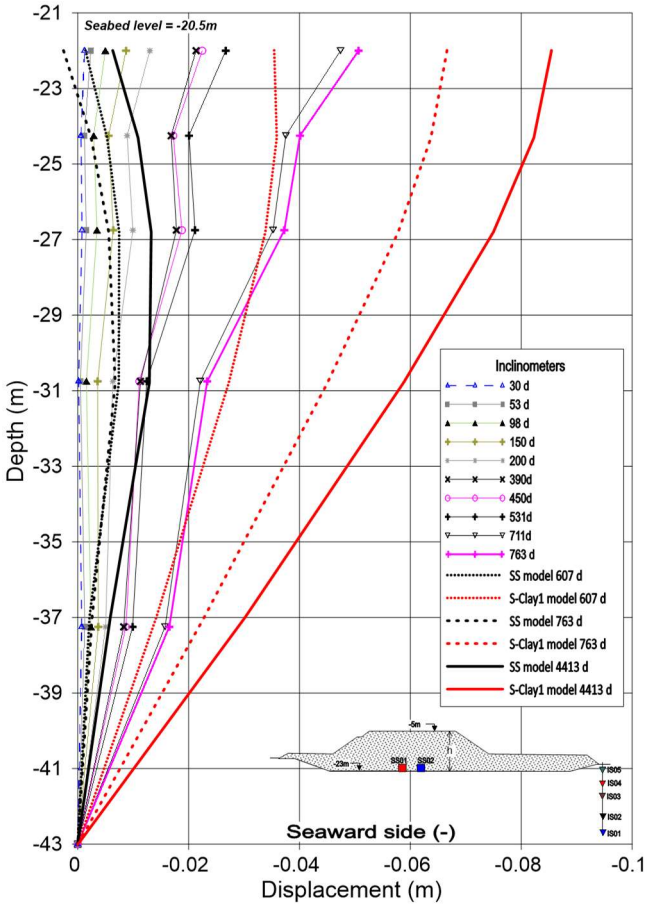

Figure 6-10. Lateral displacement predicted with the FEM

In Figure 6-11 the total displacement contours are shown for the two models used (SS and S-Clay1) at the end of construction (607 days), at an intermediate time (763 days) and after 10 years of consolidation (4413 days). The same scale is used for all models in order to highlight the differences. At the end of construction, the displacements predicted by the S-Clay1 (Figure 6-11b) extend much further, both laterally and depth wise, than predicted by the SS model (Figure 6-11a) and, in general, the predicted displacements are higher than predicted by the SS model. This is likely to be due to the deviatoric hardening part of the S-Clay1 model, activated during undrained embankment construction.

When the results are compared at the end of consolidation and in an intermediate time (Figure 6-11c to f) the trend remains the same, the displacements under the breakwater load extend deeper when using the S-Clay1 model.

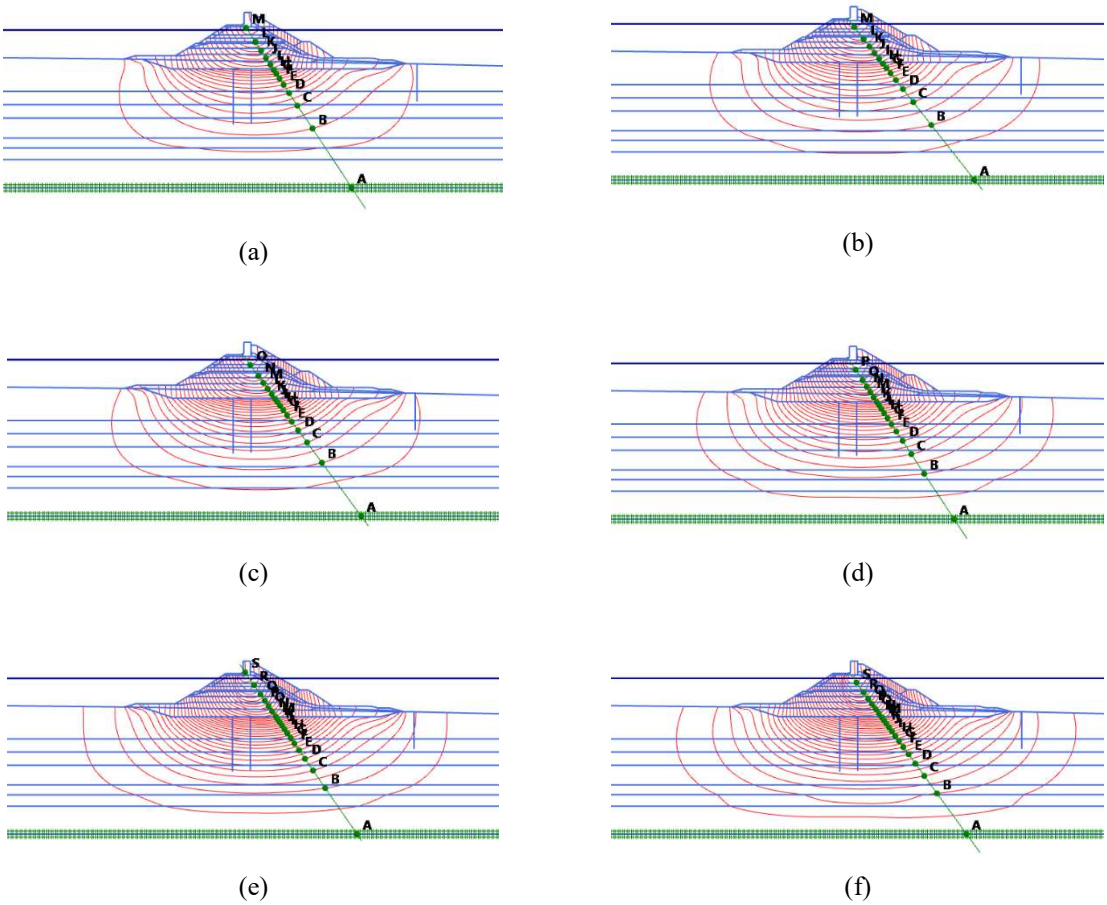

[m] A: 0.0 B:0.25 C: 0.50 D: 0.75 E: 1.00 F: 1.25 G: 1.50 H: 1.75 I: 2.00 J: 2.25 K:2.50 L: 2.75 M: 3.00 N: 3.25 O: 3.50 P:3.75 Q: 4.00 R: 4.25 S: 4.50 T:4.75

Figure 6-11. Total displacement contours (a) SS after construction (b) S-Clay1 after construction (c) SS 763days (d) S-Clay1 763 days (e) SS long term (4413days) (f) S-Clay1 long term (4413days).

In Figure 6-12, the volumetric strains contours have been plotted for the two models used SS and S-Clay1. During construction, the larger volumetric strains occur in the 10m upper layer of soil below the breakwater. As seen in Figure 6-12 (a) and (b) the predictions by the two models are very similar. In the long term, the predicted volumetric strains reach deeper layers with the S-Clay1 model than the SS

model as shown in Figure 6-12 (c) and (d). The patterns of volumetric strains predicted by the two models are practically identical.

The deviatoric strain contours are plotted in Figure 6-13 at the end of construction (a) and (b) and after 10 years of consolidation (c) and (d). The deviatoric strain predictions by the two models are very similar. With a slightly deeper influence in case of S-Clay1 for the long term behaviour. Overall, the two different modelling approaches (isotropic and anisotropic) reproduce similar patterns of behaviour.

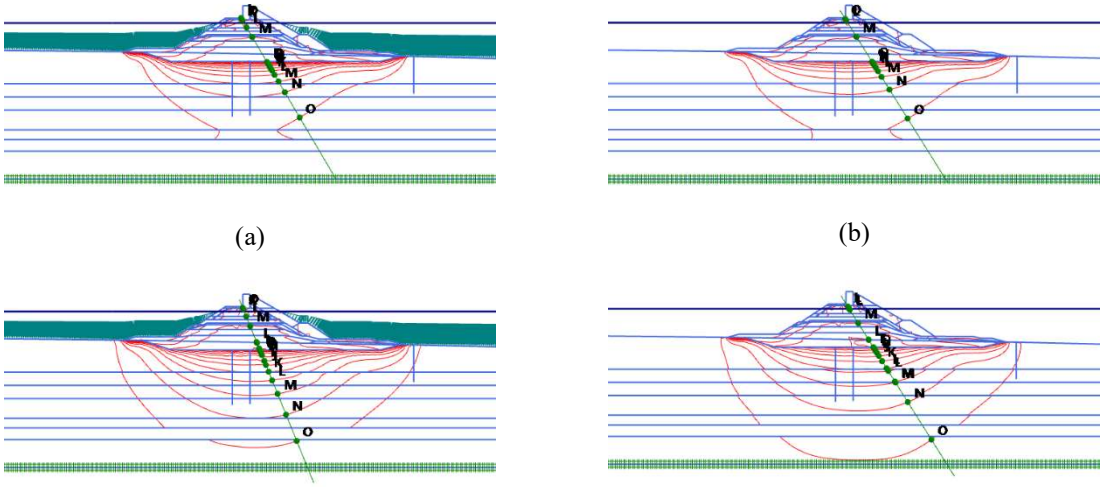

(a) (b)

(c) (d)

[%] A: 15.00 B:14.00 C:13.00 D:12.00 E:11.00 F:10.00 G:9.00 H:8.00 I:7.00 J:6.00 K:5.00 L:4.00 M:3.00 N:2.00 O: 1.00

Figure 6-12. Total volumetric strain contours (a) SS immediately after construction (607 days) (b) S-Clay1 immediately after construction (607 days) (c) SS after 10 years of consolidation (4413 days) (d) S-Clay1 after 10 years of consolidation (4413 days).

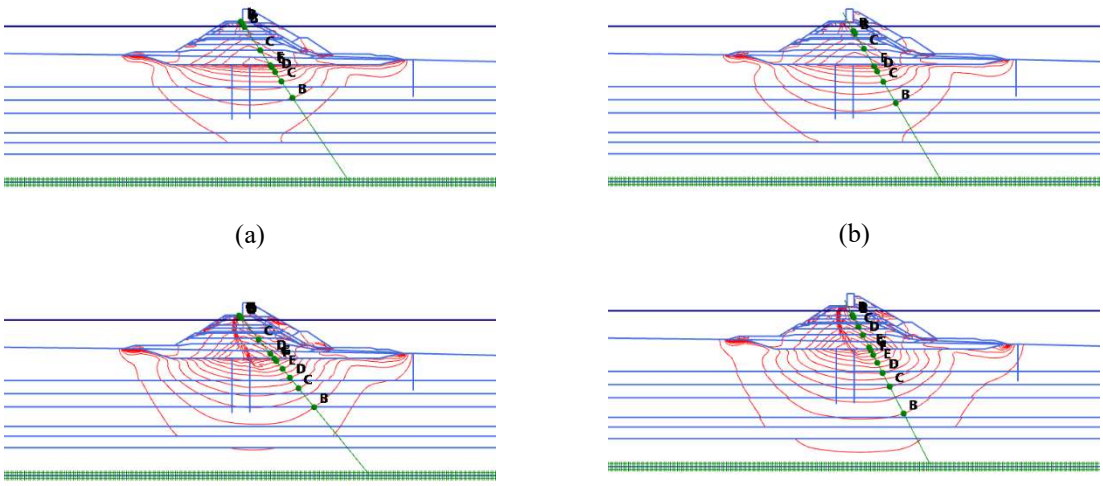

(a) (b)

(c) (d)

[%] A: 0.00 B:2.00 C:4.00 D:6.00 E:8.00 F:10.00 G:12.00 H:14.00 I:16.00 J:18.00 K:20.00 L:22.00 M:24.00 N:26.00 O: 28.00

Figure 6-13. Total deviatoric strain contours (a) SS immediately after construction (607 days) (b) S-Clay1 immediately after construction (607 days) (c) SS after 10 years of consolidation (4413 days) (d) S-Clay1 after 10 years of consolidation (4413 days).

The projections of the predicted stress paths on the p'-q plane is examined in Figure 6-14. Four selected points below ground level underneath the centreline of the breakwater (Figure 6-14a) and two additional points at a depth of 12m under the berm are considered (Figure 6-14b). These points reflect the evolution of effective stresses during the construction of the breakwater and subsequent consolidation. Initially, the models predict elastic behaviour, which is explained by the previous unloading stage due to dredging. It is observed that the value of p' increase as the construction progresses, which is expected due to the dissipation of pore pressure during soil consolidation, but some stages of undrained load can also be noted. Although the predictions by the SS model are rather similar to the ones by the S-CLAY models, there are differences in the predicted stress paths during the undrained loading, which is understood to be because of the differences in the yield curve shape. During the last stage of construction, some points under the centreline passed close to failure (corresponding to M = 0.772) but, after that, they move away as the consolidation proceeds. This means that the last stage of construction was the most critical, and also that the sequence of construction with periods of consolidation was key to ensure that the construction was carried out safely. An examination of the plastic points (Figure 6-15) obtained with the SS model shows a restricted critical area below the central part of the breakwater, which demonstrates the effectiveness of placing a long berm when building on soft soils.

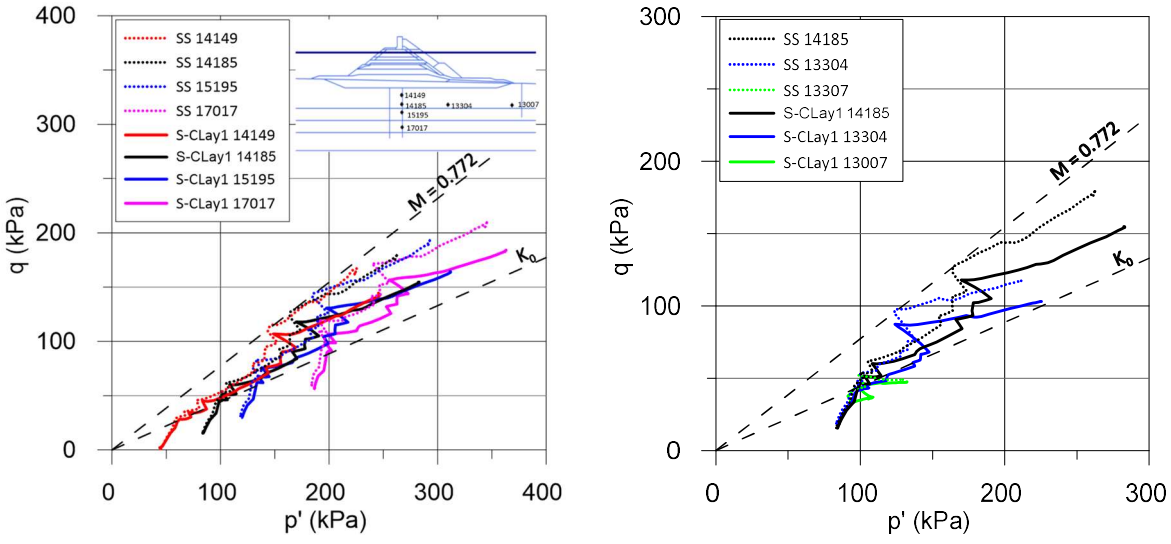

Figure 6-14. Stress path at various points (a) on the centreline (b) horizontal line at 14m below the seabed.

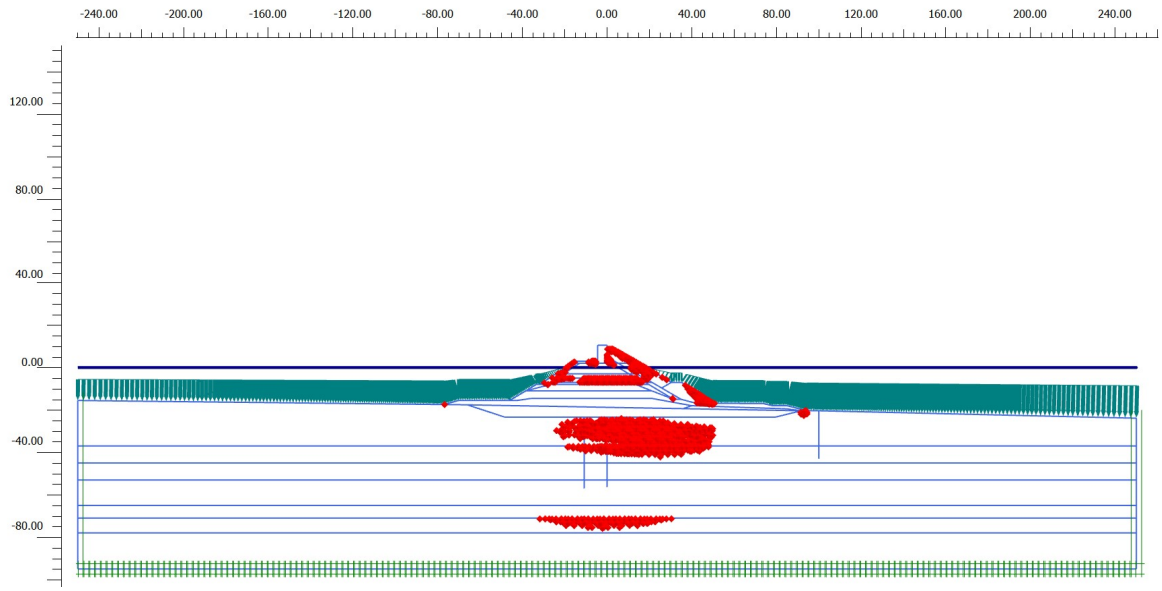

Figure 6-15. Plastic points obtained at last stage of construction with the SS model.

6.2.5.2 Section 2

The response observed in the instruments installed in this section was similar to Section 1, with stages of loading and dissipation of pore pressure. Three models were used with this section: The Soft Soil model (SS), the Soft Soil Creep model (SSC) and the anisotropic model S-Clay1. The parameters used for the SSC model were selected from the preload test (see section 4.4.3.2) using an average value for each layer. It is observed that all the models predict better the upper piezometers (levels -28, -34 and -39), but the response of lower piezometers (levels -49 and -57m) seem to be far from the predicted value, especially in the first stages of construction (Figure 6-16). The dissipation rate is initially well captured by the models, although it tends to deviate with each additional load increase. Finally, the post-construction rate of dissipation is again well captured by the models (see Figure 6-16). The lower piezometers that initially showed an extremely low dissipation rate, in the final stage of consolidation show dissipation rate consistent with the prediction of the models.

The predicted excess pore water pressure profile under the centreline of the breakwater at different times is presented in Figure 6-17. As seen in this figure, the predictions of the models are similar in the different times examined, but in case of pore pressure computed immediately after caisson construction (866 days), it is observed that the prediction is noticeably different at levels from -30 to -50m. The SS, SSC and S-Clay1 models predict a maximum excess pore water pressure of about 90, 125 and 107 kPa, respectively. It is also observed that the predictions at the end of the construction of the embankment (330 days), are very close to the measurements during the first 15m, but at greater depth, the pore pressures are overestimated. After the consolidation of the embankment load (700 days) the predictions show a better agreement with the measurements.

Figure 6-18 shows a comparison between measured settlements during construction and post-construction. Models seem to reproduce quite well the settlements measured during construction and post-construction. Long term settlements are better predicted with the SSC model. Note that embankment settlements were measured at the base of the embankment while the caissons settlements were measured with topographic control points placed at the top of caissons. After the construction of the breakwaters, 5 geodetic control points were installed in the south breakwater, one of them was placed in the caisson area (caisson 27). These points are part of the topographic network of the port. The Port Authority of Barcelona, maintains periodic control of these points, taking readings of settlements every 2 to 3 years as shown in Figure 6-18.

Figure 6-19 shows the horizontal profile of settlements at different times of construction. The profile was taken at the base of the embankment at the horizontal level of -26m. It can be seen that the different models produce quite similar results. However, the SSC model produces greater settlements, due to the time dependence inherent in the approach of the model. This can be seen by the calculated settlements (0.4-0.5m) in the direction towards the boundaries of the model, which correspond to not loaded zones of the model.

Predicted settlements versus time at different nodes below the breakwater centerline are presented in Figure 6-20 for a consolidation time of about 10-years. During embankment construction the settlement predicted with the SSC model is greater than that calculated with the SS or S-Clay1 model. However, during caisson placement (day 700) and subsequent consolidation, the SSC model initially shows lower settlements, but in the long term, the settlements calculated with this model are equal to or greater than those calculated with the SS or S-Clay1 model.

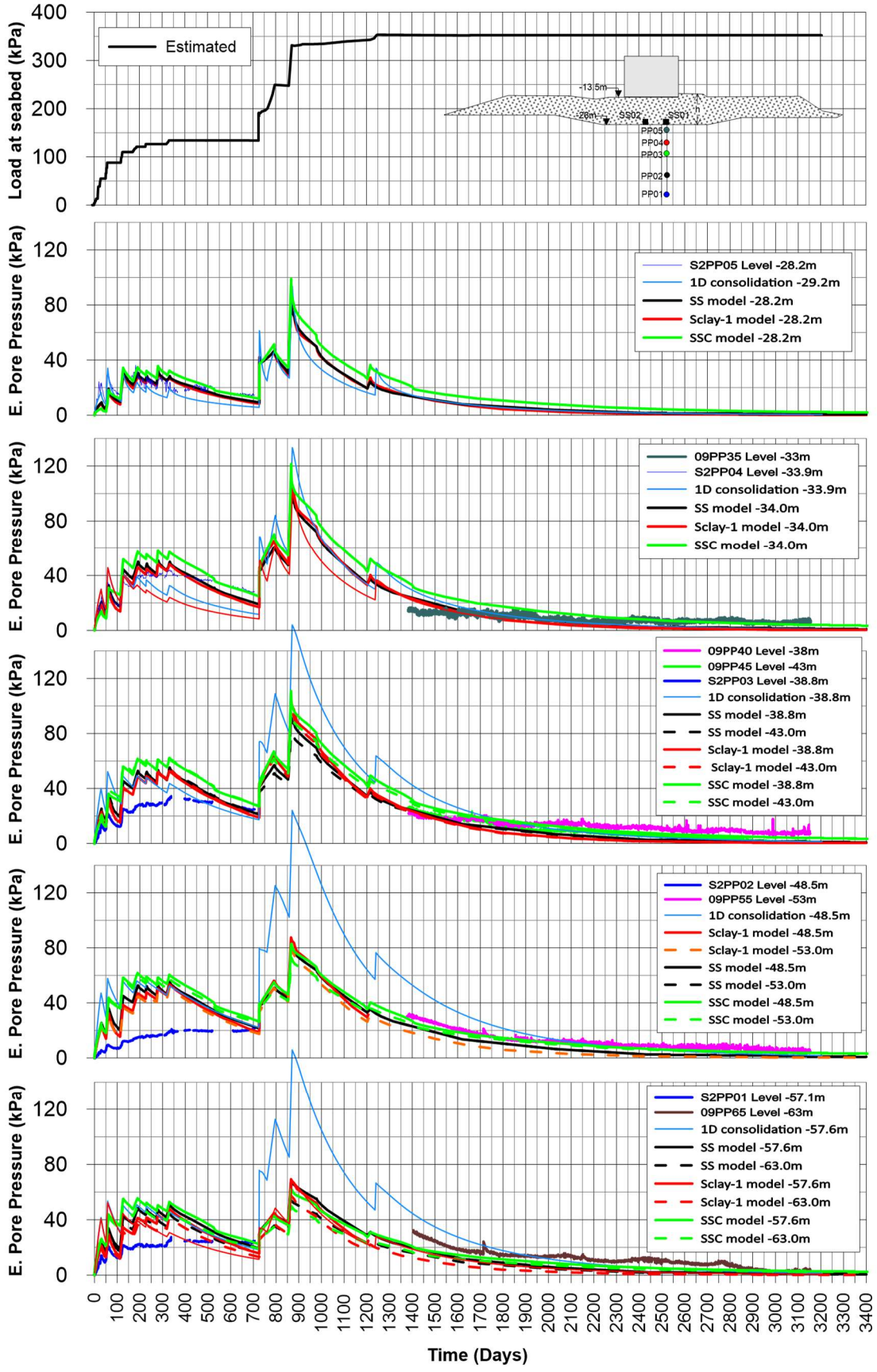

Figure 6-16. Pore pressures evolution computed with the SS, SSC and SClay-1 models.

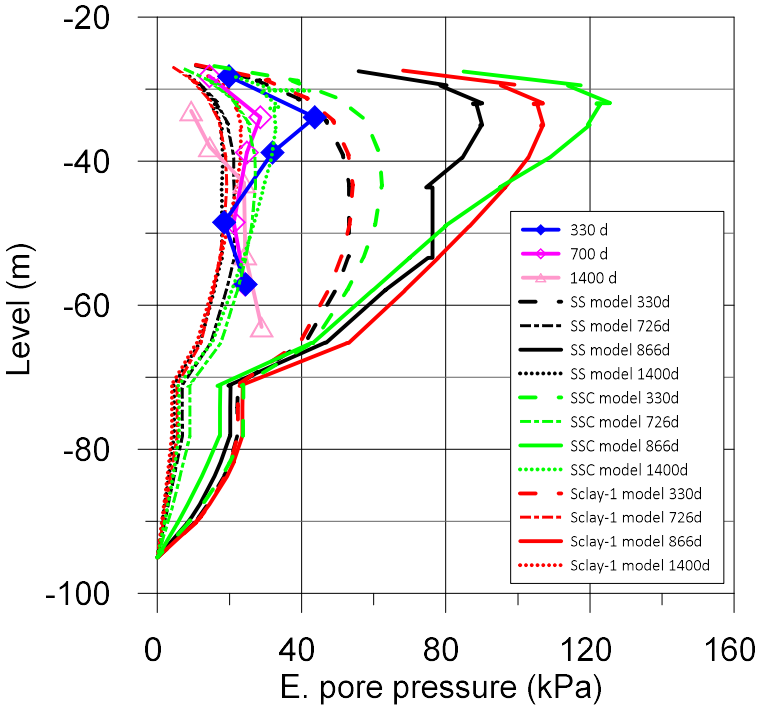

Figure 6-17. Excess pore pressure profile at center of Section 2.

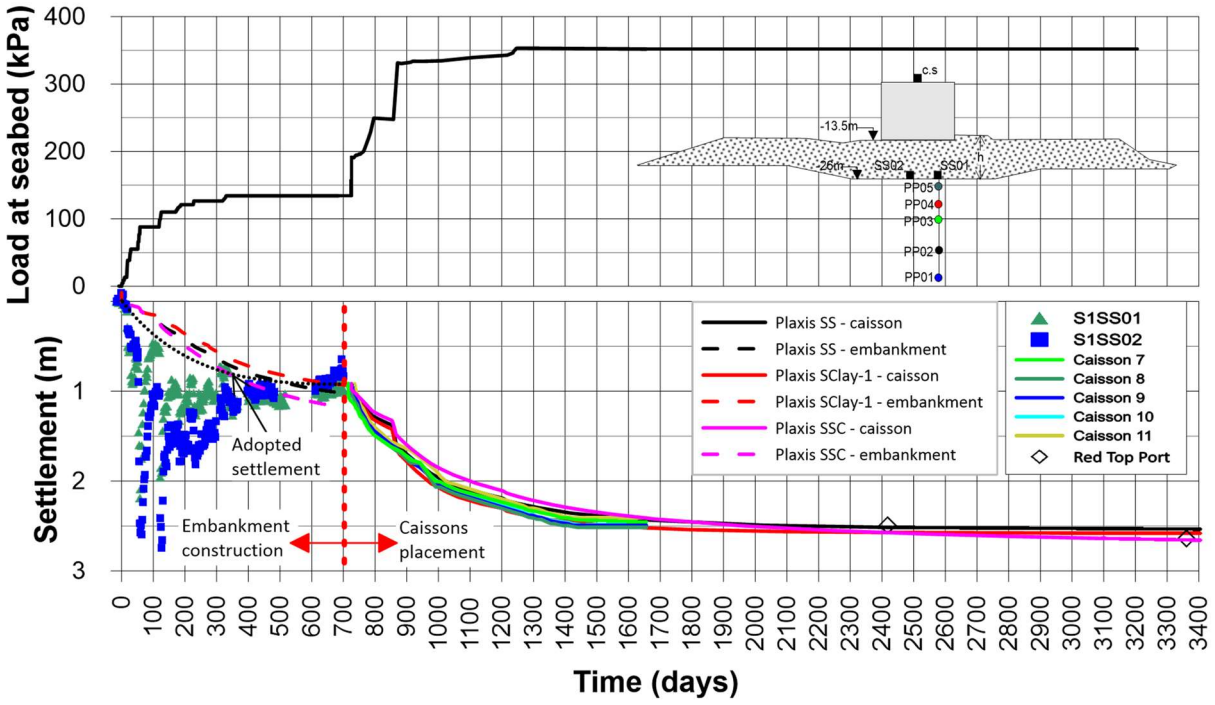

Figure 6-18. Evolution of settlements predicted and measured at Section 2 (Red Top Port = Port topographic network),

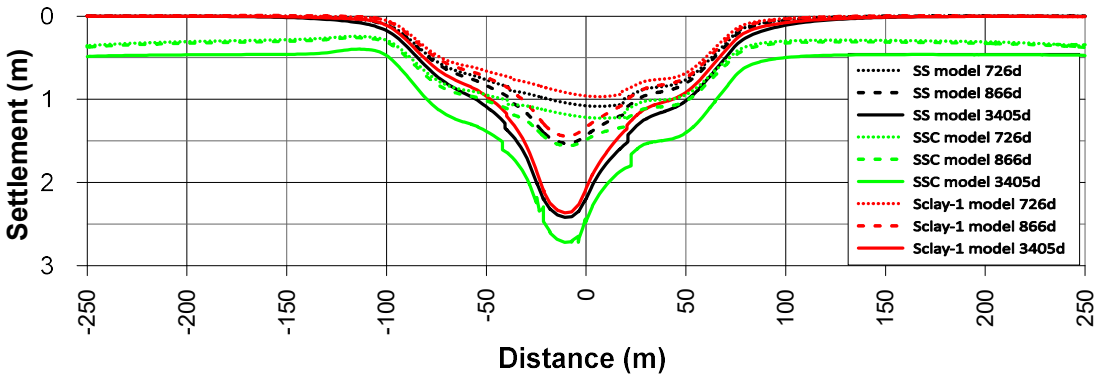

Figure 6-19. Horizontal profile of settlements at embankment base of Section 2.

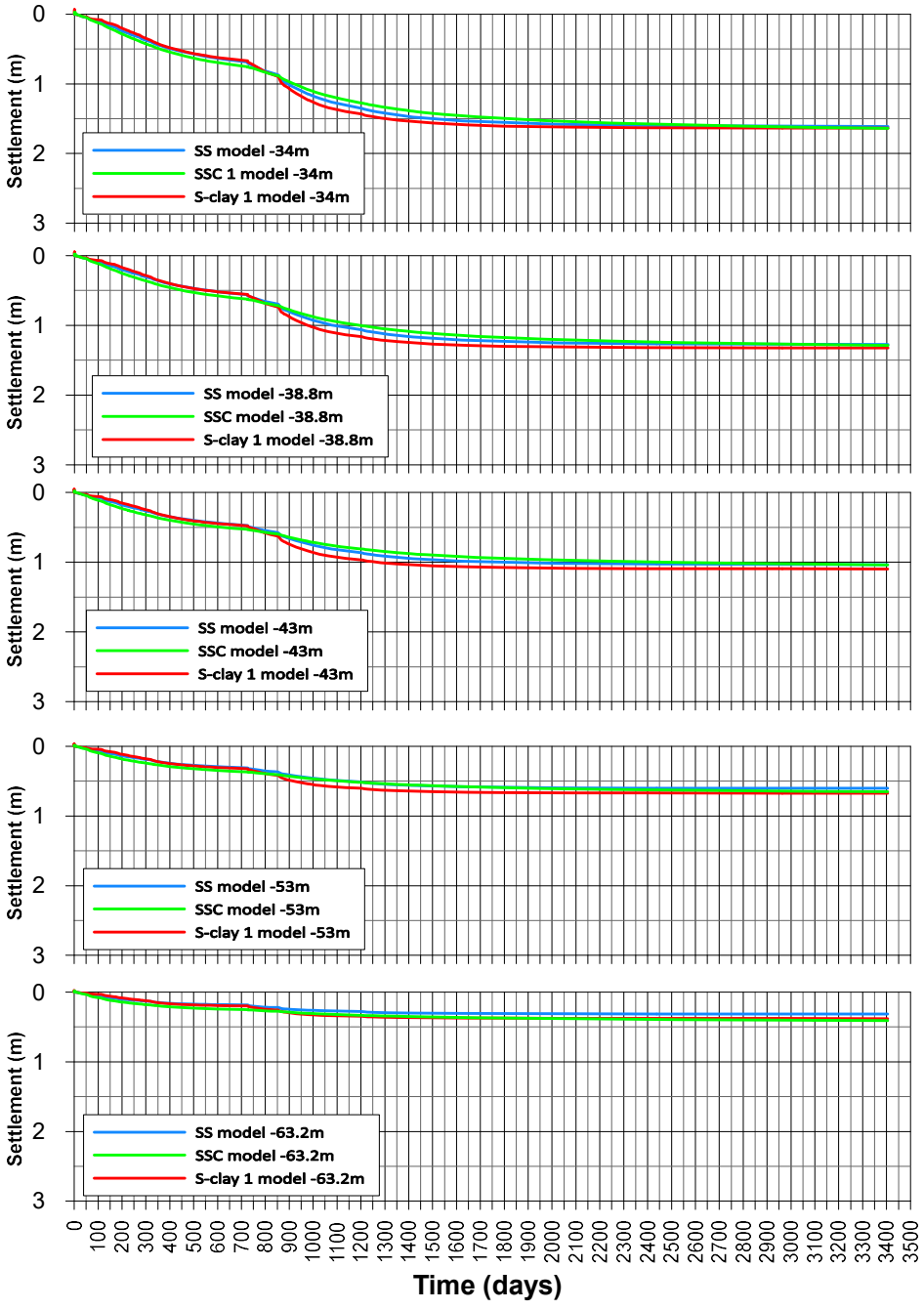

Figure 6-20. Settlements at several depths predicted with the FEM models in Section 2.

Inclinometer readings after 717 days of construction, shows only a small lateral displacement with an irregular pattern of movement, probably due to the location under the central part of the embankment (at 31m from the centerline), where compression is dominant. In this case, prediction with the models shows a different pattern of behaviour as shown in Figure 6-21. SSC model was adjusted with compressibility parameters decreasing with depth, while the other models used a single compressibility parameter at each layer. At x = 100m from centerline SS and SSC models show displacement towards the seaward side (-) while the S-Clay1 model shows displacement towards the port side (+). At x = 31m the behaviour is very similar in the short term with the three models, but in the long term the SSC model differs from the others, by showing much greater displacements towards the port side in the upper stratum. This behaviour is most likely a consequence of the higher compressibility used in the upper layer.

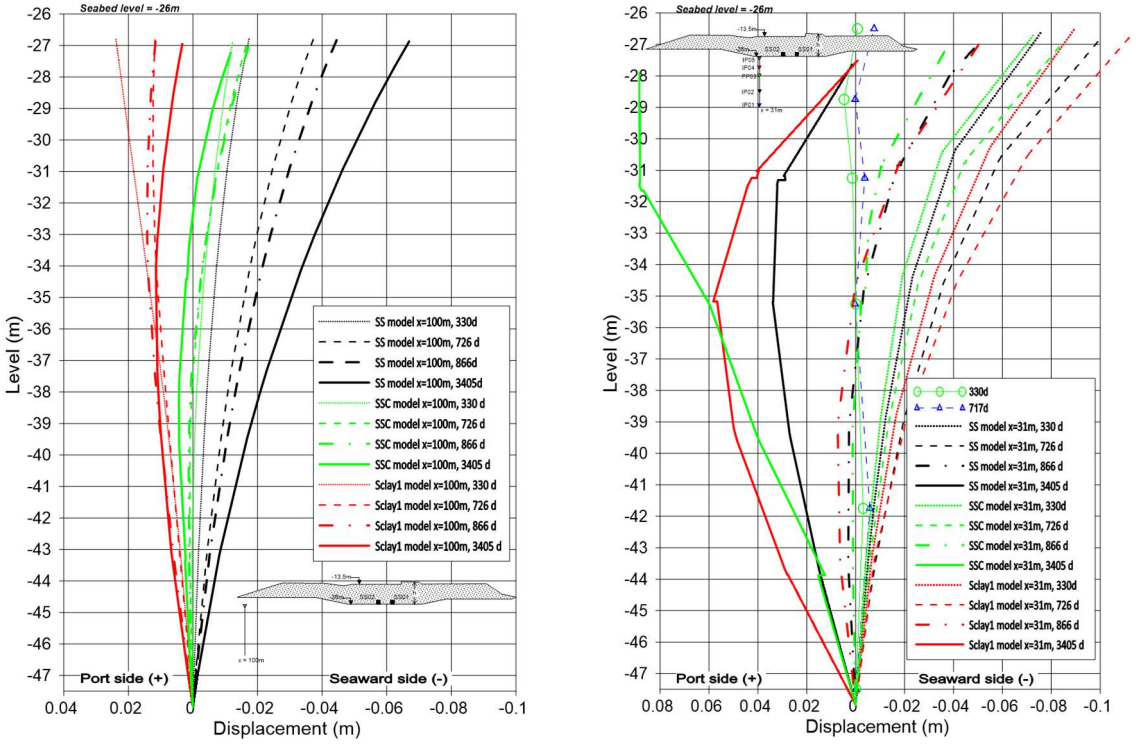

(a) (b)

Figure 6-21. Lateral displacement measured and predicted with the FEM models (a) At 100m from centerline (b) at 31m from the centerline.

The total displacement contours are shown in Figure 6-22 for the three models used (SS, SSC and S-Clay1). Displacements were calculated at the end of construction (886 days) and after 10 years of consolidation (3405 days). The SS and S-Clay1 models show similar behaviour, the latter being the one that reaches deeper displacements (see Figure 6-22b and d). In the case of the SSC model, the contours show a much wider displacement extension (Figure 6-22c), because they depend on time.

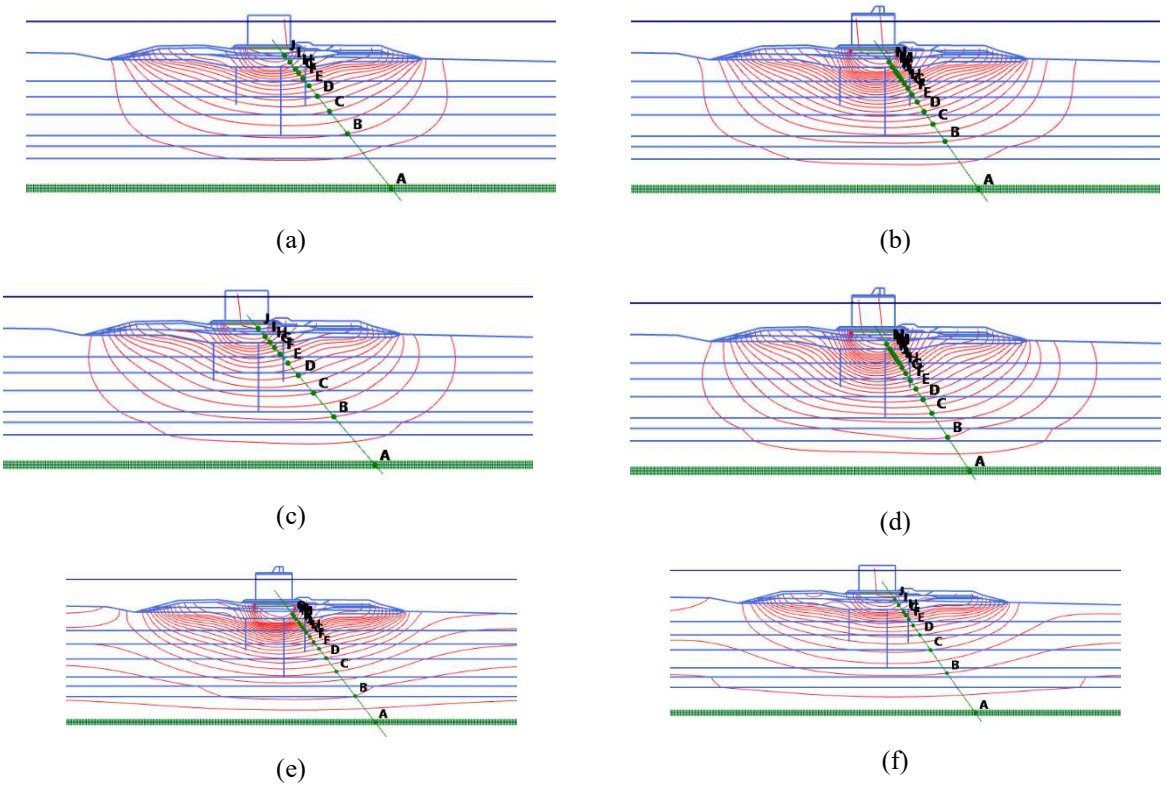

[m] A: 0.0 B:0.25 C: 0.50 D: 0.75 E: 1.00 F: 1.25 G: 1.50 H: 1.75 I: 2.00 J: 2.25 K:2.50 L: 2.75 M: 3.00 N: 3.25 O: 3.50 P:3.75 Q: 4.00 R: 4.25 S: 4.50 T:4.75

Figure 6-22. Total displacement contours (a) SS after caisson construction 866 days (b) SS long term (3405 days) (c) S-Clay1 after caisson construction 866 days (d) S-Clay1 long term (3405days) (e) SSC after caissom construction 866 days (f) SSC long term (3405 days).

In Figure 6-23, the total volumetric strains contours have been plotted for the models. During construction (866 days), the larger volumetric strains occur in the upper layer below the breakwater. As seen in Figure 6-23 (a), (c) and (e) the predictions by the models are very similar. In the long term, the predicted volumetric strains reach deeper layers with the SSC model (see Figure 6-23f). The volumetric deformation patterns predicted by the SS and S-Clay1 models are practically identical, while those of the SSC model shows a discontinuous pattern of contours because the compressibility parameters used are different in each layer.

The deviatoric strain contours are plotted in Figure 6-24 at the end of construction (a), (c) and (e) and after 10 years of consolidation (b), (d) and (f). The deviatoric strain predictions by all the models are very similar, with a slightly deeper influence in case of SSC for long-term behaviour.

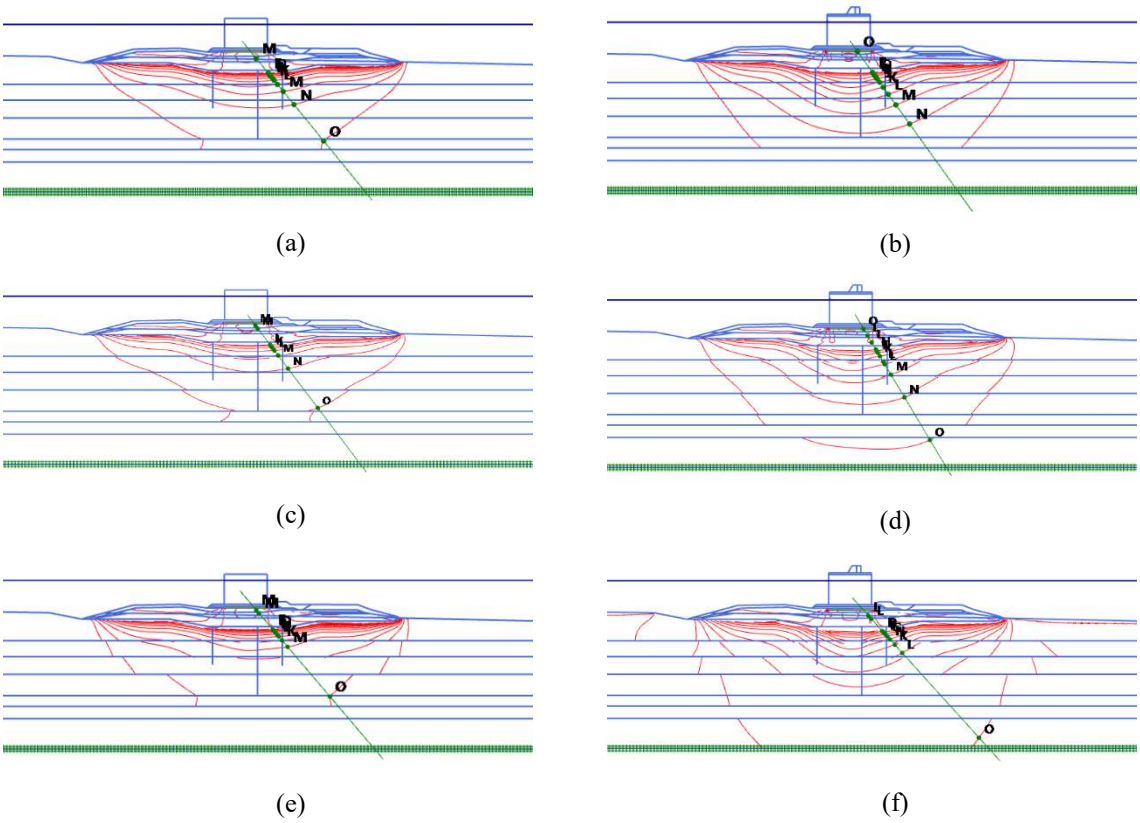

Figure 6-23. Total volumetric strain contours (a) SS immediately after caisson construction (866 days) (b) SS after 3405 days of consolidation (c) S-Clay1 immediately after caisson construction (866 days) (d) S-Clay1 after 3405 days of consolidation (e) SSC after 3405 days of consolidation (f) SSC after 3405 days of consolidation (f).

The projections of the predicted stress paths on the p'-q plane are examined in Figure 6-25. The stress paths obtained with the SS and S-Clay1 models are compared in Figure 6-25a for a vertical profile through the centre of the breakwater and in Figure 6-25b for a horizontal section of the model. In the same way, Figure 6-25(c) and (d) show the results obtained with the SSC and S-Clay1 models. It can be seen that the models respond in a similar way to the loading, unloading and soil consolidation stages followed during construction. During the last stage of caisson filling, some points under the centreline approach the failure line (corresponding to M = 0.772) but, after that, they move away as consolidation proceeds. As expected, the caissons placement stage was the most critical. In this sense and to ensure the stability of the breakwater, two aspects of the project stand out: first, the construction progress in stages, with intermediate times to consolidate the soil (it was also necessary that the caissons were filled in stages) and the atypical geometry of the embankment, with a very wide berm (approximately 180m).

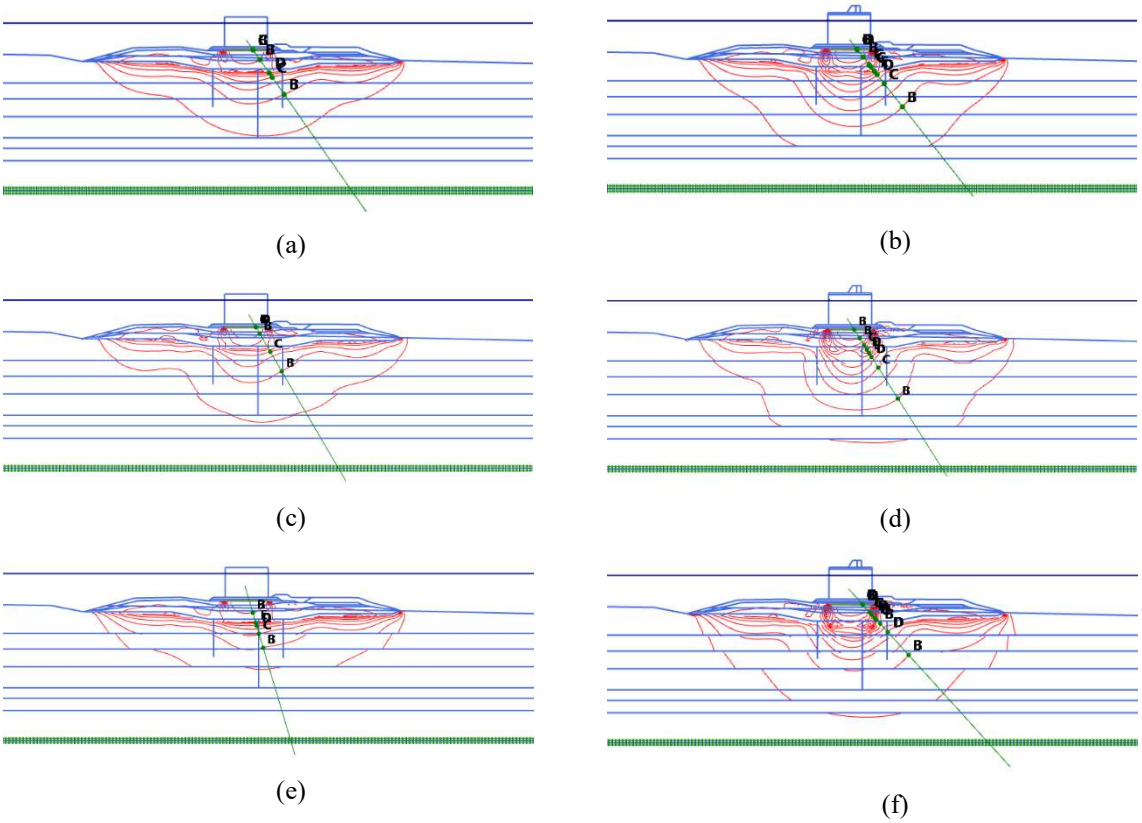

Figure 6-24. Total deviatoric strain contours (a) SS immediately after caisson construction (866 days) (b) SS after 3405 days of consolidation (c) S-Clay1 immediately after caisson construction (866 days) (d) S-Clay1 after 3405 days of consolidation (e) SSC immediately after caisson construction (866 days) (f) SSC after 3405 days of consolidation.

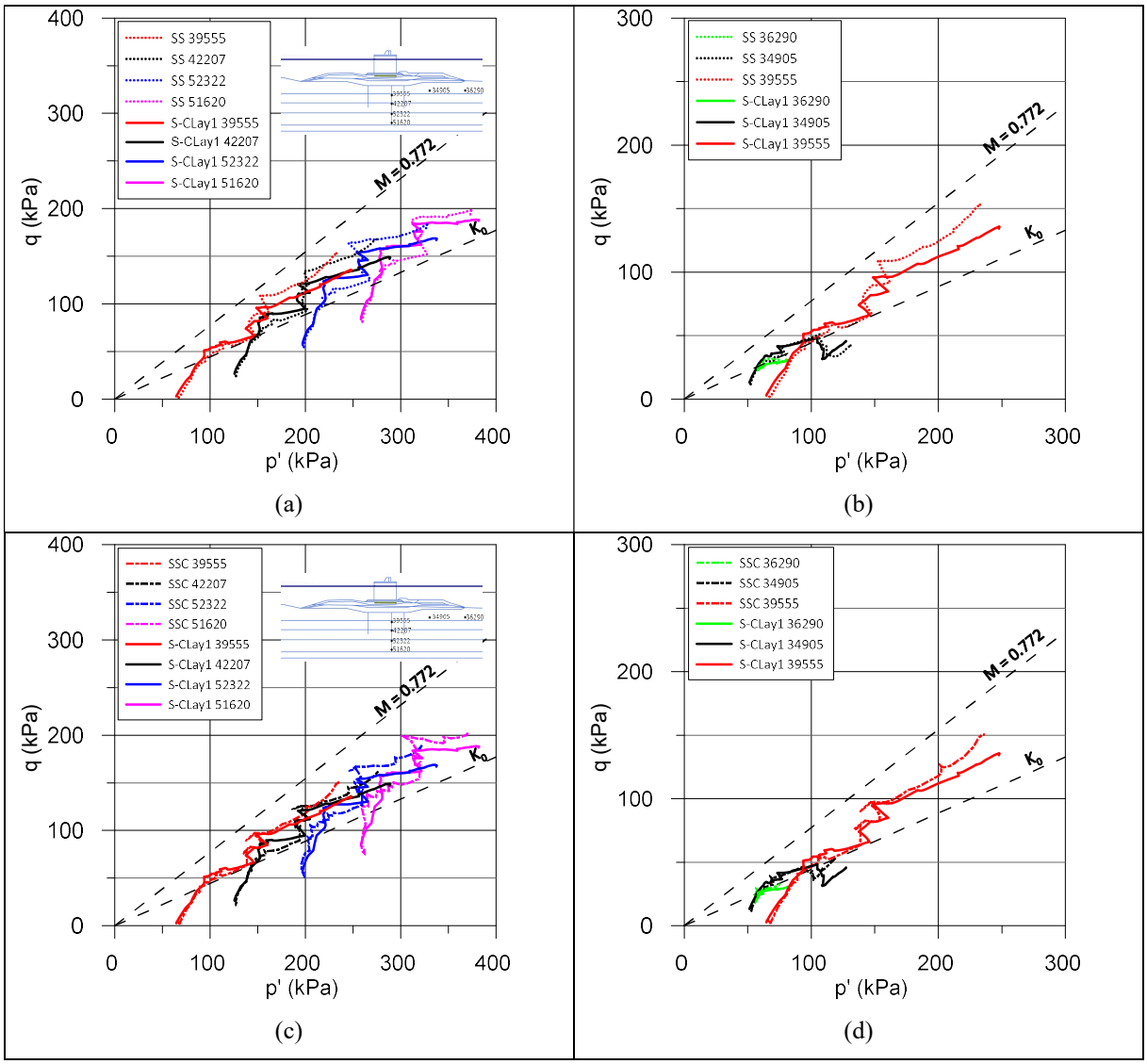

Figure 6-25. Stress path at various points (a) on the centreline (b) horizontal line at 10m below the seabed.

6.2.5.3 Section 3

The excess pore pressures calculated with the SS and S-Clay1 models are shown in Figure 6-26. Predictions with Olson's one-dimensional consolidation model are also included in this figure. These predictions are compared with the post-construction pore pressures measured. The predictions fit quite well with the measurements made, especially on the lower piezometers (levels -52 and -62m).

Figure 6-27 shows the pore pressure profile with depth. The pressures at the end of the period of consolidation of the embankment were very similar computed with the two models (SS and S-Clay1). It is observed that the greatest difference in the prediction of pressures between the models corresponds to the stage of placement of the caissons (903 days). Later, and after a period of pressure dissipation (1417 days), the predictions of the two models are again very similar. It should be noted that these pore pressures predictions resulted in values higher than the values measured in the ground.

Settlement predictions were also made in this section. Figure 6-28 shows the calculated settlements at the base of the embankment and also in the caissons. The settlements measured employing topographical controls in caisson 23 are also shown in this figure. It is observed that both models reproduce the measured settlements quite well. The settlement prediction in this section is 10cm greater than that calculated in Section 2

Figure 6-29 shows the profile of settlements in a horizontal section through the base of the embankment. The shape of the settlement profile is consistent with the geometry of the breakwater and extends approximately 30m on both sides. The maximum settlements (at 3147 days) are very similar to those obtained in Section 2.

Likewise, settlements at different depths in the central axis of the breakwater were calculated with the two models (see Figure 6-30). It is observed that both models calculate practically the same long-term settlement value. During the construction of the embankment and filling of the caissons, some difference is observed in the calculation of settlement, probably due to the different dissipation of pore pressures between the two models.

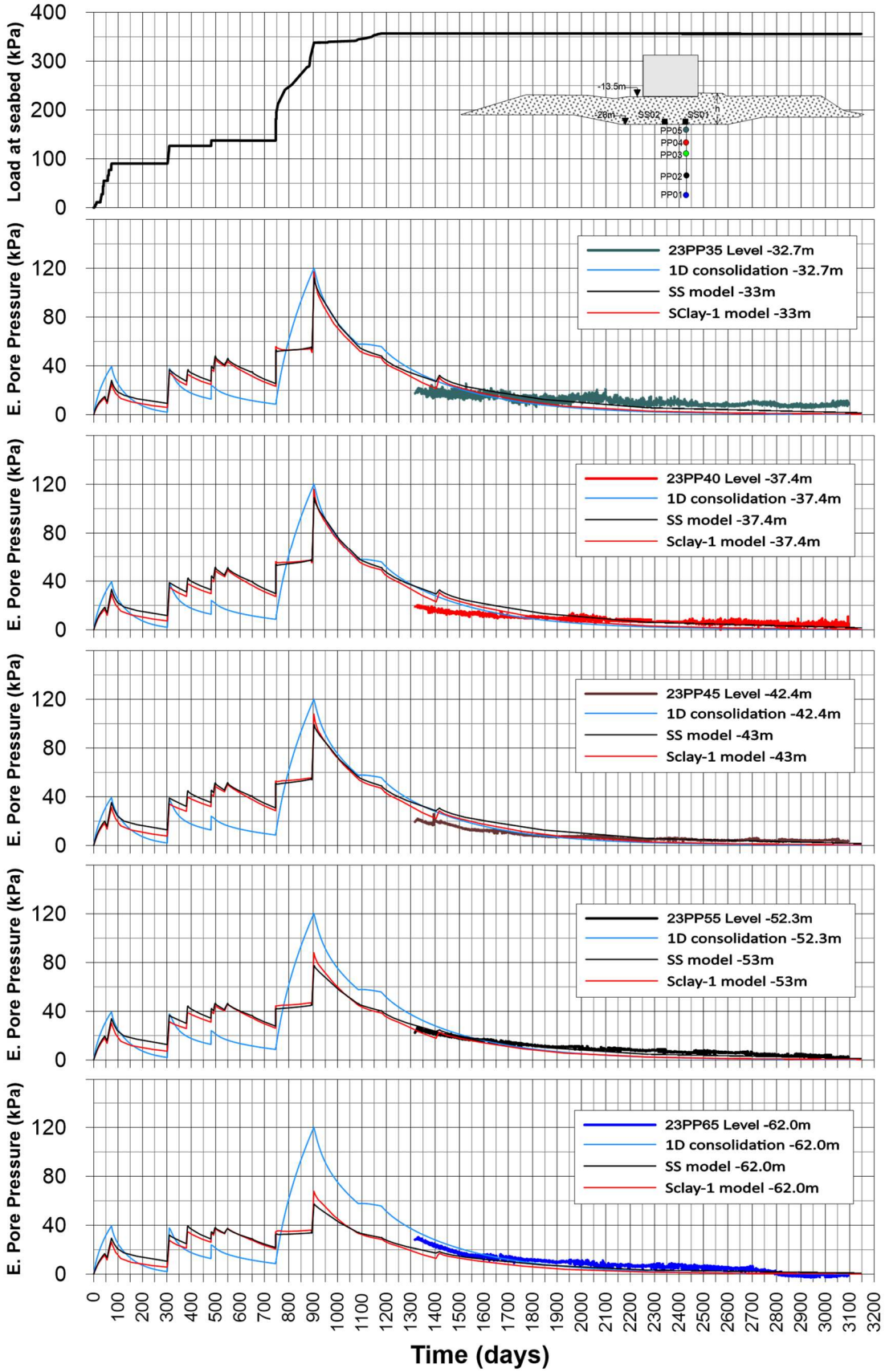

Figure 6-26. Pore pressures evolution computed with the SS and SClay-1 models.

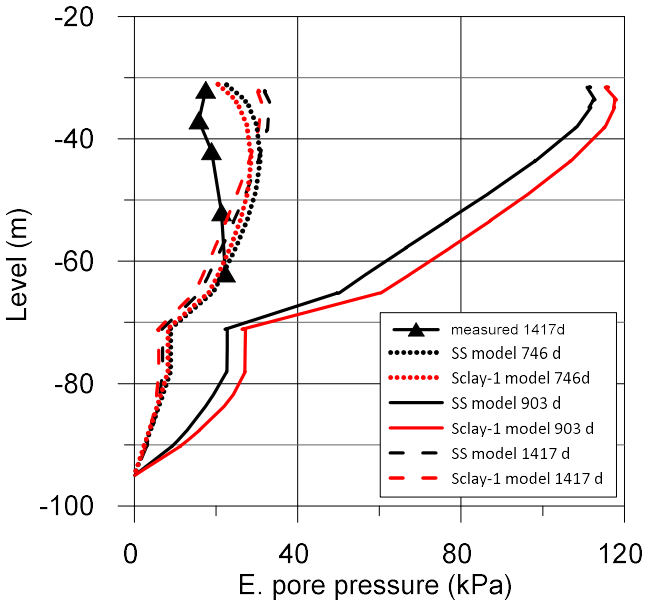

Figure 6-27. Excess pore pressure profile at the centre of section 3

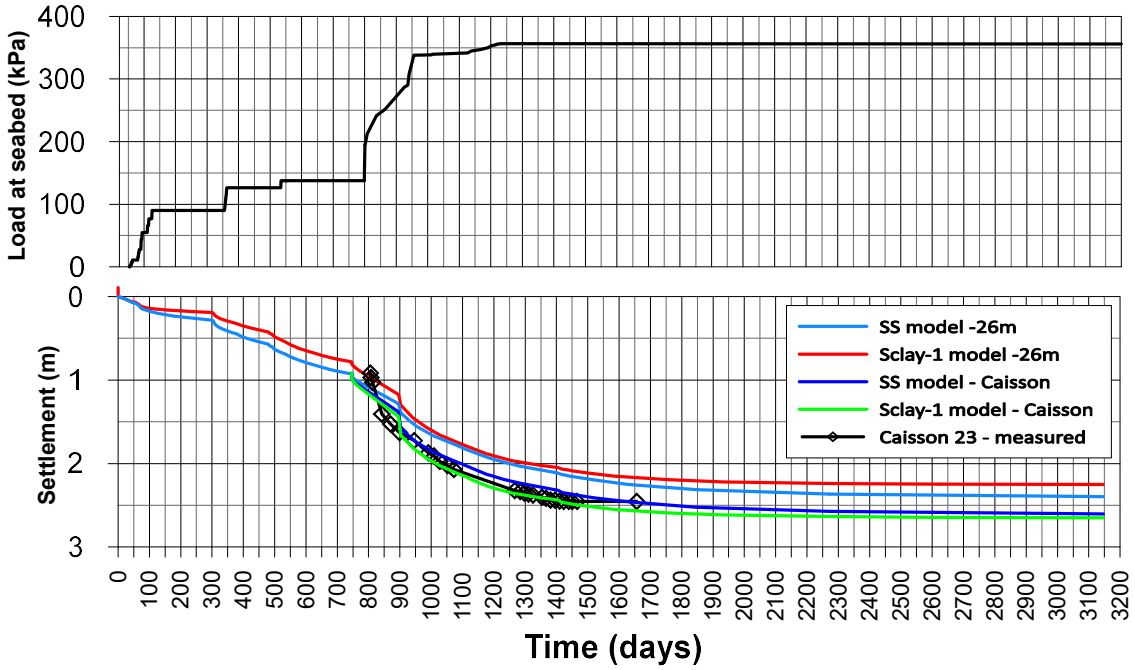

Figure 6-28. Evolution of settlements predicted in Section 3.

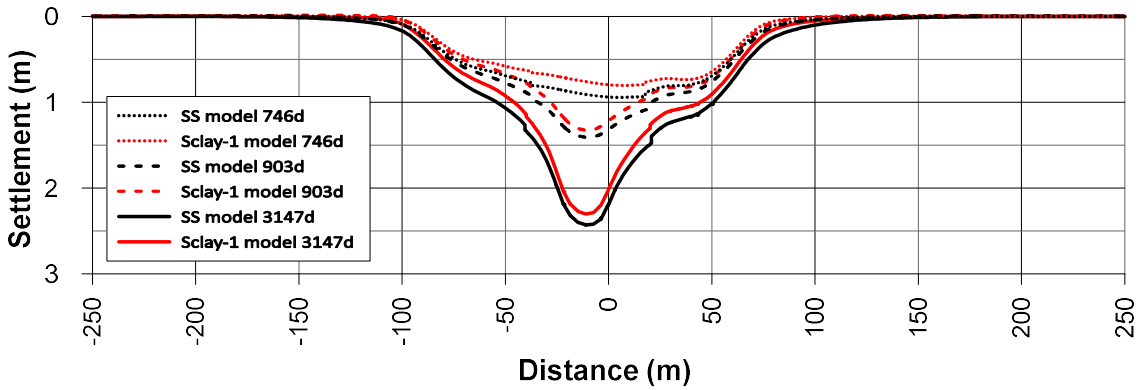

Figure 6-29. Horizontal profile of settlements at embankment base of Section 3.

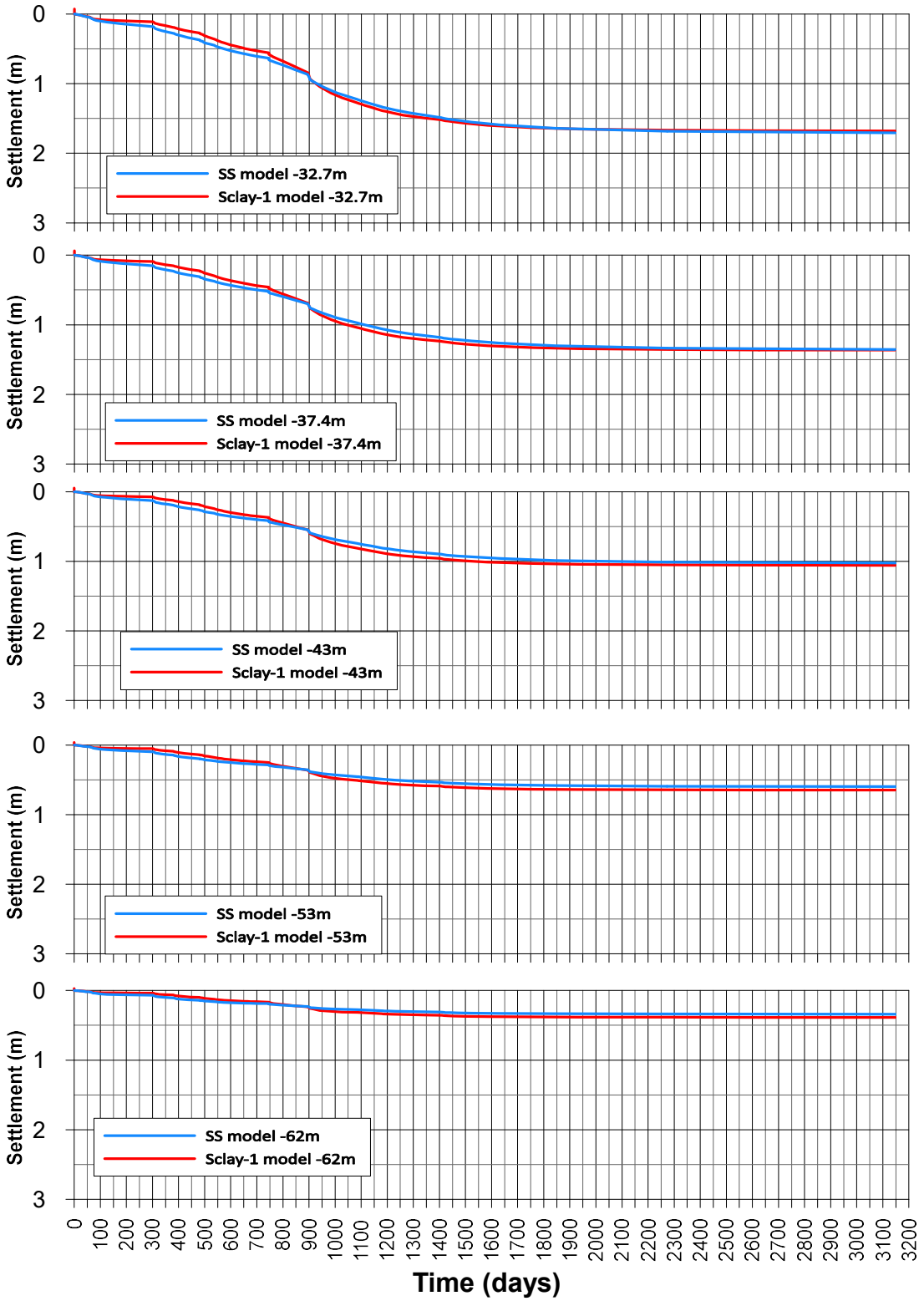

Figure 6-30. Settlements at several depths predicted with the FEM models in Section 3.

The total displacement contours under the breakwater are shown in Figure 6-31. It can be seen that the SS and S-Clay models produce similar contours. However, it is observed that the displacement contours calculated with the S-Clay1 model, extend further towards the seaside and in depth to the lower clay layer (see Figure 6-31b and d).

Finally, the contours of volumetric deformation (see Figure 6-32) and deviatoric deformation (Figure 6-33) are also examined. The results are similar to those obtained in Section 2. The largest volumetric deformations are observed in the first stratum under the breakwater; however, these extend to the intermediate sand layer at 50m depth. A result that is consistent with the measurements made in the preload test (see section 3.5.2). On the other hand, the shear deformations calculated with both models show a larger intensity in the area immediately under the caisson in the long-term (Figure 6-33c and d).

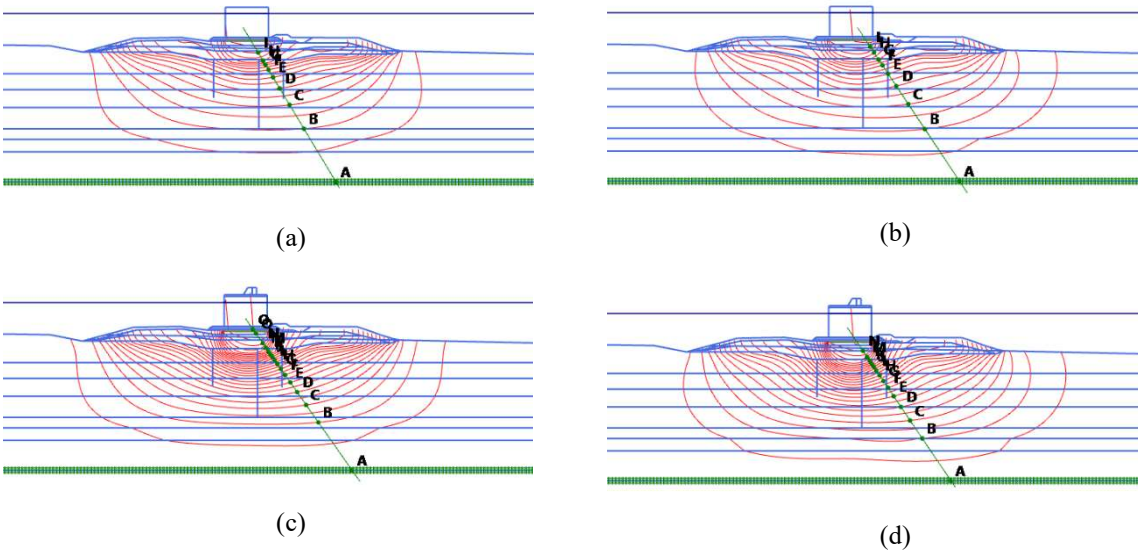

[m] A: 0.0 B:0.25 C: 0.50 D: 0.75 E: 1.00 F: 1.25 G: 1.50 H: 1.75 I: 2.00 J: 2.25 K:2.50 L: 2.75 M: 3.00 N: 3.25 O: 3.50 P:3.75 Q: 4.00 R: 4.25 S: 4.50 T:4.75

Figure 6-31. Total displacement contours (a) SS after construction (b) S-Clay1 after construction (c) SS long term (3147) (d) S-Clay1 long term (3147 days).

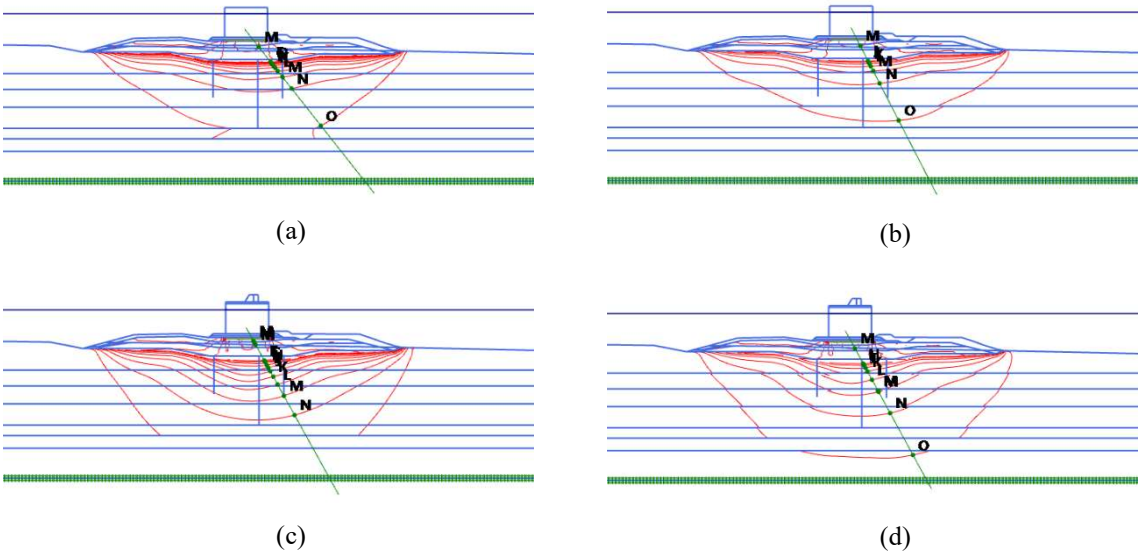

Figure 6-32. Total volumetric strain contours (a) SS immediately after construction (903 days) (b) S-Clay1 immediately after construction (903 days) (c) SS after 3147 days of consolidation (d) S-Clay1 after 3147 days of consolidation.

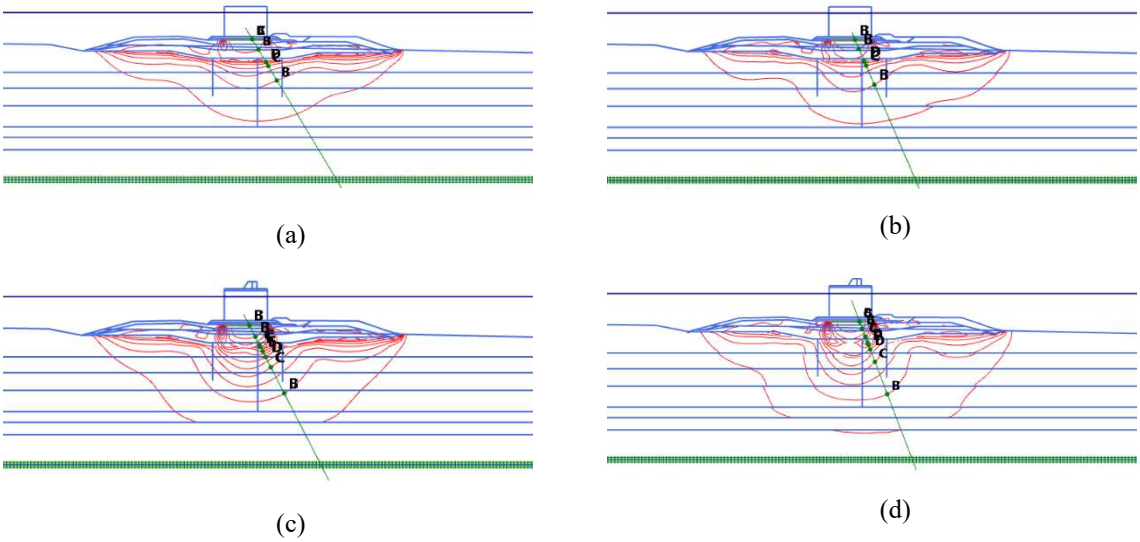

(a) (b) (c) (d)

Figure 6-33. Total deviatoric strain contours (a) SS immediately after construction (903 days) (b) S-Clay1 immediately after construction (903 days) (c) SS after 3147 days of consolidation (d) S-Clay1 after 3147 days of consolidation.

The stress paths of different points in the model of Section 3 are shown in Figure 6-34. Four selected points under the central zone of the breakwater show a similar trend to that obtained in Section 2. The mean effective stress p' increases as the construction progresses, while the undrained loads move the stress path in the direction of the failure line. The stress paths obtained with the SS model are closer to the failure line. It is clear that due to the stage construction process all the points examined remain within the safe zone of stress. In Figure 6-34b, two additional points under the embankment are examined at a depth of about 10m, these points maintain a tendency to follow the K_0 line.

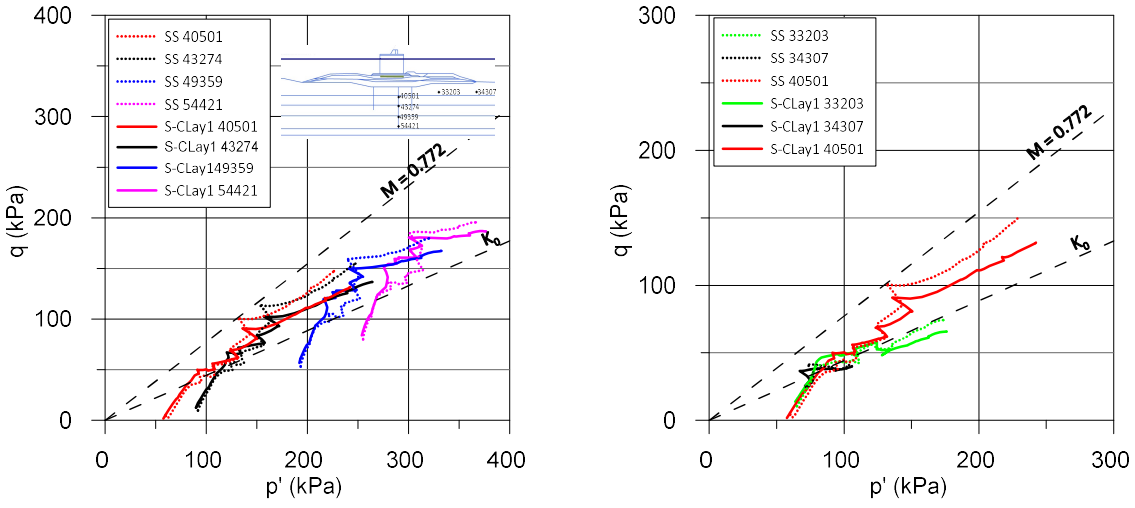

(a) (b)

Figure 6-34. Stress path at various points (a) on the centreline (b) horizontal line at 10m below the seabed.

6.2.5.4 Section 4

The excess pore pressures calculated with the SS and S-Clay1 models are shown in Figure 6-35. Again, as was done with the previous section, the pore pressure predictions with Olson's one-dimensional

consolidation model are included in this figure. These predictions are compared with the post-construction pore pressures measured with the instrumentation. The predictions fit quite well with the measurements made, especially on the lower piezometers (levels -52 and -62m). The upper piezometers also recorded data during the breakwater construction. The prediction of the models concerning these data resulted in slightly overestimated pore pressures.

Figure 6-36 shows the pore pressure profile with depth. It is observed that the greatest difference in the prediction of pressures between the models corresponds to the stage of pore pressure dissipation. The predicted pressures at 558 and 1314 days (during partial consolidation of the embankment and caisson, respectively) were different with the two models (SS and S-Clay1), which is explained by a different dissipation rate. The maximum pore pressures were obtained under caisson undrained load (day 859), being similar with both models. It should be noted that these pore pressure predictions resulted in values higher than the values measured in the ground, but the S-Clay1 model shows slightly better prediction.

Settlement predictions are shown in Figure 6-37. Two different control points are shown in this figure: one under the embankment base and the other corresponding to the caisson. The settlements measured using topographical controls in caisson 35 are also shown in this figure. It is observed that the S-Clay1 model underestimates the final settlement, showing a significant difference with respect to the SS model predictions, something that was not observed in the other sections evaluated, and explained by the different construction history. Apparently, the S-Clay1 model is more affected by the load history than the SS model. The variation of the final settlement prediction ranged between 2.40 and 2.65 m in the S-Clay1 model, while with the SS model it ranged between 2.53 and 2.61m in the three sections analysed.

Figure 6-38 shows the profile of settlements in a horizontal section through the base of the embankment. The shape of the settlement profile is consistent with the geometry of the breakwater and extends approximately 30m on both sides. As expected for this section, the maximum settlements computed with the SS model (at 3026 days) is much higher than the S-Clay1 model prediction.

As in the previous cases, the settlements at different depths in the central axis of the breakwater were calculated with the two models (see Figure 6-39). It is observed that both models calculate practically the same settlement value at the lower levels (level >-43m), while in the upper strata the difference is noticeable.

The total displacement contours under the breakwater are shown in Figure 6-40. It can be seen that the SS and S-Clay models produce similar contours. However, it is observed that the displacement contours calculated with the S-Clay1 model, extend slightly further in depth towards the lower clay layer (see Figure 6-40b and d).

The contours of volumetric deformation and deviatoric deformation are shown in Figure 6-41 and Figure 6-42, respectively. The largest volumetric deformations are observed in the first stratum under the breakwater; which is consistent with the settlement profile. Volumetric deformation intensity extends

up to the intermediate sand layer at 50m depth. On the other hand, the shear deformations calculated with both models show a larger intensity in the area immediately under the caisson (Figure 6-42c and d), which shows a punching mechanism typical of foundation on soft soil.

The stress paths of different points in the model of Section 4 are shown in Figure 6-43. Four selected points under the central zone of the breakwater show a similar trend to that obtained in Sections 2 and 3. The mean effective stress p' increases as the construction progresses, while the undrained loads move the stress path in the direction of the failure line. No point touches the failure envelope line as pore pressure was controlled during construction. The stress paths obtained with the SS model are closer to the failure line. In Figure 6-43b, two additional points under the embankment are examined at a depth of about 10m, these points maintain a tendency to follow the K_0 line.

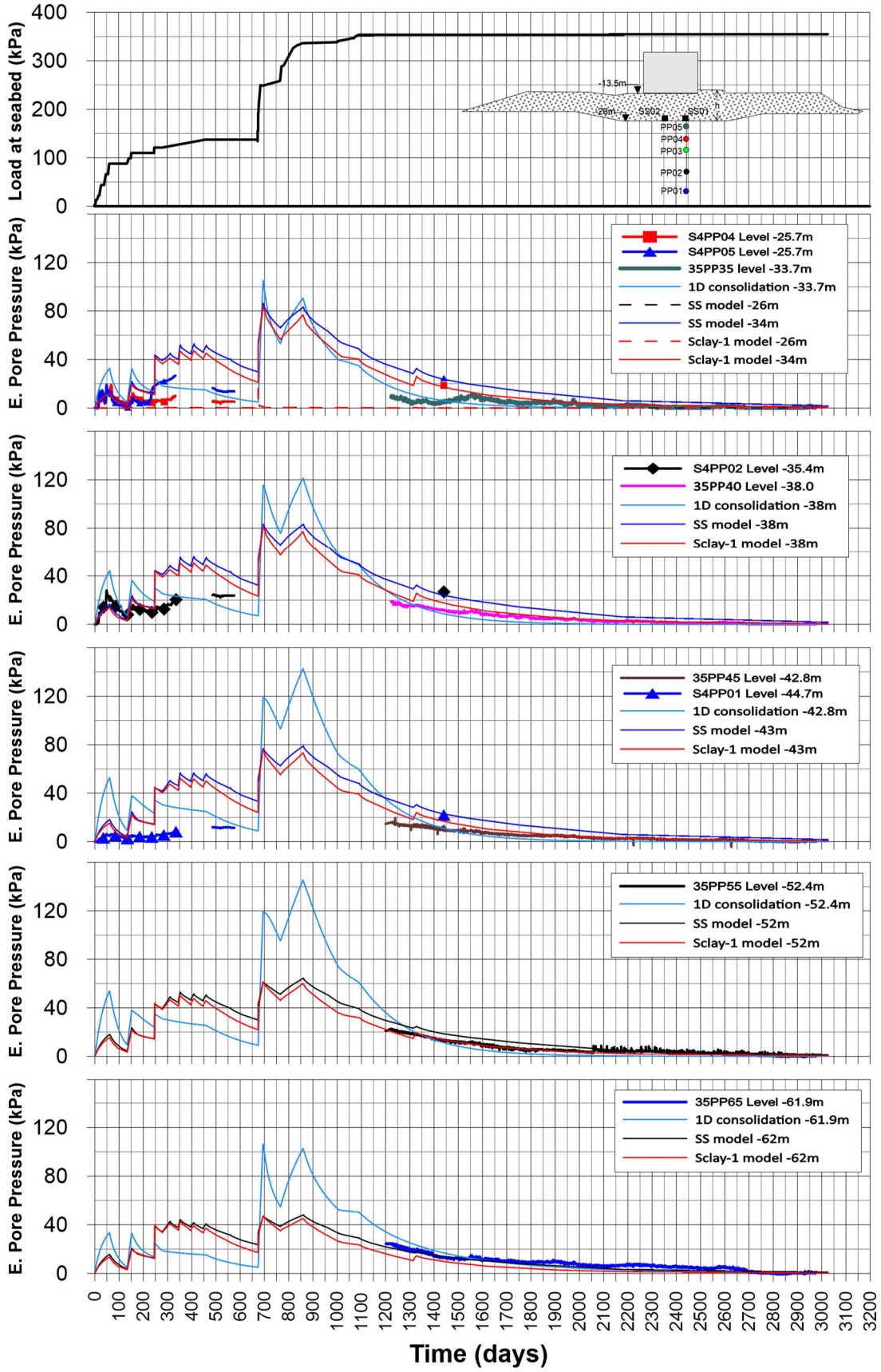

Figure 6-35. Pore pressures evolution computed with the SS and SClay-1 models in Section 4.

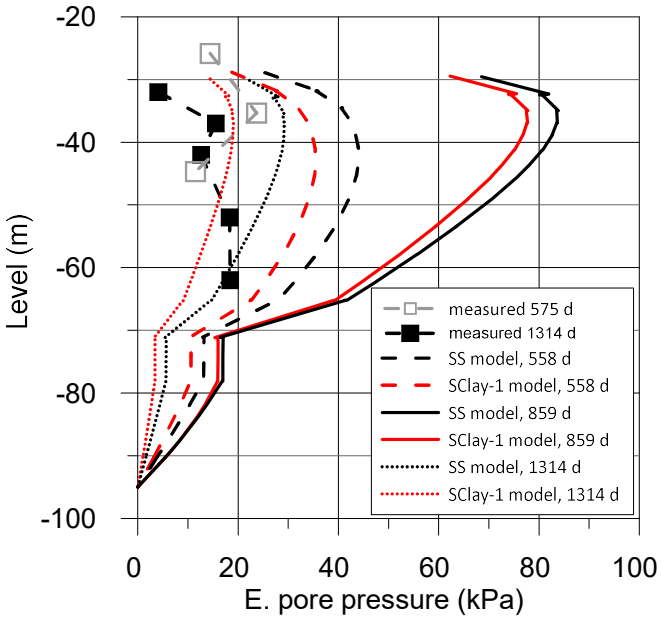

Figure 6-36. Excess pore pressure profile at the centre of section 3

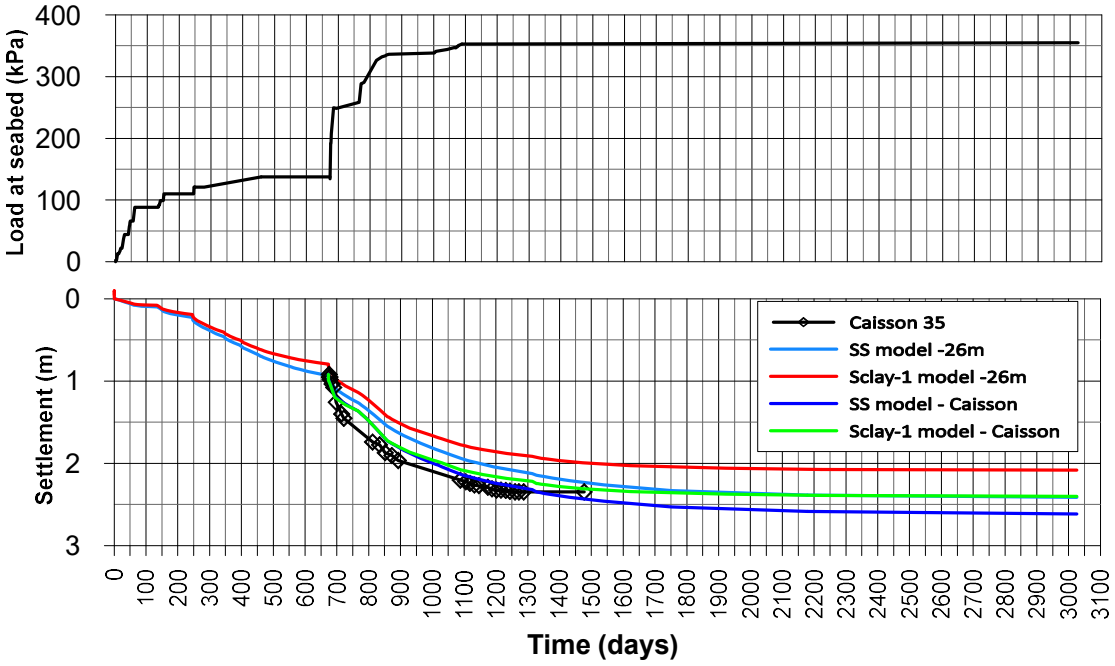

Figure 6-37. Evolution of settlements predicted in Section 4.

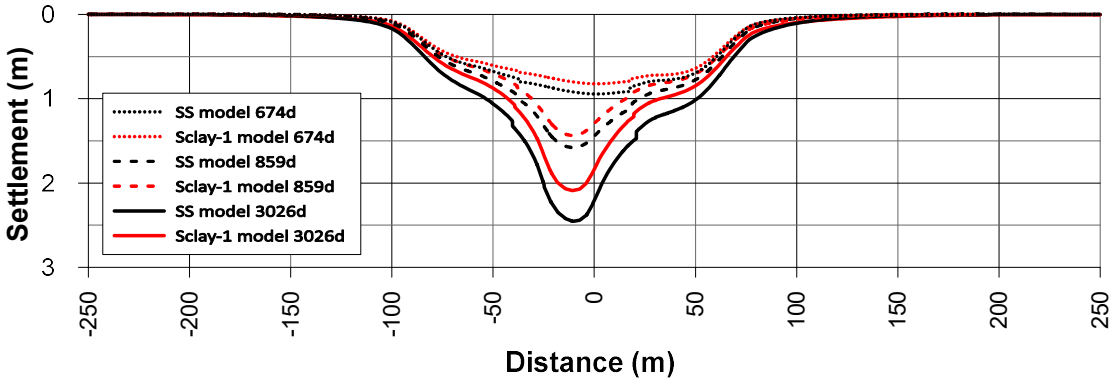

Figure 6-38. Horizontal profile of settlements at embankment base of Section 4.

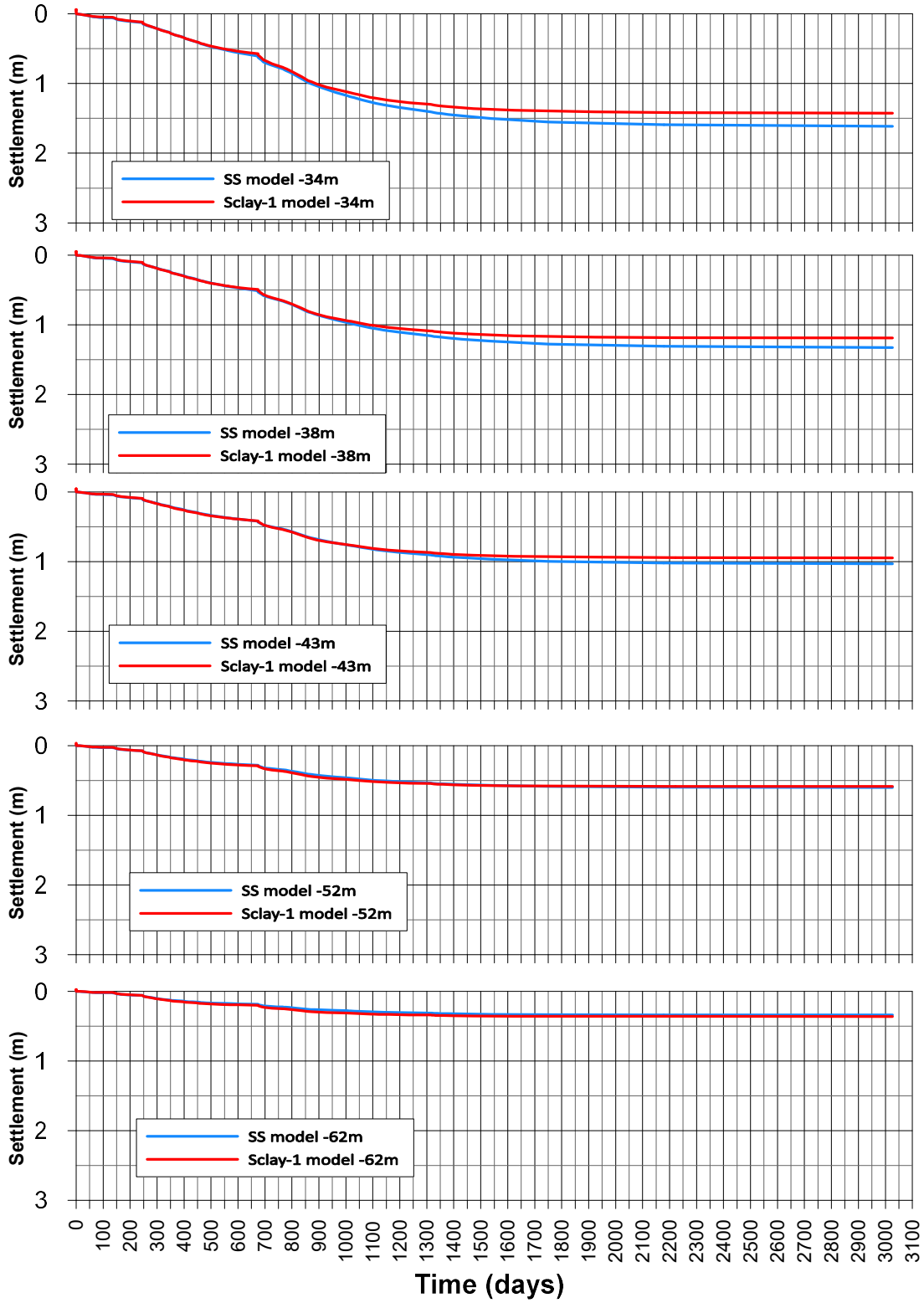

Figure 6-39. Settlements at several depths predicted with the FEM models in Section 4.

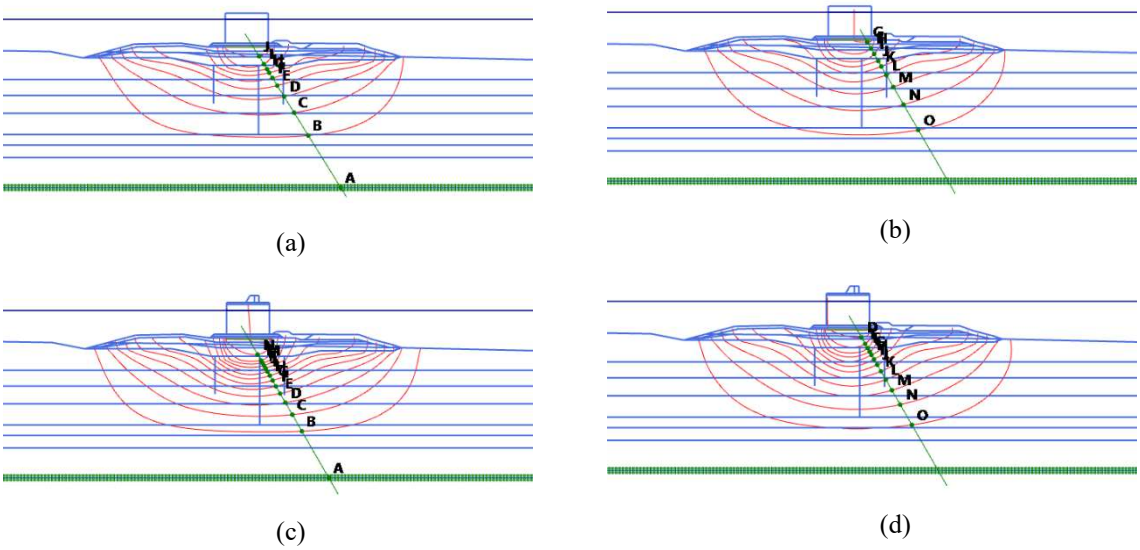

Figure 6-40. Total displacement contours (a) SS after construction (b) S-Clay1 after construction (c) SS long term (3026days) (d) S-Clay1 long term (3026days).

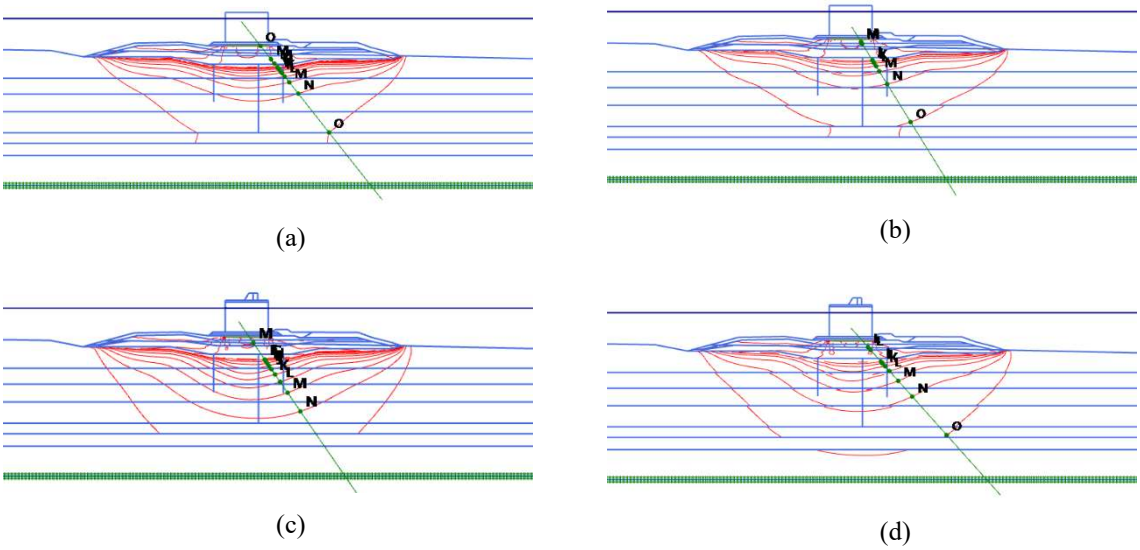

Figure 6-41. Total volumetric strain contours (a) SS immediately after construction (859 days) (b) S-Clay1 immediately after construction (859 days) (c) SS after 3026 days of consolidation (d) S-Clay1 after 3026 days of consolidation.

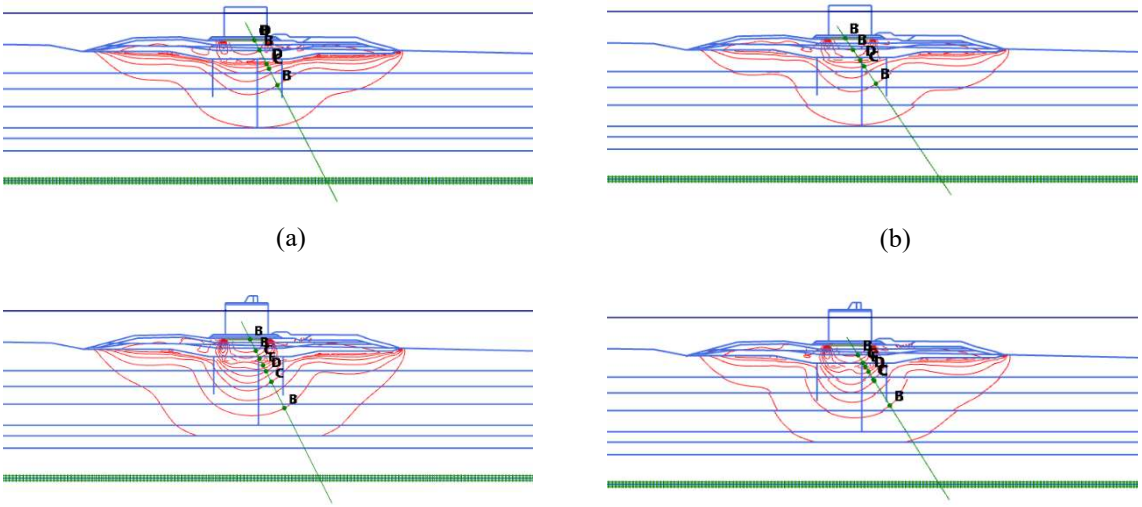

(a) (b)

(c) (d)

Figure 6-42. Total deviatoric strain contours (a) SS immediately after construction (859 days) (b) S-Clay1 immediately after construction (859 days) (c) SS after 3026 days of consolidation (d) S-Clay1 after 3026 days of consolidation.

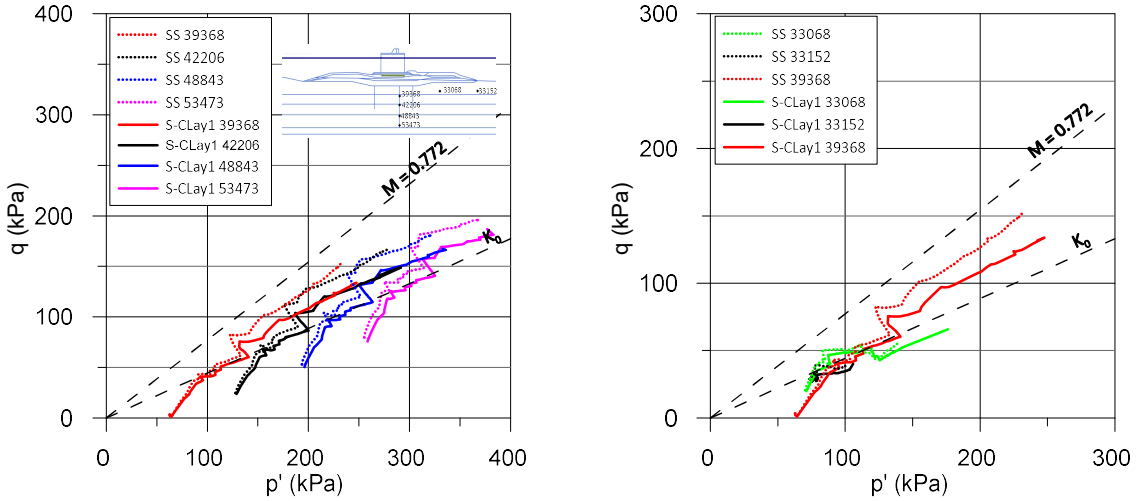

(a) (b)

Figure 6-43. Stress path at various points (a) on the centreline (b) horizontal line at 10m below the seabed.

6.3 PERFORMANCE UNDER CYCLIC LOAD

6.3.1 Domain discretization

Based on the Kuhlemeyer and Lysmer (1973) study, the average length of the element size should be less than or equal to one-eighth of the wavelength associated with the maximum frequency component f_{max} of the input wave (the highest frequency component that contains appreciably energy):

$$AverageElementSize \leq \frac{\lambda}{8} = \frac{v_{s,\min}}{8 f_{\max}} \qquad 6.5$$

$V_{s,min}$ is the lowest wave velocity, which corresponds to the first clay stratum. Based on shear stiffness (35-65 MPa) and the unit weight of soil, $V_{s,min}$ is estimated at 130-180 m/s. Wave load frequency varies between 0.07 – 0.1 Hz. Therefore, for this analysis conditions, the average element size is higher than 100m, which means that contrary to what occurs in seismic deformation analysis, in the case of sea wave load analysis, the size of the element is not relevant. Taking into account the nature of this research effort, the mesh used was refined to 5,000 triangular elements, with element sizes ranging from 0.18 m in the breakwater area to 12.67 m close to the boundaries.

6.3.2 Boundary conditions

During the static analysis, both the horizontal and vertical directions are fixed against movement at the base of the model. The lateral vertical boundaries allow vertical movement, but are laterally "fixed" to prevent horizontal movements. Flow across the boundary is permitted at the lateral and bottom of the model. A hydrostatic stress state is defined by the phreatic surface.

For dynamic analysis, appropriate boundary conditions must be established, which are able to simulate the far-field behaviour by absorbing the increment of stresses caused by dynamic loading and avoiding spurious wave reflections inside the soil body. The viscous boundary type, based on the method of Lysmer and Kuhlmeyer (1969) was chosen to simulate the far-field behaviour at the boundary of the model. A damper is used in the boundaries, which ensures that an increase in stress on the boundary is absorbed without rebounding. This type of boundary is suitable for problems where the dynamic source is inside the mesh.

The normal and shear components absorbed by the damper in the x-direction are: $\sigma_n = -C_1 \rho V_p \dot{u}_x$ and $\tau = -C_2 \rho V_s \dot{u}_y$ where ρ is the density of the materials, V_p and V_s are the compressional and shear wave velocity and u_x and u_y are the normal and shear particle velocities, C_1 and C_2 are relaxation coefficients to modify the effect of the absorption. The use of $C_1 = 1$ and $C_2 = 1$ results in a reasonable absorption of any waves reaching the boundaries.

6.3.3 Construction stages

The principal purpose of the static analyses (pre-storm) is to obtain the initial distribution of effective stresses and pore pressures within the breakwater and foundation soils at the beginning of the dynamic analysis (establishing the pre-storm initial conditions). In this sense, the construction sequence of section 2 (item 6.2.3) was adopted to establish the initial states before the dynamic analyses.

The dynamic analysis is performed in the time domain, using the wave pressure records measured with the instrumentation of the caisson at various depths, during a storm. At the location of each pressure sensor, a point load is introduced and the measured pressure records are entered as load multipliers. Due to the enormous amount of data measured on each sensor, approximately 8 hours of recording with a

sampling rate of 100 hz (about 3 million data per sensor), which greatly exceeds the conventional computation possibilities for dynamic analysis, it was necessary to extract a 600 s sector from the most active part of the storm. The section between 7:00 p.m. to 7:10 p.m. was selected to perform the dynamic analyzes. It was verified that the frequency content was equivalent to the complete storm record. Figure 6-45 shows the Fourier spectrum obtained with different size of sections extracted from the pressure record (600, 3600, 10800 and 21600s), showing that the predominant frequency content (mainly between 0.065 and 0.1 Hz) does not vary with the length of the sample.

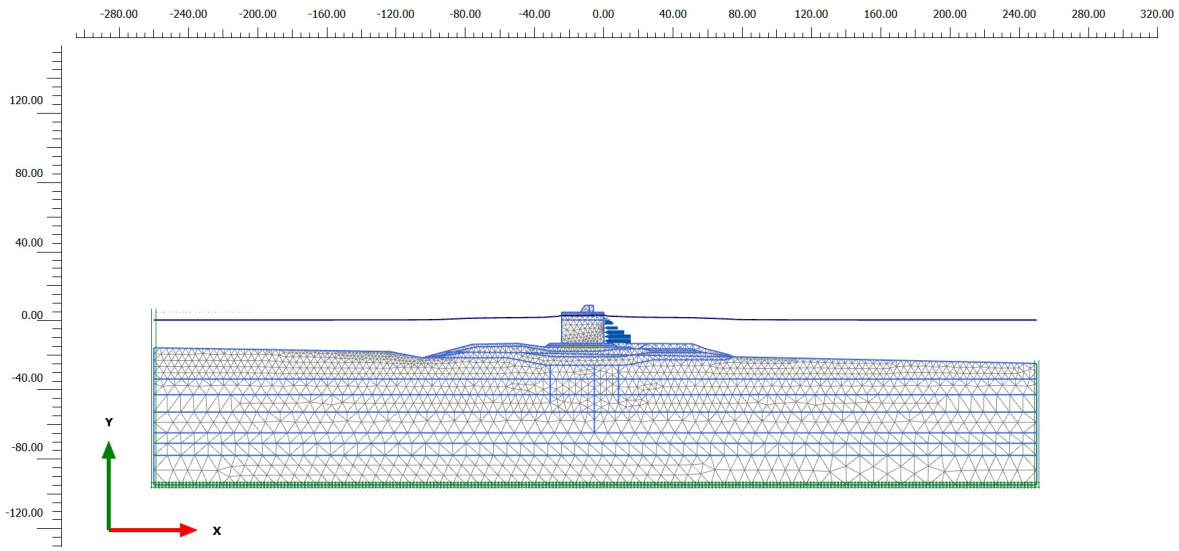

Figure 6-44. Geometry and mesh of the finite element model for dynamic analysis. Section 2.

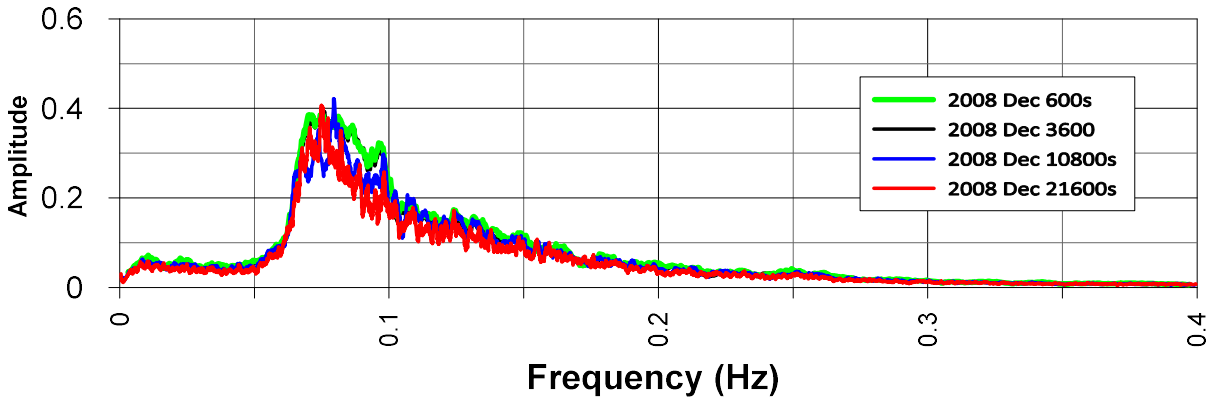

Figure 6-45. Normalized Fourier spectrum of 2008 storm for different size sections extracted from the pressure record (sensor 4).

6.3.4 Viscous damping

Some amount of viscous damping is needed to remove or reduce energy carried as high frequency "noise" generated in the numerical analyses. The use of too much viscous damping, however, can overdamp the mesh and can reduce the overall dynamic response; producing potentially unconservative calculations of cyclic pore pressure generation and induced cyclic deformations.

Viscous damping is applied in Plaxis as a Rayleigh damping formulation. The damping matrix, C is given by a combination of the mass matrix M and the stiffness matrix K, both affected by the Rayleigh coefficients, α (the mass-proportional damping constant) and β (the stiffness-proportional damping constant), in the following way: [C]=α[M] + β[K]. To calibrate both coefficients, it is necessary to define two target damping ratio ξ (which are generally chosen between 0.5 a 2 %), with their related frequencies. Following the procedure proposed by Hudson, Idriss & Beirkae (1994) the first frequency f_1 is set to the fundamental frequency of the whole soil layer and the second frequency f_2 as the closest odd number given by the ratio of the fundamental frequency of the input signal and the fundamental frequency of the whole soil layer.

The fundamental frequency of soil deposit can be estimated as $f = V_s/4H$, where V_s is the shear wave velocity and H is the thickness of the soil layer. It is estimated that the value of V_s varies between 136 (G=35 MPa) and 291 m/s (G=160 MPa) and considering that the soil deposit is 70m thick, then f_1 varies between 0.46 and 1 Hz. The fundamental frequency of the input signal was conservatively adopted as 0.1 Hz. Therefore, the frequency target f_2 is 0.1/0.46= 0.22Hz, and it can be set equal to 1Hz.

Within the range of the frequencies f1 and f2, the damping is less than the target damping (1%), whereas outside this range the signal it is overdamped. To produce the target damping, Rayleigh coefficients were selected at α = 0.03959 and β = 0.00218 (See Figure 6-46). As indicated by Beaty (2017) the mass-proportional damping does not impact the timestep, may reduce large displacements, and does not significantly damp high frequencies, whereas the stiffness-proportional damping is good at damping high frequencies, does not impact low frequencies as much, and can significantly reduce the timestep.

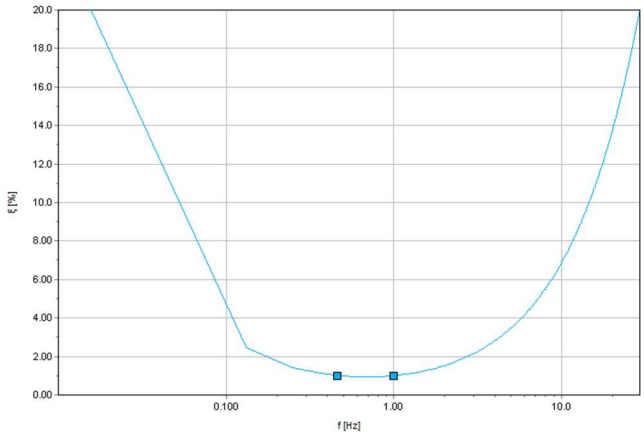

Figure 6-46. Rayleigh damping introduced in the dynamic model

6.3.5 Results and discussion

The UBC3D-PLM constitutive model for cyclic behaviour of liquefiable soils have been calibrated to match behaviours of laboratory cyclic test (see item 4.3.1). Of course, laboratory stress path not always follows the field stress path, principal stress rotation or the behaviour changes associated with void redistribution during cyclic analysis. Therefore, some deviation from the measured pore pressure

response during a storm could be expected. In addition, post cyclic resistance is not well simulated with the UBC3D-PLM model, as recognized by Beaty and Byrne (2011), who indicated that the UBCSAND will predict a significantly softened stress-strain behaviour after liquefaction, and the resulting mobilized strength may not be consistent with common interpretations of residual strength.

Chowdhury (2018) suggested that, in case of seismic analysis of dams, a better criteria to define the onset of liquefaction in field conditions is based on the occurrence of a cyclic pore pressure ratio $R_{u,seis} \geq 0.7$ and development of a peak shear strain of $\gamma \geq 10\%$. $R_{u,seis}$ is the ratio of the pore pressure seismically generated (or cyclically generated) and the initial vertical effective stress. $R_{u,seis}$ can be expressed as:

$$R_{u,seis} = 1 - \left(\sigma'_v / \sigma'_{v,i} \right) = \Delta u_{cyclic} / \sigma'_{v,i} \tag{1.6}$$

where σ'_v is the current effective vertical stress and $\sigma'_{v,i}$ is the initial (pre-earthquake) vertical effective stress, and Δu_{cyclic} is the cyclically induced change in pore pressure. $R_{u,seis}$ differs from the more commonly calculated pore pressure ratio r_u ($r_u = u/ \sigma'_v$), in that σ'_v is the initial major principal effective stress (before starting the breakwater construction).

Figure 6-47 shows the relationship of cyclic stress ratio (CSR) and the number of cycles to liquefaction (N_{liq}) computed with several set of parameters of the UBC3D-PLM model under a vertical effective stress σ'_v of 133 kPa. Also included in this figure, it is the relationship obtained from the cyclic interaction diagram (item 3.4.1) and results of CDSS tests of Port Barcelona clay. It is observed that although several parameters were tried (see Table 6-10), the slope of CSR – N result almost the same with all models used and slightly higher than the reference value obtained from the cyclic interaction diagram ($\tau_{ave}/\sigma'_v = 0$ and $\tau_{ave}/\sigma'_v = 0.16$). Two sets of parameters were selected for the analysis. The conservative set (Model 2: UBC7) was used for post-cyclic stability analysis and the other set (Model 1: UBC3) was used for evaluation of breakwater performance. None of them could correctly predict deformation.

Table 6-10. List of parameters used to probe the UBC3D model

	UBC1	UBC2	UBC3/9/10	UBC4	UBC5	UBC6	UBC7/11/12	UBC8
k_B^e	300	300	300	1500	1500	2500	2000	2000
k_G^e	150	150	150	750	750	750	750	750
k_G^p	8000	8000	8000	8000	8000	8000	8000	4000
me	0.5	0.5	0.5	0.5	0.5	0.8	0.8	0.8
ne	0.5	0.5	0.5	0.5	0.5	0.5	0.5	0.5
np	0.5	0.5	0.5	0.65	0.5	0.5	0.5	0.5
f_{dens}	0.2	0.2	0.2	0.5	0.5	0.5	0.5	0.5
f_{Epos}	0.2	0.2	0.2	0.2	0.2	0.2	0.2	0.2
ϕ_{cv}	28	29	29	29	29	29	29	29
ϕ_p	30	30	30	30	30	30	30	30
c	9	9	1	1	1	1	1	1
N	5	5	5	5	5	5	5	5

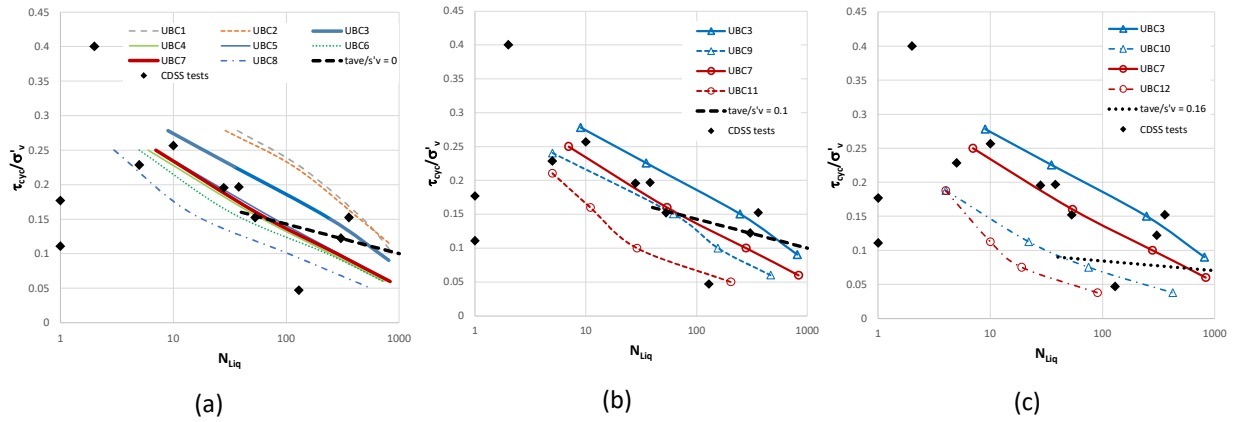

Figure 6-47. Relationship of the number of cycles to liquefaction (N_{liq}) and cyclic stress ratio (CSR) from cyclic direct simple shear (CDSS) test results and CDSS simulations. (a) τ_{ave}/σ'_v =0 (b) τ_{ave}/σ'_v =0.1 (c) τ_{ave}/σ'_v =0.16.

Figure 6-48 shows the stress state just before the start of the cyclic analysis. Under the embankment, the initial stress ratios K are mostly around 0.7 and 0.9, which is consistent with the commonly observed stress rotation of embankments. There are values higher than K > 0.9 at specific locations, such as at the base and the toe of the embankment, soils in these areas are considered to be potentially liquefiable materials. The predictions for the static state are reasonable for the conditions present after breakwater construction and soil consolidation.

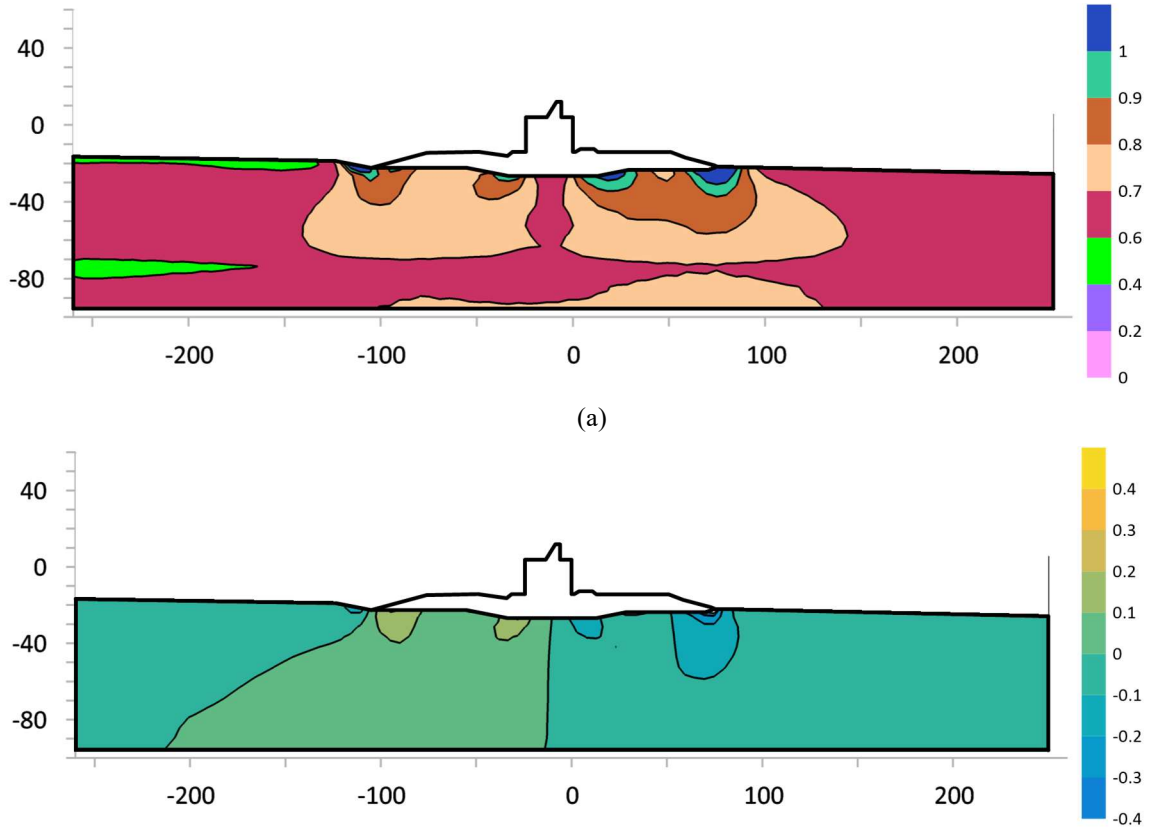

Figure 6-48. Initial stress state at the start of the dynamic analysis. (a) Initial stress ratio K = σ'_x/σ'_y contours. (b) Initial static shear stress ratio $\alpha = \tau_{xy}/\sigma'_y$ contours.

Figure 6-49 presents the maximum of the excess pore water pressure ratio r_u contours at the end of the cyclic loading computed with the two models tested. Based on the contours of r_u, that varies between 0.1 to 0.4, the soils are mainly affected by cyclic mobility up to the level of -38m (around 18m thick). Cyclic mobility is more significant under the berms of the embankment. Both models show a similar definition of the zones affected by cyclic mobility. Contours of $R_{u,seis}$ were also computed and these are shown in Figure 6-50. Cyclic mobility zones are quite similar to those shown with the r_u contours, but, in this case, a zone with negative pore pressure is noted (especially noted in model 1), which is explained as a result of the flow rule implemented in the UBC3D-PLM model.

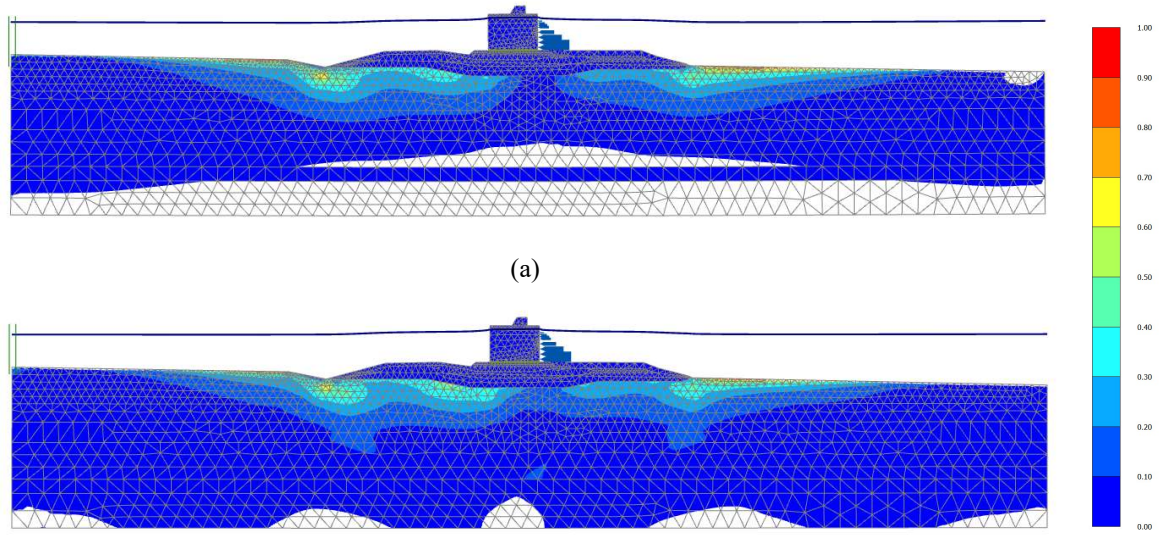

(a)

(b)

Figure 6-49. Excess pore water pressure ratio ($r_u = u/\sigma_v$) contours at the end of the cyclic loading (a) Model parameters UBC3 (b) Model parameters UBC7.

Figure 6-51 shows the wave pressures record of the storm in December of 2008 and also the response of subsoil recorded with the piezometers installed at several depths. Also, the results of the dynamic finite element analysis are shown in this figure. It is clear that the computed pressure with the UBC3D model overestimates the response observed, but in no case the liquefaction condition is reached.

Finally, the dominant vibration frequency of the model was verified, calculating the dynamic response at a point located at the top of the caisson and another at the bottom of the caisson. The Fourier spectrum results in a frequency of 0.47 Hz, a value quite similar to that calculated in Section 2.5 with the analytical model (0.53Hz), indicating that the dynamic model responds as expected.

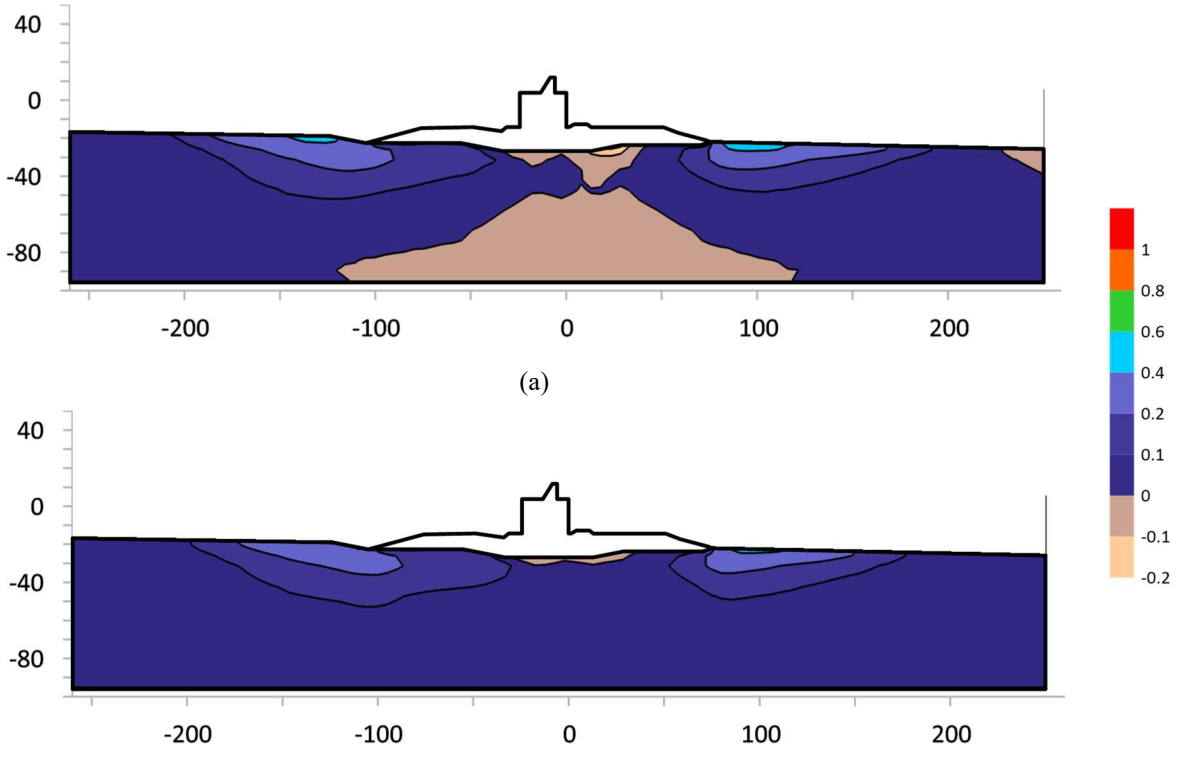

(a)

(b)

Figure 6-50. Excess pore water pressure ratio ($R_{u,seis}$) contours at the end of the cyclic loading (a) Model parameters UBC3 (b) Model parameters UBC7.

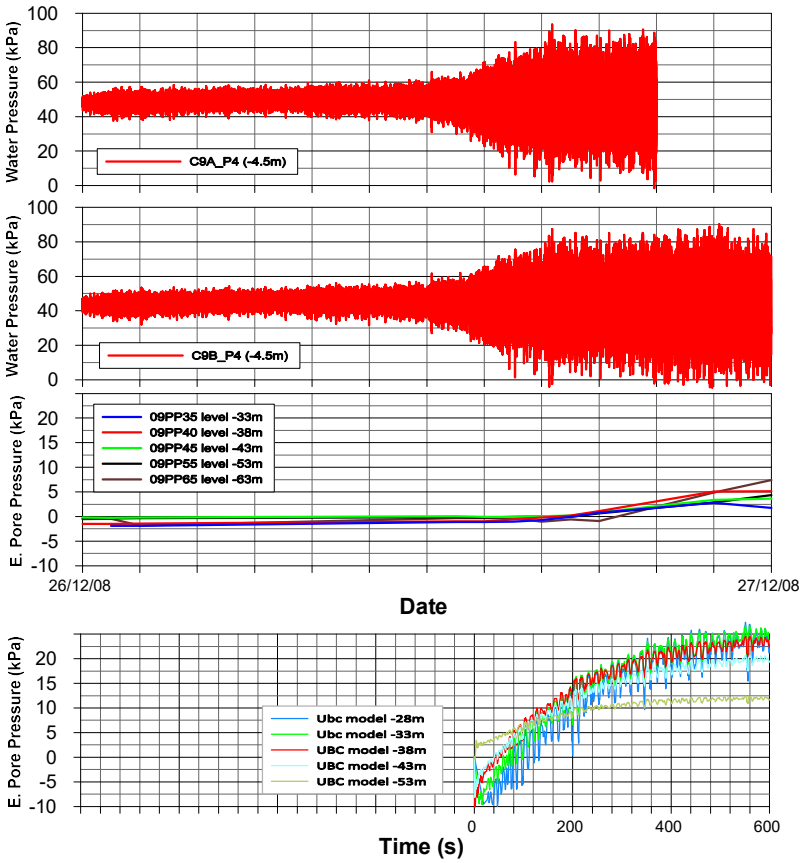

Figure 6-51. Excess pore pressure computed with the UBC model during a large storm recorded at 2008, compared with the pore pressure measured in the foundation soils.

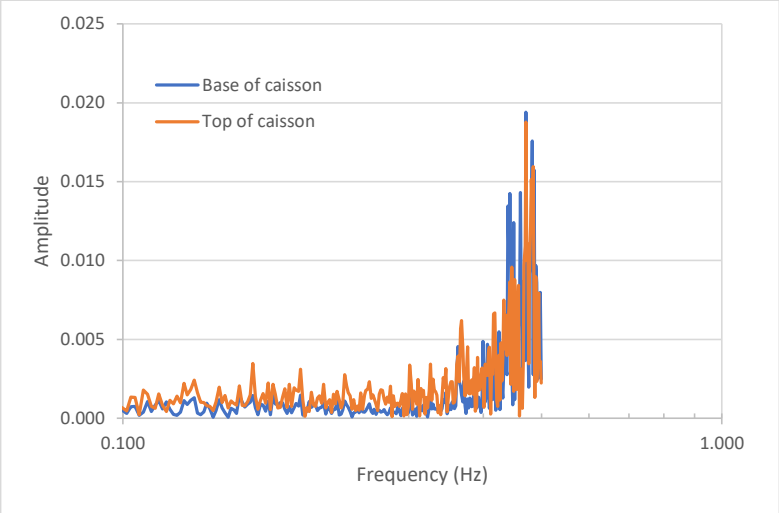

Figure 6-52. Fourier spectrum computed with the dynamic finite element model.

6.4 CONCLUSIONS

This chapter describes the numerical simulation of the breakwater construction for Barcelona Harbour using different constitutive models (Soft Soil, S-Clay1 and Soft Soil Creep model). All models are implemented into Plaxis finite element code. Analyses are performed on four instrumented sections to monitor pore pressures, settlements, and horizontal displacements. The first of these sections corresponds to the slope-type dike and the other to the caisson dike. The data from the first section were used to calibrate the model during construction because according to the work schedule it was the first section to record data. In this way, the model was used to predict settlements and assess the stability of the caissons dike. The soil parameters were adjusted to simulate the undrained strength obtained in simple shear tests. The main conclusions from this study are given as follows:

This chapter revealed that the elastoplastic methods of analyses were successful in reproducing the performance of a breakwater founded on soft soil based on pore pressures and settlements measured during construction and post-construction. The simulations also aim to compare the overall response predicted by the advanced models to the results obtained using the isotropic models that are often employed in practice. It was concluded that despite the still existing limitations of simple isotropic models, careful simulations carried out using elastic-plastic models and coupled consolidation can provide a good prediction of settlements and pore pressures of breakwaters constructed over soft clays. Although, in general, all the model calculations were found to be inaccurate for predicting horizontal deformations, but the S-Clay1 model seems to perform better in this regard, which is an important advantage considering that the horizontal displacements are associated with instability of breakwaters as shown by Chung et al 2006.

Measuring stresses in-situ is very complex and most of the publications in the field of breakwaters are concerned with caisson settlements. Even so, it is interesting to examine the stress path calculated at different points in the model. The observed effective stress paths at points vertically below the centre of

the breakwater and at the toe of the embankment slope are consistent with the loading and consolidation stages during breakwater construction. From these curves, it can be seen that during construction the dike with a sloping section came dangerously close to the instability zone, which did not occur in the case of the caissons breakwater. This is explained by the fact that the rate of construction that took place in the case of the sloping dike was much higher than the rate of construction of the caissons dike. The slope-type breakwater was built by tipping material from dump trucks while the embankment of caisson breakwater was dumped with barges. In the case of the slope-type breakwater, the 10-month suspension that was established in order to dissipate pore pressures was essential for stability. This demonstrates the effectiveness of the staged construction method for breakwaters on soft soils.

The undrained cyclic behaviour was also investigated with aid of a full dynamic finite element model together with the constitutive model UBC3D-PLM included in Plaxis. The model parameters were calibrated using laboratory tests. As has been demonstrated, the model hardly reproduces the cyclic interaction diagram described in chapter 3. However, the parameters were selected under a conservative criterion. The hydrodynamic forces acting on the wall of the caisson measured during the December 2008 storm were put into the model at the position of each sensor. A random 600 s sector was selected from the pressure records, verifying that its frequency content is representative of the frequency content of the entire record.

It is clear from results of the model that the ratio of excess pore pressure to stress increment (r_u) varies between 0.1 to 0.4, with higher values in areas located below the extremes of the embankment, mainly due to less confinement. The areas located below the caissons are also affected by cyclic mobility but to a lesser extent, in this case, the embankment provides sufficient confinement. These results highlight how important it is to have an embankment with long berms, to reduce the development of areas with cyclic mobility.

Chapter 7

STABILITY ANALISYS OF BARCELONA VERTICAL BREAKWATER

7.1 INTRODUCTION

The behaviour of the soft soil under the breakwater was examined in previous chapters using the results of the geotechnical instrumentation and different numerical models. The instrumentation allowed to measure settlements of the order of about 2.5 m as a result of the construction of the breakwater. Also, construction generated an increase of pore pressures to maximum values above 120 kPa. The evolution of pore pressure during construction was kept under control so that the stress state was kept away from the failure condition at all times.

In this chapter, the numerical model used to evaluate the performance of the vertical breakwater, as described in the previous chapter, is expanded, so that it will be used to evaluate the stability at different stages of the construction process, identifying the critical states of the work. In order to evaluate stability, it was necessary to define different types of safety factors, associated with the load requirements due to the waves and the weight of the structure. Finite element analysis was used with the adjusted SS model to produce the undrained resistance in simple shear mode. In addition, the stability under cyclic loading conditions is examined, using a simplified procedure and the interaction diagram developed in Chapter 3.

7.2 FACTOR OF SAFETY

Usually, the study of the stability of a breakwater is associated with the corresponding failure mechanisms. ROM 0.5 establishes 4 geotechnical failure modes for vertical breakwaters (Overturning, sliding, bearing capacity and global stability), which have been described in section 2.6. However, bearing capacity and global stability correspond to the same failure mechanism, therefore, within the framework of finite element analysis carried out in this thesis, only the global stability is considered. Overturning and sliding mechanisms are implicitly integrated into the analyses through the use of 'joint elements' to improve the soil-structure interaction.

Two different types of analysis were used to computed the safety factors: Increasing the external loads (caissons weight and wave loads) until a limit load is found and reducing strength parameters (cohesion and angle of friction) until a collapse mechanism is found. The last one produce similar result to that obtained with the limit equilibrium method, as described by Griffith and Lane (1999).

The procedure of increasing loads is motivated by issues such as the uniqueness of the bearing mechanism and global stability, and by the uncertainty in the value of horizontal wave loads, which could lead to sliding failure. In these circumstances, it would be convenient to know the critical collapse load to compare with the initial estimates of the sea wave forces.

When the safety factor was computed by the progressive reduction of strength parameters (c, $\tan\phi$), the method led to the most critical failure mechanism, which in all cases can be called global instability. As a reference, Table 7-1 shows the minimum desired safety factor for different failures mechanism, in vertical breakwater stability analysis. For Barcelona breakwater analysis, it was proposed to adopt a minimum safety factor of 1.5 for short-term failures under self-weight and 1.25 when low-probability wave forces act. This proposal is more conservative than the ROM recommendation that sets the previous safety factors at 1.3 and 1.1, for global stability cases.

Table 7-1. Minimum safety factor for vertical breakwater proposed for ROM 0.5-0.5.

Ultimate limit state	Load Case		
	Quasi-permanent actions	variable actions	Accidental actions
Sliding	1.3	1.1	1.0
Bearing failure	1.8	1.5	1.2
Overturning	1.3	1.2	1.1
Global stability	1.3	1.1	1.0

Factors of safety by Increasing loads

The safety factor is defined as the relation between the limit load to produce collapse and the initial value of this load. Three different situations were established:

FS1*, Increasing caisson weight

FS2*, increasing simultaneously the caisson weight and wave load

FS3, Increasing wave load

The symbol * indicates that the weight of caisson was considered submerged, that is, discount the weight of the volume of displaced water to the weight of caisson.

Factor of safety by reducing strength parameters

The safety factor is defined as the value by which cohesion and the tangent of the angle of friction are divided to produce soil collapse. Two cases were distinguished:

CF1, reducing c and tg(φ) without wave load

CF2, reducing c and tg(φ) with wave load

7.3 STABILITY ASSESSMENT

7.3.1 Review of stability before breakwater construction

The construction of the caisson breakwater was developed in 4 construction phases defined in the construction project. These phases are described in item 5.2. For the stability calculations indicated in this chapter the following phases were considered: Phases II (placement of the caissons), Phase III (Construction of the superstructure) and Phase IV (filling behind the caissons).

7.3.1.1 Undrained effective stress analysis with undrained strength parameters

At the stage of design, the stability of different phases of the project was computed using the limit equilibrium method. Details of this limit equilibrium analysis can be found in the Technical Construction File (GPO-Europrincipia, 2001). In this section, the undrained stability was investigated with the finite element method. The limit equilibrium method has been found to provide acceptable result in many applications and is widely used in the engineering practice, so in this case, it will be used only as a reference. Geometry, materials and conditions of analysis were almost the same in order to compare results from these two different methodologies. General description of the finite element analyses and main results of the analysis are presented in this section.

The lineal elastic model was used to simulate the caissons and concrete slab behaviour, while the Mohr-Coulomb model was selected for the soft clay, rubble-mound, rockfill, and backfill materials. Soft clay was assumed to have undrained behaviour (with development of excess pore pressure). All other materials were considered drained (without development of excess pore pressure).

Strength parameters values were defined at section 6.2.2, with the exception of that for the Mohr-Coulomb parameters to define the undrained behaviour of the soft clay, which were established in the following way:

- From the various field and laboratory tests performed, it is obtained that the undrained shear resistance s_u in the dominant shear mode varies depending on the effective vertical stress as follow:

$$s_u(z) = 0.25\sigma'_{v0}(z) \qquad 7.1$$

  Where $\sigma'_{v0}(z)$ is the effective vertical stress in the initial conditions at depth z.

- In the areas under load, the equation that defines the variation of su with depth is as follows:

$$s_u(z) = 0.25[\sigma'_{v0}(z) + \Delta\sigma'_v(z)] \qquad 7.2$$

Where $\Delta\sigma_v^{'}(z)$ is the increase in the effective vertical stress produced by the load applied to the natural ground. This increase is calculated using Boussinesq formulas (Poulos and Davis, 1974) for infinite elastic half-spaces corresponding to the type of load applied.

- Subsoil was divided into several strips of material with different strength. In each of these strips, the properties of the natural ground are modified according to the corresponding effective vertical stresses. In this way, the gain in undrained resistance as consolidation progress is introduced in the model following the construction process.

Horizontal loads were included in the analysis in order to simulate wave loads. Different types of safety factors as defined in section 7.2 were computed for the situations considered more relevant.

Finite elements mesh of the model in the final stage of construction is show in Figure 7-1, 1917 triangular elements of 15 nodes were used.

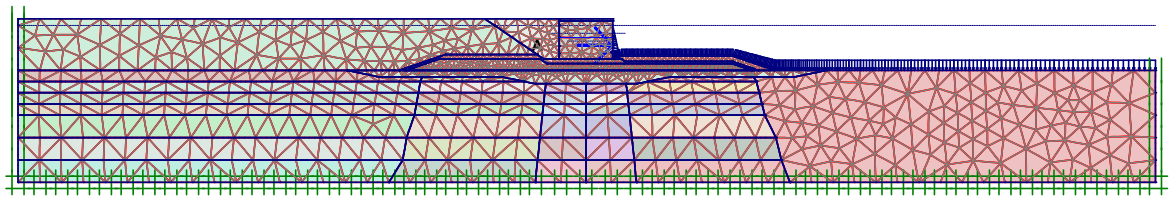

Figure 7-1. Finite element mesh at the final stage of construction

Figure 7-2 shows the several phases of construction considered in the analysis. It could be observed how the undrained shear strength of the foundation soil is changed at each phase to represent an increase of strength due to soil consolidation (undrained analysis with undrained parameters). Changes of the undrained strength was based on the vertical effective stress as explained before, in the same way as it was done for the limit equilibrium analysis.

Results

The ability of the finite element analysis to reach a state of collapse (increasing loads or reducing resistance parameters) brings the opportunity to examine the failure mechanisms in details. The advantage of the finite element method is that it avoids the need to assume a failure mechanism because the process of computation itself develop the most critical failure mechanism. This feature is especially useful in the case of a caisson breakwater, due to its complex geometry.

In addition, given the great influence of pore pressure distribution on the stability of geotechnical structures, the finite element method is more appropriate because the distribution of pore pressure is consistent with the equilibrium condition of the problem. This feature is not assured in the limit equilibrium method.

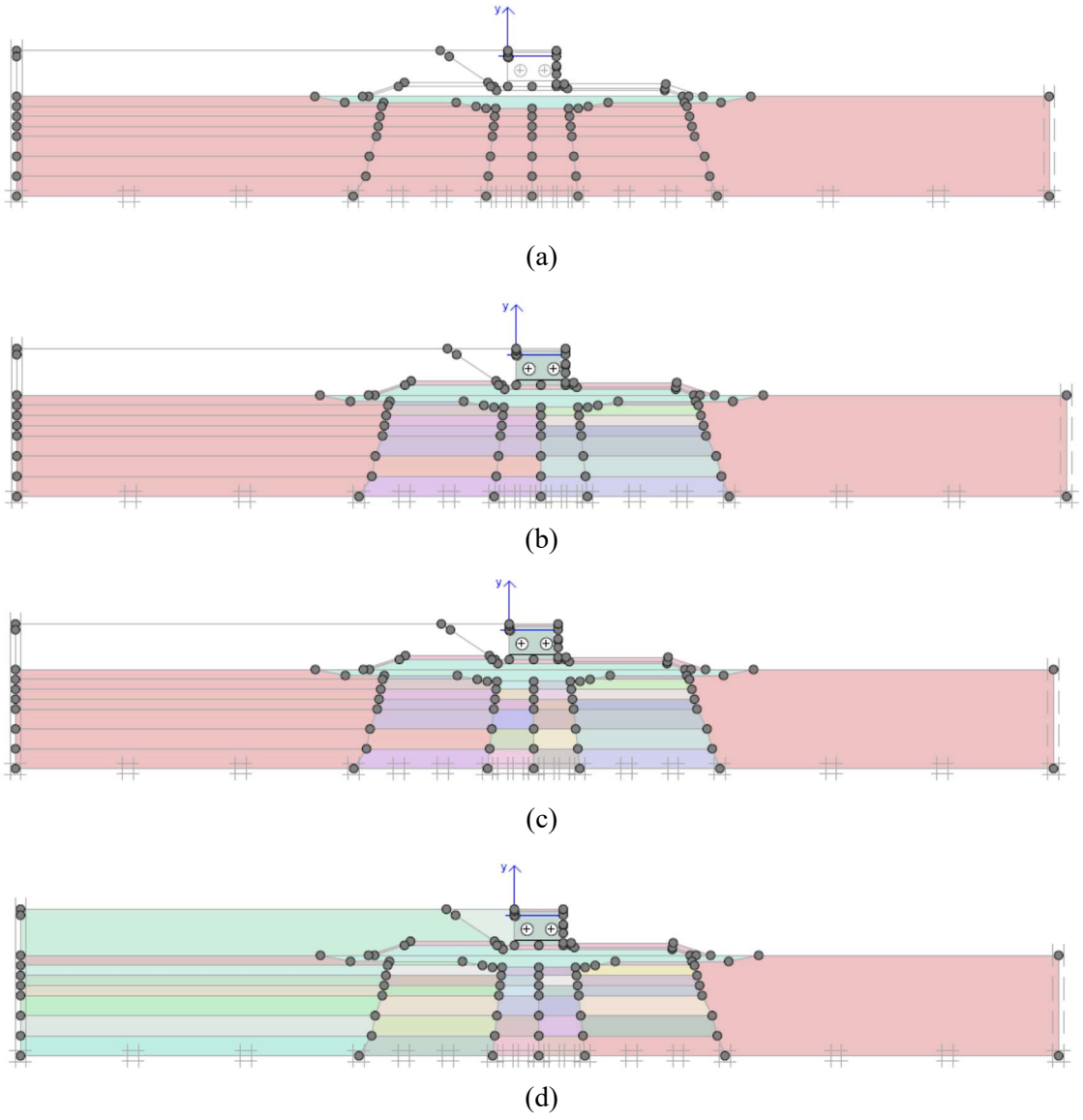

Figure 7-2. (a) Dredged and filling with rubble mound material (b) Embankment construction and caissons placement (c) Superstructure and shoulder construction (d) Backfill at the inner harbour

Soft clays are generally characterised by its low permeability, which implies a slow dissipation of excess pore pressure. In this condition, stability analyses under undrained condition are usually recommended. The Plaxis code offers the possibility of undrained effective stress analysis (Material type = Undrained) with the direct input of the undrained shear strength (s_u). This option was used in conjunction with the Mohr-Coulomb model. Note that when using the Mohr-Coulomb model, the improvement of soft soil as a result of consolidation is not considered, also the stiffness modulus is not stress-dependent, so these soil parameters had to be changed as the construction process progresses in the computations, as explained before. Furthermore, it should be noted that whenever the material type parameter is set to undrained, effective values must be entered for the stiffness parameters (Young's modulus E and Poisson ratio ν) in the analysis.

Figure 7-3 shows typical failure mechanism obtained with the finite element models; the sliding surface follows the geometry of the problem and distribution of undrained strength of foundation soil. In all the cases studied, the failure mechanism observed is of the global instability type.

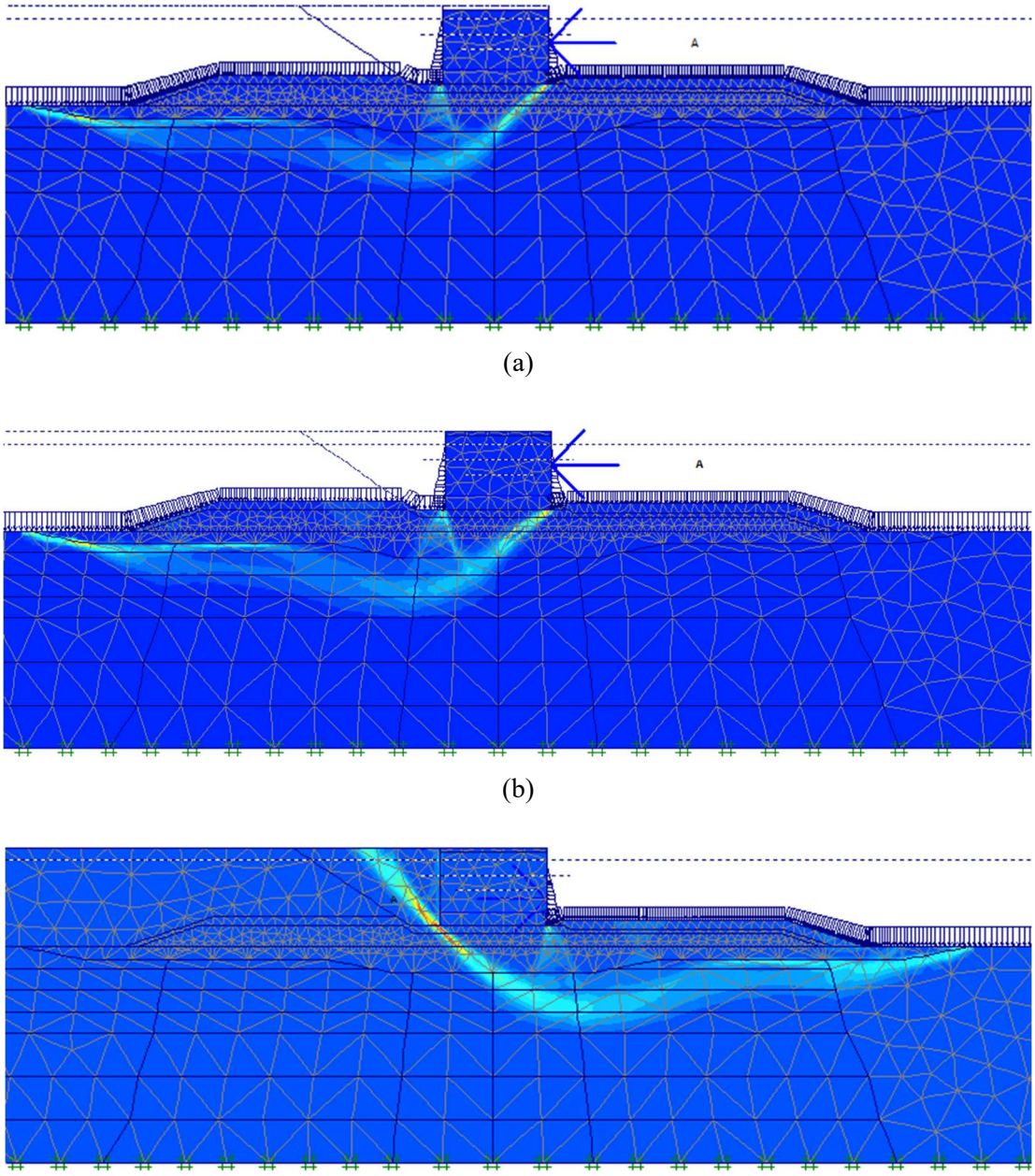

(a)

(b)

(c)

Figure 7-3. Some failure mechanisms obtained by the finite element analysis at different stages of construction, using the phi-c reduction method with wave load (a) Phase 2, CF2=1.33, (b) Phase 3, CF2=1.27, (c) Phase 4, CF2=1.37.

Safety factors obtained in the finite element analyses are shown in Table 7-2. The most critical phase of construction corresponds to the superstructure construction under the action of wave load. Both increasing loads and phi-c reduction methods (FS2, FS3 and CF2) produce the most critical safety factors at this stage.

Table 7-2. Safety factors obtained with the finite element method. Undrained effective stress analysis with undrained strength parameters (c_u, ϕ_u).

PHASE II (crest)	FS1*	1.75	CF1	1.62
	FS2*	1.43	CF2	1.33
	FS3	1.90		
PHASE III (crest)	FS1*	1.96	CF1	1.75
	FS2*	1.34	CF2	1.27
	FS3	1.59		
PHASE IV (sine)	FS1*	2.00	CF1	1.59
	FS2*	1.64	CF2	1.37
	FS3	3.00		

7.3.1.2 Undrained effective stress analysis with effective strength parameters

Additional finite element undrained effective stress analyses were carried out using effective strength parameters. The Mohr-Coulomb model was replaced by the more advanced Soft Soil model. The advantage of using these models in a consolidation analysis is that the increase of undrained shear strength with consolidation is automatically obtained.

In the geotechnical investigation of soft soils sometimes effective strength parameters are not always available, and one has to deal with measured undrained shear strength (s_u) as obtained from undrained tests, or commonly by in situ tests. Undrained shear strength, however, cannot easily be used to determine the effective strength parameters ϕ' and c'. Moreover, even if one would have proper effective strength parameters, care has to be taken as to whether these effective strength parameters will provide the correct undrained shear strength in the analysis. This is because the effective stress path that is followed in an undrained analysis may be different from that followed in reality, due to the limitations of the applied soil model and their ability to recognise features of soils, like anisotropic effects. Even in advanced models which usually consider the reduction of mean effective stress in undrained loading, it is generally advised to check the mobilised shear strength against the available (undrained) shear strength. The effective parameters of the soft soil model used in the analysis were calibrated in order to reproduce the undrained strength established from laboratory tests (see chapter 4).

Results

Figure 7-4 shows typical failure mechanisms obtained in the undrained analyses with effective strength parameters. These mechanisms are very similar to that obtained in the effective analysis with undrained parameter.

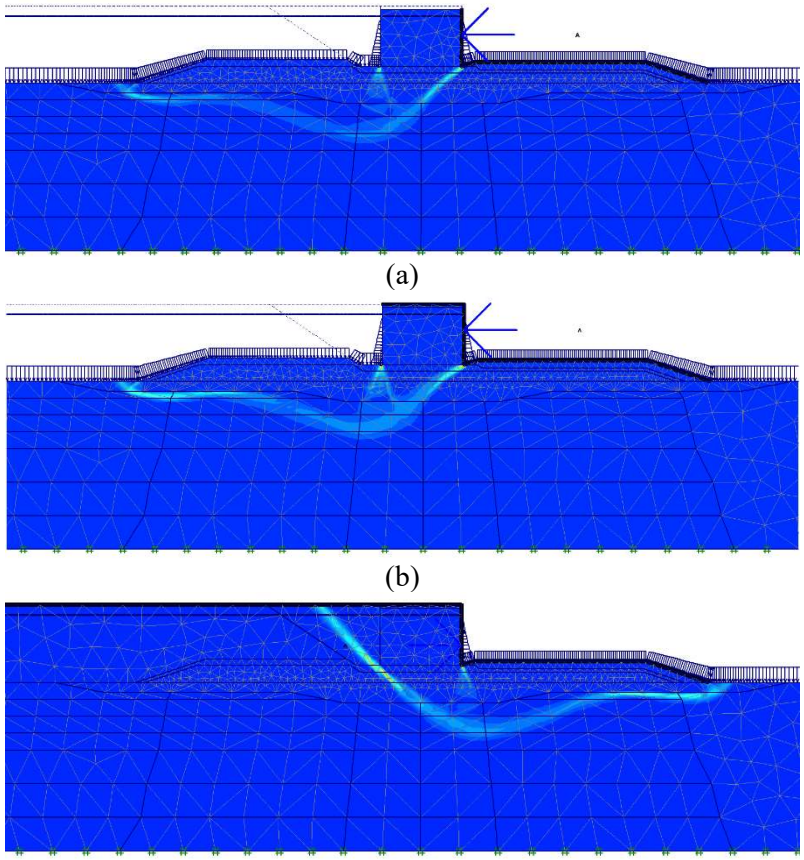

Figure 7-4. Some failure mechanisms obtained by the finite element analysis at different stages of construction, using the phi-c reduction method with wave load (a) Phase 2 CF2=1.42, (b) Phase 3 CF2=1.40, (c) Phase 4 CF2=1.51.

Safety factors computed at distinct phases of construction are shown in Table 7-3. Again, the most critical safety factors correspond to the phase of superstructure construction. All computations were performed with the standard iterative procedure without arc-length control. It is interesting to note that the safety factors obtained using effective stress strength parameters are approximately 0.10 to 0.15 greater than the factors obtained with the calculation procedure employing undrained parameters. Differences should be expected as the increase of undrained shear strength due to consolidation is better reproduced using effective stress models.

Table 7-3. Safety factors obtained with the finite element method. Undrained effective stress analysis with effective strength parameters (c', ϕ').

PHASE II (crest)	FS1*	1.91	CF1	1.77
	FS2*	1.52	CF2	1.42
	FS3	2.09		
PHASE III (crest)	FS1*	2.06	CF1	1.96
	FS2*	1.51	CF2	1.40
	FS3	1.85		
PHASE IV (sine)	FS1*	2.35	CF1	1.75
	FS2*	1.89	CF2	1.51
	FS3	3.30		

7.3.2 Safety during breakwater construction

During construction, the stability of breakwaters built on soft soil depends on the degree of improvement of undrained strength of soils as the process of consolidation occurs in successive phases of construction. The main uncertainty in this type of processes is the estimation of the time necessary to reach enough excess pore pressure dissipation. This fact led to the decision to install a geotechnical instrumentation system (see Chapter 5) to provide information about the development of the consolidation process. The main parameters to be measured were:

- Pore pressure, to supply a direct measure of built-up pressures and dissipation.
- Settlements, which are related to the progress of consolidation.
- Horizontal movement, which indicated the development of instability phenomena.

Data obtained from the monitoring instrumentation during construction were crucial to calibrate the FE model which reproduces the best approximation to real pore pressure dissipation. In this regard, the model results have permitted establishing a constructive sequence that ensured an appropriate safety factor at each phase of construction. The Soft Soil model was used to investigate stability during breakwater construction. The characteristics and calibration of this model are described in detail in Chapter 4.

Table 7-4 shows the different characteristics of the seawave force and uplift force considered in the static analyzes of different construction phases.

Table 7-4. Seawave force and uplift force used at several phases of construction in static analysis.

Phase	Crown wall height [m]	Wave height, Hs [m]	Wave period, Ts [s]	Wave force [kN/m]	Application point [m]	Uplift force [kN/m]
II	Without crown	5	9	1036.3 (crest)	9.48	525.1
III	+6	5.91	12.7	1436.1 (crest)	10.36	878.2
IV	+11	8.04	12.7	748.9 (trough)	6.10	766.2

Results

Pore pressures induced in the soft foundation soil during construction showed a significant difference compared to the original design (GPO-Europrincipia, 2001), especially in the phase of placement and filling of caissons, which was considered fully consolidated in the design. Including these pore pressures in the finite element analysis reduced drastically the safety factor at all stages of construction.

Permeability of clays layers was adjusted to match the computed pore pressure with the corresponding measured value as described in chapter 6. In general, a good fit was achieved with the model, although

the better agreement with observations was obtain in the shallow layers. Deep layers show a dissipation pattern that the model was not able to simulate well.

Distribution of excess pore pressures at several stages of caissons placement is shown in Figure 7-5. Maximum pore pressure changes from 30 kPa before caisson placement to about 120 kPa after the complete procedure of caissons placement and fill. The area immediately under the caissons is the most affected; of course, a strong reduction of effective stress is expected in these zones, which increase the potential for a bearing capacity failure of the caissons.

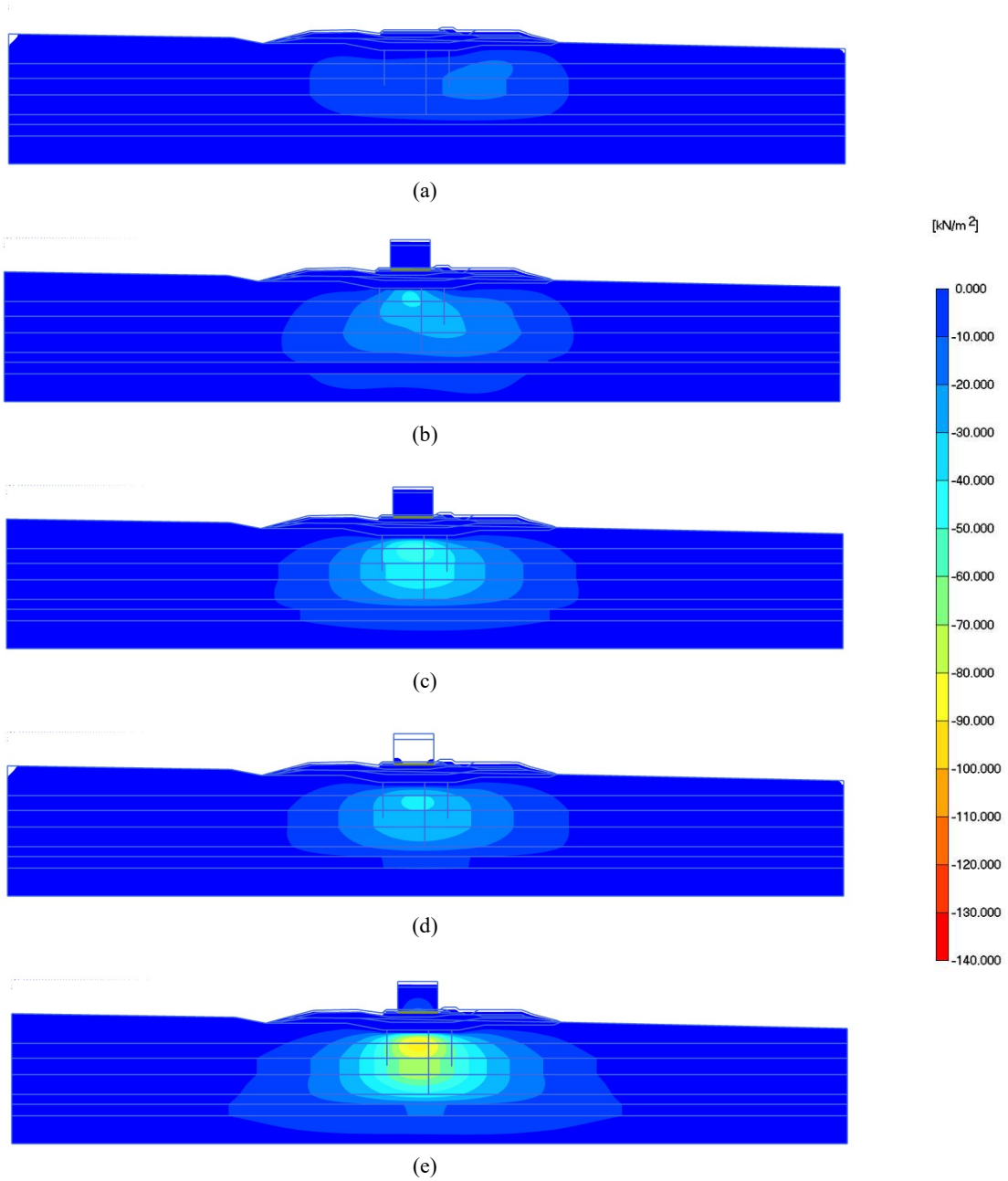

Figure 7-5. Excess pore pressure (a) before caissons placement (b) caisson filled with water (c) partial filling of caissons (d) after consolidation (e) totally filling of caisson

The safety factors calculated under these conditions (residual pore pressure after embankment construction and a rather slow dissipation rate before caisson placement), resulted in unacceptable safety factor values (CF1 = 1.05 and CF2 = <1.0). In order to improve these results, the fill volume of the cells was reduced by 5%. In other words, the unit weight of the caisson and fill decreases from 19.8 to 19.1 kN/m^3. This action slightly improved the safety factors, but still not enough (CF1 = 1.11 and CF2 = <1.0). An alternative procedure of construction was established to ensure the stability during placement and filling of the caissons: after placement of the caissons only 40% of cells would be filled with sand (this is equivalent to a unit weight of 15.2kN/m^3, enough to avoid failures due to sliding of the caissons). Total filling of the caissons (until reaching a unit weight of 19.1kN/m^3) could only proceed after a period of consolidation to gain enough soil strength to allow subsequent phases of construction to proceed. Different periods of consolidation were tested in the model. In case of considering 1 month of consolidation the computed safety factors were CF1 = 1.25 and CF2 = 1.06 and with 4 months of consolidation the safety factors resulted in CF1 = 1.45 and CF2 = 1.25, which was found acceptable. Table 7-5 shows the calculated safety factors during the placement and filling of the caissons. To verify the validity of the calculations made during this construction phase, the settlements measured at the topographic control points were compared with the settlement predictions from the model. A good agreement between computed and observed settlements provided the required confidence to allow the progress of work with a sufficient margin of safety. Figure 7-6 shows the typical failure surface obtained under the action of the wave load and self-weight of caisson at Phase II.

Table 7-6 shows the safety factors obtained in the analysis of several phases of construction, after the construction of Phase II during the filling stages indicated above. To compare the previously computed safety factor (section 7.3.1.1 and 7.3.1.2) with the updated safety factor during construction (unit weight 19.1), an additional computation set with caisson unit weight of 19.8 kN/m^3 has been included. Seawave forces considered in these analyses are indicated in Table 7-4.

Table 7-5. Factors of safety during caisson placement and filling (Phase II)

Stage	Unit weight kN/m^3	Phi-c reduction		Failure mechanism
Caisson sinking	11.5	CF1	1.83	Embankment slope
		CF2	<1.00	Local failure
Partial filling	15.2	CF1	1.84	Embankment slope
		CF2	1.51	Local failure
Consolidation 4 months	15.2	CF1	1.84	Embankment slope
		CF2	1.49	Local failure
Full filling	19.1	CF1	1.45	Global failure
		CF2	1.25	Global failure

Table 7-6. Factors of safety at different stages of construction after filling of caisson in stages

	$\gamma_{caisson}$= 19.1 kN/m^3				$\gamma_{caisson}$= 19.8 kN/m^3			
	Increasing loads		Phi-c reduction		Increasing loads		Phi-c reduction	
PHASE II (crest)	FS1*	1.78	CF1	1.45	FS1*	1.68	CF1	1.40
	FS2*	1.55	CF2	1.25	FS2*	1.51	CF2	1.21
	FS3	1.87			FS3	1.88		
PHASE III (crest)	FS1*	1.98	CF1	1.59	FS1*	1.96	CF1	1.54
	FS2*	1.42	CF2	1.23	FS2*	1.49	CF2	1.21
	FS3	1.71			FS3	1.69		
PHASE IV (trough)	FS1*	1.97	CF1	1.52	FS1*	1.99	CF1	1.50
	FS2*	1.68	CF2	1.31	FS2*	1.63	CF2	1.30
	FS3	2.61			FS3	2.30		

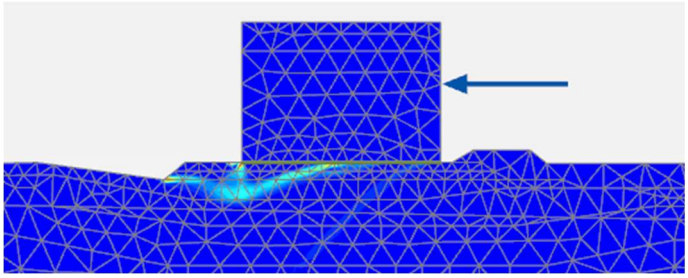

(a)

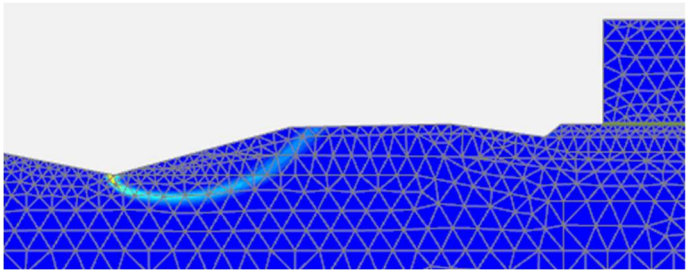

(b)

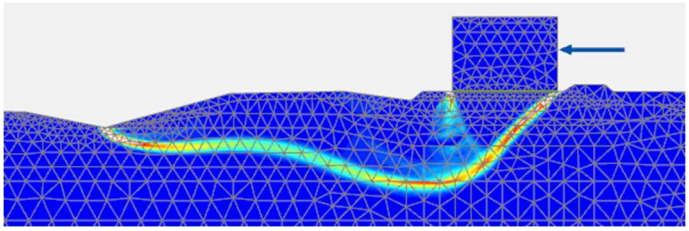

(c)

Figure 7-6. Failure mechanism under the action of the wave loads and self-weight of caisson in phase II (phi-c reduction method) (a) Local failure (b) failure of embankment slope (c) global failure.

7.3.3 Discussion

7.3.3.1 Factors of safety

Safety factors obtained with the limit equilibrium and finite element method are generally consistent between them once the differences in the procedures of calculation and adopted definitions for the safety

factors are taken into account. It was considered during design that these values provided enough margin of safety for all phases of the project. Furthermore, the similarity in the safety factors obtained with the limit equilibrium method and the finite element with effective parameters methodology shows the consistency of the analyses carried out with two completely different methods and reinforces the idea of a unique failure mechanism. Table 7-7 shows the results of limit equilibrium and finite element analyses. It is observed that the safety factors in the construction stage are lower than those calculated during design. This is due to the fact that during construction the pore pressures were not completely dissipated, as observed with the piezometers, thus reducing the available resistance of the soil.

Table 7-7. Comparison of factors of safety obtained with the limit equilibrium and finite element methods.

Phase	Case	FS limit equilibrium (design)	FS-FEM, undrained parameters (design)	FS-FEM, Effective parameters (design)	FS-FEM Effective parameters (construction)
II	Self-weight	2.00	1.62(CF1)	1.77(CF1)	1.40(CF1)
II	Wave load (crest)	1.40	1.33(CF2)	1.42(CF2)	1.21(CF2)
III	Self-weight	2.00	1.75(CF1)	1.96(CF1)	1.54(CF1)
III	Wave load (crest)	1.40	1.27(CF2)	1.40(CF2)	1.21(CF2)
IV	Self-weight	1.48	1.59(CF1)	1.75(CF1)	1.50(CF1)
IV	Wave load (sine)	1.35	1.37(CF2)	1.51(CF2)	1.30(CF2)

As previously indicated, complementary finite element analyses were carried out comparing the collapse load with the design loads (FS1, FS2, FS3). In the situation of a fully undrained problem (without drained materials) the safety factors computed as a load ratio or as a strength ratio are theoretically the same. When drained and undrained condition exists in the same problem, the equality of both types of factor breaks down. The criterion adopted in this research was to consider that the bearing capacity and the global stability mechanism are identical. The differences between FS1 and CF1 in the simple case of self-weight show this characteristic (Table 7-3). For the cases evaluated, the difference between both measures of safety is small (phases II and III) indicating that the safety is essentially controlled by the undrained strength of the clay.

Unfortunately, the definition of safety factor as a load ratio (collapse and design load) becomes complex when different loads are identified (i.e. self-weight, horizontal loads and others). This has led to the definition of additional measured of safety like FS3, useful to assess the uncertainty related to the wave loads only and the possibility of the development of an overturning mechanism. The meaning of other safety factors definition like the search of the collapse load by the simultaneous increase of self-weight and horizontal load and relating them with the design loads are more straightforward.

7.3.3.2 Failure mechanism

A detailed examination of the displacement and strains computed with the finite element analysis can give insight into the failure mechanism of the caisson breakwater foundation. Incremental strains at the final step (when plastic failure occurs) give an indication of the likely failure mechanism. Also, a vector representation of the displacement field shows the pattern of movement of the soil mass as failure progresses.

Comparisons of failure surfaces obtained for each safety factor definition are shown in Figure 7-7. Although both FS1 and CF1 were established to evaluate safety under self-weight load, the shape of the corresponding failure surfaces shows a different pattern of movement. FS1 (increasing caissons weight) produces a failure surface similar to that of a bearing capacity problem on a two-layer system, which crosses through the embankment and the soft foundation soil. In contrast, the sliding surface obtained from the CF1 computation pass predominantly through the foundation soil. In this case, the reduction of soil strength parameters which applies to the whole model, softens the soil under the embankment, creating a weak zone in the contact of the embankment with the foundation soil and producing a distortion of the failure surface typical of a bearing capacity problem.

On the other hand, although computations of factors FS2 and CF2 are completely different, sliding surfaces have almost the same shape. As mentioned before, under some conditions the undrained strength of foundation soil controls the bearing capacity of the caissons. In these conditions the same safety factor (defined as a relation of the forces to produce instability to the resistance forces) should be obtained, regardless of how it is computed (reducing resisting force or increasing the acting forces), and of course, the same failure mechanism is expected in both cases, provided that the directions of acting load stay constant. In the case of FS3, the relation between the weight of caisson and the horizontal wave load is changed (compared to the FS2 case) producing a more superficial failures mechanism.

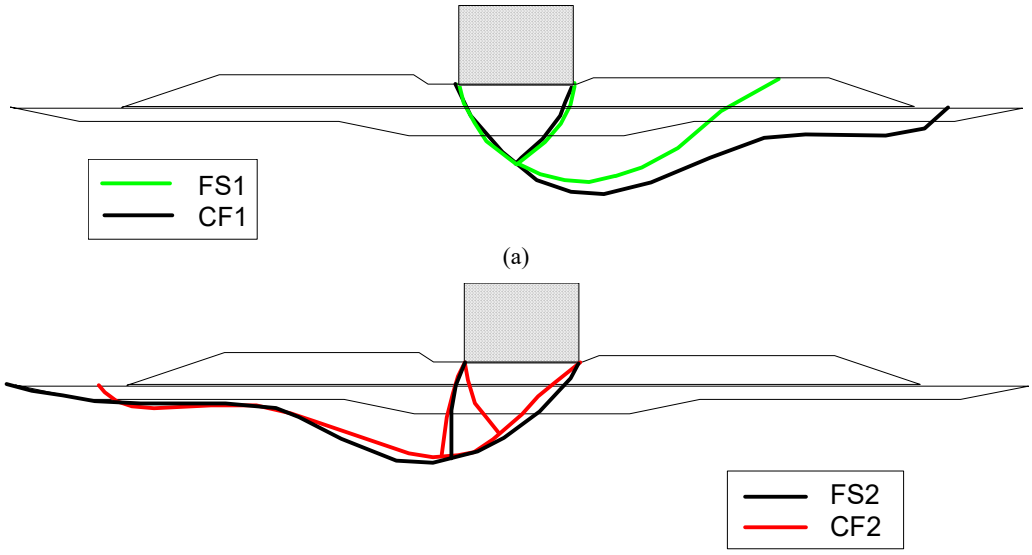

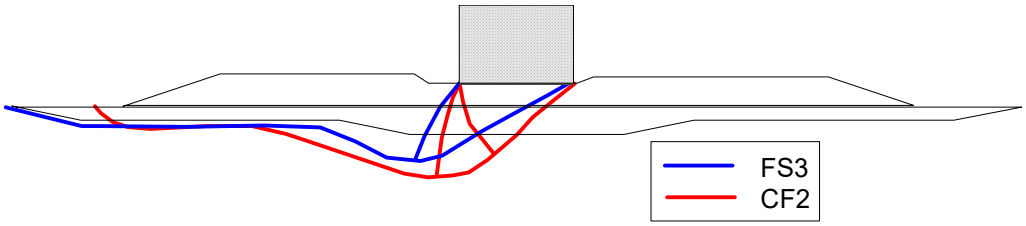

(c)

Figure 7-7. Comparison of different failure mechanism

7.4 STABILITY UNDER CYCLIC LOADS

In the previous analysis, the design storm was considered in the analysis as the action of two loads: a horizontal static load and an uplift pressure into the granular embankment. These loads correspond to the maximum likelihood impact of wave load computed with the Goda's formula. However, in reality, it is known that the storm applies repetitive loads with several intensities and frequencies (Oumeraci et al, 2001). Wave studies (INHA, 2000) indicated that the number of waves which are relevant to the breakwater stability is about a hundred. The period of wave impact is in the range of 10 - 20s. In other words, the foundation soil is under the action of cyclic loading and with a low capacity to drain, taking into account the low permeability of the foundation soils. A conservative assumption is to suppose that the foundation soil effectively behaves undrained under the action of the storm wave.

Applying shear stresses to the natural soil under undrained condition generate positive pore pressures, which are accumulative under load repetitions, creating the possibility that some zones lose partially their strength, a phenomenon described as 'cyclic instability'. The limit case is when the soil loses its total strength, corresponding to the concept of liquefaction.

Therefore, it is of interest to know in what magnitude the possible drop of foundation soil resistance, due to the repetitive action of wave load may affect the stability of the breakwaters. Analyses were performed for the construction phase 3, when the soils have completed consolidated under the action of the embankment and caissons weight and the wall crown has been recently constructed. The risk of cyclic instability does not affect the fill materials because they tend to behave in a drained way due to their high permeability.

7.4.1 Simplified analysis using the interaction diagram

The response of the foundation soils under cyclic loads due to sea wave loads was investigated with a simplified procedure using the cyclic Interaction diagram in connection with the results of a static finite element model. This type of analyses permits a preliminary evaluation of the breakwaters, with the advantage of a reduced computation time.

7.4.1.1 Loads definitions

Wave load definition is described in section 2.2.3.

7.4.1.2 Analysis procedure

If the design storm can be represented as the application of a number of waves impacts of a certain magnitude, then a static analysis can be used to identify areas in the foundation soil where the stress state exceeds the stability criteria defined by the interaction diagram. Of course, waves are of several magnitudes, adding complexity to the analysis; in order to simplify the analysis, a conservator criterion was assumed.

Two loads intensities were chosen from the wave magnitudes shown in Table 2-4: A high load of 1011.5 kN/m and a low load of 341.6 kN/m. The former is supposed to act only a few tens of times (N=40) and the latter about a thousand times (N=1000). In this way, it was possible to establish two safety zones in the interaction diagram for a simple shear mode of failure, which is shown in Figure 7-8.

The safety zone for the load application N=40 is limited for the condition $\tau_{cyc}/\sigma'_v = 0.16$ and for the static failure condition $\tau_{cyc}/\sigma'_v + \tau_{ave}/\sigma'_v = 0.25$. The safety zone for the load application N=1000 is limited for the condition $\tau_{cyc}/\sigma'_v = 0.10$ and the same static failure condition (Figure 7-8).

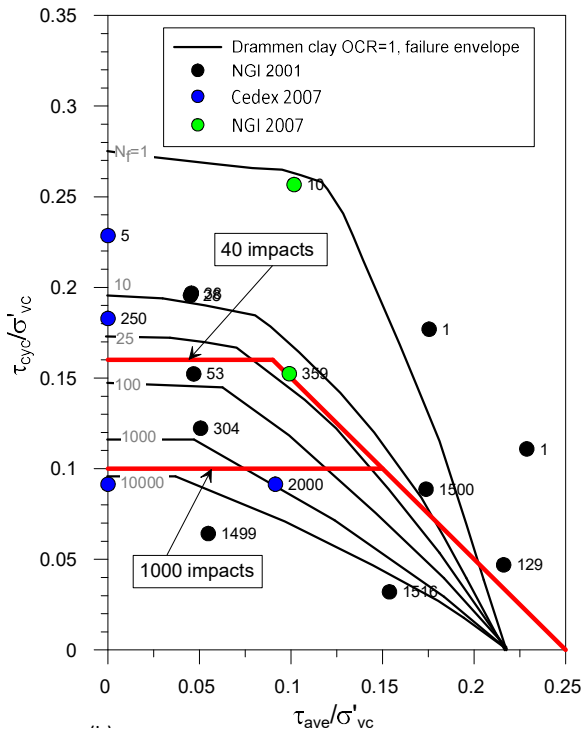

Figure 7-8. Zones defined in the interaction diagram based on simple shear tests for the N=40 and N=1000 load applications.

The following phases were performed in the analysis:

- Computation of the cyclic shear stress and average stress (τ_{cyc}, τ_{ave}) in the foundation soil under the action of the two horizontal wave loads (F_x = 341.6 kN/m and F_x = 1011.5 kN/m). The action of these loads involves also the application of a dynamic uplift force on the base of the caisson, which was

assumed as a triangular pressure distribution and maximum forces of 223.4kN/m and 310.5 kN/m, respectively. Calculating the normalized stress state τ_{cyc}/σ'_v y τ_{ave}/σ'_v comprises two stages:

a) The average shear stress τ_{ave} corresponds to the state reached after the construction and consolidation of the caissons. Caissons load produces an asymmetric distribution of shear stress into the foundation soil. An excel subroutine was programmed to search each Gauss points of the model and normalize the computed shear stresses corresponding to the clay foundation with respect to the effective vertical stresses.
b) A new computation including the horizontal wave load and the associate uplift forces was performed. This computation produces a new shear stress distribution. It was assumed that the cyclic shear stress τ_{cyc} can be obtained as the difference between the shear stresses computed in this stage and the previous computation (due to embankment and caisson weight). The normalization vertical effective stress σ'_v is that computed in the previous stage.

- Normalized (τ_{cyc}/σ'_v, τ_{ave}/σ'_v) computed in the foundation soil are compared with the safe and unsafe zones of the interaction diagram. A search algorithm was programmed in Excel to identify which gauss points are located in an unsafe zone. Points outside the envelope for N=1000 (Fx=342 kN/m) are shown in Figure 7-9. These points correspond to locations with high average shear stress ($\tau_{ave}/\sigma'_v > 0.2$) that are not able to support additional cyclic shear stress.

  Figure 7-10 and Figure 7-11 show for the two cases analysed, the zones where unsafe points are located in the section of the breakwater. The areas identified as likely to be affected by the cyclic mobility are concentrated in specific areas below the caissons. In these areas critical combinations of stresses exist, where the shear stress tends to be maximum and the vertical stress decrease rapidly when moving away from the central zone of the caissons.

- An additional safety computation is performed, using a reduced value of the undrained shear strength in the unsafe zones identified in the previous stage. The criteria chosen has been to assume that in unsafe areas the initial shear strength remains, that is, in these areas no resistance gain due to the action of the preload from the embankment or the caisson's placement is considered. In Figure 7-10 and Figure 7-11 the zones chosen to represent the liquefied undrained strength are plotted.

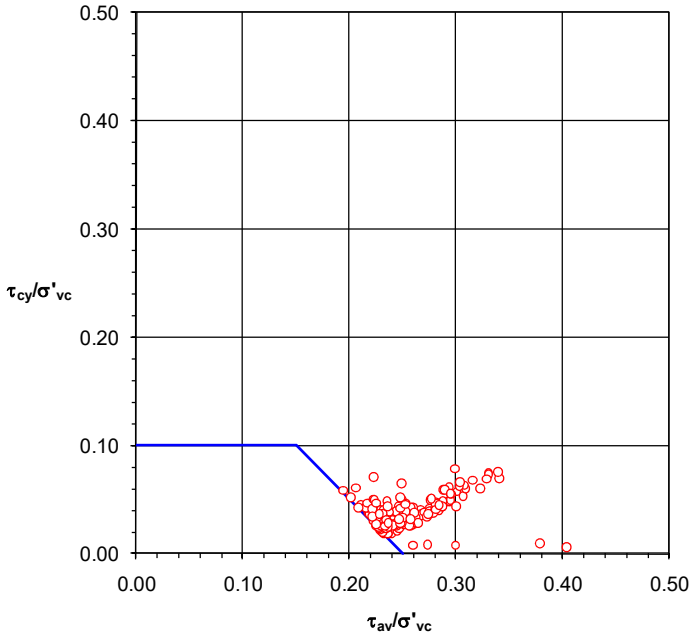

Figure 7-9. Points of cyclic mobility, Phase 3, F=342kN/m

7.4.1.3 Results

The safety factors calculated are shown in Table 7-11Table 7-11 (Phase III).

Areas potentially affected by cyclic mobility phenomena are confined from the top by the granular embankment and laterally by "no damaged" natural ground. Therefore, a kinematically admissible failure is only possible through areas that affect zones of the clay not damaged by cyclic loading. It also shows that the size of the area "unsafe" increase with increasing intensity of the horizontal load.

The undrained strength available in the "damaged areas" can be evaluated from cyclic shear tests carried out by NGI (2002). Table 7-8 shows that after the application of cyclic loading (up to 1500 cycles) an undrained resistance similar to the initial one is still available. However, if the number of load cycles were to increase, it is possible that some of the values τ_F/σ'_n shown in Table 7-8 would be reduced due to the accumulation of higher positive water pressure during cyclic loading.

Table 7-8. Values of normalized undrained resistance τ_f/σ'_n after the application of cyclic shear (NGI, 2002).

Sample		Clay content	τF (kPa)	σ'n (kPa)	τF/σ'n
S5	M2-2	32.4	55	169.8	0.32
S5	M6-2	16.9	30.8	279.8	0.11
S10	M1-2	6.3 (sand)	128.1	179.9	0.71
S10	M2-2	38.8	55	199.7	0.27
S10	M3-2	9.9 (silt)	115.7	219.9	0.52
S10	M4-2	31.5	66.3	260	0.255
S11	M4-2	22.7	66.9	230	0.291
S11	M5-2	32.0	68.8	259.7	0.26

The undrained strength available in damaged areas shown in Figure 7-10 and Figure 7-11 can be found easily. The effective vertical stresses at the four corners of the areas "damaged" in these figures are shown in Table 7-9. The finite element calculation provides the stresses for Phase III and the initial stresses can be computed as a function of depth below the seabed (with $\gamma_{sum} = 8.5$ kN/m^3). The undrained strength is also indicated ($s_u = 0.25\ \sigma'_v$). The last column shows the ratio of the initial undrained strength in the field and available in Phase III. The reduced undrained strength used in the damaged areas is shown in the column called "initial" (undrained strength) in Table 7-9. This resistance is equivalent to using ratios of $s_u/\sigma'_v = 0.125$ in the higher elevations of the damaged areas (in contact with the berm) and $s_u / \sigma'_v = 0.17$ in the lower bounds. These values are considerably lower than the experimental data shown in Table 7-8 which introduces additional safety to the calculations presented below.

Finally, the computation of the safety factor for the cases shown in Figure 7-10 and Figure 7-11 was carried out. Mohr-Coulomb model in undrained conditions was used and the foundation soil was zoned to reflect the improvement induced by the consolidation under the embankment and caissons. In the damaged areas, s_u value was reduced to its initial values, which is equivalent to using relations $s_u / \sigma'_v = 0.125$ to 0.17 as mentioned.

The two load cases considered are specified in Table 7-10. The dynamic uplift pressure acts only in the area of the embankment beneath the caissons. Uplift pressures vary horizontally from zero at the port side to a value Δp_{max} on the seaside, so that, the resultant of the horizontal distribution matches the resulting dynamic uplift force (SD).

The safety factors calculated are shown in Table 7-11 (Phase III). The critical case calculated (cyclic loading, dynamic uplift pressure and 40 impacts of a horizontal load of 1011.5 kN/m) produce a safety factor CF2 = 1.18. This safety factor increases to 1.48 when 1000 impacts of a horizontal force H = 341.6 kN/m is used. This table also indicates the corresponding static values in order to observe the drop in safety attributable to cyclic loading events.

In the light of the analysis performed and the conservative assumptions setting out, it is considered that the configuration of the breakwater provides adequate safety in case of cyclic loading.

Table 7-9. Undrained strength in the areas affected by cyclic mobility

			Depth below seabed (m)	Effective vertical stress		Undrained strength kN/m^3		r
				Initial	Phase III	Initial	Phase III	
F_x = 341.6 kN/m	Upper Corners	1	6.2	52.7	128	13.1	32	0.41
		2	7.4	62.9	107	15.7	26.7	0.59
	Lower corners	1	14.7	124.9	184	31.2	46	0.68
		2	15.1	128.3	194	32	48.5	0.66
F_x = 1011.5 kN/m	Upper Corners	1	6.2	52.7	102	13.1	25	0.52
		2	6.2	52.7	119	13.1	29.7	0.44
	Lower corners	1	16.8	142.8	194	35.7	48.5	0.74
		2	18.4	156.4	226	39.1	56.5	0.69

$r = s_{u\_ini}/s_{u\_phaseIII}$

Table 7-10. Load cases considered. Analysis of cyclic loading

Phase	H kN/m	d (m)	SD kN/m	Δp_{max} kN/m^2
III (crest)	341.6	10.36	223.4	18.31
III (crest)	1011.5	10.36	310.5	25.45

H: Horizontal force; d: Distance from point of application of force H to the caisson base; SD: Resulting dynamic uplift force; Δp_{max}: Maximum value of uplift pressure.

Table 7-11. Strength reduction Safety Factor CF2. Effect of the cyclic mobility on the foundation soils. Phase III

	Dynamic Uplift	CF2	
		H = 341.6 kN/m 1000 impacts	H = 1011.5 kN/m 40 impacts
Cyclic mobility	NO	1.51	1.23
	YES	1.48	1.18
Static analysis	NO	1.67	1.42
	YES	1.55	1.40

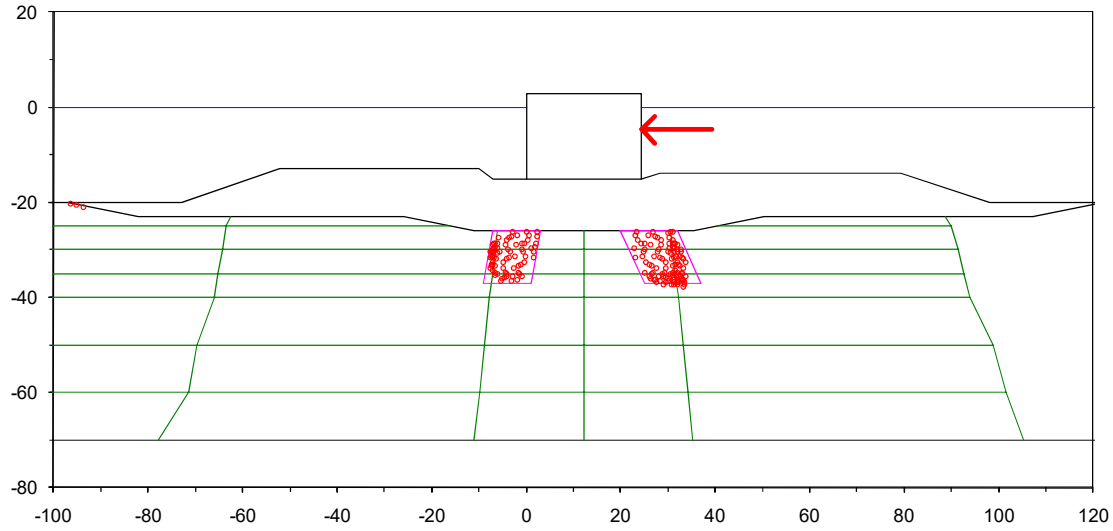

Figure 7-10. Case with horizontal force F = 341.6 kN/m. Red circles indicate gauss points with high cyclic mobility potential. Phase 3.

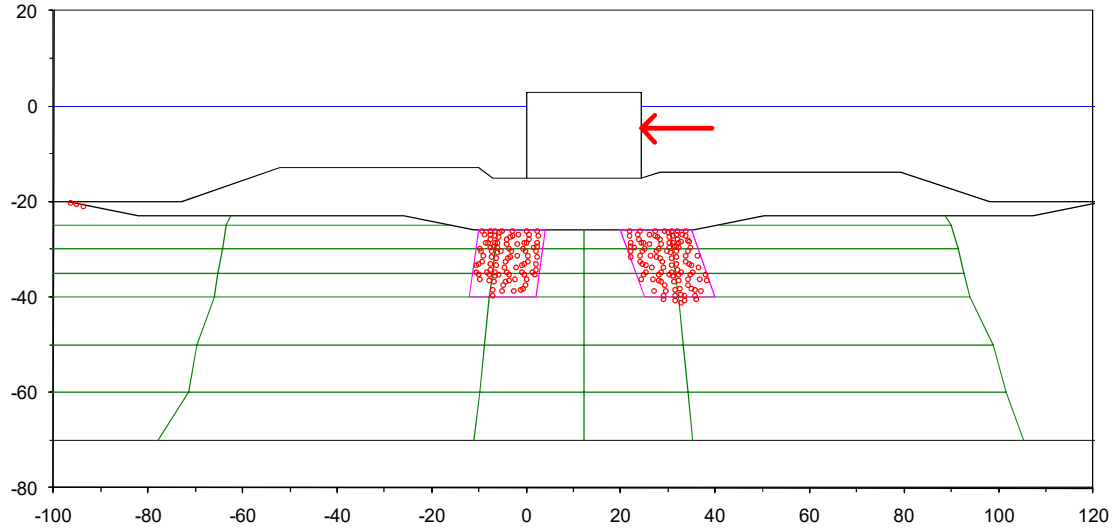

Figure 7-11. Case with horizontal force F = 1011.5 kN/m. Red circles indicate gauss points with high cyclic mobility potential. Phase 3.

7.5 CONCLUSION

As usual in large projects, the design goes through different stages, with the evaluation of stability being one of the most important aspects. Initially, stability evaluations were carried out using the limit equilibrium method that allowed defining the geometric characteristics of the dike. With the development of further investigation of both hydraulic aspects through physical models and complementary geotechnical experimentation, finite element models were developed that allowed the identification of additional requirements for the stability of the dike. Among which, highlights the design of a long berm, not usual in vertical breakwaters, but which was essential to ensure the stability of the dike.

The safety of a vertical breakwater project on soft ground depends fundamentally on the evaluation of its stability in all phases of the work. Analysis of the stability of a vertical breakwater in low-strength cohesive soils raises some specific questions about the definition of safety factors that must be carefully considered. In this sense, 3 types of safety factors were defined by increasing the weight loads of the caisson and the horizontal sea wave force, in order to investigate different failure mechanisms, thus increasing the weight of the caissons aims to investigate the failure mechanism of bearing capacity, while the increase in the horizontal sea wave force is associated with the sliding mechanism and the simultaneous increase in the horizontal force and the weight would allow investigating the overturning mechanism.

To verify that the project hypotheses are fulfilled, especially those related to consolidation rate, an instrumentation system was installed to measure displacements and pore pressures in the foundation of the dike. The stability calculation models were calibrated with the instrumentation, and the stability was verified as new data were obtained, adjusting the consolidation periods if necessary, under this form of work, the uncertainties associated with the ground were reduced, allowing factors of safety of the order of 1.20-1.25 in critical stages of the project.

The undrained cyclic shearing tests performed (triaxial and simple direct shear) indicate that the silt-clay foundation soil maintains a residual undrained shear resistance, after the stage of cyclic loads, similar to static resistance. In this material the concept of “cyclic mobility” (as an alternative to the concept of liquefaction) is appropriate. The soil deforms during the cyclic shearing stage but maintains a very acceptable residual resistance. The cyclic interaction diagram defined from the tests on samples allows estimating the extent of the cyclic mobility phenomena associated with the expected loads for the design storm. The procedure involves a simplification of a complex problem and allows the analysis to be carried out using static calculations in the manner described in this Chapter.

Additional stability calculations were carried out, by reducing the resistant parameters until critical conditions were found. In these calculations, conservative values, significantly lower than those measured, were assigned to the residual resistance of the areas affected by cyclic mobility. The areas identified as susceptible to being affected by cyclic mobility are confined at the top by the granular fill of the embankment and laterally by the natural ground “not damaged” by the action of the sea waves. Therefore, there are no conditions for the affected areas to give rise to failure mechanisms located exclusively on “damaged” soil. Taking into account the exceptional nature of the actions introduced and the additional conservative assumptions on the reduction of the resistance to undrained shear stress, the calculated safety factor of 1.18 is considered acceptable.

Chapter 8

CONCLUSIONS AND RECOMMENDATIONS FOR FURTHER STUDIES

8.1 CONCLUSIONS

Two main breakwaters were constructed as part of the Barcelona Port expansion. The East breakwater is of a rubble mound type whereas the South breakwater includes two different types: rubble mound and vertical caissons. Most of the foundation soil immediately under the breakwaters consists of weak sediments of clayey silts and silty clays that require a careful assessment of their bearing capacity at all stages of construction and are bound to produce significant settlements. The South breakwater section where caissons are employed has a length of 2095m and is the main subject of this investigation. Vertical breakwaters are subject to complex loadings and, when founded on soft ground, they are prone to failures and to excessive settlements. Cyclic loading due to storm wave loading increases the complexity and uncertainty of the system. Those issues have been examined using a range of experimental, field, monitoring and computational techniques. The caisson section of the South breakwater has provided a focal point to bring together the different strands of the work that constitute the material reported in the Thesis.

Initially, the thesis investigates the types of waves that impact on the breakwater, concluding that for a significant wave height (H_s) of less than 4m, quasi-static wave loads are generated whereas for H_s greater than 4m, impact type wave loads occur. Impact loads with a period of 12 to 14s were subsequently shown to transmit enough energy to the foundation to generate pore pressures that accumulate with time, as observed during the December 2008 storm.

Further context is provided by examining the state of stresses under a breakwater. They can be described through stress paths and the corresponding principal stress directions. Similar to what is observed in embankments, three failure modes can be distinguished in plane strain conditions: active, simple shear and passive. Therefore, the use of anisotropic models, such as S-Clay1 model, can be appropriate to assess safety. However, in case of breakwaters with long berms, like the Barcelona case, it is observed that the predominant mechanism is the simple shear mode. In such situations, it is feasible to perform the stability evaluation of the breakwater using an isotropic constitutive model, such as the soft soil model, provided it is adjusted to correctly reproduce the undrained strength in simple shear mode.

Several soil behaviour characteristics have been given special attention in the characterisation of the foundation ground: undrained shear strength, small strain stiffness, compressibility, and cyclic loading

effects especially as they affect undrained strength. The key role of the undrained shear resistance on the performance and stability of a breakwater has been stressed throughout the investigation. Undrained shear strength is a complex parameter that depends on several variables such as anisotropy, preconsolidation pressure, rate and direction of the load. Its assessment requires an extensive testing campaign. However, in those cases in which it is possible to establish a predominant failure mode that coincides with the simple shear mode, as in the case of Barcelona Port, the determination of the undrained shear resistance can be done through direct simple shear tests and in situ CPTu tests. These two types of tests have yielded very similar results through the parameter N_k, established as N_k=15 for the clay of the Port of Barcelona. In more complex situations, such as the incorporation of gravel columns in the foundations, or if small berms are used, it is necessary to establish the undrained resistance by means of extension, compression and simple shear tests. For these cases, advanced calculation models that incorporate anisotropy should be used.

The stiffness characteristics at small strain level was investigated with the resonant column test. The data from these tests were merged with the triaxial tests results to produce a unique stiffness curve using the rate-effect adjustment proposed by Vardanega and Bolton (2011a). This curve was used in conjunction with the Plaxis HSS model to simulate the construction of the breakwater. No significant improvement of the predictions was achieved with the use of this formulation, compared to other simpler models, such as the Soft Soil model. This is explained because the high compressibility of the soil in the Port of Barcelona produces settlements of the order of 2.5m, rending the effect of small strain stiffness marginal.

Estimates of the breakwater expected settlements were also made for the different construction phases. Compressibility characteristics for settlement analysis were first studied with standard oedometric tests and then verified with a large-scale instrumented preload test. Results show that the compressibility coefficients obtained in the laboratory tests match quite well the preload results, something that is not observed in relation to the swelling coefficient. In this case, the preload produces lower values, possibly as a result of stratification with stiffer soils. The large differences between the consolidation coefficients obtained from compression tests and those obtained from dissipation tests of in situ CPTu are also noted. Dissipation tests yielded values of coefficient of consolidation at least one or two orders of magnitude higher.

Another fundamental factor in the study of vertical breakwaters is related to the cyclic behaviour of the foundation soil. In this regard, two aspects are of great interest in relation to breakwaters: the first one is related to the generation of pore pressures that could lead to cyclic mobility of the foundation and, potentially, it could affect the stability of the dyke. The second refers to the undrained resistance available during and after the cyclic event. To investigate these aspects, several cyclic triaxial and simple shear tests were carried out. The results show a direct relationship between the normalized deviatoric

stress and the pore pressure ratio r_u, indicating that the induced pore pressure increases with the increase in deviatoric stress. It is also observed that the initial stress state has less influence. The most critical condition is obtained when the tests involve stress reversal. Dobry et al (1982) found similar results in the study of sand liquefaction due to seismic effects. For the foundation soil of the Barcelona breakwater, a maximum r_u value of the order of 0.6 was observed in the laboratory.

The undrained resistance available after the application of the cyclic load was observed to remain the same or even sometimes become greater than the static shear strength. This latter behaviour was observed mainly in samples with a low clay content (<9%). When the cyclic deviator and the initial shear stress exceed a threshold, however, the specimen fabric is disturbed and the sample post cyclic shear strength reduces.

Construction of vertical breakwaters on soft soil frequently presents significant difficulties. The stage of caisson placement and filling is especially critical. Ensuring that a sufficient degree of consolidation has been achieved is therefore key to ensure the stability of the caissons immediately after placement and filling. Development of large settlements due to the high compressibility of the foundation soil is also a significant feature during construction and post-construction. To check the assumptions made during design, extensive geotechnical instrumentation has been deployed to assist in the process of construction of both vertical and rubble mound breakwaters. Data provided by the instrumentation were used to calibrate a numerical model developed to study stability conditions and to predict settlements at different stages of construction. Instrumentation has proved to be a very useful tool to provide the necessary information to carry out the works and to schedule activities in an efficient and safe manner.

Some important characteristics about the behaviour of the foundation soils can be observed from the instrumentation measurements:

- Every fill placing over an instrumented section resulted in an increase of pore water pressure that partially dissipated with time.
- The settlements are progressively developed in response to the increase of the applied load and the consolidation of the soil.
- The horizontal displacements measured are very small, at the limit of accuracy of the instruments, which indicated that the vertical strains are dominant, corroborating the one-dimensional assumption of deformations, at least under the centre of the breakwater.
- The behaviour of pore water pressure in all the instrumented sections was similar, suggesting a degree of homogeneity in the characteristics of the ground that control the generation and dissipation of water pressure.

Well documented case studies are a necessary requirement for the advancement of geotechnical knowledge. In this regard, validation of existing models against real cases should improve our confidence in available models. Several commercially available constitutive models were tested for their ability to reproduce undrained strength and deformations in a real boundary value problem. Anisotropic models have advantages over isotropic models in that they are able to predict the undrained resistance under the 3 load modes (compression, extension and simple shear) that are expected to occur in a breakwater. On the contrary, isotropic models should be adjusted to reproduce the dominant failure mode, according to the conditions of each breakwater. Furthermore, to better reproduce the deformation behaviour, especially in the long term, it is recommended to use models that incorporate soil creep behaviour. In this regard, the SSC model has proven to be effective to reproduce the oedometric tests, the preload test, and the long-term settlements of the dyke, including the effects of secondary compression as well as the influence of OCR, load increment size and the current stress state, on the calculation of the deformation.

For the evaluation of the stability of vertical breakwaters and other marine structures, many design codes (e.g. ROM 0.5) recommended to investigate 3 failure mechanisms: overturning, sliding and global stability. This distinction is not necessary if Finite Element analysis is used as it will automatically identify the most critical failure mechanism. Two different procedures to compute safety factor were adopted: increasing loads or reducing strength parameters. In the first case, 3 types of safety factors were defined increasing the horizontal load until failure, increasing the weight of the caisson until failure, and simultaneous increase of the weight of the caisson and the horizontal wave force. The procedure of reducing the strength parameters was used to investigate the overall stability under caisson weight and under caisson weight plus wave load action. The hypothesis of total dissipation of pore pressures and improvement of the characteristics of the ground due to its consolidation was adopted in the design stage before construction. However, during construction, with the aid of geotechnical instrumentation, it was observed that the pore pressure dissipation rate was slower than expected. When introducing the residual pore pressure in the analysis, the safety factors were significantly reduced, forcing to reschedule the work. These results highlight the value of having a foundation instrumentation system during the construction process of large projects on soft soils.

The analysis of the failure modes of caisson breakwaters has revealed the importance of considering dynamic effects for stability analysis, since the build-up and subsequent dissipation of pore pressures affect the mechanical behaviour of soils. The simulation of this type of dynamic problems involves a fairly large effort in terms of computing resources, for which it is necessary to have a formulation and appropriate constitutive models. In contrast to what happens in seismic problems, where the structure is subjected to a few minutes of seismic activity, in the case of breakwaters, the action of storms on the caisson usually lasts several hours or even days. In this respect, the use of a simplified analysis model has been proposed, based on the cyclic interaction diagrams of the soil in combination with a

conventional finite element model. In parallel, a dynamic finite elements model was also performed using Biot's coupled formulation and the UBC3D-PLM constitutive model. This model, although it is more appropriate for sand, reveals some interesting characteristics, such as the increase in pore pressures in areas under the caisson susceptible of being affected by cyclic mobility, which coincide with the areas identified in the simplified analysis model. The coincidence of results provides greater confidence on the use of the simplified method in practical engineering. Also, the design of a long berm, was shown to be essential to ensure the stability of the dyke for both static and dynamic loading conditions.

8.2 RECOMMENDATIONS FOR FURTHER STUDIES

Although the longitudinal geometry of the caisson breakwaters makes them suitable for adopting 2D models, the construction process undoubtedly involves 3D effects as not all the breakwater is built simultaneously. Therefore, performing the numerical simulations using 3D models would allow a better reproduction of the field measurements. The first attempts made during the development of this thesis revealed the difficulties to reproduce a complex 3D geometry by means of the tools available to carry out the meshing and subsequent calculation process. Although these tools are now used more frequently, it is still very time-consuming for their application in practical engineering, especially when it comes to dynamic models.

Other interesting aspects to investigate is related to the generation of pore pressures in response to the cyclic actions produced by the sea waves. Unlike earthquakes, which last only a few seconds, marine structures, such as breakwaters, are subjected to thousands of load cycles during a storm. Under these conditions, the constitutive models developed mainly to simulate the response of the ground to earthquakes, usually predict a high accumulation of volumetric strains or pore pressures (under undrained conditions) in a few load cycles. The development of models to reproduce the behaviour of soils subjected to thousands of loading cycles has recently acquired great interest in the geotechnical community and therefore it is naturally a research line to follow.

Finally, the development of numerical procedures that allow the calculation of the fluid-soil-structure interaction in a satisfactory way continues to be a challenge for the engineering community, especially in the field of offshore structures and breakwaters interacting with large waves. Different proposals have been developed in this regard, among which, the Particle Finite Element Method (PFEM) is a promising numerical technique for solving fluid-soil-structure interaction (Oñate et al 2012). Another line of work is that developed by Elsafti (2013) based on two separated solvers for the governing equations: (i) a hydrodynamic solver to simulate the wave motion and the wave-induced loads and (ii) a structural solver for the analysis of the dynamic response of the structure and the soil foundation. The fluid pressure is transferred to the structural model at sampling points over time.

REFERENCES

Almeida, M.S.S, Britto, A.M and Parry, R.H.G. (1986). Numerical modelling of a centrifuged embankment on soft clay. Canadian Geotechnical Journal, Vol. 23, pp. 103-114.

Alonso, E.E., Gens, A., Lloret, A. (2000). Precompression design for secondary settlement reduction. Geotechnique Vol. 50, No. 6, pp. 645-656

Alonso, E., Lloret, A., Gens, A., and Salvadó, M. (2002). Efectos de la sobreconsolidación en la velocidad de asentamiento secundario. Cedex. Revista Ingeniería Civil, 125, p. 41.

Andersen, K.H. (1976). Behavior of clay subjected to undrained cyclic loading. Int. Conf. on Behaviour of Offsh. Struct., BOSS'76. Trondh., Proc. (1): 392–403.

Andersen, K.H. (2009). Bearing capacity of structures under cyclic loading; offshore, along the coast and on land. 21st Bjerrum Lecture presented in Oslo 23 November 2007. Can. Geotech. J. 46: 513.535.

Andersen, Knut. (2015). Cyclic soil parameters for offshore foundation design. The 3rd McClelland Lecture. Conference: Frontiers in Offshore Geotechnics III, ISFOG'2015, Meyer (Ed). Taylor & Francis Group, London, ISBN: 978-1-138-02848-7. At: Oslo. Volume: 1, p. 5-82.

Andersen, K.H. and Lauritzsen, R. (1988). Bearing capacity for foundations with cyclic loads. ASCE, J. of Geotech. Engrg, 114 (5): 540–555.

Anderson, D.G. and Richart, F.E. Jr. (1976) Effects of straining on shear modulus of clays. J. Geotech. Engrg. Div. ASCE, 1- 27.

Andresen, A., T. Berre, A. Kleven and T. Lunne (1979). Procedures used to obtaind soil parameters for foundation engineering in the North Sea. Marine Geotechnology, Vol. 3, Nº3, pp. 201-266.

Autoridad Portuaria de Barcelona. (2007). Informe sobre las causas de la avería del Muelle Prat del Puerto de Barcelona acaecida el 1º de enero de 2007.

Beaty, M.H. (2017). Application of UBCSAND to the LEAP Centrifuge Experiments. Soil Dynamics and Earthquake Engineering, Vol. 104, pp. 143-153

Beaty, M. and Byrne, P. M. (1998). An effective stress model for predicting liquefaction behaviour of sand. Geotechnical Earthquake Engineering and Soil Dynamics III. Edited by P. Dakoulas, M. Yegian, and R. Holtz (eds.), ASCE, Geotechnical Special Publication 75 (1): 766-777.

Beaty, M. H., and Byrne P. M. (2011). UBCSAND constitutive model version 904aR. Documentation report: UBCSAND constitutive model on Itasca UDM Website.

Benz, T. (2006). Small-Strain Stiffness of Soils and its Numerical Consequences. Phd thesis, Universität Stuttgart.

Biot M.A. (1941). General theory of three-dimensional consolidation. J Appl Phys;12(2):155–64.

Biot MA (1955) Theory of elasticity and consolidation for a porous anisotropic solid. J Appl Phys 26:182–185

Biot, M. A. (1956). 'Theory of propagation of elastic waves in a fluid saturated porous solid', J. Acoust. Soc. of America, 28, 168-191.

Biot, M. A. (1962a). 'Mechanics of deformation and acoustic propagation in porous media', J. Appl. Phys. 33, 1482-1498.

Biot, M. A. (1962b). 'Generalized theory of acoustic propagation in porous dissipation media', J. Acoust. Soc. of America, 34, 1254-1264.

Bishop, A.W. and Wesley L.D. (1975). A hydraulic triaxial apparatus for controlled stress path testing Geotechnique, 25 (4), pp. 657-670

Bjerrum, L. (1967). Engineering geology of Norwegian normally-consolidated marine clays as related to settlements of buildings. Seventh Rankine Lecture. Geotechnique, 17, 81-118.

Bjerrum, L. (1972). Embankments on soft ground, Proceedings of the ASCE Conference on Performance of Earth-Supported Structures, Purdue University, 2, 1-54.

Bjerrum, L. and Landva, A., (1966). Direct Simple Shear Tests on a Norwegian Quick Clay, Geotechnique, Vol. 16, pp. 1–20.

Boulanger, R. W., and Ziotopoulou, K. (2017). PM4Sand (version 3.1): A sand plasticity model for earthquake engineering applications. Report No. UCD/CGM-17/01, Center for Geotechnical Modeling, Department of Civil and Environmental Engineering, University of California, Davis, CA, March, 112 pp.

Brinch-Hansen, J. (1970). A revised and extended formula for bearing capacity. DGI Bulletin, No28, 5-11. Danish Geotechnical Institute.

Brinkgreve, R.B.J. (1994). Geomaterial models and numerical analysis of softening. Ph.D. dissertation, Delft University of Technology, Delft, the Netherlands.

Brinkgreve, R. B. J., Kumarswamy, S. and Swolfs, W. M. (2017). Plaxis 2D 2017 Manual. Plaxis bv. Delft, Netherlands.

Brugger, P. J., Almeida, M. S. S., Sandroni, S. S. and Lacerda, W. A. (1998). Numerical analysis of the breakwater construction of Sergipe Harbour, Brazil. Canadian Geotechnical Journal, vol. 35 (6), pp. 1018-1031.

Buisman, A. S. K. (1936): Results of long duration settlement tests. 1st International Conference on Soil Mechanics and Foundation Engineering, Cambridge, Mass. Proceedings, Vol. I, pp. 103–106.

Burland, J. 1990. On the compressibility and shear strength of natural clays. Geotechnique 40, No. 3, 329-378.

Burland, J.B. (1965). The yielding and dilation of clay. Géotechnique, 15, 211–214.

Butterfield, R. (1979). "A natural compression law for soils (an advance on e-log p)." Geotechnique, 29(4), 469–480.

CEDEX. 2008. Informe sobre los resultados de los ensayos dinámicos de laboratorio realizados con dos muestras procedentes del Puerto de Barcelona. Informe parcial N°17. Julio 2008.

Chowdhury, K.H. 2018. Evaluation of the State of Practice Regarding Nonlinear Seismic Deformation Analyses of Embankment Dams Subject to Soil Liquefaction Based on Case Histories. Ph.D. Thesis, University of California, Berkeley, CA, USA.

Chung, S. G., Kim, S. K., Kang, Y. J., Im, J. C. & Nagendra Prasad, K. (2006). Failure of a breakwater founded on a thick normally consolidated clay layer. Geotechnique 56, No. 6, 393–409.

Darendeli, M. B. (2001). "Development of a new family of normalized modulus reduction and material damping curves." Ph.D. thesis, Univ. of Texas at Austin, Austin, TX.

De Borst,R.& Vermeer,P.A. 1984. Possibilities and limitations of finite elements for limit analysis. *Geotechnique*, **34,** 199-210.

De Groot M, Bolton M, Foray P, Meijers P, Palmer A, Sandven R, et al. Physics of liquefaction phenomena around marine structures. J Waterway Port Coast Ocean Eng 2006;132(4):227–43.

De Groot, M.B.; Andersen, K.H. ; Burchart, H.F.; Ibsen, L.B. ;Kortenhaus, A.; Lundgren, H.; Magda, W. ; Oumeraci, H.; Richwien, W. (1995): Foundation design of caisson breakwaters. *Final version MAST II,MCS Project, June 1995*

De Groot, M. (2001). Geotechnical Aspect. In Kortenhaus & Voortman (Ed.), Probabilistic Desing Tools for Vertical Breakwaters (pp. 157-223). Lisse, Netherland, Balkema.

DiBiagio, E. 1977. Field Instrumentation –A Geotechnical Tool. Norwegian Geotechnical Institute Publication No. 115: 29-40.

D'Ignazio, M. (2016). Undrained shear strength of Finnish clays for stability analyses of embankments. Tampere University of Technology. Publication; Vol. 1412. Tampere University of Technology.

Dobry, R., Ladd, R.S., Yokel, F.Y., Chung, R.M., Powell, D., 1982. Prediction of pore pressure buildup and liquefaction of sands during earthquakes by the cyclic strain method. Building Science Series 138. National Bureau of Standards, U.S. Department of Commerce, Washington, D.C.

Donofrio, A., Silvestri, F. & Vinale, F. (1999). Strain rate dependent behaviour of a natural stiff clay. Soils and Foundations. Vol 39. No. 2, 69-82.

Dos Santos, J.A. and Correia, A.G. (2001). Reference threshold shear strain of soil. Its application to obtain a unique strain-dependent shear modulus curve for soil. 15th International Conference on Soil Mechanics and Geotechnical Engineering. Istanbul, Turkey, volume 1, 267-270

Duncan, J. M., and Chang, C.-Y. (1970). "Nonlinear analysis of stress and strain in soils". J. Soil. Mech. and Found. Div., 96(5), 1629–1653.

Duncan, J.M., Wright S.G. & Brandon T.L. 2014. Soil Strength and Slope Stability2nd edition. Chapter 3, Soil mechanics principles. Published by John Wiley & Sons, Inc., Hoboken, New Jersey.

Dunnicliff J. (1993). Geotechnical Instrumentation for Monitoring Field Performance, John Wiley & Sons, Inc., 608pp.

EM 1110-2-1100. 2002. Coastal Engineering Manual. U.S. Army Corps of Engineers

Elsafti H. (2015). Modelling and analysis of wave-structure-foundation interaction for monolithic breakwaters. PhD thesis. Leichtweiss-Institute for Hydraulic Engineering and Water Resources, TU-Braunschweig, Germany

Elsafti, H. and Oumeraci, H. (2016). A numerical hydro-geotechnical model for marine gravity structures. Computers and Geotechnics, 79, 105-129.

Erken, A., Ülker, B.M.C. (2008). The post cyclic shear strength of fine-grained soils. The 14 Word conference on Earthquake Eng, China.

EURO GEOTÉCNICA S.A. 1999. Campaña de Reconocimientos Complementarios. Octubre de 1999.

Fatahi, B., Minh, T. and Khabbaz, H. 2012. Effects of initial stress state on performance of embankments on soft soils. Australian Geomechanics Vol 47, No3, September 2012.

Franco, L. 1994. Vertical breakwaters: the Italian experience. Coastal Engineering, vol 22, Issues 1–2, 31-55.

Fukuoka, M. & A. Nakase. 1973. Problems of soil mechanics of the ocean floor. Proc. 8th Int. Conf. Soil. Mech. Foundat. Engng, 4.2, 205-22.

Gens A. 1982. Stress-strain and strength of a low plasticity clay. Phd Thesis. University of London.

Gens, A. & Nova, R. 1993. Conceptual bases for a constitutive model for bonded soils and weak rocks. In Geotechnical Engineering of Hard Soils—Soft Rocks, Athens, Greece, Anagnostopoulos et al. (eds.). Balkema, Rotterdam: 485–494.

Gao YF, Shen Y, Zhang J, Li B (2011) Analysis of wave-induced liquefaction in seabed deposits of silt. China Ocean Eng 25(1):31–44

Geremew A (2013) Pore-water pressure development caused by wave-induced cyclic loading in deep porous formation. Int J Geomech 13(1):65–68

Georgiannou, V. N., Rampello, S. & Silvestri, F. (1991). Static and dynamic measurement of undrained stiffness of natural overconsolidated clays. Proc.10th Eur. Conj Soil Mech., Florence 1,91-96.

Goda, 1974. A new method of wave pressure calculation for the design of composite breakwaters. Proc. 14th Conf. Coast. Eng., ASCE, Copenhagen.

Goda, Y., 1985. Random seas and design of marine structures. Tokyo: University of Tokyo Press, 323 pp.

Goulois, A.M., Whitman, R.V., and Hoeg, K. (1985). Effect of sustained shear stress on the cyclic degradation of clay. Proceedings, Symposium on strength Testing of Marine Sediments, R.C. Chaney and K.R. Demars, eds., ASTM STP 883, ASTM, Philadelphia, pp. 336-351.

GPO-Europrincipia. 2001. Proyecto Constructivo del Dique de Abrigo Sur. Tramo I y II. Anejo 7. Ensayos en modelo reducido.

Griffiths D.V. and Lane P.A. (1999). Slope stability analysis by finite elements. Geotechnique, Volume 49, Issue 3, pp. 387-403.

Gutierrez R. & Grassa, J. M. 2015. Diseño, construcción y explotación de diques de abrigo portuario en España desde finales del siglo XX. RIBAGUA – Revista Iberoamericana del Agua Vol. 2, No2, pp. 80–96

Gutierrez-Serret, R., Grass, J.M., Grau, J.I. 2010. Breakwater development in Spain. The last ten years. Coasts, marine structures and breakwaters: Adapting to change: Proceedings of the 9th international conference organised by the Institution of Civil Engineers and held in Edinburgh on 16 to 18 September 2009.

Hardin, B.O. (1978) The Nature of Stress-Strain Behaviour for Soils. Proceedings of Earthquake Engineering and Soil Dynamics, ASCE, Pasadena, 19-21 June 1978, 3-89.

Hardin B. O. and Drnevich V. P. 1972. “Shear Modulus and Damping in Soil: Design Equations and Curves,” Journal of the Soil Mechanics and Foundations Division, Vol. 98, No. 7, 1972, pp. 667-692.

Hight, D. W., Jardine, R. J. & Gens, A. 1987. The behaviour of soft clays. Chapter 2, Embankment on soft clays, pp. 33-158. Athens: Public Works Researcd Centre of Greece.

Houlsby, G.T. and Wroth, C.P. (1991) “The Variation of the Shear Modulus of a Clay with Pressure and Overconsolidation Ratio”, Soils and Foundations, Vol. 31, No. 3, September, pp 138-143, ISSN 0038-0806

Hsu, C., and Vucetic, M. (2004). “Volumetric threshold shear strain for cyclic settlement.” J. Geotech. Geoenviron. Eng., 10.1061/(ASCE) 1090-0241(2004)130:1(58), 58–70.

Hsu, C., and Vucetic, M. (2006). "Threshold shear strain for cyclic porewater pressure in cohesive soils." J. Geotech. Geoenviron. Eng., 10.1061/(ASCE)1090-0241(2006)132:10(1325), 1325–1335.

Hudson, M., Idriss, I. and Beirkae, M. (1994). Quad4m user's manual.

Hunter G. and Fell R. 2003. Prediction of impending failure of embankments on soft ground. Can. Geotech. J. 40: 209–220

Indraratna, B., Perera, D., Rujikiatkamjorn, C. & Kelly, R. (2015). Soil disturbance analysis due to vertical drain installation. Proceedings of the Institution of Civil Engineers: Geotechnical Engineering, 168 (3), 236-246.

Indraratna, B., Baral, P., Ameratunga, J. & Kendaragama, B. (2017). Potential biological and chemical clogging of piezometer filters in acid sulphate soil. Australian Geomechanics Journal, 52 (2), 79-85.

INHA. (2000). Ensayos 2D para comprobar la estabilidad y rebase del Proyecto de construcción de la ampliacion del dique sur del Puerto de Barcelona.

Isenhower, W. M. (1979), "Torsional Simple Shear/Resonant Column Properties of San Francisco Bay Mud," M.S. Thesis, The University of Texas at Austin, 1979, 307 pp.

Jaky, J., 1948. Pressure in silos. In: Proceedings of the 2nd International Conference on Soil Mechanics and Foundation Engineering, vol. 1, pp. 103–107

Jamiolkowski, M., Ladd, C.C., Germaine, J.T. and Lancellotta, R. (1985). New developments in field and laboratory testing of soils. Proceedings, 11th International Conference on Soil Mechanics and Foundation Enginering, Vol 1, San Francisco, pp. 57-153.

Jardine, R. J., Symes, M. J. and Burland J. B. (1984). The Measurement of soil stiffness in the triaxial apparatus. Geotechnique 34, 3, 323-340

Jardine, R. J. & Hight, D. W. 1987. The behaviour and analysis of embankments on soft clay. Chapter 3, Embankment on soft clays, pp. 159-245. Athens: Public Works Research Centre of Greece.

Jeng DS, Cha DH, Lin YS, Hu PS (2001). Wave-induced pore pressure around a composite breakwater. Ocean Eng 28:1413–1435

Jeng DS, Seymour B (2007). Simplified analytical approximation for pore-water pressure buildup in marine sediments. J Waterw Port Coast Ocean Eng 4(309):309–312

Jeng D. 2003. A general finite element model for wave-seabed-structure interaction. Numer Anal Model Geomech 59–100.

Jeng, D. and Li, J. (2006). "Numerical model for wave-induced residual pore pressure in a porous seabed around the head of a breakwater." Coastal Engineering, 4533.

Jeng D-S, Cha D. 2003. Effects of dynamic soil behavior and wave non-linearity on the wave-induced pore pressure and effective stresses in porous seabed. Ocean Eng; 30(16):2065–89.

Jeng D-S, Ou J. 2010. 3D models for wave-induced pore pressures near breakwater heads. Acta Mech;215(1–4):85–104.

Juran I., Elias V. 1991. Ground Anchors and Soil Nails in Retaining Structures. In: Fang HY. (eds) Foundation Engineering Handbook. Springer, Boston, MA

Karstunen, M., Krenn, H., Wheeler, S.J. Koskinen, M. & Zentar, R. 2005. Effect of anisotropy and destructuration on the behaviour of Murro test embankment. ASCE International Journal of Geomechanics 5(2): 87–97.

Karstunen, M., Wiltafsky, C., Krenn, H., Scharinger F. and Schweiger, H. F. 2006. Modelling the behaviour of an embankment on soft clay with different constitutive models. Int. J. Numer. Anal. Meth. Geomech., 2006; 30:953–982

Kirca VSO, Sumer BM, Fredsøe J (2013) Residual liquefaction of seabed under standing waves. J Waterw Port Coast Ocean Eng 139:489–501

Konder, R. L. (1963). “Hyperbolic stress-strain response: Cohesive soils”. J. Soil Mech. and Found. Div., 89(1), 115–143.

Kortenhaus, A. and Oumeraci, H. 1998. Classification of wave loading on monolithic coastal structures. Proceedings International Conference Coastal Engineering (ICCE), ASCE, No 26. Vol. 1, Copenhagen, Denmark, pp-. 867-880.

Koutsoftas, D.C., and Ladd, C.C. 1985. “Design strengths for an offshore clay.” J. Geotech. Eng., ASCE, 111, 337-355.

Kovari K, Amstad Ch. (1982). A new method of measuring deformations in diaphragm walls and piles. Geotechnique 32(4):402–406

Kovari K, Amstad Ch., Köppel, J. (1979). New developments in the Instrumentation of underground openings. Proc. 4th Rapid Excavation and Tunnelling Conference, Atlanta, Ga., USA.

Koskinen, M., Karstunen, M., Wheeler, S.J. 2002a. Modelling destructuration and anisotropy of natural soft clay. Proc. Of 5th European Conference on Numerical Methods on Geotechnical Engineering (NUMGE02), 4-6 September, Paris, France, pp. 11-20. Paris: Presses de l’ENPC/LCPC.

Kramer, S. L. 1996. Geotechnical Earthquake Engineering. Prentice Hall, New Jersey, 653 pp

Kudella M, Oumeraci H, De Groot M, Meijers P. 2006. Large-scale experiments on pore pressure generation underneath a caisson breakwater. J Waterway Port Coast Ocean Eng;132(4):310–24.

Kudella M, Oumeraci H. 2004. Pore pressure development in the sand bed underneath a caisson breakwater. Coastal engineering conference, vol. 29-4. ASCE American society of Civil Engineers; 2004. p. 3800.

Kuhlemeyer, R.L. and Lysmer. J. (1973) Finite Element Method Accuracy for Wave Propagation Problems. Journal of the Soil Mechanics and Foundations Division, 1973, Vol. 99, Issue 5, Pg. 421-427.

Kulhawy, F.H. & Mayne, P. (1990). Manual on Estimating Soil Properties for Foundation Design. Report EL-6800, Electric Power Res. Inst., Palo Alto.

Ladd, C.C. and Foott, R., 1974. New design procedure for stability of soft clays. ASCE Journal of Geotechnical Engineering 100 (7), 763–786.

Lacasse and B. Raadim (1987): Comparison of truly undrained and constant volume direct simple shear tests. Geotechnique, Vol.37, No.1, pp. 3-10.

Ladd and Edgers, 1972. Consolidated-Undrained Direct-Simple Shear Tests on Saturated Clays. Research report R72-82. Soils Publication 284. MIT

Ladd, C.C., Foote, R., Ishihara, K., Schlosser, F., and Poulos, H.G. (1977). Stress-Deformation and Strength Chracteristics. Proceedings, 9th International Conference on Soil Mechanics and Foundation Enginering, Vol 2, Tokio, pp. 421-494.

Ladd, C., Whittle, A., and Legaspi, D. (1994). Stress-deformation behavior of an embankment on Boston blue clay. Proceedings of ASCE conference on vertical and horizontal deformations of foundations and embankments, College Station, Texas, 2: 1739–1759.

Ladd, C.C. & R. Foott. 1974. New design procedure for stability of soft clays. J. Geotecj. Engng. Div., ASCE 100 (GT7), 763-86

Lade, P. V. & de Boer, R. (1997). The concept of effective stress for soil, concrete and rock. Geotechnique 47, No. 1, 61-78

Lee, S. Y., Huynh, T. C., Kim, J. T., Yoon, H. S and Han. S.H. 2013. Vibration Characteristics of Gravity-Type Caisson Breakwater Structure with Water-Level Variation. International Journal of Distributed Sensor Networks Volume 2013, Article ID 261396, 10 pages

Leroueil S, Magnan J-P, Tavenas F. 1990. Embankments on Soft Clays. Ellis Horwood: Chichester, England.

Leroueil S., Tavenas F., Brucy F., La Rochelle P. & Roy M. 1979. Behaviour of destructured natural clays. ASCE Journal of Geotechnical Engineering, 105(6): 759–778.

Leonards, G.A. and Altschaeffl, A.G. 1964. Compressibility of Clay. Journal of the Soil Mechanics and Foundations Division, American Society of Civil Engineers 90:133-154.

Likitlersuang, S., Teachavorasinskun, S., Surarak, Ch., Oh, E., Balasubramaniam, A. 2013. Small strain stiffness and stiffness degradation curve of Bangkok Clays. Soils and Foundations; 53(4): 498–509.

Lo Presti, D.c.F., 1989, Proprietà Dinamiche dei rerreni, proceedings XIV conferenza geotecnica di torino, Department of structural Engineering, Pólitecnico di Torino. (in Italian).

Lo Presti, D. C. F., Jamiolkowski, M., Pallara, O., Cavallaro, A. & Pedroni, S. (1997). Shear modulus and damping of soils. Geotechnique 47, No. 3, 603-617

Lundgren, H. 1969. "Wave Shock Forces: An Analysis of Deformations and Forces in the Wave and in the Foundation," *Proceedings of the Symposium on Research on Wave Action*, Delft Hydraulics Laboratory, Emmeloord, The Netherlands, Vol II, Paper 4.

Lunne, T & Kleven A. (1981a) Role of CPT in North Sea foundation engineering. Proceedings of Geotechnical Engineering division Session, ASCE National Convention, St. Louis, Missouri 76-107.

Lysmer, J. Kuhlmeyer, R.L. (1969). Finite dynamic model for infinite media. ASCE J. of the Eng. MEch. Div. 859-87.

Marsland, A., and Powell, J.J.M. 1977. The behaviour of a trial bank constructed to failure on soft alluvium of the River Thames. In Proceedings of the International Symposium on Soft Clay, Bangkok. Edited by R.P. Brenner and E.W. Brand. Asian Institute of Technology. pp. 505–525.

Mayne, Paul & Kemper, JB. (1988). Profiling OCR in Stiff Clays by CPT and SPT. Geotechnical Testing Journal – vol. 11, No. 2, pp 139-147.

Meijers, P. (1994): Spring and dashpot parameters from large scale tests. *MAST II/ MCS - project,* Delft Geotechnics, BO-330040/49, 32 pp

Meyerhof, G. G. (1953). The bearing capacity of foundations under eccentric and inclined loads. 3rd International Conference on Soil Mechanic and Foundations Engineering 1, 440-445. Miche, R. 1944. Mouvements ondulatories des mers en profunder constante on décroissant. Annals des Points et Chaussées, pp. 25-78.131-164,270-292, 369-406.

NAVFAC DM-7.1 (1986). Soil Mechanics. Design Manual 7.1, Department of the Navy, Naval Facilities Engineering Command, Alexandria, Va., 364 pp.

Näätänen, A., Wheeler, S., Karstunen, M., and Lojander, M. 1999. Experimental investigation of an anisotropic hardening model for soft clays. In Proceedings of the 2nd International Symposium on Pre-failure Deformation Characteristics of Geomaterials, Torino, Italy, 28–30 September, Edited by M. Jamiolkowski, R. Lancellotta, and D. Lo Presti. A.A. Balkema, Rotterdam. pp. 541–548.

Negro, V., Varela, O., Garcia, J. & Lopes, J.S. 2001. Diseño de diques verticales. Colegio de Ingenieros de Caminos, Canales y Puertos. Colección Seinor 26. España.

NGI (1998b): MAST III - PROVERBS, Effect ofcyclic loading on capacity and stiffness, design diagrams. *NGI report No. 524094-2,*December 1998

NGI. 2002. Port de Barcelona. Laboratory testing. Geotechnical Testing Report. March, 2002.

NGI. 2009. Laboratory testing Muelle Ports. 2008 Laboratory test result. January 2009.

Olson, R. E. (1977). Consolidation under time-dependent loading. J. Geotech. Engng Div., ASCE 103, No. GT1, 55-60.

Oñate, E., Celigueta, M., Idelsohn, S., Salazar, F., Larese, A., Rossi, R., Suárez B. and Morán, R. (2012). Analysis of fluid-soil-structure interaction problems with the Particle Finite Element Method (PFEM). CIMNE Research Report, Nº PI374

Oumeraci,H., Kortenhaus,A., Allsop,W., De Groot,M., Crouch,R., Vrijling,H. & Voormant,H. 2001. Probabilistic Design Tools for Vertical Breakwaters. A.A.Balkema Publishers.

Oumeraci. 1994. Review and analysis of vertical breakwater failures — lessons learned. Coastal Engineering. Volume 22, Issues 1–2, January 1994, Pages 3-29

Oumeraci, H., Burchart, H.F., De Rouck, J., Juhl, J., Losada, M. 1995. Coastal structures – overview of MAST-2 projects, XXVIth IAHR Congress-Hydra 2000, Seminar 1: The EC Marine Science and Technology Programme (MAST), London, UK, 37 pp.

Oumeraci, H.; Partenscky, H.-W.; Tautenhain, E.; Nickels, H. 1991. Large scale model investigations: a contribution to the revival of vertical breakwaters. *Proceedings of the Conference on Coastal Structures and Breakwaters*, ICE, London, U.K.: Thomas Telford Ltd., pp. 207-220.

Oumeraci, H. & Kortenhaus, A. (1994) Analysis of the dynamic response of caisson breakwaters. Coastal Engineering, vol. 22, nos 1-2, pp. 159-183.

Oumeraci, H.; Partensky, H.W.; Kohlhase, S.; Klammer, P. (1992): Impact Loading and dynamic response of dynamic breakwaters - Results of large-scale model tests. *In. Proc. 23rd ICCE, ASCE, Vol 2, pp. 1475-1488*

Papa, V., Silvestri, F. & Vinale, F. (1988). Analisi delle proprieta di un tipico terreno piroclastico mediante prove di taglio semplice. In Atti de1 I Convegno de1 Gruppo Nazionale di Coordinamento per gli Studi di lngegneria Geotecnica, Monselice, pp. 265-286.

Pastor, M., Drempetic, V., Merodo, J.A.F., y Mira, P., 2006. Una metodología racional para el estudio de cimentaciones de estructuras marinas. Ingeniería Civil CEDEX 141, 37–48.

Pita E., Vasquez J. & GT-1 ATPC. 2007. Análisis de estructuras bidimensionales mediante programas de estabilidad de taludes. Puertos N 138.

Pedersen, J. (1997): Dynamic Response of Caisson Breakwaters Subjected to Impulsive Wave Loading - Design Diagrams for Dynamic Load Factors - *2nd Project Workshop, Las Palmas, 18-22 February 1997*

Petalas, A. and Galavi, V. 2013. Plaxis liquefaction model UBC3D-PLM. Report

Press, W. H., Flannery, B. P., Teukolsky, S. A. & Vetterling, W. A. [1988] Numerical Recipes in C (Cambridge University Press).

Potts, D. M.& Zdravkovic,L. 2001. Finite element analysis in geotechnical engineering II: Application. T. Telford, London.

Potts, D. M, 2002, Guidelines for the use of advanced numerical analysis, London, Publisher: Thomas Telford

Poulos H.G., and Davis E.H. 1974. Elastic solutions for soil and rock mechanics. John Wiley & Sons, Inc., New York.

Prior DB, Suhayda JN, Lu NZ et al (1989) Storm wave reactivation of a submarine landslide. Nature 341(7):47–50

Puebla, H., Byrne, P.M. & Phillips, R. (1997). Analysis of CANLEX liquefaction embankments: prototype and centrifuge models. Can. Geotech. Journal, Vol. 34, No. 5: 641-657.

Puzrin, A.M., Alonso, E.E., Pinyol, N.M. 2010. Geomechanics of failures. Chapter 5. Springer Dordrecht Heidelberg London New York.

RODIO. 1996. Reconocimiento Geotécnico de los Nuevos Diques del Puerto de Barcelona. Informe, Tomo I, Mayo 1996.

ROM 0.5. 2005. Recomendaciones Geotécnicas para Obras Marinas. Ministerio de Fomento, Puertos del Estado.

Richwien, W., Wang, Z., 2000. The mechanism of seaward tilting of vertical breakwaters. Some aspects on subsoil failure of vertical breakwaters. Forschungsberichte aus dem Fachbereich Bauwesen. Universität Essen 83, 54–69.

Rocchi, G., Vaciago, G., Fontana, M., Da Prat, M. (2013). Understanding sampling disturbance and behaviour of structured clays through constitutive modelling. Soils and Foundations, 53(2), pp 315–334

Roscoe K H and Burland J B 1968 On the Generalised Stress-Strain Behaviour of Wet Clay In Heyman, J. and Leckie, F. A. (eds) Engineering Plasticity, Cambridge University Press. 535-609.

Rowe, P.W. (1971): Theoretical meaning and observed values of deformation parameters for soil, Stress Strain Behaviour of Soils (ed. by Parry, R.G.H.), 143-194.

Rowe, P. W. (1962). The Stress-Dilatancy Relation for Static Equilibrium of an Assembly of Particles in Contact. Proceedings of the Royal Society A: Mathematical, Physical and Engineering Sciences, 269(1339), 500–527.

Rundgren, L. 1958. “Water Wave Forces”, Bulletin No. 54, Royal Institute of Technology, Division of Hydraulics, Stockholm, Sweden.

Sainflou, M. 1928. “Treatise on Vertical Breakwaters,” *Annals des Ponts et Chaussee*, Paris, France (Translated by W. J. Yardoff, U.S. Army Corps of Engineers.)

Santagata, M.; Germaine, J.T.; and Ladd, C.C. 2007. Small-Strain Nonlinearity of Normally Consolidated Clay. Journal of Geotechnical and Geoenvironmental Engineering, Vol. 133, No. 1. 728-82.

Savinov, O.A. (1955) Machine Foundations, (in Russian), Leningrad.

Schanz, T., Vermeer, P.A., Bonnier, P.G. (1999). The hardening-soil model: Formulation and verification. In R.B.J. Brinkgreve, Beyond 2000 in Computational Geotechnics, Balkema, Rotterdam. 281–290.

Scholte‘s L, Chareyre B, Michallet H, Catalano E, Maraougui D (2015) Modeling wave-induced pore pressure and effective stress in a granular seabed. Continuum Mech Thermodyn 27:305–323

Sekiguchi,H.& Ohmaki,S. 1992. Overturning of caissons by storm waves. *Soils and Foundations*, **32,** 144-155.

Sekiguchi, H., Kita, K., Okamoto, O., 1995. Response of poroelastoplastic beds to standing waves. Soils and Foundations 35 (3), 31–42.

Shibuya, S., Hwang, S. C., and Mitachi, T. (1997). “Elastic shear modulus of soft clays from shear wave velocity measurement.” Geotechnique, 47(3), 593–601.

Silvestri, F. (1991). Stress-strain behaviour of natural soils by means of cyclic/dynamic torsional shear tests. In Experimental characterization and modelling of soils and soft rocks, pp. 7-73. University of Napoli Federico Il.

Skempton, A. W. (1954). The pore pressure coefficients A and B, Geotechnique 4, No. 4, 143-147.

Sloan,S.W.& Randolph,M.F. 1982. Numerical prediction of collapse loads using finite element methods. *International Journal for Numerical and Analytical Methods in Geomechanics*, **6,** 47-76.

Stark, T., Ricciardi, P., and Sisk, R. 2018. Case Study: vertical drain and stability analyses for a compacted embankment on soft soils. Journal of Geotechnical and Geoenvironmental Engineering. 144(2): 05017007.

Stickle, M.M., 2010. Sobre la Respuesta Dinámica del Terreno Bajo la Acción del Olaje en Cajones Fondeados en Suelos Arcillosos. (Ph.D. thesis). Universidad Politécnica de Madrid, Madrid, Spain.

Stickle M, De La Fuente P, Oteo C, Pastor M, Dutto P. 2013. A modelling framework for marine structure foundations with example application to vertical breakwater seaward tilt mechanism under breaking wave loads. Ocean Eng;74:155–67.

Sumer SK, Sumer BM, Dixen FH, Fredsoøe J. 2008. Pore pressure buildup in the subsoil under a caisson breakwater. In: Proceedings of the ISOPE, 6th–11th July. Canada: Vancouver; 2008. p. 664–71.

Sumer BM (2013) Liquefaction around marine structures. World Scientific, London

Takahashi, S., and Hosoyamada, S. 1994. "Hydrodynamic Characteristics of Sloping Top Caissions," *Proceedings of International Conference on Hydro-Technical Engineering for Port and Harbour Construction*, Port and Harbour Research Institute, Japan, Vol 1, pp 733-746.

Takahashi, S., Tanimoto, K., and Shimosako, K. 1994. "Wave Pressure on Perforated Wall Caissons," *Proceeding of International Conference on Hydro-Technical Engineering for Port and Harbor Construction*, Port and Harbour Research Institute, Yokosuka, Japan, pp 747-764.

Tanimoto, K., and K. Kimura. 1985. A Hydraulic Experimental Study on Trapezoidal Caiison Breakwater. Tech. Note 528, Port and Harbour Research Institute, Yokosuka, Japan.

Tarragó, D. 2021. Hydraulic fills liquefaction effect on quay stability. Phd Thesis. Universitat Politecnica de Catalunya, Barcelona

Tavenas F. & Leroueil S. 1980. The behaviour of embankments on clay foundations. Canadian Geotechnical Journal, 17(2): 236-260.

Terzaghi,K. (1943). *Theoretical soil mechanics*. John Wiley & Sons, Inc., New York.

Tsegaye, A. 2010. Plaxis liquefaction model. Report 1. Plaxis knowledge base.

Tsuchida, T. (2000). Evaluation of undrained shear strength of soft clay with consideration of sample quality. Soils and Foundations, 40 (3), pp. 29-42

Ukritchon,B., Whittle,A.J. & Sloan,S. 1998. Undrained limit analysis for combined loading of strip footings on clay. *Journal of Geotechnical and Geoenvironmental Engineering*, **124,** 265-276.

Ülker M, Rahman M, Jeng D-S. 2009. Wave-induced response of seabed: various formulations and their applicability. Appl Ocean Res; 31(1):12–24.

Ülker, M.B.C., Rahman, M.S., and Guddati, M.N. 2012. Breaking wave-induced response and instability of seabed around caisson breakwater. Int. J. Numer. Anal. Meth. Geomech. 2012; 36:362–390.

Ulker, M.B.C., Rahman, M.S., Guddati, M.N., 2010. Wave-induced dynamic response and instability of seabed around breakwater. Ocean Engineering 37, 1522–1545.

UPC. 1997. Ensayos sobre muestras procedentes del Puerto de Barcelona. Laboratorio de Geotecnia. Departamento de Ingenieria del Terreno, UPC.

UPC. 2001. Ensayos especiales sobre muestras procedentes del Puerto de Barcelona. Laboratorio de Geotecnia. Departamento de Ingeniería del Terreno, UPC.

UPC. 2008. Informe de los ensayos de identificación, edométricos, permeabilidad y triaxiales. Puerto de Barcelona. Julio 2008

Vardanega, P. J. and Bolton, M. D. 2013. Stiffness of Clays and Silts: Normalizing Shear Modulus and Shear Strain Journal of Geotechnical and Geoenvironmental Engineering, Vol. 139, No. 9, pp. 1575-1589.

Vardanega, P. J., and Bolton, M. D. (2011a). "Practical methods to estimate the non-linear shear stiffness of clays and silts." Proc., 5th Int. Conf. On the Deformation Characteristics of Geo-materials, IOS Press, Amsterdam, Netherlands, 372–379.

Vázquez-Suñé, E. 2003. Urban Grounwater. Barcelona City Case Study. Phd Thesis. Universitar Politecnica de Catalunya (UPC).

Vermeer, P.A., Neher, H.P., 1999. A soft soil model that accounts for creep. In: Proceedings of the Plaxis Symposium on Beyond 2000 in Computational Geotechnics, Amsterdam, pp. 249–262.

Vesic, A.S. (1975). Bearing capacity of shallow foundations. In: Foundation engineering handbook (ed e.H.F.Winterkorn and H.Y.Fang), pp. 121-145. Van Nostrand Reinhold, New York.

Vicinanza, D., Di Lauro, E., Contestabile, P., Gisonni, C, Lara, J., and Losada, I. 2019. Review of Innovative Harbor Breakwaters for Wave-Energy Conversion. J. Waterway, Port, Coastal, Ocean Eng., 2019, 145(4).

Viggiani, G. & Atkinson, J.H. (1995). Stiffness of fine-grained soil at very small strains. Geotechnique 45, No2, 249-265.

Vucetic, M. (1994). Cyclic threshold shear strains in soils. Journal of Geotechnical Engineering, ASCE, vol 120, No 12, pp. 2208-2228.

Wang, Y., Lei, J., Gong, X., Wang Y., Yang, P. (2018). Post-cyclic undrained shear behavior of marine silty clay under various loading conditions. Ocean Engineering, vol. 158, pp 152–161

Wang JG, Nogami T, Karim MR (2001). Analysis of transient response of saturated porous elastic soil under cyclic loading using element-free Galerkin model. Int J Solids Struct 39(24):6011–6033

Wang JG, Zhang BY, Nogami T (2004). Wave-induced seabed response analysis by radial point interpolation meshless method. Ocean Eng 31:21–42

Wang JG, Karim MR, Lin PZ (2007). Analysis of seabed instability using element free Galerkin method. Ocean Eng 34:247–260

Wijewickreme, Dharma, Dabeet, Antone, and Byrne, Peter, "Some Observations on the State of Stress in the Direct Simple Shear Test Using 3D Discrete Element Analysis," Geotechnical Testing Journal, Vol. 36, No. 2, 2013, pp. 1–8, doi:10.1520/GTJ20120066. ISSN 0149-6115.

Wheeler, S.J. 1997. A rotational hardening elasto-plastic model for clays. In Proceedings of the 14th International Conference on Soil Mechanics and Foundation Engineering, Hamburg, A.A. Balkema, Rotterdam. Vol. 1, pp. 431–434.

Wheeler, S., Näätänen, A., Karstunen, M., & Lojander, M. (2003). An anisotropic elastoplastic model for soft clays. Can. Geotech. J. vol. 40, 403-418.

Wood, D. M. (1990) Soil behaviour and critical state soil mechanics. Cambridge University Press (462pp)

Wroth, C. & Wood, D. (1978). The correlation of index properties with some basic engineering properties of soils. Canadian Geotechnical Journal. 15. 137-145.

Wroth, C.P. and Houlsby, G.T. (1985) "Soil Mechanics – Property Characterization and Analysis Procedures", Invited Paper, Proceedings of the 11th International Conference on Soil Mechanics and Foundation Engineering, San Francisco, August 12-16, Vol. 1, ISBN 90-6191-561-9, pp 1-55

Yan, SW., Zhao, L., and Fan, Z. 2010. Soft Soil Improvement to Resist Strength Softening Caused By Wave. Twentieth International Offshore and Polar Engineering Conference, Beijing, China

Ye, G., Leng, J., Jeng, D. (2018). Numerical testing on wave-induced seabed liquefaction with poro-elastoplastic model. Soil dynamic and earthquake engineering 105:150-159

Yu, H.S.& Netherton,M.D. 2000. Performance of displacement finite elements for modelling incompressible materials. *International Journal for Numerical and Analytical Methods in Geomechanics*, **24,** 627-653.

Zhang X, Lee F, Leung C. Tilt displacement of caisson breakwater due to wave loading. Géotechnique 2009;59(1):17–27.

Zhang, J., Andrus, R. D., and Juang, C. H. (2005). "Normalized shear modulus and material damping ratio relationships." J. Geotech. Geoenviron. Eng., 131(4), 453–464.

Zienkiewicz O. C. (1982). Field equations for porous media under dynamic loads. Num. Meth. in Geomech., D. Reidel, Boston, U.S.A.

Zienkiewicz O.C. and Shiomi T. (1984). Dynamic behaviour of saturated porous media: The generalized Biot formulation and its numerical solution, Int. J. Num. Anal. Geomech., 8, 71 – 96.

Zienkiewicz O.C., Chan A. H. C., Pastor, M., Paul D.K., Shiomi T. (1990a). Static and dynamic behaviour of geomaterials – A rational approach to quantitative solutions, Part I – Fully saturated problems, Proc. Roy. Soc. Lond., A429, 285-309.

Zienkiewicz O.C., Xie Y.M., Schrefler B.A., Ledesma A. and Bicanic N. (1990b). Static and dynamic behaviour of soils – A rational approach to quantitative solutions, Part II – Semi-saturated problems, , Proc. Roy. Soc. Lond., A429, 310-323.

Zienkiewicz, O.C. & Chan, Andrew & Pastor, Manuel & Schrefler, Bernhard & Shiomi, Tadahiko. (1999). Computational Geomechanics With Special Reference to Earthquake Engineering. Edition: 1st Publisher: John Wiley & Sons.

Zienkiewicz, Chang C, Bettess P. 1980. Drained, undrained, consolidating and dynamic behaviour assumptions in soils. Geotechnique 1980;30(4).

APPENDIX I

GEOTECHNICAL INSTRUMENTATION OF SOUTH BREAKWATER

I.1 INTRODUCTION

The expansion of the Port of Barcelona has required the construction of 2 new dikes, which were built on the soft soil of the port. Due to the soft nature of the soil, it was necessary to increase soil strength through carefully planned consolidation stages. In order to verify that a sufficient degree of consolidation has been achieved, an instrumentation system was deployed. It included pore pressure measurements and settlement measurements at various depths as well as inclinometer measurements of horizontal movements.

In this Appendix, the instrumentation that was deployed in the South Breakwater is described, with special attention given to the difficulties encountered. The original instrumentation was active from February 2004 to March 2006 and was replaced by a new instrumentation once the placement of the caissons was completed, which remained active from July 2007 to September 2009. With the exception of the inclinometers, the new instrumentation kept the same sensor configuration and was only placed in the caissons area (3 sections). Figure I-1 shows a plan view of the 4 instrumented sections in the South Breakwater. Finally, results from the instrumentation are presented.

The specialized company SOLDATA was in charge of installing and maintaining the instrumentation. This appendix is primarily based on the reports provided by SOLDATA. The Norwegian Geotechnical Institute (NGI) provided advice about the design, deployment and installation of the monitoring system.

I.2 OBJECTIVES OF THE INSTRUMENTATION

The main objectives of the instrumentation were:

- To monitor the progress of consolidation under the embankment to help to assess the gain of undrained shear strength required for stability during the phase of placing and filling the caissons.
- To monitor the progress of soil movements during all phases of construction, preferably including both total settlements and their distribution with depth. Measurement of horizontal movements as an additional check of stability conditions.
- To monitor distributions of displacements on the surface to assess the development of the tilting of the caissons.

Marine instrumentation involves additional difficulties to the standard practice in geotechnical instrumentation projects. Working conditions are extremely unfavourable and it is necessary to ensure the survival of the instruments in an aggressive medium. Probably these are the principal reasons why very few instrumentations of breakwater have been reported.

To overcome these problems, a non-traditional method for installing the instruments was developed as explained below. The period available to perform the installation works was the winter of 2003/2004, so bad weather conditions were expected. In view of that situation, it was decided to set up chains of instrument onshore which were delivered to the working platform for installation. Cables and connectors had to be specially designed by the supplier, in order to reduce the work done by the diver team. It was also decided that all piezometers and inclinometers had to be of commercial type and well proved to work in difficult conditions.

In addition, the construction of the embankment involved dumping stone rocks with a maximum weight of about 1 ton (Project specifications), so it was necessary to design an effective protection system for the instruments and connecting cables.

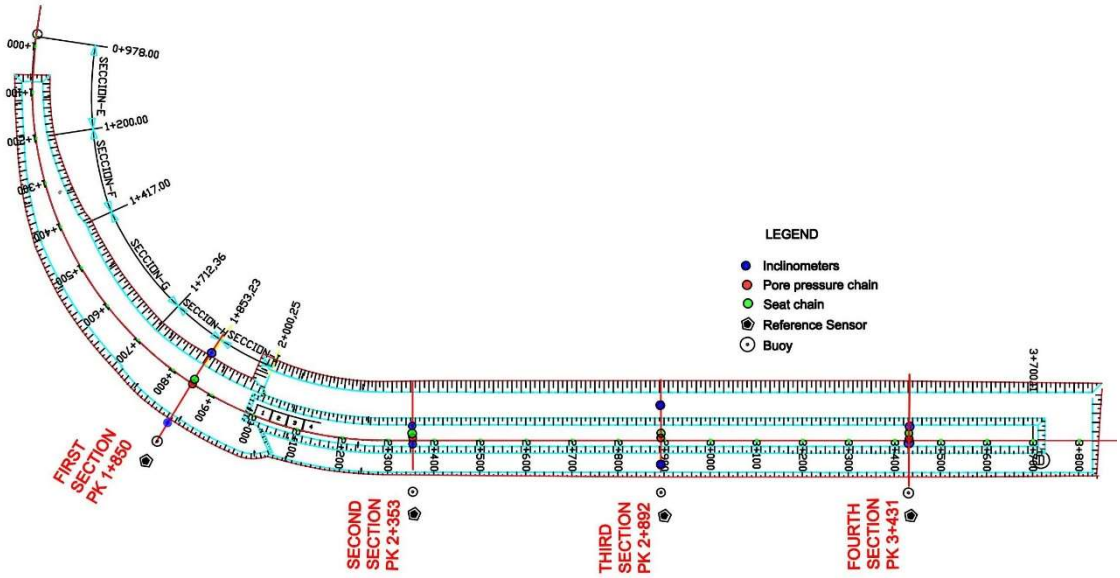

Figure I-1. Location of instrumented sections in the South Breakwater.

I.3 DESCRIPTION OF THE INSTRUMENTATION SYSTEM

The project envisaged that 4 sections should be instrumented about one section every 500 m of the most critical areas of the south breakwater (three sections were located in the caisson area). Due to the importance of monitoring the progress of consolidation, it was checked by two independent measurements: pore pressures and settlements. Particular importance was given to the top 20 m of the foundation soil where critical instability surfaces are likely to be located. Two typical cross-sections of

instrumentation for the two different types of breakwater cross-section are shown in Figure I-2 and Figure I-3.

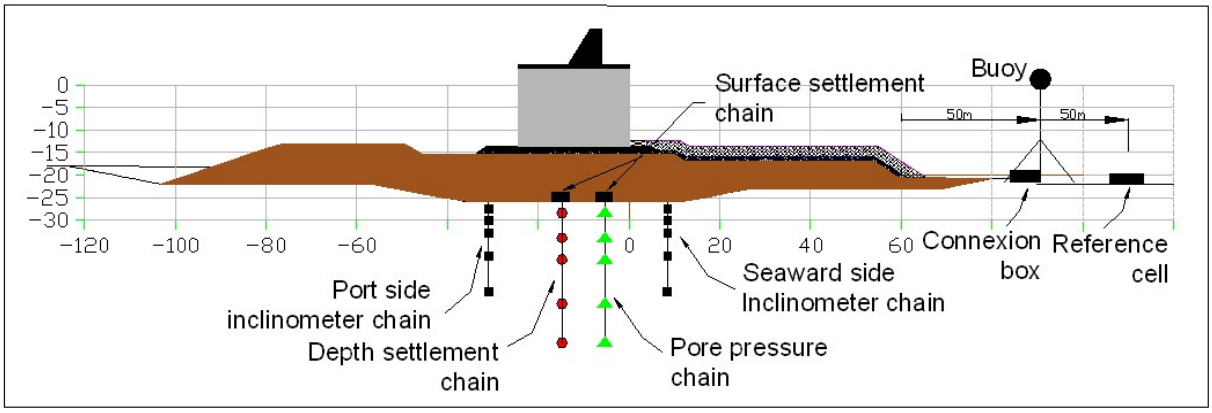

Figure I-2. Typical cross section for vertical breakwater instrumentation.

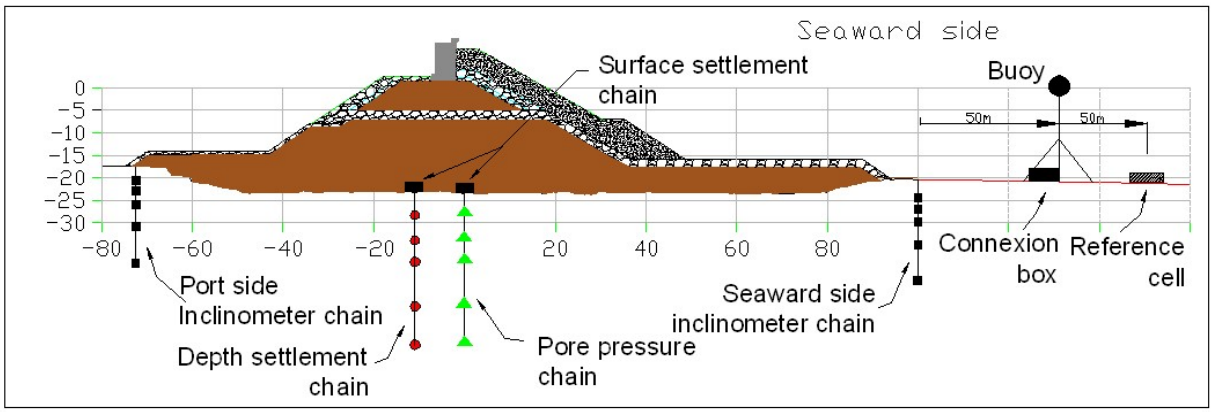

Figure I-3. Typical cross section for rubble mound breakwater instrumentation.

Each instrumentation section has been connected to its own autonomous system of power data transmission. In summary each section is provided with the following instruments:

- 2 chains of in-place inclinometers, with 5 sensors each, installed at several depths down to 20m. They were placed at the two ends of the section.

- 1 chain of pore pressure measurement cells placed at the center of each section. This consists of 5 piezometers installed down to a maximum depth of 35m below sea bed.

- 1 chain of depth settlements measurement cells, with 5 sensors installed down to a depth of 35m below sea bed.

- 2 cells of surface settlement measurement, placed at the seabed/embankment contact, with approximately 5 m of distance between them.

- Also, one cell was installed outside the influence area of settlements, as a reference cell for settlements.

- 1 buoy for power supply and data transmission.

Pore pressure measurements system

A chain consisting of 5 dual vibrating wire piezometers (range of 1.0Mpa) was installed to obtain the pore pressure profile. Excess pore pressure is computed as the difference between the actual reading (PP_f) and the initial hydrostatic reading (PP_i). Figure 6-31 shows a representative sketch of the pore pressure system.

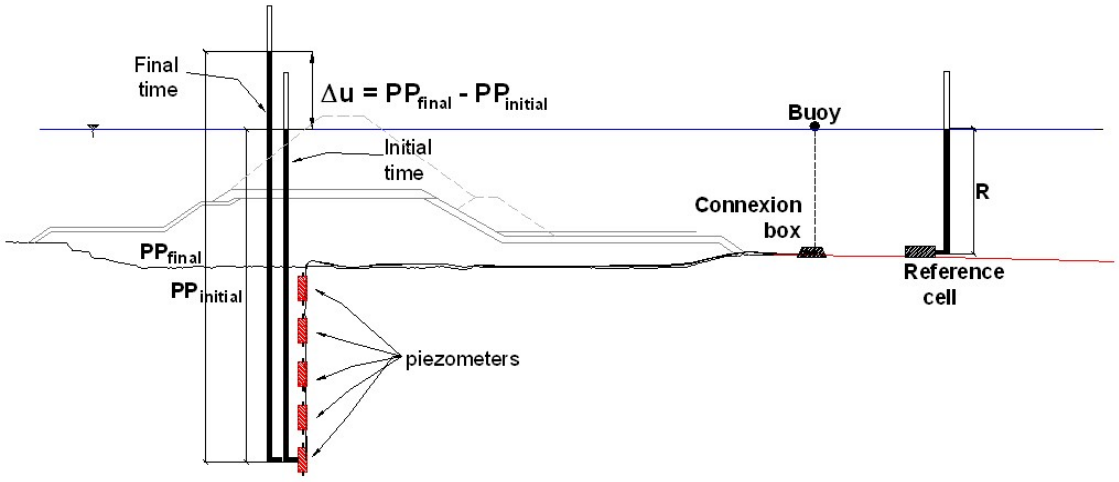

Figure I-4. Pore pressure measurements, basic principle

The pore pressure piezometers installed were a Geokon model 4500HDX heavy duty dual piezometers (range of 1.0 MPa). Each piezometer was delivered with sufficient cable attached to reach after installation the surface of sea above the buoy location, to facilitate subsequent cable connections. One chain of 5 dual piezometers was installed per section of monitoring.

Prior to the installation of the pore pressure piezometers, their zero values were determined. This procedure was carried out ensuring the piezometer was in thermal equilibrium and out of direct sunlight by immersion in a bucket of clean water. The actual zero reading was recorded with the piezometer diaphragm at or very slightly below the level of the surface of the water. Also, prior to the installation, the piezometer was kept inside a bucket of water for at least 3 hours.

The cables for the five double pore pressure piezometers were spliced together and joined to a common multi-conductor connector by the instrument manufacturer. Hence the depths of installation were pre-determined (5m, 10m, 15m, 25m and 35m below seabed). The cables were marked such that each installation is identifiable.

Each instrument was assembled inside of a geotextile sock. This sock was about 0.5m long. Its sole aim is to fix the instrument and its cable to a stainless steel cable (see figures below), without straining the data cable. The sensor was positioned upside down to avoid air trapping in the sensor. The piezometer was attached along a supporting stainless steel cable. In between the sensors, cylinders of dense foam

material (material used for temperature protection of pipes for example) were also attached to the cable. There were 2 cylinders of 0.5m length between each pair of piezometers, as well as 2 further cylinders above the top piezometer. The supporting steel cable and the data cables were run inside that cylinder, that was filled with resin, to prevent any hydraulic connection along the cables.

The strings were assembled onshore and delivered to the working platform for installation. The following figures show some details of the installation of the instruments.

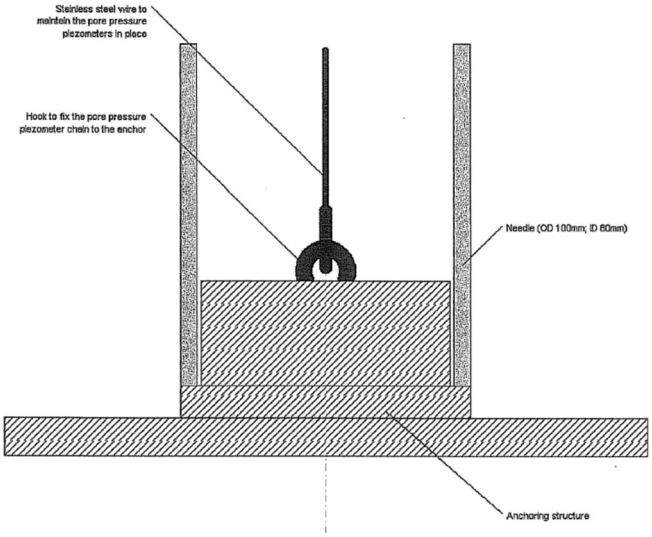

Figure I-5. Botton of the pore pressure gauge chain in the needle

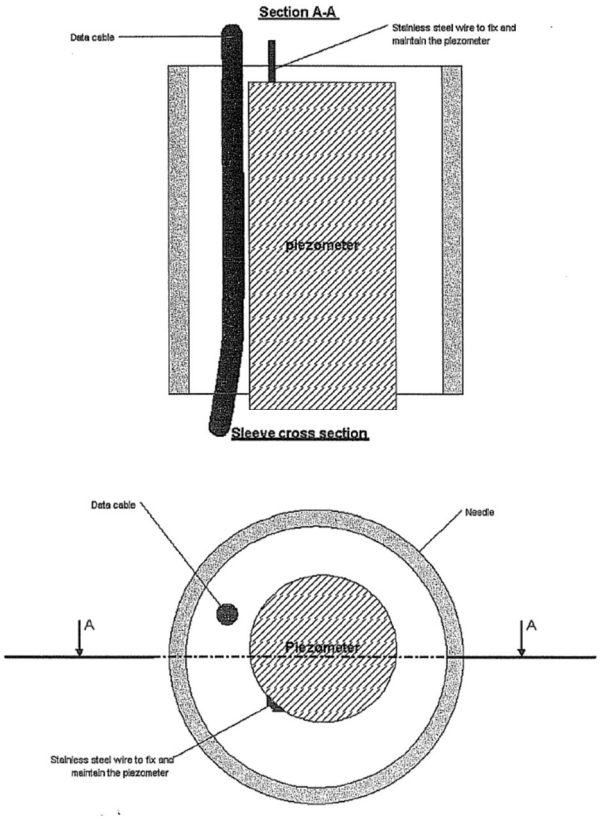

Figure I-6. Pore pressure gauge cross section

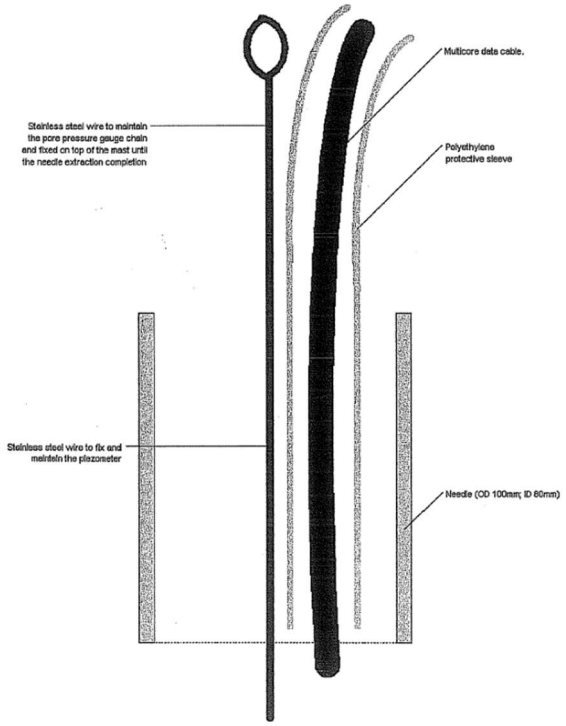

Figure I-7. Top of the needle

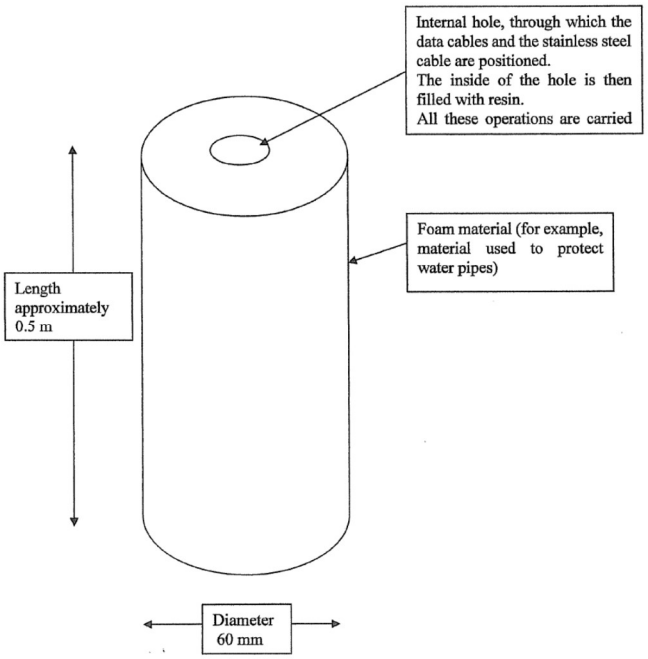

Figure I-8. Foam ‘plug’

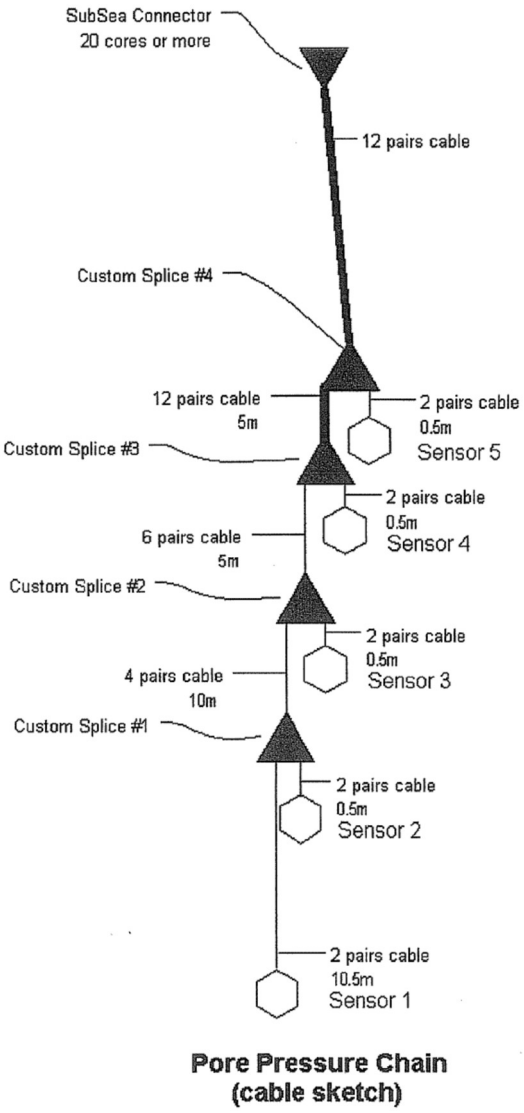

Figure I-9. Pore pressure chain (cable sketch)

Surface settlement gauges

The surface settlement measurement chain consists of two sensors, which were arranged under the dike as follows: Water pressure sensors were assembled inside a flexible polyethylene pipe, to avoid measuring the excess pore pressure developed during the construction of the embankment. In this way, the water pressure sensors only measure differences in water levels due to settlement.

A reference cell was installed on the seabed 50m away seaward from the buoy location. This enables the correction of data for variations in the tidal level. This reference was used as well to correct the data of the "At depth settlement gauges". Figure 6-37 show the basic principle for surface settlement.

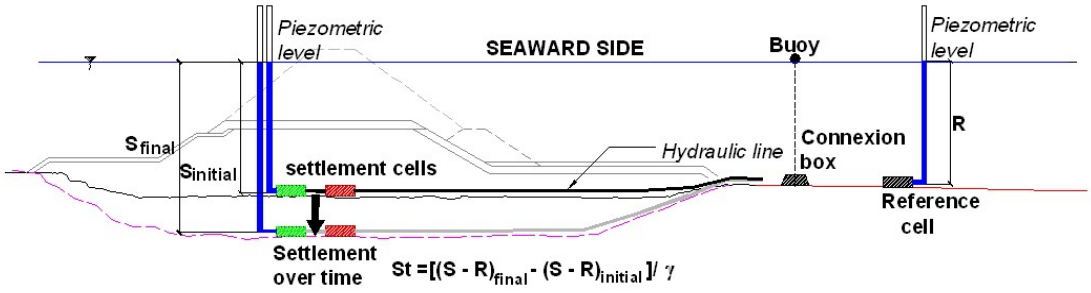

Figure I-10. Surface settlement gauge, basic principle.

The settlement cells were Geokon model 4500HD heavy duty dual piezometers (range 0.70MPa). Each cell was delivered with sufficient cable attached to reach after installation the surface of the sea above the buoy location, to facilitate subsequent cable connections.

All piezometers were prepared and verified for zero reading and saturation, as explained before for the pore pressure piezometers.

The cells were placed inside of a protective flexible pipe (Type agricultural drain). The pipe is soft and contained holes, so it did not float too much. The data cable was installed forming loops inside the pipe (considering the minimum bending radius of the cables), in order to provide 20% spare length of slack and avoid tension.

Above the cells, a steel plate 1 x 1 m of approximately 10mm thickness was fixed to the pipe. This was to provide some protection to the cell and to help it to remain at the surface. Additionally, some sandbags were located above the steel plate to provide additional protection and damping of the stone impacts.

The soft pipe and its data cable were protected similarly to the other instrument cables.

The two settlement cells were installed inside the same pipe, whereas the reference cell was installed separately.

The strings were assembled onshore and delivered to the working platform for installation.

A diver placed the pipe with its cells in the correct position on the seabed. The diver also attached the cable to a temporary buoy to free the installation platform to move onto the next location. The following figures show some details of the installation.

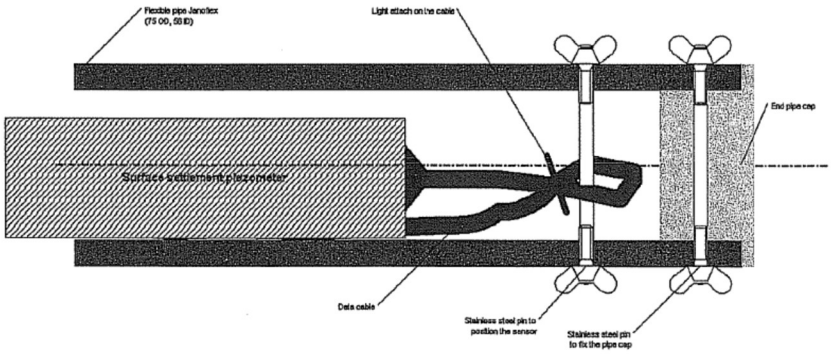

Figure I-11. End of pipe and sensor under the dyke

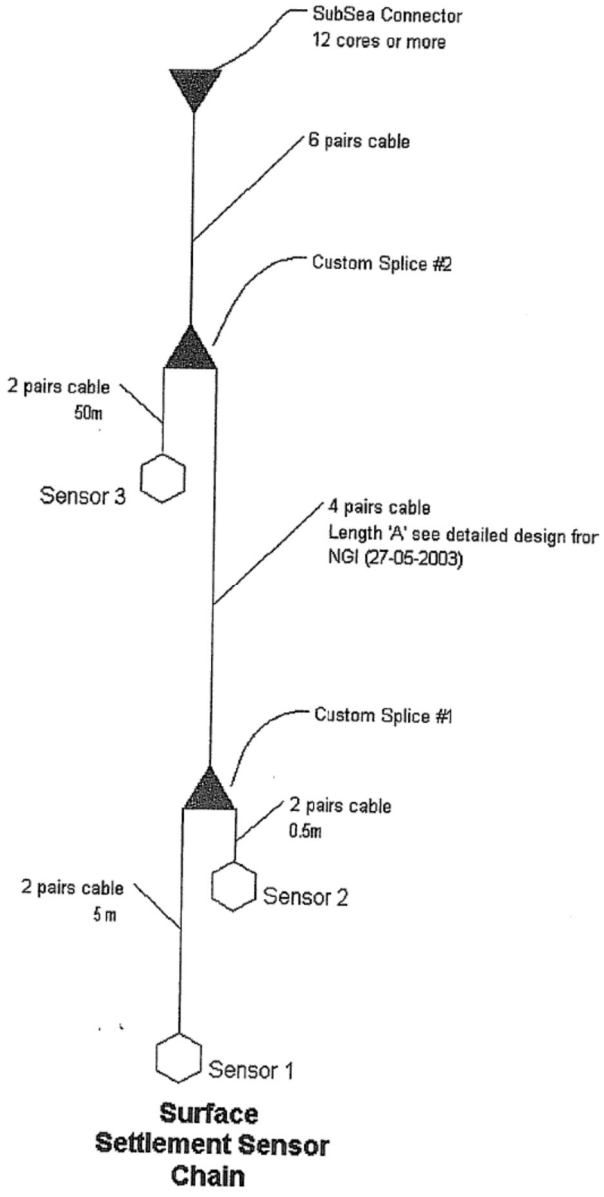

Figure I-12. Surface settlement sensor chain

"At depth" settlement gauges

The "At depth" settlement measurement chain has 5 sensors at depths of 5, 10, 15, 25 and 35m. This chain is based on the same conceptual design as the surface settlement gauges, that is: water pressure sensors were assembled inside a flexible polyethylene pipe, to avoid measuring the excess pore pressure developed during the construction of the embankment. When settlement occurs the sensors only measure differences in water levels. Also, the measurements were corrected with a reference sensor. Figure 6-40 show the basic principle for depth settlement measurement.

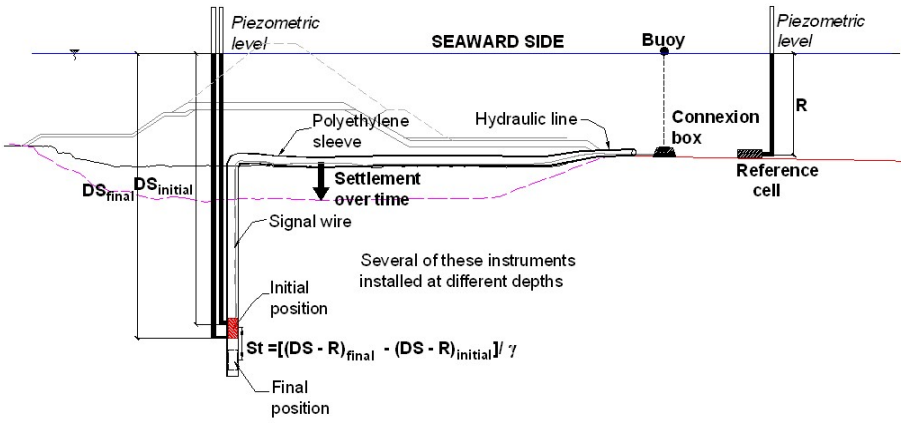

Figure I-13. "At depth" settlement gauge, basic principle.

The settlement cells were a Geokon model 4500S piezometer (range 0.70MPa). Each cell was delivered with sufficient cable attached to reach after installation the surface of the sea above the buoy location, to facilitate subsequent cable connections.

All piezometers were prepared and verified for zero reading and saturation, as explained before for the pore pressure piezometers.

The cables for the five single cells were spliced together and joined to a common multi-conductor connector by the instrument manufacturer, at the pre-determined depths. The cables were marked such that each installation was identifiable.

The instruments were assembled inside of plastic sleeves. These sleeves are essentially polyethylene cable ducting: Type Janoflex 63R. This product can compress by 16% under 25 kg, and by up to 30% for large applied forces. It can also bend easily, hence accommodating more settlements.

The sensor was placed upside-down so that a loop was created below each sensor.

The settlement cells were supported inside of the sleeves at the required depths using a stainless steel cable and stainless steel pins pushed through the skin of the sleeves and the loop below the sensor.

The Janoflex tubing was only installed up to the surface of the seabed. Its buoyancy is too large for the horizontal section all the way to the buoy. At the level of the seabed, the Janoflex was connected to an agricultural drain with holes. The protection was extended all the way to the outside of the breakwater.

The strings were assembled onshore and delivered to the working platform for installation.

The following figures show some details of the installation of the instrument.

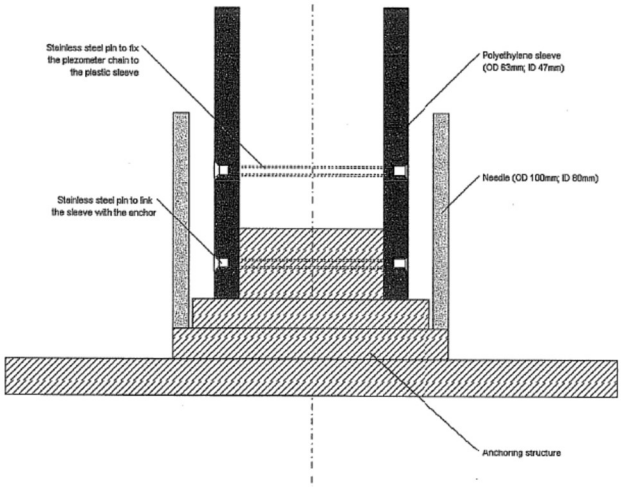

Figure I-14. Bottom of the "at depth settlement gauge" sleeve in the needle

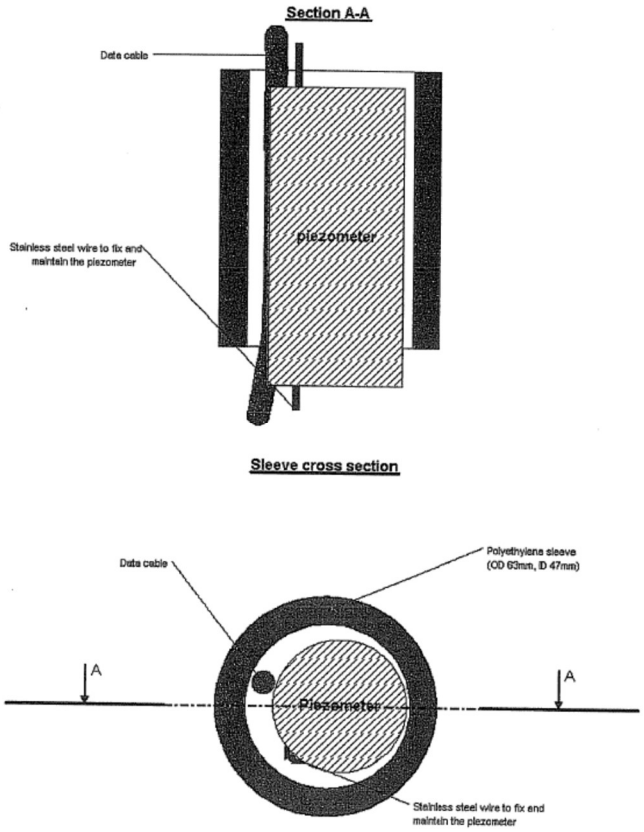

Figure I-15. Plastic sleeve and "At depth" settlement gauge cross-section

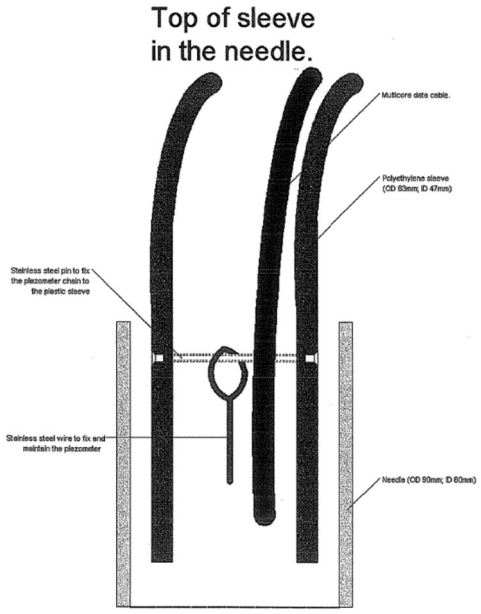

Figure I-16. Top of sleeve in the needle

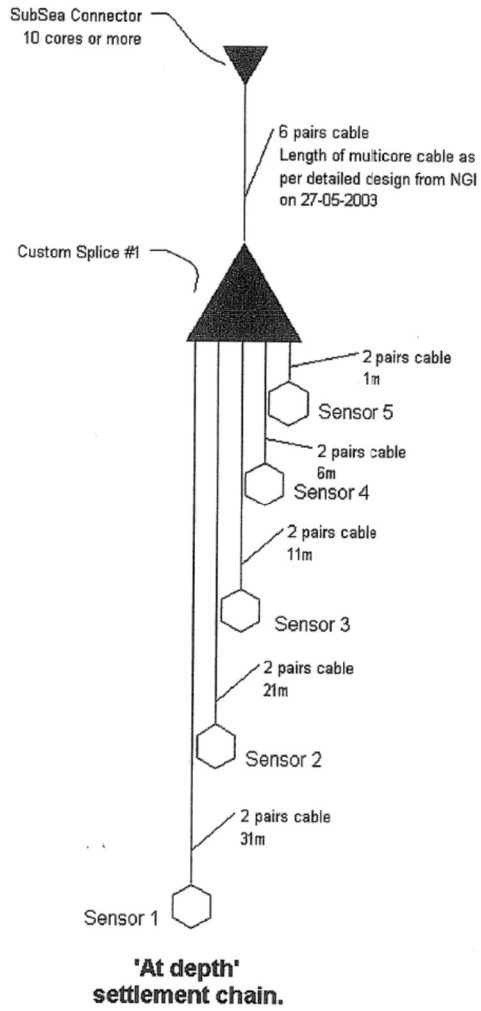

Figure I-17. ‘At depth’ settlement chain

Inclinometer for global stability monitoring

Two chains of in-place inclinometer were installed at lateral sides of each breakwater section. The chain consists of a string of 5 inclinometer probes (Sisgeo model S410P, +/-10 degree, uni-axial, magneto-resistivity vertical in-place inclinometer) assembled inside of ABS inclinometer casing. The inclinometer sensor was attached to a stainless steel cable at each required depth inside the casing. The tilt of individual inclination sensors is recorded; giving a vertical profile of inclinations that allows lateral movements to be calculated by integration. A sketch of the in-place inclinometer system is shown in Figure I-18.

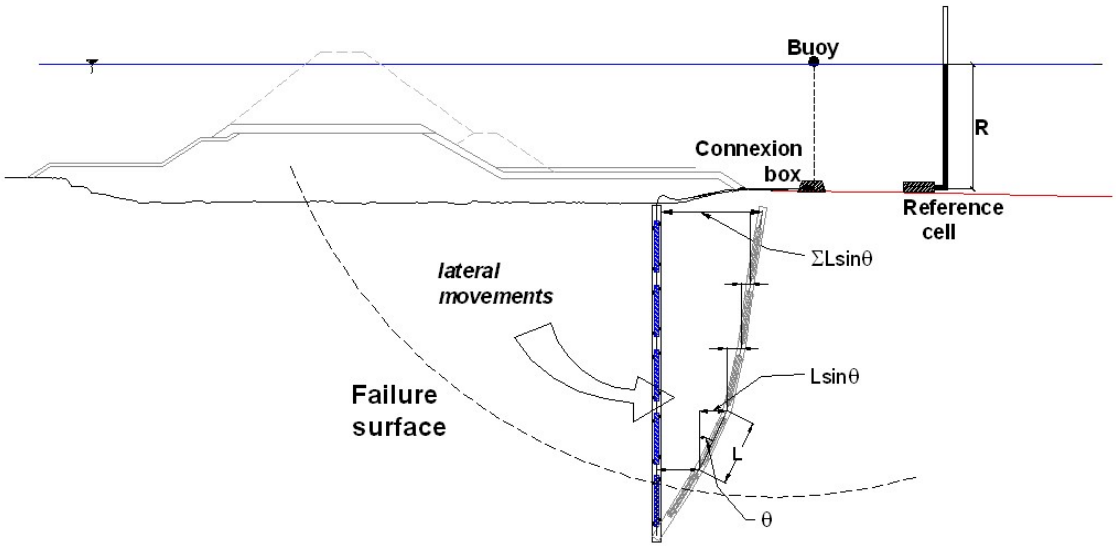

Figure I-18. In-place inclinometers, basic principle

Each inclinometer was delivered with sufficient cable attached to reach after installation the surface of the sea above the buoy location, to facilitate subsequent cable connections. Each of the 5 sensors had its own cable up to 0.5 meters above the highest one, where all of them were spliced together in a muti-pair cable. The length of the multi-pair cable was defined according to the inclinometer chain position, with 20% spare length.

The cables for the five inclinometers were spliced together and joined to a common multi-conductor connector by the instrument manufacturer. Hence the depths of installation were pre-determined (2m, 4m, 7m, 12 m and 20 m below seabed). The cables were marked such that each installation was identifiable.

The instruments were assembled inside of ABS inclinometer casing with flush couplings. The inclinometer sensors were attached along a stainless steel cable at each required depth. The string composed of the cable and the sensors were fixed both at the top and at the bottom of the inclinometer tube. In addition, each inclinometer was fixed at its level with a pin through the casing. The strings were assembled onshore and delivered to the working platform for installation. The top of the inclinometer

casing was such that it ends just above the highest sensor. A janoflex flexible plastic tube (diameter 56/63) was riveted onto the casing and provided a flexible vertical extension toward the surface. Note that this was rendered necessary by the fact that the inclinometers are installed underneath the breakwater, and therefore suffer vertical settlement.

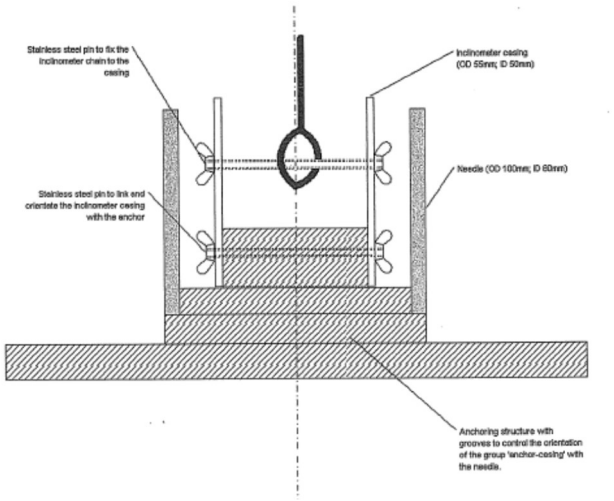

Figure I-19. Bottom of inclinometer casing in the needle

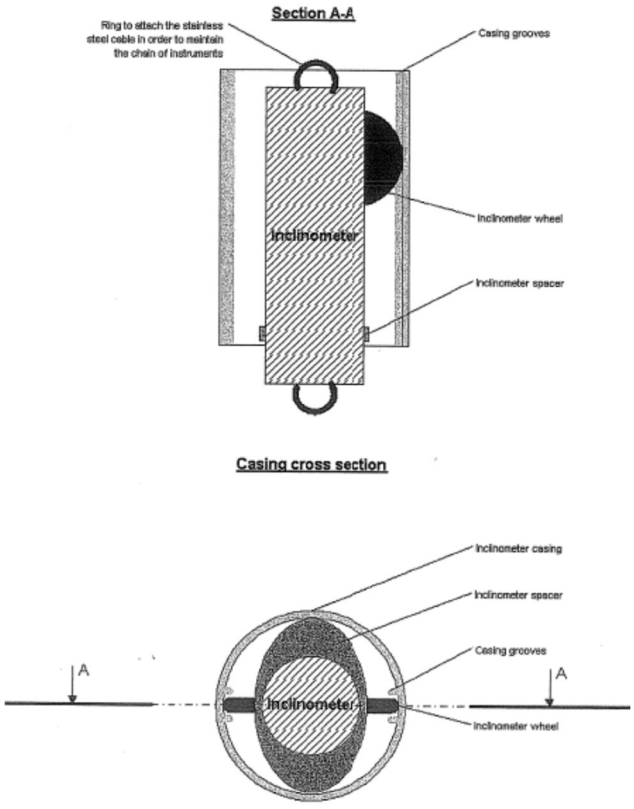

Figure I-20. Casing and Inclinometer cross-section

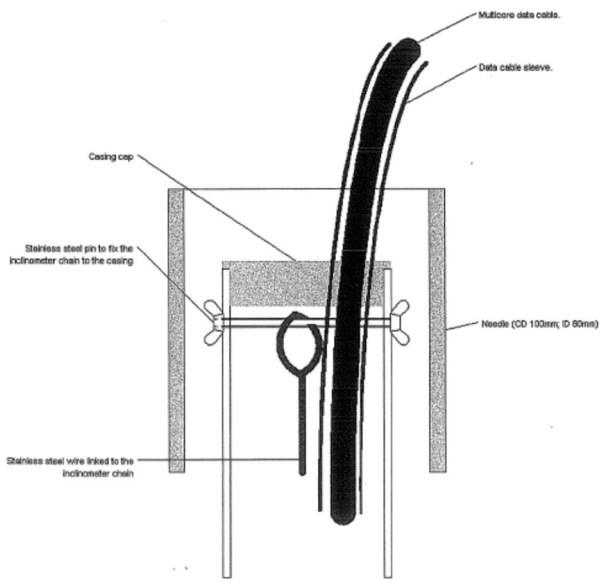

Figure I-21. Top of inclinometer casing in the needle

Cabling

The data cable of each chain of instruments was laid on the seabed from the instrument location to the buoy location with sufficient protection and additional spare length (about 20%).

Each instrument was connected to a single twisted & shielded data cable pair. All the single cables were protected by an external layer made of polyurethane. All the single cables from the same chain of the instruments were spliced (by the instrument supplier) to a unique multipair data cable a few meters from the last sensor of the chain (see Figure I-14).

Each chain of instruments was connected by a multipair twisted & shielded data cable laid on the seabed up to the buoy location. All the multipair cables were protected by an external layer made of polyurethane.

All the multipair data cables were gathered to the buoy location where they were connected to a junction box. This junction box was linked to 36 pairs armored data cable going from the seabed up to the buoy itself.

All the cable connections (cable-junction box) were done by using sub-sea connectors (SubConn, Micro series). Sub-sea connectors located at the extremity of the cable of instruments chain were assembled in situ by the supplier technician and tested electrically to certify the quality of the connections. The junction box (36p armoured cable and sub-sea connectors) was fully manufactured in the supplier factory and was tested for electrical signalling and waterproofing.

The junction box was done by splitting the 36 pair armoured cable into 6 standard cables (sample of the data cables used for the instrument chains) ending by subsea connectors. Each pair of cable was

connected to a corresponding pair of cable. All the data cable connections were sealed in a moulded block (‘pigtail’ shape).

Each of the 36 pairs was protected by an external layer made of polyethylene. The 36 pairs were shielded all together. The armoured cable was protected by 2 layers of polyurethane separated by mechanical armour made of ‘kevlar’

The armoured cable was fixed to the buoy and each of the 36 pairs was connected to a data connection panel located in a waterproof compartment of the buoy structure located 2 meters above sea level.

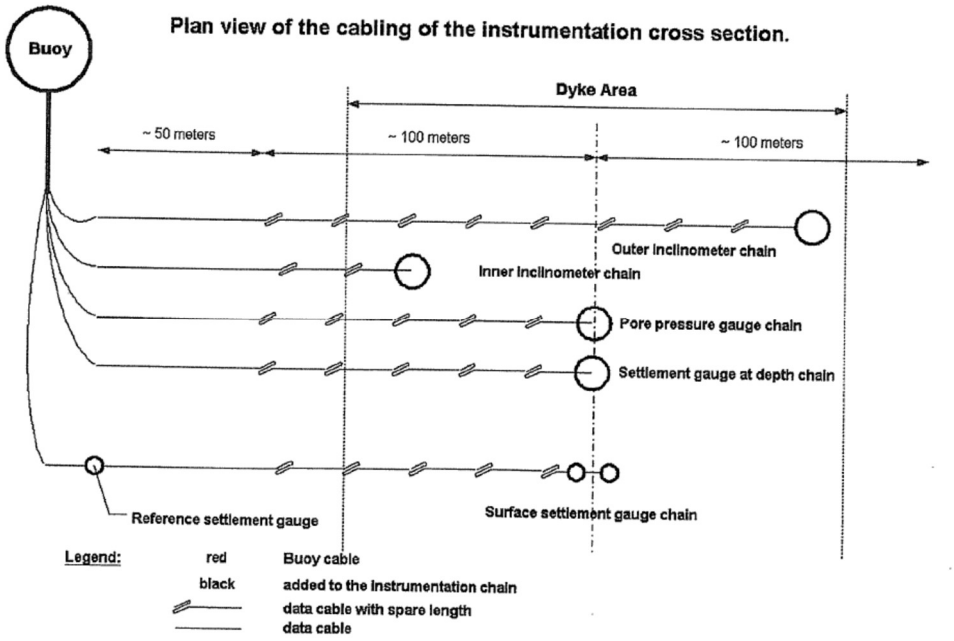

Figure I-22. Plan view of the cabling of the instrumentation cross-section

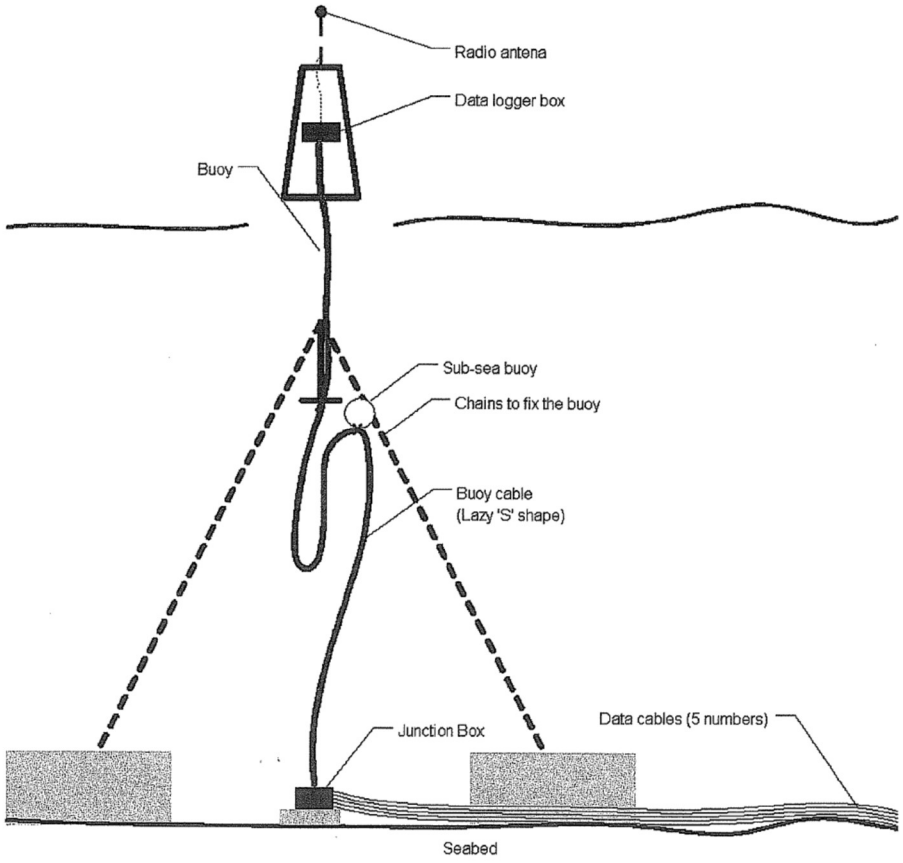

Figure I-23. Cabling from the seabed to the buoy

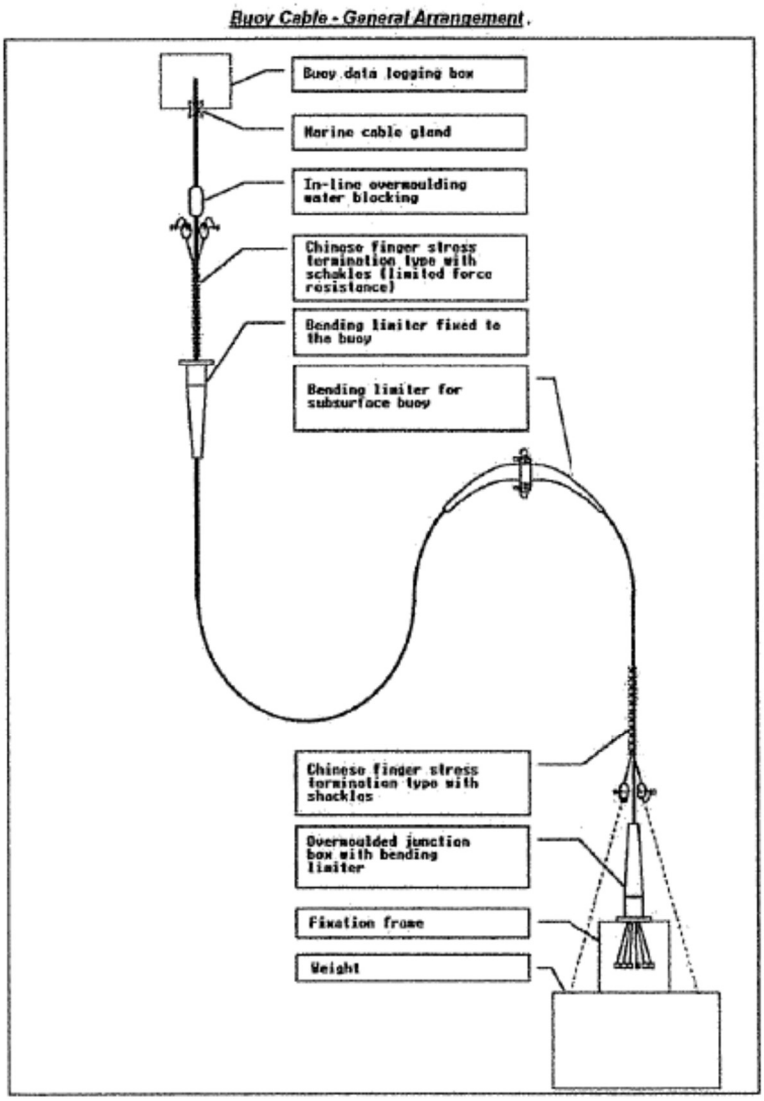

Figure I-24. Buoy cable, general arrangement

Cables protection

Each multipair data cable (one for each chain of instruments) was laid on the seabed from the instrument location to the buoy location. It was protected by a flexible plastic structure.

The flexible plastic structures were gathered by the divers and placed under the steel structure (U-shape sheet piles) to protect them from the materials used to build the breakwaters. The sheet-piles were placed by pieces of 3 meters long overlapping to prevent cables and plastic tube shearing.

The sheet-piles were placed by the divers and pinned together to join them in a continuous protective structure.

Where U shape steel protection could not be installed (instrument locations, the area where plastic tube are gathered in one line), the data cable in plastic tubes were covered by sandbags or gravel bags 0.5 meters thick.

The steel protection was limited to the area covered by materials used for the construction of the breakwater (dyke edge point more than 10 to 15 meters).

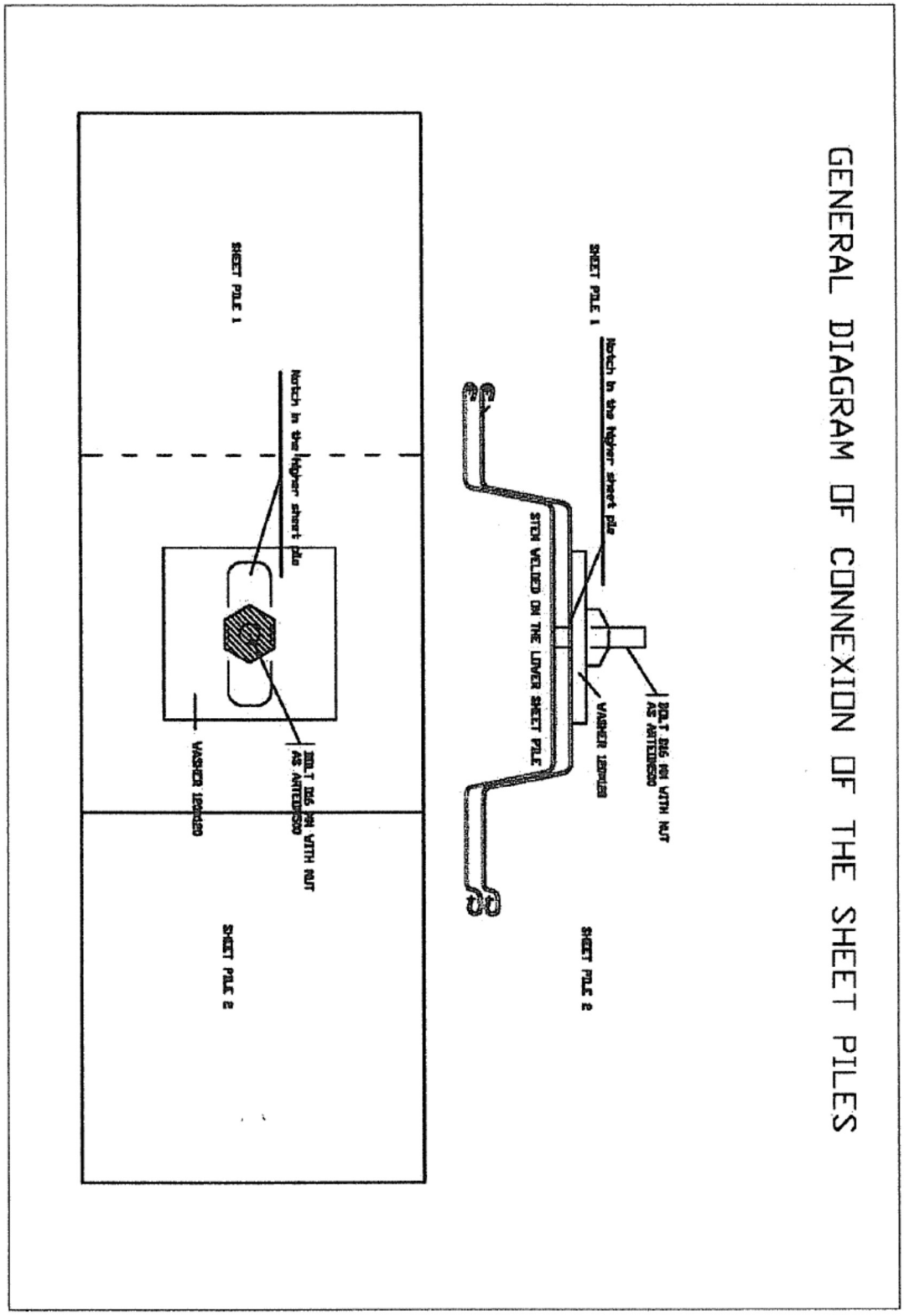

Figure I-25. Buoy cable, general arrangement

Data logger

The instruments in each monitoring profile were connected to a data logger installed on a waterproof box located on a buoy outside of the dike. The buoy also carried all of the equipment necessary to facilitate the autonomous operation of the data logger i.e. battery, voltage regulator, solar panels for recharging the battery, etc. The power system was located in a second compartment.

The data logger was a Campbell Scientific CR10X with multiplexers and the instrumentation interfaces required to take readings from the instruments connected to it. These were installed in a waterproof box (IP68) connected to the instrument cables through a waterproof marine gland.

The data logger was programmed to take readings from the instruments (including the battery level) at the required intervals and store the data internally and in the modus register for capture by the central data acquisition PC running GeoScope SMACS software.

Figure I-26. Data logger Scientific CR10X

Radio Network

A radio modem was installed on the buoy inside of the waterproof box housing the data logging equipment. The antenna was mounted on the top of the buoy to facilitate communication with a radio modem base station onshore. The cable between the radio modem and the antenna was laid inside the buoy structure through a marine waterproof gland.

The radio modem 'base station' antenna was mounted on the roof of the 'Faro del Llobregat' with a line of sight to the data logging buoys. The frequency of transmission was within 868 and 870 MHz with a maximum power of 100mW.

The central GeoScope SMACS monitoring PC, located in the office of the Port Authoriry, was connected to the radio modem 'base station'. The SMACS software integrated the data loggers via the radio modems at regular intervals in order to download and display the latest reading. All data stored in the server was also available via internet connection with the GeoScope Web software installed at the UPC.

Instrument installation

Soil conditions are too weak to use jack-up platforms, so an anchored barge was adopted.

Traditional methods for installing buried instruments require drilling boreholes and grouting operations but this process is time consuming. Weather conditions could make these operations very difficult. An innovative method of installing the sensors was suggested: to push a casing containing the chain of instruments into the ground until the required depth is reached.

Precise marine operations were planned to execute the tasks of installing sensor chains in the right location. The barge was positioned by four mooring anchors and was operated along the profile of instrumentation by electric winches. The precision of this operation was controlled by the GPS located at the head of the crane.

Once the barge was at the right position, the chain of instruments was introduced into the driving mandrel, in a horizontal position. The instrument cables are wound onto a drum attached to the masthead of the mandrel rig. The steel suspension cable is also wound onto a drum.

After affixing the shoe at the foot of the sleeves the mandrel rig was lowered onto the seabed using the crane, mounted on the working platform, whilst its position is controlled with a GPS unit mounted on the masthead (see Figure I-27). The verticality of the mast was controlled by means of an inclinometer. Divers were used to verify that the rig was safely placed on the seabed.

When the mast is in position some check readings of the instruments were made using a portable readout connected to the multi-conductor connector. The mandrel was driven into the seabed by the rig, which has various sensors to monitor inclination, applied load, depth, etc during the procedure.

A casing containing the sensors was driven to the required depth by static thrust using the weight of the mast as a reaction force. Once the mandrel has reached the required depth it was withdrawn leaving the instruments in the ground. During this process, the instrument cable was fed through the mandrel, and the stainless steel suspension cable was kept in tension so that the string of sensors remains in place.

The suspension steel wire is tensioned all along the process up to the complete retraction of the mandrel. Once the mandrel is above ground level, the suspension cable is disconnected.

Once the mandrel has been recovered the cable connector (protected by a cap) is passed through the annulus of the mandrel as the mandrel rig is lifted back onto the installation platform. The divers dealt with the cable to free the installation platform to move onto the next location.

Protection against dumping of core materials was provided by sheet piles placed over the connecting cables and surfaces instruments. A divers' team carried out this work placing sheet piles on top of the sleeves of cables. Special joints were designed to prevent accidental cutting of cables. To complete these protective activities, 1 meter of fine gravel was dumped covering the instrumentation area.

Figure I-27. Lifting the mast to driving position.

Data Management

Sensors corresponding to each monitored cross-section have been connected to a data logger installed on a waterproof box located in a buoy away from the breakwater (Figure I-28). This buoy also holds all the equipment necessary to allow the autonomous operation of the data logger i.e battery, voltage regulator, solar panels for recharging the battery, etc. The power system is located in a compartment inside the buoy. The data acquisition was done every hour and the data transfer to the display computer was done 5 times a day. The internal memory of the Cambell logger allows about 30 days of raw data storage.

The data logger was in communication by radio modem with the PC running the monitoring software, to display the latest instrument data. A suitable representation of the instrumented area was used as a background for the instrumentation data display.

The software GeoScope was used for data collection, storage and processing. The program has a built-in examination facility (Geoscope shell), which allows data to be displayed and exported into an MS Excel worksheet format. The GeoScope Manager keeps a daily summary of the measurements including the first value, the latest value, the mean, the average, the smallest value, and the largest value and for each of those values, the time when the measurement was taken.

The GeoScope SMACS PC computer was situated in a weatherproof air-conditioned office with reliable mains electricity supply and UPS system. A dedicated telephone and internet connection was available to ensure e-mail notification of alarm messages.

Figure I-28. Buoy place in position with two solar panels.

Difficulties and problems

In spite of the fact that special routes to navigate near the working areas were defined and a special agreement with local fishermen was reached, part of the instrument system was damaged by maritime traffic either by vessels entering/leaving the port or by the associated to sport fishing activities. Buoys and data cables were affected continuously (see Figure I-29 and Figure I-30). Even though precautions were taken, it has not been possible to avoid frequent damage. Repairs costs have amounted to almost 30% the initial cost estimate. In addition, this problem caused an important delay in completing the instruments installation. A number of instruments were lost, but important information could eventually be obtained from the instrumentation.

Figure I-29. Buoy after damage, floating body has been broken.

Figure I-30. Data cable found cut.

Monitoring

Evolution in time of excess pore pressures measurements at several depths is presented in Figure I-31 to Figure I-34 for each cross-section instrumented. Dumping activities of the core material are also shown in the same figures.

Figure I-35 shows the surface settlement measured at the contact embankment/seabed and settlements at various depths with time of Section 1, also the history of load (fill thickness) is included. Unfortunately, measurements in this section were only possible until August 2005, because the system was damaged on that date. A similar figure was done for Section 2, under the zone of vertical breakwaters (see Figure I-36). The settlements measured for sections 3 and 4 showed an anomalous response (see Figure I-37 and Figure I-38) and therefore were not considered in the analyses.

Inclinometers data produces horizontal displacements profiles for Section 1 at the seaward side (Figure I-39) and for Section 2 at the port side (Figure I-40).

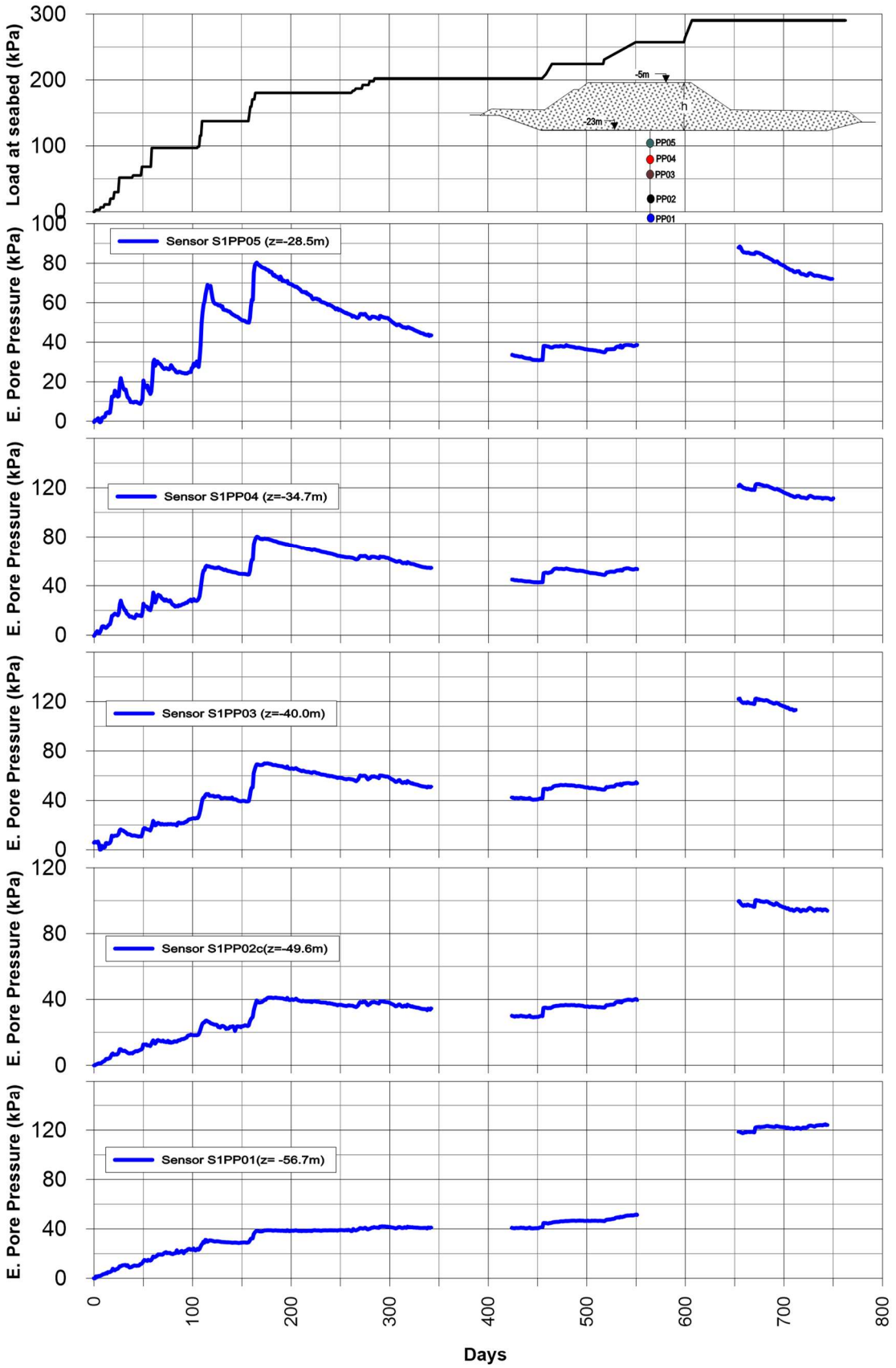

Figure I-31. Excess pore pressure recorded in section 1

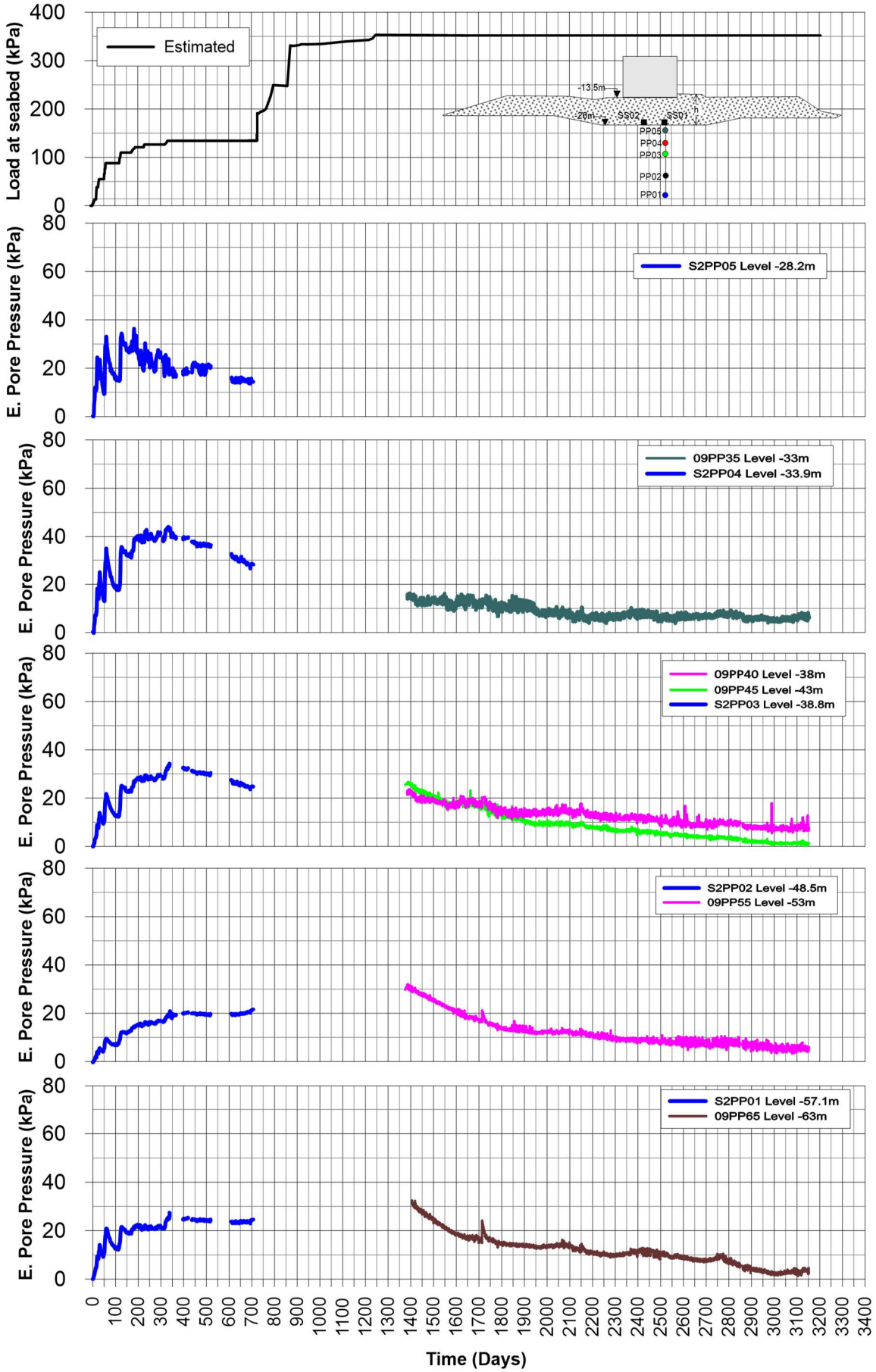

Figure I-32. Excess pore pressure recorded in section 2

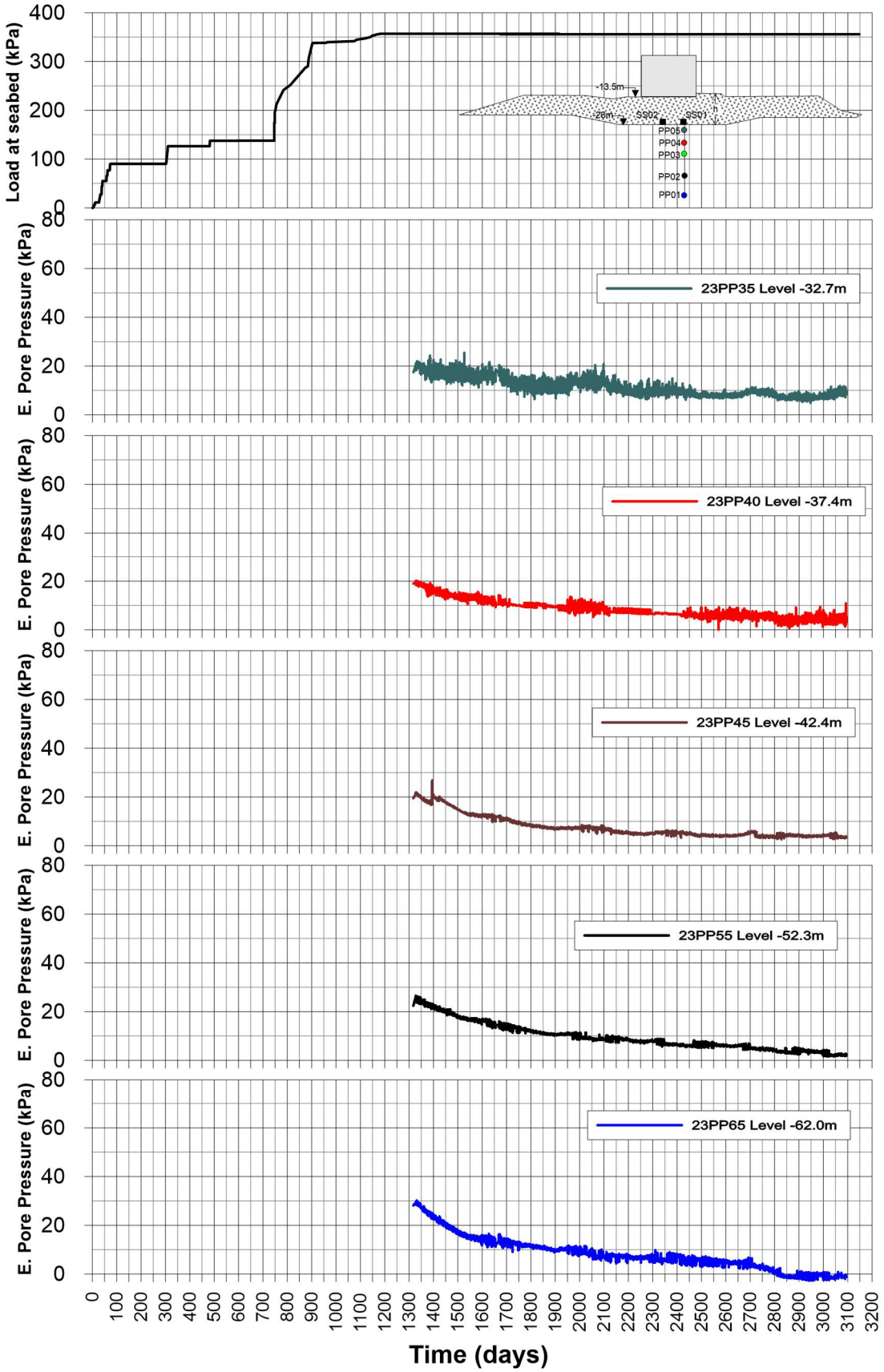

Figure I-33. Excess pore pressure recorded in section 3

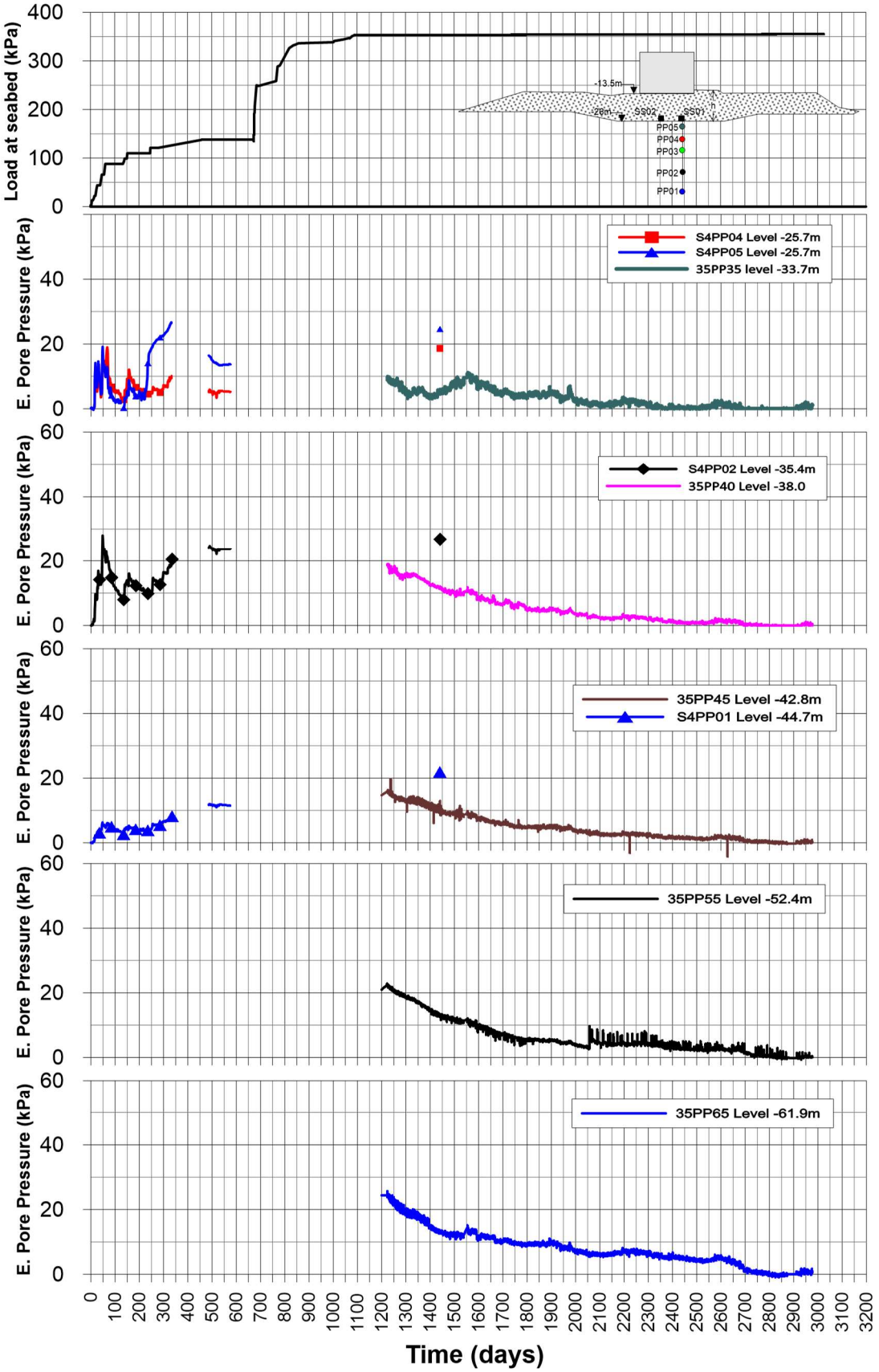

Figure I-34. Excess pore pressure recorded in section 4

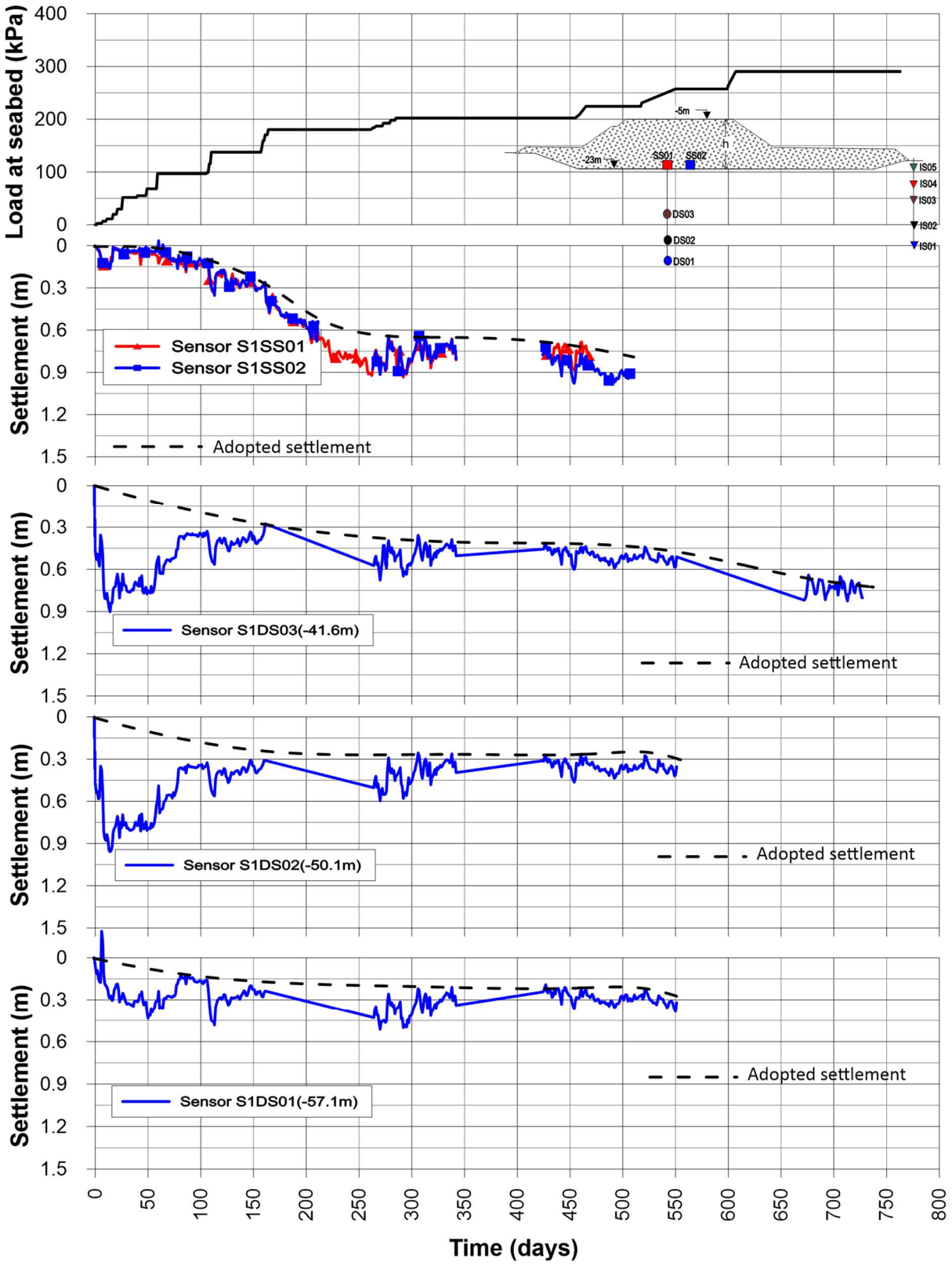

Figure I-35. Developed of settlements at various depths with time at section 1 of instrumentation.

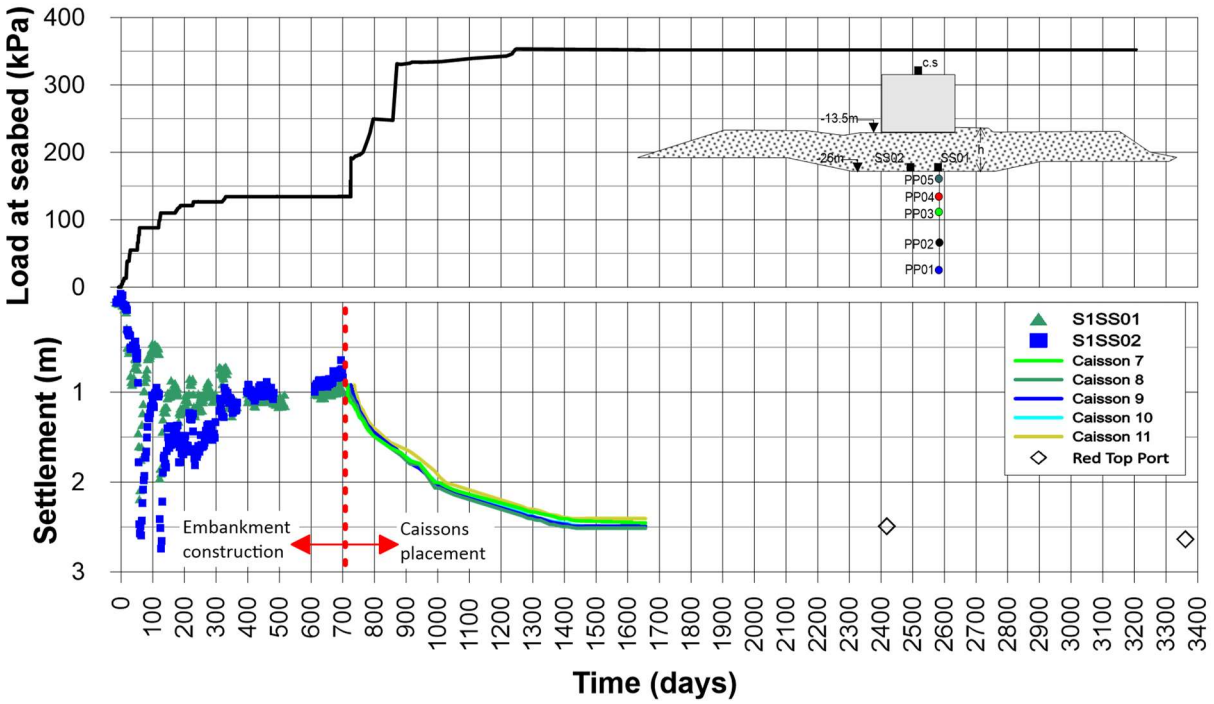

Figure I-36. South breakwater, history of dumping, and settlement at section of instrumentation 2.

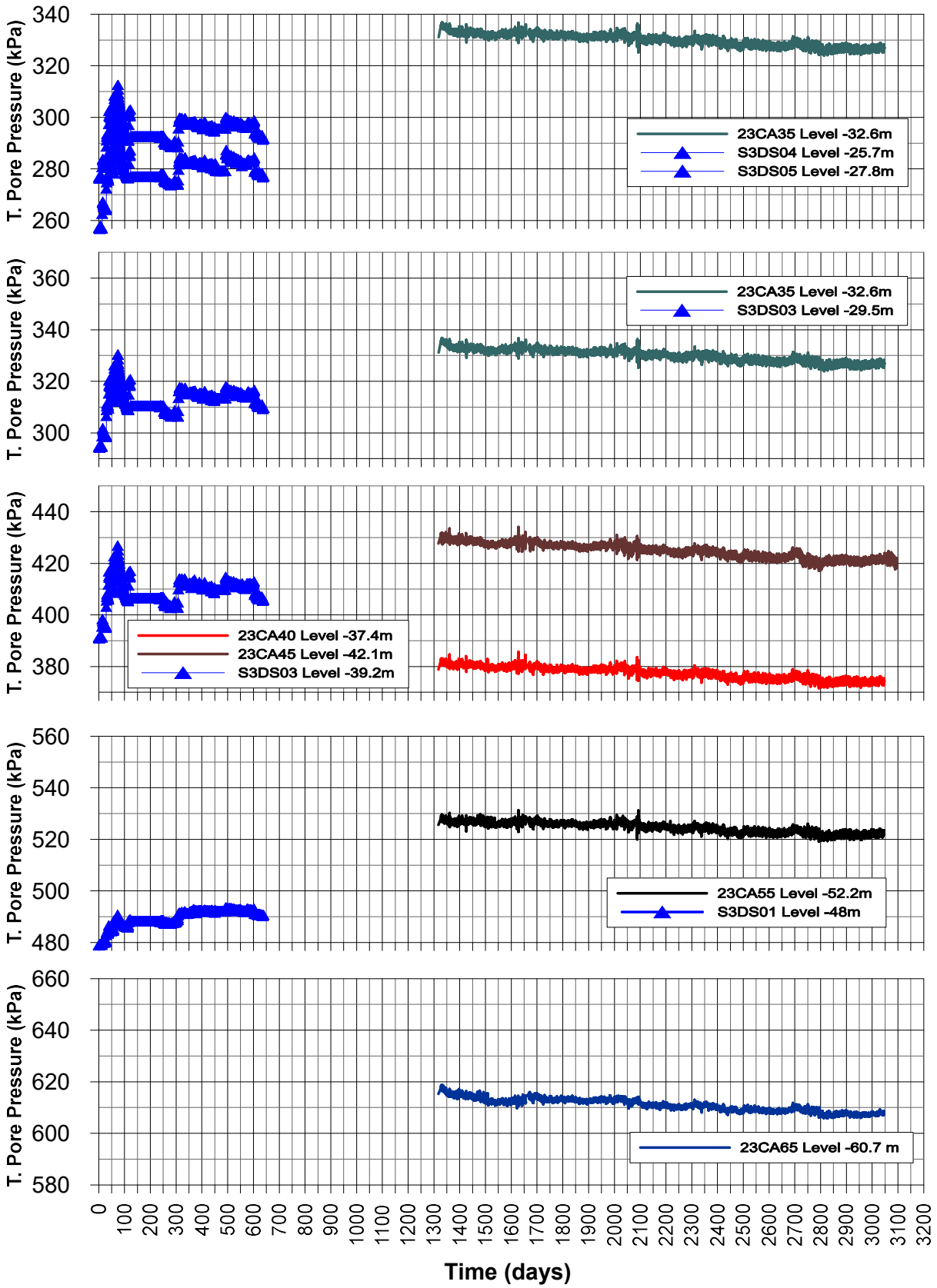

Figure I-37. Developed of settlements at various depths with time at section 3 of instrumentation.

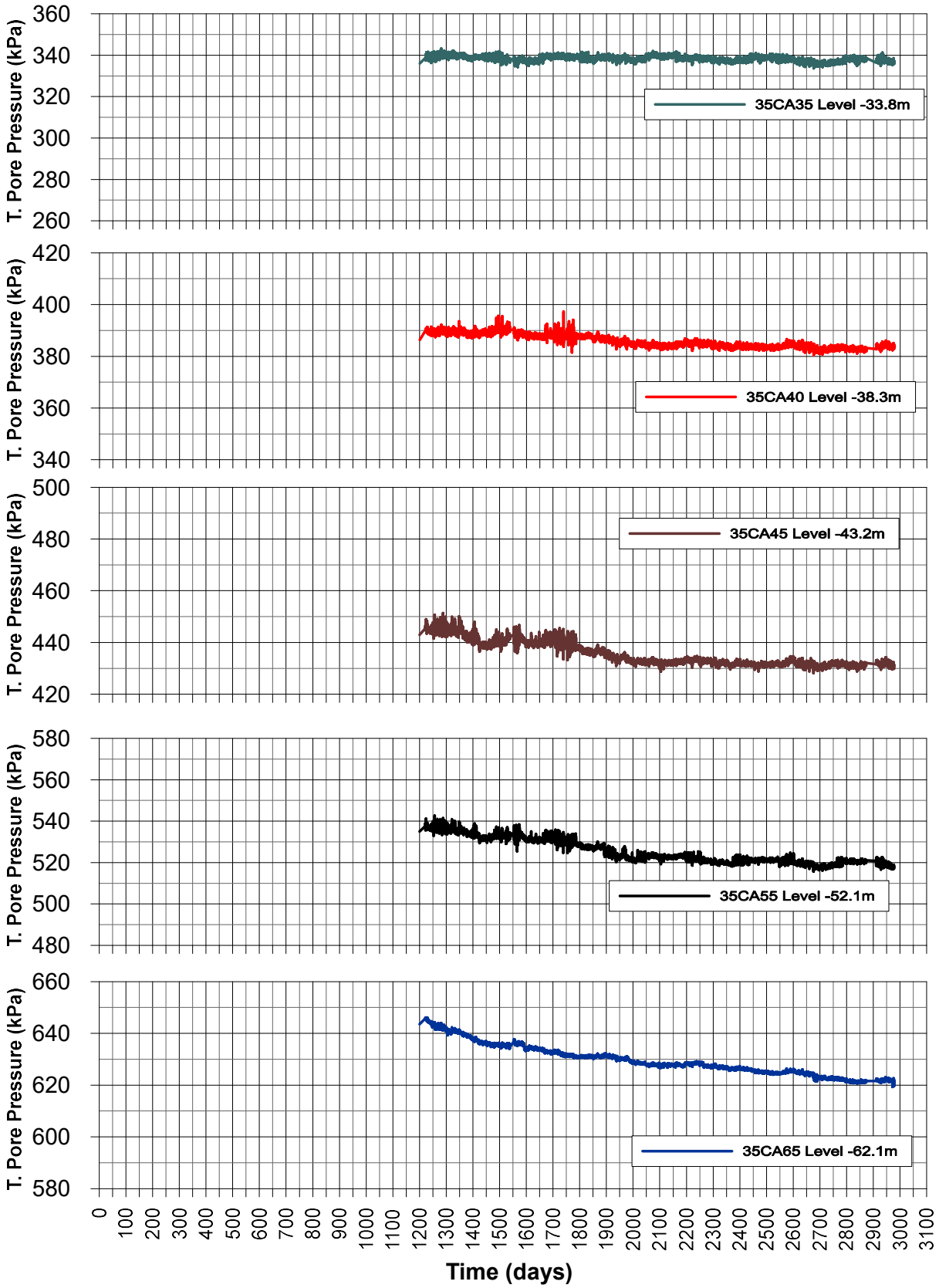

Figure I-38. Developed of settlements at various depths with time at section 4 of instrumentation.

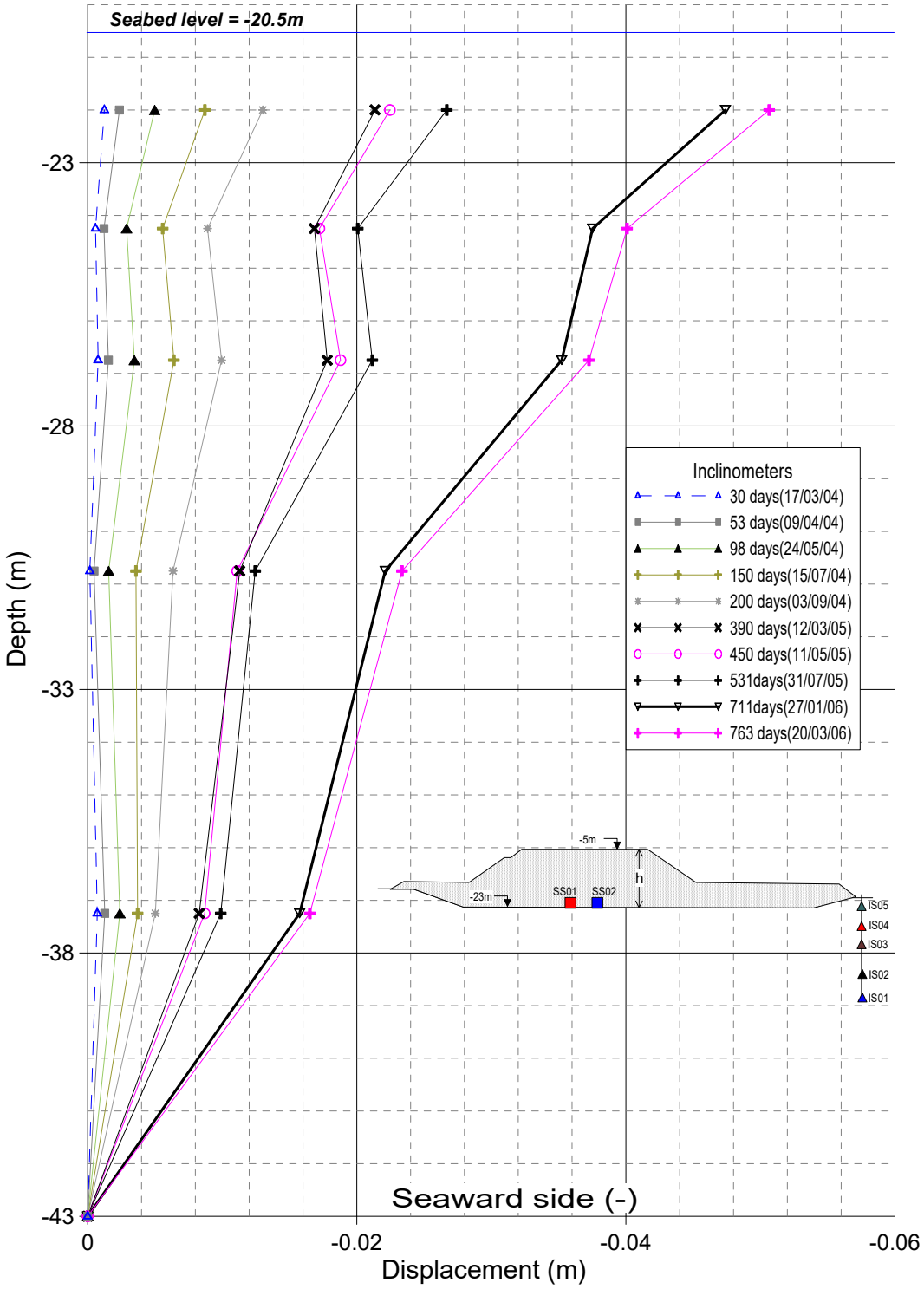

Figure I-39. Profile of horizontal displacement at inclinometer installed in section 1, seaward side.

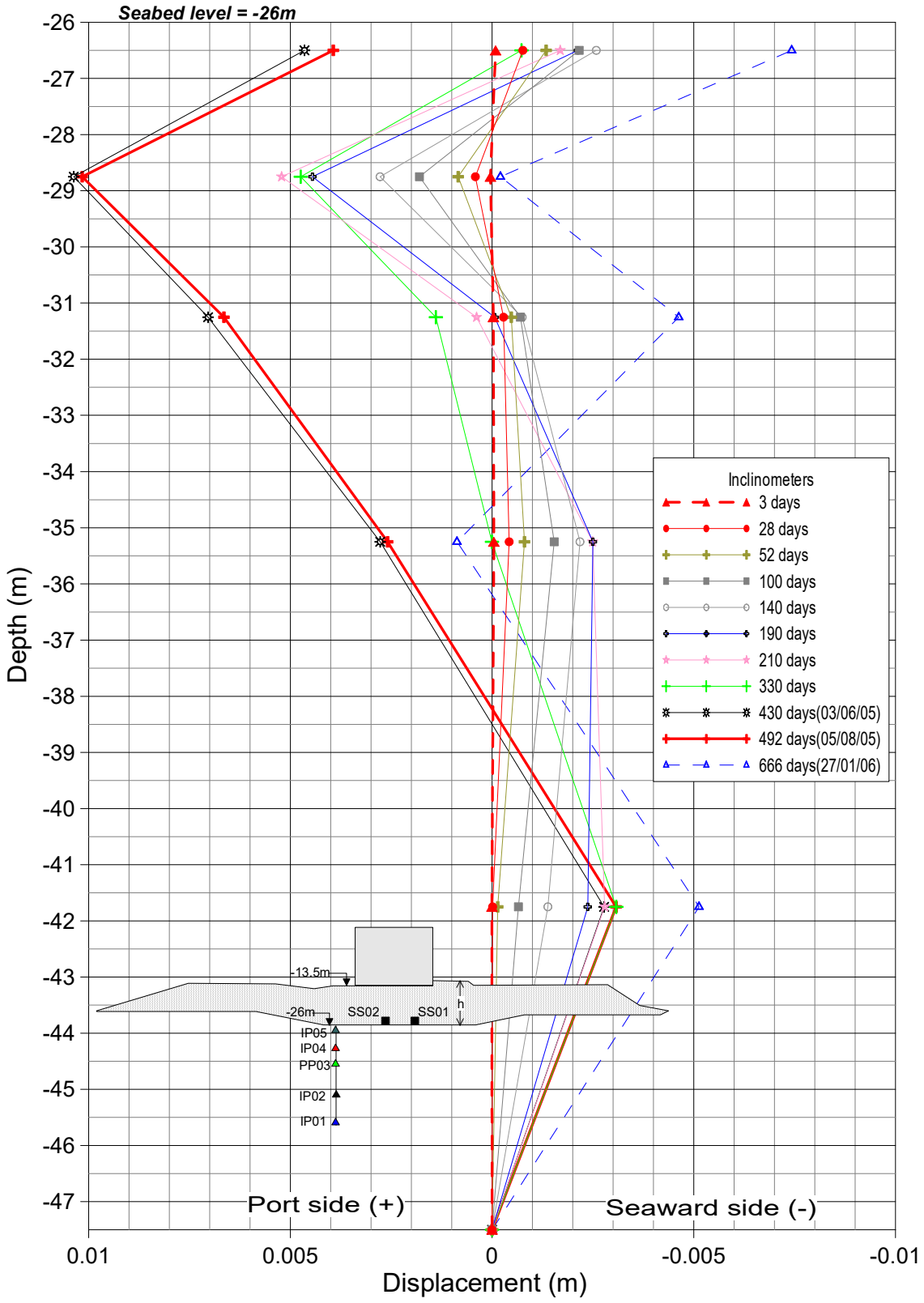

Figure I-40. Profile of horizontal displacement at inclinometer installed in section 2, Port side.

APPENDIX II

HYDRAULIC INSTRUMENTATION. WATER PRESSURE MEASUREMENT ON CAISSON

II.1 INTRODUCTION

Due to the experience of 2001, with the collapse of 4 caissons in the new port entrance and later the failure of 14 caissons at the Prat quay in 2007, it was decided to implement one of the caissons of the south breakwater in order to have information on the force of the waves and verify the designs of the breakwater. Caisson 9 was selected, coinciding with geotechnical instrumentation section 2.

The instrumentation installation work was assigned to the company ALAVA INGENIEROS. This appendix is based primarily on the installation reports made by the contractor.

II.2 DESCRIPTION OF THE INSTRUMENTATION

Water pressure sensors

Due to the typical conditions of the marine environment, with high chemical and biological aggressiveness, a type of sensor with proven resistance under those conditions was required. The transducers used were from the DRUCK firm, model PTX 164-3303, with a titanium body and diaphragm, for measurements on the wall, the crown and the base of the caisson. These sensors had already been used in similar applications in the Ports of Las Palmas and Malaga with satisfactory results.

The sensors incorporate an integral cable resistant to the environment and of sufficient length for direct connection to the data acquisition system, so that interruptions, splices or connections that could introduce errors in the measurement are avoided.

The assembly of the 16 wall sensors was carried out in two alignments (8 in each alignment) using two 120mm diameter PVC pipes that the box has by construction. These vertical ducts are provided, for each measurement point, with 90 ° angled outlets at the heights specified for each sensor, ending in a Delrin housing with three 120 ° screws and blanking cap. The sensors have been placed in these outlets at different depths by means of the final Delrin housings, turned and internally threaded, with internal housing adapted to the sensor and with internal threaded part for its fixing and location of accessories for protection against biofouling and protection grid. against external aggressions. Likewise, this threaded interior serves as a housing for the tools, or future accessories for the periodic inspection and cleaning of the sensors. The cables have been routed through the conduits to the common interconnection boxes that communicate with the Data Acquisition and Communications System.

Likewise, (8) uplift pressure transducers have been installed at the base of the caissons (four per alignment), using (8) existing perforations channeled with high pressure polyethylene tubes of 120 mm internal diameter, which had been preventively sealed. Likewise, 8 Packer-type inflatable shutters have been mounted to fix the sensors to the duct so as to avoid any upstream or downstream of the water column that could disturb the measurement. They incorporate lifting rails made of polyethylene, approximately 18 m long. The sensors have been isolated inside a plastic casing, with all its accessories, similar to those of the wall but of sufficient length, and conical termination, to avoid or minimize the contact of the aggregates with the diaphragm surface. As a complement, this housing contains the relevant accessories for the protection of the sensors in this difficult environment. The housing is fixed to the Packer, through which the sensor cable passes, it is guided internally through the rod to the surface and following the existing pipes it was connected to the Data Acquisition System (DAS). The inflation hose has also been channeled through the inside of the rod, thus reaching the surface chamber.

It had been planned to install 10 uplift sensors, however, since the caisson was built with 8 holes for the sensors, it was decided to use the excess material, in the installation of 4 additional measurement points on the crown (2 in each alignment). Figure II-1 shows the set up of the instrumentation.

Data adquisition sytem

All the cables from the different sensors terminate (through the corresponding pipes) in two boxes specifically designed for this installation and its environmental conditions, with sealing and protection characteristics comparable to an IP65 level, which had already been sufficiently tested in the facilities of the Port of Malaga and the Port of Las Palmas. These boxes were placed inside the booths built inside the crown itself, one for each alignment of the sensors (wall, crown, and uplift pressure). A niche was built connected to each of the booths, in the upper part of the portside face of the crown, to house the data transmission antenna, protected by a transparent plastic cover to transmit the radio link. Both boxes are connected to each other by means of a synchronization and communications cable of approximately 15m.

The main role of these boxes is to house and protect the following equipment from the environment:

- Rippers for conversion of 12 VDC to 24VDC and to the different services for powering the Ethernet HUB and transmitting antenna.
- Electric interconnection rails, for configuration and feeding of the different subsystems.
- Pneumatic interconnection rails, for integration and moisture filtration from the reference conduits and future CNIS of the sensors.
- Atmospheric pressure sensor.
- Data transmission system, long distance / high security Wireless
- Desiccant silica gel filters for the pneumatic rail.

- DATA ACQUISITION SYSTEM, of the IMC firm, model CRONOS PL-3.

The general power supply of the systems, was carried out by means of two fuel cell systems (one per tower), each consisting of a 12V 50W methanol battery and two fuel tanks containing 50 litres each, and two back-up batteries for maneuvering and maintenance.

The data is transmitted from the base station connected to the DAS through the directional antenna and received at a similar station located in the Llobregat lighthouse, with direct vision between the antennas. In this location, the Ethernet and 220VAC cables were routed to communicate the receiving antenna to the supplied PC, which is connected to the APB's Local Network. The necessary software (IMC devices for system configuration, data display and saving data) has been installed on this PC. In this way, the data can be viewed by the Port Authority or Ports of the State with a dedicated application or with another application called "on-line Famos", specific to this system, which through calls to the corresponding IP address allows analysis and calculations in real time. The "off-line Famos" version was also available for the subsequent treatment of the acquired data and the generation of reports. However, for this thesis, the data was worked entirely in Matlab. The interconnection protocol was TCP/IP, with an air bandwidth of 11 Mbps.

II.3 DATA RECORDS OF STORM

Below are the records obtained in the 3 most important storms recorded during the time the instrumentation was active.

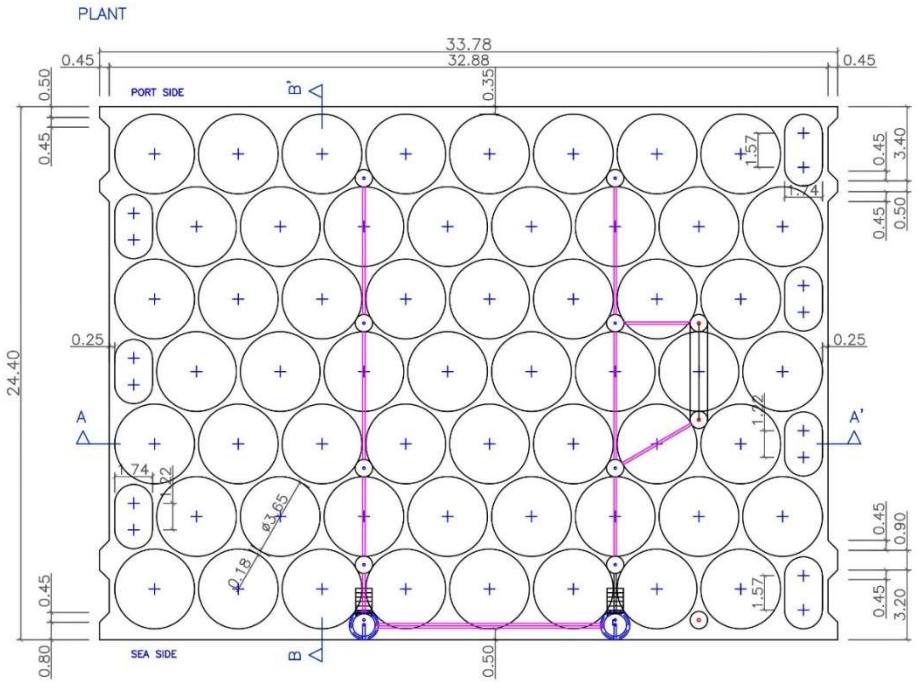

(a)

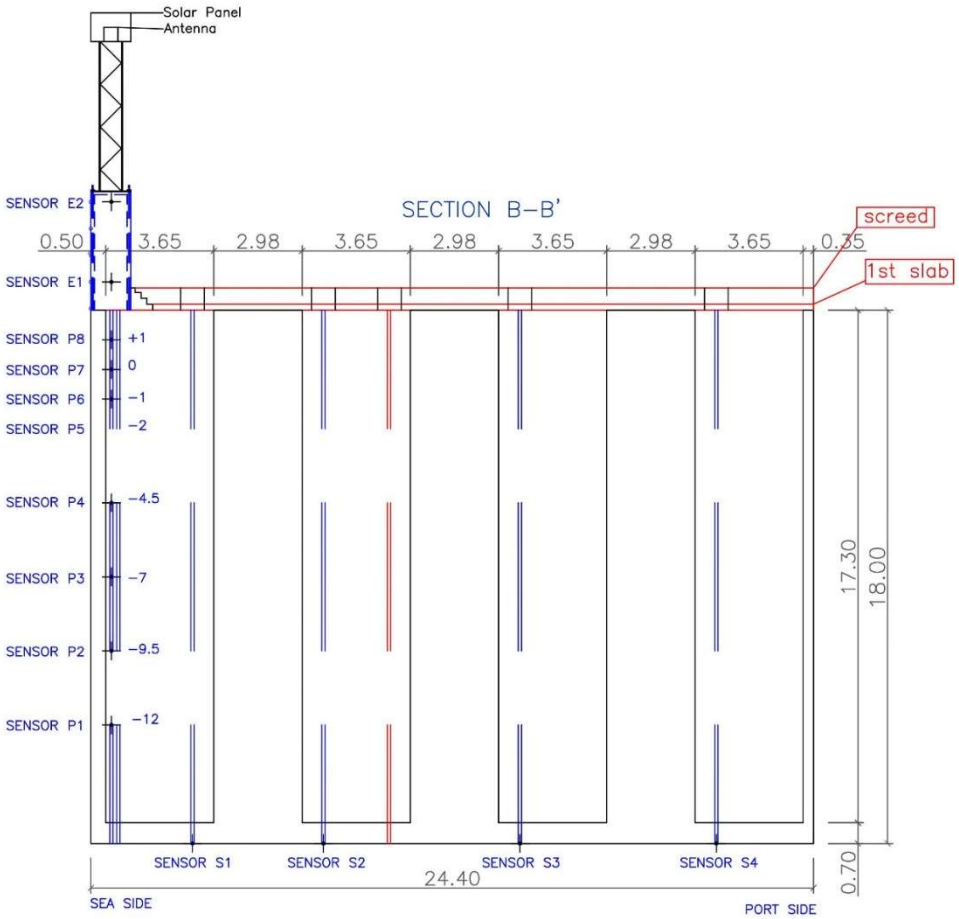

(b)

Figure II-1. Setup of the instrumentation (a) Plan view (b) Cross-section

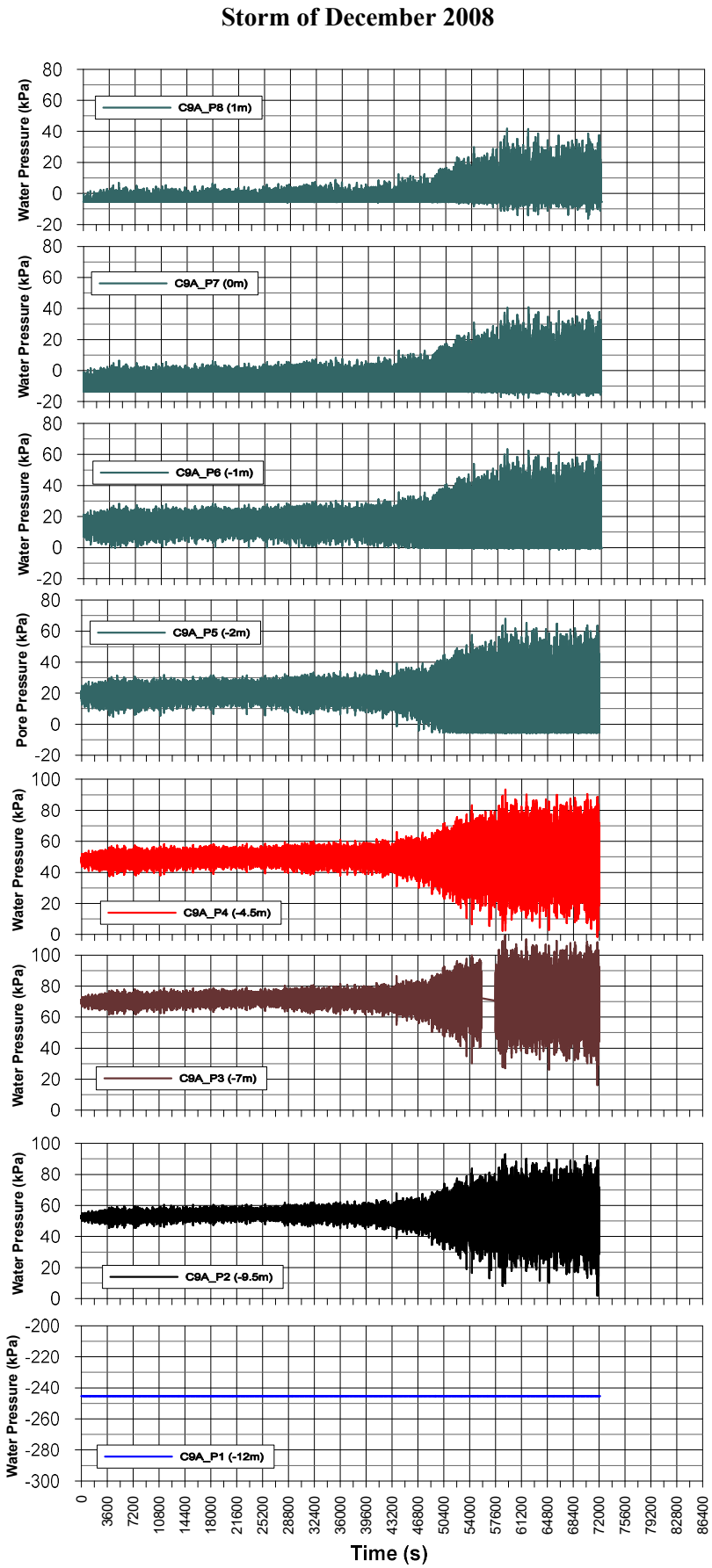

Figure II-2. Sea wave pressure on the caisson wall, alignment A, December 26, 2008

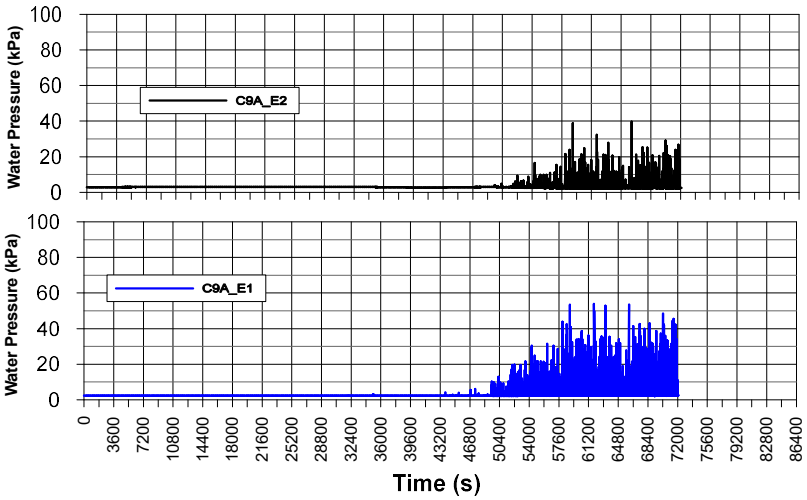

Figure II-3. Wave pressure on the crown, alignment A, December 26, 2008

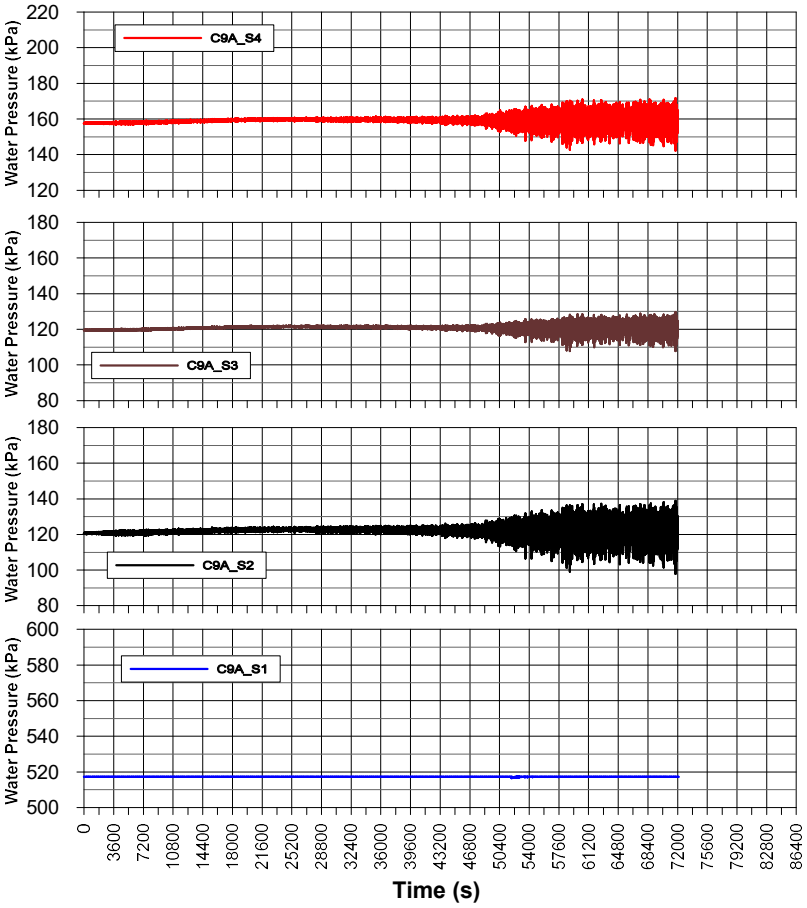

Figure II-4. Uplift pressure on the caisson base, alignment A, December 26, 2008

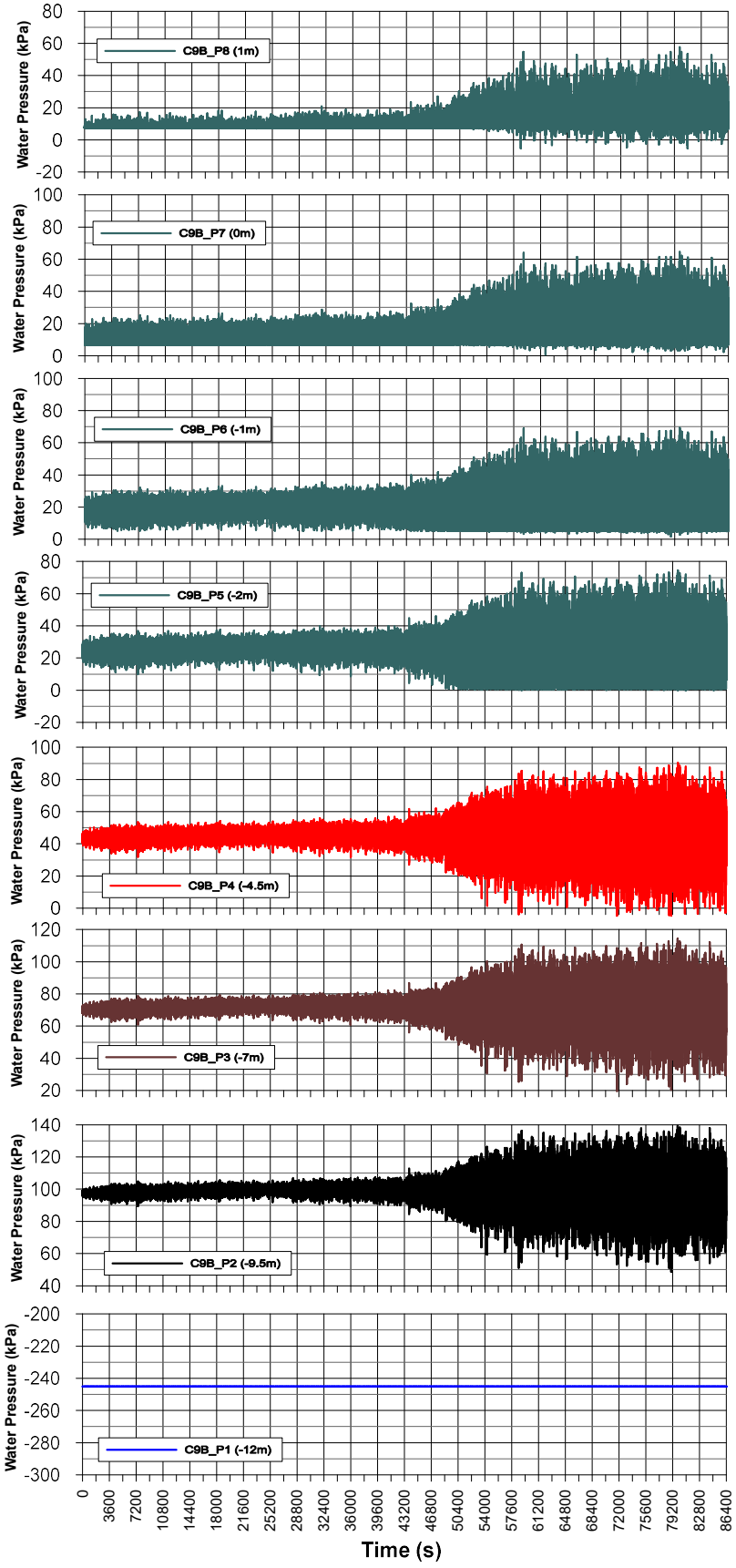

Figure II-5. Sea wave pressure on the caisson wall, alignment B, December 26, 2008

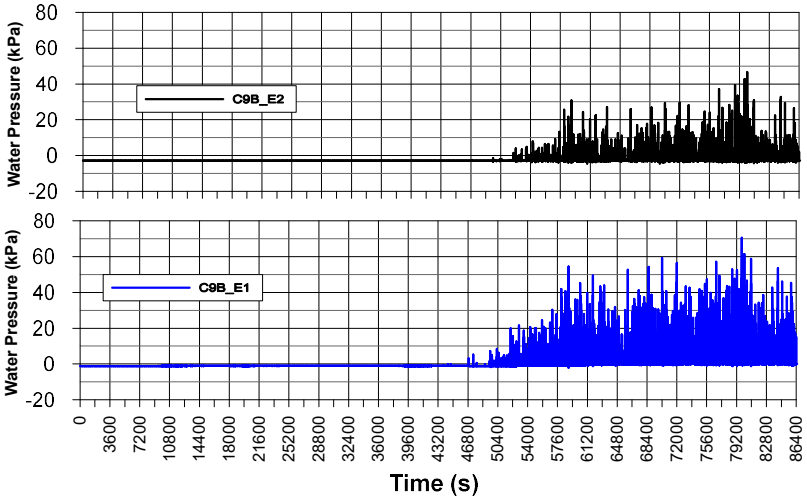

Figure II-6. Wave pressure on the crown, alignment B, December 26, 2008

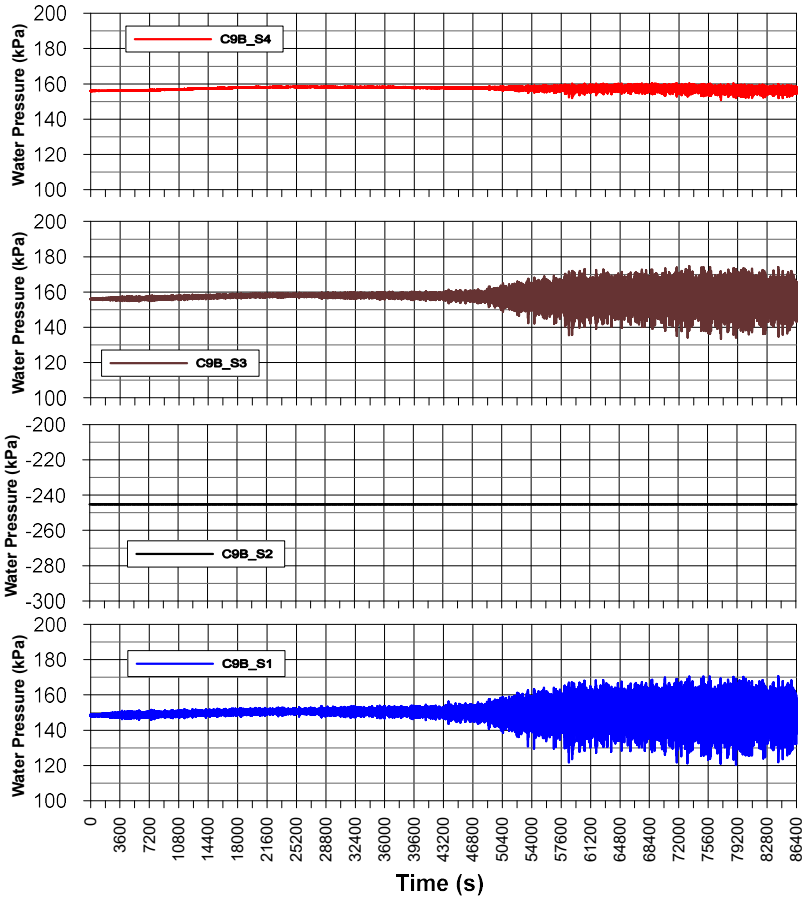

Figure II-7. Uplift pressure on the caisson base, alignment B, December 26, 2008

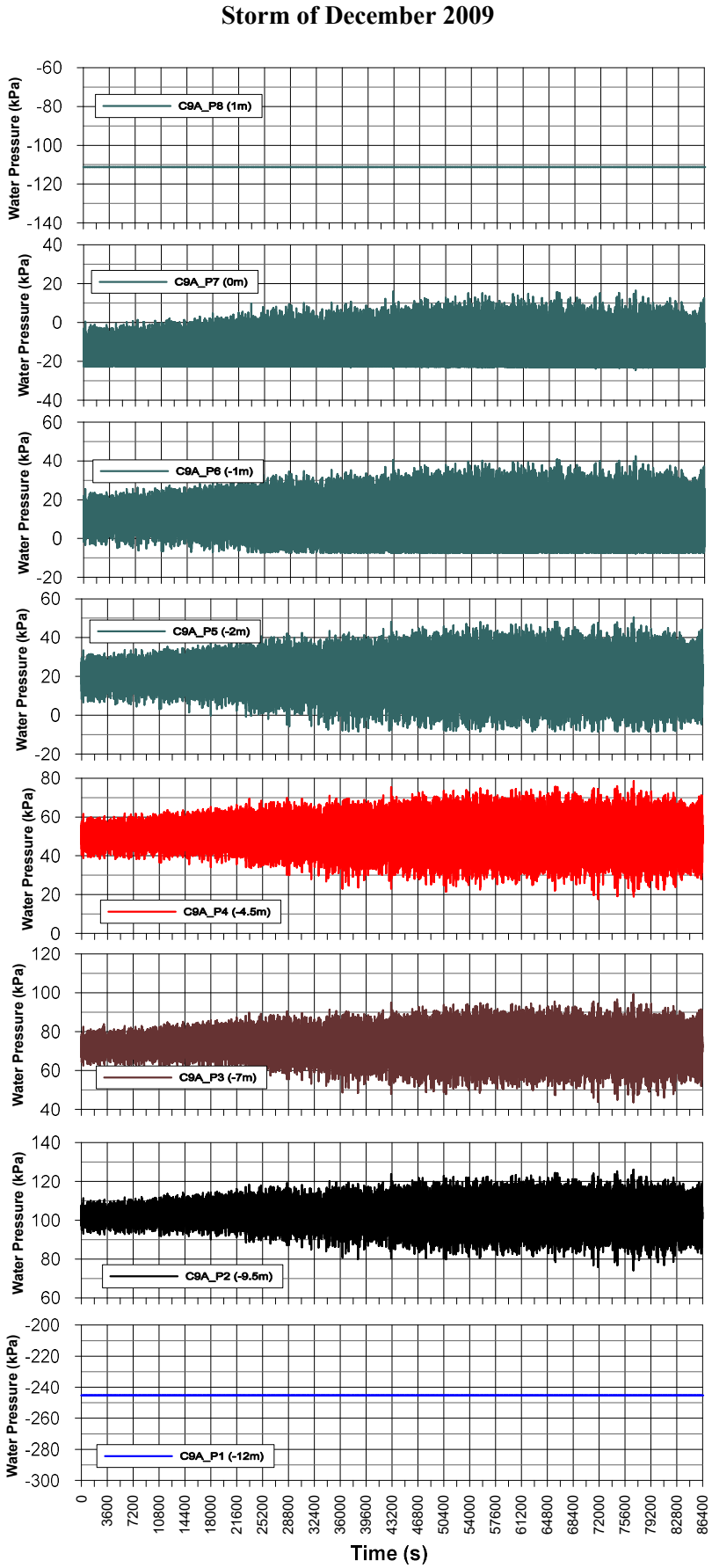

Figure II-8. Sea wave pressure on the caisson wall, alignment A, December 14, 2009

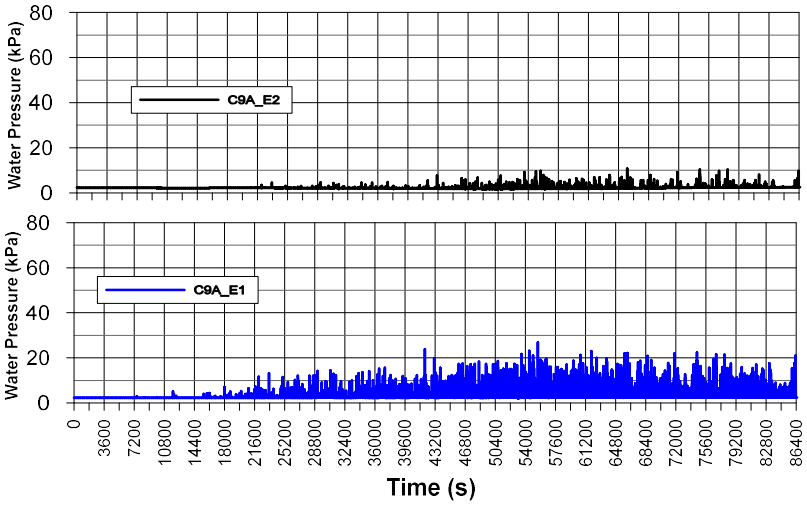

Figure II-9. Wave pressure on the crown, alignment A, December 14, 2009

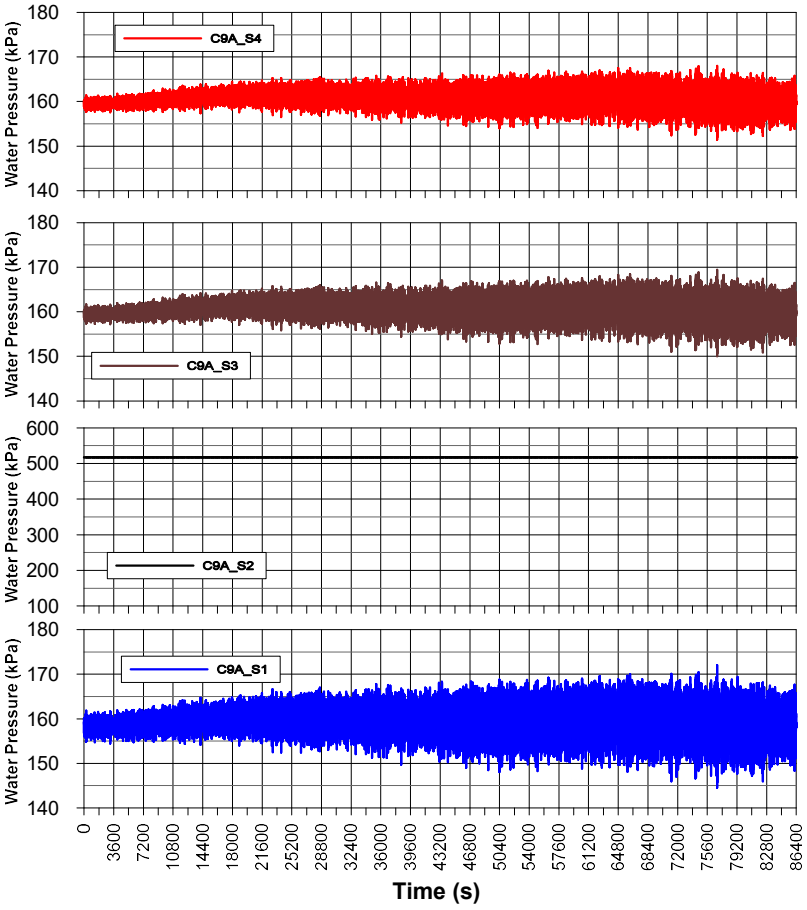

Figure II-10. Uplift pressure on the caisson base, alignment A, December 14, 2009

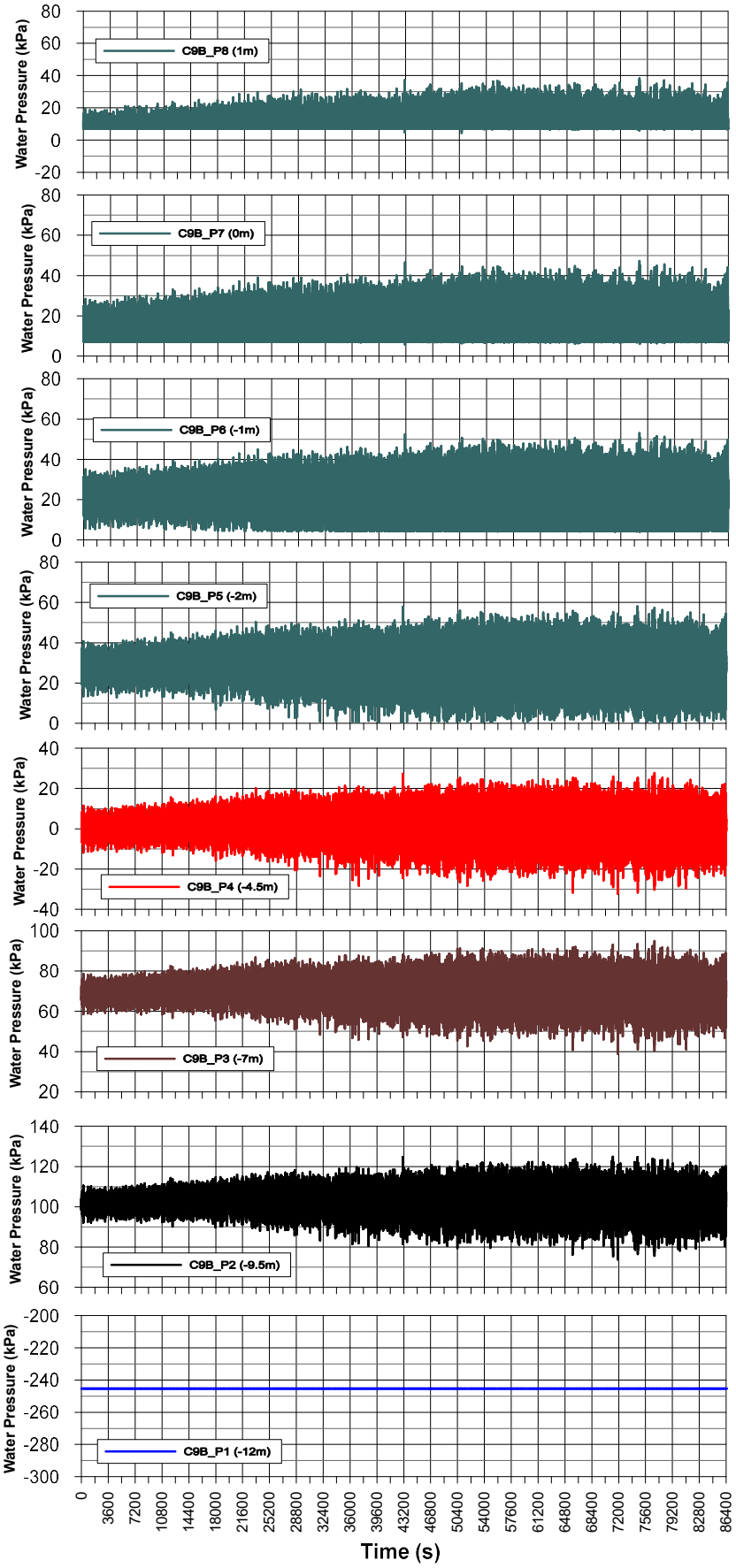

Figure II-11. Sea wave pressure on the caisson wall, alignment B, December 14, 2009

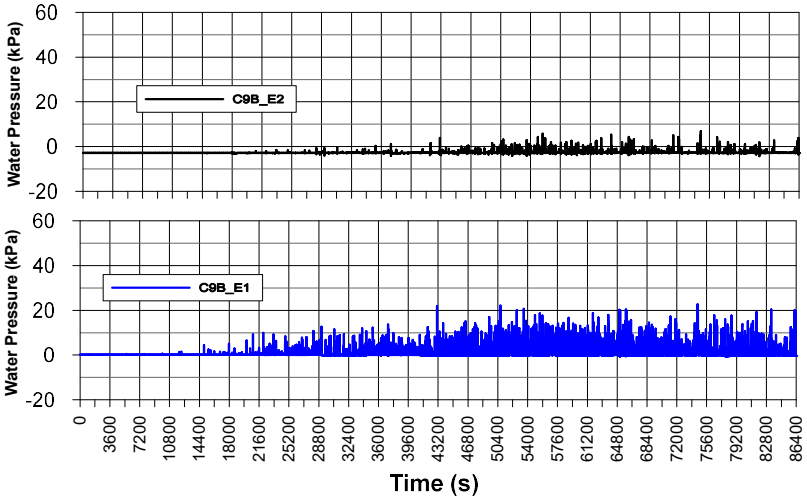

Figure II-12. Wave pressure on the crown, alignment B, December 14, 2009

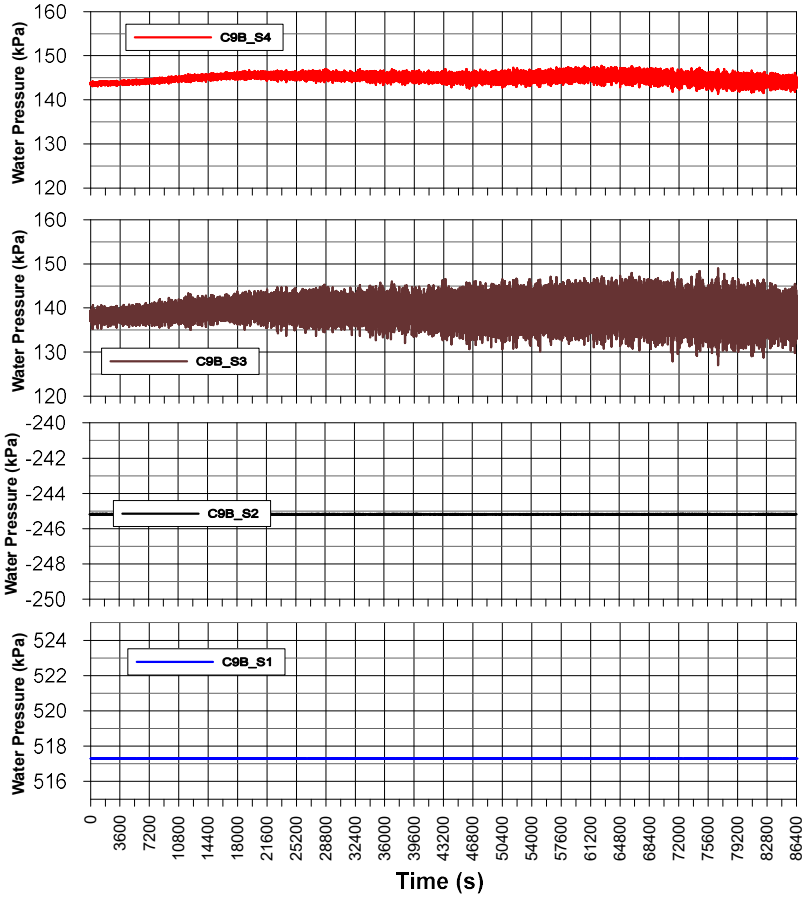

Figure II-13. Uplift pressure on the caisson base, alignment B, December 14, 2009

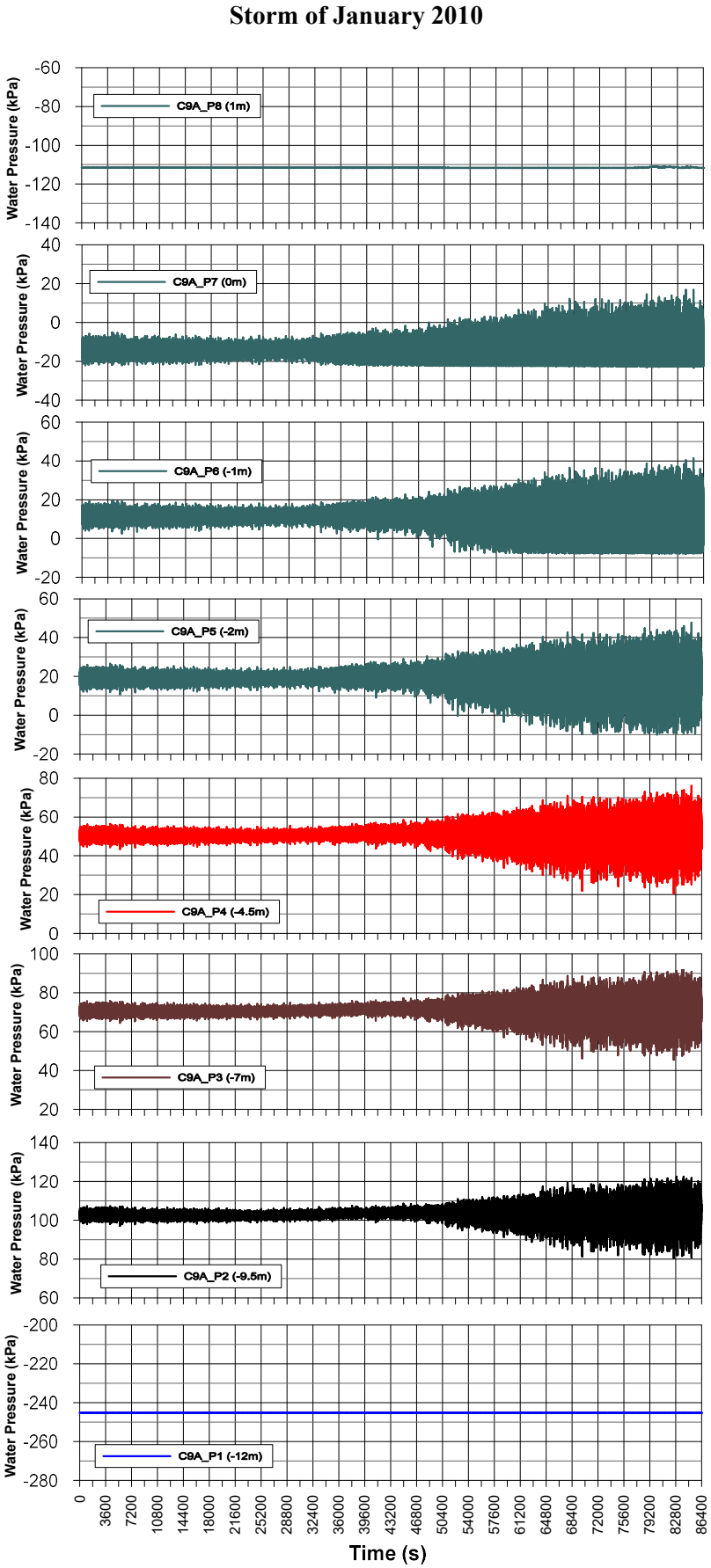

Figure II-14. Sea wave pressure on the caisson wall, alignment A, January 7, 2010

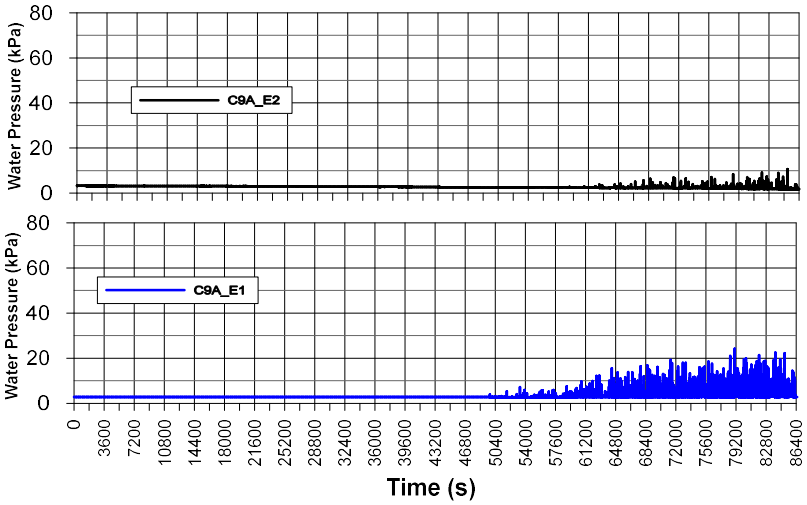

Figure II-15. Wave pressure on the crown, alignment A, January 7, 2010

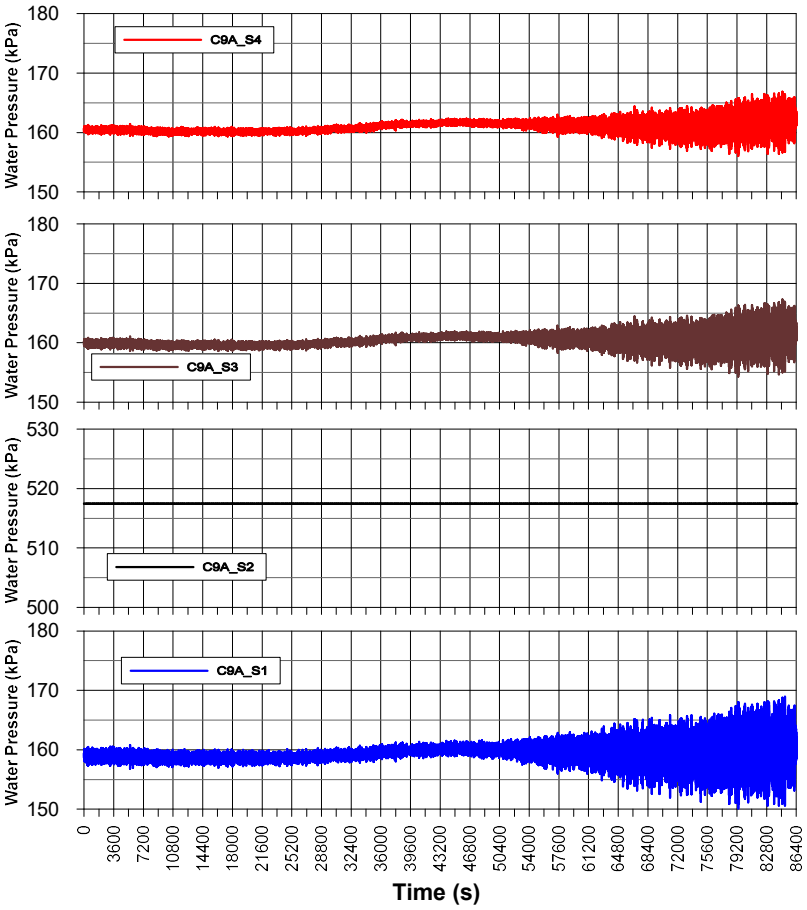

Figure II-16. Uplift pressure on the caisson base, alignment A, January 7, 2010

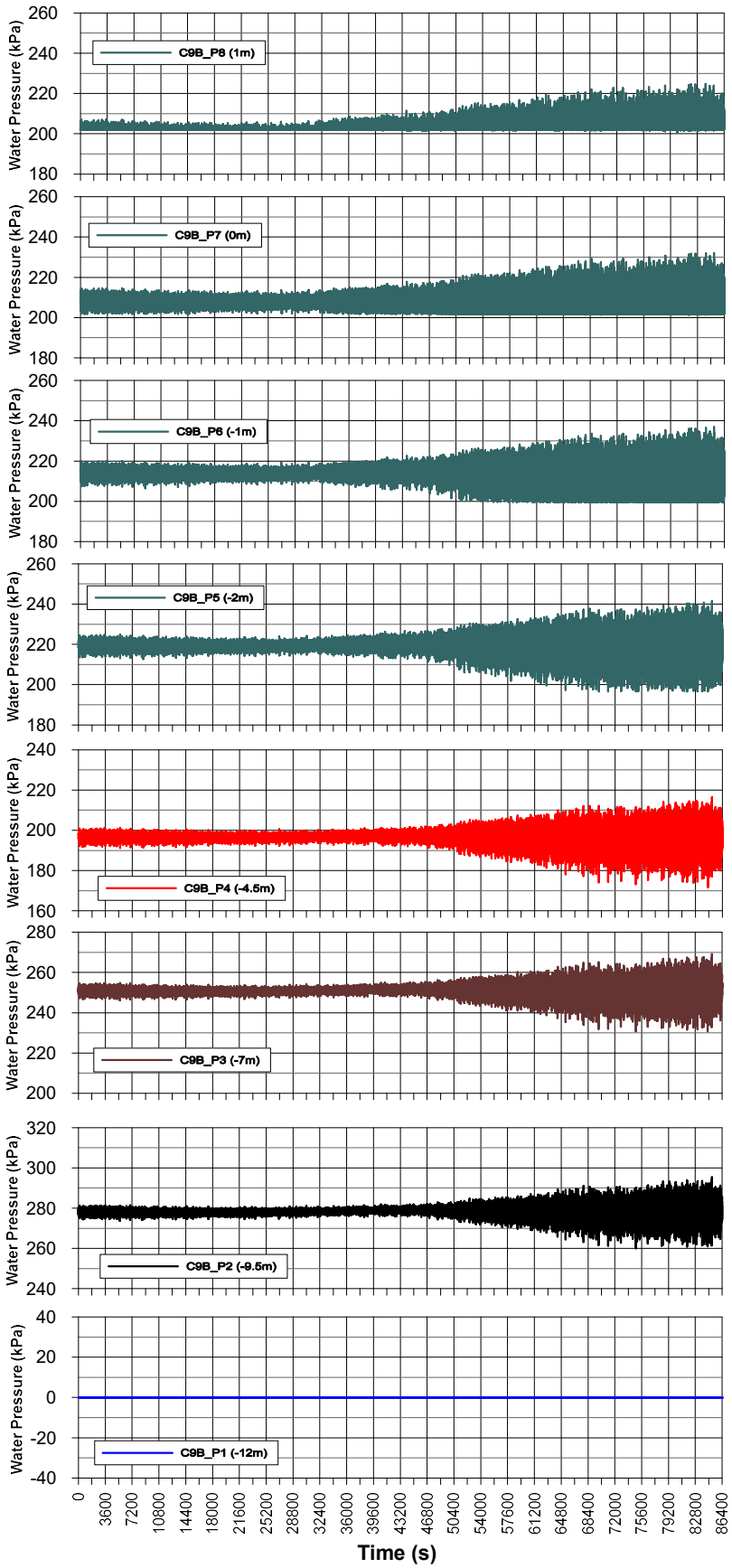

Figure II-17. Sea wave pressure on the caisson wall, alignment B, January 7, 2010

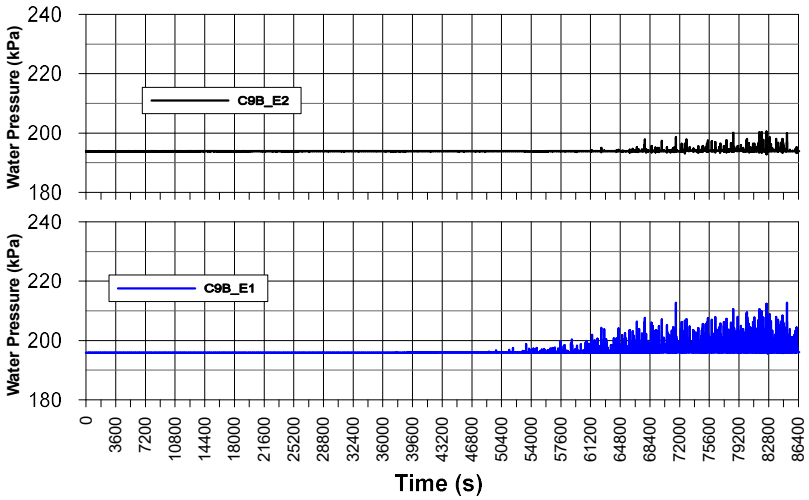

Figure II-18. Wave pressure on the crown, alignment B, January 7, 2010

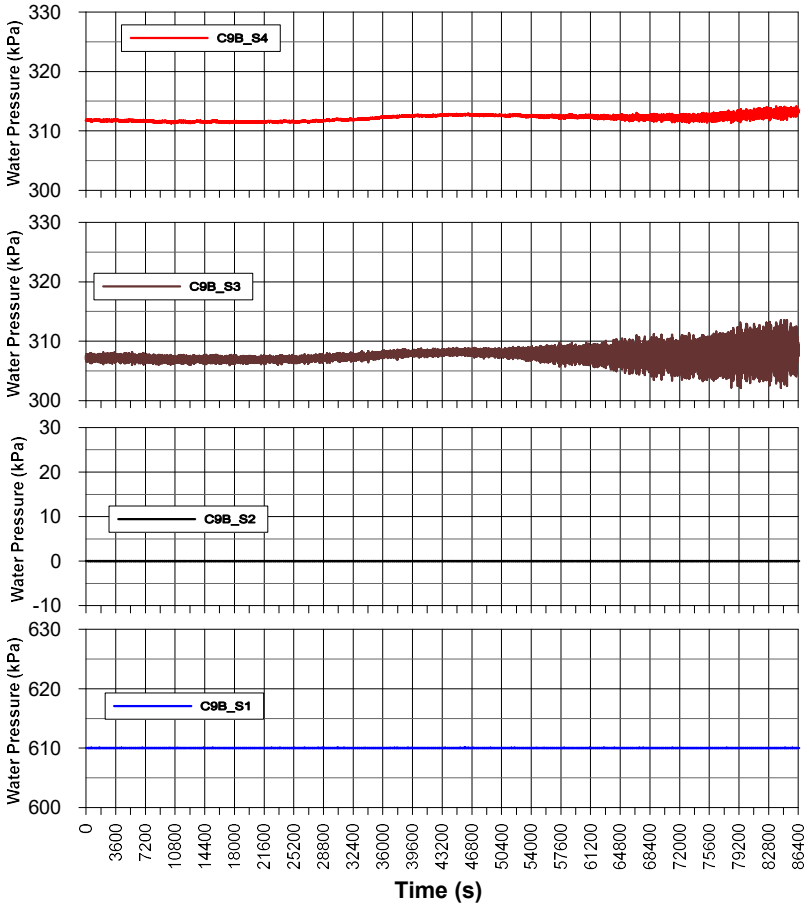

Figure II-19. Uplift pressure on the caisson base, alignment B, January 7, 2010